One-Dimensional Spectral/hp Element Simulation of Wave Propagation in Human Arterial Networks

by

Victoria Eleanor Franke

Department of Aeronautics

Imperial College London

Prince Consort Road

London SW7 2BY

This thesis is submitted for the degree of Doctor of Philosophy of the University of London

2003

BEST COPY

AVAILABLE

Variable print quality

Abstract

This thesis is concerned with the modelling of blood flow and wave propagation in arterial systems using computational fluid dynamics. The arterial networks are simplified to one-dimensional systems and the governing equations are solved using a high order spectral/hp element method with a discontinuous Galerkin discretisation.

Two different human systemic arterial networks are considered. The first is a composite network that has been studied by other investigators. A number of different parameters such as the inflow and outflow boundary conditions and cardiac period are varied and the effects on the pressure and velocity waveforms discussed. The second network is entirely new and is constructed from in-vivo geometry data obtained using magnetic resonance imaging of a single human subject. The numerically computed waveforms are compared with clinical measurements for the same human subject obtained using Doppler ultrasound and applanation tonometry. The effects of arterial taper and ill-matched bifurcations are assessed. The effect of geometrical alterations to the network are investigated and the impact on the predicted waveforms of artificial devices, such as bypass grafts and stents, presented.

Wave propagation is also investigated in placental arterial networks focusing on monochorionic placentas where twin fetuses share a single placenta in which the blood vessels of the two fetoplacental circulations are often joined. The geometry and connectivity of the placental arterial networks are obtained by producing a plastic cast of the recently delivered placentas. The one-dimensional code is used to investigate the dynamic interaction between the two fetoplacental circulations. The volume fluxes are calculated and the predicted waveforms are compared with in-vivo measurements.

The conclusions discuss the usefulness and further applications of the numerical modelling and make suggestions for the incorporation of additional parameters.

To Peter

Acknowledgements

My first thank you must go to my husband, Peter, who has supported and helped me throughout my PhD. Without his encouragement there would be no thesis.

I would like to thank my supervisor Spencer Sherwin for all his help with the numerical methods and one-dimensional code and for coming up with many good ideas and opportunities.

Special thanks must go to Kim Parker in the Bioengineering department, although he was not officially my supervisor, he has helped me to understand waveforms in arterial systems and has given me a great deal of invaluable advice. I would also like to thank him for spending many hours proof reading my thesis.

I would also like to thank Joaquim Peiró for his help and for proof reading Chapter 2 and Daniele Lamponi from EPFL for providing results for a numerical comparison of the codes. I am grateful to Professor Fisk and Ling Wee from Queen Charlotte's Hospital for helping me to understand the medical terminology and anatomical features and pathologies of monochorionic placentas.

There are also a number of people who have helped me to acquire all of the new data in the thesis. I am grateful to David Firmin and Lindsey Crowe at the Royal Brompton Hospital for acquiring the MRI data, especially to Lindsey, who spent many hours scanning my body; Robert Merrifield from the computing department for explaining the use of CMRtools to measure the arterial data from the MR images; Andrew Zambanini for taking pressure and flow waveforms in the arteries of my body and Sheila Byrd from St. Mary's Hospital, London, for providing typical arterial data for the circle of Willis.

Finally, I would like to say how much I enjoyed casting the placentas with Kim Parker, Ling Wee and Nick Watkins. It was one of the highlights of my PhD.

Contents

Abstract **2**

Table of contents **5**

List of tables **10**

1 Introduction **13**

1.1 Pressure and velocity waveforms in the arterial system 13

1.1.1 The circulatory system 13

1.1.2 Clinical tools 15

1.2 Modelling arterial systems 15

1.2.1 Previous research into wave propagation in arterial networks . 17

1.2.1.1 Early work 17

1.2.1.2 Sources of the features of the in-vivo waveforms . . . 18

1.2.1.3 Modelling of waveforms in arterial networks 19

1.2.1.4 Modelling parameters 21

1.3 Objectives 22

1.3.1 The human systemic arterial networks 23

1.3.2 Monochorionic placentas 24

1.4 Thesis organisation 25

2 Governing equations and numerical modelling **27**

2.1 Governing equations for a single vessel 28

2.1.1 Mass conservation in a single vessel 30

2.1.2 Momentum conservation in a single vessel 30

2.1.3 Pressure-area relationship 30

2.1.4 The distensibility of the blood vessel 31
2.2 Mass and momentum conservation systems 32
2.2.1 Mass and momentum conservation, (A, u) system 32
2.2.2 Mass and momentum conservation, (p, u) system 32
2.2.3 Linearisation of the mass and momentum equations, (A, u) system 33
2.3 Numerical modelling - discontinuous Galerkin method 36
2.3.1 Using discontinuous Galerkin method to solve the advection equation 37
2.3.2 Using discontinuous Galerkin method to solve the governing equations for a single vessel 41
2.4 The characteristic system 43
2.4.1 Non-linear (A, u) system 43
2.4.2 Non-linear (p, u) system 45
2.4.3 Linear (A, u) system 46
2.4.4 Linear (p, u) system 47
2.5 Numerical boundary conditions 48
2.5.1 Inter-elemental flux upwinding 48
2.5.2 Vessel junctions - bifurcations and anastomoses 49
2.5.2.1 Bifurcations 50
2.5.2.2 Anastomoses 51
2.6 Inflow boundary conditions and terminal resistance 53
2.6.1 Inflow boundary conditions 53
2.6.1.1 Absorber boundary condition (BC1) 54
2.6.1.2 Velocity boundary condition (BC2) 56
2.6.1.3 Velocity boundary condition with reversed flow (BC3) 56
2.6.1.4 Absorber/reflector boundary condition (BC4) 56
2.6.2 Terminal resistance 57
2.7 Reflection coefficients at bifurcations 58

3 Validation of the computational code **63**
3.1 Sources of error 64

3.2 Stability 64
3.3 Convergence testing 66
3.3.1 Convergence in a single tube 66
3.3.2 Convergence in an arterial network 68
3.3.2.1 Convergence to a time periodic solution 69
3.3.2.2 Convergence with polynomial order 71
3.3.2.3 Convergence with number of elements per artery . . 73
3.3.2.4 Convergence with time step 74
3.4 Linear and non-linear analysis 77
3.4.1 Simple tube 77
3.4.2 Simple bifurcation 81
3.5 Comparison with the Taylor-Galerkin numerical scheme 85

4 The well-matched network **88**
4.1 Introduction 88
4.2 Clinical waveforms in arterial systems 89
4.3 A network of 55 well-matched arteries 93
4.3.1 Inflow boundary conditions 94
4.3.2 Source of reflections in the system 99
4.3.3 Terminal resistance 101
4.3.4 Waveforms in systems with large reflection coefficients 106
4.3.5 Reflections in a simple tube 107
4.3.6 Period size 109
4.3.7 Comparison of waveforms for the well-matched system with the results of Wang and Parker 112
4.3.8 Comparison of waveforms for different inflow boundary conditions with typical in-vivo waveforms throughout the network 115
4.3.9 Magnitudes of pressure and velocity in the well-matched arterial network 120
4.4 A comparison of the waveforms obtained using linear and non-linear analysis in the well-matched network 123
4.4.1 The waveforms in the network with no terminal resistance . . 123

4.4.2 The well-matched network with terminal resistance 125

5 The new tapered MRI network **128**

5.1 Creation of the arterial network from the MRI images 128

5.1.1 MRI angiography, imaging and the new arterial network . . . 128

5.1.2 The computational network and boundary conditions 135

5.1.3 Clinical measurements - Doppler ultrasound and applanation tonometry readings 136

5.2 Results for the tapered network 140

5.2.1 Inflow boundary conditions 140

5.2.2 Reflection sites - the effect of taper and ill-matched bifurcations 143

5.2.3 Change in waveforms along the length of an artery 148

5.2.4 Waveforms in the tapered network 150

5.2.5 Comparison of the effects of the inflow boundary conditions . 151

5.2.6 Comparison of the calculated and clinical results 153

5.2.7 Magnitudes of pressure and velocity waveforms in the MRI arterial network 161

5.2.8 Comparison of computed waveforms in the MRI network with the well-matched network 166

5.2.9 Terminal resistance in the MRI network 167

5.3 Alterations to the geometry of the arterial tree 172

5.3.1 Arteries branching from the aorta 172

5.3.2 Arteries in the head (Circle of Willis) 180

5.4 Wavespeed and ageing in arteries 184

5.4.1 Wavespeed 184

5.4.2 Ageing 186

5.5 Surgical interventions 188

5.5.1 Stents 189

5.5.2 By-pass grafts 191

5.6 Damping in the system 196

5.7 Summary 201

6 Monochorionic placentas **205**

6.1 The fetal circulation 206

6.2 Twin-to-twin transfusion syndrome 207

6.3 Casting the placentas 209

6.4 The plastic casts of the placentas 215

6.4.1 Placenta A - large AAA 215

6.4.2 Placenta B - medium AAA 216

6.4.3 Placenta C - small AAA 217

6.4.4 Placenta D 217

6.4.5 Placenta E 217

6.4.6 Placenta F 218

6.4.7 Placenta G 218

6.4.8 Summary of cast placentas 219

6.5 One-dimensional modelling of placental arterial networks 225

6.6 A detailed study of placenta A 227

6.6.1 Single placenta waveforms 228

6.6.1.1 Terminal resistance 231

6.6.2 Waveforms in the joined monochorionic placenta 232

6.6.2.1 Identical heart rates and phases 232

6.6.2.2 Different heart rates 235

6.6.2.3 Different inputs 237

6.6.2.4 Terminal resistance 239

6.6.2.5 Different inputs and terminal resistance 241

6.6.2.6 Anastomosis area 242

6.7 A study of placenta B 246

6.7.1 Single placenta waveforms 247

6.7.2 Monochorionic placenta waveforms 247

6.8 A study of placenta C 251

6.8.1 Single placenta waveforms 252

6.8.2 Monochorionic placenta waveforms 252

6.9 Summary 256

7 Conclusions and suggestions for further work **259**

7.1 Conclusions 259

7.1.1 Numerical model 259

7.1.2 Human arterial tree 260

7.1.3 Monochorionic networks 262

7.2 Suggestions for further work 263

A Human arterial network data **265**

A.1 55 well-matched arterial data 266

A.2 MRI tapered arterial network 268

B Monochorionic arterial network data **270**

B.1 Data for placenta A 271

B.2 Data for placenta B 272

B.3 Data for placenta C 273

Bibliography **274**

List of Tables

3.1 Table of reflection coefficients and vessel properties in the bifurcation. 81

5.1 Table of pressures for the clinical waveforms obtained using applanation tonometry, for the same subject as the MR data. 138

5.2 Table of measured reflection coefficients in a sample of arteries in the tapered network due to taper (calculated from computational results) and due to the bifurcation at the end of the numbered vessel (calculated from linear theory). 144

5.3 Volume fluxes in the ascending aorta. 155

6.1 Table of fluxes in the intertwin network, showing the effect of varying different parameters in the network. 245

6.2 Table of fluxes in the monochorionic network of placenta B for the same magnitude inputs, but with different periods. 250

6.3 Table of fluxes in the arterial network of the monochorionic placenta C for the same input pressure magnitudes, but different heart rates. . 254

A.1 Data for the well-matched network. (Density, $\rho = 1021\ kg/m^3$). . . . 266

A.2 Table of parameters for the well-matched network. 267

A.3 Data for the MRI tapered network. (Density, $\rho = 1021\ kg/m^3$). . . . 268

A.4 Table of parameters for the MRI tapered network. 269

B.1 Data for placenta A (large AAA). Young's modulus = 0.4 MPa, density, $\rho = 1021\ kg/m^3$ and $c_0 = 4.43\ m/s$ for each vessel. 271

B.2 Data for placenta B (medium AAA). Young's modulus = 0.4 MPa, density, $\rho = 1021\ kg/m^3$ and $c_0 = 4.43\ m/s$ for each vessel. 272

B.3 Data for placenta C (small AAA). Young's modulus = 0.4 MPa, density, $\rho = 1021\ kg/m^3$ and $c_0 = 4.43\ m/s$ for each vessel. 273

Chapter 1

Introduction

1.1 Pressure and velocity waveforms in the arterial system

1.1.1 The circulatory system

The circulatory system in the human body is composed of a continuous circular network of blood vessels, the heart and blood itself. The fact that blood travels in a loop was first considered by William Harvey in the 17th century [53] at a time when others thought the blood was produced in the liver. The main function of the circulatory system is to deliver required substances throughout the body, via the blood [78, 99]. The required products are mainly those required for metabolism and hence cell survival and include oxygen, glucose, vitamins and water and to remove the associated waste products including carbon dioxide, urea and creatinine. The distributing network of blood vessels consists of arteries, arterioles, capillaries, venules and veins. The arteries deliver the high pressure blood from the heart to the major organs and they also branch rapidly into smaller arterioles which in turn branch into the very narrow capillaries. It is in the capillaries that the transfer of metabolic products takes place. The blood then flows into the venules, which join together to form veins and deliver the blood back to the heart.

The heart is the component of the circulatory system that pumps the blood around the body. The ventricles of the heart act as a type of bellows pump, contracting approximately 80 times a minute in the human body and producing a pressure and flow pulse, that propagate throughout the arterial system. The portion of

the heart beat when the ventricle is contracting is known as (ventricular) systole and the portion when there is no output through the aortic valve into the arterial network is termed (ventricular) diastole. The network of blood vessels is composed of two loops, the pulmonary circulation, which is supplied by the right ventricle of the heart and takes the blood to the lungs to exchange respiratory gases, and the larger systemic circulation, which supplies blood throughout the rest of the body and it is the latter that is considered throughout this work. The vessel that receives the blood from the left ventricle of the heart into the systemic circulation is the ascending aorta, which branches into several other large arteries. These major arteries are highly distensible, which allows them to expand and receive the blood when the heart ejects the blood (systole) and to contract during diastole. This smooths the intermittent blood flow from the heart into a more continuous stream.

The arteries therefore perform a vital role in the preservation of life, but unfortunately, they are susceptible to disease and degradation. This can be due to alterations occurring in the arterial system, such as the arterial properties changing with age or a build up of fatty plaques on the arterial walls, atherosclerosis. These changes can compromise the distribution of blood throughout the body and can also cause additional stress on the heart itself. Surgical interventions may be performed to mitigate the effects of these changes (section 5.5), but these are not always successful and their effects on the blood flow distribution are not known in advance. Attempts have also been made to diagnose circulatory problems such as the presence of stenoses by examining the flow and pressure patterns. Certain characteristic features have been suggested, however the knowledge of the origin of these features is incomplete, section 1.2.1.2. There is therefore, a great deal of motivation for better understanding the pressure and velocity distributions and waveforms in arterial networks and how they are related to the arterial geometry, connectivity and material properties. These parameters can be difficult to investigate in-vivo, or experimentally, but the advent of cheap powerful computers means that numerical modelling is now a feasible alternative, section 1.2.1.3 and Chapter 2.

1.1.2 Clinical tools

Clinicians use many tools to help diagnose problems in the arterial system. Pressure and velocity waveforms in the large arteries of the human network can be recorded in-vivo using techniques such as applanation tonometry and Doppler ultrasound respectively [95]. These waveforms have characteristic features and clinicians often take these measurements routinely to check that everything appears normal. Abnormal waveforms can indicate a pathological state and provide a means for diagnosing various ailments in clinical practise. For example the dicrotic wave in the aorta is diminished in some patients suffering from vascular disease or diabetes [95, 75, 76, 32, 106] and an increase in systolic pressure and a less pronounced dicrotic wave [95, 106, 5, 64] is thought to be caused by an increased stiffness of the arterial wall, which often occurs with age, in people who smoke and with hypertension and is a significant risk factor for heart attacks and other coronary problems [4]. A greater understanding of the waveforms and the causative factors of the different features may allow improvements to be made with regard to the diagnosis of different problems.

Another tool that has recently become available to clinicians is Magnetic Resonance Imaging (MRI) which allows internal features of the body to be investigated non-invasively and without side-effects [59]. Such techniques can be used to obtain reasonably accurate data of the geometry of the blood vessels. These MR images could be studied to detect any abnormalities in the geometry, such as blockages in the arterial vessels. This would be an expensive and lengthy procedure and it would be preferable to diagnose problems more rapidly through simple analysis of the waveforms. However, it does provide an opportunity for us to obtain reasonably accurate in-vivo geometry data as described in section 5.1.1.

1.2 Modelling arterial systems

Physiologists and mathematicians have been trying to mathematically model the arterial system for hundreds of years, however, the properties of blood and the structure of the arterial wall and the geometry of the arteries are very complex. The arterial wall is constructed primarily of three different components, smooth muscle

cells, elastin and collagen, which all have different properties. The arrangement of these different materials in the arterial wall means that the behaviour of the artery in response to a change in transmural pressure is non-linear, anisotropic and viscoelastic [95, 110, 89, 78, 85]. Blood is a suspension of many different cells in plasma and therefore exhibits non-Newtonian properties, although these effects are most significant for vessels with diameters of less than 100 μm and for larger vessels blood is generally considered Newtonian [110, 24, 23, 21, 17]. The presence of the large number of red blood cells also affects the homogeneity of the blood in small diameter vessels, but for the vessels we investigate blood can be considered homogeneous and incompressible.

Modelling the geometry of arterial networks is also challenging because there are a large number of vessels, which vary in cross-section and curvature and also differ between subjects. These differences in the physical features of the network can therefore affect the blood flow and wave propagation, hence waveforms in one human can be different to those in another. There is also a lack of physiological geometry available to study for the in-vivo human arterial system, with most data being for composite networks from many different subjects and for ex-vivo data, section 1.2.1.3. The accurate measurement of the geometry of excised arteries is complicated by a number of features including vasoconstriction, simulating the correct physiological pressure and ensuring the arteries are under the correct longitudinal tension [29].

Ideally we would like to model all of the physiological properties of the circulatory system as well as the full geometry, but this is computationally unfeasible and the precise mathematical definitions of some of the properties are also unknown, hence modelling assumptions need to be made. The particular problem to be investigated will determine which properties of the blood and arteries are most significant and consequently which modelling assumptions should be used. In recent years the advances in computational power have rendered the solution of some arterial problems using numerical methods more feasible. Increasingly complex problems have been modelled, such as the determination of wall shear stress and particle transport in local sections of three-dimensional by-pass geometries [44], flows in reconstructions of in-vivo arteries [28] and unsteady flows in small arterial sections [136], as well

as one-dimensional wave propagation in large geometries, such as arterial networks [45, 163]. This thesis will concentrate on the latter and the one-dimensional wave propagation will be modelled in two arterial networks. This sort of modelling is attractive because it allows waveforms and flow distributions to be obtained for a whole network, rather than just for a very small section of geometry.

Using the clinical tools described in section 1.1.2 we hope to improve our understanding of arterial networks by obtaining accurate in-vivo geometry data for the major arteries from MR images as input data for our mathematical modelling. The in-vivo waveforms which are also typically one-dimensional can then be compared with the results of our modelling. We can simplify the arterial network to a single dimension, because the arteries can be thought of as a network of long thin elastic vessels. A system of hyperbolic equations can then be used to describe the velocity and pressure waveforms in the network, Chapter 2.

This simplification to a single dimension is relatively well known and in the following section some of the related research which has been performed previously is briefly discussed.

1.2.1 Previous research into wave propagation in arterial networks

Many studies have been performed and much has been written with regard to the circulatory system and the patterns of pressure and blood flow that occur within the different vessels. A brief summary of some of this work focusing on the mathematical and numerical modelling of the pressure and flow waveforms is presented in the following sections. For a broader discussion regarding blood flow and wave propagation in arteries and wave propagation in general the books of Nichols and O'Rourke [95], Lighthill [82], Whitham [173], Milnor [89] and Pedley [110] are of particular interest.

1.2.1.1 Early work

The earliest work on the modelling of the transmission of the pressure pulse throughout arterial networks appears to begin with that of Euler who derived the equations governing conservation of mass and momentum [31], but it is not until the work of Young [178] that the interaction of the fluid and the elastic vessels was described

mathematically using an analogy with Newton's theory of sound in gases. Moens [90] and Korteweg [69] independently derived the equations governing pulsatile flow in thin walled elastic vessels, which we now know as the Moens-Korteweg equations (section 2.1.4) some 70 years later. Shortly before this, Riemann had developed the method of characteristics [125], which have since been applied successfully to arterial flows [139, 146, 147].

An early model considering the entire arterial network was suggested by Hales [50] who noted that intermittent pumping of early fire engines was smoothed into a relatively constant outflow and bore similarities to the persistence of flow after ventricular ejection in arterial networks. From this he proposed what became known as the Windkessel model, but it was not until 1899 that it was quantified by Frank [41]. Since that time it has been used extensively in the description of the circulatory system, but not without controversy.

1.2.1.2 Sources of the features of the in-vivo waveforms

The first investigators to recognise that the features of the in-vivo waveforms are related to the properties of the arterial tree were the Weber brothers, who identified that the pressure waveforms were composed of both forward travelling and reflected waves [164]. Since that time there has been significant debate as to whether the differences between the pressure and flow waveforms in the ascending aorta can be explained in terms of reflected waves alone [163]. However, the majority of authors believe that reflections are important and much research has been performed in an attempt to identify the source of reflected waves [89, 43, 170, 172, 87, 123, 13, 119]. Three different sources are commonly mentioned: the arterial bifurcations, the peripheral bed and the tapered nature of the arteries themselves and indeed these are all sources of change in impedance, and consequently will generate reflections [169].

Westerhof *et al* [169] found that reflections occur at bifurcations in the large proximal arteries and that reflections also occur in the periphery with high levels of reflections when arterioles are constricted and low levels when they are dilated. Other studies also suggest that reflections arise at the bifurcations in the major arteries [92, 73, 171, 122, 168] and the smaller arteries have also been suggested as

the principal reflection sites by many studies [89, 102, 12, 113]. Work on determining effective reflection lengths also places the primary reflection sites in the vascular bed [86, 104], however the concept of an effective length is at best an approximation and need not bear any relationship to the locations of the reflection sites in-vivo [15]. Discrete locations within the arterial tree have also been identified as the primary sources of reflection, including the aorto-iliac bifurcation [51, 92], the abdominal aorta [107], the renal arteries [74, 65] and a site located distal to the terminal aortic bifurcation [74]. However, other in-vivo experiments have found that induced waves at the femoral could not be detected at the aorta [112] and that an induced wave in the aorta produced no discernible reflections [142].

It has also been suggested from area measurements that the arterial system should be well-matched for forward travelling waves [48], however reflection coefficients at bifurcations are direction sensitive [52, 79]. A continuous change in characteristic impedance has been identified in the aorta, which is consistent with a continuous reflection [89]. Segers and Verdonck [133] have investigated tapered vessels representing the aorta and found that they produced continuous reflection with an effective length corresponding to the location of the renal arteries, which would be hidden in the input impedance pattern and may explain some of the previous observations. They conclude that the measured in-vivo aortic reflections are a consequence of at least two interacting phenomena: a continuous wave reflection due to the arterial tapering and local reflections from the level of the diaphragm.

1.2.1.3 Modelling of waveforms in arterial networks

The Windkessel model is a lumped parameter model, where the cardiovascular system can be represented by two components, one representing the left ventricle and one the systemic arteries [40]. Indeed Windkessel models have proved to be quite useful for estimating the stroke volume and arterial compliance [95, 163]. However, there are a number of drawbacks, not least that the wavespeed is infinite and that the wave reflections are not incorporated [89, 95]. An extension of the Windkessel model is to consider the arterial network as a set of lumped vessel segments where the flow and pressure in a single segment are represented by an average value in that vessel. Properties of the vessel can be considered in electrical terms with the effects

of blood viscosity equivalent to the electrical resistance and the compliance of the vessels represented by capacitance [94, 89, 40]. The model can be extended to incorporate inertial effects using impedance to account for the phase lag between flow and pressure [40, 167] and even a fourth parameter has been suggested [144]. Indeed a number of models have been constructed using passive electric circuits [98, 167]. These extended lumped parameter models are actually distributed networks incorporating transmission line theory [175, 62] through the impedance term [144] and more recently these electrical models have been simulated on computers [6]. These models allow for the simulation of the pulse propagation and reflections. Lumped and distributed parameter models are, however, limited by the need for defining a large amount of parameters that have little, or no physiological, or anatomical significance [140]. It is also difficult to draw conclusions about the influence of specific features of the system [140].

The majority of the studies have been performed in the frequency domain [167, 6, 13, 119], which can be difficult to relate to the actual physiological and the clinical waveforms which are obtained in the time domain [162]. There are also a number of modelling limitations of a frequency based analysis including the fact that the arterial system is assumed to be in a state of steady oscillation, which is not the case, and there is also no way of distinguishing between systole and diastole, hence the behaviour of the aortic valve cannot vary depending on the time as is the case physiologically [111, 134].

More recently investigations have been performed in the time domain often making use of the method of characteristics and using a variety of numerical methods [45, 134, 111, 137, 160, 163, 140, 38, 159]. These methods provide results that can be compared directly to haemodynamic measurements, including pressures, flow and dimensions, at each heart beat and interpretation of the results is straightforward [162]. Further separating the waveforms into the forward and backward travelling components allows the composition of the waveforms and the sources of the features to be analysed. This can be extended further using "wave intensity analysis", which identifies forward and backward travelling compression and expansion waves [148]. The only alterations of the wave motion identifiable in the frequency domain are the subtle and perhaps ambiguous variations in the impedance spectra [162].

Although a number of investigations have been performed into the human arterial tree, the effect of geometry does not appear to have been considered to any great extent. In fact the majority of the studies [167, 145, 6, 160, 163, 98, 130] are based on the original data of Noordergraaf [97] and the subsequent modifications of Westerhof [167]. This is a composite network of ex-vivo data for the major arteries from a number of different subjects and actually includes appropriately scaled data for a dog [167].

As well as studying the waveforms in the arterial tree, a number of smaller arterial systems have been modelled and the effects of a variety of different parameters and interventions studied. These include the modelling of fetoplacental circulations [45, 166], the coronary vessels [140], the circle of Willis [56], the effects of stenoses [145], grafts [159, 143], stents [111, 39] and discontinuities in wall properties [157]. One-dimensional models have also been linked with local three-dimensional solvers [37, 117] and have been suggested as tools for surgical planning [159, 143, 150].

1.2.1.4 Modelling parameters

Although we have limited our modelling to a single spatial dimension, there are still many choices for the parameters and features that could be incorporated into the governing equations. Different effects have been incorporated by previous workers including the viscosity of blood, where a number of different velocity profiles have been assumed [140, 145], the non-linearity of the pressure area relationship of the artery wall [145], wall inertia [111, 38], longitudinal tethering [89, 38] and the viscoelasticity of the artery wall [111, 114, 89]. Models have also been developed to simulate the losses occurring at vessel junctions arising from the three-dimensional nature of the flow in these geometries [143, 38]. However, experimental studies suggest that the effect of the branch angle on the reflections at junctions is small [129]. The overall effect of the different parameters is dependent upon the network examined, but it is thought that the viscoelastic wall terms are more significant than those in the fluid in large arteries [114, 110] and that the wall inertia term is not significant in physiological cases due to the relatively low wall velocity and accelerations [114, 110].

In addition, it is possible to use both linear and non-linear models for the govern-

ing equations [134]. Non-linear models are much more versatile in that they allow the vessel wall properties and cross-sectional area to vary within a segment and also more accurately model the speed of wave propagation as being dependent on the local vessel wall conditions and the flow velocity. The effects of non-linearities are noticeable and may or may not be significant depending on the accuracy required and the modelling performed [63, 115, 134].

Another area that has received a great deal of attention is the modelling of the microcirculation. These vessels cannot be modelled individually due to their abundance and small cross-sectional area. A number of different models have been used from a simple reflector condition [163, 134], to complex multiparameter fractal based approaches [100]. Windkessel and other lumped parameter models have also been linked to the one-dimensional model to represent the vascular bed [140, 145, 141], however a large number of parameters are required to define such models.

Often the waveforms are found to be sensitive to the modelling parameters that are employed. This can make it very difficult to ensure that the parameters incorporated in the one-dimensional model are acting in a physiological manner, because they are hard to measure accurately and are also case specific. Indeed Stergiopulos *et al* conclude that the major limitation of their one-dimensional model is the requirement for a great amount of parameter data, much of which is not available and is difficult to estimate [145].

1.3 Objectives

The aim of this thesis is to improve the understanding of the blood flow and pressure waveforms in human arterial networks, with particular emphasis on the effects of geometry. To this end we develop a computational tool that solves the hyperbolic equations governing one-dimensional blood flow in distensible tubes. A high order discontinuous Galerkin method is used to solve the governing equations for single arterial vessels and the technique is extended to networks of vessels through the method of characteristics and conservation of mass and total pressure. This solution procedure exhibits a fast convergence rate which enables us to reasonably undertake parametric studies of the effect of different boundary conditions and domain

parameters on the calculated waveforms.

Two different arterial systems are modelled: the human arterial tree and the arterial networks in monochorionic placentas. Due to the lack of data available and the possible sensitivity of the waveforms to the geometry of different subjects, we aim to obtain new geometry data for these arterial networks from single subjects. We also aim to obtain in-vivo data for waveforms in these networks so that we have a direct comparison between the waveforms calculated using the one-dimensional model and the in-vivo waveforms for the same network. The effects that the geometry, inflow boundary conditions and arterial properties have on the waveforms will be investigated. However, these parameter changes will be limited as far as possible to properties for which we have reliable in-vivo data and to simple, general, physiologically justifiable assumptions. Limiting the investigations in this manner will allow us to determine whether the waveforms in a single subject can be modelled using simple generic conditions and measurable data. The studies of the effects of geometry and parameter changes will aid us in determining the sources of the features of the waveforms and identifying the important variables, as well as providing further insight into the modelling assumptions that should be improved, or incorporated in order to develop a more accurate numerical simulation of blood flow in arterial networks.

1.3.1 The human systemic arterial networks

The human arterial tree is probably the best studied arterial network and two versions will be investigated. Initially, the one-dimensional model will be used to determine the waveforms in the well-matched network previously investigated by Wang and Parker [163]. This network is based on the vessel data of Noordergraaf [97] and is a composite network of ex-vivo data from many sources, section 1.2.1.3. The results from this model will be compared with typical in-vivo measurements and also with Wang and Parker's results in order to validate our techniques and to assess the effects of a number of parameters. Wang and Parker, in common with many other investigations, have used linear rather than nonlinear modelling, therefore a comparison between linear and non-linear modelling is also presented.

As described in section 5.1.1 MRI can be utilised to obtain in-vivo geometry data

of the arterial tree and these methods will be employed to obtain the dimensions and connectivity for an entirely new network of a single adult female human subject. In-vivo waveforms for velocity and pressure are obtained using applanation tonometry and Doppler ultrasound for a variety of arteries in the same subject. This is one of the main advantages of creating a new network because these waveforms can be compared directly with the results from the one-dimensional model. The geometry of the arterial network is analysed to determine the features that affect the computed pressure and velocity waveforms and primarily considers the reflections due to taper and ill-matched bifurcations. Modelling assumptions are assessed, such as the inflow boundary conditions, terminal resistance, the accuracy of the artery wall data, and whether extensions to the geometry of the network would improve the waveforms. Once the new arterial network has been assessed for a healthy human, computations are made investigating the effects that surgical interventions may have on the waveforms in the system, to enable us to understand the likely post-operative situation.

1.3.2 Monochorionic placentas

The velocity waveforms and volume fluxes in placentas are also studied. This is an area that has received relatively little attention, particularly from a modelling perspective and is of particular interest in twin pregnancies where a single placenta is shared between two fetuses (monochorionic twin pregnancies). In these cases the fetoplacental circulations are almost always linked by anastomoses between arteries and arteries, arteries and veins or more rarely veins and veins. Connections of these types result in an unbalanced transfusion of blood from one fetus (the donor) to the other (the recipient), which can adversely affect the development of the fetuses and can lead to a condition known as twin-to-twin transfusion syndrome (TTTS), that can be fatal [132, 156]. To obtain data for these networks the fetoplacental circulations of monochorionic placentas are cast using plastic resin and measurements are made from the arterial plastic models. Placental circulations are not as uniform in connectivity and structure as the human arterial tree and are therefore good candidates for assessing the effects of geometry. We study three different placentas linked by arterio-arterial anastomoses of different sizes.

In such networks unusual wave patterns can occur in the arterio-arterial anastomoses and also in the umbilical arteries. Our investigations therefore focus on the interactions between the two sides of the network. The dynamic situations are modelled with the one-dimensional propagation code and are compared with in-vivo Doppler ultrasound readings. Since the transfusion of blood from one twin to the other is so important, we also focus on the flow distribution. Parameters of the network are altered and these effects on the imbalances between the two fetoplacental networks is assessed by calculating the volume fluxes entering and leaving each side. We investigate whether the one-dimensional modelling is capable of replicating the in-vivo waveforms and also what combination of parameters are required to enable the two sides of the system to balance.

1.4 Thesis organisation

Chapter 2 outlines the one-dimensional mathematical representation of flows in distensible arterial networks and the numerical implementation of these equations in the time domain. Firstly, the hyperbolic system of governing equations and the simplifications necessary to reduce the complex three-dimensional flows to a one-dimensional approximation are considered. Both the linear and non-linear models are derived and discussed. The numerical discretisation using the discontinuous Galerkin method with a one-dimensional spectral/*hp* element spatial approximation is then explained. The modelling of junctions in the arterial network using the method of characteristics is described as are the inflow and outflow boundary conditions.

The numerical model is then validated in Chapter 3 and the appropriate time-steps and discretisation determined to ensure that the results produced will be sufficiently accurate.

The first set of results obtained using the one-dimensional model are shown for the well-matched network in Chapter 4 and our results are compared with those of Wang and Parker. The effects of a number of parameters on the waveforms are assessed and the differences between the results obtained using linear and non-linear analysis are discussed.

Chapter 5 describes the construction of in-vivo data for a new tapered arterial network of a single human using magnetic resonance images. This network was modelled using the nonlinear one-dimensional code and the computed waveforms are compared with in-vivo clinical readings for the same subject, as well as with the well-matched network. The relative contributions of both taper and ill-matched bifurcations to the reflections within the system and the waveforms are assessed. The impact of extending the network by the addition of arteries that could not be resolved in the MRI scans is investigated and finally various surgical interventions are modelled and their effect on the flow and pressure waveforms considered.

A completely different arterial network is discussed in Chapter 6 where the waveforms in monochorionic placentas are examined. The potential complications associated with monochorionic placentas are first explained in detail and then the casting processes used to obtain the arterial geometry and connectivity are described. A number of cast placentas are discussed and three that have different sized connections are studied using the one-dimensional code. The effects of different parameters on the mass fluxes into and out of the placentas and the waveforms in the umbilical arteries and anastomoses are assessed.

Finally, in Chapter 7 conclusions regarding the usefulness of one-dimensional modelling of arterial networks are drawn and suggestions for further work are presented.

Chapter 2

Governing equations and numerical modelling

In this chapter the equations governing one-dimensional wave propagation in a single vessel and in a network of vessels are derived and the numerical methods used to solve them described. In sections 2.1 and 2.2 the non-linear hyperbolic system of governing equations describing one-dimensional blood flow in arterial networks and an algebraic relationship between pressure and area are introduced. The governing equations are further simplified by linearising the equations. This enables the comparison between the linear and non-linear analyses discussed in Chapters 3 and 4. The numerical discretisation of the governing equations using a discontinuous Galerkin formulation with a spectral/*hp* element spatial approximation is described in section 2.3. The characteristic system is explained in section 2.4 and in section 2.5 the solution procedure for a single vessel is expanded to permit the modelling of a network of vessels. This involves the method of characteristics combined with conservation of mass and total pressure at the elemental boundaries. Finally, in section 2.6 the inflow and outflow boundary conditions of the system are described and in section 2.7 an analytic expression for a reflection coefficient at a bifurcation is derived. The derivations are a slightly expanded version of those given in our publications [134, 137, 111].

2.1 Governing equations for a single vessel

Before deriving the one-dimensional wave propagation equations in a vessel, it is instructive to first define and discuss the assumptions that are required to reduce a complex three-dimensional system, such as the human arterial tree, to a system that can be modelled in a single dimension. These assumptions relate to the geometry of the network, the properties of the vessel wall and of course the flowing blood itself.

Arteries in the human body can be thought of as elastic distensible tubes. Assuming that the geometry is one-dimensional requires the vessels to be modelled with a straight central axis and with uniform properties around the circumference and the velocity profiles must be similar within the vessel, although they can change in magnitude. The vessels are further assumed to have invariant central axes and therefore remain straight during the wall motion. Although, the arteries within a human are quite clearly three-dimensional and exhibit both in- and out-of-plane curvature [18, 19] these assumptions are not unreasonable, because other than in the aortic arch the curvature is relatively small when compared with the diameter of the vessels and the vessels are typically long and thin. Arteries are also close to circular in cross-section in-vivo but the lower pressure veins can adopt more complex shapes. The arterial wall properties are generally relatively uniform around the circumference, although this may not be the case in certain pathological conditions.

The assumption that the velocity profiles are similar is not valid in the vicinity of curves and branches, where the flows are three-dimensional, but the secondary components are generally assumed to be small. Even in the aortic arch, where there is evidence of secondary flow with radial components of velocity, the axial flow is found to be dominant [110]. We therefore neglect the effects of the branch angle of the bifurcations and curved vessels. We further simplify our flow modelling by assuming the velocity profile to be flat. This means we are neglecting the effects of blood viscosity, which would tend, in steady flow in a circular cylinder, to cause the flow to adopt a parabolic velocity profile (Poiseuille flow). We ignore the effects of blood viscosity, because the arteries we consider are relatively large in diameter, hence the Reynolds numbers are moderate (100-1000) and the viscous effects are confined to a relatively narrow boundary layer for entrance flows and the flow is

unsteady with moderate Womersley numbers and long wavelengths compared with the vessel diameters, which tend to make the velocity profiles relatively flat. Indeed in-vivo observations, including those by Schlutz [131], have found that the velocity distribution in the major arteries is relatively flat and uniaxial under normal conditions and Paulsen and Hasenkam [109] asserted that this is the case even in the ascending aorta.

Beyond the arterial wall the external pressure is assumed to be constant on each section and body forces are also neglected. Gravity is the most significant body force, but it is reasonable for Chapter 5, because the measurements for the MRI network were taken with the subject lying down, therefore the effects of gravity will have been small. This is not the case in a standing human where gravity tends to cause a pooling of blood in the legs.

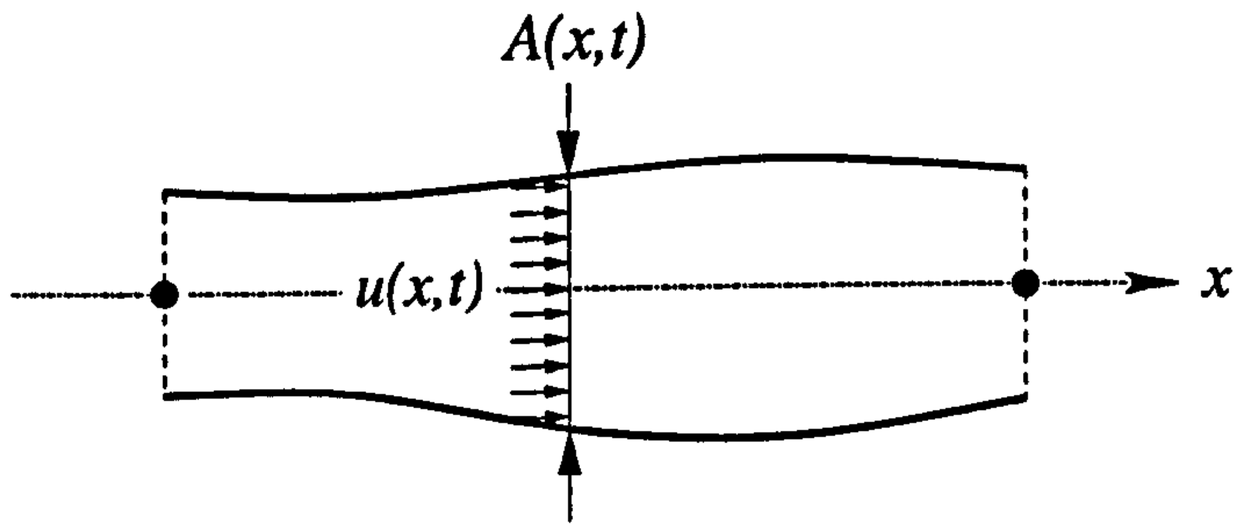


Figure 2.1: Schematic of a one-dimensional blood vessel showing that the domain is axially symmetric and the blood velocity profile has been simplified further and is assumed to be flat.

The simplified blood vessel is shown in figure 2.1, where the centreline of the vessel is aligned with the x-axis and the domain and flow are axisymmetric. The cross-sectional area, $A(x,t)$, can vary with both axial location and time as can the fluid velocity $u(x,t)$, which has no radial dependence as it is averaged across a section.

In the arterial wall itself the properties are assumed to be uniform and the arteries to behave elastically. As mentioned in Chapter 1 the arterial wall is a complex structure of elastin, collagen and smooth muscle cells of which elastin is the only purely elastic material [110]. In the larger arteries, which we are to study, the arterial walls are composed of a high percentage of elastin, therefore the elastic assumption is thought to be reasonable. Smaller arteries and arterioles have a significant proportion of smooth muscle cells and therefore if we were to study smaller

arteries then other vessel properties would become increasingly important.

2.1.1 Mass conservation in a single vessel

We now detail some of the important fundamental equations from which we derive our one-dimensional governing equations for fluid flow in distensible tubes. The mass conservation for a simple vessel can be thought of, using control volume techniques, as: the rate of change (in time) of mass within a vessel plus the net flux of mass out of the vessel is equal to zero. For an incompressible fluid, such as blood, this can be written in one-dimensional form as:

$$\frac{\partial A}{\partial t} + \frac{\partial Au}{\partial x} = 0 \tag{2.1}$$

where A is the cross-sectional area of the vessel, u is the local velocity, t is time and x is distance.

2.1.2 Momentum conservation in a single vessel

For inviscid flow in a distensible blood vessel conservation of momentum requires the rate of change of momentum (in time) within the vessel plus the net flux of momentum out of the vessel to equal the applied pressure forces. For a single dimension and for an incompressible fluid this leads to the following equation:

$$\frac{\partial u}{\partial t} + u\frac{\partial u}{\partial x} = -\frac{1}{\rho}\frac{\partial p}{\partial x} \tag{2.2}$$

where ρ is density and p is pressure.

2.1.3 Pressure-area relationship

The flow in a single vessel is governed by equations (2.1) and (2.2), but there are three independent variables, u, p and A and only two equations. Therefore in order to close the system a relationship between the pressure, p, and area, A, of the vessel needs to be defined. For simplicity, in our modelling we have assumed that there is a simple linear relationship between vessel radius and pressure and that the vessel walls are elastic, therefore pressure is a simple function of area alone. This assumption neglects many of the properties of a real artery, such as viscoelasticity.

The arterial sections are further assumed to behave independently of one another.

$$p = P_0 + \beta(\sqrt{A} - \sqrt{A_0}) \tag{2.3}$$

We further limit the modelling to include only thin walled vessels, hence β in the relationship between p and A can be defined as:

$$\beta = \frac{Eh_0\sqrt{\pi}}{A_0}$$

where $h_0 = h_0(x)$ and $A_0 = A_0(x)$ represent the vessel thickness and cross-sectional area at diastole, $E = E(x)$ is the Young's modulus and P_0 is the diastolic pressure. More details of the derivation can be found in [111, 118, 95].

Assuming the vessel walls to be thin when compared with their diameter is only a minor approximation in the larger arteries that we consider, where vessel wall thicknesses are $\sim$ 10 % of the arterial radius. Further down the arterial tree the vessel walls become thicker in relation to the vessel diameter [78].

This form of β does not include any of the effects relating to radial compression of the vessel wall that would require the Poisson ratio to be incorporated. The assumption is that if the vessel walls are thin enough the changes in wall thickness with distension are small and may be neglected, which assumes that the Poisson equals zero [89]. An equivalent relation for thick walled tubes is $\beta = \frac{Eh_0\sqrt{\pi}}{A_0(1-\nu^2)}$ and more details are given in [89, 95].

2.1.4 The distensibility of the blood vessel

A property that is often used in the assessment and description of distensible systems, such as this, is the distensibility, D. This is related to the arterial wall properties and is defined as:

$$D = \frac{1}{A}\frac{\partial A}{\partial p}, \tag{2.4}$$

We also define c^2 as:

$$c^2 = \frac{A}{\rho}\frac{\partial p}{\partial A} = \frac{1}{D\rho}. \tag{2.5}$$

where c is a characteristic velocity, often termed the wavespeed. This is discussed further in section 2.4, where the reasons for this formulation and terminology become clear [110].

For thin walled vessels we can obtain c in terms of A from the pressure-area relationship and the definition of β. Differentiating p with respect to A in equation (2.3), gives $\frac{\partial p}{\partial A} = \frac{\beta}{2\sqrt{A}}$ and c can thus be written as:

$$c^2 = \frac{A}{\rho}\frac{\partial p}{\partial A} = \frac{\beta A^{1/2}}{2\rho}. \tag{2.6}$$

Note for linear analysis substituting β into equation (2.6) gives $c = \sqrt{\frac{Eh_o}{2\rho R}}$, where R is the radius of the vessel A. This is the well-known Moens-Korteweg equation, which is valid for thin walled vessel [90, 69, 95, 89].

2.2 Mass and momentum conservation systems

The mass and momentum equations can be expressed in terms of A and u or p and u. These are shown in the following sections together with the linearised equations for an (A, u) system.

2.2.1 Mass and momentum conservation, (A, u) system

To write the mass and momentum equations in terms of A and u we must assume that pressure can be written as a function of area $p = f(A(x,t))$ then:

$$\frac{\partial p}{\partial x} = \frac{\partial p}{\partial A}\frac{\partial A}{\partial x}$$

Substituting the definition of c^2 from equation (2.5) into the above equation gives:

$$\frac{\partial p}{\partial x} = \frac{\partial p}{\partial A}\frac{\partial A}{\partial x} = \frac{c^2\rho}{A}\frac{\partial A}{\partial x}$$

By simple manipulations the momentum equation (2.2) can be expressed in terms of A and u as follows:

$$\frac{\partial u}{\partial t} + u\frac{\partial u}{\partial x} + \frac{c^2}{A}\frac{\partial A}{\partial x} = 0 \tag{2.7}$$

Equations (2.1) and (2.7) now form the mass and momentum conservation equations for an (A, u) system.

2.2.2 Mass and momentum conservation, (p, u) system

The system of equations in (2.1) and (2.2) can also be expressed in a (p, u) system. In this case it is the continuity of mass equation (2.1) that needs re-writing, this time in terms of p.

Expanding equation (2.1) gives:

$$\frac{\partial A}{\partial t} + u\frac{\partial A}{\partial x} + A\frac{\partial u}{\partial x} = 0 \tag{2.8}$$

If cross-sectional area is a function of local transmural pressure only, $A = f(p(x,t))$, then we can write $\frac{\partial A}{\partial t} = \frac{\partial A}{\partial p}\frac{\partial p}{\partial t}$ and $\frac{\partial A}{\partial x} = \frac{\partial A}{\partial p}\frac{\partial p}{\partial x}$. Substituting these into equation (2.8) we can re-write it in terms of p as:

$$\frac{\partial A}{\partial p}\frac{\partial p}{\partial t} + u\frac{\partial A}{\partial p}\frac{\partial p}{\partial x} + A\frac{\partial u}{\partial x} = 0 \tag{2.9}$$

Multiplying equation (2.9) by $\frac{\partial p}{\partial A}$ and substituting c^2 from equation (2.5), section 2.1.4, gives:

$$\frac{\partial p}{\partial t} + u\frac{\partial p}{\partial x} + \rho c^2\frac{\partial u}{\partial x} = 0 \tag{2.10}$$

Equations (2.10) and (2.2) now form the mass and momentum conservation equations for a (p,u) system.

2.2.3 Linearisation of the mass and momentum equations, (A,u) system

A further simplification is to linearise the governing equations (2.1) and (2.2) and previous work by other authors has used simplified linear models rather than solving the non-linear governing equations defined above. For example Wang and Parker [163] used linear theory to calculate the waveforms in a whole arterial tree. For ease of comparison of results and in order to investigate the differences between the two sets of governing equations we have also performed calculations using the linear model. Results obtained from our linear model are compared with the results of Wang and Parker in Chapter 4. In this chapter we also compare results from the linear and non-linear analysis. Linear analysis is only valid for constant area vessels, therefore the vessels are unable to taper, which limits the geometries that can be considered. Hence, the non-linear code is required so that we can evaluate more complex features of the arterial networks, such as the tapered system studied in Chapter 5.

For linear theory the wavespeed in a vessel does not vary, i.e. when the area increases in a vessel the wavespeed remains constant, which clearly is not true as we would expect c to increase with increasing area.

For a linearised system we assume that the wavespeed is much greater than the velocity of the blood, $c >> u$ [110]. Therefore a small change in u is negligible in terms of the wave propagation, although in-vivo u could be $> 20\%$ of c in some areas, particularly the aorta.

The system of equations (2.1) and (2.2) will be perturbed by a small amount a', u' and p' about A_0, U_0 and P_0, where A_0, U_0 and P_0 are values at diastole which satisfy (2.1) and (2.2).

Equations (2.1) and (2.2) can be re-written in terms of $A = A_0 + a'$, $U = U_0 + u'$ and $p = P_0 + p'$.

$$\frac{\partial(A_0 + a')}{\partial t} + (U_0 + u')\frac{\partial(A_0 + a')}{\partial x} + (A_0 + a')\frac{\partial(U_0 + u')}{\partial x} = 0 \qquad (2.11)$$

$$\frac{\partial(U_0 + u')}{\partial t} + (U_0 + u')\frac{\partial(U_0 + u')}{\partial x} = -\frac{1}{\rho}\frac{\partial(P_0 + p')}{\partial x} \qquad (2.12)$$

Velocity, u, is initially assumed to be at rest, therefore $U_0 = 0$. The terms $\frac{\partial A_0}{\partial t}$ and $\frac{\partial A_0}{\partial x}$ are zero, due to the fact that A_0 does not vary with time, t, and length, x (i.e. no taper). P_0 also does not vary with x and $\frac{\partial P_0}{\partial x}$ also becomes zero. The mass and momentum equations can now be written as:

$$\frac{\partial a'}{\partial t} + u'\frac{\partial a'}{\partial x} + (A_0 + a')\frac{\partial u'}{\partial x} = 0 \qquad (2.13)$$

$$\frac{\partial u'}{\partial t} + u'\frac{\partial u'}{\partial t} + \frac{1}{\rho}\frac{\partial p'}{\partial x} = 0 \qquad (2.14)$$

As u', a' and p' are small, quadratic terms are considered to be small and neglected which leaves:

$$\frac{\partial a'}{\partial t} + A_0\frac{\partial u'}{\partial x} = 0 \qquad (2.15)$$

$$\frac{\partial u'}{\partial t} + \frac{1}{\rho}\frac{\partial p'}{\partial x} = 0 \qquad (2.16)$$

Assuming that p is a function of A, $\frac{\partial p'}{\partial x}$ can be written as $\frac{\partial p'}{\partial x} = \frac{\partial p}{\partial A}|_{A_0}\frac{\partial A}{\partial x}|_{A_0} = \frac{\partial p}{\partial A}|_{A_0}\frac{\partial a'}{\partial x}$ therefore the momentum equation (2.16) becomes:

$$\frac{\partial u'}{\partial t} + \frac{1}{\rho}\frac{\partial p}{\partial A}|_{A_0}\frac{\partial a'}{\partial x} = 0 \qquad (2.17)$$

Linearising c in equation (2.5) gives $c_0 = \sqrt{\frac{A_0}{\rho}\frac{\partial p}{\partial A}|_{A_0}}$ and therefore $\frac{1}{\rho}\frac{\partial p}{\partial A}|_{A_0} = \frac{c_0^2}{A_0}$, which can then be substituted into equation (2.17) to give:

$$\frac{\partial u'}{\partial t} + \frac{c_0^2}{A_0}\frac{\partial a'}{\partial x} = 0 \tag{2.18}$$

Equations (2.15) and (2.18) are the mass and momentum equations respectively linearised in terms of A and u. Differentiating equation (2.18) with respect to x and equation (2.15) with respect to t and combining them leads to the classical wave equation.

2.3 Numerical modelling - discontinuous Galerkin method

To obtain a numerical solution for a fluid flow problem using finite element/spectral element methods the solution domain has to be decomposed into subdomains or elements. For spectral element methods the solution in each element is also represented by a polynomial expansion. The accuracy of the numerical solution can be improved either by increasing the number of elements in the mesh (h-type refinement) or by increasing the order of the polynomial (p-type refinement). Convergence of the numerical solution to the actual solution for elliptic problems, is exponential for p-type refinement, but only algebraic for h-type refinement, and similar differences are seen for hyperbolic problems, hence spectral element methods can greatly improve the accuracy of the numerical solution for a given computational time. Spectral methods also propagate waves throughout the domain with minimal dispersion and is a key advantage over other numerical techniques that can exhibit significant dispersion errors when applied to hyperbolic problems. The advantages of using spectral/hp element methods are that computational work is relatively low for a high accuracy, complex geometries can be represented accurately by high order polynomial expansions and accuracy can be improved (and parametric studies performed) without the need to re-mesh the domain [66, 49, 16].

To solve the system of governing equations, a high order discontinuous Galerkin formulation with a 1D spectral/*hp* element spatial approximation is applied. A discontinuous formulation is attractive because it enables discontinuous systems to be solved. Such discontinuities occur in one-dimensional representations of arterial systems at junctions, where there is likely to be a discontinuity in area and possibly β, and also locally within arteries where β may change suddenly due to the presence of an artificial device, such as a stent, or disease and calcification. For explicit problems it also only requires a local matrix to be assembled rather than a large global matrix for the entire domain, which is usually needed for continuous Galerkin methods, and therefore saves computational power, particularly since this global matrix needs inverting.

In the following section a simple example of the use of the discontinuous Galerkin method is introduced to solve: the linear advection equation. Then in section 2.3.2

the discontinuous Galerkin formulation is applied to the governing equation for flow in an elastic vessel, equations (2.1) and (2.7). The linear advection example is shown first because it is a simple introduction to the concepts of the discontinuous Galerkin method, which can then be applied to the more complicated system of equations we wish to solve.

An important feature of the flows in arterial networks that makes high order spectral methods attractive is that the characteristic system is subcritical, i.e. ($\lambda_1 > 0$ and $\lambda_2 < 0$) and shock waves will not be present in the system. Indeed under physiological conditions the wave propagation speeds in the arteries are an order of magnitude greater than the flow speeds. Continuous solutions such as these exhibit rapid convergence of both the diffusion and phase properties with order of the *hp* scheme [135]. The discontinuous Galerkin method is also an appealing formulation for the high-order discretisation of the conservation laws because waves are propagated for many periods with minimum numerical diffusion and dispersion.

2.3.1 Using discontinuous Galerkin method to solve the advection equation

To understand the fundamental concepts involved in solving a partial differential equation using spectral/hp elements, we first analyse the relatively simple linear scalar advection equation and following the work of Cockburn and Shu [22] and Lomtev, Quillen and Karniadakis [83] we proceed as follows.

$$L(u) = \frac{\partial u}{\partial t} + a\frac{\partial u}{\partial x} = 0 \tag{2.19}$$

where a is a real constant and $L(u)$ is a linear operator.

To solve this system we first discretise the domain $\Omega = (a, b)$ into a mesh of N_{el} non-overlapping elemental regions $\Omega_e = (x_e^L, x_e^U)$, such that $x_e^U = x_{e+1}^L$ for $e = 1, \ldots, N_{el}$, and

$$\bigcup_{e=1}^{N_{el}} \overline{\Omega}_e = \overline{\Omega},$$

The approximation of the solution is C^0 continuous within every elemental domain, Ω^e, but need not be at the interface of each element for discontinuous Galerkin methods. This is unlike the majority of finite/spectral element methods, where C^0 continuity is required throughout.

Multiplying equation (2.19) by a test function $v(x)$ and integrating over each elemental domain Ω_e gives the inner product of $L(u)$ with $v(x)$ for each element.

$$(v, L(u))_e = \int_{\Omega_e} v \left[\frac{\partial u}{\partial t} + a \frac{\partial u}{\partial x} \right] dx \;=\; 0 \qquad (2.20)$$

Integrating the second term by parts gives:

$$\sum_{e=1}^{Nel} \left[\int_{\Omega_e} v \frac{\partial u}{\partial t} dx - \int_{\Omega_e} a \frac{\partial v}{\partial x} u dx + [avu]_{x_e^L}^{x_e^U} \right] \;=\; 0 \qquad (2.21)$$

where x_e^U and x_e^L are the upper and lower boundary points of each element.

The solution $u(x)$ is now approximated by a discretised expansion denoted by $u^\delta(x)$ (trial function) and the expansion $v(x)$ (test function) is also replaced by a finite expansion denoted by $v^\delta(x)$.

Although u^δ may be discontinuous across inter-element boundaries, to obtain a global solution information must propagate between the elemental regions. This is achieved by upwinding the boundary flux in the third term of equation (2.21). Denoting the upwinded flux as u^u, the discrete weak (i.e. integral) formulation can be written as:

$$\sum_{e=1}^{Nel} \left[\int_{\Omega_e} v^\delta \frac{\partial u^\delta}{\partial t} dx - \int_{\Omega_e} a \frac{\partial v^\delta}{\partial x} u^\delta dx + [a v^\delta u^u]_{x_e^L}^{x_e^U} \right] \;=\; 0 \qquad (2.22)$$

If we were now to define a polynomial basis and choose a quadrature rule we would have a semi-discrete scheme. However, the calculation of the second term can be difficult to implement, therefore this term is once again integrated by parts to give:

$$\sum_{e=1}^{Nel} \left[\int_{\Omega_e} v^\delta \frac{\partial u^\delta}{\partial t} dx + \int_{\Omega_e} a v^\delta \frac{\partial u^\delta}{\partial x} dx + [a v^\delta [u^u - u^\delta]]_{x_e^L}^{x_e^U} \right] \;=\; 0 \qquad (2.23)$$

Note this second integration is a mathematical manipulation using integration by parts so that the second term is in the standard form (i.e. the derivative is on u rather than v) which is typically easier to implement.

The information is propagated between elements by the third (boundary) term which is the difference between the upwinded and the local fluxes, $\left[a v^\delta \left[u^u - u^\delta \right] \right]_{x_e^L}^{x_e^U}$. This method can be thought of as a penalty method with an automatic procedure for determining the penalty parameter.

To calculate the upwinded flux for the linear advection equation we only take information from the upwind direction:

i.e. if $a \geq 0$ then

$$u^u = \begin{cases} u_{e-1}^U & \text{at} \quad x_e^L \\ u_e^U & \text{at} \quad x_e^U \end{cases}$$

and if $a < 0$ then

$$u^u = \begin{cases} u_e^L & \text{at} \quad x_e^L \\ u_{e+1}^L & \text{at} \quad x_e^U \end{cases}$$

where the superscripts U and L again refer to information at the upper and lower boundary of the element.

Rearranging equation (2.23) we obtain:

$$\sum_{e=1}^{Nel} \int_{\Omega_e} v^\delta \frac{\partial u^\delta}{\partial t} dx = -\sum_{e=1}^{Nel} \left[\int_{\Omega_e} a v^\delta \frac{\partial u^\delta}{\partial x} dx + [a v^\delta [u^u - u^\delta]]_{x_e^L}^{x_e^U} \right] \tag{2.24}$$

For ease of implementation each local element is mapped onto a reference element called the standard element which is denoted by Ω_{st} [127], where:

$$\Omega_{st} = \{-1 \leq \xi \leq 1\} \tag{2.25}$$

Hence, we can define the elemental mapping as:

$$\chi_e(\xi) = x_e^L \frac{(1-\xi)}{2} + x_e^U \frac{(1+\xi)}{2}. \qquad \xi \in \Omega_{st} \tag{2.26}$$

and the inverse of the linear transformation $\chi(\xi)$ is:

$$\xi = \chi_e^{-1}(x) = 2\frac{x_e - x_e^L}{x_e^U - x_e^L} - 1. \qquad x_e \in \Omega_e \tag{2.27}$$

Having defined the finite element framework in terms of the Galerkin formulation, the different types of expansion bases for the one-dimensional case can be considered. We therefore choose the expansion bases to be a polynomial space of order P on each element, e, and expand our solution on each element in terms of orthonormal Legendre polynomials $L_p(\xi)$, i.e.:

$$u^\delta|_{\Omega_e}(\chi_e(\xi), t) = \sum_{p=0}^{P} L_p(\xi) \hat{u}_e^p(t). \tag{2.28}$$

The choice of discontinuous discrete solution and test functions means that the problem is decoupled on each element, with the only link being the upwinded boundary fluxes.

We now consider the Galerkin projection of a smooth function $f(x)$ in the elemental domain Ω_e onto the polynomial expansion u^δ

$$(v^\delta, u^\delta)_e = (v^\delta, \mathbf{f})_e \tag{2.29}$$

for all $v^\delta \in V$, where $(v, u)_e$ is the inner product for each element.

If the left hand side of equation (2.29) represents the left hand side of equation (2.24) and the right hand side of equation (2.29) represents the right hand side of equation (2.24) and letting $u^\delta = v^\delta$, which is the traditional Galerkin approach, then equation (2.24) is equivalent to solving the mass matrix equation:

$$\mathbf{M}_e \hat{\mathbf{u}}_e = \mathbf{f}_e \tag{2.30}$$

where the local mass matrix $\mathbf{M}_e$ is a square matrix of order (P+1) and equals:

$$\mathbf{M}_e^{pq} = (L_p, L_q) \tag{2.31}$$

and

$$\hat{\boldsymbol{u}}_e = [\hat{u}_e^0, ..., \hat{u}_e^p]^T, \qquad \boldsymbol{f}_e^p = (L_p, f_e).$$

for $0 \leq p, q \leq P$ and $1 \leq e \leq N_{el}$. The local mass matrix can then be inverted to determine the solution:

$$\hat{\mathbf{u}}_e = [\mathbf{M}_e]^{-1} \mathbf{f}_e \tag{2.32}$$

However, $[\mathbf{M}_e]^{-1}$, is trivial as $\mathbf{M}_e^{pq}$ is an identity matrix, I, because the Legendre polynomials are orthonormal and therefore the basis is orthogonal with respect to the $L^2(\Omega_e)$ inner product. Hence, equation (2.32) is equivalent to solving $\hat{\mathbf{u}}_e = \mathbf{f}_e$. Solving equation (2.24) for each element, e, gives:

$$J_e \frac{\partial \hat{u}_e^p}{\partial t} = -J_e \left(L_p, a \frac{\partial u_e}{\partial x} \right)_{\Omega_e} - \left[L_p a \left[u_e^u - u_e(u^\delta) \right] \right]_{x_e^L}^{x_e^U} = 0, \quad p = 0, \ldots, P \tag{2.33}$$

where J_e is the Jacobian of the elemental mapping, $J_e = \frac{1}{2}(x_e^U - x_e^L)$, from the standard region, $\Omega_{st} = [-1, 1]$.

We substitute the Legendre expansion given by equation (2.28) for the solution, u^δ, into the first term of equation (2.24) which gives the inner product $J_e(L_p, \sum \frac{\delta \hat{u}_e^p}{\delta t} L_q)$. However, as $\frac{\delta \hat{u}_e^p}{\delta t}$ is not a function of space it can be brought out of the inner product

and as (L_p, L_q) is the identity matrix then the first term can be written without the inner product as $J_e \frac{\delta \hat{u}_e^p}{\delta t}$.

The final step required to complete the discretisation is a time integration scheme and we have employed an Adams-Bashforth scheme [47].

2.3.2 Using discontinuous Galerkin method to solve the governing equations for a single vessel

We will now describe the solution procedure for our governing equations [137, 134]. The one-dimensional hyperbolic system, equations (2.1) and (2.2), can be expressed in a conservative form as shown in section 2.2.1, which can be re-written as:

$$\frac{\partial U}{\partial t} + \frac{\partial F}{\partial x} = 0 \tag{2.34}$$

where

$$\boldsymbol{U} = \begin{bmatrix} U_1 \\ U_2 \end{bmatrix} = \begin{bmatrix} A \\ u \end{bmatrix} \qquad \boldsymbol{F} = \begin{bmatrix} F_1 \\ F_2 \end{bmatrix} = \begin{bmatrix} uA \\ \frac{u^2}{2} + \frac{p}{\rho} \end{bmatrix}.$$

We solve this system in a domain $\Omega = (a, b)$ using the same steps as for the advection equation of the previous section.

The mesh is discretised into N_{el} non-overlapping elements similar to section 2.3.1. Then we construct the weak, integral, form of equation (2.34) by multiplying by a test function $\psi(x)$ to give the inner product:

$$\left(\psi, \frac{\partial \mathrm{U}}{\partial t}\right)_{\Omega} + \left(\psi, \frac{\partial \mathrm{F}}{\partial x}\right)_{\Omega} = 0 \tag{2.35}$$

Decomposing the integral into elemental regions we obtain:

$$\sum_{e=1}^{N_{el}} \left[\left(\psi, \frac{\partial \mathrm{U}}{\partial t}\right)_{\Omega_e} + \left(\psi, \frac{\partial \mathrm{F}}{\partial x}\right)_{\Omega_e}\right] = 0. \tag{2.36}$$

Once again we integrate the second term by parts letting $\mathbf{U}^\delta$ be the finite space of $L^2(\Omega)$ functions which are polynomial of degree P and denoting the upwinded flux as $\mathbf{F}^u$, the discrete weak formulation can be written as:

$$\sum_{e=1}^{N_{el}} \left[\left(\psi^\delta, \frac{\partial \mathbf{U}^\delta}{\partial t}\right)_{\Omega_e} - \left(\frac{d\psi^\delta}{dx}, \mathbf{F}(\mathbf{U}^\delta)\right)_{\Omega_e} + \left[\psi^\delta \mathbf{F}^u\right]_{x_e^L}^{x_e^U}\right] = 0, \tag{2.37}$$

Again, following the traditional Galerkin approach, we choose the test function within each element to be in the same discrete space as the numerical solution $\mathbf{U}^\delta$

and integrating the second term by parts again we obtain:

$$\sum_{e=1}^{N_{el}} \left[\left(\psi^\delta, \frac{\partial \mathbf{U}^\delta}{\partial t} \right)_{\Omega_e} + \left(\psi^\delta, \frac{\partial \mathbf{F}(\mathbf{U}^\delta)}{\partial x} \right)_{\Omega_e} + \left[\psi^\delta \left[\mathbf{F}^u - \mathbf{F}(\mathbf{U}^\delta) \right] \right]_{x_e^L}^{x_e^U} \right] = 0. \qquad (2.38)$$

where $\mathbf{F}(\mathbf{U}^\delta)$ is the local flux and in the third term is calculated at x_e^U and x_e^L using u^δ rather than u^u. Unlike the linear advection equation in section 2.3.1, the upwinded flux, $\mathbf{F}^u$, is calculated by taking information arriving from both directions at both the upper and lower boundaries of element e. For example at the point x_e^L we take forward travelling information at the upper boundary of element $e-1$ and backward travelling information at the lower boundary of element e, i.e. we consider information which is arriving at the boundary and ignore information which is moving away.

We again expand our solution on each element e in terms of orthonormal Legendre polynomials $L_p(\xi)$:

$$\mathbf{U}^\delta|_{\Omega_e}(\chi_e(\xi), t) = \sum_{p=0}^{P} L_p(\xi) \hat{\mathbf{U}}_e^p(t).$$

to give:

$$J_e \frac{\partial \hat{U}_{i,e}^p}{\partial t} = -J_e \left(L_p, \frac{\partial F_i}{\partial x} \right)_{\Omega_e} - \left[L_p \left[F_i^u - F_i(\mathbf{U}^\delta) \right] \right]_{x_e^L}^{x_e^U} = 0, \quad p = 0, \ldots, P, \quad i = 1, 2 \qquad (2.39)$$

where

$$\boldsymbol{U} = \begin{bmatrix} U_1 \\ U_2 \end{bmatrix} = \begin{bmatrix} A \\ u \end{bmatrix} \qquad \boldsymbol{F} = \begin{bmatrix} F_1 \\ F_2 \end{bmatrix} = \begin{bmatrix} uA \\ \frac{u^2}{2} + \frac{p}{\rho} \end{bmatrix}.$$

For an explicit time integration scheme this equation can be solved in an analogous manner to the linear advection equation for each component, $i = 1, 2$.

Again we complete the method by using the Adams-Bashforth scheme for the time integration. We explain the implementation of the upwinding fluxes for this system in detail in section 2.5. It should also be noted that the upwinding process is used to impose the characteristic boundary conditions through the flux at the ends of the global domain Ω. For more information regarding discontinuous Galerkin and spectral/hp methods see the publications of Sherwin and co-workers [66, 135].

2.4 The characteristic system

In order to solve the algebraic system for the one-dimensional model (equations (2.1) and (2.2)) in more than one element we need to determine the upwinded flux terms at the boundaries of the elements. This is essentially a Riemann problem that can be solved numerically using the characteristic form of the hyperbolic system. This technique can be further extended to incorporate discontinuities in area and wall properties by applying conservation of mass and conservation of total pressure. Discontinuities in area will occur at bifurcations and other junctions. The upwinded fluxes are discussed further in section 2.5, but first we derive the characteristic equations for the different systems of governing equations.

2.4.1 Non-linear (A, u) system

The (A, u) system of equations (2.1) and (2.7) can be expressed in a conservative form:

$$\frac{\partial \boldsymbol{U}}{\partial t} + \boldsymbol{H}\frac{\partial \boldsymbol{U}}{\partial x} = \begin{bmatrix} A \\ u \end{bmatrix}_t + \begin{bmatrix} u & A \\ c^2/A & u \end{bmatrix} \begin{bmatrix} A \\ u \end{bmatrix}_x = \begin{bmatrix} 0 \\ 0 \end{bmatrix} \tag{2.40}$$

Matrix $\boldsymbol{H}$ has two real eigenvalues $\lambda_{1,2}$

$$\left| \boldsymbol{H} - \lambda \boldsymbol{I} \right| = \begin{vmatrix} u-\lambda & A \\ c^2/A & u-\lambda \end{vmatrix} = (u-\lambda)^2 - c^2 = 0 \tag{2.41}$$

Therefore $\lambda_{1,2} = u \pm c$ and the two corresponding eigenvectors are:

$$\mathbf{q_1} = \alpha \begin{bmatrix} A \\ c \end{bmatrix}, \qquad \mathbf{q_2} = \beta \begin{bmatrix} -A \\ c \end{bmatrix} \tag{2.42}$$

and the eigenmatrix $\boldsymbol{Q}$ is:

$$\boldsymbol{Q} = \left[\mathbf{q_1}, \mathbf{q_2} \right] = \gamma \begin{bmatrix} A & -A \\ c & c \end{bmatrix} \tag{2.43}$$

where α, β and γ are arbitrary scaling factors.

We can now write $\boldsymbol{HQ} = \boldsymbol{Q\Lambda}$ therefore the matrix $\boldsymbol{H} = \boldsymbol{Q\Lambda Q^{-1}}$, where $\boldsymbol{\Lambda}$ is the diagonal matrix formed by the eigenvalues of $\boldsymbol{H}$.

Substituting this into equation (2.40):

$$\frac{\partial \boldsymbol{U}}{\partial t} + \boldsymbol{Q\Lambda Q^{-1}}\frac{\partial \boldsymbol{U}}{\partial x} = 0 \tag{2.44}$$

and premultiplying equation (2.44) by $\boldsymbol{Q}^{-1}$ gives:

$$\boldsymbol{Q}^{-1}\frac{\partial \boldsymbol{U}}{\partial t} + \boldsymbol{\Lambda}\boldsymbol{Q}^{-1}\frac{\partial \boldsymbol{U}}{\partial x} = 0 \tag{2.45}$$

If there exists a quantity $\boldsymbol{W} = \boldsymbol{W}(\boldsymbol{U})$ such that:

$$\frac{\partial \boldsymbol{W}}{\partial \boldsymbol{U}} = \boldsymbol{Q}^{-1} \tag{2.46}$$

then using this relation, equation (2.45) can be written as:

$$\frac{\partial \boldsymbol{W}}{\partial t} + \boldsymbol{\Lambda}\frac{\partial \boldsymbol{W}}{\partial x} = 0 \tag{2.47}$$

and hence can be transformed into a decoupled system of equations for the characteristic variables, which component wise reads

$$\frac{\partial W_1}{\partial t} + \lambda_1 \frac{\partial W_1}{\partial x} = 0 \tag{2.48}$$

$$\frac{\partial W_2}{\partial t} + \lambda_2 \frac{\partial W_2}{\partial x} = 0 \tag{2.49}$$

The characteristic variables can be determined by integrating the differential system since:

$$\boldsymbol{Q}^{-1} = \gamma \begin{bmatrix} \frac{1}{2A} & \frac{1}{2c} \\ -\frac{1}{2A} & \frac{1}{2c} \end{bmatrix} = \frac{\partial \boldsymbol{W}}{\partial \boldsymbol{U}} = \begin{bmatrix} \frac{\partial W_1}{\partial A} & \frac{\partial W_1}{\partial u} \\ \frac{\partial W_2}{\partial A} & \frac{\partial W_2}{\partial u} \end{bmatrix} \tag{2.50}$$

A possible choice for γ where the characteristic variables satisfy the Cauchy-Riemann condition $\left(\frac{\partial^2 W_{1,2}}{\partial A \partial u} = \frac{\partial^2 W_{1,2}}{\partial u \partial A}\right)$ is $\gamma = 2c$, since A does not depend on u [116]. Therefore if the characteristic variables exist they must satisfy:

$$\frac{\partial W_1}{\partial A} = \frac{c}{A}, \qquad \frac{\partial W_1}{\partial u} = 1, \tag{2.51}$$

$$\frac{\partial W_2}{\partial A} = -\frac{c}{A}, \qquad \frac{\partial W_2}{\partial u} = 1 \tag{2.52}$$

Integrating the differential form in equations (2.51) and (2.52) we obtain:

$$W_1 = u + \int_{A_0}^{A} \frac{c(A)}{A} dA, \tag{2.53}$$

$$W_2 = u - \int_{A_0}^{A} \frac{c(A)}{A} dA \tag{2.54}$$

These are the Riemann invariants in terms of A and u for the one-dimensional wave equations. Waves therefore propagate in the vessel with a speed of $u \pm c$ and we can see now why we chose the form we did for c and described it as a characteristic velocity in section 2.1.4.

A closed form for W_1 and W_2 can be obtained by using the relationship between p and A in equation (2.3). Equations (2.53) and (2.54) can now be written in terms of A and integrating these equations gives:

$$W_1 = u + 4\sqrt{\frac{\beta}{2\rho}}(A^{1/4} - A_0^{1/4}) = u + 4(c - c_0), \tag{2.55}$$

$$W_2 = u - 4\sqrt{\frac{\beta}{2\rho}}(A^{1/4} - A_0^{1/4}) = u - 4(c - c_0) \tag{2.56}$$

where $c_0 = \sqrt{\frac{\beta A_0^{\frac{1}{2}}}{2\rho}}$.

Since $\beta > 0$ and $\rho > 0$, we may write the variables (A, u) in terms of (W_1, W_2) as [39]:

$$A = \left[\frac{(W_1 - W_2)}{8}\sqrt{\frac{2\rho}{\beta}} + A_0^{1/4}\right]^4, \tag{2.57}$$

$$u = \frac{(W_1 + W_2)}{2}. \tag{2.58}$$

2.4.2 Non-linear (p, u) system

In this section we derive the characteristic equations for the non-linear (p, u) system. Equations (2.10) and (2.2) can be expressed as follows:

$$\frac{\partial U}{\partial t} + \boldsymbol{H}\frac{\partial U}{\partial x} = \begin{bmatrix} p \\ u \end{bmatrix}_t + \begin{bmatrix} u & \rho c^2 \\ 1/\rho & u \end{bmatrix}\begin{bmatrix} p \\ u \end{bmatrix}_x = \begin{bmatrix} 0 \\ 0 \end{bmatrix} \tag{2.59}$$

Matrix $\boldsymbol{H}$ has two real eigenvalues $\lambda_{1,2}$, which as for section 2.4.1 are $\lambda_{1,2} = u \pm c$.

However, in this case the corresponding eigenmatrix for the system is:

$$\boldsymbol{Q} = \left[\ \mathbf{q_1}, \mathbf{q_2}\ \right] = \gamma \begin{bmatrix} 1 & -1 \\ \frac{1}{\rho c} & \frac{1}{\rho c} \end{bmatrix} \tag{2.60}$$

Again writing $\boldsymbol{HQ} = \boldsymbol{Q\Lambda}$ and following the analysis for the non-linear (A, u) system we obtain the relationship between $\boldsymbol{W}$ and $\boldsymbol{Q}$ formed in equation (2.46). The characteristic variables can then be determined by integrating the differential system to give:

$$\frac{\partial W_1}{\partial p} = \frac{1}{\rho c}, \qquad \frac{\partial W_1}{\partial u} = 1, \tag{2.61}$$

$$\frac{\partial W_2}{\partial p} = -\frac{1}{\rho c}, \qquad \frac{\partial W_2}{\partial u} = 1 \tag{2.62}$$

Integrating the differential form of equations (2.61) and (2.62) we obtain:

$$W_1 = u + \int_{P_0}^{p} \frac{1}{\rho c(p)} dp, \tag{2.63}$$

$$W_2 = u - \int_{P_0}^{p} \frac{1}{\rho c(p)} dp \tag{2.64}$$

which are the Riemann invariants in terms of p and u for the one-dimensional wave equations. Again waves propagate in the vessel with a speed of $u \pm c$.

The system can be closed for thin-walled vessels using equation (2.3). Calculating c in terms of p from equations (2.3) and (2.5) gives $c = \frac{1}{\sqrt{2\rho}}(p - P_0 + \beta A_0^{1/2})^{1/2}$. Substituting this into equations (2.63) and (2.64) and integrating gives W_1 and W_2 in terms of p:

$$W_1 = u + \frac{4}{\sqrt{2\rho}}[(p + k_0)^{1/2} - A_0^{1/4}\beta^{1/2}] = u + 4(c - c_0), \tag{2.65}$$

$$W_2 = u - \frac{4}{\sqrt{2\rho}}[(p + k_0)^{1/2} - A_0^{1/4}\beta^{1/2}] = u - 4(c - c_0) \tag{2.66}$$

where $k_0 = A_0^{1/2}\beta - P_0$.

Note $W_{1,2} = u \pm 4(c - c_0)$ and $c_0 = \sqrt{\frac{\beta A_0^{1/2}}{2\rho}}$ which is consistent with the non-linear analysis for the (A, u) system.

2.4.3 Linear (A, u) system

To solve the linear mass and momentum equations (2.15) and (2.18) using the method of characteristics we first write the (A, u) system in a conservative form, equation (2.67), where the primes are dropped for convenience:

$$\frac{\partial \boldsymbol{U}}{\partial t} + \boldsymbol{H}\frac{\partial \boldsymbol{U}}{\partial x} = \begin{bmatrix} a \\ u \end{bmatrix}_t + \begin{bmatrix} 0 & A_0 \\ c_0^2/A_0 & 0 \end{bmatrix} \begin{bmatrix} a \\ u \end{bmatrix}_x = \begin{bmatrix} 0 \\ 0 \end{bmatrix} \tag{2.67}$$

Matrix $\boldsymbol{H}$ has two real eigenvalues $\lambda_{1,2}$

$$\left| \boldsymbol{H} - \lambda \boldsymbol{I} \right| = \begin{vmatrix} -\lambda & A_0 \\ c_0^2/A_0 & -\lambda \end{vmatrix} = \lambda^2 - c_0^2 = 0 \tag{2.68}$$

and therefore $\lambda_{1,2} = \pm c_0$.

The two corresponding eigenvectors are:

$$\mathbf{q_1} = \alpha \begin{bmatrix} A_0 \\ c_0 \end{bmatrix}, \qquad \mathbf{q_2} = \beta \begin{bmatrix} -A_0 \\ c_0 \end{bmatrix} \tag{2.69}$$

and the eigenmatrix Q is

$$Q = \left[\mathbf{q_1}, \mathbf{q_2} \right] = \gamma \begin{bmatrix} A_0 & -A_0 \\ c_0 & c_0 \end{bmatrix} \tag{2.70}$$

Using the relationship between W and Q formed in equation (2.46) then the characteristic variables can be determined by integrating the differential system in a similar manner to the non-linear analyses:

$$\frac{\partial W_1}{\partial a} = \frac{c_0}{A_0}, \qquad \frac{\partial W_1}{\partial u} = 1, \tag{2.71}$$

$$\frac{\partial W_2}{\partial a} = -\frac{c_0}{A_0}, \qquad \frac{\partial W_2}{\partial u} = 1 \tag{2.72}$$

which when integrated yield:

$$W_1 = u + \int_{A_0}^{A_0+a} \frac{c(A_0)}{A_0} dA, \tag{2.73}$$

$$W_2 = u - \int_{A_0}^{A_0+a} \frac{c(A_0)}{A_0} dA \tag{2.74}$$

These are the linearised Riemann invariants in terms of A and u for the one-dimensional wave equations. Waves propagate in the vessel with a speed of $\pm c_0$. $c(A_0)$ is a constant denoted by c_0, which when thin walled theory is used gives $c_0 = \sqrt{\frac{A_0}{\rho} \frac{\partial p}{\partial A}|_{A_0}} = \sqrt{\frac{\beta A_0^{\frac{1}{2}}}{2\rho}}$. Substituting this into equations (2.73) and (2.74) gives the W_1 and W_2 characteristics for linear wave propagation in thin walled vessels:

$$W_1 = u + \frac{ac_0}{A_0} = u + \frac{a}{A_0^{3/4}} \sqrt{\frac{\beta}{2\rho}}, \tag{2.75}$$

$$W_2 = u - \frac{ac_0}{A_0} = u - \frac{a}{A_0^{3/4}} \sqrt{\frac{\beta}{2\rho}} \tag{2.76}$$

We can now write the variables (A, u) in terms of (W_1, W_2) as:

$$a = \left[\frac{(W_1 - W_2)}{2}\right] \left(\frac{A_0}{c_0}\right) = \left[\frac{(W_1 - W_2)}{2}\right] A_0^{3/4} \sqrt{\frac{2\rho}{\beta}}, \tag{2.77}$$

$$u = \frac{(W_1 + W_2)}{2}. \tag{2.78}$$

2.4.4 Linear (p, u) system

Finally, it can also be shown that the Riemann invariants can be expressed in terms of a linear (p, u) system. This is achieved by linearising equations (2.63) and (2.64)

by perturbing by a small amount a', u' and p' about A_0, U_0 and P_0 respectively, where $U_0 = 0$ and dropping quadratic terms in a', u' and p'.

Integrating W_1 and W_2 between the limits of P_0 and $P_0 + p'$ and dropping primes for convenience gives:

$$W_1 = u + \int_{P_0}^{P_0+p} \frac{1}{\rho c_0} dp = u + \frac{p}{\rho c_0}, \tag{2.79}$$

$$W_2 = u - \int_{P_0}^{P_0+p} \frac{1}{\rho c_0} dp = u - \frac{p}{\rho c_0} \tag{2.80}$$

2.5 Numerical boundary conditions

In this section the application of the characteristic analysis of the previous sections to the inter-element and inter-vessel boundary conditions will be discussed. The flux upwinding applied between vessels is very similar to that applied between elements, but further information is required to close the system. At the elemental/vessel boundaries the numerical schemes (equation (2.39)) need to be complemented with boundary data $\mathbf{U}$. As we can compute the characteristics, W_1 and W_2, at the boundary we can use this information to compute $\mathbf{U}$ for non-linear analysis, from equations (2.57) and (2.58) respectively. One boundary condition needs to be imposed at each end for well-posedness of the differential problem, because the propagation speed is subcritical in physiological vessels, $c > u$, and therefore $\lambda_1 > 0$ and $\lambda_2 < 0$ and information can propagate in both directions.

In the following section the inter-elemental flux upwinding is explained for non-linear analysis; the process for the linear analysis is very similar.

2.5.1 Inter-elemental flux upwinding

Looking first at the interface between two elements, e and $e+1$ we consider a point $x = x_e^U = x_{e+1}^L$, where x_e^U is the upper boundary of element e and x_{e+1}^L is the lower boundary of element $e+1$. Consider a function, f, that is continuous on each element e and $e+1$, but possibly discontinuous at the elemental boundary x, where there may be a discontinuity in vessel properties. f_l and f_r are left and right limiting values, given by:

$$f_l = f|_{\Omega_e}(x_e^U), \quad f_r = f|_{\Omega_{e+1}}(x_{e+1}^L).$$

The appropriate characteristic information at point x is given by the forward travelling wave in the left hand element and the backward travelling wave in the right hand element.

$$W_1 = u_l + 4\sqrt{\frac{\beta_l}{2\rho}}\left(A_l^{1/4} - {A_{0l}}^{1/4}\right) \tag{2.81}$$

$$W_2 = u_r - 4\sqrt{\frac{\beta_r}{2\rho}}\left(A_r^{1/4} - {A_{0r}}^{1/4}\right) \tag{2.82}$$

When the vessel properties are continuous, $\mathbf{F}^u$ from equation (2.39) at point x is computed by posing $\mathbf{F}^u = \mathbf{F}(\mathbf{U}^u)$, where $\mathbf{U}^u = [A^u, u^u]^T$ is computed from W_1 and W_2 given by equations (2.81) and (2.82) and applying equations (2.57) and (2.58), i.e.

$$\boldsymbol{F}(\boldsymbol{U}^u) = \begin{bmatrix} F_1(\boldsymbol{U}^u) \\ F_2(\boldsymbol{U}^u) \end{bmatrix} = \begin{bmatrix} A^u u^u \\ \dfrac{(u^u)^2}{2} + \dfrac{p(A^u, u^u)}{\rho} \end{bmatrix}.$$

This upwinding is applied at all of the elemental interfaces, which includes the inflow and outflow, where W_1 (inflow) or W_2 (outflow) are specified to simulate the appropriate boundary conditions for the problem.

If the material properties are not continuous at the interface then additional information is required to close the system. We therefore assume that the mass fluxes are balanced and also conservation of momentum, which leads to conservation of total pressure. This leads to:

$$Q = u_l A_l = u_r A_r \tag{2.83}$$

$$P_r = \rho\frac{u_l^2}{2} + \beta_l(\sqrt{A_l} - \sqrt{A_{0l}}) = \rho\frac{u_r^2}{2} + \beta_r(\sqrt{A_r} - \sqrt{A_{0r}}) \tag{2.84}$$

These interface conditions maintain the conservation properties of the (A, u) system. This method allows for discontinuities in all the vessel properties including A_0 and β. The system of equations is then solved in an iterative fashion to determine the values of u_l, u_r, A_l and A_r.

2.5.2 Vessel junctions - bifurcations and anastomoses

The techniques used for discontinuities between vessels are applicable to the more complex modelling of vessel junctions, where three or more vessels meet. At such locations there is almost certainly a discontinuity in area and probably also in wall

properties in the idealised one-dimensional model. Once a vessel junction can be modelled it is then a trivial matter to extend the modelling to a complex network of vessels.

Arterial networks are primarily composed of bifurcations, arteries which split into two vessels, but there can also be anastomoses, where two arteries join to make one. Anastomoses are relatively uncommon in arterial networks, but occur in the placenta where the umbilical arteries join at the Hyrtyl's equilibrating anastomosis and in the human arterial tree there is an anastomosis in the head at the basilar artery and bypass grafts form anastomoses when the graft rejoins the host artery. There are also a number of trifurcations (arteries split into three), but these are rare and we will not consider them in our modelling. We discuss the modelling of bifurcations and anastomoses in the two following sections.

2.5.2.1 Bifurcations

From the governing system of equations written in terms of the characteristic variables W_1, W_2 (equations (2.55) and (2.56)) we know that the system can be interpreted in terms of a forward and a backward travelling waves. A typical bifurcation is shown in figure 2.2 where the parent vessel is denoted 1 and the upper and lower daughter vessels are labelled 2 and 3, respectively. At the bifurcation, x, there are six unknowns: (A_1, u_1) in the parent vessel; (A_2, u_2) in the upper daughter vessel and (A_3, u_3) in the lower daughter vessel.

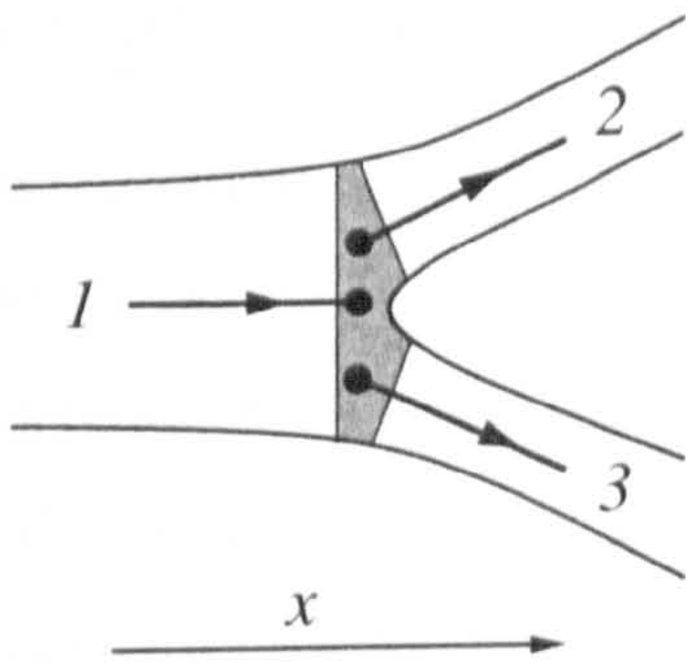


Figure 2.2: Bifurcation - One vessel joining into two.

From a characteristic perspective, information can only reach the bifurcation, x, from within vessel 1 by means of a forward travelling wave, W_1^1, of (A_1, u_1) in a similar manner to the inter-elemental boundaries. However, information can propagate

back to the bifurcation by backwards travelling waves within both daughter vessels 2 and 3, denoted $W_2^2(A_2, u_2)$ and $W_2^3(A_3, u_3)$. The travelling waves are functions of A and u and are governed by equations (2.81) and (2.82) and it is the hyperbolic nature of the problem that allows the system to be reduced to the three characteristic variables. The hyperbolic nature of the problem reduces the incoming information to three characteristic variables W_1^1, W_2^2 and W_2^3. The first three equations of the Riemann problem are obtained by specifying that the characteristic variables in each vessel remain constant along the characteristic lines. The characteristic variables for the non-linear system, can be written in terms of c as:

$$u_1 + 4(c_1 - c_0^1) = W_1^1 \tag{2.85}$$

$$u_2 - 4(c_2 - c_0^2) = W_2^2 \tag{2.86}$$

$$u_3 - 4(c_3 - c_0^3) = W_2^3 \tag{2.87}$$

where c_0^1, c_0^2, c_0^3 are the values of the wave speed c evaluated using the equilibrium area A_0 in vessels $1, 2$ and 3, respectively.

We now close the system using the conservation of mass and total pressure. For the bifurcation this results in a mass flux balance where $Q_1 = Q_2 + Q_3$ and that total pressure $p + \frac{1}{2}\rho u^2$ are continuous at the boundary, therefore:

$$A_1 u_1 = A_2 u_2 + A_3 u_3 \tag{2.88}$$

$$p_1 + \frac{1}{2}\rho u_1^2 = p_2 + \frac{1}{2}\rho u_2^2 \tag{2.89}$$

$$p_1 + \frac{1}{2}\rho u_1^2 = p_3 + \frac{1}{2}\rho u_3^2. \tag{2.90}$$

The whole set of equations is a non-linear system of algebraic equations which can be solved to determine the values (A_1, u_1), (A_2, u_2) and (A_3, u_3) at the bifurcation and provide an upwind flux at the junction. The inputs to the system are the material properties of the vessels, β, the equilibrium area at the bifurcation, A_0, and the values of W_1^1, W_2^2 and W_2^3 which can be evaluated from the initial equilibrium state (A^i, u^i) in each vessel.

2.5.2.2 Anastomoses

The solution technique at anastomoses is very similar, but here the flows are converging, rather than diverging. As stated this is relatively rare, but is obviously very

common on the venous side. A typical anastomosis is shown in figure 2.3

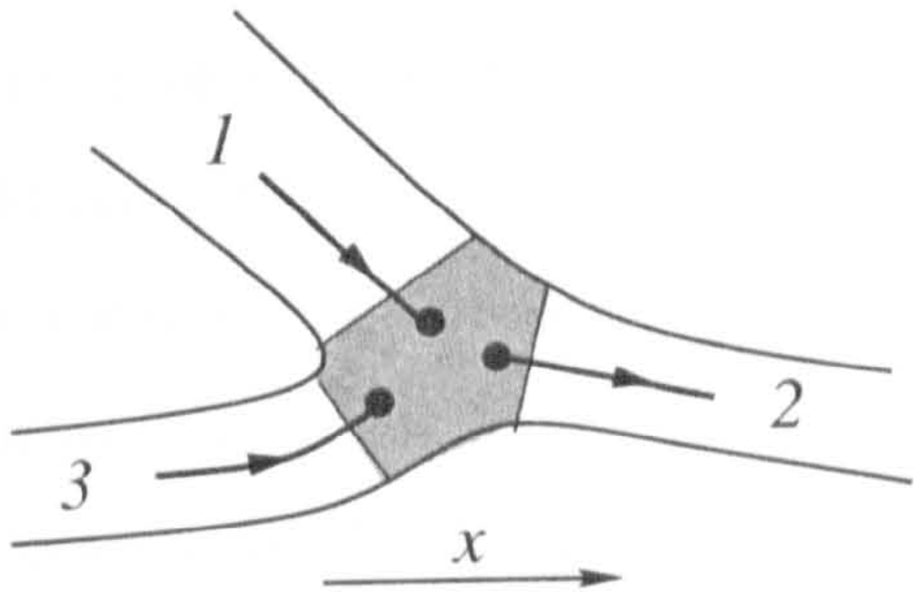


Figure 2.3: Anastomoses - Two vessels joining into one.

The information in this situation can reach the bifurcation through the forward travelling characteristic waves in both vessels 1 and 3 and through backward travelling waves in vessel 2, which result in the following characteristic equations:

$$u_1 + 4(c_1 - c_0^1) = W_1^1 \tag{2.91}$$

$$u_2 - 4(c_2 - c_0^2) = W_2^2 \tag{2.92}$$

$$u_3 + 4(c_3 - c_0^3) = W_1^3. \tag{2.93}$$

Mass conservation now becomes

$$A_1 u_1 + A_3 u_3 = A_2 u_2. \tag{2.94}$$

but continuity of total pressure remains unchanged and equations (2.89-2.94) define the algebraic equations which determine the values (A_1, u_1), (A_2, u_2) and (A_3, u_3).

As mentioned in section 2.1 this modelling does not consider the geometry of the junction, for example the branch angle has no effect. A modification to this modelling that accounts for the geometry of the bifurcation based on the ideas proposed by Holden and Risebro [58] is presented by Formaggia *et al* [38].

2.6 Inflow boundary conditions and terminal resistance

To complete the construction of the one-dimensional model we need to apply appropriate boundary conditions for both the analytic hyperbolic system and its discretisation. The subsonic nature of the problem means that a boundary condition is required at all boundaries of the domain, i.e. at the inflows and outflows. The boundary conditions are essentially the upwinded fluxes of the boundary elements and therefore are imposed through the characteristic representation of the system. We now describe the different inflow and outflow conditions we have investigated.

2.6.1 Inflow boundary conditions

At the inflow to the arterial tree, for example at the heart for the human arterial networks in Chapters 4 and 5, we can prescribe a value of velocity u, or area A, which means that the inflow boundary acts as a reflector for outgoing waves. Alternatively, given a variation in time of velocity u and area A we can determine the variation of the incoming characteristic $W_1(t)$ and impose this value through the upwinded flux in the discontinuous Galerkin formulation. This type of boundary condition acts as a pure absorber to outgoing waves.

Four different boundary conditions have been imposed at the inflow of the ascending aorta in the arterial networks in Chapters 4 and 5. Boundary conditions 1 and 4 have been imposed as a W_1 characteristic and boundary conditions 2 and 3 have been imposed as a velocity, u. They are all essentially a periodic half sine wave with a period of ~ 0.3 seconds, which approximates the period the aortic valve is open for. In the following section we explain how the different boundary conditions are implemented. The physical meaning of each boundary condition is explained in greater detail in the results section 4.3.1, Chapter 4.

We do not know the precise boundary conditions at the inflow to the arterial networks therefore we have had to investigate a number of different inflow boundary conditions. Although, it may in future be possible to obtain the in-vivo boundary conditions this requires an extra level of information about the system that is specific to the physiological state when the data was recorded. It would be more general if we could merely model the action of the heart and assessing these different boundary

conditions may be very revealing.

2.6.1.1 Absorber boundary condition (BC1)

The first boundary condition is imposed through the forward characteristic, W_1. It is specified as a pure absorber at the ascending aorta, which means that no waves are reflected back into the system at the inlet. A half sine wave is imposed as a W_1 characteristic for the first 0.3 seconds in every time period, T and then the characteristic is zero for the rest of the cycle. This boundary condition can be imposed for both the non-linear analysis through:

$$W_1 = u_l + 4\sqrt{\frac{\beta}{2\rho}}(A_l^{1/4} - A_0^{1/4}) \tag{2.95}$$

where

$$u_l = u_0 = 0, \quad A_l = \begin{cases} A_0 + \Delta A_{lmax} \sin\left(\frac{\pi t^*}{0.3}\right) & 0 < t^* < 0.3 \\ \\ A_0 & 0.3 < t^* < T \end{cases}$$

where t^* is the time within the cycle and is given by $t^* = t - (cycle * T)$ and $cycle$ is the cycle number of the periodic input,

or for linear analysis through:

$$W_1 = u_0 + \frac{a_l}{A_0^{3/4}}\sqrt{\frac{\beta}{2\rho}} \tag{2.96}$$

where

$$u_0 = 0, \quad a_l = \begin{cases} \Delta a_{lmax} \sin\left(\frac{\pi t^*}{0.3}\right) & 0 < t^* < 0.3 \\ \\ 0 & 0.3 < t^* < T \end{cases}$$

and ΔA_{lmax} and Δa_{lmax} are the maximum change in A_l and a_l for the W_1 characteristic in the non-linear and linear analysis respectively.

Note A_l is not the physical area of the artery, but is the characteristic area or Riemann state which is imposed at the inlet. The physical area, A^*, can be calculated at the inlet from the left and right travelling characteristics using equation (2.57). However, the exact value of the physical area can only be explicitly imposed through the W_1 characteristic when there are no reflections in the system and the W_2 characteristic is zero. Otherwise to enforce a fixed value of A^* requires W_1 to be a function of W_2.

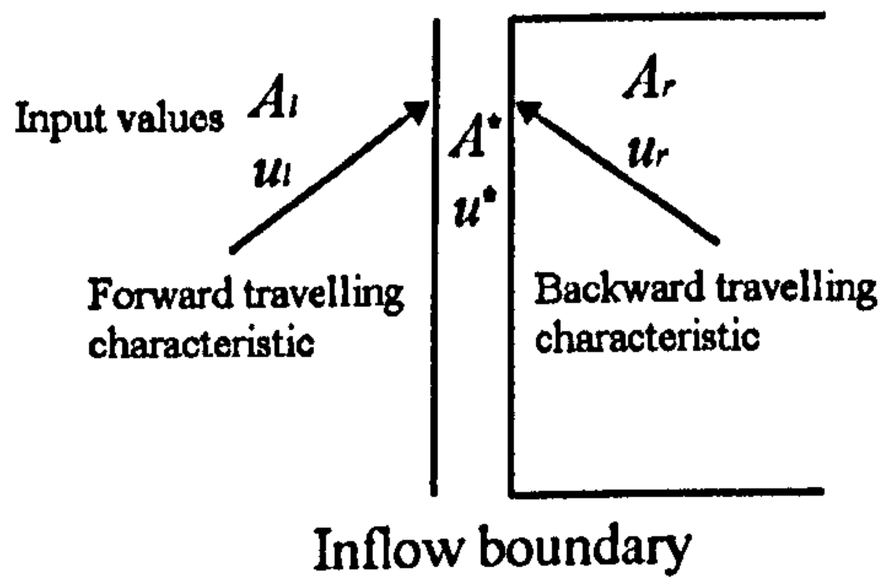


Figure 2.4: Characteristic information at the inflow boundary. $A^\star$ is dependent on both the forward and backward travelling characteristics.

For non-linear analysis substituting W_1 and W_2 at the inlet into equation (2.57) we obtain:

$$A^\star = \left(\frac{A_l^{1/4} + A_0^{1/4}}{2} \right)^4, \tag{2.97}$$

Rearranging this relationship and subtracting A_0 gives ΔA_l, which we can write in terms of the maximum values as:

$$\Delta A_{lmax} = A_{lmax} - A_0 = (2(A^\star_{max})^{1/4} - A_0^{1/4})^4 - A_0 \tag{2.98}$$

Therefore we have a relationship between the imposed characteristic, A_l, and the desired physical area, $A^\star$.

For linear analysis substituting W_1 and W_2 at the inlet into equation (2.77) and rearranging gives:

$$\Delta a_{lmax} = 2(A^\star_{max} - A_0), \tag{2.99}$$

These characteristic areas are those that we impose to give the desired maximum physical area change.

In this formulation the desired physical area can only be prescribed when there are no reflections in the system. As for most of our modelling there are reflections in the system, the desired value of $A^\star_{max}$ is only approximately enforced at the inflow.

The area to be imposed can also be calculated from a desired pressure, P, using equation (2.3). For example, for a desired maximum change of pressure, ΔP_{max}, in our system we can rearrange equation (2.3) to give:

$$A^\star_{max} = \left[\frac{\Delta P_{max}}{\beta} + \sqrt{A_0} \right]^2. \tag{2.100}$$

2.6.1.2 Velocity boundary condition (BC2)

Velocity boundary conditions are rigidly imposed through the characteristic variables, which are now coupled, i.e. $W_1 = f(W_2)$. For simplicity we detail only the desired resultant velocity used in our modelling. For boundary condition 2 the velocity at the ascending aorta was prescribed as a half sine wave for 0.3 seconds of the cycle followed by zero flow for the rest of the cycle. For both linear and non-linear analysis this was specified as:

$$u = \begin{cases} u_{max} \sin\left(\frac{\pi t^*}{0.3}\right) & 0 < t^* < 0.3 \\ \\ 0 & 0.3 < t^* < T \end{cases} \tag{2.101}$$

Prescribing u in this manner means that the inflow acts as a reflector boundary condition. Where $u = 0$ we know from equation (2.58) that $W_1 = -W_2$, therefore the backwards travelling wave is totally reflected at the inflow.

2.6.1.3 Velocity boundary condition with reversed flow (BC3)

Boundary condition 3 was also prescribed as a velocity, but the profile is more physiological. A small region of negative velocity is specified following the half sine wave, which was then followed by zero velocity. This is given for linear and non-linear analysis as:

$$u = \begin{cases} u_{max} \sin\left(\frac{\pi 25 t^*}{7}\right) & 0 < t^* < 0.28 \\ \\ u_{min}\left(\frac{t^* - 0.28}{0.02}\right) & 0.28 < t^* < 0.3 \\ \\ u_{min}\left(\frac{0.31 - t^*}{0.01}\right) & 0.3 < t^* < 0.31 \\ \\ 0 & 0.31 < t^* < T \end{cases} \tag{2.102}$$

2.6.1.4 Absorber/reflector boundary condition (BC4)

Boundary condition 4 was imposed as an absorber, W_1 characteristic, for the first 0.3 seconds and therefore was imposed in exactly the same way as for boundary

condition 1 for $t < 0.3$ seconds of the cycle. For the next 0.01 seconds the W_1 characteristic varies linearly between 0 and -W_2, to simulate the aortic valve closing. For the rest of the cycle it acts as a pure reflector at the inlet of the aorta, since the inflow characteristic wave is set to be equal to the negative of the backwards travelling wave, $W_1 = -W_2$, and therefore $u = 0$.

2.6.2 Terminal resistance

The human arterial system is a branching network consisting of many vessels. The main arteries split into smaller vessels, which in turn bifurcate into first arterioles and then the capillaries that comprise the micro-circulation.

Even using the rapid numerical techniques described in section 2.3 it is impractical to model the vast number of vessels in the microcirculation individually, not least because of the difficulties in obtaining the geometry data. Since we are primarily interested in the waveforms in the larger arteries we therefore reduce the problem in size and model only the major arteries of the network. This, of course, means that a model is required to simulate the effects of the more distal vessels and bifurcations. These will be reflecting the waves and therefore we choose to model their effect by prescribing a reflection coefficient on the terminal vessels. We denote this as the terminal resistance, R_t, which we define in terms of the forward and backward travelling waves, W_1 and W_2, as:

$$R_t = -\frac{W_2}{W_1}. \tag{2.103}$$

The reflection condition therefore sets the incoming, W_2 characteristic to be equal to the outgoing characteristic wave, W_1, scaled by the local reflection coefficient for each of the terminal vessels [111].

The definition assumes that W_1 and W_2 have been defined with respect to the equilibrium condition (equation (2.55) and (2.56)), thus a value of $R_t = 1$ implies total reflection of the outgoing wave, whereas $R_t = 0$ corresponds to no reflection, i.e. $W_2 = 0$ and is termed an absorbing outflow. Since $u = (W_1 + W_2)/2$ the definition (equation (2.103)) implies that $u = W_1(1 - R_t)/2$, thus a total reflector boundary condition means that the vessel is completely blocked and that on the

outflow, velocity equals zero.

In order to impose this type of boundary condition we again use the characteristics of the system. The velocity at the boundary, u^*, is given by equations (2.103) and (2.58):

$$u^* = \left[\frac{(u_0 + u_l)}{2} + 2(c_l - c_0)\right](1 - R_t) \tag{2.104}$$

where u_0 and c_0 are the values at the equilibrium state. The subscript l and r represent the values to the left and the right of the outflow boundary, taken to be at $x = L$. We also assume that $u_0 = 0$. The characteristic variable W_1 remains unaltered at the outflow boundary and is given as:

$$W_1 = u_l + 4c_l = u^* + 4c^*$$

where c^* at the boundary is:

$$c^* = \left[\frac{u_l - u^*}{4}\right] + c_l. \tag{2.105}$$

The incoming reflected wave, W_2, is given by:

$$W_2 = u_r - 4c_r = u^* - 4c^*. \tag{2.106}$$

If we now substitute equations (2.104) and (2.105) into equation (2.106) and assume that $c_l = c_r$ at the boundary, the values of u_r and A_r, which provide the outflow boundary conditions are given by:

$$\begin{aligned} u_r &= (1 - R_t)[(u_0 + u_l) + 4(c_l - c_0)] - u_l \\ A_r &= A_l. \end{aligned}$$

The boundary conditions for linear analysis are derived in a similar manner.

2.7 Reflection coefficients at bifurcations

To conclude the theory behind the one-dimensional modelling we note that for linear theory an exact reflection coefficient can be calculated at bifurcations. This is the relationship between the incoming perturbation of velocity and area with the change in perturbation at the bifurcation and is useful as an indication of the effect on the waveforms at different bifurcations.

We can derive this reflection coefficient, originally determined by Frank [42], using linear characteristic analysis and in the following section we do so for the (A, u) system, equations (2.1) and (2.7). We consider a simple bifurcation consisting of three vessels: a main vessel, 1, which splits into two daughter vessels 2 and 3. The equilibrium states in these vessels are denoted $\bar{u}_1$ & $\bar{a}_1$, $\bar{u}_2$ & $\bar{a}_2$ and $\bar{u}_3$ & $\bar{a}_3$ respectively. Initially, the equilibrium state in vessel 1 is perturbed by a small amount Δu_1 and Δa_1, so that there is a forward travelling wave in this vessel, figure 2.5 (a).

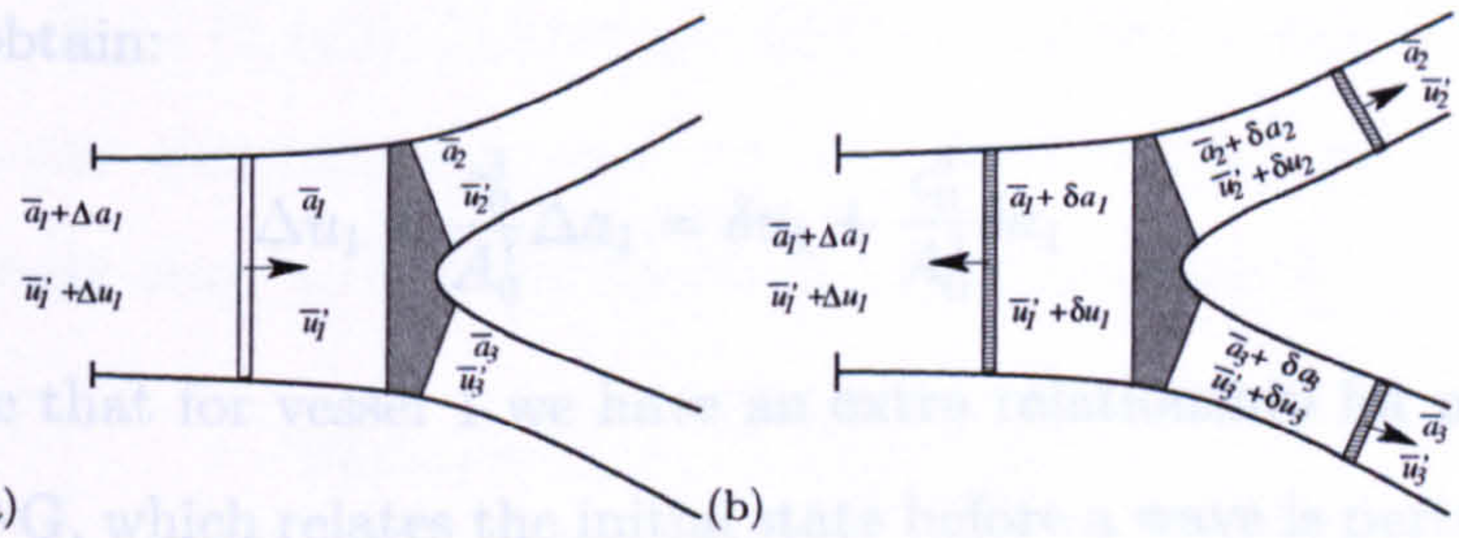


Figure 2.5: Simple bifurcation (a) The equilibrium state in vessel 1 is perturbed by a forward travelling wave. (b) The state in all vessels once the wave has reached the bifurcation.

Once this wave reaches the junction there is a change in the equilibrium states of all the vessels so that the perturbations are δa_i and δu_i. There is now a wave travelling in all three vessels δa_i and δu_i where i is the identity of the vessel, figure 2.5 (b).

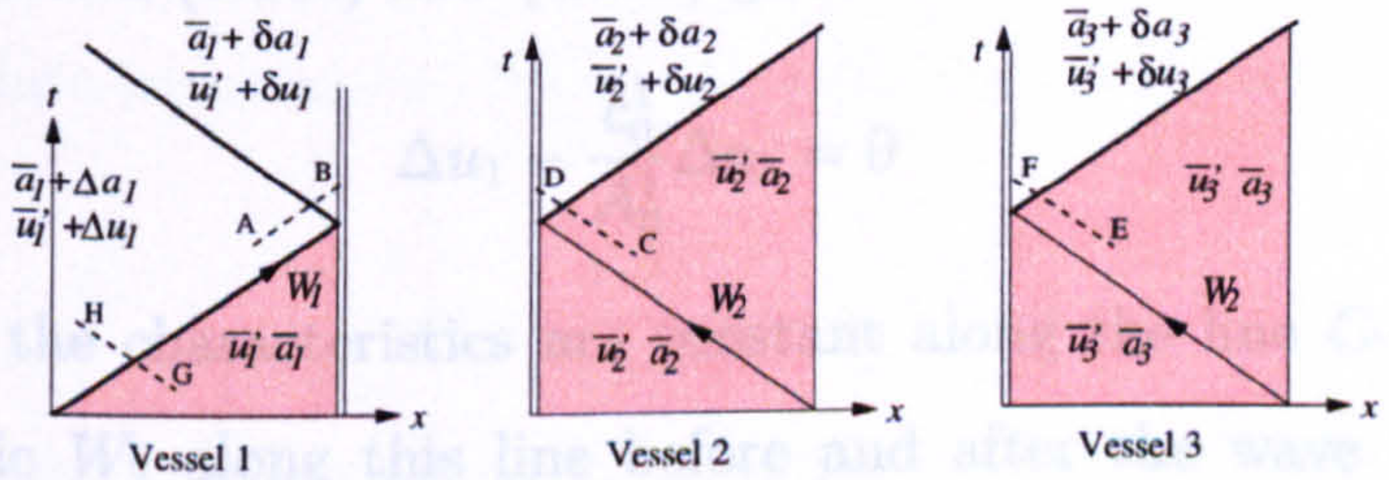


Figure 2.6: The characteristics at the different states in all three vessels.

In order to calculate the linear reflection coefficients at a bifurcation we write the relationships between the characteristics, before and after the wave has reached the bifurcation. Before the wave reaches the bifurcation we know that along a characteristic, say A-B, in figure 2.6, vessel 1, W_1^1 must be constant, therefore along

this characteristic:

$$W_1^1 = \bar{u}_1 + \Delta u_1 + \frac{c_0^1}{A_0^1}(\bar{a}_1 + \Delta a_1) \tag{2.107}$$

and after the wave has reached the bifurcation, W_1^1 must also be constant along this characteristic A-B but is given by:

$$W_1^1 = \bar{u}_1 + \delta u_1 + \frac{c_0^1}{A_0^1}(\bar{a}_1 + \delta a_1) \tag{2.108}$$

Substituting equation (2.108) into equation (2.107), so that W_1^1, $\bar{u}_1$ and $\bar{a}_1$ are eliminated we obtain:

$$\Delta u_1 + \frac{c_0^1}{A_0^1}\Delta a_1 = \delta u_1 + \frac{c_0^1}{A_0^1}\delta a_1 \tag{2.109}$$

We also note that for vessel 1 we have an extra relationship for a characteristic along the line H-G, which relates the initial state before a wave is perturbed in vessel 1:

$$W_2^{10} = \bar{u}_1 - \frac{c_0^1}{A_0^1}\bar{a}_1 \tag{2.110}$$

with the state once the wave is perturbed:

$$W_2^{10} = \bar{u}_1 + \Delta u_1 - \frac{c_0^1}{A_0^1}(\bar{a}_1 + \Delta a_1) \tag{2.111}$$

Substituting equation (2.110) into (2.111) gives:

$$\Delta u_1 - \frac{c_0^1}{A_0^1}\Delta a_1 = 0 \tag{2.112}$$

For vessel 2 the characteristics are constant along the line C-D and therefore the characteristic W_2 along this line before and after the wave has reached the bifurcation are given by:

$$W_2^2 = \bar{u}_2 - \bar{a}_2\frac{c_0^2}{A_0^2}, \tag{2.113}$$

$$W_2^2 = \bar{u}_2 + \delta u_2 - \frac{c_0^2}{A_0^2}(\bar{a}_2 + \delta a_2) \tag{2.114}$$

which when combined gives:

$$\delta u_2 - \frac{c_0^2}{A_0^2}\delta a_2 = 0 \tag{2.115}$$

Similarly for vessel 3, W_2^3 are constant along the line E-F and can be combined to give:

$$\delta u_3 - \frac{c_0^3}{A_0^3}\delta a_3 = 0 \tag{2.116}$$

We also assume continuity of mass and total pressure at the bifurcation in our modelling, where the linearised mass flux at the bifurcation is:

$$A_0^1\delta u_1 = A_0^2\delta u_2 + A_0^3\delta u_3, \tag{2.117}$$

Substituting equations (2.109), (2.115) and (2.116) into the continuity of mass equation (2.117) we can eliminate δu_1, δu_2 and δu_3, we can then substitute equation (2.112) to eliminate Δu_1, and we finally obtain the relationship:

$$2c_0^1\Delta a_1 - c_0^1\delta a_1 = c_0^2\delta a_2 + c_0^3\delta a_3 \tag{2.118}$$

The linearised total pressure at the bifurcation is:

$$\delta p_1 = \delta p_2 = \delta p_3 \tag{2.119}$$

To eliminate δp in the total pressure we can write it in terms of the linearised c_0, from equation (2.5) which can be rearranged to be written as:

$$\delta p = \frac{(c_0)^2\rho}{A_0}\delta a \tag{2.120}$$

Substituting δp into equation (2.119) we can write the conservation of total pressure as:

$$\frac{(c_0^1)^2}{A_0^1}\delta a_1 = \frac{(c_0^2)^2}{A_0^2}\delta a_2 = \frac{(c_0^3)^2}{A_0^3}\delta a_3 \tag{2.121}$$

By substituting the total pressure conservation (equation (2.121)) into equation (2.118) we can eliminate δa_2 and δa_3 and rearranging gives:

$$\frac{\delta a_1}{\Delta a_1} = \frac{2\frac{A_0^1}{c_0^1}}{\left(\frac{A_0^1}{c_0^1} + \frac{A_0^2}{c_0^2} + \frac{A_0^3}{c_0^3}\right)} \tag{2.122}$$

Finally to obtain the reflection coefficient, R_c, we note that consistent with the work on surface tidal waves [71], R_c can be defined as the ratio of the change of pressure across the reflected wave, $\hat{\delta p} = \delta p - \Delta p$, to the change of pressure in the incident wave, Δp. From equation (2.120) we note that a change in pressure is

equivalent to a change in area, the reflected wave $\delta\hat{a}_1$ is defined as $\delta\hat{a}_1 = \delta a_1 - \Delta a_1$ and so the linear reflection coefficient for our problem can be written as [134]:

$$R_c = \frac{\delta\hat{a}_1}{\Delta a_1} = \frac{\left(\frac{A_0^1}{c_0^1} - \frac{A_0^2}{c_0^2} - \frac{A_0^3}{c_0^3}\right)}{\left(\frac{A_0^1}{c_0^1} + \frac{A_0^2}{c_0^2} + \frac{A_0^3}{c_0^3}\right)} \tag{2.123}$$

Chapter 3

Validation of the computational code

This thesis is, at least in part, concerned with assessing the usefulness and accuracy of modelling blood flow in arterial networks using a one-dimensional approximation. However, before the numerical results can be meaningfully compared with physiological results and the effects of different modelling assumptions assessed, it is important to ensure that the numerical scheme has been implemented correctly. In this chapter we therefore present some of the validation techniques we have used to ensure that our numerical results are accurate solutions to the problems we impose.

The numerical scheme described in Chapter 2 is consistent and convergent, but because it is an explicit scheme it is not unconditionally stable. The time step must therefore meet criteria (section 3.2) for the solution to be stable, but once this is satisfied then the solutions should increase in accuracy with increasing numbers of elements, polynomial order and decreasing time step. There is however an increase in computational cost for this improved accuracy and a compromise must be reached between accuracy and the time required for the computation. In this chapter we therefore assess the effect that different computational parameters have on the accuracy and cost of the calculations and determine a set of parameters that we can use to compute our results. We then go on to validate the code against simple analytical test problems, before finally comparing our results with those produced by a similar code on the same small network.

3.1 Sources of error

When performing any experiments it is important to be conscious of the possible sources of error in the results. This is particularly true for numerical modelling, because results are produced that appear accurate and definitive, due to the fact that they are quoted to a high number of significant figures. The temptation is therefore to accept the results unquestioningly and not to consider the likely sources of error and their impact.

For computational modelling the errors can be grouped into three categories:

1) Modelling errors

2) Discretisation errors

3) Convergence errors

Modelling errors are introduced by differences between the physical situation to be approximated and the mathematical model used. There are two distinct category of modelling errors: those introduced by the assumptions made when deriving the governing equations to simulate the physical situation and those that are due to assumptions regarding the geometry of the domains to be modelled and the boundary conditions that are applied. We clearly make a great deal of approximations both in deriving the equations (blood flow is three-dimensional not one-dimensional) and in simplifying the domain. Some aspects relating to these simplifications are discussed in both Chapter 2 and the results and much of the investigation is devoted to assessing the impact of the geometrical and boundary condition assumptions (Chapters 4 and 5).

Discretisation errors, also known as consistency, are due to the difference between the exact solution of the governing equations and the exact solution to the set of algebraic equations that are used to approximate the governing equations. Convergence errors are also related to the numerical scheme and are the differences between the exact solution and the numerical solution of the algebraic equations.

3.2 Stability

Hyperbolic systems such as those described in Chapter 2 can be considered to have two forms of error: amplitude and phase error. Numerical schemes will typically

introduce a phase error, which if related to the physical conditions, can be considered as a dispersive error, however they should not introduce an amplitude, or dissipation, error. Stability is the requirement that the magnitude of the solution is not increased with time, i.e. the amplitude error is not positive, consequently schemes where the amplitude declines are sometimes known as overstable schemes. To meet this requirement in an explicit scheme such as ours, the condition that must be satisfied is the CFL, or Courant condition which states that the Courant number must be less than or equal to a constant, C, that is dependent on the numerical scheme i.e.

$$\frac{c\Delta t}{\Delta x} \leq C$$

where the left hand side is the Courant number, Δt is the time step and Δx is the distance between discretisation points and c is the wave propagation speed. For the non-linear computations the limit becomes:

$$\frac{(c+u)\Delta t}{\Delta x} \leq C$$

where u is the velocity. For our choice of quadrature points the grid spacing, Δx, varies with $1/P^2$ and $1/N_{el}$, where P is the polynomial order and N_{el} is the number of elements per vessel.

These limits can be derived using the von Neumann stability analysis [34] approach and can be interpreted physically as the requirement that information must not propagate through more than one section of the discretised domain in a single timestep and are clearly related to the propagation of the characteristics discussed in section 2.4. For a more detailed discussion of stability see Hirsch [57]. Implicit schemes can be unconditionally stable, but difficulties arise when solving non-linear hyperbolic equations, as we do, when implicit schemes can introduce an amplitude error and hence may be unstable, or dissipative [33]. Such uncertainties have prompted us to use the explicit discontinuous Galerkin approach described in Chapter 2 which is not dissipative and has excellent phase accuracy and we simply tolerate the time-step limitation. From the following sections, where we discuss the convergence and computational times required for the solutions, we see that this is not too onerous.

3.3 Convergence testing

For a numerical method to be convergent the solution of the discretised equations must tend to the exact solution of the differential equation as the grid spacing tends to zero. The Lax equivalence theorem [124] says that "given a properly posed linear initial value problem and a finite difference approximation to it that satisfies the consistency condition, stability is a necessary and sufficient condition for convergence." For non-linear problems, where the boundary conditions have a strong influence, equivalence can only be inferred and is typically proved by example.

For an unsteady problem, such as blood flow in arterial networks there are a number of parameters that are important when determining the accuracy of the numerical solutions. We therefore present the results of our convergence tests which were computed for varying numbers of cycles, polynomial order, time steps per cycle and number of elements per artery.

Convergence tests were first performed on a wave in a simple tube with a reflector boundary condition at the outflow and an absorber boundary condition (BC1) at the inflow to validate the numerical techniques. We then performed computations on the 55 well-matched arterial network of Wang and Parker. The input to the arterial network was boundary condition 3, (described in section 2.6) with a peak velocity of 1 m/s dropping to a negative value of -0.33 m/s. The time period of the cycle was 0.75 seconds and a reflection coefficient of 0.5 was applied to the end of every terminal vessel. This well-matched network is described in more detail in Chapter 4.

3.3.1 Convergence in a single tube

We begin by analysing the convergence of the solution within a single tube. A half-sine wave is imposed at the inlet of the domain using boundary condition 1, an absorber boundary condition, and a terminal resistance of 0.5 on the outflow. Waves do not become trapped within the system and there are therefore a maximum of two waves in the tube, the imposed wave and the reflected wave. The solution was assessed for the linear code to enable a simple comparison with the analytical solution. Figure 3.1 (a) shows the convergence of the error with polynomial order

at a single time and location within the cycle and exhibits the expected exponential convergence to machine accuracy, which occurs by polynomial 8. This is in contrast to the slower algebraic convergence with linear elements shown in figure 3.1 (b).

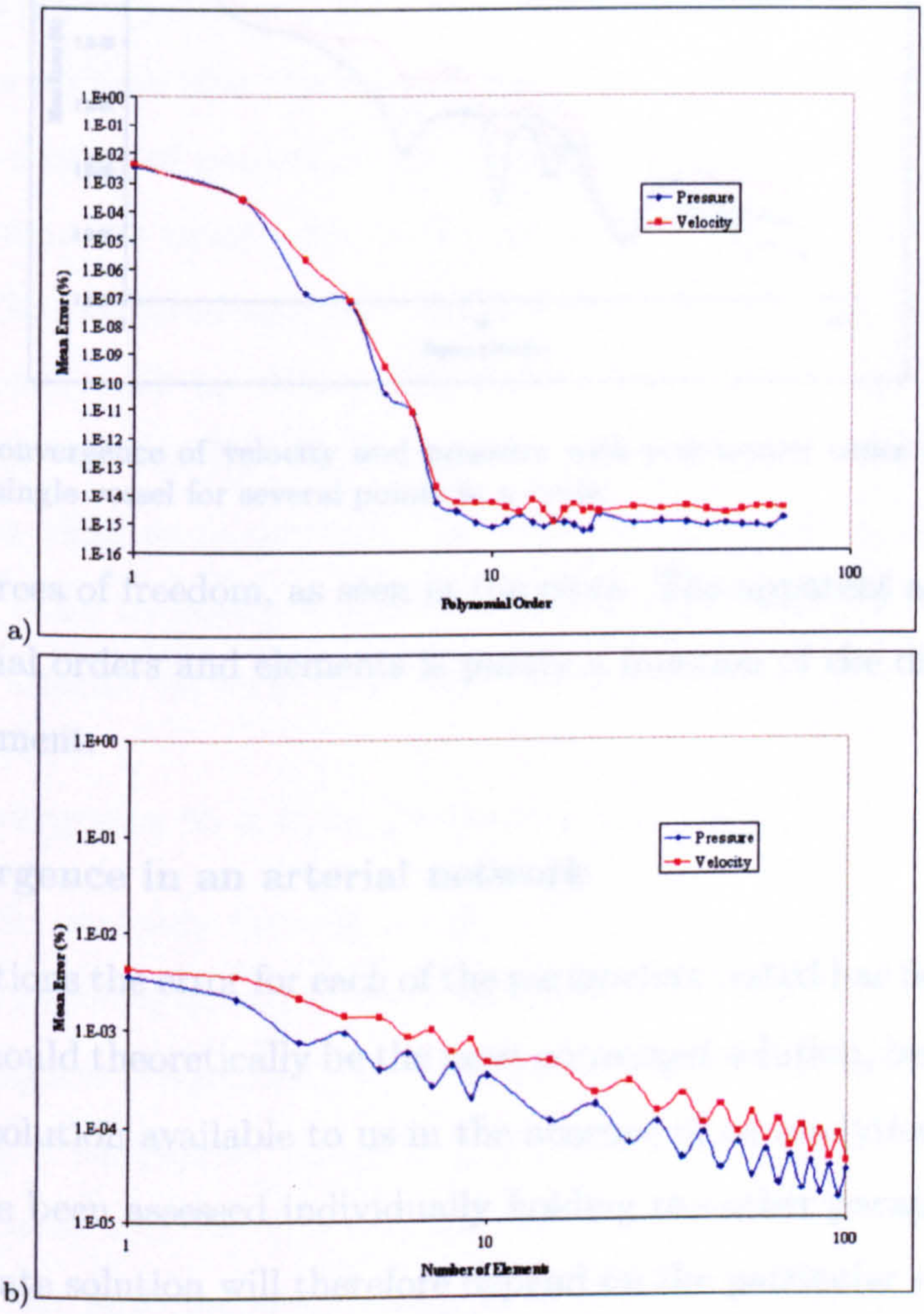


Figure 3.1: Convergence of velocity and pressure with (a) polynomial order and (b) number of elements in a single vessel at one time.

Slightly more demanding graphs are shown in figure 3.2 for convergence with polynomial order and number of elements. The elemental convergence is shown for a polynomial of order 8 on each element for this plot. The convergence with elements and polynomial order is very similar, but is not so rapid as the polynomial convergence in figure 3.1 (a). This is because the errors have been assessed at a number of discrete times within the cycle and are highlighting errors associated with the discontinuous nature of the input wave. The choice of a half sine wave means that there are two slope discontinuities, which are difficult to resolve numerically and introduce bumps into the solution. These bumps reduce in size with increasing

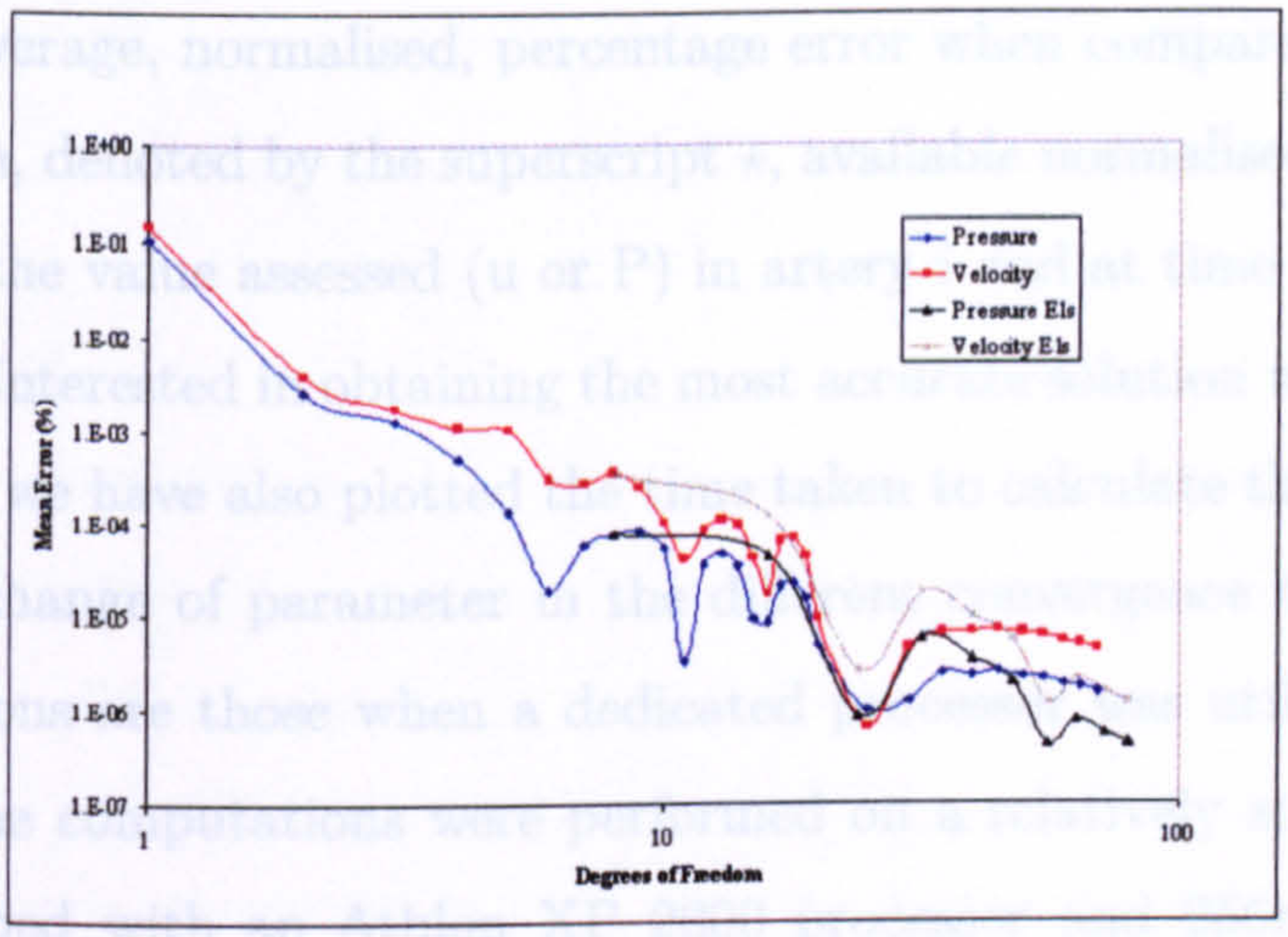


Figure 3.2: Convergence of velocity and pressure with polynomial order and number of elements in a single vessel for several points in a cycle.

numbers of degrees of freedom, as seen in the plots. The apparent accuracy of some of the polynomial orders and elements is purely a function of the discrete nature of the error assessment.

3.3.2 Convergence in an arterial network

In these calculations the error for each of the parameters tested has been assessed relative to what should theoretically be the most converged solution, because this is the most accurate solution available to us in the absence of an analytical solution. The parameters have been assessed individually holding the other parameters constant. The most accurate solution will therefore depend on the particular convergence test and will be either the solution with the most cycles, the highest polynomial order, the highest number of elements per vessel or the lowest time step. To obtain an estimate for the errors the velocity and pressure have been sampled in eight arteries of the well-matched arterial network for each convergence test and at 6 different times in the cycle. These arteries are 1, 7, 8, 27, 41, 15, 52 and 54, which provides a good sample of arteries throughout the body, with different properties, locations and sizes. In fact these are the same eight arteries for which results are shown for in Chapter 4. The errors have been normalised by reference values of pressure and velocity for each artery and have been expressed as a percentage. This can be written as:

$$\varepsilon = \sum_{i=1}^{8}\sum_{j=1}^{6}\left((\phi_{ij} - \phi^{\star}_{ij})^2\right)^{1/2} / \sum_{i=1}^{8}\sum_{j=1}^{6}\phi^{\star}_{ij} \times 100 \qquad (3.1)$$

where ϵ is the average, normalised, percentage error when compared with the most accurate solution, denoted by the superscript $\star$, available normalised by the solution itself and ϕ_{ij} is the value assessed (u or P) in artery i and at time j.

Since we are interested in obtaining the most accurate solution within reasonable time constraints we have also plotted the time taken to calculate the solution for 10 cycles for each change of parameter in the different convergence tests. The times for the calculations are those when a dedicated processor was utilised to compute the solution. The computations were performed on a relatively standard personal computer equipped with an Athlon XP 2000 processor and $256mb$ memory; the operating system was Red Hat Linux 7.3.

These results allow us to determine the most suitable discretisation parameters to be chosen in order to rapidly compute accurate velocity and pressure waveforms in the different arterial networks considered in later chapters of this thesis.

3.3.2.1 Convergence to a time periodic solution

For time-periodic unsteady flows it is not sufficient to run the computation for a single cycle to obtain an accurate solution, because the initial conditions have an effect that propagates throughout the cycle. As the solution develops the conditions at the beginning of subsequent pulses throughout the network become more similar to the time periodic solution and consequently the differences between successive cycles decrease. We have therefore assessed the number of cycles required to obtain a converged solution as a first step. The one-dimensional code was used to compute the velocity and pressure for 20 cycles (15 seconds) for the entire well-matched network. These were computed with a polynomial of 8, a time step of $\Delta t = 10^{-5}s$ and only one element in each vessel. The last cycle was assumed to be the most accurate, therefore the error for all the other cycles was calculated using this last cycle as a reference solution. The convergence graph is shown in figure 3.3, where for clarity the mean percentage difference is plotted on a log axis. This convergence can be thought of as a measure of transition into a time periodic state.

On this graph there is a linear decrease in the error with an increasing number of cycles, hence an exponential decrease in error, until approximately the 13th cycle. Beyond this point the error does not decrease significantly, which is likely to be

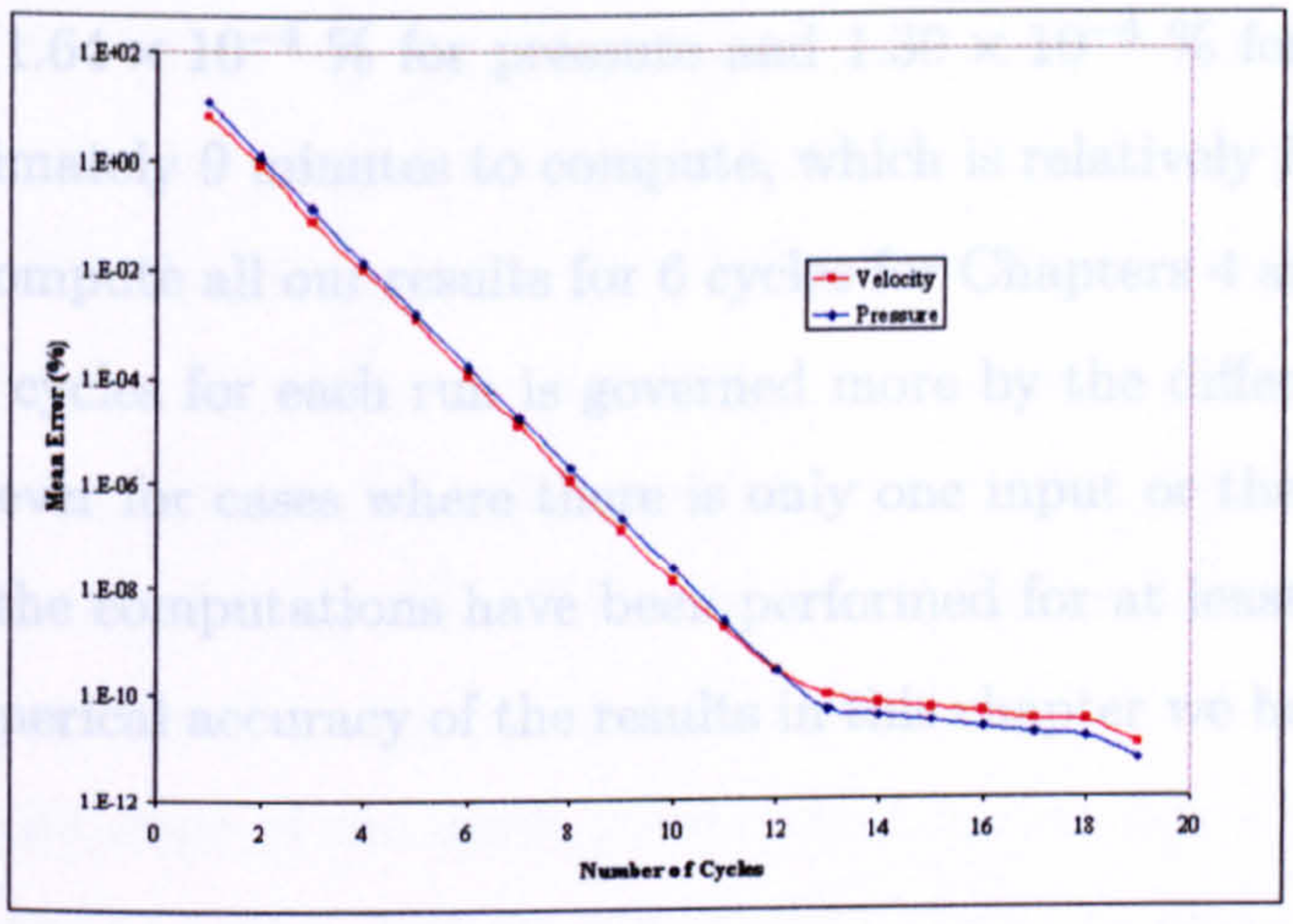


Figure 3.3: Convergence of velocity and pressure to a time periodic state with number of cycles.

due to the solution only being written out to 12 significant figures and also the computations are approaching the machine accuracy of the computer. The error by cycle 13 is very small, approximately 4.91×10^{-11} % for pressure and 8.40×10^{-11} % for velocity.

The velocity and pressure waveforms are shown for 10 cycles (7.5 seconds) in figure 3.4 for the ascending aorta (artery 1) at the beginning of the network and the posterior tibial (artery 54) at the end of the arterial network. The main features of the waves have appeared in the first cycle and the waves are almost fully established and visually close to convergence as early as cycle two. The velocity appears to converge more rapidly than the pressure, which is perhaps because the velocity has been imposed at the inflow.

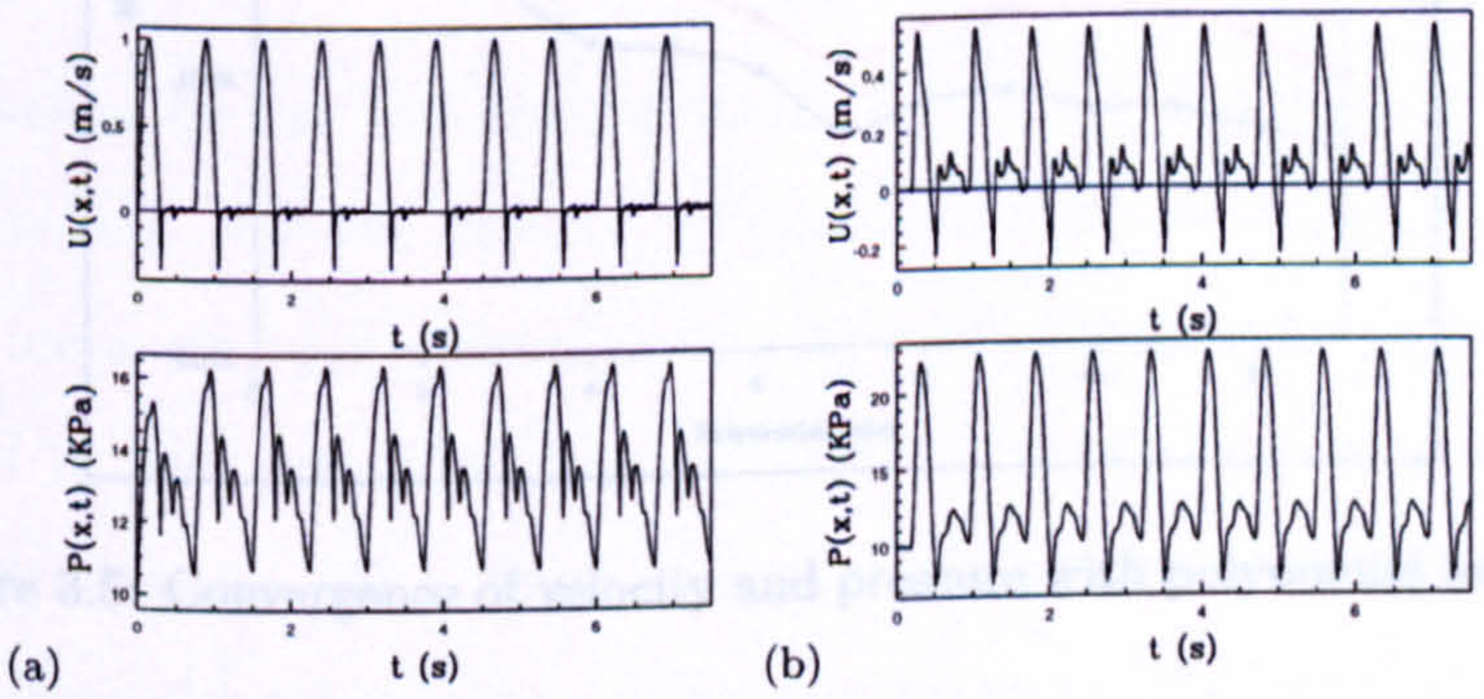


Figure 3.4: Waveforms in artery 1 (a) and artery 54 (b) for the first 10 cycles showing that the waves are very similar as early as the 2nd cycle.

It took approximately 28 minutes of processor time for 20 cycles of the arterial waveforms to be computed, however the solution appears adequately converged by

the sixth cycle (1.64×10^{-4} % for pressure and 1.30×10^{-4} % for velocity). This will take approximately 9 minutes to compute, which is relatively fast, therefore we have chosen to compute all our results for 6 cycles for Chapters 4 and 5. In Chapter 6 the number of cycles for each run is governed more by the differences in the two input rates, however for cases where there is only one input or the inputs have the same frequency the computations have been performed for at least 6 cycles. When assessing the numerical accuracy of the results in this chapter we have actually used 10 cycles.

3.3.2.2 Convergence with polynomial order

To assess the convergence of the solution with Polynomial order the waveforms in the well-matched network were computed for polynomial orders of 1 to 15. These were computed for 10 cycles with a time step of $\Delta t = 10^{-5}s$ and 1 element per vessel. The errors for the polynomial order solutions were calculated relative to the reference solution, polynomial order 15. Again the ensemble average of the percentage error was calculated for the 8 arteries and the six time points in the tenth cycle (equation (3.1)).

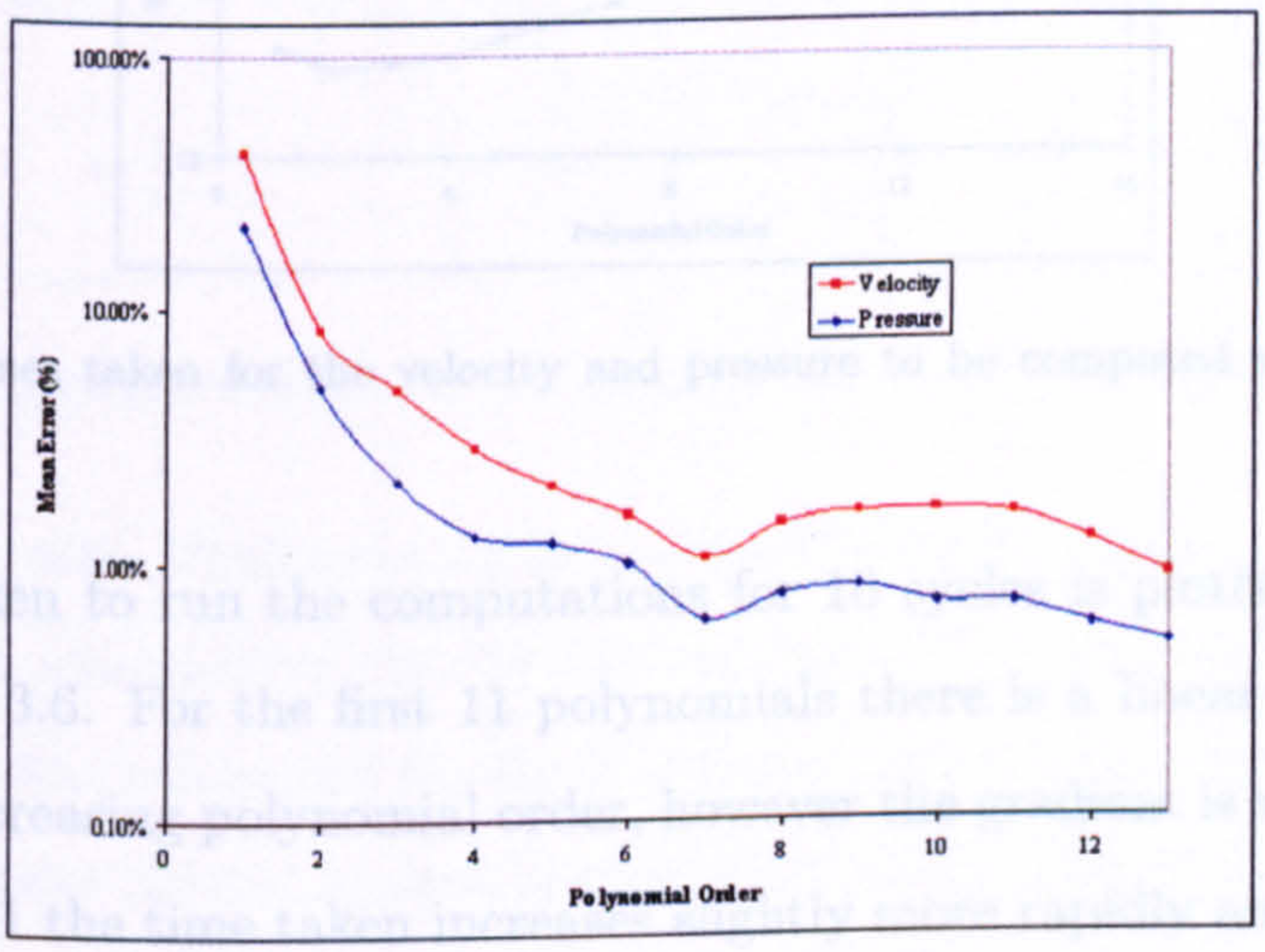


Figure 3.5: Convergence of velocity and pressure with polynomial number.

The mean percentage error is plotted on a log scale against the polynomial order in figure 3.5. As can be seen there is a very large error for polynomial 1, approximately 21.48 % for pressure and 42.09 % for velocity, but by polynomial order 7 the error is relatively small, approximately 0.6 % for pressure and 1.04 % for veloc-

ity. The velocity (red line) has a slightly higher error than the pressure (blue line). The convergence rate slows beyond this point and the errors are still relatively large when compared with the convergence plots for the number of cycles and time step. A possible explanation for this is that the large errors occur where the gradients are large and that as the polynomial order increases the results become better resolved in time, which can therefore greatly affect the results, but not necessarily is a consistent manner throughout the network. Another source of error is introduced by the discontinuity in the slope of the input wave caused by the use of a half sine wave. The dispersion errors (section 3.2) are also likely to be most affected by changes in the spatial discretisation. The errors will also have a tendency to accumulate due to the reflector boundary conditions on the inflow and outflows of the network, which will lead to the waves being trapped for great lengths of time and allows the errors to accumulate.

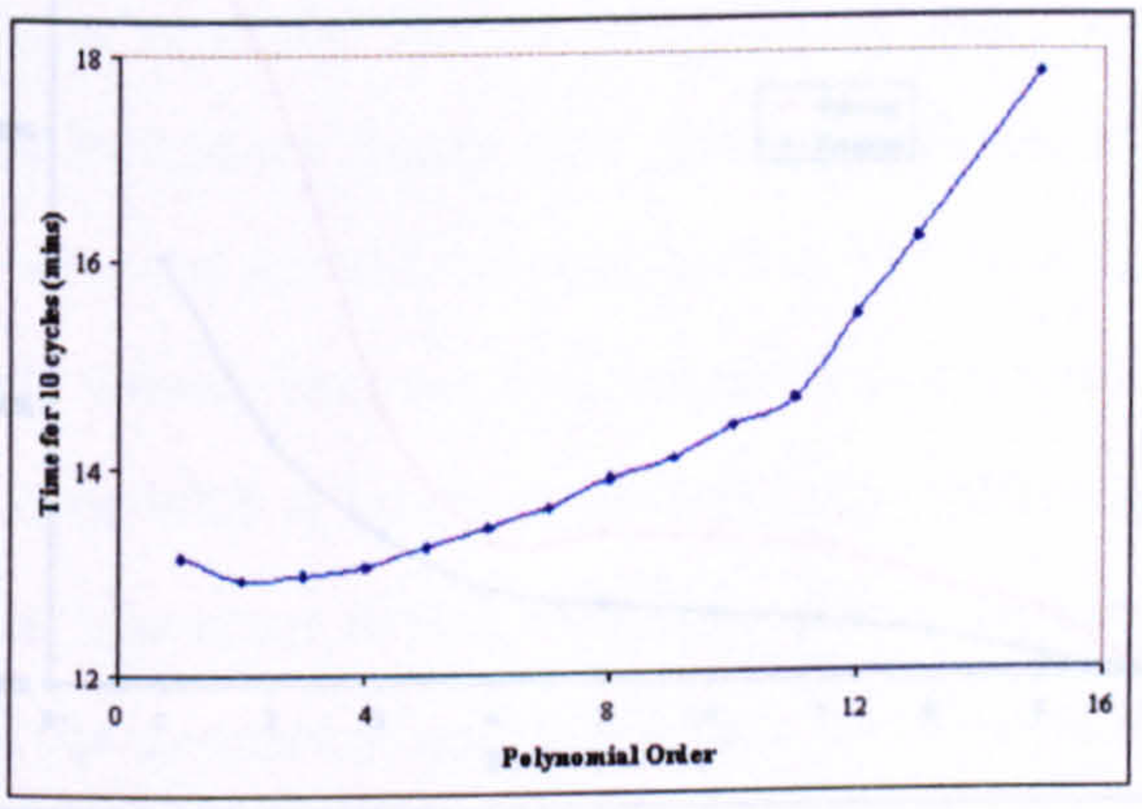


Figure 3.6: Times taken for the velocity and pressure to be computed with polynomial number.

The time taken to run the computations for 10 cycles is plotted for each polynomial in figure 3.6. For the first 11 polynomials there is a linear increase in time required with increasing polynomial order, however the gradient is very shallow. After polynomial 11 the time taken increases slightly more rapidly and polynomial 15 takes nearly 18 minutes. All of these computations are however relatively fast, there is only approximately 4.5 minutes difference between the fastest and the slowest calculation, which shows that the computational cost of increasing the polynomial order within this range is relatively minor. From these results and those in section 3.3.1 it appears that choosing the polynomial to be 8 provides a good combination of accuracy, stability and speed and thus this is what we have used to compute the

results for the thesis.

3.3.2.3 Convergence with number of elements per artery

To calculate the convergence of the solution with an increasing number of elements per artery, each vessel was evenly divided into a number of elements for each different element test. The velocity and pressure waveforms for the arteries were calculated for 10 cycles at polynomial number 8 and using a time step of $\Delta t = 2 \times 10^{-6} s$. Not all calculations would compute with the larger time step of $\Delta t = 10^{-5} s$, which was used in the previous tests, for a high number of elements per vessel, so a lower time step had to be used. The lack of convergence was due to the stability criteria being violated as the number of degrees of freedom increased and hence Δx decreased.

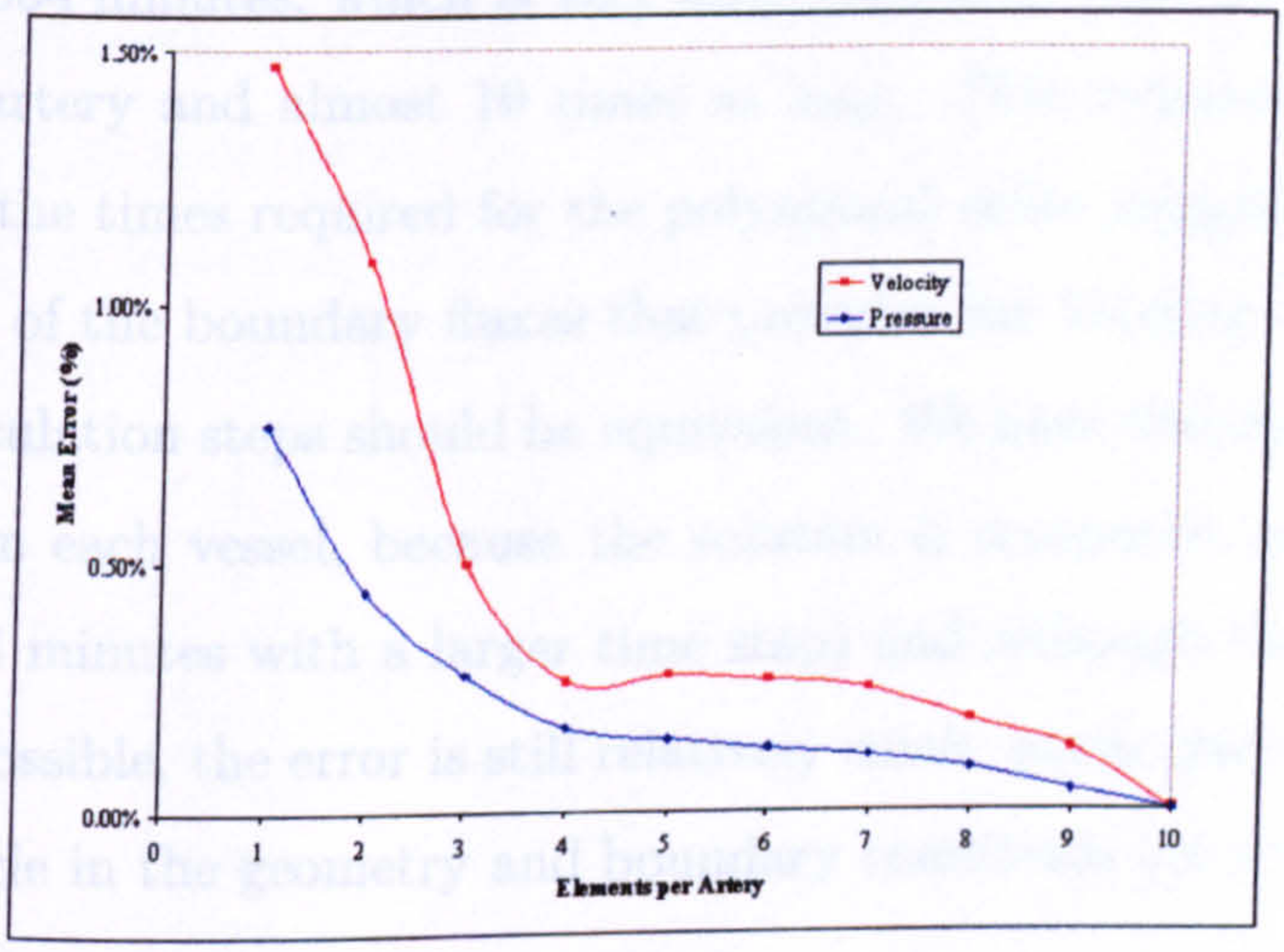


Figure 3.7: Convergence of velocity and pressure with number of elements per artery.

The solution with 10 elements was assumed to be the most accurate and the errors have been assessed relative to this solution. The ensemble average of the percentage error was calculated for the 8 arteries and at 6 time points in the tenth cycle and the error is plotted against elements per artery in figure 3.7. The accuracy improves significantly up to 4 elements per artery where the difference is less than 0.25 %, but beyond this the improvement in accuracy is slow and relatively linear. The accuracy is actually still quite good with only one element with differences that are not very large, only 0.77 % for pressure and 1.47 % for velocity.

The time taken to compute 10 cycles for each case of different numbers of elements per artery was also calculated and is shown in figure 3.8. The time increases

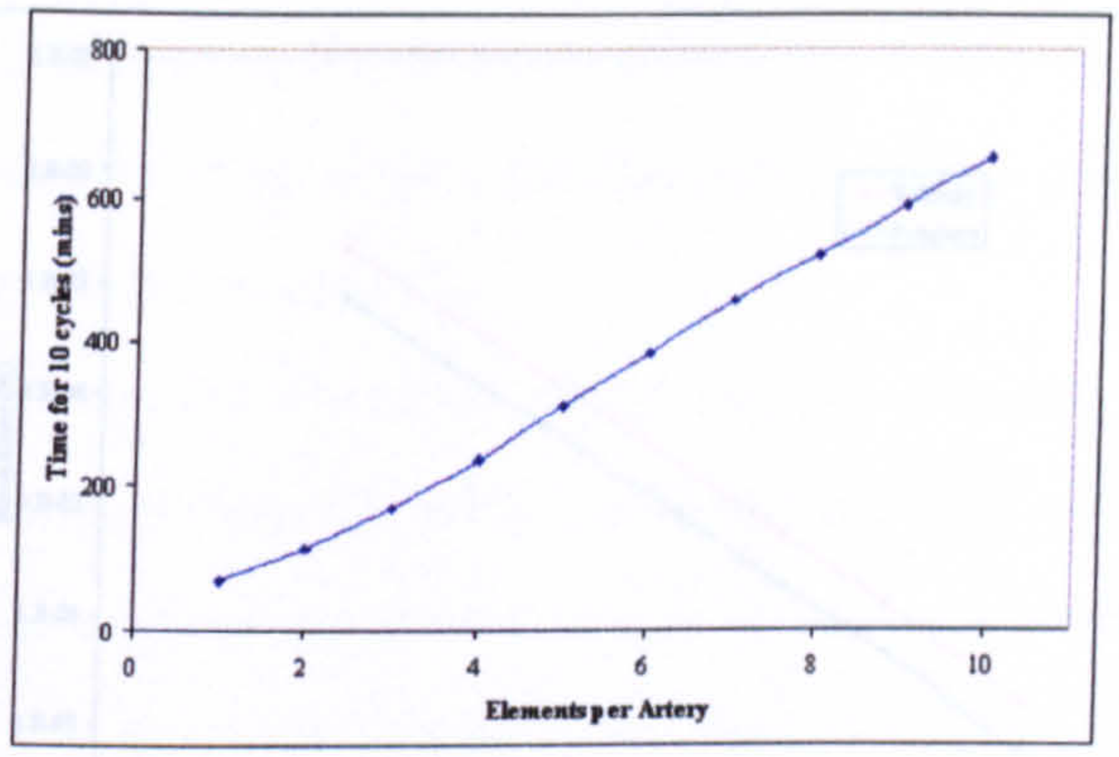


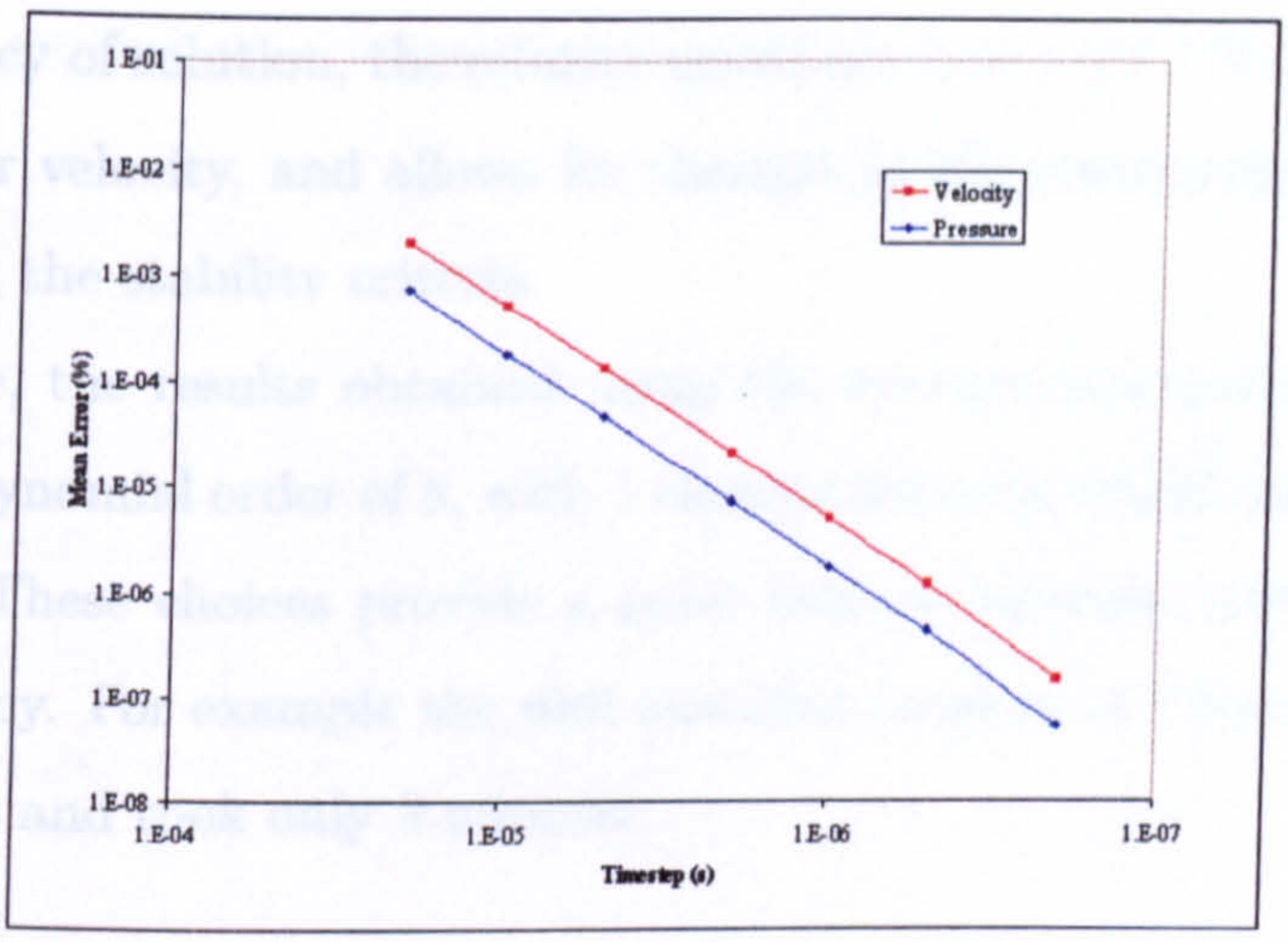
Figure 3.8: Times taken for the velocity and pressure to be computed with elements per artery.

linearly with number of elements per artery but it is the gradient that is significant. With 10 elements per artery the time taken to compute the solution for 10 cycles is approximately 654 minutes, which is very large compared with 69 minutes for only 1 element per artery and almost 10 times as long. This increased gradient when compared with the times required for the polynomial order suggests that it may be the calculations of the boundary fluxes that provides the limiting step as the number of other calculation steps should be equivalent. We have therefore chosen to use just 1 element in each vessel, because the solution is computed extremely quickly for 10 cycles (14 minutes with a larger time step) and although the solution is not as accurate as possible, the error is still relatively small, particularly when the large assumptions made in the geometry and boundary conditions are considered.

3.3.2.4 Convergence with time step

The final convergence test is to determine the sensitivity of the solution to the size of the time step. The velocity and pressure waveforms have been computed with a polynomial order of 8, using 1 element in each vessel and for 10 cycles. Again, the ensemble average of the percentage error was calculated for the 8 arteries and for 6 time points in the tenth cycle and was assessed relative to the solution with a time step of $\Delta t = 10^{-7}s$, 1 element and a polynomial of 8. The percentage error is plotted against the time step, both on log scales, in figure 3.9.

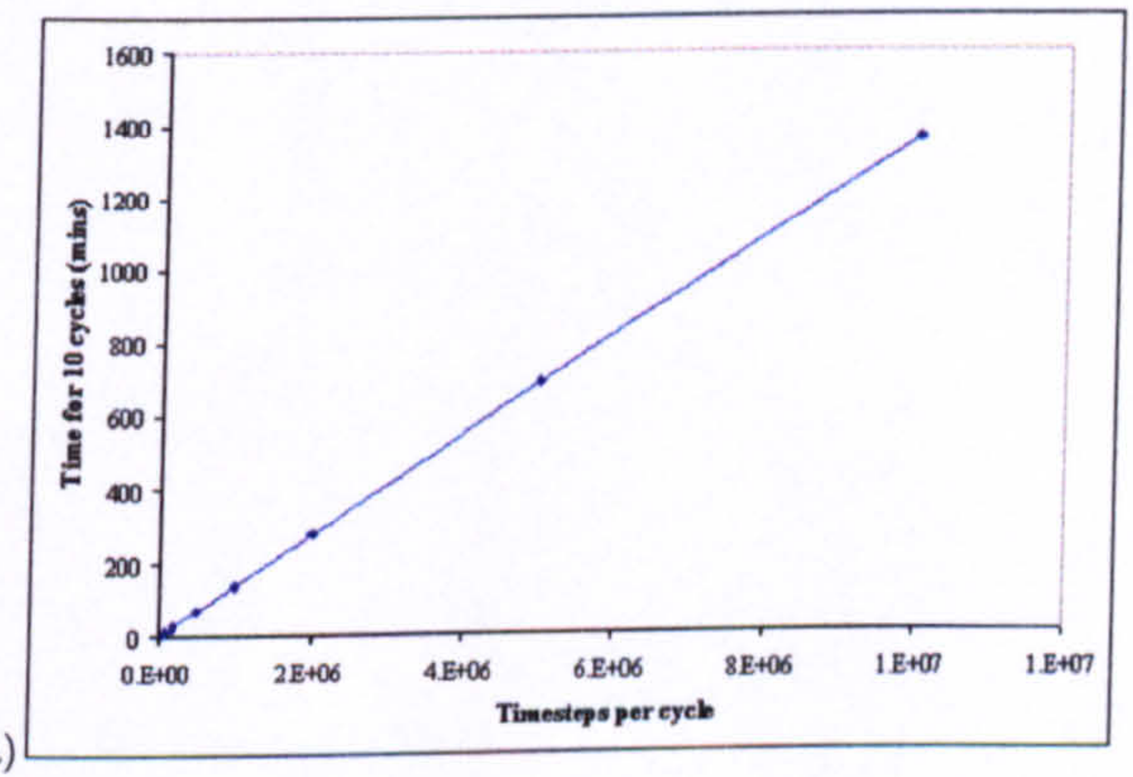
On this log/log graph there is a linear relationship between the variables, where decreasing the time step also decreases the mean error. The effect of the time step



(a)

Figure 3.9: Convergence of velocity and pressure with time step.

on the solution is relatively minor, because the errors for the largest time step that the solution would converge for are the order of 0.001%, thus if the solution is stable it is automatically of good accuracy. The gradient of these slopes are both 2, which is consistent with a second order accurate, $O(\Delta t^2)$, solution technique, such as the Adams Bashforth method we have employed.



(a)

Figure 3.10: Times taken for the velocity and pressure to be computed with timesteps per cycle.

The time taken for each computation is plotted in figure 3.10 which shows that the time varies linearly with the number of time steps per cycle. The smaller the time step the longer it takes for the solution to be calculated for 10 cycles and halving the time step doubles the time required. Using a small time step is not therefore attractive, for example $\Delta t = 10^{-7}s$ takes 1362 minutes to calculate the solution. We have therefore chosen to use a time step of $\Delta t = 10^{-5}s$ for all computations in this thesis, which ensures the computations are relatively fast, but still maintains a

very good accuracy of solution, the relative errors are 1.80×10^{-4} % for pressure and 5.10×10^{-4} % for velocity, and allows for changes in the parameters of the system without violating the stability criteria.

To summarise, the results obtained using the one-dimensional code were computed using a polynomial order of 8, with 1 element for each vessel and at a timestep of $\Delta t = 10^{-5} s$. These choices provide a good balance between computational expense and accuracy. For example the well-matched network of Chapter 4 was computed for 6 cycles and took only 9 minutes.

3.4 Linear and non-linear analysis

In Chapter 2 the governing equations for linear and non-linear one-dimensional wave propagation were derived. In order to compare and validate the implementation of these different models we have calculated the waveforms in a simple straight tube and in a simple bifurcation for linear and non-linear analysis in sections 3.4.1 and 3.4.2. Observing the differences for the two solutions and checking that the linear solution matches the expected analytical results allows us to validate the one-dimensional code.

3.4.1 Simple tube

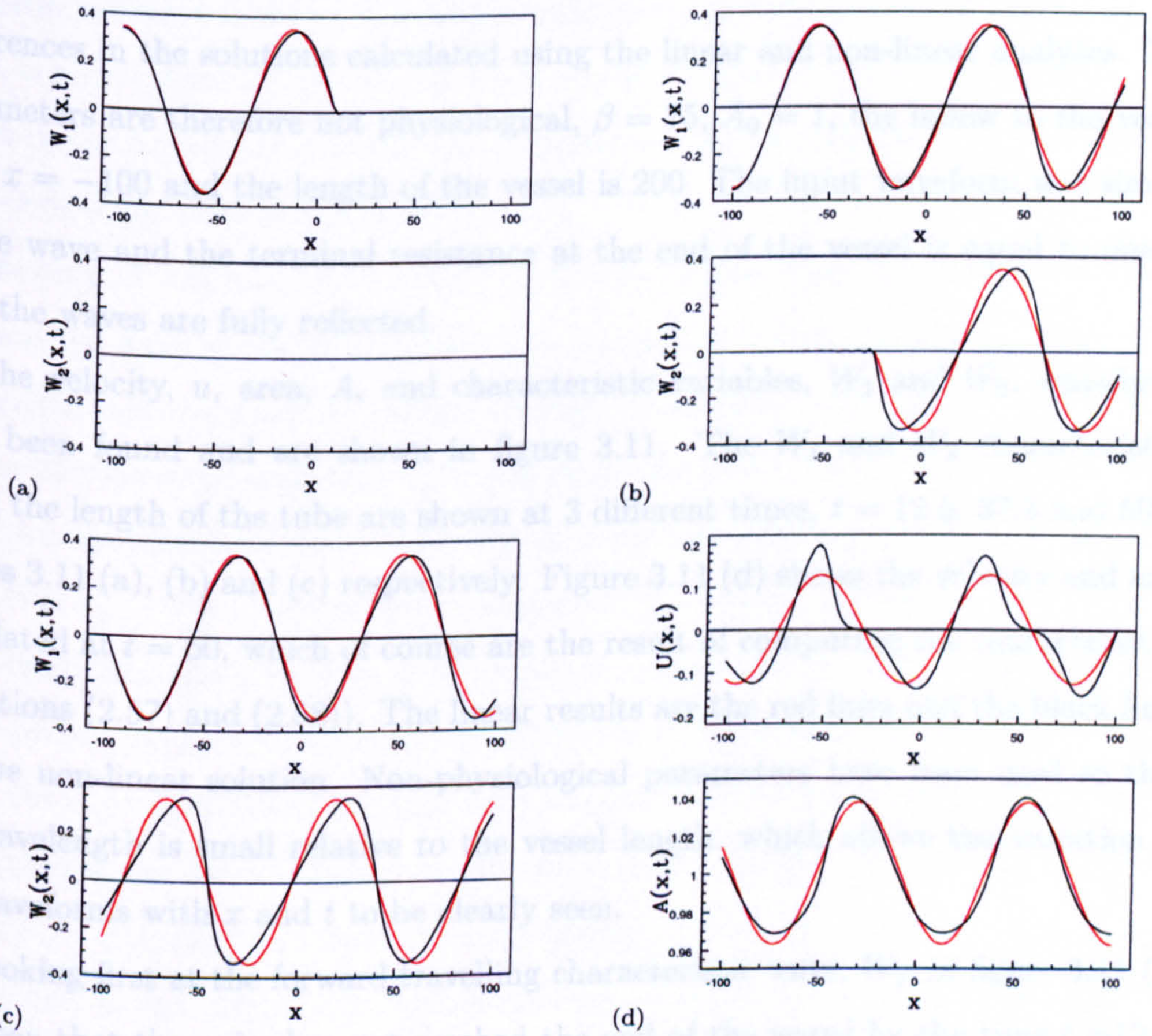


Figure 3.11: (a), (b) and (c) Characteristic waveforms along the lengths of a simple tube calculated with linear (red) and non-linear (black) analysis at three different times, t = 12.5, 37.5 and 50 respectively. (d) Velocity and Area waveforms calculated at t = 50.

For our first test case we consider the flow in the simplest geometry: a constant cross-section, single tube. The parameters have been chosen to clearly illustrate the

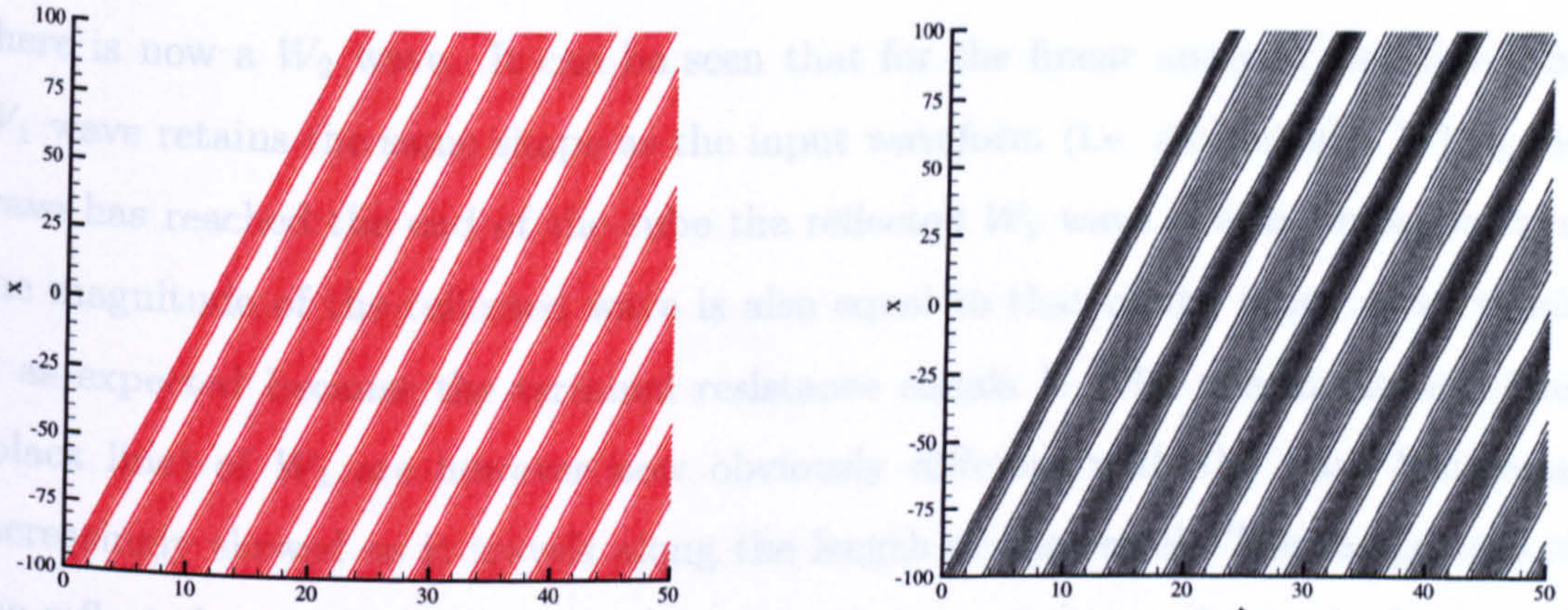


Figure 3.12: Contours of the characteristic variable, W_1, in the simple tube showing the effect of the non-linear modelling. (a) Linear solution (gradient is c_0) and (b) non-linear solution (gradient is $u + c$).

differences in the solutions calculated using the linear and non-linear analyses. The parameters are therefore not physiological, $\beta = 75$, $A_0 = 1$, the inflow to the vessel is at $x = -100$ and the length of the vessel is 200. The input waveform was simply a sine wave and the terminal resistance at the end of the vessel is equal to one so that the waves are fully reflected.

The velocity, u, area, A, and characteristic variables, W_1 and W_2, waveforms have been found and are shown in figure 3.11. The W_1 and W_2 characteristics along the length of the tube are shown at 3 different times, $t = 12.5$, 37.5 and 50 in figures 3.11 (a), (b) and (c) respectively. Figure 3.11 (d) shows the velocity and area calculated at $t = 50$, which of course are the result of computing the characteristics (equations (2.57) and (2.58)). The linear results are the red lines and the black lines are the non-linear solution. Non-physiological parameters have been used so that the wavelength is small relative to the vessel length, which allows the variation of the waveforms with x and t to be clearly seen.

Looking first at the forward travelling characteristic wave, W_1, in figure 3.11 (a) it is seen that the pulse has not reached the end of the vessel by the time t =12.5, therefore there are no reflections and hence the characteristic variable, W_2, is equal to zero. There are however slight differences in the solutions from the two modelling approaches.

The waveforms are more interesting at time equal to 37.5, figure 3.11 (b), where

the W_1 wave has reached the end of the tube and as consequence of the reflection there is now a W_2 wave. It can be seen that for the linear analysis (red line) the W_1 wave retains the same shape as the input waveform (i.e. sinusoidal). When the wave has reached the end of the tube the reflected W_2 wave is also sinusoidal and the magnitude of the reflected wave is also equal to that of the input wave which is as expected because the terminal resistance equals 1. The non-linear solutions (black line) of W_1 are however now obviously different with the wave becoming increasingly skewed as it travels along the length of the vessel. The magnitude of the reflected wave has stayed the same, but the wave becomes increasingly skewed as it propagates back through the domain and travels further.

At time equal to 50, figure 3.11 (c), the W_2 wave has reached the inflow, where as a reflected wave it is free to leave the tube because the reflection coefficient at this point is zero. There is therefore no effect on the W_1 characteristic at the inflow. The waves in the non-linear analysis are very skewed by the time the W_2 characteristic has reached the inlet of the vessel.

Skewing of the wave occurs only in the non-linear case, because in the linear solution the wave speed, c, is modelled as a constant within a vessel. In section 2.4 it is shown that the wave propagates through the domain with a speed equal to $u+c$ for the non-linear analysis and c_0 for the linear analysis. For the more realistic non-linear solution the local value of the speed of wave propagation therefore varies with local area (i.e. when area increases c increases) and local velocity, u. This causes the forward travelling wave to travel more rapidly as the pressure or velocity rises, which causes the peak to catch up with the start of the pressure pulse and conversely when the area falls below the original value or the velocity becomes negative the wave propagates more slowly. As the wave travels further the non-linear effects accumulate and the wave becomes increasingly skewed. These effects are all seen very clearly in the characteristic plots. In this simple test case both the change in u and c are significant. In the well-matched physiological network the most significant difference between the linear and non-linear wave propagation speeds occurs in the ascending aorta, where the change of c is $\sim 0.32ms^{-1}$ and the peak u is $\sim 1ms^{-1}$, whereas c_0 is $\sim 4.66ms^{-1}$. In the more peripheral vessels, for example artery 54, the change of wavespeed is about the same, $\sim 0.34ms^{-1}$, but the peak u is $\sim 0.55ms^{-1}$,

and c_0 is $\sim 9.69ms^{-1}$. Therefore the change in c is relatively more important in artery 54 than for the ascending aorta and is now relatively close to the peak u. However, the significance of both effects in artery 54 has declined because c_0 is twice as large, therefore the linear and non-linear solutions should be closer.

Studying the behaviour of the W_1 and W_2 waves also helps to explain the differences in the values of velocity, u, and area, A, for the two solution methods, which are also shown for time equal to 50 in figure 3.11 (d). There is a significant difference between the linear and non-linear solution for the velocity waveform. The non-linear solution is much more complicated than the linear solution with the speeding and slowing of the waves both having an effect, in contrast the differences in the area waveforms are relatively minor. These significant differences between linear and non-linear analysis are greatly exaggerated when compared with the physiological case. The parameters are not physiological and this means the wavelength has been decreased relative to the domain so that the features of the different solutions can be observed. In the physiological case the time and distance for the initial wave to travel through the network is relatively small so differences have less opportunity to accumulate, however this is not necessarily true for the wave as a whole that may be repeatedly reflected.

Figure 3.12 shows the contours of the characteristic variable, W_1, and is a plot of distance, x, against time, t in the vessel. The characteristic lines remain parallel for the linear solution and their gradient is c_0, figure 3.12 (a). The wavespeed, c_0, for this tube is 8.66 m/s, the gradient was checked and indeed this was found to be 8.66. For the non-linear solution the gradient is $(u + c)$ and both u and c vary. These contours of the characteristic variable, W_1, diverge and converge, which is again as expected.

From these results we are confident that are numerical algorithms have been implemented correctly for flows in a single tube. We have also gained an insight into the differences between the linear and non-linear models for one-dimensional blood flow. We therefore now proceed to test more of our code by examining the results in a simple network of vessels.

3.4.2 Simple bifurcation

To validate the implementation of the code in a network and to highlight some of the differences between the linear and non-linear analysis we have calculated the waveforms in a simple bifurcation using both solution methods. The simple bifurcation is shown in figure 3.13. The input to the bifurcation is a sinusoidal pressure pulse (boundary condition 1) and is applied to the top of artery 1. No terminal resistance has been applied to the ends of arteries 2 and 3, therefore the only reflections which develop in the system are as a result of the bifurcation. Three computations were performed in which the areas and properties were the same for arteries 2 and 3, but these areas were altered so that the theoretical reflection coefficient was different for each computation. The details are summarised in table 3.1. This allows us to investigate the reflection due to the bifurcation for the two solution methods.

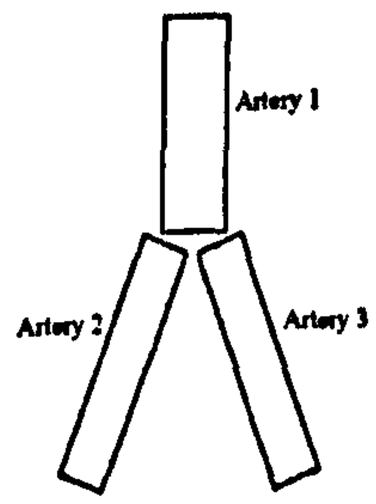


Figure 3.13: Simple bifurcation. Arteries 2 and 3 are altered so that the reflection coefficient due to the bifurcation changes.

The waveforms for vessel 1 are shown for the start and the end of the artery in figure 3.14. The waveforms are shown for velocity, u, and pressure, P, in the first column of figures, and the characteristic variables, W_1 and W_2, are shown in the second column of figures. The linear solution is coloured red at the start of the vessel and green at the end and the non-linear solution is coloured black at the start of the vessel and blue at the end.

Case	Artery 1 A_0 (m^2)	Artery 1 c_o (m/s)	Arteries 2 & 3 A_0 (m^2)	Arteries 2 & 3 c_o (m/s)	Linear R_c from eqn. (3.2)	Linear R_c from fig. 3.14	Non-Linear R_c from fig. 3.14	Linear velocity from theory	Linear pressure from theory
1	1.3E-04	4.43	9.73E-05	4.43	-0.2	-0.2	-0.275	0.754	11,460
2	1.3E-04	4.43	6.48E-05	4.43	0.0	0.0	0.0	0.553	12,330
3	1.3E-04	4.43	4.32E-05	4.43	0.2	0.2	0.25	0.352	13,180

Table 3.1: Table of reflection coefficients and vessel properties in the bifurcation.

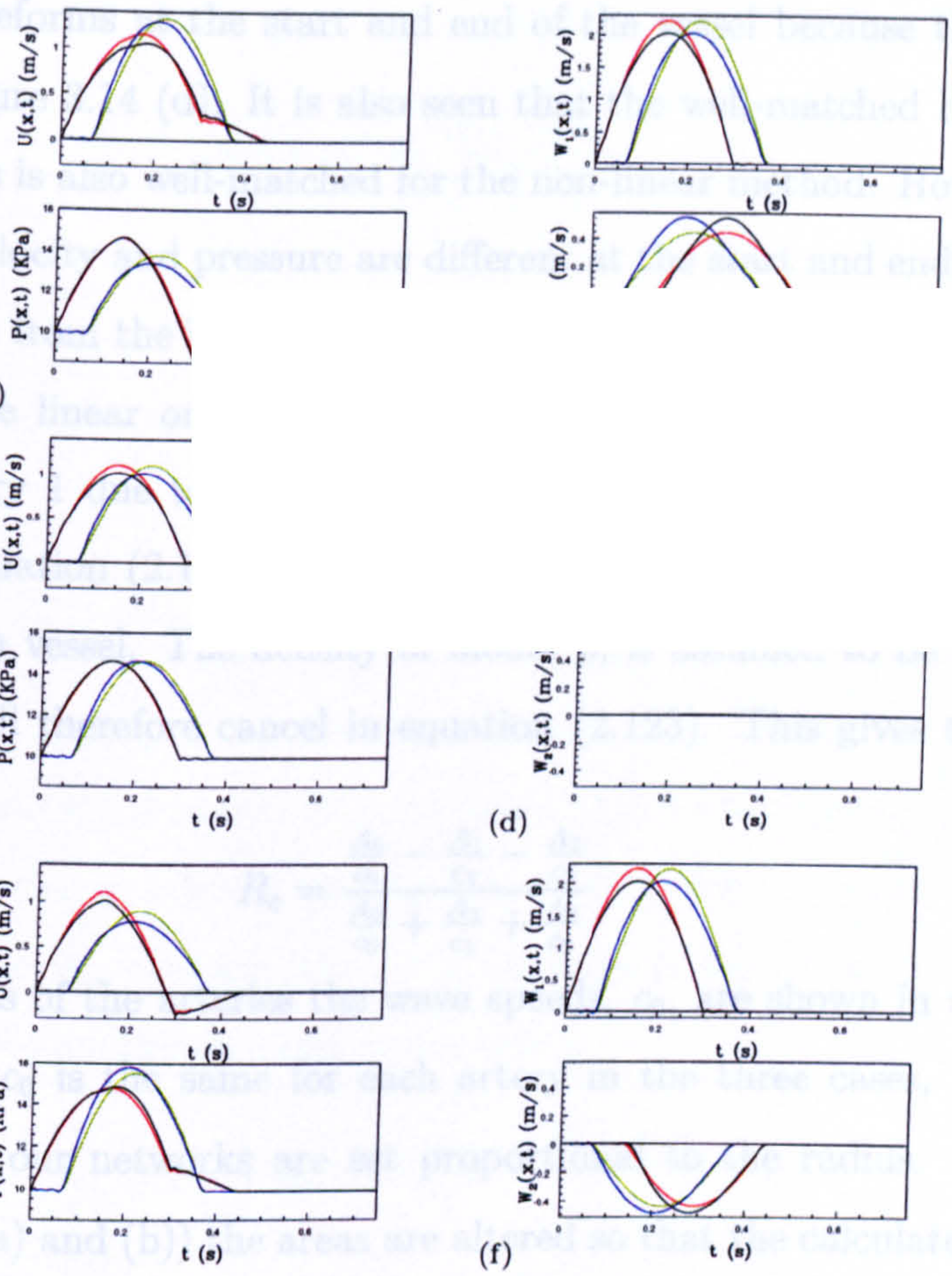


Figure 3.14: Linear (red and green) and non-linear (black and blue) waveforms of velocity, pressure and characteristic variables at the start (red and black) and end (blue and green) of vessel 1. The reflection coefficient due to the bifurcation in (a) and (b) equals R_c = -0.2, (c) and (d) equals $R_c = 0.0$ and (e) and (f) equals $R_c = 0.2$.

From the figures it can be seen that the waveforms for the linear and non-linear analyses are very similar. The same input pressure has been imposed for both the linear and non-linear cases, which can be clearly seen from the case where there is no reflection from the bifurcation, figure 3.14 (c) and (d). To impose the same pressure the imposed W_1 characteristic will be slightly different for the two solution methods and this results in a slightly different input velocity magnitude.

In figure 3.14 it is shown that the magnitudes of W_1 and W_2 are the same at the start and at the end of the vessel for each of the two solution methods. Obviously the waves are further on in time depending on whether we are looking at the W_1 or W_2 characteristic and whether it is at the start or end of the vessel. This is as expected for straight sided constant property vessels. For the cases where there is no reflection due to the bifurcation there are no differences seen in the velocity

and pressure waveforms at the start and end of the vessel because there is no W_2 characteristic, figure 3.14 (d). It is also seen that the well-matched bifurcation for the linear analysis is also well-matched for the non-linear method. However, for the other two cases velocity and pressure are different at the start and end of the vessel, due to a reflection from the bifurcation and hence a change in W_2.

To validate the linear one-dimensional code we have calculated the expected reflections in artery 1 due to the bifurcation by calculating the R_c at the end of the vessel with equation (2.123) from section 2.7, where c_1, c_2, c_3 and A_1, A_2, A_3 are known for each vessel. The density of blood, ρ, is assumed to be the same for each vessel and will therefore cancel in equation (2.123). This gives the following equation:

$$R_c = \frac{\frac{A_0}{c_0} - \frac{A_1}{c_1} - \frac{A_2}{c_2}}{\frac{A_0}{c_0} + \frac{A_1}{c_1} + \frac{A_2}{c_2}} \tag{3.2}$$

As well as the areas of the arteries the wave speeds, c_0, are shown in table 3.1 for the 3 cases. Note c_0 is the same for each artery in the three cases, because the wall thicknesses in our networks are set proportional to the radius. In the first case, (figures 3.14 (a) and (b)) the areas are altered so that the calculated reflection coefficient due to the bifurcation is -0.2, for the second case the reflection coefficient is 0.0, (figures 3.14 (c) and (d)) and in the third case the calculated reflection coefficient due to the bifurcation is 0.2, (figures 3.14 (e) and (f)).

These theoretical reflection coefficients can now be compared with the computational results showing the effect of the bifurcation on the W_1 and W_2 characteristic waveforms shown in the second column of figures. The reflection coefficients can be calculated from $R_c = -\Delta W_2/\Delta W_1$ for both linear and non-linear waveforms and these reflection coefficients are shown in table 3.1. As expected the reflection coefficients calculated from the linear waveforms are exactly the same as the reflection coefficients calculated from equation (3.2). The reflection coefficients calculated from the non-linear waveforms are similar, however there are slight differences, which are due to c varying with pressure.

As a final check the velocity, u, and pressure, P, for linear analysis can be calculated at a distance, x, and at time, t, from the above known parameters of the

vessel.

$$W_1 = u_0 + \frac{a_l}{A_0^{3/4}}\sqrt{\frac{\beta}{2\rho}} \tag{3.3}$$

where

$$u_0 = 0, \quad a_l = \begin{cases} \Delta a_{lmax} \sin\left(\frac{\pi t^*}{0.3}\right) & 0 < t^* < 0.3 \\ 0 & 0.3 < t^* < T \end{cases}$$

where t^* is the time within the cycle and is given by $t^* = t - (cycle * T)$ and cycle is the cycle number of the periodic input and T is the time period of the cycle and in this case $T = 1$. Δa_{lmax} is the maximum change in a_l for the W_1 characteristic in linear analysis and is calculated from equation (2.99) and $\frac{\Delta a_{lmax}}{A_0^{3/4}}\sqrt{\frac{\beta}{2\rho}} = 2.2124$.

Using the reflection coefficient and the time taken for the wave to propagate we can calculate the W_2 characteristic at a distance x, and time, t, from the W_1 characteristic at the appropriate earlier time using:

$$W_2 = -R_c \times W_1\left(t^* - \frac{2l - x}{c_0}\right) \tag{3.4}$$

where l= 0.312 and is the length of artery 1. The expected velocity, u, and area, A, are calculated from equations (2.77) and (2.78) in section 2.4.3 and the pressure, P, is calculated using (2.3). The calculated pressure and velocity are in table 3.1 at time, t =0.25 and at x =0. These can be checked with the values for the numerical results seen in figure 3.14 and indeed these are the same.

These results have illustrated some of the differences between the linear and non-linear analyses . Further comparisons are made in Chapter 4, section 4.4 where the differences in a whole arterial network are examined.

The numerical results are also in accord with analytical predictions and therefore we are confident that our algorithms have been implemented correctly and that we can calculate the waveforms in arterial networks. We check this for a larger network in the next section.

3.5 Comparison with the Taylor-Galerkin numerical scheme

Finally, to check our solution method the waveforms computed in a simple arterial network constructed of 7 arteries were compared with those calculated using a different numerical scheme, Taylor-Galerkin finite elements. The 7 arterial network was constructed by simplifying the 55 well-matched arterial network, described in section 4.3 Chapter 4. The input to the arterial network is boundary condition 1 with a time period of 1. The terminal resistance is different on the ends of these vessels and the range is from 0.724 to 0.893.

The one-dimensional code we compare ours with is a finite element solver which uses a Taylor Galerkin type of discretisation that maintains accuracy in space and time and is similar to the classical Lax-Wendroff scheme. This was developed by Formaggia *et al* [39]. The waveforms for the 7 arterial network are shown in figures 3.15 and 3.16 for all 7 arteries. The first column of results are the flow rates in each vessel and the area of each vessel is shown in the second column.

The number next to the figures characterises which artery in the system the waveform belongs to and there are three figures per column for each artery. The top figures for each artery are the results generated using our discontinuous Galerkin solver, the middle results show the results from the Taylor-Galerkin solver and the bottom figure shows the relative error between the two. The waveforms calculated using the Taylor-Galerkin scheme and the relative error between the two waveforms were provided by Daniele Lamponi from EPFL in a personal communication [72].

As can be seen from the figures there is a very small error for the area, which is in the order of 10^{-3}. The flow rates have a slightly larger error in the order of 10^{-2}, but these differences are still very minor. It can be seen from the larger peaks in the relative error figures that the most significant errors occur when there are sharp changes in the solution for the area or for the flow rates in each vessel.

These results show that there are only small differences between the two solution methods, which gives us the final check of our one-dimensional solver. We are therefore confident in the implementation and accuracy of all aspects of our numerical scheme and now proceed to calculate the waveforms in a larger and more physiological network of arteries.

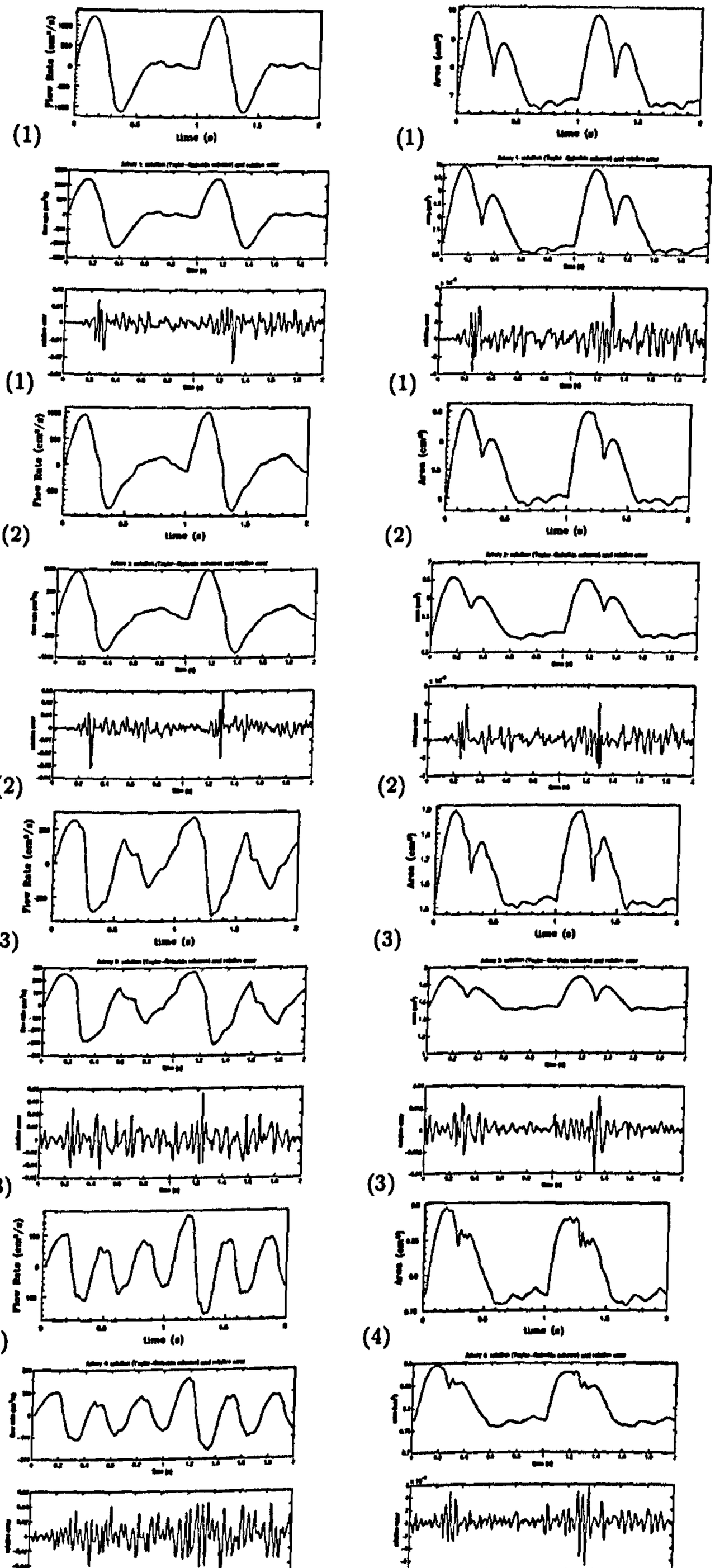


Figure 3.15: Comparison of the velocity and area waveforms calculated using the discontinuous Galerkin method (top figures) and Taylor Galerkin method (bottom figures) in a 7 arterial network. Numbers in brackets represents the artery. Bottom figure for each artery is the relative error between the two solution methods.

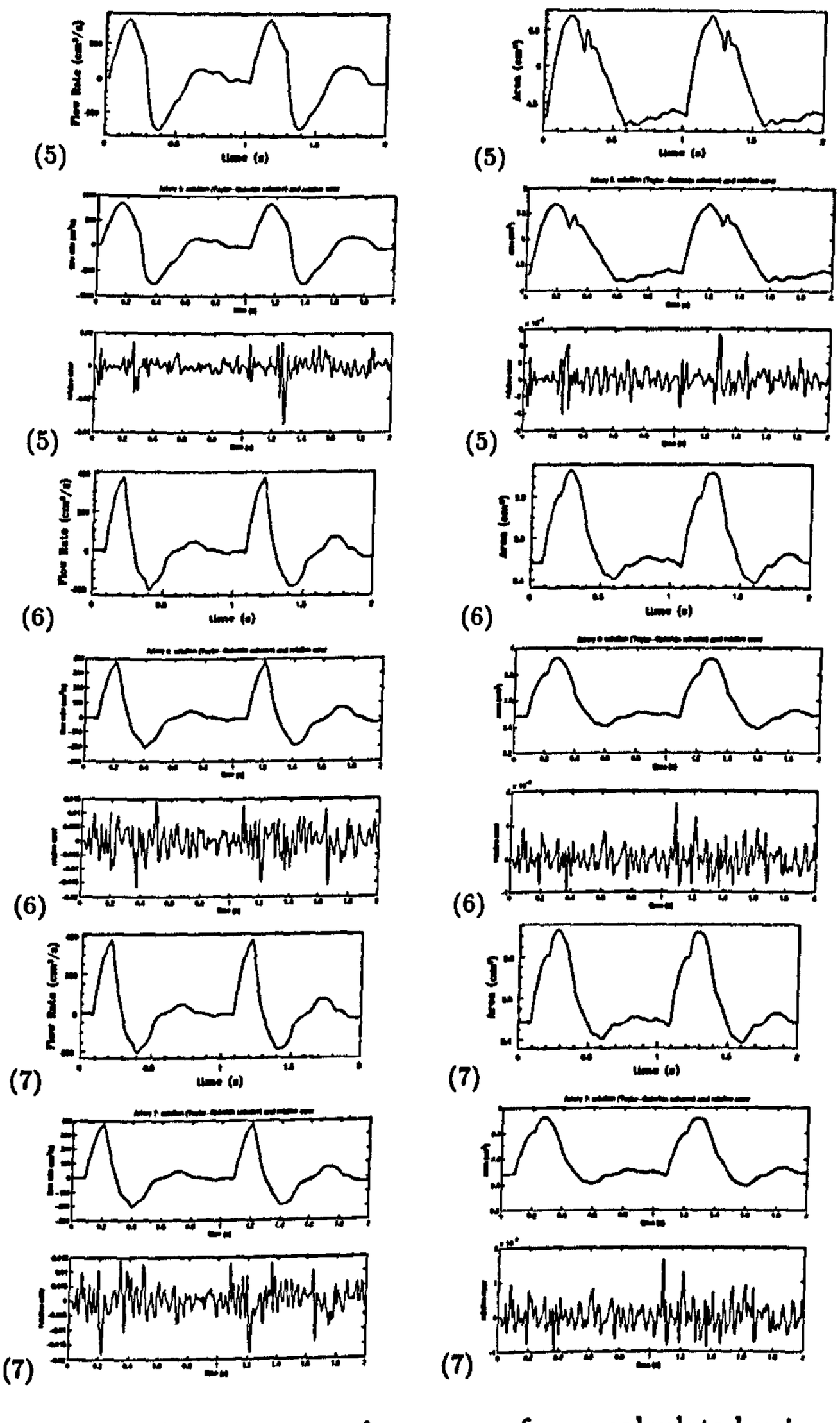


Figure 3.16: Comparison of the velocity and area waveforms calculated using the discontinuous Galerkin method (top figures) and Taylor Galerkin method (bottom figures) in a 7 arterial network. Numbers in brackets represents the artery. Bottom figure for each artery is the relative error between the two solution methods.

Chapter 4

The well-matched network

4.1 Introduction

An interesting network for study using the one-dimensional wave propagation model is the arterial tree of the adult human. Clinicians can diagnose abnormalities in a patient from observing unusual velocity and pressure waveforms using techniques such as applanation tonometry and Doppler ultrasound, section 1.1.2. Clinical interest is such that the waveforms throughout the body are relatively well studied and therefore typical physiological waveforms are available for many of the major arteries. These provide a means for validating our numerical results and models. Once validated, numerical simulation of human arterial networks has the potential to assist in the understanding of the causes of different features of the waveforms, to predict the effects of surgical interventions and also to assist as a diagnostic tool.

There have been a number of previous attempts to model the human arterial tree which include the modelling of a simplified arterial network containing the 55 largest arteries in the human body. These provide valuable information and comparisons and include methods using electric circuits in 1969 by Westerhof [167], slightly modified versions of this network modelled using a non-linear model, but where the area was assumed to be constant, Stergiopulos [145] and using a linearised one-dimensional model in space/time variables by Wang and Parker [163], section 1.2.1.3. We have taken the network of Wang and Parker as a starting point and some comparisons are made between their results and assumptions and the current work. The results produced by our code using both linear and non-linear models

are presented in sections 4.3 and 4.4. In Chapter 5 we extend our modelling to investigate wave propagation in a new tapered arterial network. This network has been produced using magnetic resonance imaging (MRI) data from a single, healthy adult human female. This is a useful set of information, because not only does it provide data about the variation in cross-section of the arteries, but also it is for a single subject, unlike previous networks which are composites of different patients. The wave propagation in this arterial tree was computed using the non-linear code which is required in order to model the tapered vessels.

The effects of many parameters on the computed waveforms are assessed in the following sections. These include different inflow boundary conditions, different levels of terminal resistance, varying heart rates and in Chapter 5 the impact of tapered vessels. The results are presented, compared with one another and with clinical results and the modelling conditions are discussed with respect to their physiological relevance.

4.2 Clinical waveforms in arterial systems

Some typical waveforms of pressure and velocity in the human arterial network are shown in figure 4.1 taken from Nichols and O'Rourke [95]. This diagrammatic figure shows how the waveforms in the arterial system change as they travel away from the heart, with the main features being that the pulsatile pressure difference increases and the flow oscillation decreases.

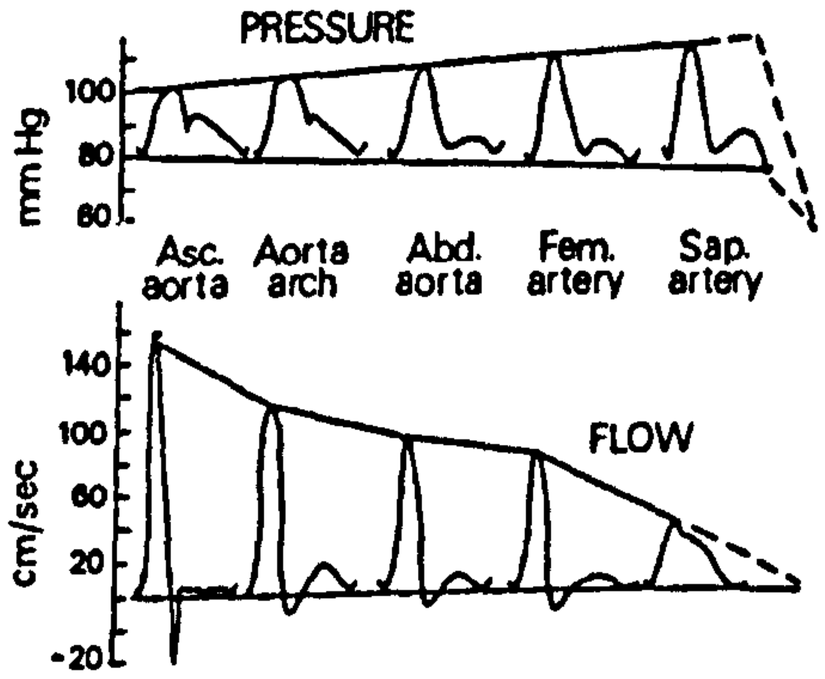


Figure 4.1: Diagrammatic flow and pressure waves in the human arterial vessels as they travel away from the heart [95]. They show that the magnitude of the pressure pulse increases, although the mean pressure slightly decreases, and that the velocity pulse decreases the further away from the heart the waveforms are measured.

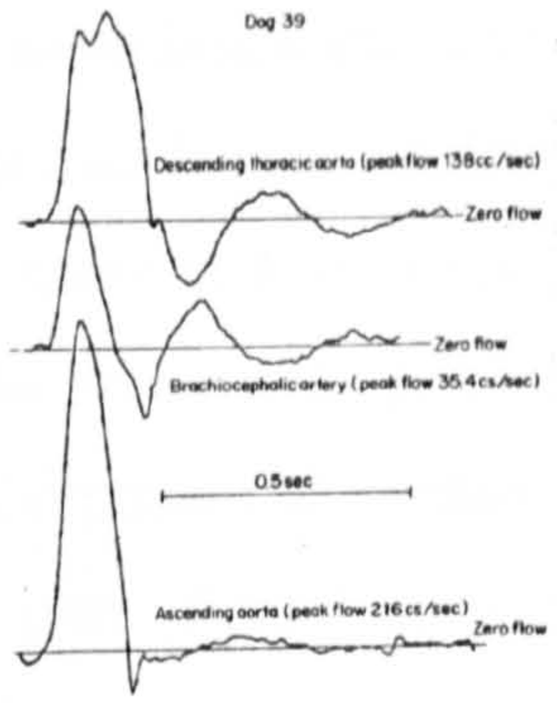


Figure 4.2: (a) Flow waves measured in a dog in the descending thoracic aorta, brachiocephalic artery and ascending aorta [101]. These are thought to be similar in shape to human waveforms.

The pressure and velocity waveforms are relatively well studied in the ascending aorta and in arteries near to the heart. Clinical measurements for pressure and flow waveforms for humans and dogs are shown in figures 4.2, 4.3, 4.4, 4.5 and 4.6. Dog waveforms are relevant to those in humans, because the velocity waveform in the ascending aorta is very similar for many different animals [95]. The flow waveforms are shown in figure 4.2 for the descending aorta, the brachiocephalic artery and the ascending aorta of a dog. The flow in the ascending aorta has a sharp peak of velocity, usually between 0.8 - 1.5 m/s [95], in the first third of systole and then a short dip of negative flow followed by no flow at all during diastole. It can be seen from figure 4.2 that the main difference in the waveforms further away from the heart is that there is flow during diastole. The peak waveform is also more rounded in the descending aorta, there is a larger period of reversed flow in the descending aorta and the brachiocephalic compared with the flow in the ascending aorta. There is also a second peak of positive and negative flow seen during diastole.

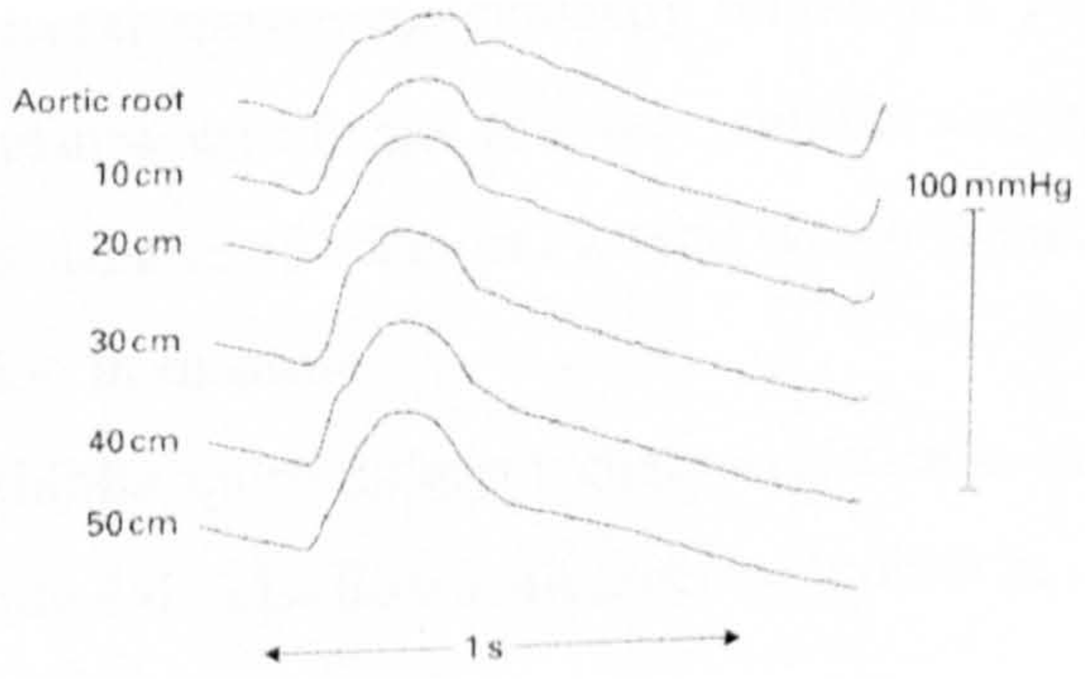


Figure 4.3: Pressure waves measured in a human adult showing the change in waveform from the ascending aorta to the femoral artery [95].

The pressure waveform in the ascending aorta has two distinct types of waveforms in animals. For example in dogs and human adolescents the pressure wave has a rounded systolic peak and then there is a secondary positive wave following the dicrotic notch in diastole. For older humans the pressure wave rises to a later systolic peak and the pressure falls in an exponential manner after the dicrotic notch. The pressure waveforms in the upper part of the body e.g. brachiocephalic artery and descending aorta, are similar in shape to the pressure seen in the ascending aorta.

The pressure waveforms for a human, recorded between the ascending aorta and the femoral artery, are shown in figure 4.3. From these plots it can be seen that the foot of the pressure wave occurs later in the cycle the further away from the heart the measurement is taken. In the ascending aorta the peak of the pressure occurs in late systole. In diastole the pressure declines exponentially with time for all the waves down the aorta and there is no second peak.

A three-dimensional pressure waveform for a dog and a contour plot along the length of the aorta are shown in figure 4.4, these are not thought to be as quite as similar to the adult human as the velocity waveforms mentioned earlier, but are more similar to waveforms seen in younger humans. The dicrotic notch can be clearly seen, as can a small second peak of pressure during diastole further down the aorta, which is a characteristic feature of waveforms in young adults and dogs. The peak pressure in systole is seen to rise the further along the aorta the clinical measurements are taken. Note from the contour plot of pressure, where distance down the length of the aorta is plotted against time, figure 4.4 (b), the local wavespeed can be calculated from the gradient of the contour, i.e. distance over time.

Figure 4.5 shows several waveforms typically found in a younger human. The brachial and radial pressure waveforms are very similar and they both have two peaks of pressure, whilst that in the femoral artery, which is further from the heart, exhibits a smooth decline in diastole.

A waveform that exhibits quite different characteristics is the flow waveform in the common carotid figure 4.6. The flow is all positive, unlike in other major arteries in the body, and the mean velocity is also relatively large.

There is less data available on other arteries, but there is usually no back flow seen in the small peripheral arteries such as the saphenous artery shown in the

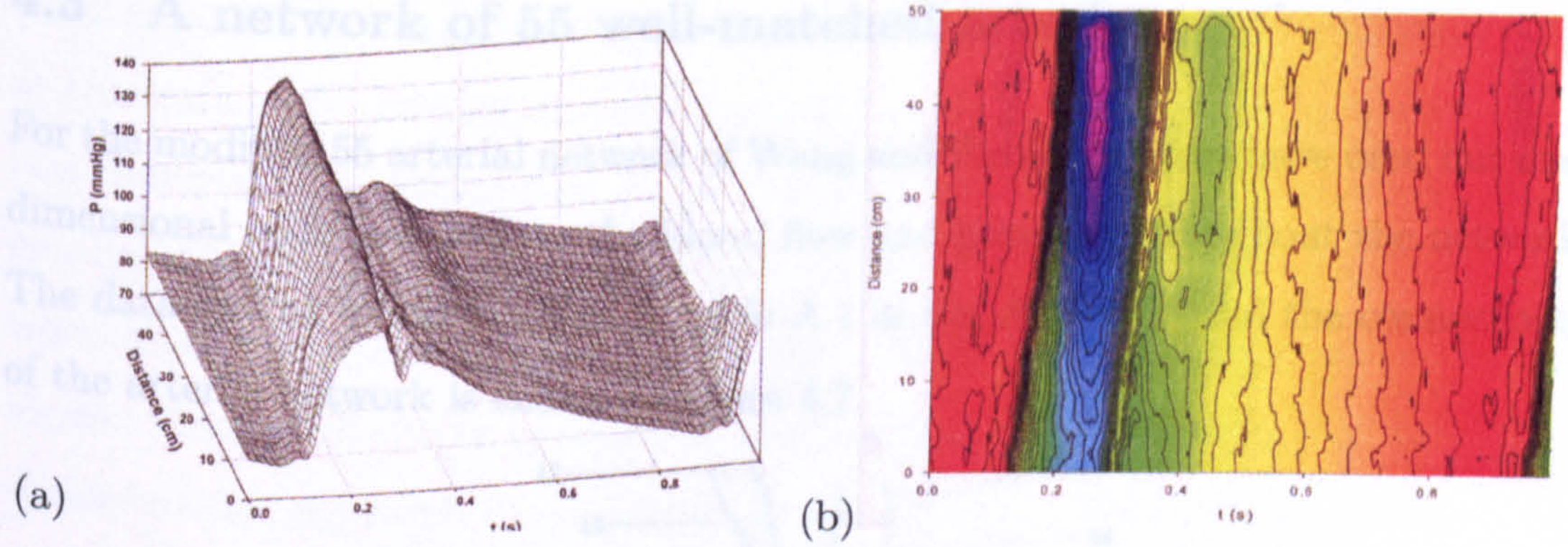


Figure 4.4: a) A three-dimensional pressure wave taken in a dog from the ascending aorta to the bottom of the aorta. Pressure measured every 2 cm down the length of the aorta b) Same data but with pressure shown as a contour. The local wavespeed can be calculated from the gradient of the contours [161].

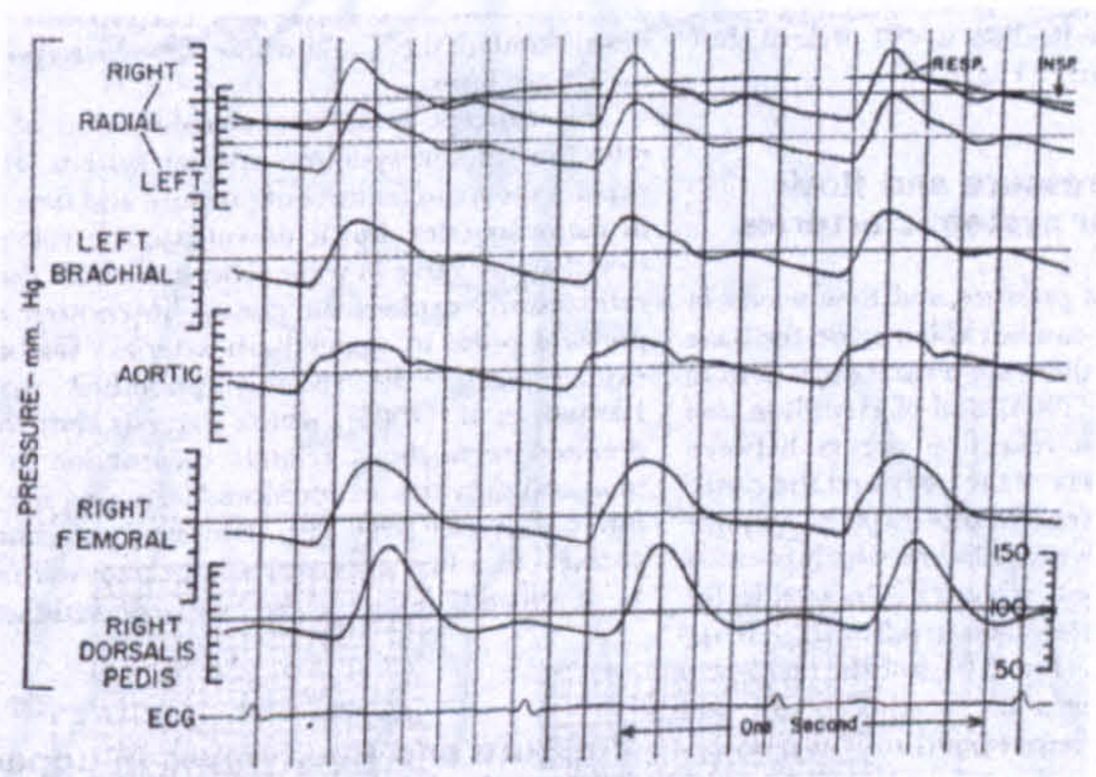


Figure 4.5: Pressure waves measured in a younger human adult in several different arteries of the body [70].

diagrammatic figure 4.1. Also, no back flow is seen in the renals and superior and inferior mesenteric that branch off the aorta. This is thought to be due to the fact that at the end of those vessels the peripheral resistance is low. This is borne out by the fact that the features of the flow and pressure waveforms are similar.

A similar phenomenon is observed when vasodilation is induced pharmacologically in peripheral vascular beds, with the flow wave resembling the pressure wave. This suggests that reflections due to small peripheral vessels are significant in the end arteries [95, 169].

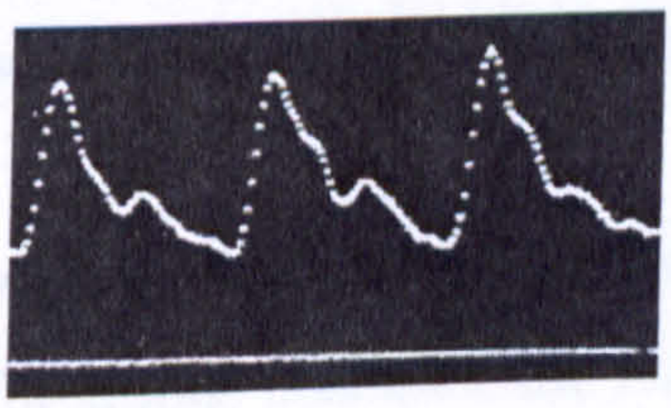


Figure 4.6: Flow in the common carotid of a human adult [1].

4.3 A network of 55 well-matched arteries

For the modified 55 arterial network of Wang and Parker [163] we have used our one-dimensional code to calculate the blood flow and pressure throughout the network. The data for the model is given in table A.1 in the Appendix and the connectivity of the arterial network is shown in figure 4.7.

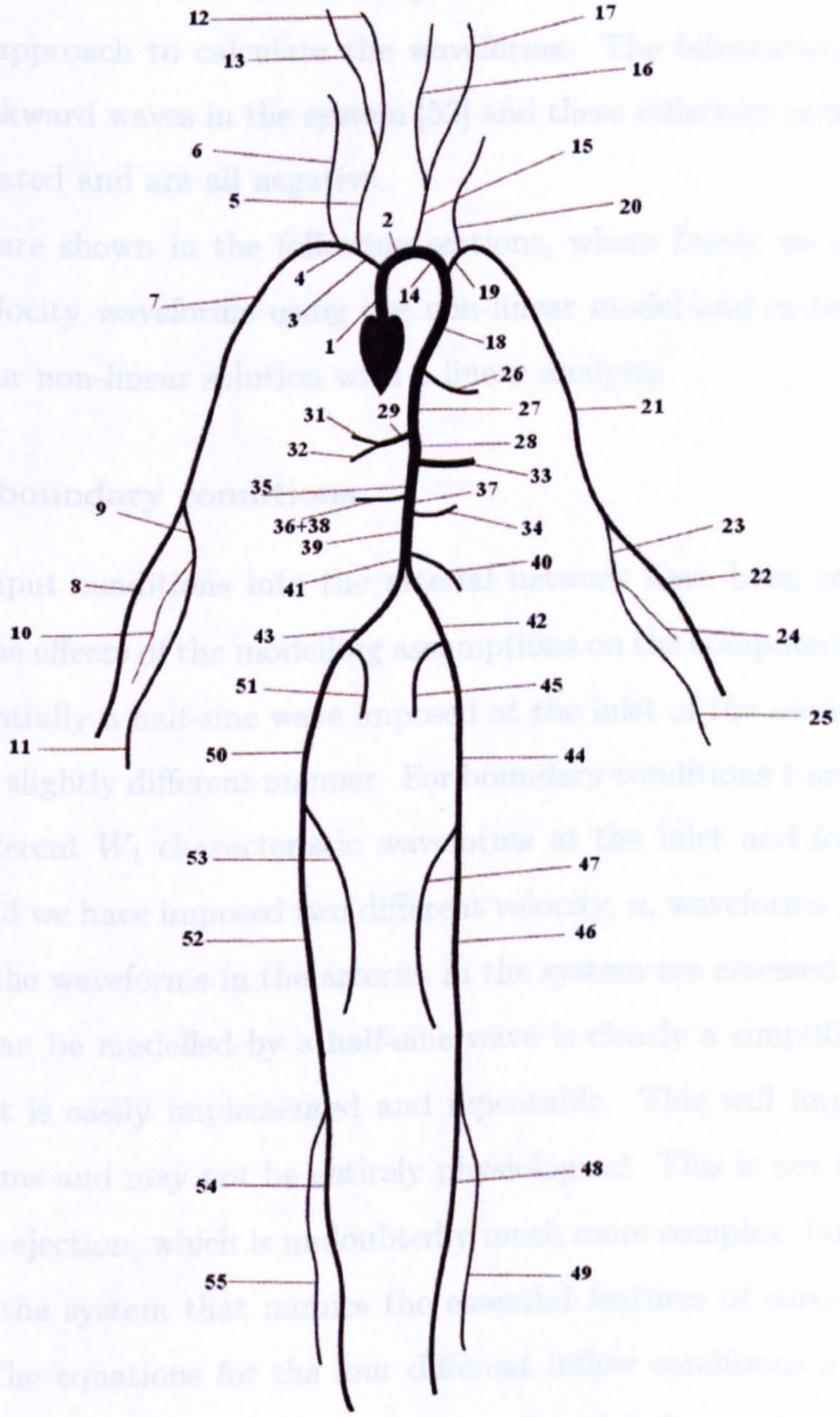


Figure 4.7: Diagrammatic representation of the connectivity and numbering of the arteries in the well-matched network.

This is essentially the network of Westerhof, but Wang and Parker found that reflections from some of the bifurcations obscured the reflections from terminal vessels and wanted to investigate the influence of terminal reflection in a simpler model.

They adjusted the diameters in the 55 arterial network so that no reflections occur at bifurcations for forward travelling waves (i.e. for a well-matched network reflection coefficients for forward waves are equal to zero (section 2.7)) and justified this by suggesting that there is evidence from the work of Papageorgiou *et al.* [108], that most arterial junctions in the human body are well-matched for forward travelling waves. Wang and Parker used linear analysis based on a book-keeping method of characteristics approach to calculate the waveforms. The bifurcations will be ill-matched for backward waves in the system [52] and these reflection coefficients have also been calculated and are all negative.

Our results are shown in the following sections, where firstly we calculate the pressure and velocity waveforms using the non-linear model and in section 4.4 we then compare our non-linear solution with a linear analysis.

4.3.1 Inflow boundary conditions

Four different input conditions into the arterial network have been considered in order to assess the effects of the modelling assumptions on the computed waveforms. All four are essentially a half-sine wave imposed at the inlet of the ascending aorta, but imposed in a slightly different manner. For boundary conditions 1 and 4 we have imposed two different W_1 characteristic waveforms at the inlet and for boundary conditions 2 and 3 we have imposed two different velocity, u, waveforms at the inlet. Their effects on the waveforms in the arteries in the system are assessed. Assuming that the inflow can be modelled by a half-sine wave is clearly a simplification, but is a function that is easily implemented and repeatable. This will impact on the resultant waveforms and may not be entirely physiological. This is not taken to be a realistic cardiac ejection, which is undoubtedly much more complex, but as a well-defined input to the system that mimics the essential features of cardiac ejection into the aorta. The equations for the four different inflow conditions are given in Chapter 2, section 2.6.1. For boundary conditions 2 and 3 the maximum velocity, u_{max}, is imposed as 1 m/s and for boundary condition 3 the minimum velocity, u_{min}, is -0.333 m/s. A pulse pressure, ΔP, of 5 kPa is imposed at the inlet for boundary conditions 1 and 4. These are all imposed on the base value 9.9 kPa.

The waveforms of pressure, velocity and the characteristic variables, W_1 and W_2,

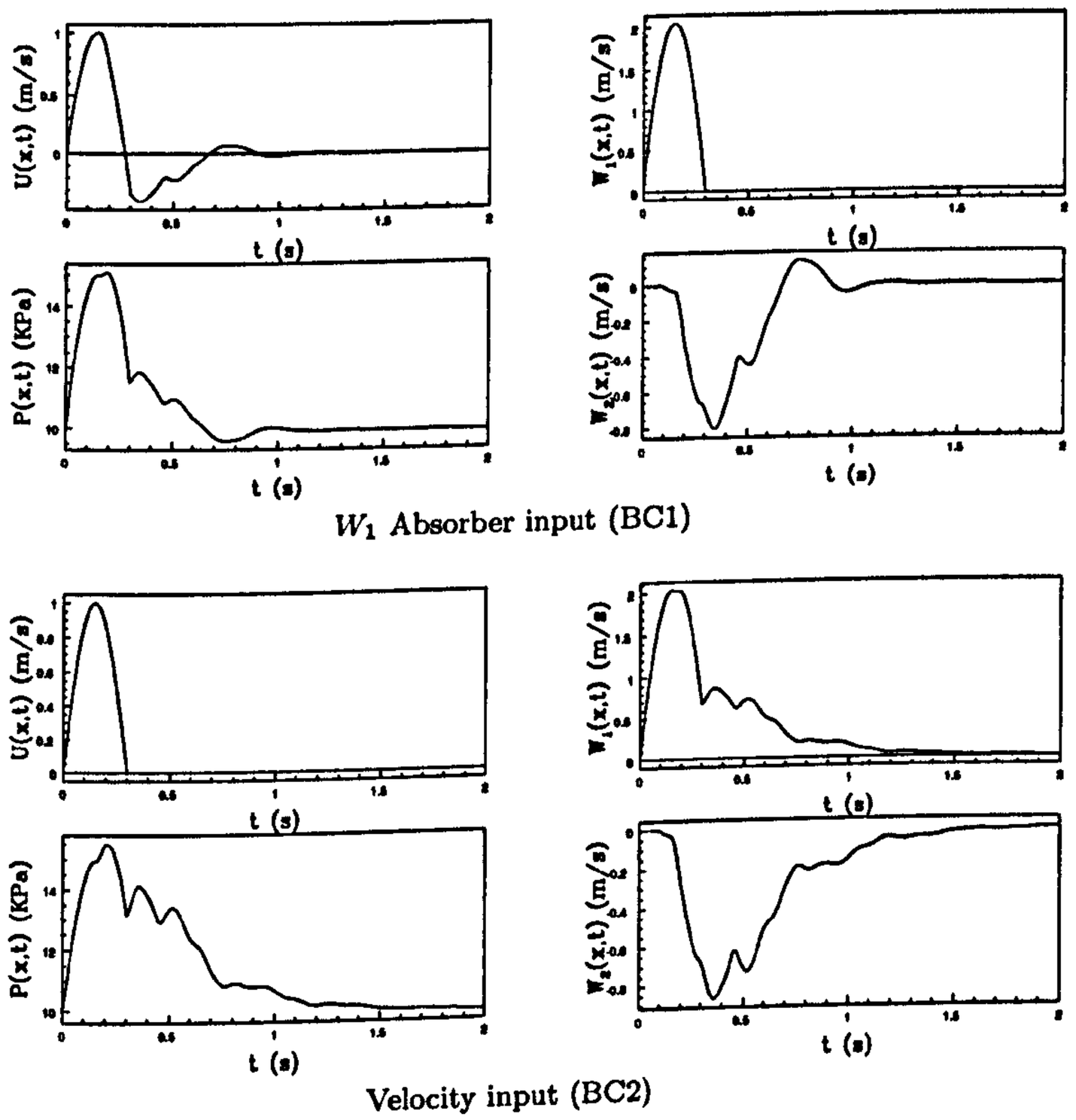


Figure 4.8: Velocity, pressure and characteristic variable waveforms at the start of the ascending aorta for boundary conditions 1, 2, 3 and 4. Results are shown for only a single heart beat with a reflection coefficient of 0.5 on the terminal vessels of the well-matched network.

are shown in figure 4.8 for a single heart beat in the ascending aorta. The results are only shown for one heart beat so that reflections from previous heart beats will not have an effect on the waveform and with time the wave can eventually die away. This enables the different features of the reflections to be studied more easily. The waveforms have been recorded at the start of the ascending aorta, $x = 0.0$. The W_1 characteristic shows the forward waves entering the system from the heart and the W_2 characteristic waveforms show the reflections from the system returning to the ascending aorta. These have occurred due to reflections from the terminal vessels and from waves travelling back up the arterial network reflecting at the bifurcations, which are ill-matched for backward waves. Note that no reflections occur from forward waves at bifurcations for this well-matched system. The results are shown for cycle 6 and with a reflection coefficient of 0.5 on all terminal vessels.

The top four graphs in figure 4.8 are for boundary condition 1 (BC1) and show results obtained when the heart acts as a pure absorber, i.e. no reflections occur at the aortic valve. This has been modelled by imposing a half-sine wave through the W_1 characteristic at the ascending aorta for the first 0.3 seconds and then zero for the rest of the cycle.

For both boundary conditions 2 and 3, the velocity was prescribed at the inflow boundary. For boundary condition 2, figure 4.8 (BC2), the velocity was imposed as a half-sine wave for the first 0.3 seconds and then for the rest of the cycle it equals zero. For boundary condition 3, figure 4.8 (BC3), the velocity is imposed as a half-sine wave for the first 0.28 seconds and then there is a sharp peak of flow reversal for 0.03 seconds. This is a more physiologically correct velocity than the one prescribed in boundary condition 2. The W_1 and W_2 characteristics are calculated from the prescribed velocity and the reflections occurring in the system. The pressure is then calculated from the W_1 and W_2 variables. Due to imposing $u = 0$, after $t > 0.3$ and $t > 0.31$ in boundary conditions 2 and 3 respectively, the W_1 characteristic variable is forced to equal the negative of the W_2 characteristic (which has occurred due to the reflections in the system), so that this condition for velocity is met. The heart is therefore now acting as a total reflector for this part of the cycle, i.e. $W_1 = -W_2$. The pressure waveforms in the ascending aorta for boundary conditions 2 and 3 are broadly similar in shape, but boundary condition 3 produces a sharp increase

in pressure when the velocity increases rapidly from a negative value to zero, also boundary condition 3 has a stronger secondary peak than boundary condition 2, which is not observed in-vivo.

The bottom four figures, boundary condition 4, figure 4.8 (BC4), shows results for the heart acting as an absorber for the first 0.3 seconds by imposing a half-sine wave through the W_1 characteristic at the ascending aorta and then as a reflector for the rest of the cycle. The half-sine wave corresponds to the aortic valve being open during ventricular systole and the waves are assumed to be dispersed in the ventricle. For the remainder of the cycle, the valve is closed and is assumed to perfectly reflect the backwards travelling waves in the ascending aorta, which has been modelled by setting $W_1 = -W_2$. There is a transition region to simulate the aortic valve closing and opening and this has been modelled by linearly varying W_1 from zero to equal $-W_2$. This transition takes 0.01 seconds and can be seen in the W_1 characteristic plot, figure 4.8 (BC4), between the times 0.3 to 0.31 seconds as the sharp increase in the W_1 characteristic until it equals minus the W_2 characteristic. Making the transition continuous in this manner greatly aids the numerical stability of the solution. This is similar to prescribing the u value, but requires less knowledge about the particular features of the network. No assumptions are made about the velocity or pressure distribution. Imposing the W_1 characteristic corresponds to the emanation of the forward travelling wave (pressure/velocity) from the aortic valve and is a more general boundary condition. Note that the notch of negative velocity and positive pressure is characteristic of physiological waveforms and is reproduced using this boundary condition.

We now look at the results in detail. For boundary conditions 1 and 4 the input was imposed by specifying the W_1 characteristic. To better understand the results, recall that the pressure and velocity are directly related to the characteristic variables, W_1 and W_2, by equations (2.57) and (2.58). Thus the negative W_2 characteristic has an additive effect on the pressure wave, which is clearly seen in figure 4.8 (BC1) and (BC4). The initial portion of the cycle is similar to the input (W_1 characteristic) for both boundary conditions. For the case where the heart is modelled as a pure absorber, figure 4.8 (BC1), the pressure slowly declines after the initial pressure rise, in contrast to the case where the heart acts as reflector for time

$t > 0.31$, shown in figure 4.8 (BC4). The pressure increases sharply as the aortic valve closes and then slowly declines. The increase in pressure for this case is due to the increase in magnitude in the W_1 characteristic which results from the requirement for W_1 to equal the negative of W_2 for a total reflector boundary condition. The pressure waveform in this case appears more physiologically correct, however the presence of a second notch in the pressure wave is not normally observed in-vivo.

The negative W_2 characteristic has a subtractive effect on the velocities, as shown in figure 4.8 (BC1) and (BC4). Again in the velocity waveforms the initial flow is similar in both cases; they have a primary peak value, which is approximately 1 m/s, and then a reversed portion of flow. When the input is an absorber, figure 4.8 (BC1), the flow slowly increases after $t > 0.3$, but when the heart acts as a reflector, figure 4.8 (BC4), the velocity waveform shows a small period of flow reversal before the velocity increases quickly until it reaches zero flow for the rest of the cycle, corresponding to $W_1 = -W_2$ and the characteristic variables cancel each other. This flow reversal is consistent with in-vivo measurements in the human body.

It can be seen in all of the W_2 characteristic waveforms that there are no reflections in the ascending aorta for approximately the first 0.15 seconds and therefore the velocity and pressure waveforms for this initial part of the cycle are similar to the input, W_1 characteristic or velocity for all four cases.

The W_1 characteristic for boundary conditions 1 and 4 are the same for the first 0.3 seconds and are also similar to the W_1 characteristics for boundary conditions 2 and 3, but for the remainder of the cycle the W_1 characteristic for boundary condition 1 is quite different to all the other boundary conditions due to this condition being defined as a pure absorber and the others acting as reflectors. The W_2 characteristics are similar in shape for the four different inputs, which is due to the reflection coefficients in the system being the same. The change in magnitude of W_2 has occurred due to the different amount of waves being trapped in the system at the aortic valve. A lower value of terminal reflection coefficient is required to produce similar results when the heart is a reflector than when it is an absorber, boundary condition 1, due to the greater trapping of waves in the former cases.

Boundary conditions 3 and 4 have very similar waveforms for both velocity and pressure. However, the second notches in these pressure waveforms are more pro-

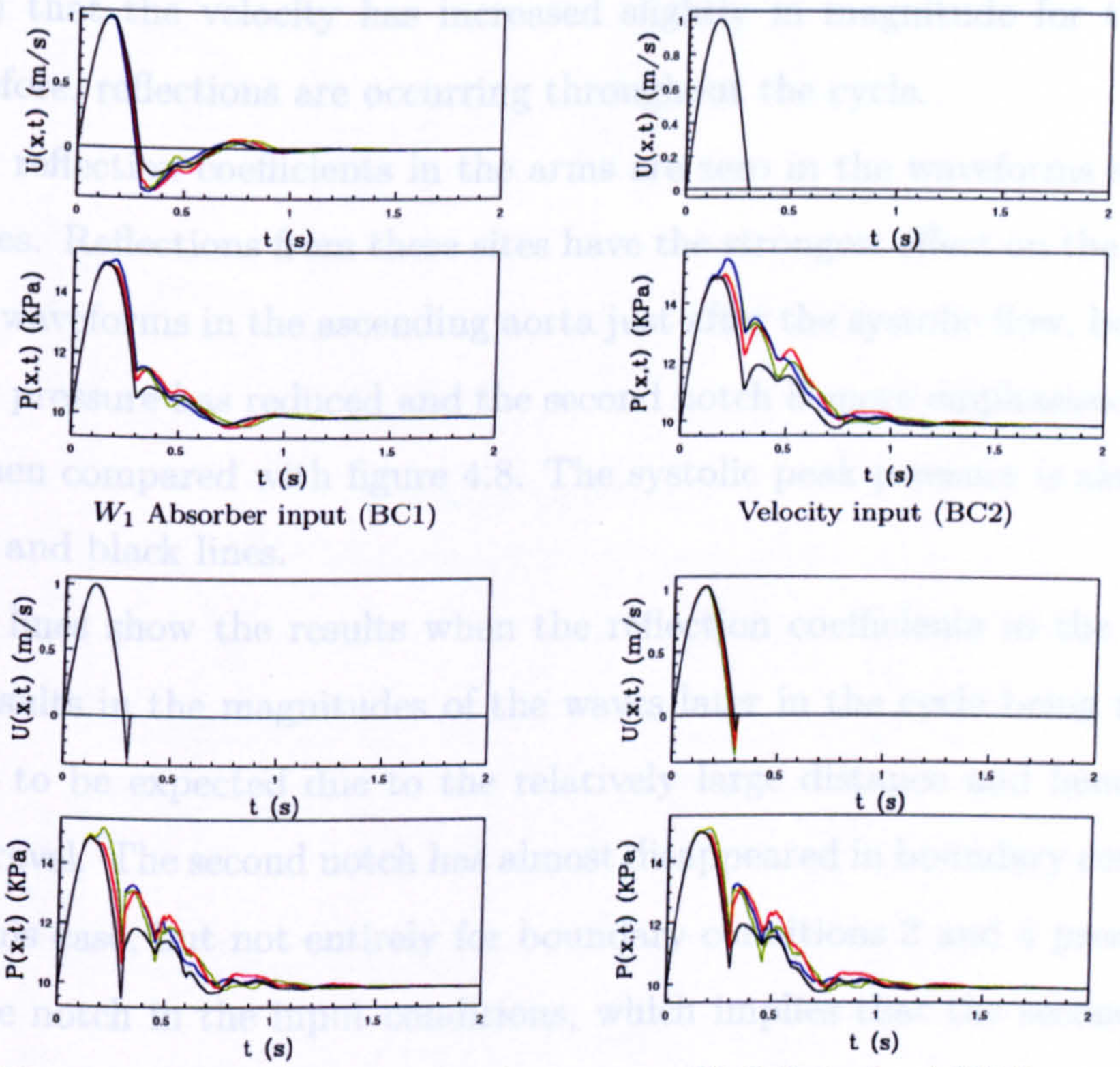
nounced than for the other two boundary conditions. This appears to have been emphasised by the sharp decrease in velocity. This notch is seen for all four inputs but is more pronounced in the reflector cases due to a total reflection occurring at the ascending aorta and therefore a larger number of reflections being trapped in the system. It can be seen that the notch has approximately doubled in size from figure 4.8 (BC1) to (BC2). Since this second notch is in the ascending aorta for all four boundary conditions, it could imply that this is a feature of this network and this non-physiological feature may be due to a lack of reflection sites in the simplified tree.

The results show a large sensitivity of waveforms to input condition into the network, but there are good physiological justifications for the part reflector/part absorber model (BC4), which simulates valve closure and the results are encouraging.

4.3.2 Source of reflections in the system

The results shown for all four cases are those obtained when a reflection coefficient of 0.5 was applied to the outflows of the terminal vessels of the arterial network. To analyse the source of some of the features of the waveforms in the ascending aorta, we have eliminated reflections occurring at the terminal vessels of groups of arteries by setting the terminal reflection coefficients to equal zero. Four sections of arteries have been considered: those in the region of the thoracic and abdominal arteries (arteries 26, 31, 32, 33, 34, 36 and 40), the cerebral arteries (arteries 6, 12, 13, 16, 17 and 20), those in the arms (arteries 8, 10, 11, 22, 24 and 25) and those in the legs (arteries 45, 47, 48, 49, 51, 53, 54 and 55). When the waves travel down arteries where the reflection coefficients are zero the waves will leave the arterial system and no reflections will re-enter from this segment of the network.

Figure 4.9 show results for the pressure and velocity waveforms with different sections of the network set to have a terminal resistance equal to zero. The results are shown at the origin of the ascending aorta and have been coloured to represent a different section of the network with no terminal resistance on the end vessels and are shown for the four different boundary conditions. These can be compared with the results in the previous section, which had terminal resistance applied on all terminal vessels of the network, figure 4.8.



W_1 Absorber input (BC1) | Velocity input (BC2)

Velocity with reversed flow input (BC3) | W_1 Reflector input (BC4)

Figure 4.9: Computational pressure and velocity waveforms in the ascending aorta. Different sections of the network have zero terminal resistance applied to the terminal vessels whereas the rest of the network has a reflection coefficient of 0.5 on the end vessels and are coloured as follows: aorta = black, carotids=red, arms=green and legs=blue. These figures show which set of reflection sites affect the features of the waveforms the most.

The black lines show results where the reflection coefficients on the terminal vessels coming off the thoracic and abdominal arteries are zero. For all four boundary conditions the pressure is lower earlier in the cycle and there is not as much reversed flow early in the cycle as in the case where all the terminal vessels had an R_t of 0.5, figure 4.8. This implies that reflections from the vessels in the thorax and abdomen affect the wave patterns in the ascending aorta predominantly at the beginning of the cycle. This is to be expected as the waves do not have so far to travel and thus their effects are seen relatively early in the cycle. It is interesting that the pressure waveforms also appear slightly lower than all the other coloured lines in the later part of the wave, which shows how much of the reflection seen in the ascending aorta is due to reflections from the aorta.

The red lines show the results when the terminal reflection coefficients in the cerebral arteries are zero. The pressure in the ascending aorta is reduced when compared with the original waves, figure 4.8, and it can be seen for the W_1 absorber

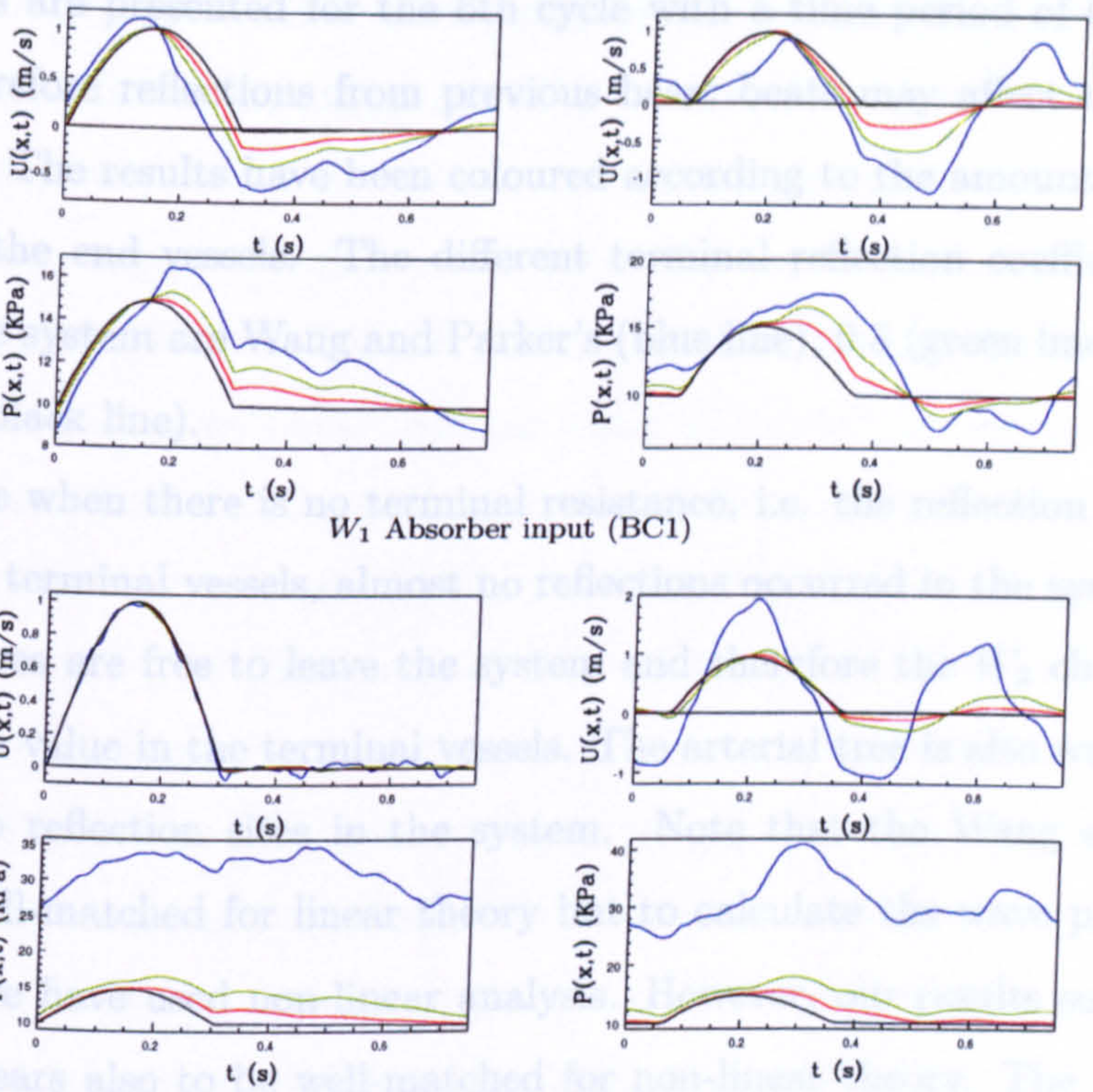
input (BC1) that the velocity has increased slightly in magnitude for the whole cycle. Therefore, reflections are occurring throughout the cycle.

Terminal reflection coefficients in the arms are zero in the waveforms shown by the green lines. Reflections from these sites have the strongest effect on the pressure and velocity waveforms in the ascending aorta just after the systolic flow, because at this time the pressure has reduced and the second notch is more emphasised later in the cycle, when compared with figure 4.8. The systolic peak pressure is also higher than the red and black lines.

The blue lines show the results when the reflection coefficients in the legs are zero. This results in the magnitudes of the waves later in the cycle being reduced. Again this is to be expected due to the relatively large distance and hence times these waves travel. The second notch has almost disappeared in boundary conditions 1 and 2 for this case, but not entirely for boundary conditions 3 and 4 presumably because of the notch in the input conditions, which implies that the second bump occurred at least in part due to later reflections in the system, associated with the legs.

4.3.3 Terminal resistance

In the computations up to this point the reflection coefficients on the terminal vessels have all been set to 0.5. We now analyse the effect of different levels of reflection from the peripheral vessels on the waveforms throughout the arterial network. To do this we have applied a range of reflection coefficients from 0 to Wang and Parker's reflection coefficients (0.63 - 0.96) given in Appendix A.1. Pressure and velocity waveforms are shown for the ascending aorta (artery 1) and the brachial (artery 7) for Wang and Parker's well-matched network for all four boundary conditions in figure 4.10. The results are shown for a point mid-way along the ascending aorta. However, the waveforms can still be compared to those in the previous sections, because they are taken only 0.02 m away from the inlet and there is little difference between the waveforms over such a short distance. The only minor difference is in the velocity waveform, where previously the velocity was equal to zero, corresponding to $W_1 = -W_2$, but now it is near zero flow for the rest of the cycle since the characteristics do not exactly cancel.



W_1 Absorber input (BC1)

Velocity input (BC2)

Velocity with reversed flow input (BC3)

W_1 Reflector input (BC4)

Figure 4.10: Computational velocity and pressure waveforms in the well-matched network for the ascending aorta (artery 1), in the first column, and the brachial (artery 7), in the second column, for all four boundary conditions with different values of reflection coefficients applied to the terminal vessels, black = 0.0, red = 0.25, green = 0.5 and blue = Wang and Parker's reflection coefficients. Note the pressure and velocity waveforms are on different scales for the different boundary conditions.

The results are presented for the 6th cycle with a time period of 0.75 seconds per cycle, therefore reflections from previous heart beats may affect the shape of the waveform. The results have been coloured according to the amount of terminal resistance on the end vessels. The different terminal reflection coefficients to be modelled in the system are Wang and Parker's (blue line), 0.5 (green line), 0.25 (red line) and 0.0 (black line).

For the case when there is no terminal resistance, i.e. the reflection coefficients are zero on the terminal vessels, almost no reflections occurred in the system (black lines). The waves are free to leave the system and therefore the W_2 characteristic does not change value in the terminal vessels. The arterial tree is also well matched so there are no reflection sites in the system. Note that the Wang and Parker network was well-matched for linear theory but to calculate the wave propagation in the system we have used non-linear analysis. However, our results suggest that the system appears also to be well-matched for non-linear theory. The waveforms when the terminal reflection coefficient in the terminal vessels is zero look like the input waveform and bear no resemblance to the physiological case. The velocity and pressure waveforms for boundary condition 1 and 4 are the same shape as the half sine wave that was imposed as the W_1 characteristic into the system at the ascending aorta.

As the reflection coefficients are increased on the terminal vessels the effect of the reflected waves on the pressure waveform in the ascending aorta can be clearly seen, with pressure being greater throughout the cycle and most obviously after the main pulse. The patterns are quite similar for the different levels of reflection coefficient for each of the boundary conditions, however the magnitudes increase with increasing terminal reflection coefficient. As discussed in section 4.3.1, the dicrotic notch is much more pronounced for boundary conditions 3 and 4, and also the waveforms for these boundary conditions are very similar for the lower levels of reflection coefficient, but are plotted on a very different scale.

Comparing the resultant velocity waveforms for the cases where the W_1 characteristic is prescribed at the inflow, although the pressure waveforms for boundary conditions 1 and 4 exhibit similar features the velocity waveforms are quite different. For the case when the W_1 characteristic is imposed as an absorber (BC1), there is a

very large region of negative flow after the main systolic injection, which is followed by a small positive flow. The magnitude of each increases with reflection coefficient, but for boundary condition 4 the velocity waveforms are much more physiological with a small sharp region of negative velocity at the end of systole. It is interesting to note that this reversed velocity and dicrotic notch in the pressure are solely due to the reflections in the network. Neither notch is present for the zero reflection coefficient case and both increase in magnitude with increasing reflection coefficient.

In contrast, the velocity waveforms in the ascending aorta for boundary conditions 2 and 3, figures 4.10 (BC2) and (BC3), are the same for all reflection coefficients tried in the system, because these boundary conditions involve prescribing the velocity at the inflow. The pressure again increases with increasing reflection coefficient and the shapes of the pressure waves are similar to those for the imposed W_1 characteristic boundary conditions (BC1) and (BC4). Both the pressure and velocity waves for boundary condition 2 are similar to those of boundary condition 3 except that the boundary condition 3 waves all have a similar sized notch after the main pulse. The notch is prescribed for the velocity wave and apparently is the direct cause of the notch in the pressure wave. When there is no terminal reflection coefficient the pressure in boundary condition 3 dips below the norm due to the reversed flow prescribed at the inlet.

A major difference between the boundary conditions is apparent when the reflection coefficients are set to those used by Wang and Parker shown by the blue lines in figure 4.10. For the imposed velocity boundary conditions the pressure has increased by a very large amount and for boundary condition 4 the results do not look at all physiological. For this level of reflection coefficient where the heart acts as an absorber (BC1) the pressure looks the most physiological, although the velocity does not.

The results for high levels of terminal reflection coefficients suggest that when the heart acts as a reflector the waves become trapped in the arterial tree and interact with one another to a large extent. There appears to be far too much reflection in the system with reflections from the previous pulses having a large effect on the waveforms so that they do not follow the same pattern as for lower reflection coefficients. The reflection coefficients were not all a uniform value as in the other

cases; so this may have affected the shape of the waves. However, the differences in wave shape for the high reflection coefficient cases is more likely to be due to wave trapping, because for boundary condition 1, where the heart acts as an absorber and thus there are far fewer reflections in the system, the wave pattern does look similar to the lower levels of reflection coefficient, but more pronounced.

For the results when the reflection coefficient is equal to 0.25 at the terminal vessels (red line) there does not appear to be enough reflection back in the ascending aorta to cause a significant pressure build up. The results when the reflection coefficients equal 0.5 (green line) on the terminal vessels are very similar to the results for one heart beat in figure 4.8. In figure 4.8 it can be seen that the reflections have not quite died down by 0.75 second so for this case the previous beat will have had an effect on the waveform, but probably not very large as the results appear very similar.

The pressure and velocity waveforms for the brachial (artery 7) are also shown in figure 4.10 (second column). Again with zero reflection coefficient on the terminal vessels the pressure and velocity waveforms (black line) are the same shape as the inflow boundary condition. The shapes of the waveforms for reflection coefficients of 0.25 and 0.5 are similar, but the secondary features increase in magnitude due to increased reflections as the terminal reflection coefficient is raised. When the reflection coefficients of Wang and Parker are applied to the terminal vessels, the waveforms for velocity and pressure do not look at all physiological especially where the heart acts as a reflector. There is a large build up of pressure for boundary conditions 2 and 3 and for boundary condition 4 the waveforms become very ragged.

We conclude that there is a strong interaction between the inflow boundary condition and the reflection coefficient applied to the terminal vessels and a reflection coefficient that provides reasonable results for an absorber inflow boundary condition produces poor results when used with a reflector inflow boundary condition. Increasing the terminal reflection coefficient increases the reflections in the system and the magnitudes of the secondary features of the waveforms, however the shapes are relatively similar for all values of reflection coefficient below some limiting value. The main features of the physiological pressure waves can be replicated by choosing an appropriate reflection coefficient for all the inflow boundary conditions but only

boundary conditions 3 and 4 are capable of producing reasonable velocity waves and also the dicrotic notch is more pronounced for these inflow boundary conditions.

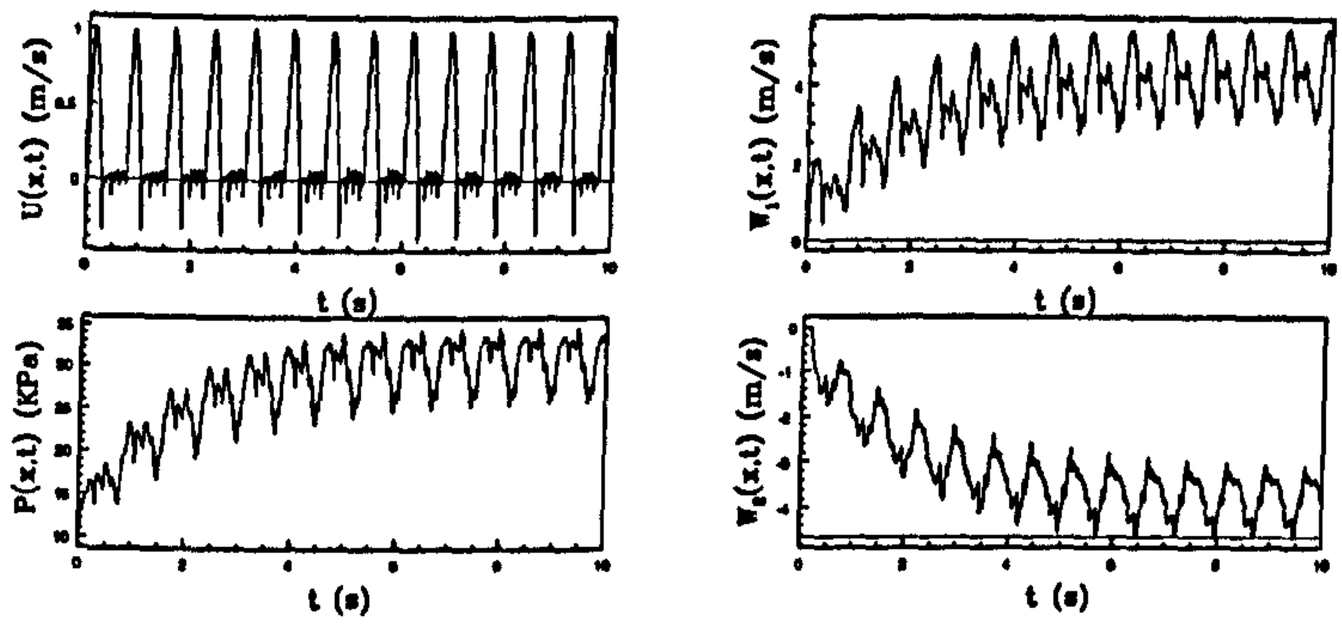
The most physiological combinations appear to be boundary conditions 3 and 4 with a reflection coefficient of 0.5, because they provide a reasonable pressure waveform with a physiological velocity waveform particularly in the ascending aorta.

We note that when a parameter is altered, such as the terminal reflection coefficient, the imposed volume flux at the ascending aorta may also change. For example for the imposed velocity boundary conditions (BC2) and (BC3) there will be an increase in volume flux into the system with a higher terminal resistance, due to the increase in pressure and consequently area. To maintain the same volume flux as the model for the output from the heart would require an iterative procedure that would greatly increase the computational expense of our parametric studies, but could be examined in future research.

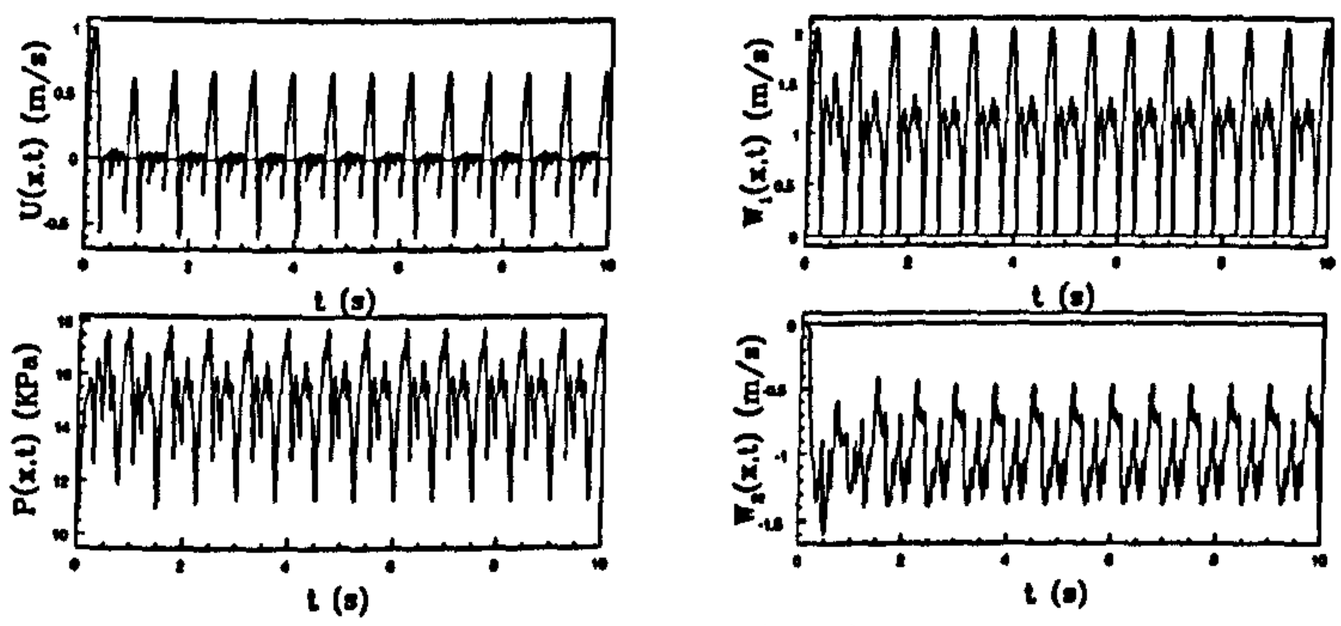
4.3.4 Waveforms in systems with large reflection coefficients

We now examine in more detail the large differences in waveforms when high reflection coefficients are used. Figure 4.11 shows waveforms for velocity, pressure and the characteristic variables in the arterial network when Wang and Parker's terminal reflection coefficients are applied. Results are shown for boundary conditions 3 (top figures) and 4 (bottom figures) for the first 10 seconds of the calculated results starting from rest.

Other than the velocity for boundary condition 3, which was prescribed, none of the waveforms look physiological and there appears to be far too much reflection in the system for both models. For boundary condition 3 there is a large build up of pressure, which has occurred during the first 6 cycles. This suggests that it is a result of reflections from previous heart beats not dying out substantially before the the next heart beat. For boundary condition 4 the pressure has increased for the rest of the cycle though not as much as for boundary condition 3 but this jagged pattern certainly does not look physiological. Also there is a large spike of reversed flow before and after the main velocity wave due to more reflections and hence a larger change in the W_2 characteristic. These two boundary conditions appeared very similar for a reflection coefficient of 0.5 in the system, but with a reflection



Velocity with reversed flow input (BC3)



W_1 Reflector input (BC4)

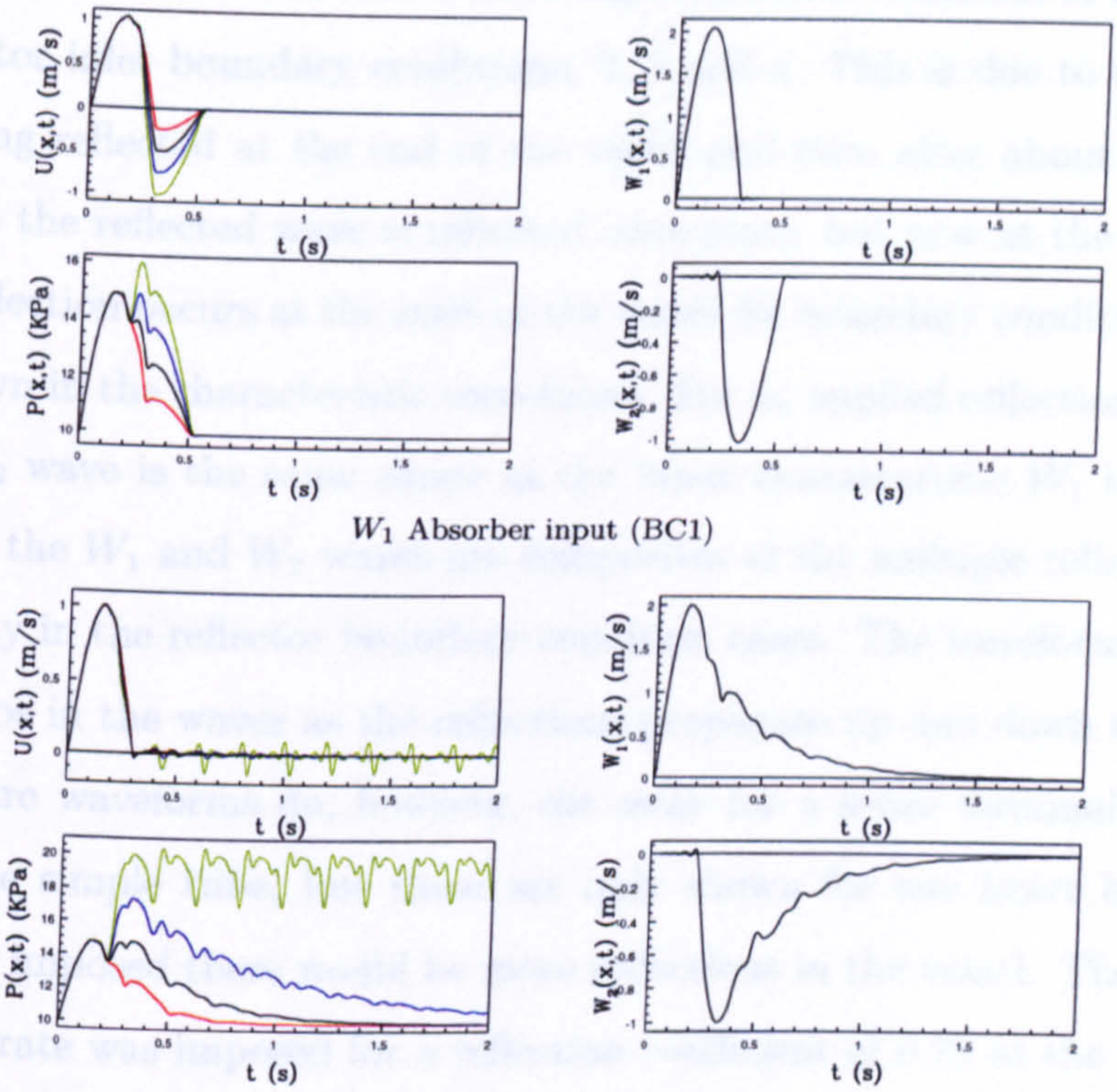
Figure 4.11: Computational velocity, pressure and characteristic waveforms for the well-matched network in the ascending aorta (artery 1) for boundary conditions 3 and 4 with the reflection coefficients of Wang and Parker's applied to the terminal vessels of the system. Note pressure and velocity are on different scales for boundary conditions 3 and 4. There is a large build up of pressure for boundary condition 3.

coefficient that is too large the waveforms appear quite different.

4.3.5 Reflections in a simple tube

In order to further understand the features discussed in the previous sections, we here examine the waveforms in a simple tube. Different terminal reflection coefficients have been applied to the end of a solitary vessel with constant cross-section. A single heart beat is imposed at the inflow for the four different boundary conditions. In the arterial network the majority of the reflections are not observed in the ascending aorta before 0.15 seconds, so we have chosen the length of the tube in order for the reflections at the inlet to occur after approximately the same time. The velocity and pressure waveforms are shown for all four boundary conditions for $R_t = 0.25$ (red), 0.5 (black), 0.75 (blue) and 1.0 (green) in figure 4.12. The W_1 and W_2 characteristic waveforms are shown for a terminal resistance of 0.5 in the second column.

There is much more reflection in the system when the terminal resistance is higher, which is to be expected. The pressure build up discussed in the previous



W_1 Absorber input (BC1)

Velocity input (BC2)

Velocity with reversed flow input (BC3)

W_1 Reflector input (BC4)

Figure 4.12: Computational velocity and pressure waveforms in a single tube for boundary conditions 1, 2, 3 and 4 and for different levels of R_t. The red lines are for a R_t of 0.25, black for 0.5, blue for 0.75 and green 1.0. The waveforms are shown for a single heart beat and show the interaction of the different boundary conditions. The forward and backward travelling waves (W_1 and W_2) are also shown for a R_t of 0.5.

section can also be seen in this tube when a high reflection coefficient of 1.0 is applied for the reflector inlet boundary conditions, 2, 3 and 4. This is due to the whole of the wave being reflected at the end of the vessel and then after about 0.3 seconds into the cycle the reflected wave is reflected once more, but now at the start of the vessel. No reflection occurs at the start of the vessel for boundary condition 1, which is clearly shown in the characteristic waveforms. For an applied reflection coefficient of 0.5, the W_2 wave is the same shape as the input characteristic W_1 but half the size, whereas, the W_1 and W_2 waves are composites of the multiple reflections that slowly die away in the reflector boundary condition cases. The waveforms show the repeated bumps in the waves as the reflections propagate up and down the tube.

The pressure waveforms do, however, die away for a lower terminal resistance than 1.0 in the simple tube, but these are only shown for one heart beat and if more beats are imposed there would be more reflections in the vessel. Therefore if a periodic heart rate was imposed for a reflection coefficient of 0.75 at the end of the vessel, the reflected waves would not have significantly reduced by the next beat and there would be a build up of pressure. These effects are similar to the well-matched network with high values of reflection coefficient applied to the terminal vessels in the 55 arterial network.

The results from this single vessel have shown how a high terminal reflection coefficient can trap large amounts of reflection in a network, and that using a reflection coefficient of 0.75 on the end vessels could be too high if there was a periodic, reflector type of inflow. We therefore continue to use the lower reflection coefficient of 0.5 on the terminal vessels of our system, because the magnitudes of the reflections in the system appear more physiologically correct. It is also interesting that the overall features of the pressure and velocity waveforms are quite similar to the waves in the ascending aorta in the arterial tree, even for such a simple geometry. The patterns are however obviously simpler due to the smaller number of reflection sites and routes the waves can travel.

4.3.6 Period size

Period size is a parameter that is variable with the current condition of a particular person, as well as between different people. Typical resting heart rates are between

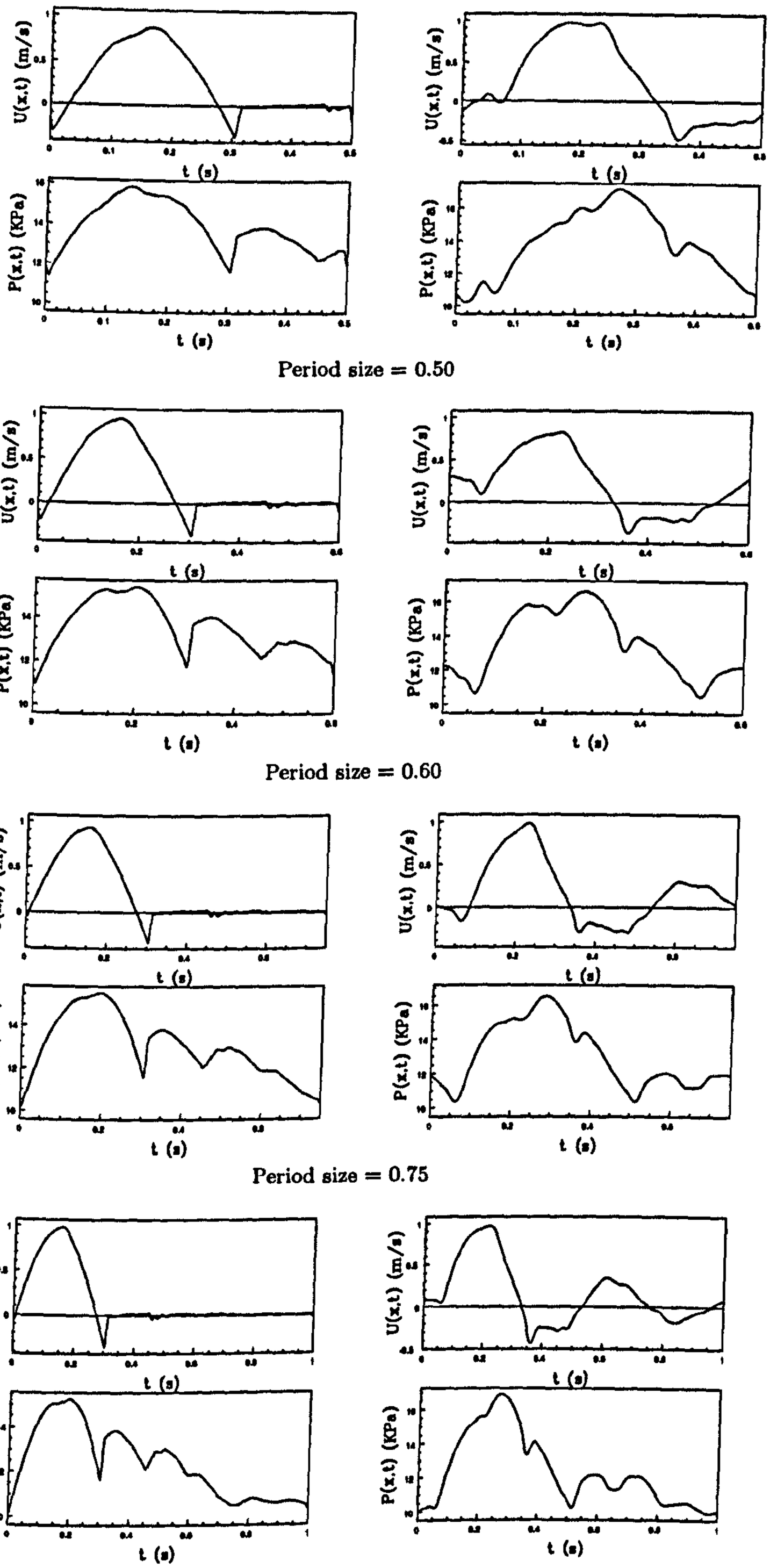


Figure 4.13: Computational pressure and velocity waves in the ascending aorta (artery 1), first column, and brachial (artery 7), second column for different heart rates for boundary condition 4. A time period of T=0.5, 0.6, 0.75 and 1.0 is imposed at the inlet, which is equivalent to a heart rate of 120, 100, 80 and 60 b.p.m. respectively.

60 and 80 b.p.m., but can exceed double this during exercise [95]. To assess the effect this has on the waveforms in the arterial tree we have calculated the pressure and velocity waves for four different heart rates: 60 b.p.m., 80 b.p.m., 100 b.p.m. and 120 b.p.m.. These correspond to a period of T=1.0 s, T=0.75 s, T=0.6 s and T=0.5 s respectively. A terminal reflection coefficient of 0.5 was applied to the terminal vessels and boundary condition 4 was imposed at the inlet. For each of these cases the same half-sine wave was imposed for the W_1 characteristic at the inlet. The period was 0.3 s and the magnitude was 5 kPa. There are transition regions of 0.01 s to simulate the aortic valve opening and closing, with $W_1 = -W_2$ for the rest of the cycle for all cases. Assuming the same inflow waveform is an approximation, because the heart acts differently during exercise, which results in different ejection forms. The results are shown in figure 4.13 for the ascending aorta and the brachial artery (arteries 1 and 7) for the four different heart rates.

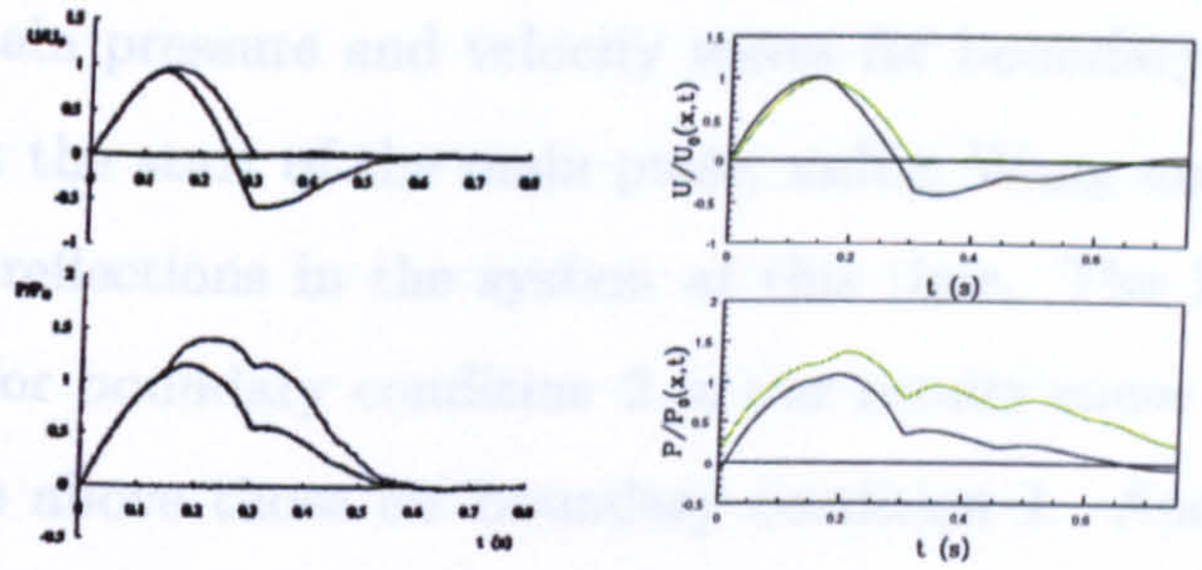
Looking at the waveforms in detail, it can be seen that the velocity waveforms for the ascending aorta are all broadly similar, although the main flow obviously occupies an increasing amount of each heart beat. As the heart rate increases there is also an increasing amount of reversed flow prior to the systolic flow and an increasing deviation of the main flow from a sinusoidal form. The pressure waves look less similar, but the main features are again the same for each heart rate. The major difference is that the later features are removed as the heart rate increases. This is because the following heart beat has commenced by the time the later reflections return to the ascending aorta and hence these reflections reinforce the initial pressure pulse. This leads to a gradually increasing pressure at the start of the cycle for faster heart rates. A similar pattern emerges for the brachial waveforms with the main features similar throughout and the later features being enveloped by the next systolic peak of pressure or flow.

Since the waveforms have relatively similar major features for all heart rates we have only investigated the results for a heart rate of 80 b.p.m. in our subsequent calculations. This rate has been chosen because it is close to a resting heart rate and therefore is most relevant to published clinical results. It is also the heart rate at which measurements were obtained in the human subject studied in Chapter 5 and therefore provides the most appropriate comparisons.

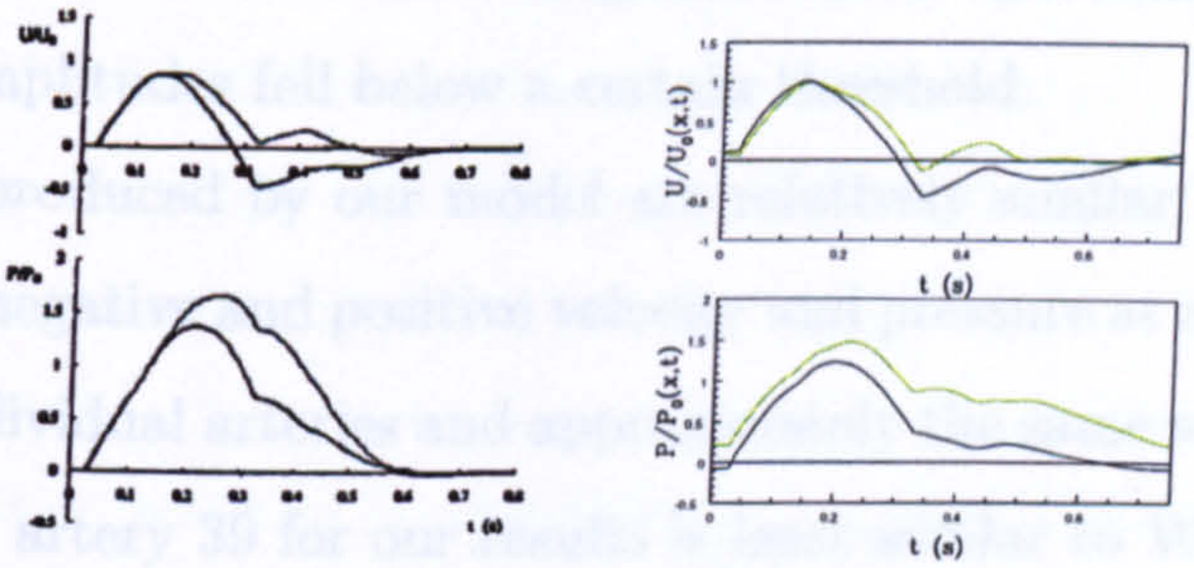
4.3.7 Comparison of waveforms for the well-matched system with the results of Wang and Parker

Our results are compared with those of Wang and Parker [160, 163] in figure 4.14 for arteries 1, 18, 39, 42 and 46 of the network. Wang and Parker modelled their network using inflow boundary conditions similar to our absorber boundary condition (BC1) and velocity boundary condition (BC2) and for clarity these are the only results shown. The waveforms for boundary condition 1 are shown in black for our results and are the lower lines for Wang and Parker's results and for boundary condition 2 our results are green and theirs are the upper traces. Their results have also been normalised by the reference values of the peak velocity, u_0, and peak pressure, P_0 we have therefore presented our data in a similar fashion and have normalised our results by the peak input pressure, 5 kPa, and the peak input velocity, 1 m/s, at the ascending aorta for boundary conditions 1 and 2 respectively.

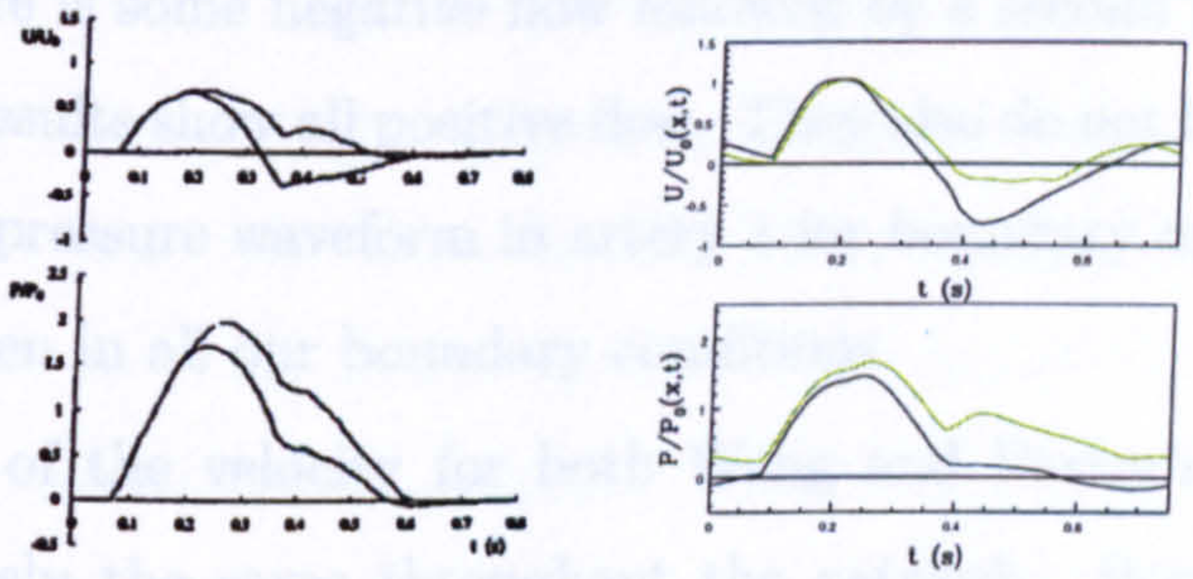
In section 4.3.3 it was found that for the reflector boundary condition (BC2) there was too much reflection in the system if similar levels of terminal resistance to Wang and Parker's were used. In common with the rest of our results, the waveforms presented here for our model are therefore for a lower terminal reflection coefficient of 0.5 for both inflow boundary conditions. This results in similar waveforms to those of Wang and Parker. A possible explanation for why similar results can be produced for different outflow boundary conditions is that their input was not periodic, so their results show only the effect of one heart beat and reflections from previous beats do not accumulate in the system. This explains why in the Wang and Parker results there is zero flow and pressure for 0.2 seconds in artery 46, because the pulse has not reached this artery until this time. However, the reflections in their system still seem small relative to ours and have died completely away after 0.65 seconds for a single wave, so perhaps the fact that they have not modelled their system as periodic does not significantly affect their results. In contrast, our results are periodic with a time period of 0.75 seconds and, as was shown in previous sections, in our model the reflected waves do not die away before the start of the following period. These trapped reflections in the system explain why in our data there is a non-zero amount of flow and pressure before the main pulse. As there are more reflections trapped in the system for boundary condition 2 than for boundary condition 1 this also



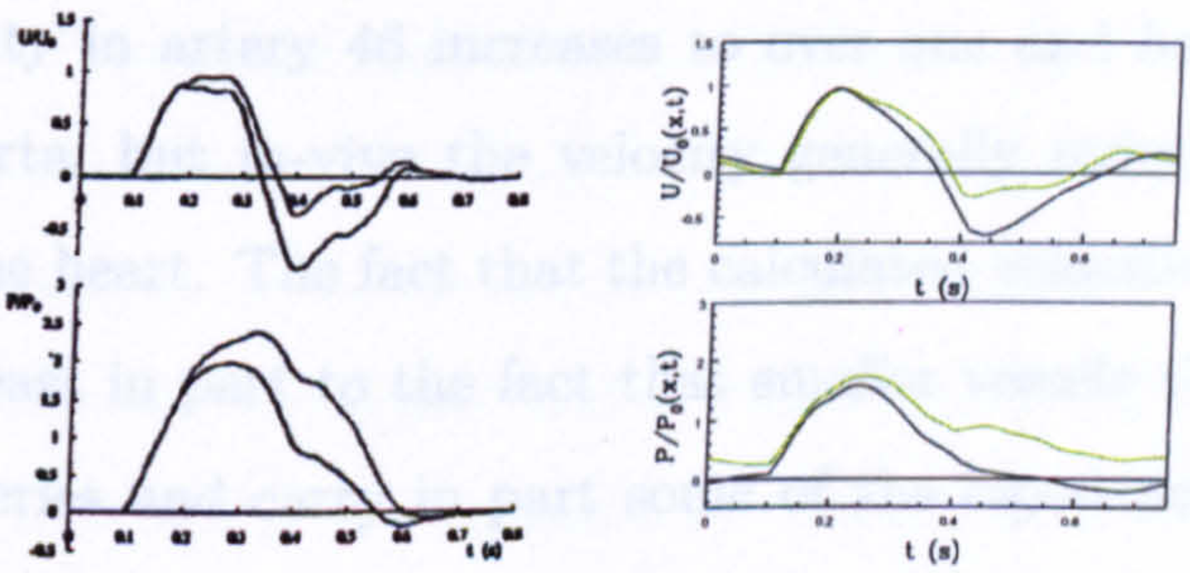
(1) Ascending Aorta



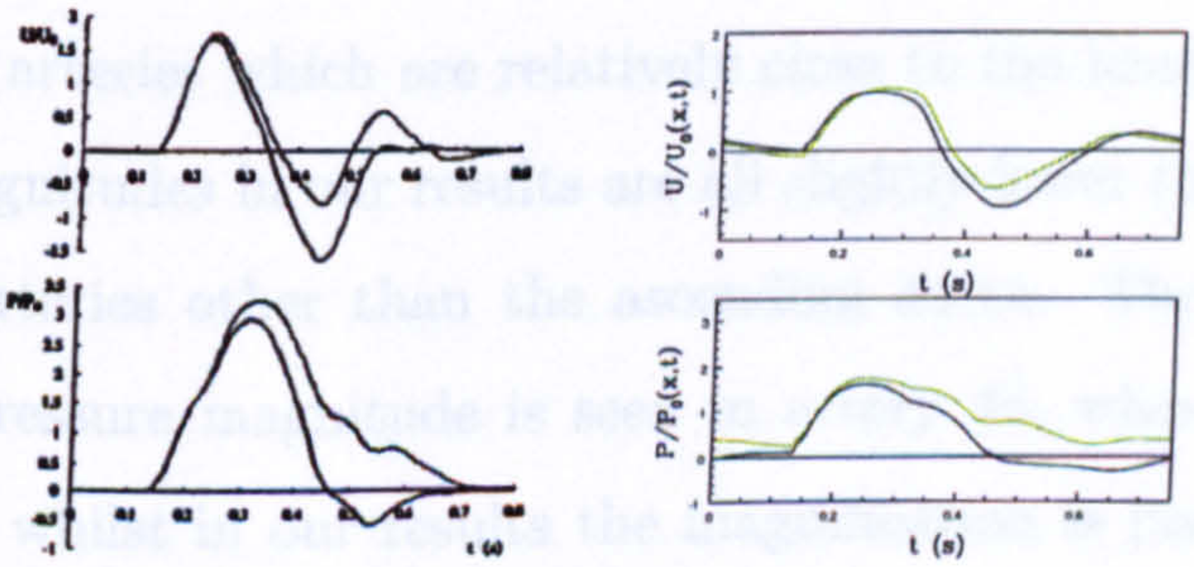
(18) Thoracic Aorta



(39) Abdominal Aorta



(42) Common Iliac



(46) Femoral Artery

Figure 4.14: Non-dimensional waveforms of pressure and velocity in the well-matched network. The waves have been non-dimensionalised by the peak values of the pulses in the ascending aorta. Results are shown for the W_1 absorber boundary condition (BC1) and for an imposed velocity (BC2). On the left are results from Wang and Parker [160, 163] for a single heart beat and on the right are our periodic results for a period of 0.75 seconds. The results for boundary condition 1 are the lower lines in Wang and Parker's graphs and black lines for our results and the results for boundary condition 2 are the upper and green lines.

explains why the main pressure and velocity waves for boundary conditions 1 and 2 do not coincide at the start of the main pulse, unlike Wang and Parker's results where there are no reflections in the system at this time. The larger amounts of trapped reflections for boundary condition 2 in our results cause the pressure and velocity waves to be above those for boundary condition 1. Another reason why there may be fewer reflections in the Wang and Parker model is that they 'killed' waves when their amplitudes fell below a certain threshold.

The waveforms produced by our model are relatively similar to those of Wang and Parker. We see negative and positive velocity and pressure at approximately the same time for the individual arteries and approximately the same wave pattern. The velocity waveform in artery 39 for our results is least similar to Wang and Parker's results, because there is some negative flow followed by a second positive section of flow, whereas their results show all positive flow. They also do not have a pronounced second notch in the pressure waveform in artery 1 for boundary conditions 1 and 2, a feature which is seen in all our boundary conditions.

The magnitudes of the velocity for both Wang and Parker's results and our own are approximately the same throughout the network. However, Wang and Parker's peak velocity in artery 46 increases to over one and half times the peak in the ascending aorta, but in-vivo the velocity generally reduces in the arteries further away from the heart. The fact that the calculated velocities are higher than expected is due at least in part to the fact that smaller vessels that would branch from these large arteries and carry in part some of the blood flow have not been modelled. However, we would not expect to see a large decline in velocity because these results are for arteries which are relatively close to the heart.

The pressure magnitudes in our results are all slightly lower than the Wang and Parker results for arteries other than the ascending aorta. The most significant difference in peak pressure magnitude is seen in artery 46, where in their results it has nearly tripled whilst in our results the magnification is just over one and a half times. Amplification of the pressure wave is known to occur in-vivo and in the femoral is likely to be 1.5-2 times that of the ascending aorta (section 4.3.9).

Some of the differences seen in the results could be due to the location where the waveforms are recorded in the artery. This set of waveforms were all recorded

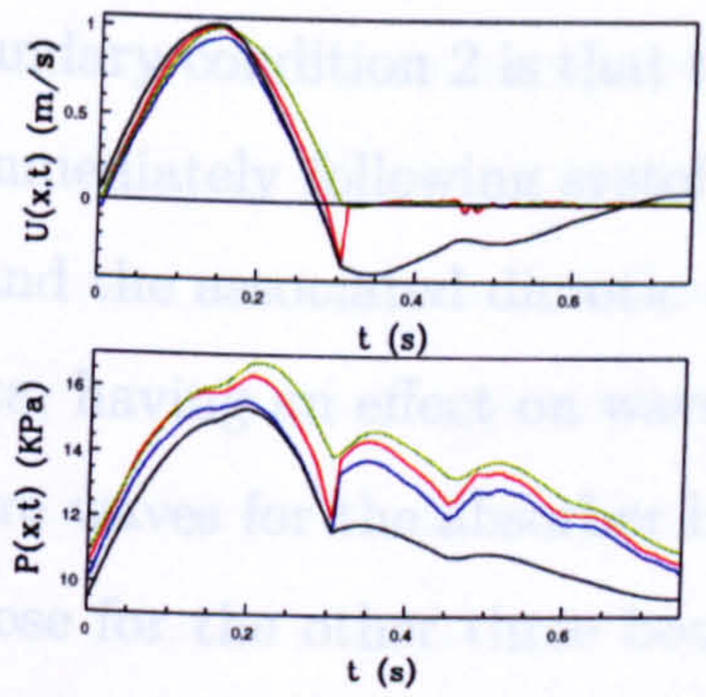
at the start of the artery for our results, except for the ascending aorta where they were recorded mid-way along the vessel, but the locations are all mid-way along each segment for Wang and Parker's results.

Overall the waveforms in the different arteries of the network computed using our model are relatively similar to Wang and Parker's results. The main difference is that we have far more reflections in our system even when we have reduced the terminal resistance to 0.5 and this is particularly noticeable late in the cycle. They appear to lose information beyond 0.65 seconds. There are also some differences in the magnitude of the different waves.

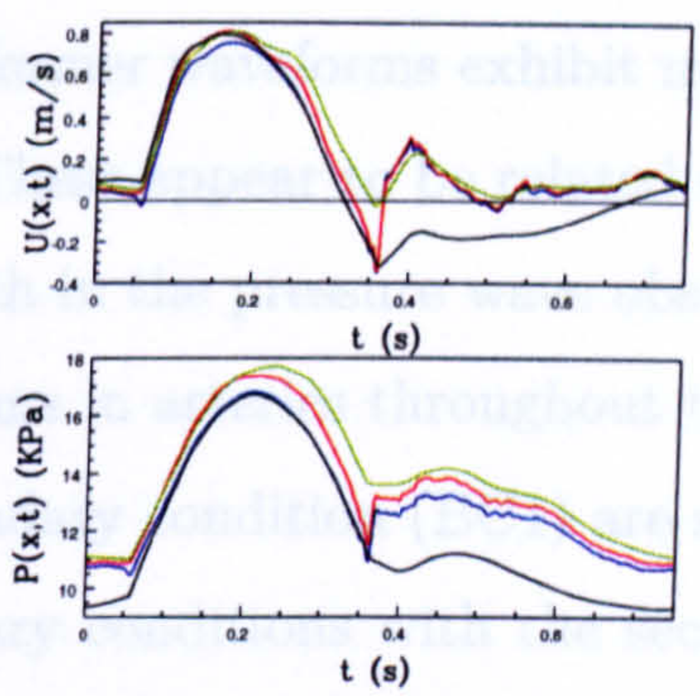
4.3.8 Comparison of waveforms for different inflow boundary conditions with typical in-vivo waveforms throughout the network

Up to this point we have primarily concentrated on the results in the ascending aorta, however we are interested in the waveforms throughout the body, hence we now examine the computational results in more of the arteries of the network. The pressure and velocity waveforms in arteries 1, 27, 41, 15, 7, 8, 52 and 54 of the 55 artery network are shown in figure 4.15 for the different boundary conditions considered previously. These arteries have been chosen to show the results at different sites in the network. The time period was chosen to be 0.75 and the terminal reflection coefficient was set as 0.5 for all the terminal vessels, because this set of parameters is physiologically justifiable and correlates best with published clinical measurements, as well as our own, discussed in Chapter 5. The locations in the arteries for which the waveforms are shown have also been chosen so that we can compare these results with our clinical measurements and the results of our new MRI model, discussed in section 5.2.3. The waveforms are coloured according to the inflow boundary conditions with black as boundary condition 1, green as boundary condition 2, red as boundary condition 3 and blue as boundary condition 4. The waveforms are shown at the start of artery 52, mid-way along arteries 1, 7, 8 and 54 and at the end of arteries 15, 27 and 41.

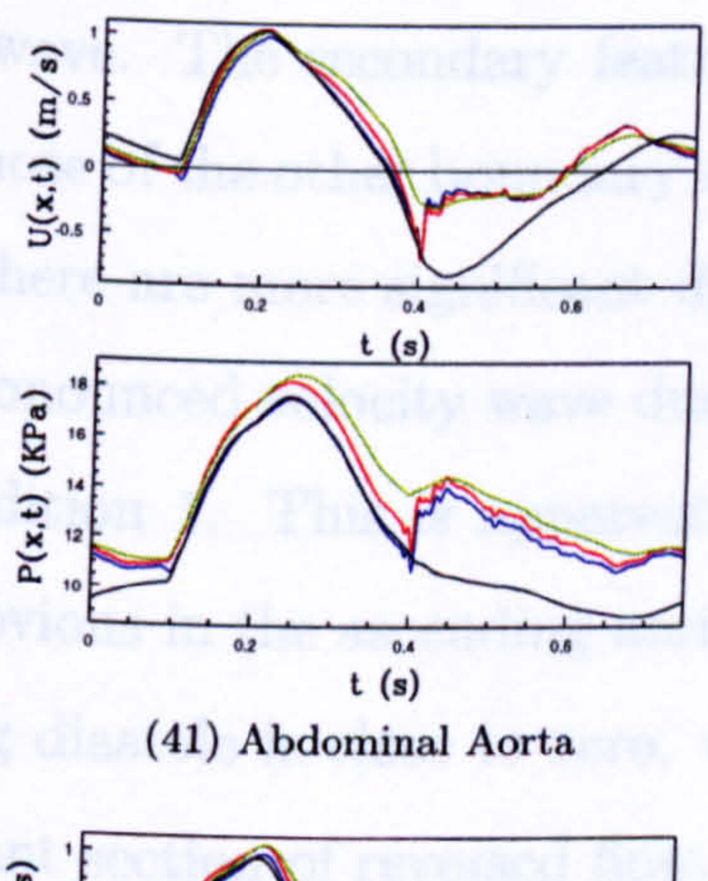
Looking first at the effects of the boundary conditions, generally the shapes of the waves in all of the arteries of the system are similar for boundary conditions 2, 3 and 4. In particular the results for boundary conditions 3 and 4 are almost identical



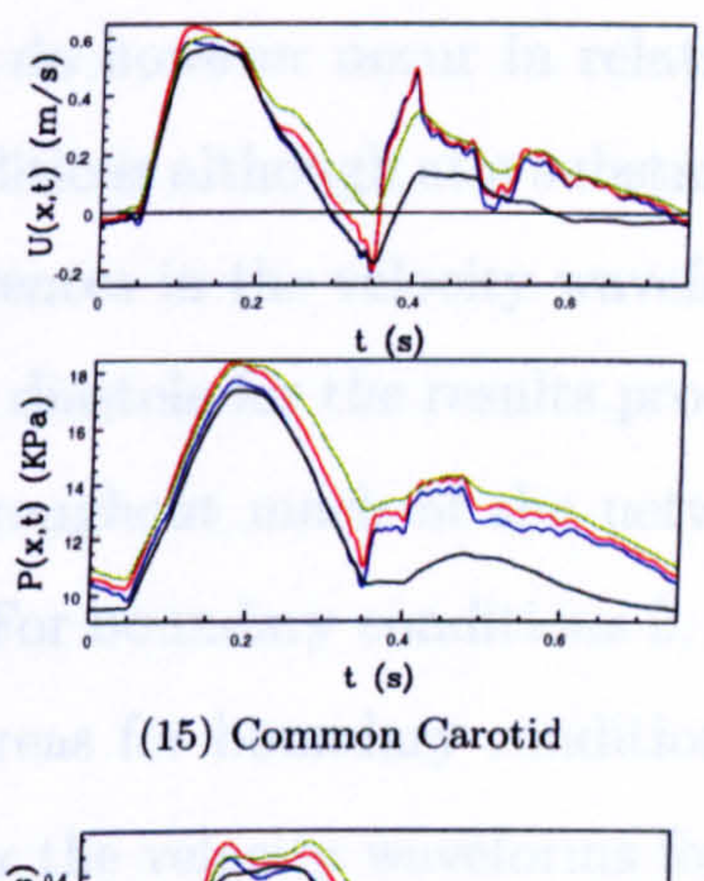
(1) Ascending Aorta



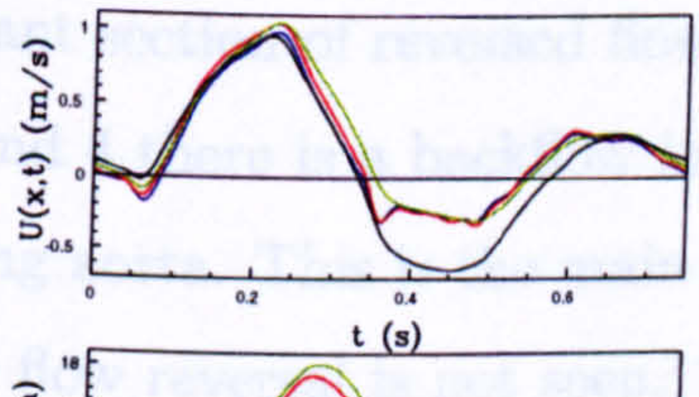
(27) Thoracic Aorta



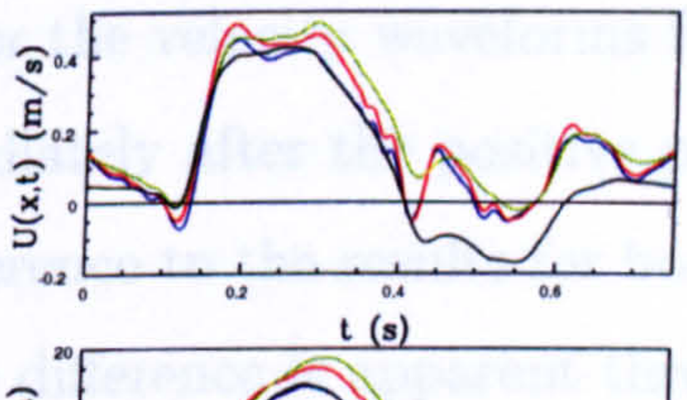
(41) Abdominal Aorta



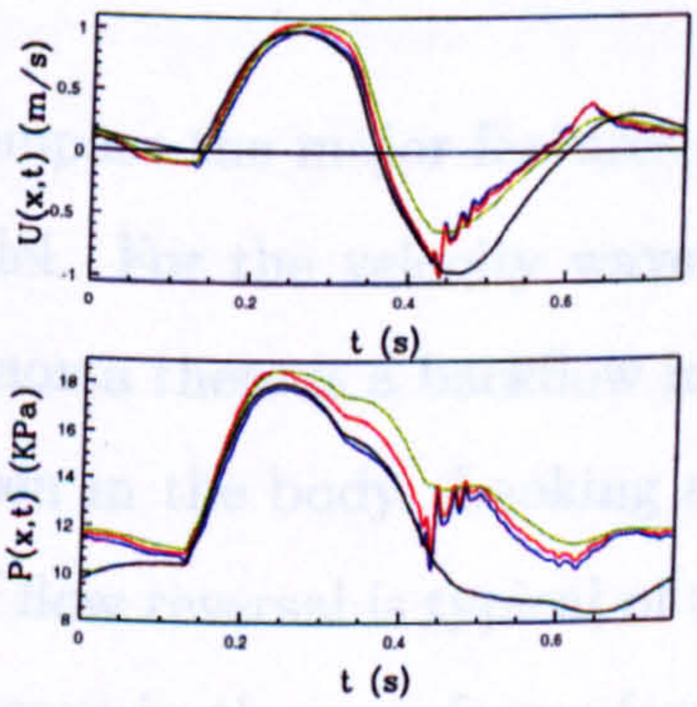
(15) Common Carotid



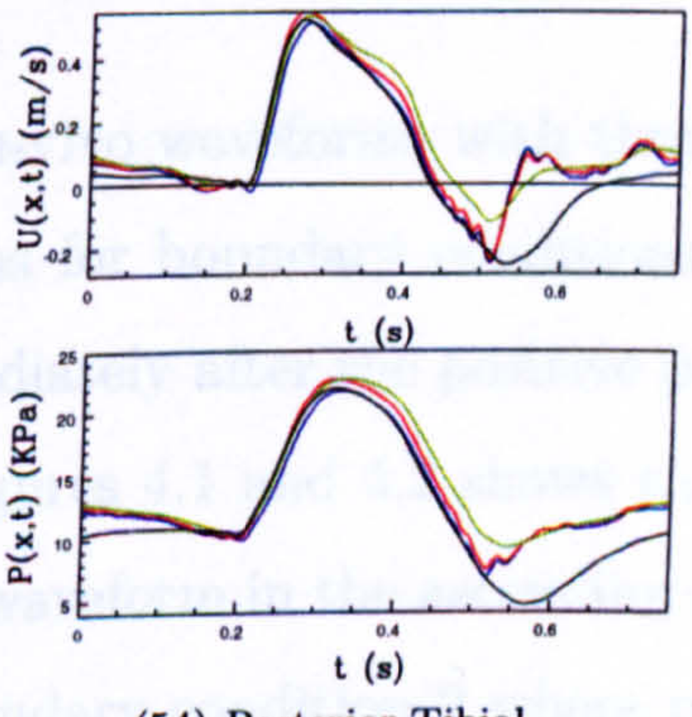
(7) Brachial Artery



(8) Radial Artery



(52) Femoral Artery



(54) Posterior Tibial

Figure 4.15: Computational results for waveforms in the well-matched network for four different inflow boundary conditions 1 (black), 2 (green), 3 (red) and 4 (blue). The waveforms have been taken in the same locations as in Chapter 5 and are for a cardiac period of 0.75 seconds, with a terminal resistance of 0.5 on the terminal vessels.

to one another. The main difference between the results for boundary conditions 3 and 4 and boundary condition 2 is that the former waveforms exhibit more notches, particularly immediately following systole. These appear to be related to the sharp flow reversal and the associated dicrotic notch in the pressure wave observed in the ascending aorta, having an effect on waveforms in arteries throughout the system.

The pressure waves for the absorber boundary condition (BC1) are significantly different to those for the other three boundary conditions with the secondary features much smaller throughout the network and hence the waves are more similar to the input wave. The secondary features do however occur in relatively similar locations to those of the other boundary conditions although at a substantially lower magnitude. There are more significant differences in the velocity waveforms with a much more pronounced velocity wave during diastole for the results produced using boundary condition 1. This is apparent throughout much of the network, but is particularly obvious in the ascending aorta. For boundary conditions 2, 3 and 4 the velocity during diastole is close to zero, whereas for boundary condition 1 there is a very significant section of reversed flow. For the velocity waveforms for boundary conditions 3 and 4 there is a backflow immediately after the positive peak velocity in the ascending aorta. This is the main difference to the results for boundary condition 2 where flow reversal is not seen. This difference is apparent throughout the network with the velocities for boundary condition 2 slightly higher and smoother than those for boundary conditions 3 and 4. However, these differences are relatively small when compared with the large diferences produced using boundary condition 1.

We now compare the major features of in-vivo waveforms with those calculated using our model. For the velocity waveforms for boundary conditions 3 and 4 in the ascending aorta there is a backflow immediately after the positive peak velocity as would be seen in the body. Looking at figures 4.1 and 4.2 shows that this very sharp region of flow reversal is typical of the waveform in the ascending aorta. Flow reversal is not seen in the waveforms for boundary condition 2 where positive flow only has been prescribed and for boundary condition 1 much more flow reversal is seen.

Looking at the pressure waves in the ascending aorta, the peak pressure in all

four boundary conditions occurs at late systole, which is physiological. For boundary conditions 3 and 4 there is a sharp increase in the pressure waveform after the systolic peak at the time of the aortic valve closure followed by a gradual decline in pressure. These features compare well with those seen in-vivo, however, for boundary condition 2 there is no sharp increase in pressure and for boundary condition 1 the pressure dips under its base value (9.9 kPa), which is not a physiologically correct feature. Another feature that is not observed in-vivo is that all the pressure waves have a second smaller dip in pressure during diastole at time 0.45 seconds.

Looking at the in-vivo measurements further down the aorta, in the thoracic aorta and the abdominal aorta (arteries 27 and 41), in figure 4.1 the dicrotic notch has a lower minimum pressure, is further away from the peak pressure and is generally less significant. These features are also observable in our results, although the reduction in the secondary pressure peak is not as great as in-vivo. However, for boundary condition 1 the results are less physiological, because there is no second peak of pressure in artery 41.

The velocity in the more distal arteries generally have some flow reversal followed by a second peak of positive flow. These features are apparent in our results, see artery 41 for example. The flow looks the most physiological for boundary conditions 2, 3 and 4, because for boundary condition 1 there appears to be too much flow reversal as is the case in the ascending aorta. However, for boundary condition 2 there is no flow reversal in the thoracic aorta, artery 27, where we would expect to see some in-vivo, therefore in arteries closer to the heart waveforms for boundary conditions 3 and 4 appear more physiological.

A well known feature of the flow in the carotid arteries is that it is all positive in a healthy body, figure 4.6. For our results, boundary condition 2 is the only case where no flow reversal appears, figure 4.15 (15), and in general the dip in the velocity is excessive.

For both the brachial artery (artery 7) and the femoral artery (artery 52) waveforms, there is a flow reversal after the peak velocity and then a secondary region of positive flow in our computations. This is likely to be seen in the femoral in the body, figure 4.1, but for all our boundary conditions the secondary peaks appear a little high. In the absence of other in-vivo flow waves in the brachial artery, we look

at our clinical measurements in Chapter 5, section 5.1.3, figure 5.7, which show that there is no flow reversal, so the waveforms from our computations do not appear to be physiologically accurate.

The pressure wave in the femoral artery in the body exhibits a gradual decline, figure 4.5 in section 4.2, but our pressure waves for this system do not appear entirely similar to the in-vivo measurements. For boundary conditions 3 and 4 there is quite a large second peak in diastole. For boundary condition 2 there is a more gradual decline but the systolic pressure wave occupies a large portion of the cycle and, although for boundary condition 1 there are no second peaks of pressure and the pressure declines smoothly, it then drops too far and then slowly starts to increase. The pressure wave for the brachial in the computations shows too many secondary peaks where it should only show one, especially for boundary conditions 3 and 4. Again for boundary condition 1 the pressure shows no secondary peaks but the pressure drops too far then slowly increases until the next pulse.

In the terminal vessels of our system, the radial artery (artery 8) and posterior tibial (artery 54), we see some negative flow and then a secondary region of positive flow for boundary condition 1 and these waveforms appear relatively physiological when compared with our in-vivo measurements, figure 5.7. The velocity waveforms in the posterior tibial for boundary conditions 2, 3 and 4 are very similar to that of boundary condition 1, however the velocity waveforms for the radial for boundary conditions 2, 3 and 4 appear less physiological and show hardly any reversed flow and two smaller peaks of velocity after the main pulse. As with the brachial, no second peak of pressure is seen after the peak pressure in the radial waveform for all four boundary conditions. The pressure waves for the posterior tibial do appear more physiological, see figure 4.5. It is roughly the shape of a half sinusoidal wave for all boundary conditions. However the waves may drop a little too far, particularly for boundary condition 1, and are perhaps not as spiked as for the in-vivo measurements.

For all four boundary conditions it can be seen that it takes longer for the waves to reach more distal vessels in the system. This is in accord with in-vivo results in the body as well as the wave speeds calculated for this network (Appendix A.1). The wave takes approximately 0.05 seconds to reach mid-way along the aorta (artery 27), 0.1 seconds to reach the distal end of the aorta (artery 41), 0.13 seconds to reach the

femoral (artery 52) and 0.2 seconds to reach the posterior tibial (artery 54). Figure 4.3 shows waveforms taken from the aorta to the femoral for a human in-vivo and illustrates the time lag between the waveforms in the aorta and the femoral artery, showing that waves propagate at a finite speed.

Overall some of the waveforms appear physiological whilst others do not. The waveforms in the aorta are probably the most physiological, but here and throughout the network the secondary features are too large. Although there are some significant differences between the different boundary conditions, the general features are relatively similar. Boundary conditions 3 and 4 exhibit more notches than the other cases, but perhaps some of this is due to an excessive reversed flow prescribed for boundary condition 3 and too much reflection for boundary condition 4. The waveforms might also be smoothed, if there were more reflections throughout the system. The model as it stands does not incorporate any dissipative effects, which may improve the waveforms, section 5.6.

To model the system by imposing boundary condition 4 at the inlet is fundamentally more attractive because we are not prescribing a sharp dicrotic notch in the pressure wave or a flow reversal and hence no assumptions are being made about the shape of the waveforms in the system, beyond the sine wave form of the input. It is interesting to note that the sharp decrease in velocity following the peak flow is a consequence of the reflections in the network.

4.3.9 Magnitudes of pressure and velocity in the well-matched arterial network

Having looked at the shape of the waveforms we now assess how the magnitudes of the velocity and pressure waves change throughout the network. To do this we have non-dimensionalised the pressure and velocity in all the arteries by the peak pressure and peak velocity in the ascending aorta for the case with the part absorber/part reflector boundary condition (BC4). The diastolic pressure in the ascending aorta has been subtracted from the pressure waves so that the non-dimensionalised pressure waveforms essentially show the pressure pulse. The time has also been non-dimensionalised by the cardiac period, 0.75 s.

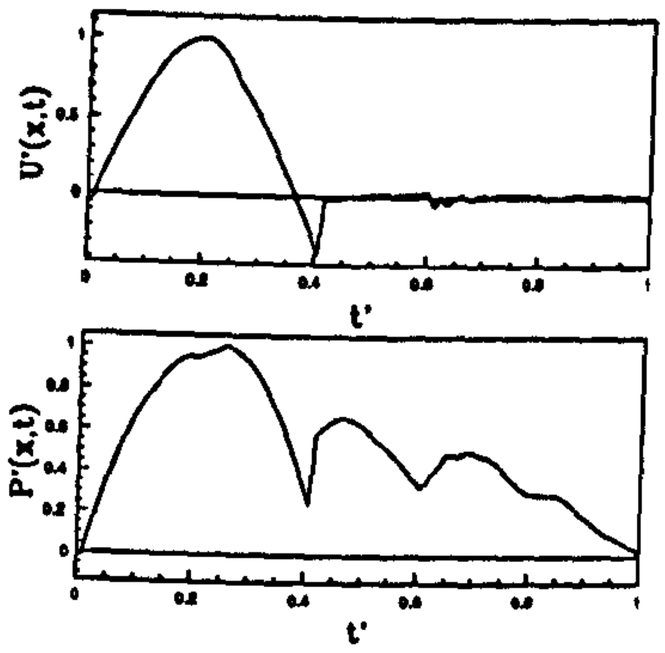
Figure 4.16 shows a comparison of the pressure and velocity waveforms in arteries

1, 27, 41, 15, 7, 8, 52 and 54 of the 55 arterial network. The figures show that the peak pressure increases and the minimum pressure decreases slowly in the arterial network with increasing distance from the heart. This is in accordance with in-vivo data, which shows that the pressure difference in a peripheral artery such as the femoral artery (52) is approximately 1.5-2 times that found in the ascending aorta (1), figure 4.1.

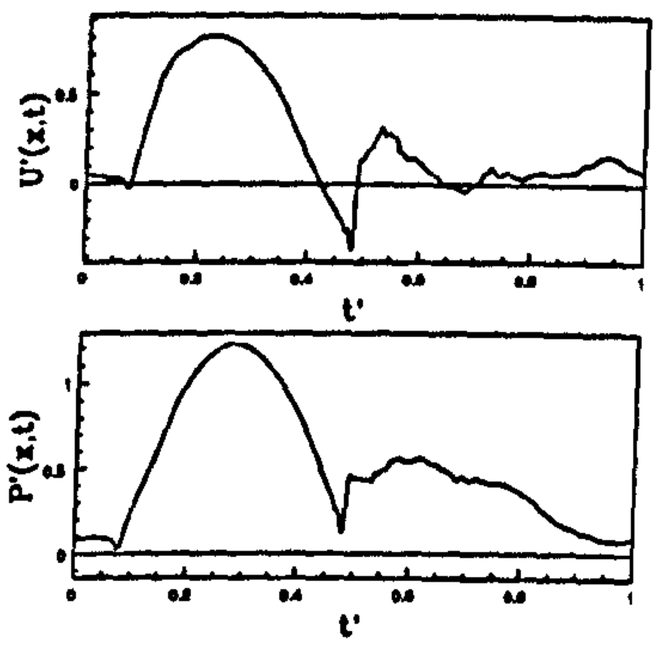
The peak pressure at the distal end of the abdominal aorta, artery 41, is higher than the peak pressure in the ascending aorta. Going a little further distally to the proximal end of the femoral, artery 52, the peak pressure has increased slightly and is nearly one and half times as large as that in the ascending aorta. In the posterior tibial, artery 54, the peak pressure has doubled. It can also be seen that the pressure has increased along the length of the arm from the brachial, artery 7, to the radial artery, artery 8, which is now one and a half times as large as that in the ascending aorta.

Figure 4.1 shows that the velocity decreases in the arterial system with distance from the heart. The velocity has significantly decreased in the terminal vessels, radial (artery 8) and posterior tibial (artery 54) and also in the common carotid (artery 15). However, it has not significantly decreased in the other arteries in the system, such as the abdominal aorta (41) and brachial artery (7), where the velocity is still approximately equal to one. It is not surprising that the velocity waveforms do not appear as physiological as the pressure waves because the velocity is very sensitive to the local arterial diameter, the relative levels of reflection coefficients on the terminal vessels and the lack of modelling of the smaller vessels.

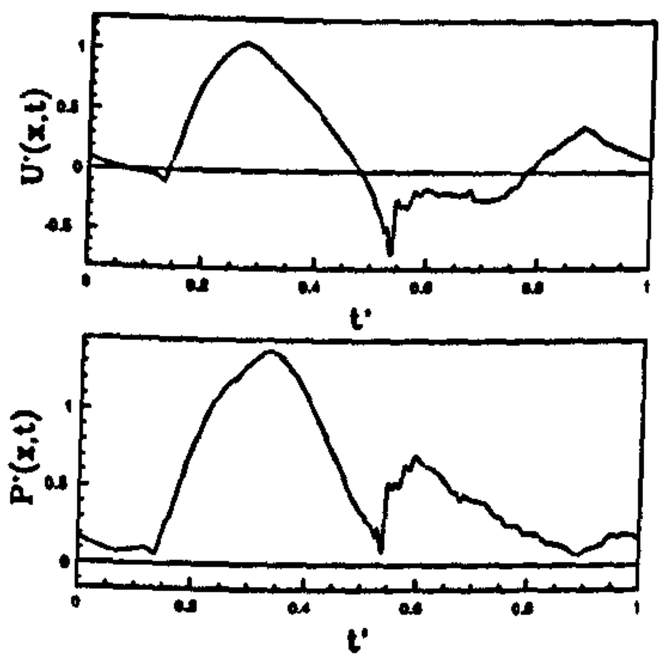
In conclusion we note that although the precise form of the physiological waves have not been modelled the overall results are very encouraging considering the relative simplicity of the simulation. We consider the effects of some of the assumptions further when we look at the new network in Chapter 5 and further discussion of the waveforms is deferred until section 5.2.



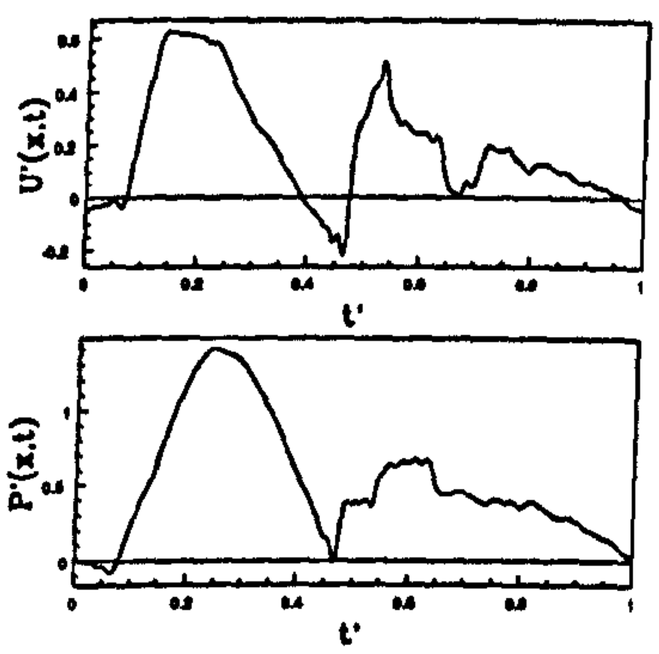
(1) Ascending Aorta



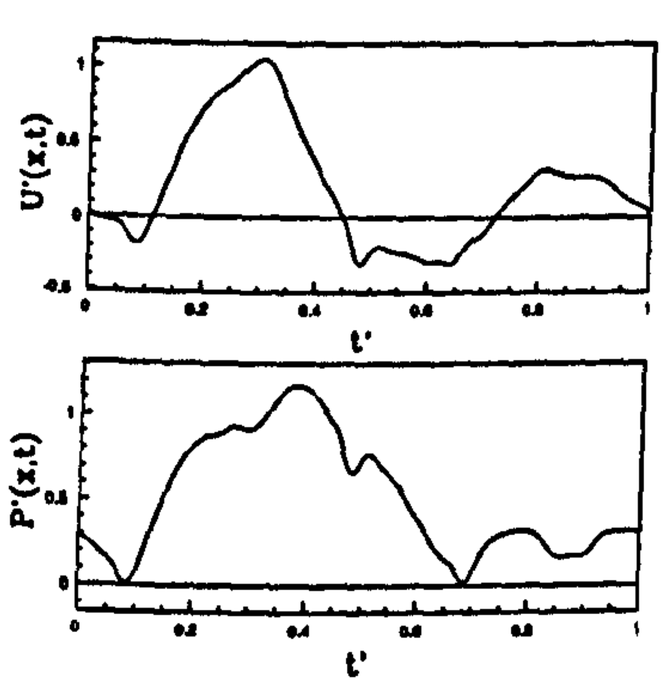
(27) Thoracic Aorta



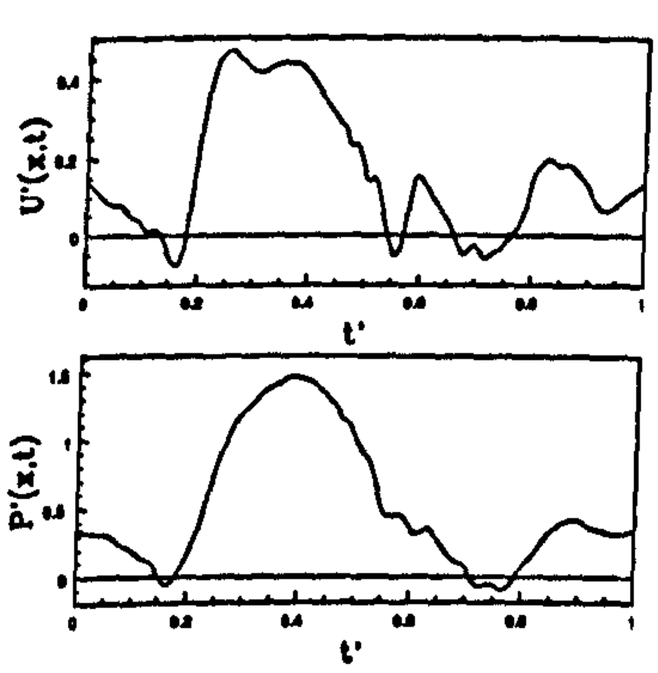
(41) Abdominal Aorta



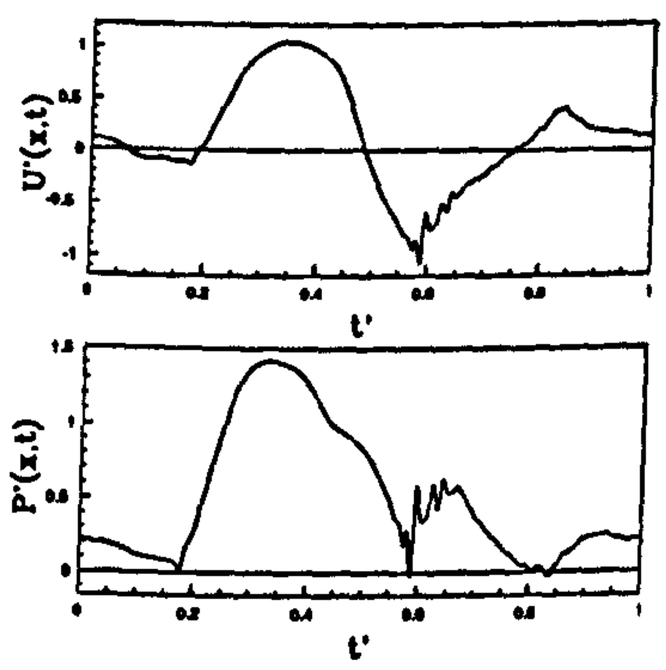
(15) Common Carotid



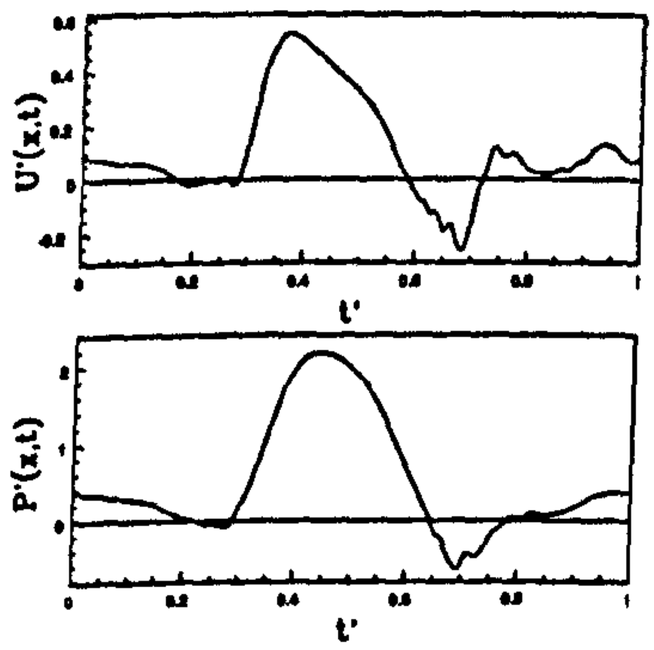
(7) Brachial Artery



(8) Radial Artery



(52) Femoral Artery



(54) Posterior Tibial

Figure 4.16: Non-dimensionalised results obtained in the well-matched network for inflow boundary condition 4. The velocities and pressures have been normalised by the peak and baseline values in the ascending aorta. Time has been normalised by the period for 1 cycle. This clearly shows the amplification of the pressure wave with distance from the heart.

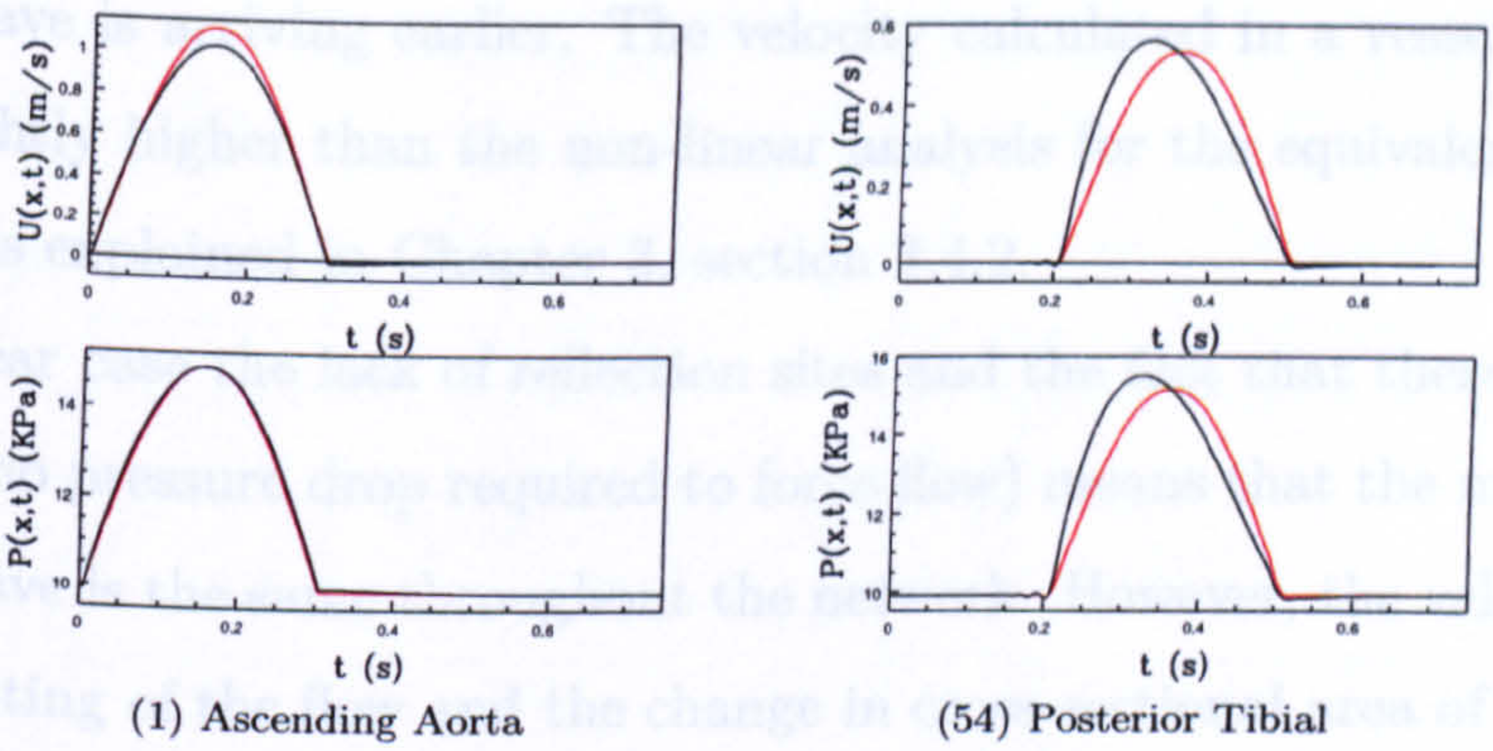
4.4 A comparison of the waveforms obtained using linear and non-linear analysis in the well-matched network

All the results in the well-matched network up to this point have been computed using the non-linear model. This avoids certain restrictions of the linearised model of the network, which include a constant wavespeed in each vessel and constant cross-sectional area arterial segments. We now apply the linearised code to the well-matched network to investigate any differences when compared with the non-linear results. The waveforms obtained using linear and non-linear models to compute the wave propagation in a single straight tube and a simple three arterial bifurcation have been discussed in section 3.4. The velocity and area waveforms were found to be different in shape in the single tube, section 3.4.1, due to a faster wavespeed in the vessel for the non-linear case when the area increased and velocity increased, however this was an exaggerated case and not a physiological example of an artery. In the bifurcation, section 3.4.2, the pressure and velocity waveforms in artery 1 were found to be very similar, but this was only in a three artery tree with no terminal resistance on the end vessels. We therefore now compare the waveforms in the physiological network of 55 arteries. Results are presented for the velocity and pressure waveforms in the well-matched system using linear and non-linear analysis both with and without terminal resistance. This allows comparison of the results of previous investigations using linear modelling and may explain some of the differences between our results and those of Wang and Parker.

4.4.1 The waveforms in the network with no terminal resistance

It was shown incidentally in the section on terminal reflection coefficients in figure 4.10, that for the non-linear modelling in the Wang and Parker arterial network very few reflections occurred in the system when there was no terminal resistance and that large reflections only appeared in the system once a reflection coefficient was applied to the terminal vessels. We now consider the differences in the waveforms in the well-matched network with no terminal resistance computed with the linear and non-linear method.

To maintain the zero reflection coefficient setup throughout, the input to the



(1) Ascending Aorta (54) Posterior Tibial

Figure 4.17: Computational waveforms of pressure and velocity at the ascending aorta and posterior tibial artery, calculated using the linear (red) and the non-linear (black) models. No terminal reflection was applied and boundary condition 1 was applied at the inflow.

network was prescribed as boundary condition 1, which acts like an absorber at the heart, i.e. backward travelling waves are free to leave at the ascending aorta. Figure 4.17 shows the waveforms of pressure, P, and velocity, u, at the root of the network, (ascending aorta, artery 1) and at the distal end of the network, (posterior tibial, artery 54). The calculated linear results are the red lines and the non-linear results the black lines.

The bifurcations are well-matched for linear theory, therefore there are no reflection sites in the network for the linear case and thus when combined with the fact that the wavespeed is constant the waveforms in the system are all the same shape as the input wave. The non-linear solution shows a small flow reversal and increase in pressure after the sine wave in the ascending aorta. This is due to the arteries only being well-matched for linear and not non-linear theory and therefore there is a small amount of reflection. However, the reflections are very minor and the fact that the waveforms are so similar despite the presence of a large number of bifurcations indicates that a well-matched system where the reflection coefficients at bifurcations have been calculated to equal zero using a linear analysis is also very close to being well-matched for non-linear analysis, which is as expected from section 3.4.2. The major difference in the waves is that the non-linear solutions of pressure and velocity clearly show that the input sine wave becomes skewed as the wave travels throughout the network. The waves in the ascending aorta are very similar but for, artery 54, where the waves have travelled for approximately 0.2 seconds from the heart, the non-linear effect of the wave speed increasing with area and velocity has had time to have an effect and the wave has been skewed so that

more of the wave is arriving earlier. The velocity calculated in a vessel with linear analysis is slightly higher than the non-linear analysis for the equivalent change in pressure, this is explained in Chapter 3, section 3.4.2.

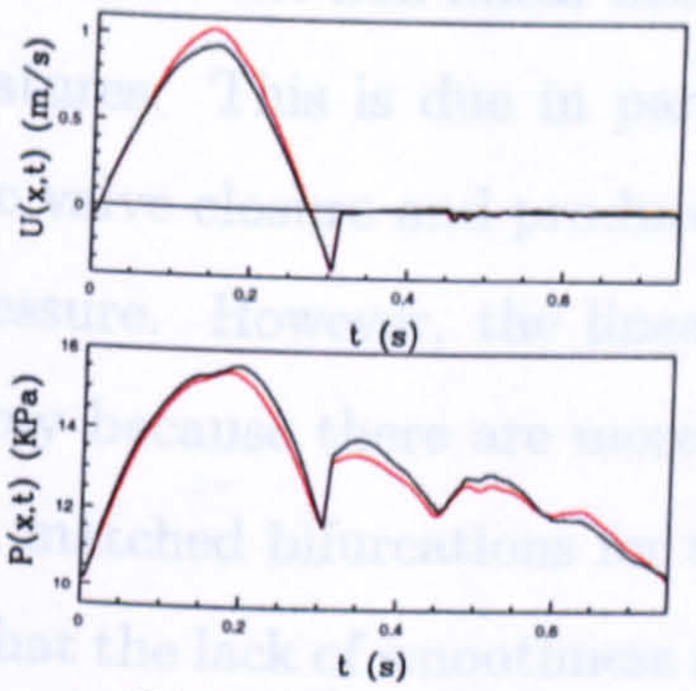
For the linear case the lack of reflection sites and the fact that there is no resistance to flow (no pressure drop required to force flow) means that the magnitude of the pressure wave is the same throughout the network. However, the velocities alter due to the splitting of the flow and the change in cross-sectional area of the vessels.

The small oscillations that occur before and after the sine wave in artery 54, figure 4.17 (54), for both solution methods are because a half sine-wave is a slope discontinuous function and is difficult to represent using a polynomial. Using more elements in each vessel would also help to minimise these oscillations.

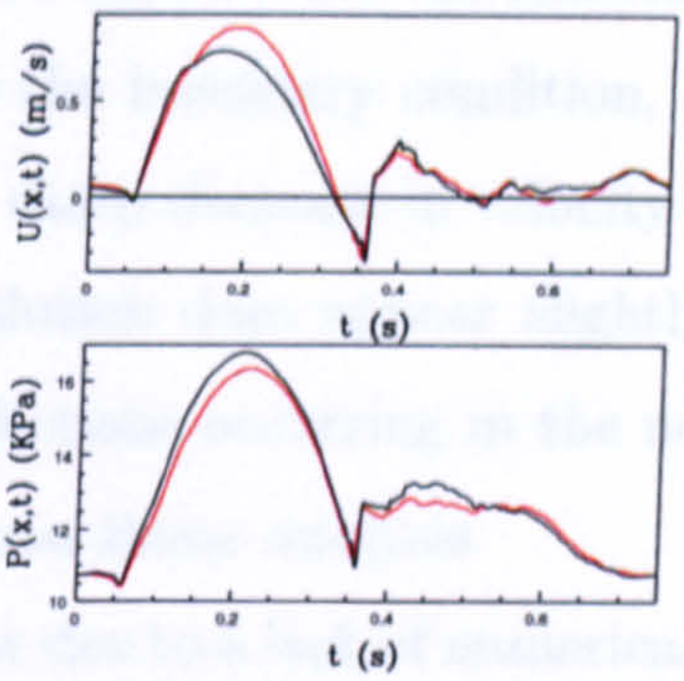
4.4.2 The well-matched network with terminal resistance

In the previous section we have seen that there is a small but significant difference between the linear and non-linear waveforms in the distal arteries, but that these differences are predominantly due to the distance the wave has travelled not to spurious reflections at the bifurcations. The differences increase as the wave travels further and since at least a portion of the waves are reflected then there will be some components of the waves that effectively travel very large distances. This may cause some differences and figure 4.18 shows a comparison of the waveforms in artery 1, 27, 41, 15, 7, 8, 52 and 54 in the 55 arterial network calculated using linear and non-linear theory. Terminal resistance has been applied to the terminal vessels therefore the waves are now reflected. They are also reflected at the heart, because we have applied boundary condition 4 at the inlet. The waveforms are shown for cycle 6 for both velocity and pressure.

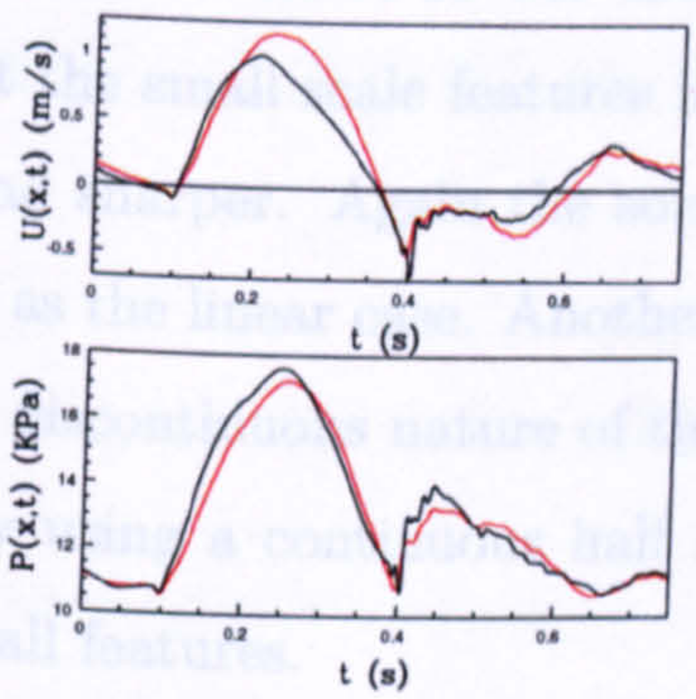
For the non-linear waveforms throughout the network the pressure is slightly higher and the velocity slightly lower than for the linear waveforms. The waveforms further away from the heart, however, are also skewed for the non-linear solution and this skewness is the main difference between the waveforms for the two solution methods. The skewness is most apparent in arteries 8, 52 and 54, which are relatively distant from the heart, hence the increase in wave speed for the non-linear case has had more time to produce an effect.



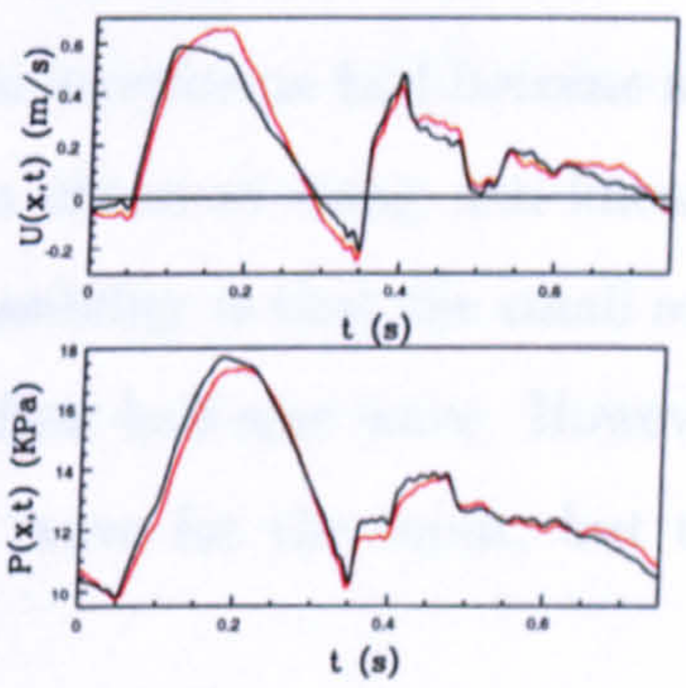
(1) Ascending Aorta



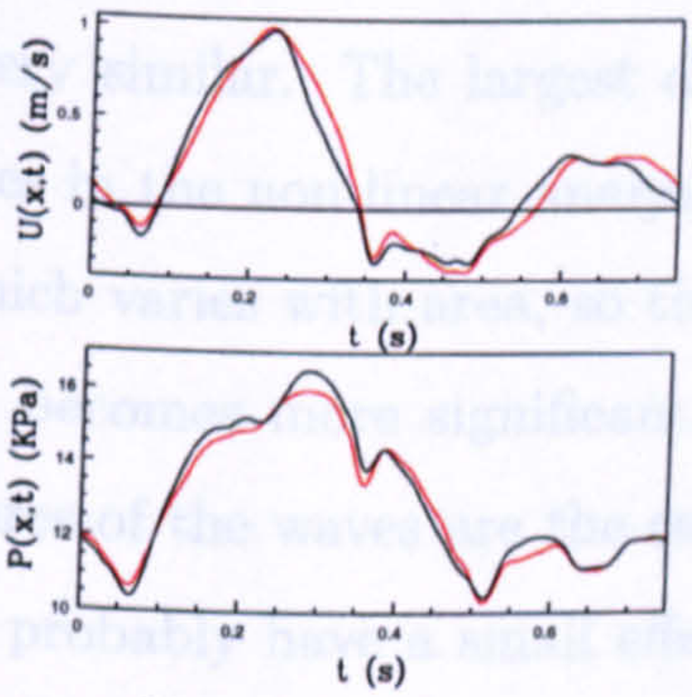
(27) Thoracic Aorta



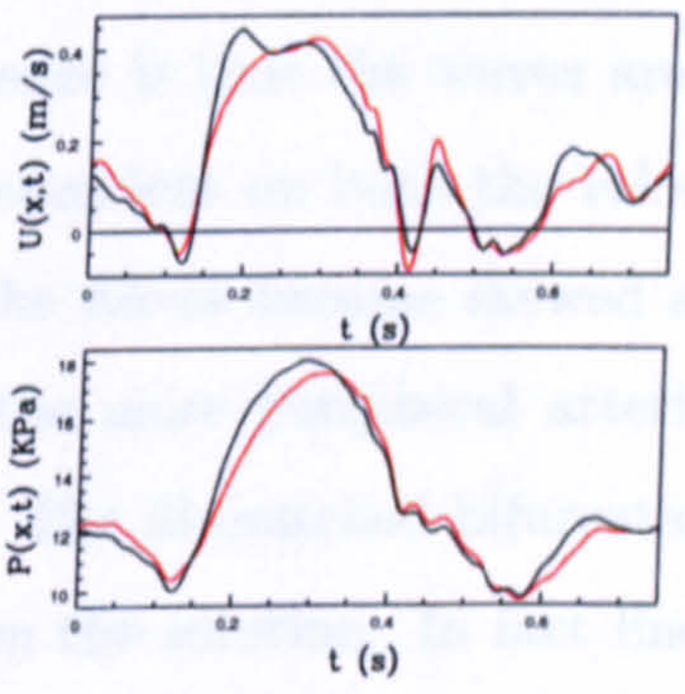
(41) Abdominal Aorta



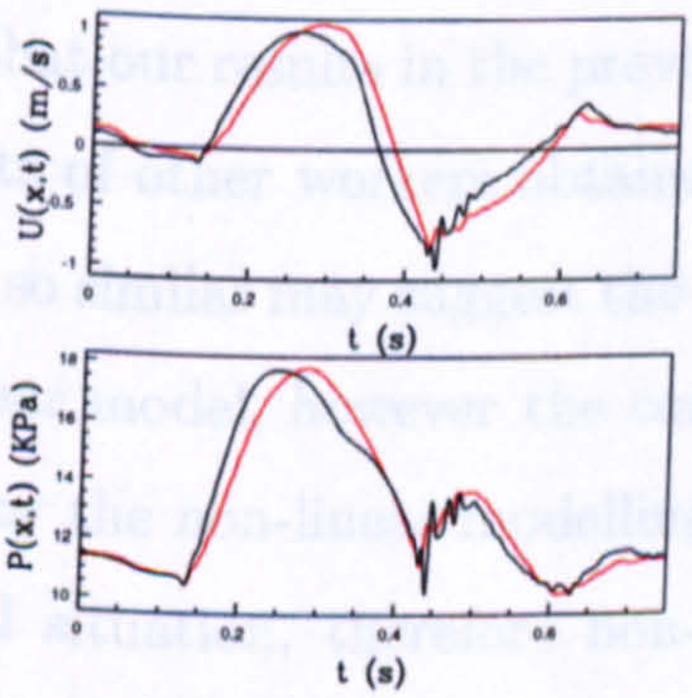
(15) Common Carotid



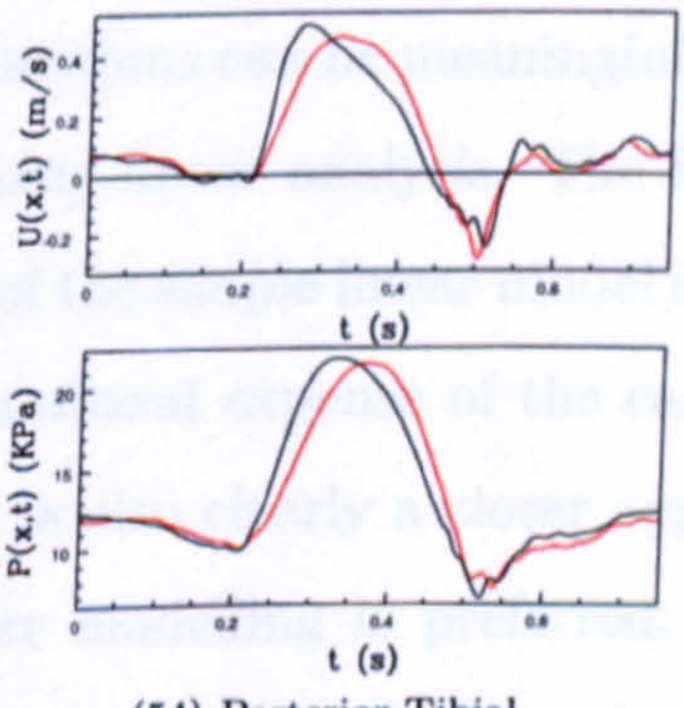
(7) Brachial Artery



(8) Radial Artery



(52) Femoral Artery



(54) Posterior Tibial

Figure 4.18: Computational pressure and velocity waveforms throughout the well-matched network for the linear (red) and non-linear (black) models. This shows that the major features of the waves are the same, although there are differences in the precise shapes. A terminal reflection coefficient of 0.5 is applied to the outflows and boundary condition 4 was used as the inflow and the cardiac period was 0.75.

The waveforms for the non-linear and linear solution are not smooth and exhibit small scale features. This is due in part to the boundary condition, which simulates the aortic valve closure and produces a sharp decrease in velocity and a sharp increase in pressure. However, the linear solution does appear slightly smoother, which is possibly because there are more reflections occurring in the network from the not so well matched bifurcations for the non-linear analysis.

To ensure that the lack of smoothness is not due to a lack of numerical resolution, a higher polynomial order of 15 was used to calculate the solution in the network. We found that the small scale features in the waveforms had become slightly more pronounced and sharper. Again the solution obtained using non-linear analysis is not as smooth as the linear case. Another possibility is that the small scale features are due to the discontinuous nature of the inflow half sine wave. However, this was investigated by using a continuous half sin^2 wave for the input, but this did not remove the small features.

Overall the pressure and velocity waveforms calculated with linear and non-linear analysis are very similar. The largest difference is that the waves are propagated at varying rates in the non-linear analysis dependent on both the velocity and the wavespeed, which varies with area, so that the waves become skewed after a time. This skewness becomes more significant in the more peripheral arteries, however the main features of the waves are the same. The ill-matched bifurcations for non-linear analysis probably have a small effect on the solution. In fact linear analysis is a good approximation for non-linear analysis of waveforms in an arterial network, which means that our results in the previous sections can be meaningfully compared with the results of other workers obtained using linear analysis. The fact that the waveforms are so similar may suggest the use of the simple linear model in preference to the non-linear model, however the computational expense of the calculations is not increased by the non-linear modelling. It is also clearly a closer approximation to the physical situation, therefore non-linear modelling is preferred. There are also a number of limitations of linear modelling, one of which is that the vessel segments must be of constant cross-sectional area. In the next chapter we therefore make improved use of the capabilities of our non-linear program and compute the waveforms in a new, tapered arterial network.

Chapter 5

The new tapered MRI network

5.1 Creation of the arterial network from the MRI images

5.1.1 MRI angiography, imaging and the new arterial network

A new human arterial network has been constructed from data obtained using Magnetic Resonance Imaging (MRI) angiography techniques. All the data for the network was obtained from the same human a 26 year old female, who was 165 cm tall and weighed 56 kg and was relatively healthy. Angiography is the imaging of blood flow in arteries and veins of the human body. Previously, x-ray angiography involved the introduction of a dye into the blood stream. The dye would therefore be transported throughout the circulatory system and because it was opaque to x-rays the blood vessels would be visible on an x-ray image. This method gave no information regarding temporal behaviour of the blood flow, but recently magnetic resonance techniques have been developed that allow the dynamics of blood flow to be measured. Although we only require static information about the arteries, we have employed these magnetic resonance techniques, because they are completely non-invasive and there is no exposure to radiation. This method also allows diameter information to be obtained because the data is acquired in numerous axial cross-sectional images.

To obtain the velocity images we have used Magnetic Resonance Angiography (MRA) time of flight techniques. This essentially involves the static tissue becoming saturated whereas the flowing blood is not, hence a distinction can be made between

the bore of the blood vessels and the surrounding tissue. There are a number of ways time of flight angiography can be performed and details can be found in the literature [59]. To ensure that only the arterial blood flow is visible on the scans a saturation band was applied parallel to the imaging plane. The purpose of the the saturation band is to presaturate the venous blood flow before it enters the imaging plane, so that is goes unrecognised in the MR image. The MRI scanner used was a Siemens Sonata 1.5 Tesla MR scanner at the Royal Brompton Hospital, London, operated by L. Crowe.

The data was obtained by acquiring sets of axial cross-sectional images, with each block composed of twenty images. These blocks were 6 cm in length and each image was 3 mm thick, therefore no gaps existed between each image. The subject was moved a further 6 cm into the MRI scanner after each block was scanned and then the next block of images was acquired. Enough blocks were taken to ensure that there were data for the subject from head to toe. The field of view was 256 x 256 pixels.

Blocks of 6cm in length are reasonably accurate as they are relatively short and therefore the images are mostly taken at or close to the 'sweet spot' of the MRI scanner i.e. where the homogeneity of the magnetic field is very good. The acquisition region was checked and the magnetic field did not change. An inaccuracy in the images arises from the fact that the images are an average of the geometry throughout the cycle.

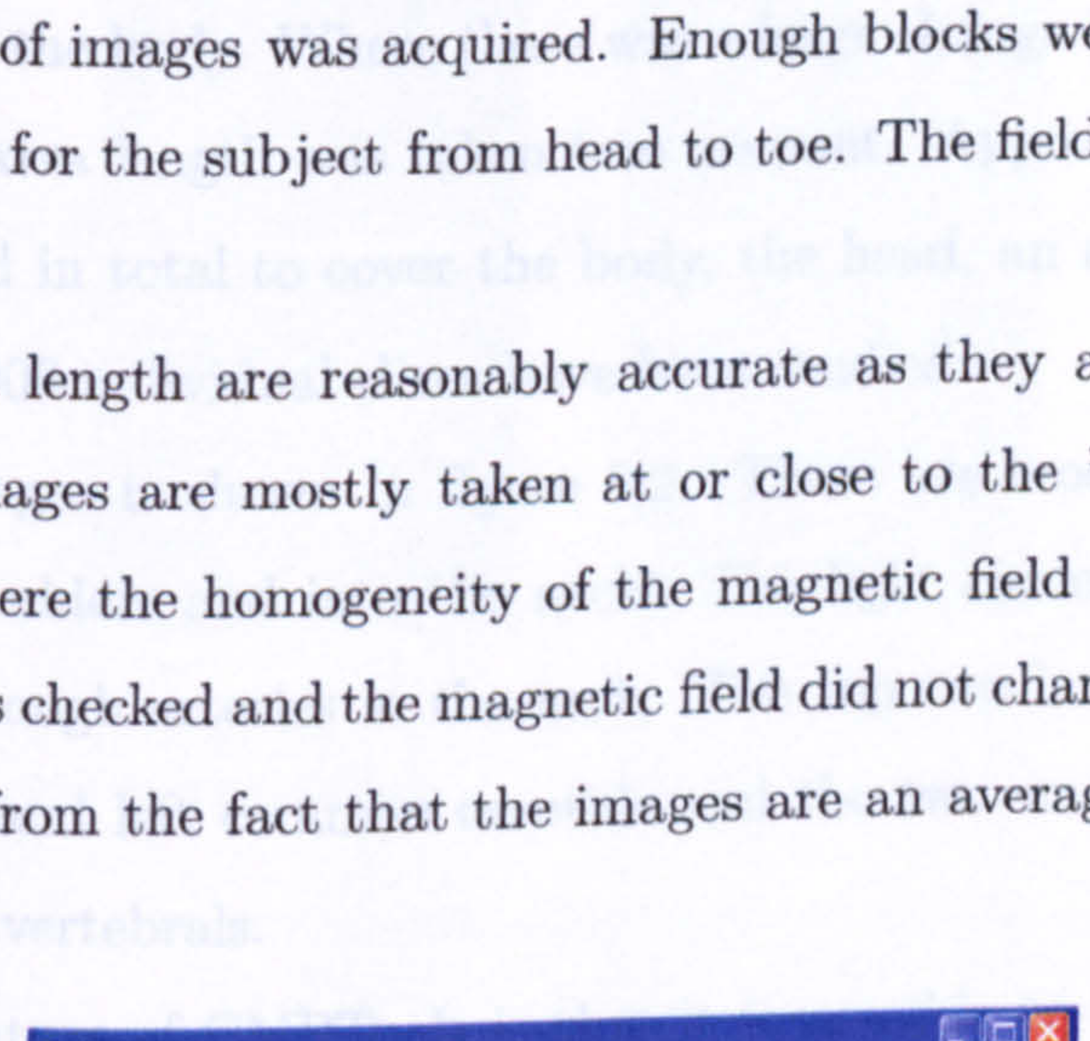


Figure 5.1: Screen shot of the image visualisation software, CMRTools [176], showing detail of a slice containing the common carotids and the vertebrals.

The DICOM files obtained from the MRI scanner were viewed and analysed using the visualisation software CMRTools [176], which was developed in the Visual Information Processing (VIP) research group at Imperial College. A screen shot of the software in operation is shown in figure 5.1. To obtain the data for the numerical model every image was examined for artery bifurcations and approximately every 2-3 slices the diameters of the arteries were measured. To allow for the non-circular cross-section of the arteries the diameter was measured twice in orthogonal directions for each acquisition and an average taken to provide the diameter for the circular geometry approximation used in the numerical model. The lengths of the arteries were calculated from the number of images the arteries appeared on and the thickness of each slice. Assuming that the lengths of the arteries can be determined from the thickness of the slices is an approximation as many of the arteries are slightly curved in the body. Where there was a large change in in-plane location of the arteries this extra length was taken into account. Approximately 60 blocks of data were acquired in total to cover the body, the head, an arm and both legs, therefore well over 1000 individual slices have been studied.

A block of 20 images is shown in figure 5.2. These are cross-sectional images at the top of the shoulders and into the neck. The light circles shows the blood entering the head through arteries in the neck. The top two larger arteries in the images are the right and left common carotids and the two smaller lower arteries are the right and left vertebrals.

Another useful feature of CMRTools is that it is possible to view the blocks of images in three dimension. This is particularly helpful for aiding in the identification of arteries in the body which is actually quite a difficult task. Figure 5.3 shows three-dimensional images of the common carotids and vertebrals reconstructed from the slices in figure 5.2 from four different angles. A three-dimensional image of the the aortic arch is shown in figure 5.4 (a) and the brachiocephalic trunk at the top left of the aortic arch can be clearly seen as can the middle artery which is the left common carotid and the right hand artery which is the left subclavian 1. This splits at the top of the figure into the left subclavian 2 and the left vertebral. The three-dimensional image in figure 5.4 (b) shows the arteries in the head. The two outer twisting arteries are the left and right internal carotids. In between these two

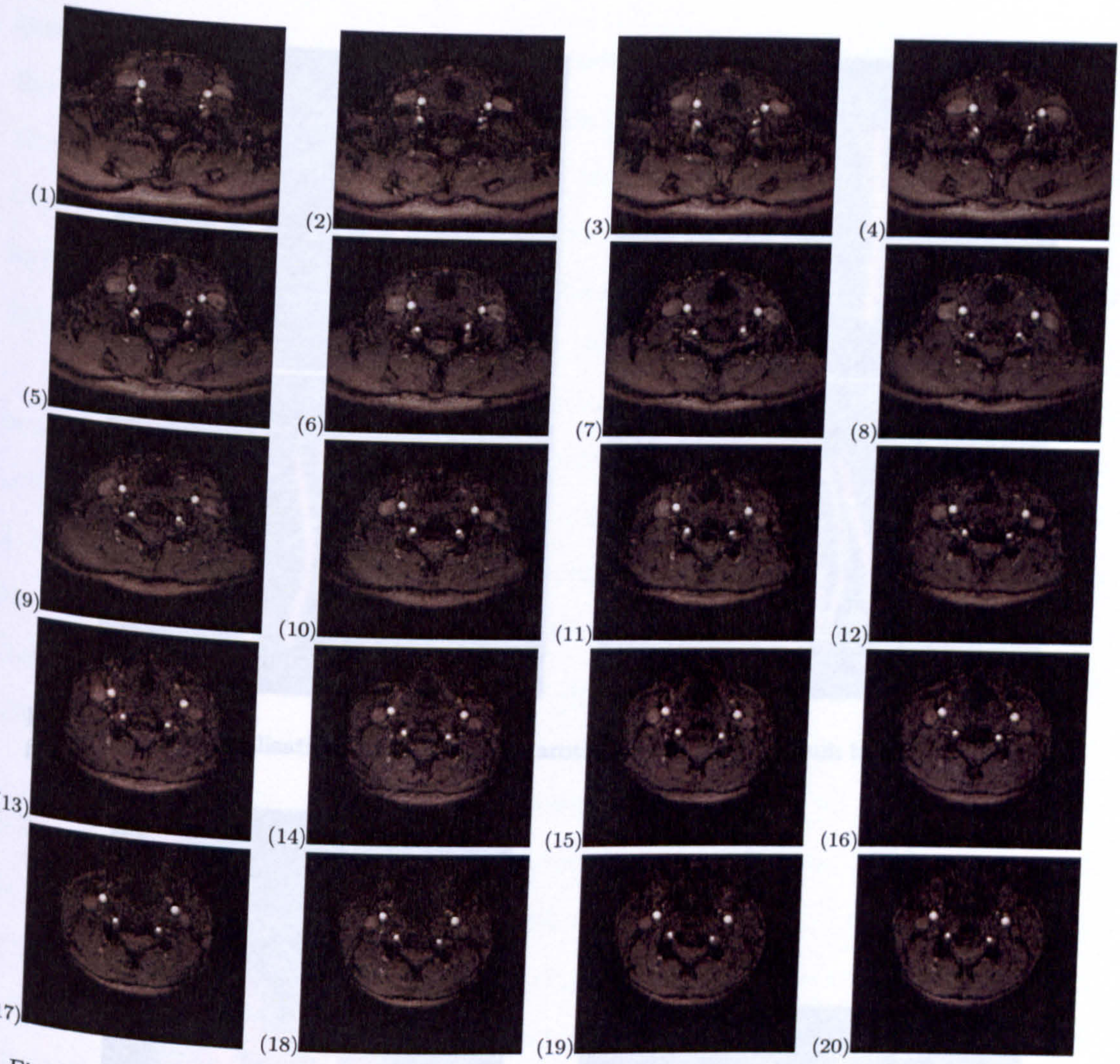


Figure 5.2: A block of 20 MR images obtained from the healthy female subject showing the major arteries in the neck and shoulders.

arteries are the left and right vertebrals, which can be seen to join into one artery, the basilar. The arteries in the head were difficult to visualise and this picture shows the arteries tilted at an angle for ease of view. The complexity means that some of these arteries were unable to be measured and hence they are not included in the numerical model. Figure 5.5 (a) is a three-dimensional picture of the two external iliacs and figure 5.5 (b) is a picture of the block of images taken directly below the images in figure 5.5 (a) which shows the external iliacs bifurcating into the femoral and deep femoral. As can be seen from these three-dimensional images we have managed to obtain quite clear data for the major arteries of the body and we are confident that the major arteries included in the numerical model are a good approximation to the actual arterial network.

Although the images are good it may have been possible to obtain details of

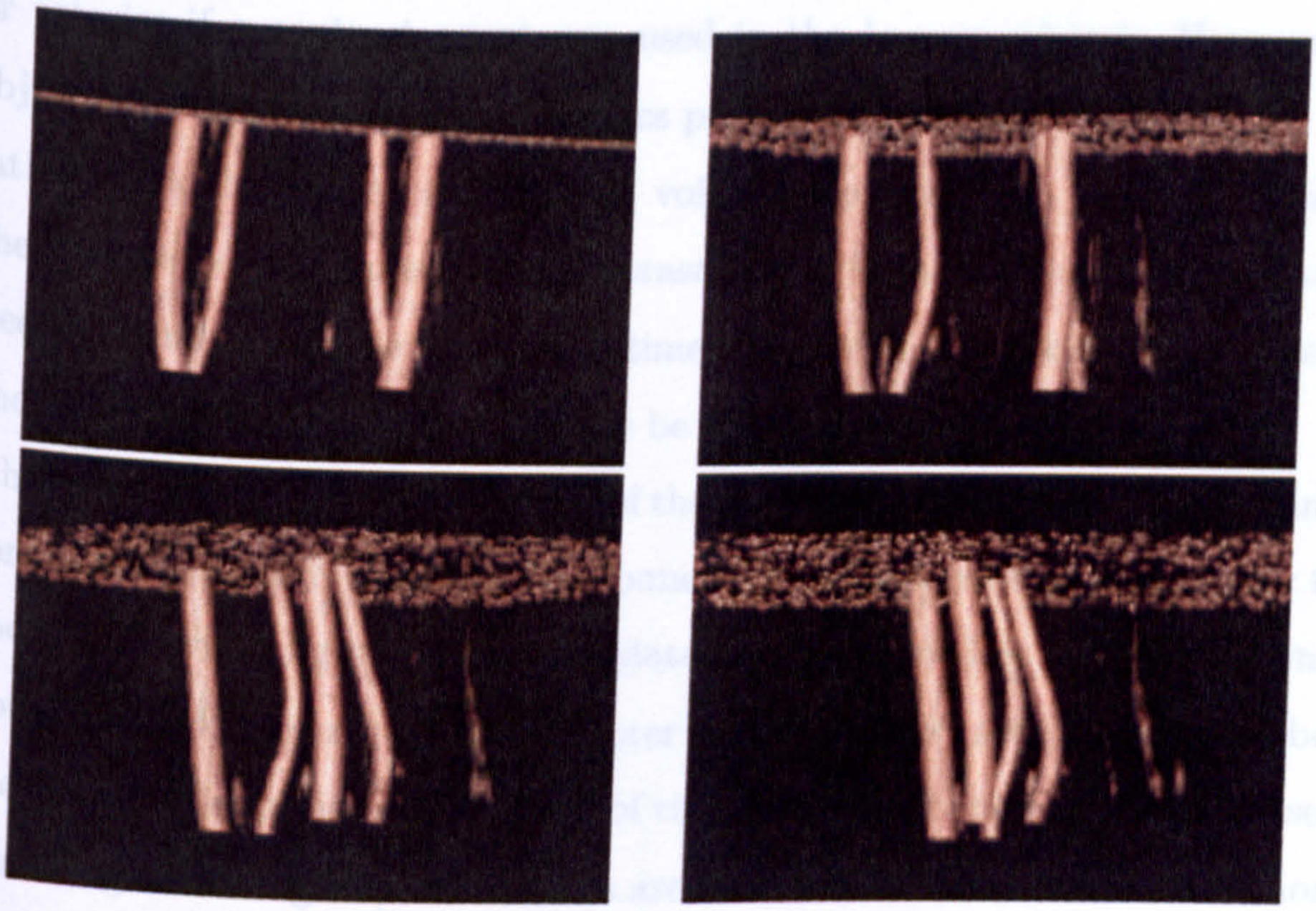


Figure 5.3: 3D visualisation of the common carotids and vertebrals from the MR data from figure 5.2.

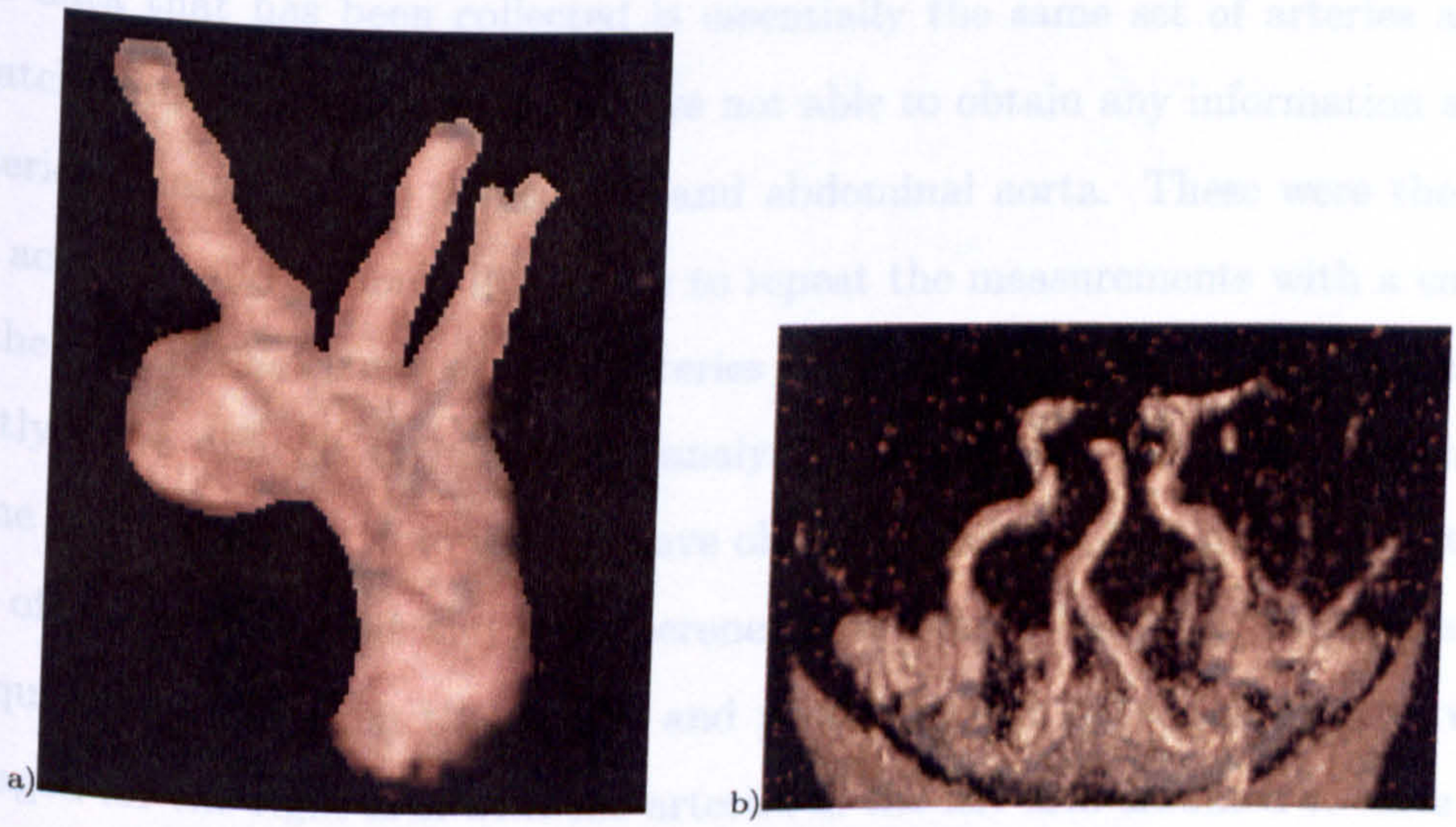


Figure 5.4: 3D visualisation of a) the aortic arch and b) the arteries in the head including basilar.

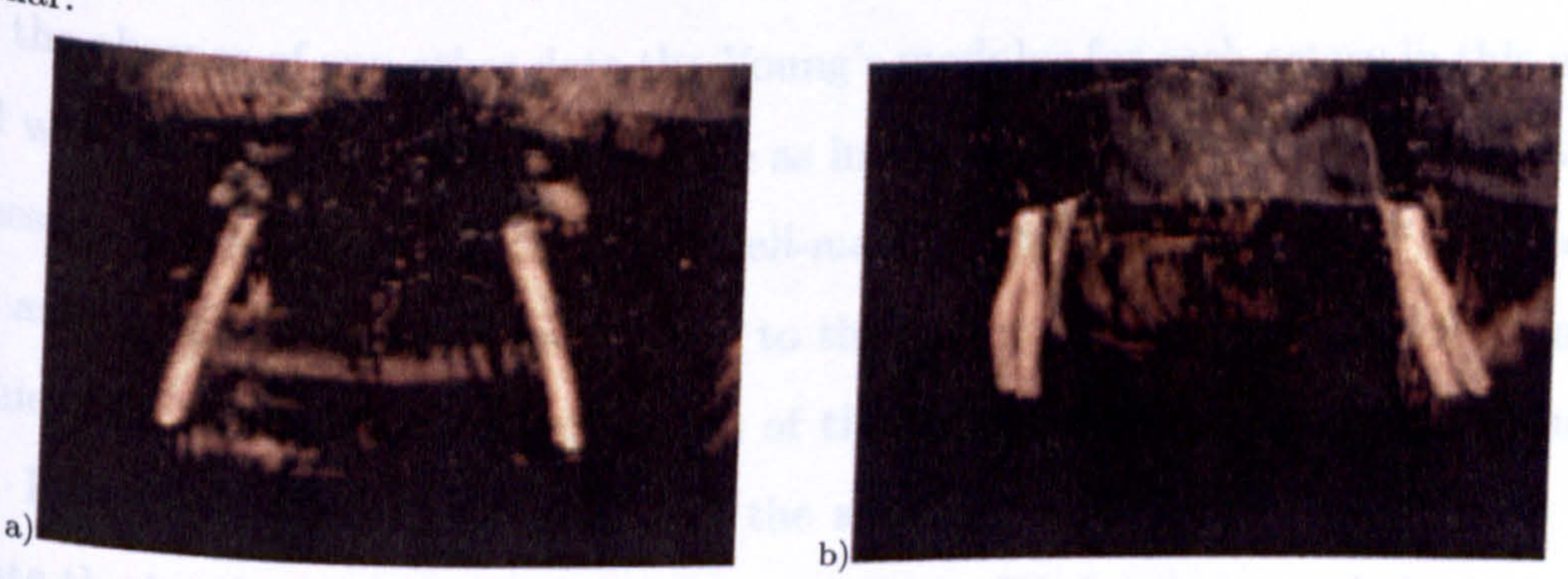


Figure 5.5: 3D visualisation of a) the iliacs and b) the immediately distal bifurcations into the femorals.

smaller arteries if a contrast agent was used in the human subject. However, as the subject was healthy then current ethics prevent the use of a contrast agent. An alternative would have been to obtain a volunteer patient who would consent to have their whole body scanned using contrast agent. However, this would probably have been difficult given the amount of time involved in producing the full set of data and of course this subject would not be a healthy one.

We have obtained a set of data for all of the major systemic arteries in the human body for the same healthy subject. The connectivity of this arterial network for this new model is shown in figure 5.6 and the data for the network is given in Appendix A.2. Note that as for the network in Chapter 4, the coronary arteries have not been modelled. One of the noticeable features of this data is that the arteries decrease in diameter along their lengths. The arteries are therefore not constant cross-sectional area tubes, but are tapered vessels.

The data that has been collected is essentially the same set of arteries as the well-matched model, except that we were not able to obtain any information about the arteries coming off the descending and abdominal aorta. These were the first images acquired and perhaps if we were to repeat the measurements with a coil on top of the subject the clarity of these arteries would be improved. These arteries are inherently more difficult to image and analyse, because they are close to being in the plane of the images. However, we have obtained an extra pair of arteries at the bottom of the legs, the left and right peroneals (artery 35 and 43). To reduce the time required for acquiring the images and processing the data, the arteries were only imaged for the right arm with the arteries in the left arm assumed to have the same lengths and diameters as those in the right arm.

In the absence of any other data the Young's modulus for each artery in this new model was assumed to be the same value as in the well-matched system. The wall thicknesses were also derived from the well-matched system, but as the diameters of the arteries are different in our model to the well-matched model we have used wall-thickness calculated as a percentage of the diameter rather than an absolute value. From measuring the diameter of the arteries in CMRtools we are able to calculate the local cross-sectional area of each artery. We have assumed that this is the mean arterial area, A_{ave}, which occurs at mean arterial pressure, P_{ave}.

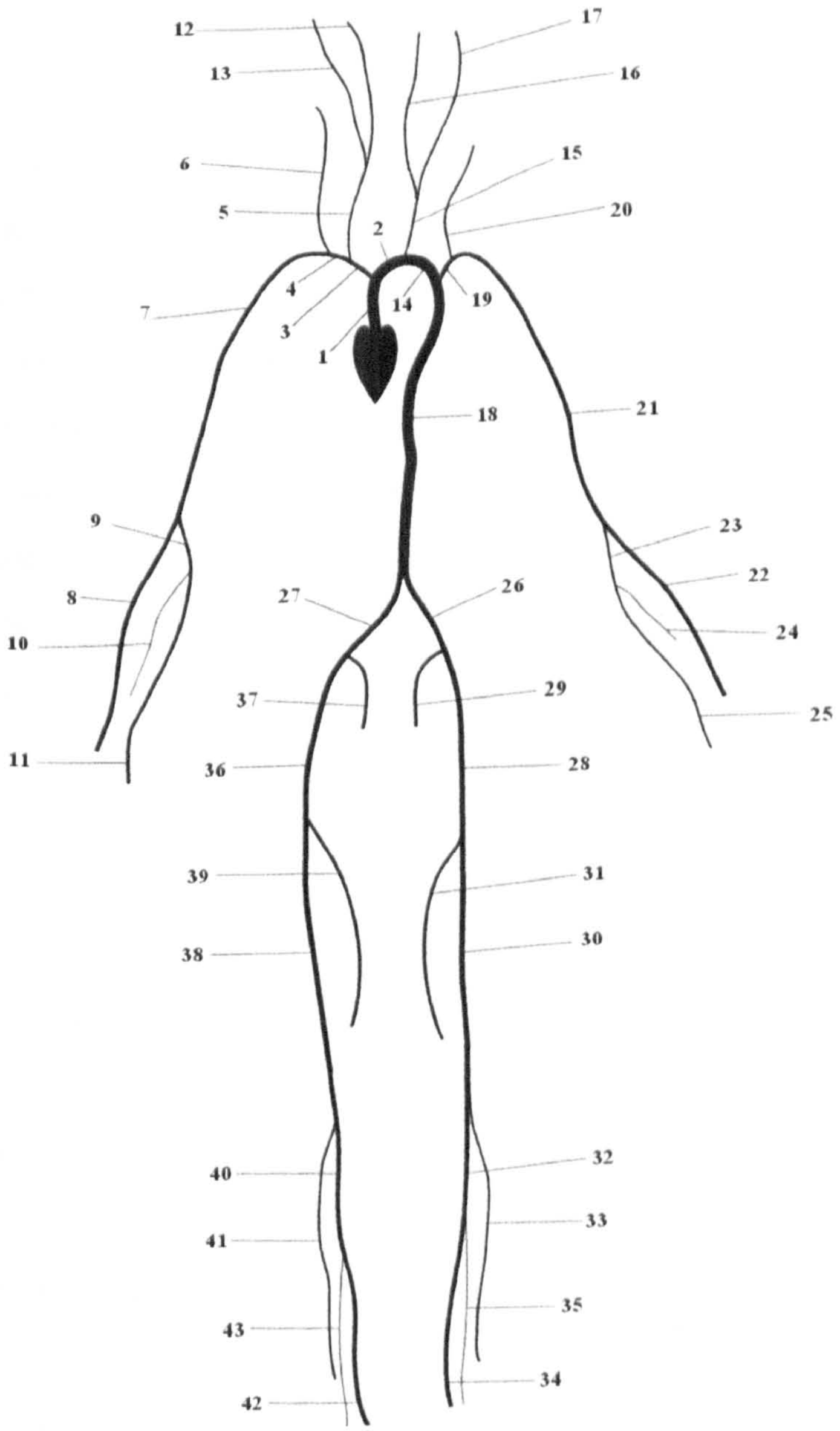


Figure 5.6: Schematic arterial network used in the numerical model obtained from MR images of a healthy female subject.

5.1.2 The computational network and boundary conditions

The fact that the network has tapered vessels means that non-linear analysis must be used to calculate the waveforms in this system. Therefore we cannot compare results for non-linear and linear analysis, unlike in Chapter 4. Four different boundary conditions have been imposed at the ascending aorta. These can be divided into two types, an area change imposed as a W_1 characteristic (boundary conditions 1 and 4) and a velocity (boundary conditions 2 and 3). These are the same four boundary conditions that were imposed for the well-matched network in Chapter 4, except the magnitudes are different. As the area of the MR images has been assumed to be at mean arterial pressure the area of the arteries in the network was scaled down to a value close to that of the diastolic area before we calculate the waveforms. If we were not to reduce the area for the system then when the velocity boundary condition is imposed the pressure waveform would not be correct, although the pressure boundary conditions could have been imposed by imposing an inflow wave with a negative base line value.

The mean arterial pressure for the system is 11.6 kPa and the approximate diastolic pressure in the ascending aorta is 9.9 kPa. The magnitude of the half sine wave (pulse pressure) to be imposed in the form of the W_1 characteristic is 3.5 kPa. These were calculated from the clinical waveforms shown in section 5.1.3. The combination of a pulse pressure of 3.5 kPa and a base value of 9.9 kPa produces a wave with magnitudes similar to those in-vivo because the pressure does not decline to the base value and the peak pressure at the ascending aorta is also higher than the imposed value. This is due to the reflections in the system, but the magnitude of the pressure pulse is maintained.

All of the arteries in the system had their measured areas reduced to values for the diastolic areas. The reductions in arterial areas were calculated using the pressure difference, ΔP, of 1.7 kPa (difference between mean arterial pressure and diastolic pressure), equation (2.3) and the relationship $h = kR_0$ where h is the wall-thickness, R_0 is the diastolic radius and k is the percentage wall thickness calculated from the well-matched system.

These equations can be rearranged to give:

$$A_0 = A_{ave}\left[\frac{\Delta P}{Ek}+1\right]^{-2} \tag{5.1}$$

where A_0 is the new diastolic arterial area, A_{ave} is the mean arterial area measured and E is the Young's modulus. The original diameters and scaled areas, A_0, are both shown in Appendix A.2.

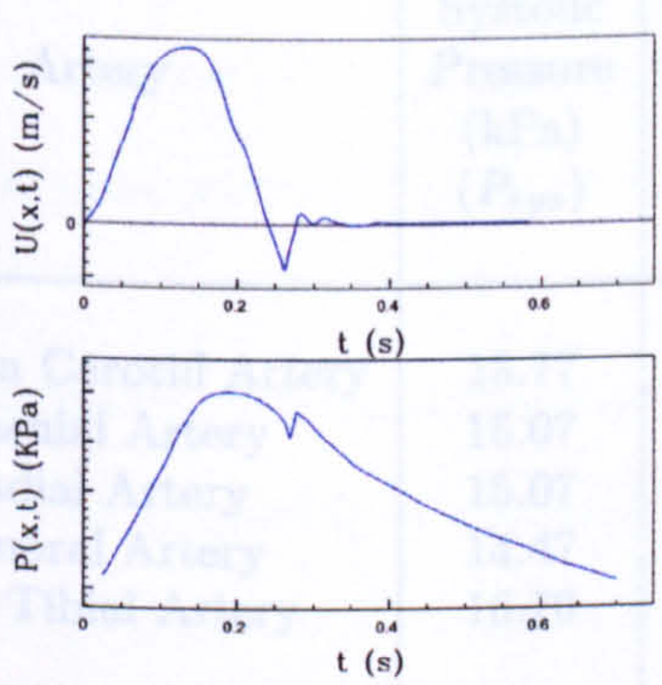
5.1.3 Clinical measurements - Doppler ultrasound and applanation tonometry readings

In order to be able to assess the validity of the computer model, clinical measurements of the pressure and velocity waveforms in some of the major arteries of the subject have been acquired. These clinical measurements are compared directly with the computational results in section 5.2.4. The measurements were taken by A. Zambanini from St. Mary's Hospital, London using Doppler ultrasound to measure the velocities and applanation tonometry to give the pressure waves [179]. All of the results are ensemble-averages of a series of approximately 10 heart beats. The clinical measurements were obtained at the following approximate locations: the origin of the left femoral, the distal end of the common carotid, mid-way along the brachial, radial and posterior tibial. The bottom five graphs, in figure 5.7, show these pressure and velocity waveforms. The top three graphs in figure 5.7 are diagrammatic representations of typical waves found in the aorta, rather than actual clinical measurements, because these could not be obtained in the subject. The figures have been arranged for ease of comparison with our computational results from the one-dimensional model in Chapters 4 and 5.

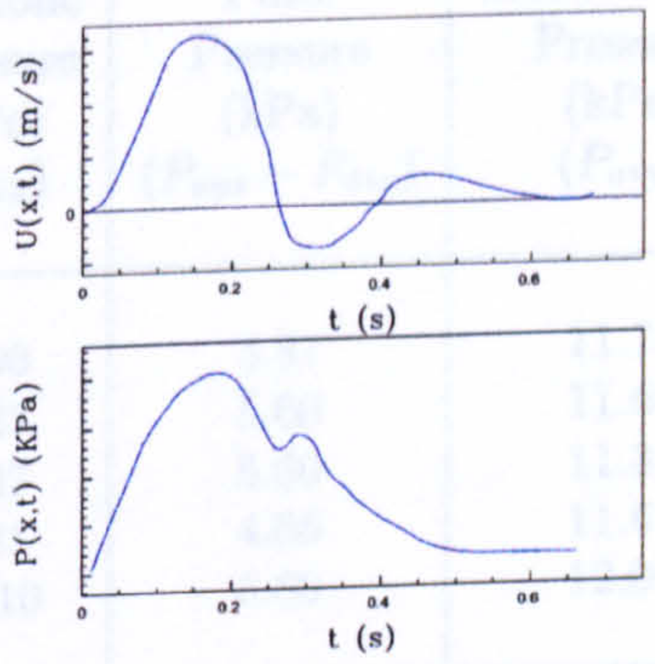
The mean arterial pressure, P_{ave}, in the subject can be calculated by integrating the clinical pressure waves. These values are shown in table 5.1 together with systolic, P_{sys}, diastolic, P_{dia} and pulse pressure (P_{sys} - P_{dia}) for each artery waveform.

Note that gravity can have an effect on the pressure in the body, but because the subject was lying down for both these clinical measurements and the MRI scans, then the effect of gravity will be minimal.

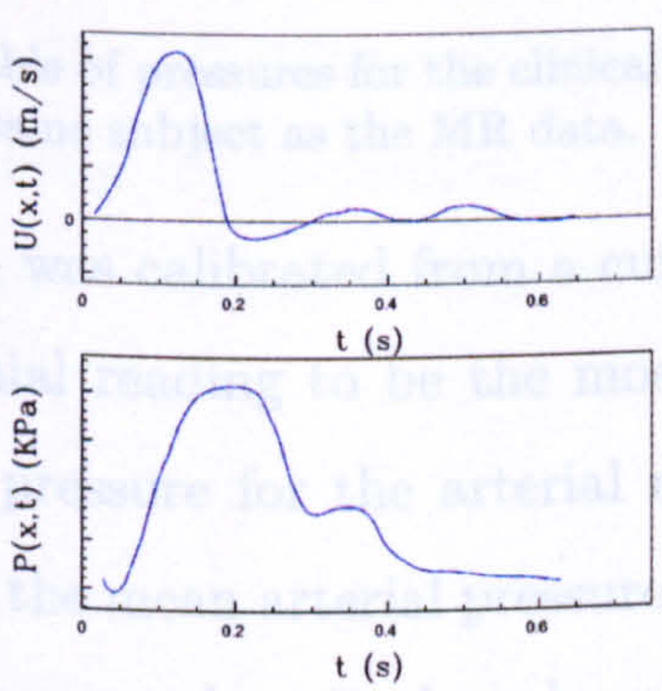
The mean arterial pressures have varied slightly in the system from one artery to the next. The pressure waveform was measured using applanation tonometry but



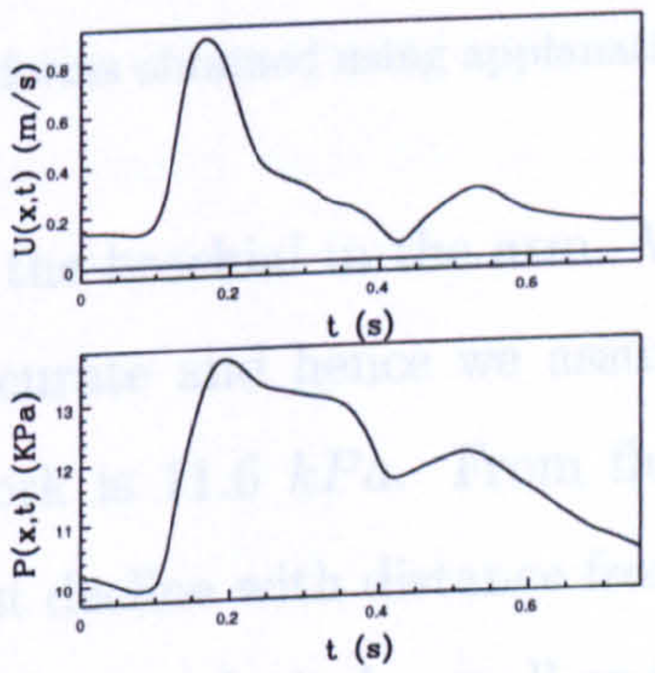
(1) Ascending Aorta



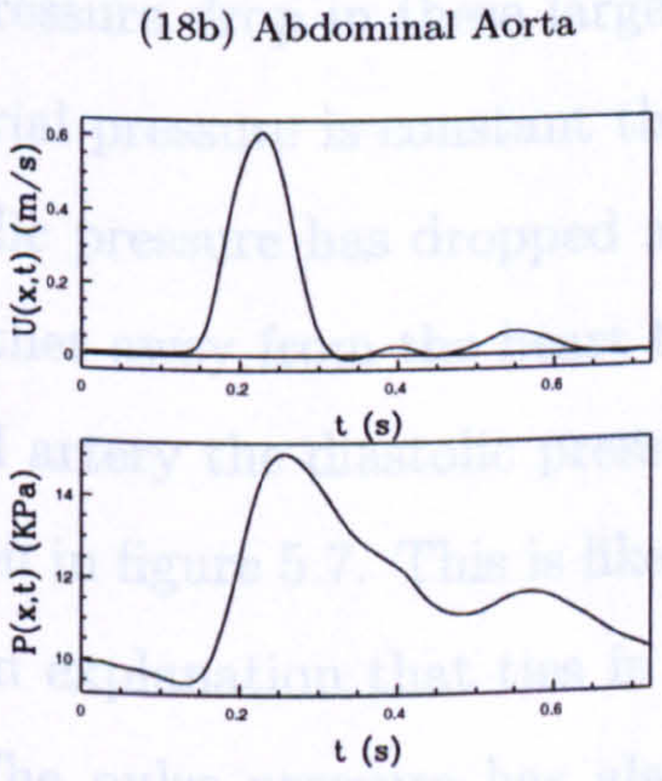
(18) Thoracic Aorta



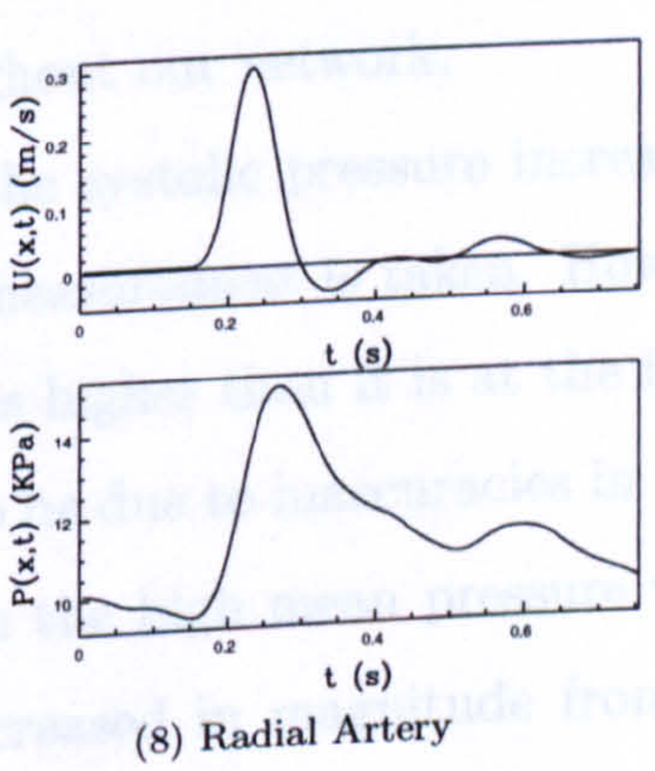
(18b) Abdominal Aorta



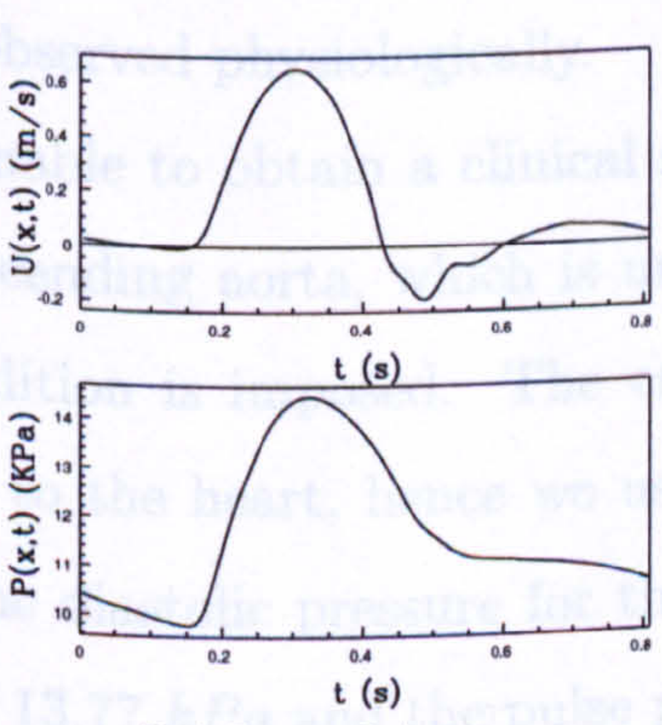
(15) Common Carotid



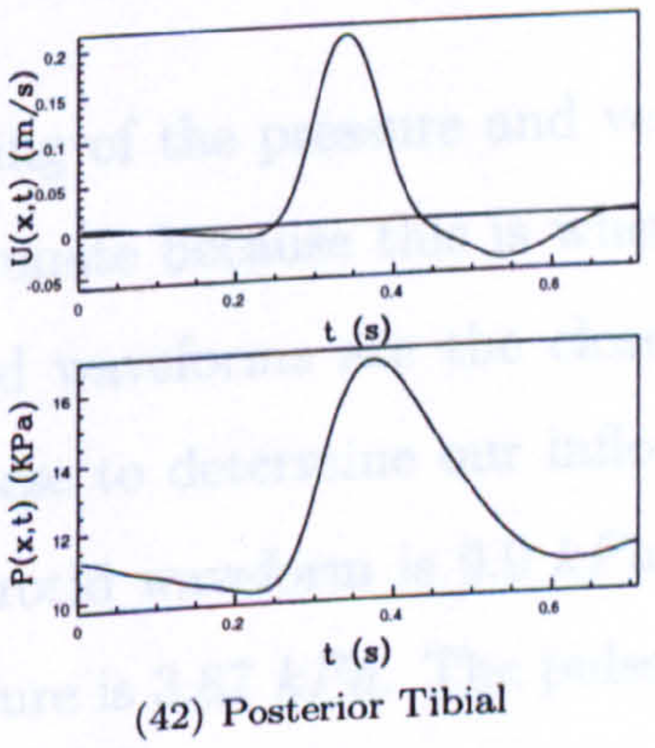
(7) Brachial Artery



(8) Radial Artery



(38) Femoral Artery



(42) Posterior Tibial

Figure 5.7: Clinical waveforms obtained from the subject in the more perpherial arteries. Diagrammatic representation of typical waveforms are given for measurements in the aorta, which could not be obtained clinically, to retain the format for ease of comparison with later results.

Artery	Systolic Pressure (kPa) (P_{sys})	Diastolic Pressure (kPa) (P_{dia})	Pulse Pressure (kPa) ($P_{sys} - P_{dia}$)	Mean arterial Pressure (kPa) (P_{ave})
Common Carotid Artery	13.77	9.90	3.87	11.75
Brachial Artery	15.07	9.47	5.60	11.60
Radial Artery	15.07	9.47	5.60	11.34
Femoral Artery	14.47	9.81	4.66	11.67
Post Tibial Artery	16.70	10.10	6.60	12.09

Table 5.1: Table of pressures for the clinical waveforms obtained using applanation tonometry, for the same subject as the MR data.

the magnitude was calibrated from a cuff at the brachial in the arm. We therefore take the brachial reading to be the most accurate and hence we assume that the mean arterial pressure for the arterial network is 11.6 kPa. From fluid dynamic considerations the mean arterial pressure must decline with distance from the heart, however the pressure drop in these large arteries is relatively small and we assume the mean arterial pressure is constant throughout our network.

The diastolic pressure has dropped and the systolic pressure increased in magnitude the further away from the heart the measurement is taken. However, in the posterior tibial artery the diastolic pressure is higher than it is at the femoral, this can also be seen in figure 5.7. This is likely to be due to inaccuracies in the pressure magnitudes, an explanation that ties in with the high mean pressure recorded for this artery. The pulse pressure has also increased in magnitude from the aorta, which is also observed physiologically.

We were unable to obtain a clinical reading of the pressure and velocity waveform at the ascending aorta, which is unfortunate because this is where the input boundary condition is imposed. The carotid waveforms are the closest available measurements to the heart, hence we use these to determine our inflow boundary conditions. The diastolic pressure for the carotid waveform is 9.9 kPa, for systole the pressure is 13.77 kPa and the pulse pressure is 3.87 kPa. The pulse pressure in the ascending aorta is likely to be slightly less than this, therefore we have assumed a pulse pressure of 3.5 kPa. We also impose a baseline pressure of 9.9 kPa at the inflow, the same as the carotid diastolic pressure, because the pressure in our results

never declines exactly to this base line value. Therefore the diastolic pressure in the ascending aorta will be slightly higher than 9.9 kPa in the results and the results will exhibit the characteristic decline in diastolic pressure with distance from the heart.

In the absence of a clinical measurement of the velocity wave in the aorta, for the results obtained by imposing a velocity inflow boundary condition, we have used a peak velocity magnitude for the half sine wave that results in a volume flow rate of approximately 4.0 litres/min. This is equivalent to the value obtained for MR data acquired during the scanning of the subject and is fairly typical of volume flow rates observed in resting female humans. This also tallies with the velocities obtained from the pressure boundary conditions.

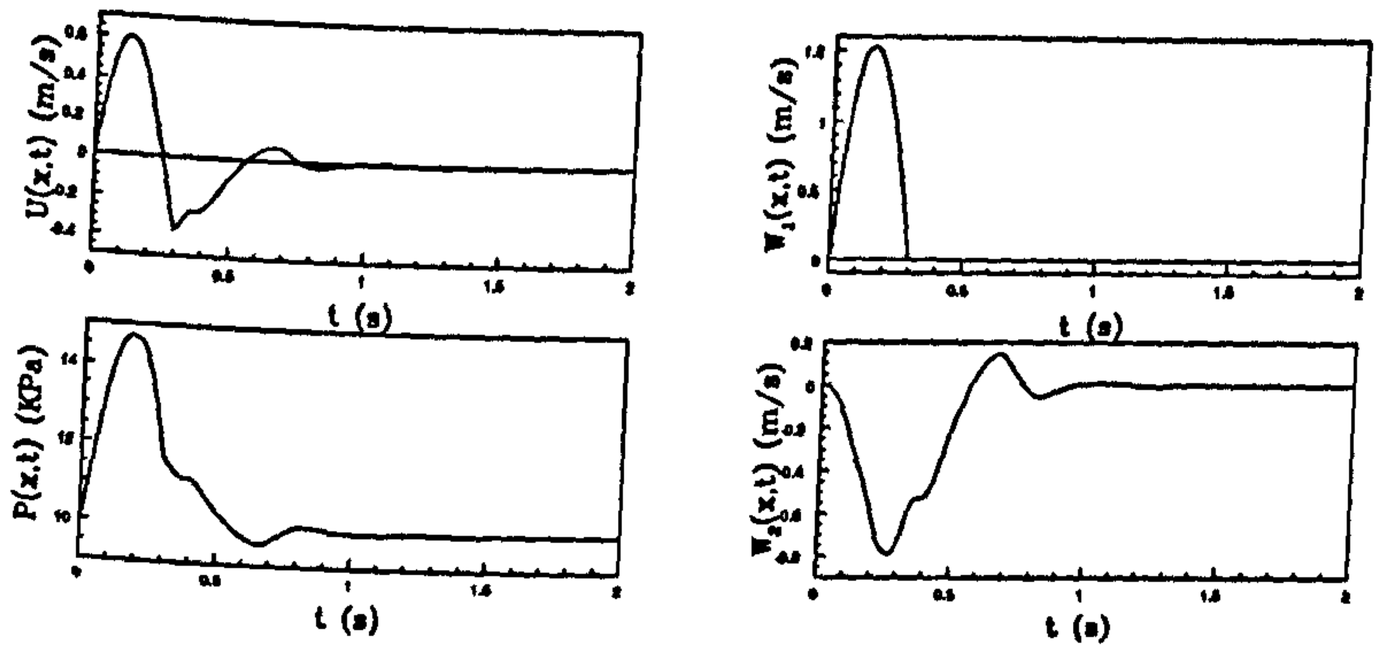
5.2 Results for the tapered network

5.2.1 Inflow boundary conditions

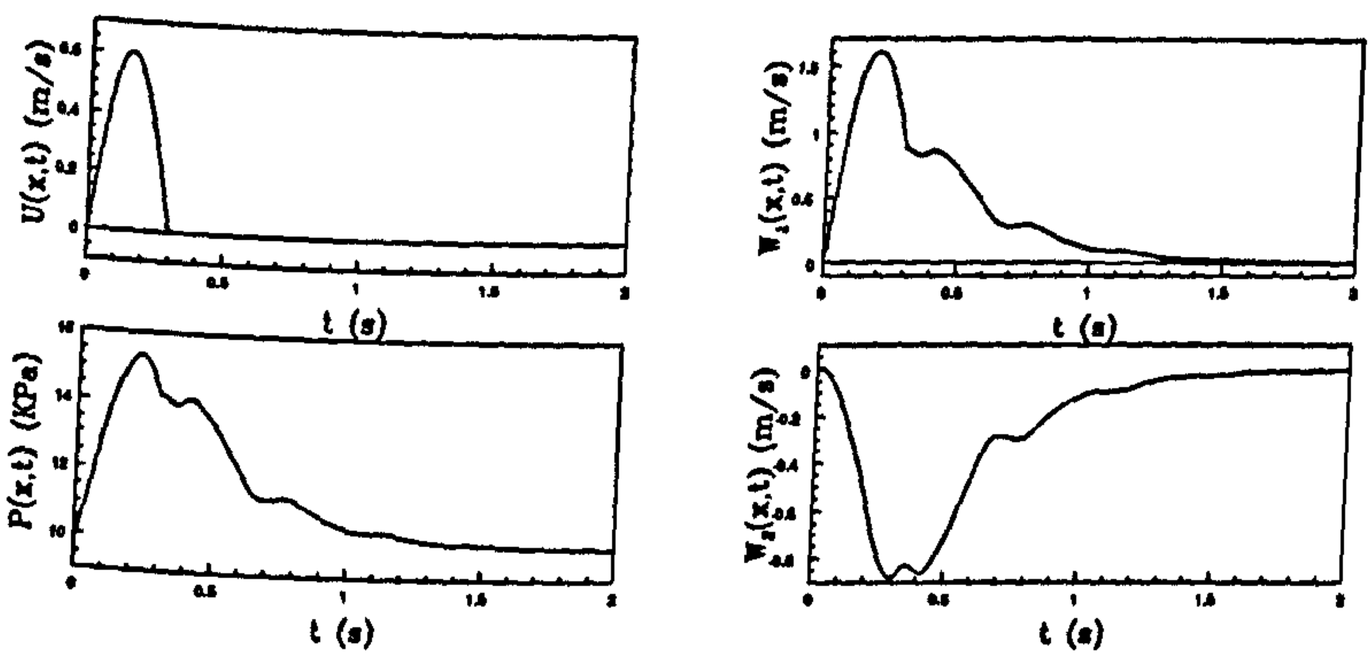
As with the well-matched network computations, four different input boundary conditions have been imposed and the effects of these modelling assumptions on the results for this network assessed. The four boundary conditions have been imposed in the same manner as the well-matched system input boundary conditions (section 4.3.1), however, the magnitudes are lower since the well-matched model is representative of a human male whereas this network is for a female. The desired change in pressure needed for the W_1 characteristic input boundary conditions, (BC1) and (BC4), is 3.5 kPa as previously described in section 5.1.3. The maximum velocity prescribed for boundary conditions 2 and 3 is 0.6 m/s and the minimum velocity prescribed for boundary condition 3 is -0.2 m/s. Precise details are given in section 2.6.1 regarding the input equations. A more significant difference between the two cases is that for most results in the well-matched system a reflection coefficient of 0.5 was imposed on the terminal vessels, but for this new model initially no terminal resistance has been imposed.

The waveforms of pressure, velocity and the characteristic variables, W_1 and W_2, for a single isolated heart beat at the start of the ascending aorta are shown in figure 5.8. The results are only shown for one heart beat so that reflections from previous heart beats do not have an effect on the waveform and with time the wave can eventually die away. This enables the different features of the reflections to be studied more easily.

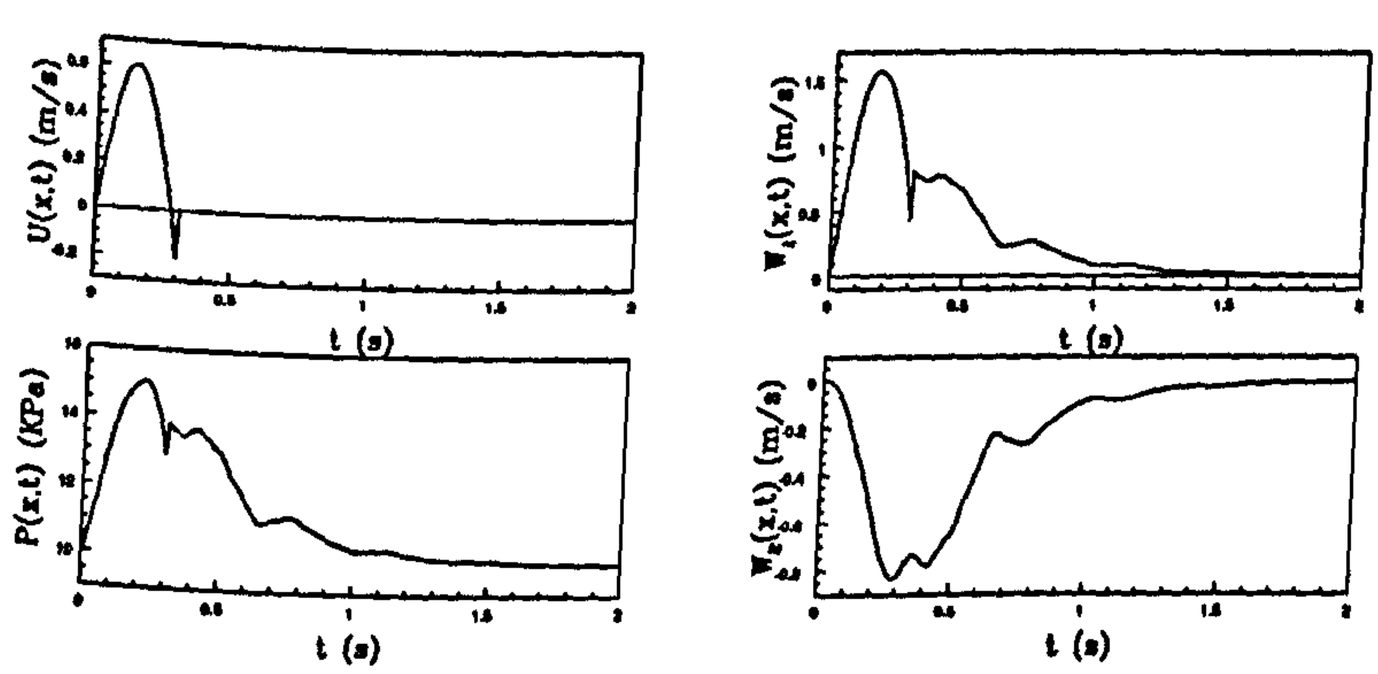
Looking at the W_2 characteristics for all four boundary conditions it can be seen that in each case there is a large amount of reflection in the ascending aorta even though no terminal resistance has been applied to the terminal vessels. This is in complete contrast to the non-tapered well-matched network. Boundary condition 1 was imposed as a W_1 characteristic in the form of a half sine wave and can be seen in the W_1 characteristic plot. The heart acts as an absorber throughout for this boundary condition i.e. no reflections occur at the ascending aorta. The velocity waveform has a reversed flow after the peak velocity for approximately 0.25 seconds and then a secondary period of positive flow. The pressure waveform declines



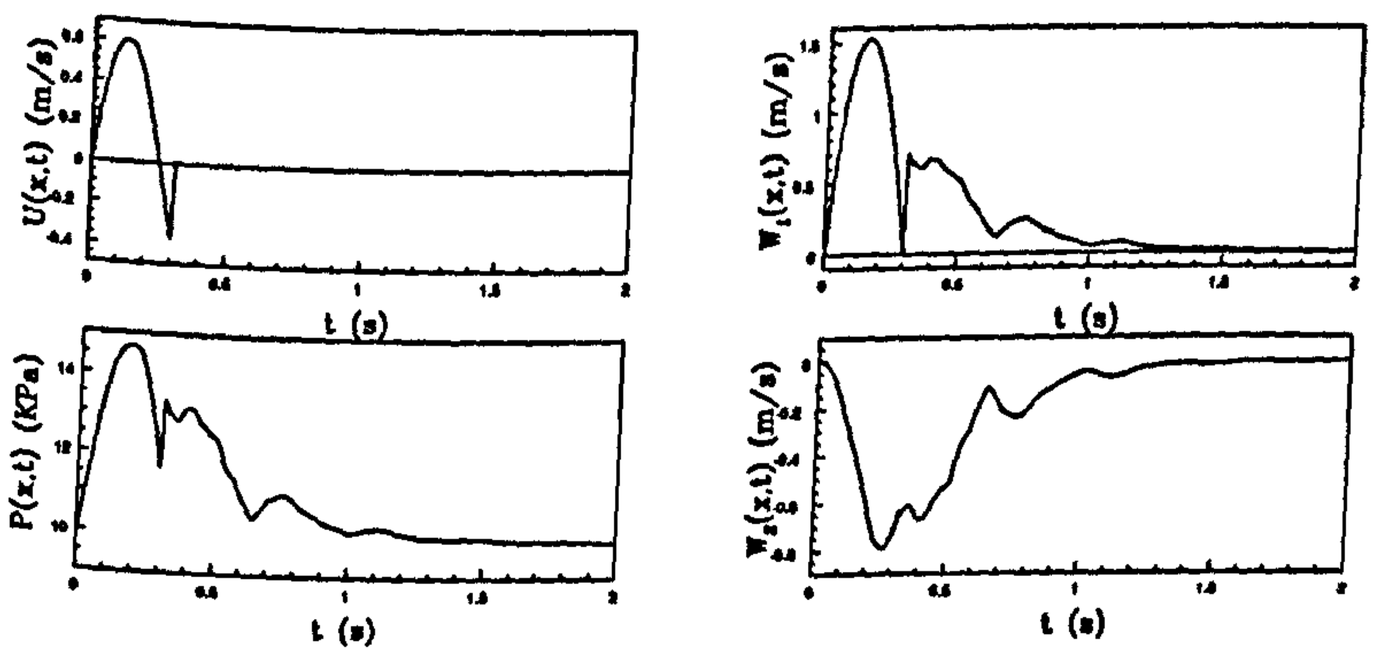
W_1 Absorber input (BC1)



Velocity input (BC2)



Velocity with reversed flow input (BC3)



W_1 Reflector input (BC4)

Figure 5.8: Velocity, pressure and characteristic variable waveforms at the start of the ascending aorta for boundary conditions 1, 2, 3 and 4. Results are shown for only a single heart beat with no terminal reflection coefficient on the tapered network.

more gradually after the systolic pressure than the waveform in the well-matched system, which had two peaks as the pressure declined. The waveform is smoother in this model, due to the more continuous nature of the reflections returning to the ascending aorta, as seen from the W_2 characteristic waveform. This figure also shows that the reflections occur in the ascending aorta almost immediately, whereas in the well-matched system the majority of the reflections only developed after approximately 0.15 seconds. This is a feature of the tapered network and for all four boundary conditions the reflections started almost immediately.

The velocity was imposed at the start of the ascending aorta for boundary condition 2 and therefore the velocity waveform is the same shape as the well-matched system for this example. The pressure waveform again declines more smoothly in this tapered system and the peak reflections occur between approximately 0.3 and 0.4 seconds of the cycle in the W_2 characteristic figure.

As in the well-matched system for boundary condition 3 the velocity was imposed with a small section of reversed flow after the peak flow as shown in the velocity figure. The waveforms produced by this boundary condition are similar to the waveforms produced by imposing boundary condition 4 as was the case in the well-matched network and are discussed below.

Again for boundary condition 4 the heart acts as an absorber for the first 0.3 seconds and then as a reflector for the rest of the cycle. There is a transition region to simulate the aortic valve closing and opening and this has been modelled by linearly varying W_1 from the constant value to equal $-W_2$. This transition takes 0.01 seconds and can be seen in the W_1 characteristic plot, figure 5.8 (BC4), between the times 0.3 to 0.31 seconds as the sharp increase in the W_1 characteristic until it equals the negative of the W_2 characteristic. In the ascending aorta for the well-matched network there was always a large second notch seen in the pressure waveform but this is not a feature in the pressure waveform for this network, although there is a smaller notch later in the cycle at approximately 0.75 seconds. The pressure waveform after the dicrotic notch declines more smoothly, which looks far more physiological. As with the well-matched results the velocity waveform looks physiological for both boundary condition 3, where it is imposed and 4, where it is a consequence of the reflections in the network. Boundary condition 4 has more reversed flow and a

greater dicrotic notch due to the differences in the W_1 characteristic. As can be seen in the W_1 plot the W_1 characteristic declines to zero after the initial pulse for boundary condition 4, but not for boundary condition 3.

It is important to remember that as there is no terminal resistance on the terminal vessels in the system the reflections can only have occurred from either ill-matched bifurcations or the tapering of the vessels. It is perhaps surprising that these effects can generate such physiological waves and we now investigate the relative importance of these two effects.

5.2.2 Reflection sites - the effect of taper and ill-matched bifurcations

To investigate the effect of the tapering vessels in the system we have examined a single tapered vessel from the system in isolation, artery 18, which is a large section of the aorta. A half sine wave was imposed as a W_1 characteristic (BC1) at the inlet and no terminal resistance was applied to the end of the vessel, therefore at the inlet and the outlet waves are free to leave the vessel and any reflections can only be due to the taper. Figures 5.9 (a) and (b) show the velocity, pressure and characteristic variables, W_1 and W_2, at the start (black) and at the end (blue) of the vessel. It can be seen in figure 5.9 (a) that the velocity at the start of the vessel is lower in magnitude than at the end and also has some reversed flow. At least some of the change in magnitude of velocity along the length of the vessel is due solely to the different local cross-sectional areas, however, this cannot account for the reversed flow. The pressure has remained at approximately the same magnitude at the start and at the end of the vessel, but the shape of the wave after the peak is different. The W_1 characteristic, figure 5.9 (b) shows the input at the start of the vessel (black) and that this has increased in magnitude by the end of the vessel (blue) in accordance with the change in vessel area. The most revealing plot is that of the W_2 characteristic, which has remained zero at the end of the vessel, indicating no terminal reflection, but has decreased in value at the start, which shows that there are actually reflections occurring in the system due solely to the taper. The fact that the W_1 and W_2 characteristics at the start and end of the vessel are different has caused the differences in the velocity and pressure waveforms at the start and end of the vessel.

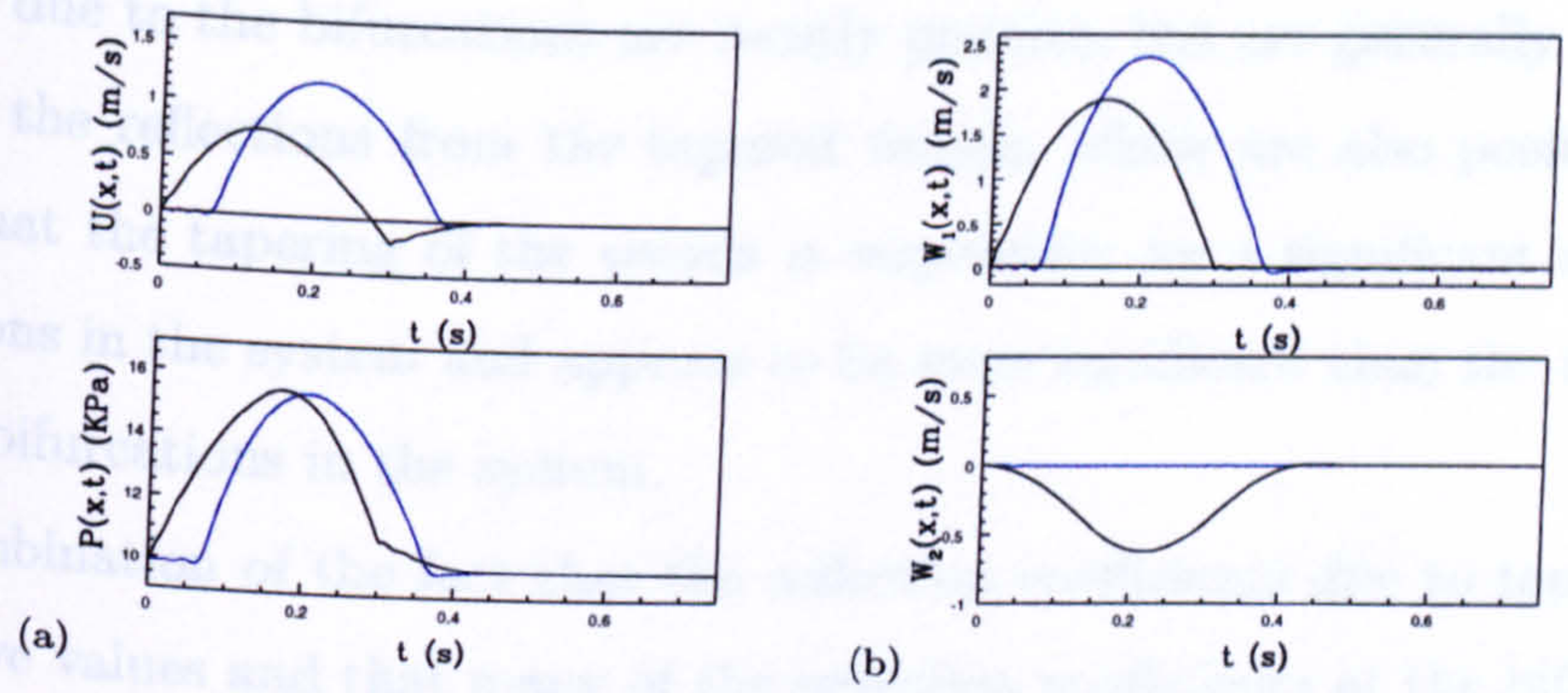


Figure 5.9: Velocity, pressure and characteristic waveforms, W_1 and W_2, at the start (black) and end (blue) in an isolated artery 18. These show the reflection due to taper in an isolated artery. Terminal resistance = 0.0 at end of the vessel.

Tapered Vessel	R_c Linear theory (bifurcation)	$R_c = -\Delta W_2/\Delta W_1$ (taper)	Tapered Vessel	R_c Linear theory (bifurcation)	$R_c = -\Delta W_2/\Delta W_1$ (taper)
5	0.119	0.041	21	-0.009	0.43
7	-0.009	0.042	26	0.102	0.065
15	0.106	0.45	27	0.010	0.15
18	0.068	0.32	30	0.293	0.33
19	0.202	0.27	38	0.271	0.19

Table 5.2: Table of measured reflection coefficients in a sample of arteries in the tapered network due to taper (calculated from computational results) and due to the bifurcation at the end of the numbered vessel (calculated from linear theory).

With no terminal resistance at the end of the vessel the large reflection at the start of the vessel must have occurred from the tapering of the vessel. An approximate reflection coefficient due to taper for the vessel can be calculated from the magnitude of the pulse of the W_2 characteristic divided by the magnitude of the pulse of the W_1 characteristic, $R_c = -\Delta W_2/\Delta W_1$, at the vessel inflow where ΔW_1 and ΔW_2 can be found from graphs such as figure 5.9 (b). For this vessel the pulse magnitude of W_1 and W_2 at the start of the vessel are 1.9 and -0.6 respectively, therefore $R_c \sim 0.6/1.9 = 0.32$. The reflection coefficients at the start of the artery due to the tapering of the vessels were calculated in a similar manner for each of the other tapered vessels in the network, again in isolation, and the results are shown in table A.4 in Appendix A.2. The reflections due to the bifurcations have also been calculated using linear theory, equation (2.123). This was found to be a good approximation for non-linear analysis in section 4.4, and the calculated reflection coefficients are also shown in table A.4. A sample of these reflection coefficients due to taper and due to the bifurcations are shown in table 5.2. The reflection

coefficients due to the bifurcations are mostly positive, but are generally smaller in value than the reflections from the tapered vessels, which are also positive. This indicates that the tapering of the vessels is responsible for a significant amount of the reflections in the system and appears to be more significant than the reflections due to the bifurcations in the system.

The combination of the fact that the reflection coefficients due to tapering are large positive values and that many of the reflection coefficients at the bifurcations are also positive explains why we have seen a large negative change in the W_2 characteristic in the ascending aorta of this tapered network even though no terminal resistance has been applied to the end vessels.

To assess the reflections in a tapered system when bifurcations are present, tests on simple tapered bifurcations were also performed. Two straight vessels were added to the single tapered vessel in the previous example, as shown in figure 5.10 (a). Vessels 2 and 3 were identical to one another and had a constant area along the length of the artery. The areas of vessels 2 and 3 were altered, so that for the three computations the reflection coefficients calculated for forward travelling waves at the bifurcations were: -0.2, 0.0 and 0.2. The results are shown in figure 5.10, where the first column shows the velocity and pressure waveforms at the start (black) and end (blue) of vessel 1 and the second column shows the characteristic waveforms, W_1 and W_2, waveforms at the start (black) and end (blue) of vessel 1.

The results for a reflection coefficient of 0.0 are shown in, figures 5.10 (c). The velocity, pressure and characteristic, W_1 and W_2 waveforms at the start and end of vessel 1 are very similar to that seen in the single tapered vessel, figure 5.9. At the start of the vessel the approximate reflection coefficient is 0.32 and at the end it is 0.0. The bifurcation has not had a significant effect on the waveform, which is expected, because the reflection coefficient at the bifurcation is zero and again shows that the linear theory calculation is also a good approximation for non-linear reflection coefficients.

Figures 5.10 (b) show results for a bifurcation with a linear theory reflection coefficient of -0.2 for forward travelling waves. It can be seen in figure 5.10 (b) that at the end of the vessel the approximate reflection coefficient calculated from the change in W_1 and W_2 is -0.29, which is solely due to the bifurcation. The change in

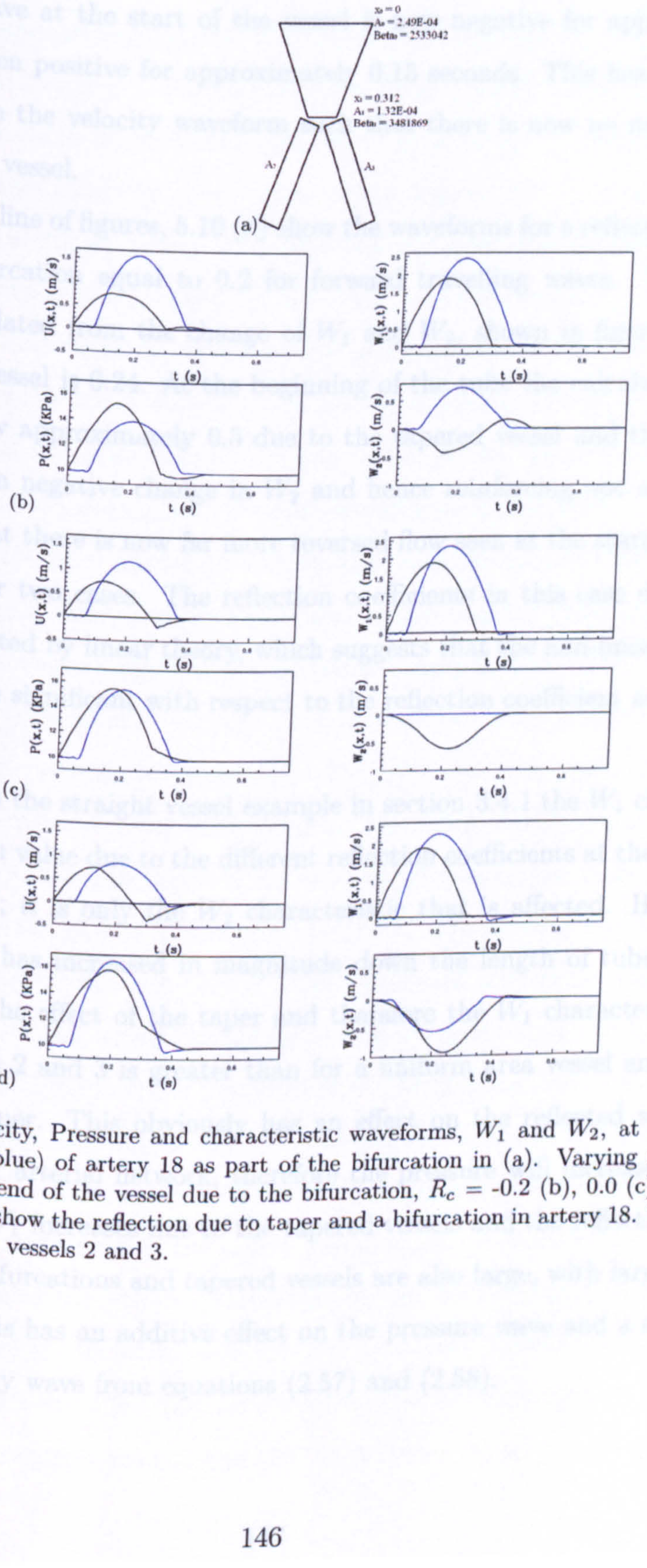


Figure 5.10: Velocity, Pressure and characteristic waveforms, W_1 and W_2, at the start (black) and end (blue) of artery 18 as part of the bifurcation in (a). Varying reflection coefficients at the end of the vessel due to the bifurcation, R_c = -0.2 (b), 0.0 (c) and 0.2 (d). These figures show the reflection due to taper and a bifurcation in artery 18. Terminal resistance = 0.0 on vessels 2 and 3.

W_2 at the start of the vessel is also quite different from the $R_c = 0.0$ case, with both positive and negative sections. The effect of the taper in the vessel in the $R_c = 0.0$ case gives a reflection coefficient of 0.32 at the start of the vessel, but now in this case the reflection coefficient at the start of the vessel is approximately $R_c = 0.24$ and the W_2 wave at the start of the vessel is now negative for approximately 0.3 seconds and then positive for approximately 0.15 seconds. This has resulted in an overall effect on the velocity waveform such that there is now no negative flow at the start of the vessel.

The bottom line of figures, 5.10 (d) show the waveforms for a reflection coefficient due to the bifurcation equal to 0.2 for forward travelling waves. The reflection coefficient calculated from the change of W_1 and W_2, shown in figure 5.10 (d), at the end of the vessel is 0.24. At the beginning of the tube the calculated reflection coefficient is now approximately 0.5 due to the tapered vessel and the bifurcation both producing a negative change in W_2 and hence reinforcing one another. This has the effect that there is now far more reversed flow seen at the start of the vessel than in the other two cases. The reflection coefficients in this case do not match with those predicted by linear theory, which suggests that the non-linear effects in a tapered vessel are significant with respect to the reflection coefficient at ill-matched bifurcations.

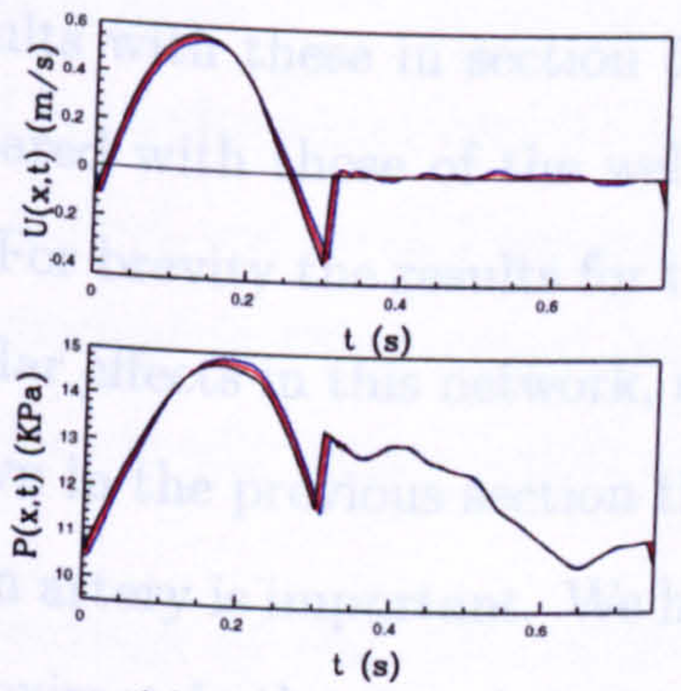
As was seen in the straight vessel example in section 3.4.1 the W_1 characteristic has not changed in value due to the different reflection coefficients at the bifurcation in the three cases; it is only the W_2 characteristic that is affected. However, the W_1 characteristic has increased in magnitude down the length of tube 1 in these examples due to the effect of the taper and therefore the W_1 characteristic transmitted into vessels 2 and 3 is greater than for a uniform area vessel and increases with increasing taper. This obviously has an effect on the reflected wave at the bifurcation. In our arterial network, therefore the pressure will increase down the network, because W_1 increases due to the tapered vessels and the reflections due to the effects of the bifurcations and tapered vessels are also large, with large negative changes in W_2. This has an additive effect on the pressure wave and a subtractive effect on the velocity wave from equations (2.57) and (2.58).

5.2.3 Change in waveforms along the length of an artery

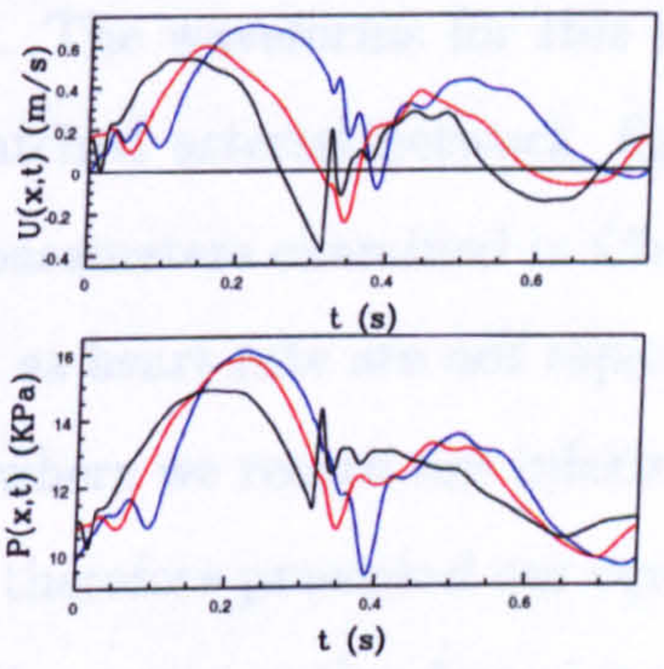
t has been shown from tests on single vessels and simple bifurcations, section 3.4.2 and 5.2.2, that waveforms vary along the length of a blood vessel. The location where the waveforms are recorded may therefore be important when comparing clinical and computational results. The waveforms may be especially sensitive to the measurement location in the arterial network of tapered vessels, particularly the velocity, section 5.2.2, because the magnitude of velocity is affected by the local cross sectional area from the mass conservation arguments. To illustrate how the waveforms vary along an artery in a physiological situation we have plotted the waveforms at three locations along the vessel for four different arteries (1, 7, 18 and 38) of the new MRI network. The velocity and pressure waveforms are shown in figure 5.11 where the black lines are the results at the start, the red lines are at the mid-point and the blue lines at the end of the artery. From figure 5.11 (1) it can be seen that the velocity and pressure waveforms at the start and end of the ascending aorta are very similar to one another and are almost overlaid. This is because the artery is untapered and the wave length is large when compared with the length of this vessel (0.036m), hence there is only a small time lag from the start to the end of the artery. Arteries 7, 18, and 38 are much longer arteries than artery 1 and it can be seen in figures 5.11 (7), (18) and (38) that the waveforms do vary quite significantly along their length. The main features of the waves are similar, but due to the time required for wave propagation, the start of the wave and any characteristic feature of the wave occurs at a later time the further down the vessel the measurements are taken. More significant is that the magnitudes of the velocity and pressure waves change quite dramatically along the length of the artery. In the previous section the magnitudes of pressure and velocity were shown to decrease or increase depending on the reflection coefficient of the bifurcation at the end of the vessel and the taper of the artery. In these figures the pressure waves are amplified along the length of the artery due to the positive reflection coefficient at the bifurcation and the velocity increases due to the reduction in area. This is not the case in artery 38 where the velocity decreases, possibly because of the effect of the large positive reflection coefficient at the end of the vessel due to the bifurcation, which mitigates the effect of the taper in this vessel. Some of the minor

features of the waves also change along the length of the artery, but this is relatively insignificant.

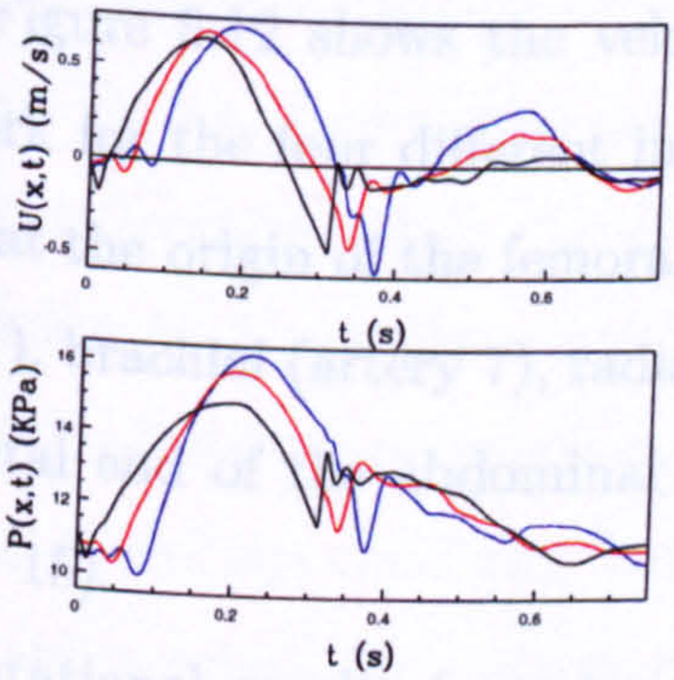
These results show that the location where the waveforms are recorded is important in the physiological situation particularly for certain arteries (long and tapered). We have therefore tried to use computational results from points in a similar position to those where the clinical readings of the waveforms in the subject were taken, as mentioned in section 5.1.3.



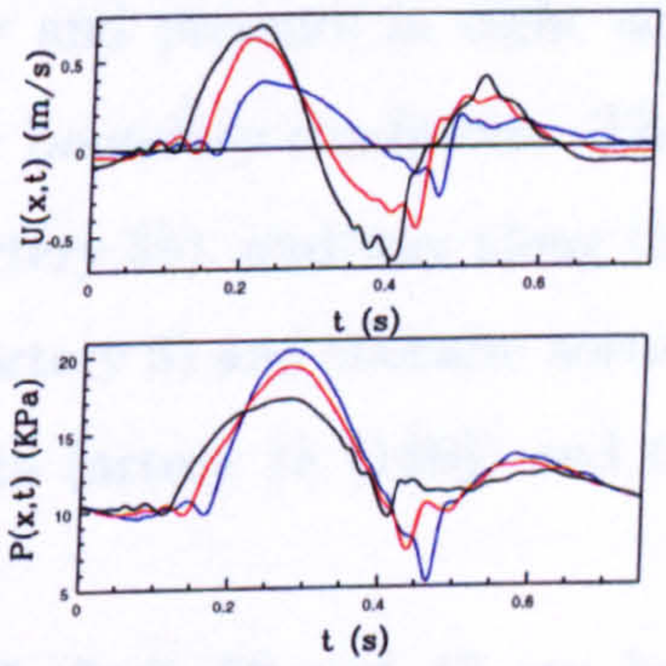
(1) Ascending Aorta



(7) Brachial Artery



(18) Thoracic Aorta



(38) Femoral Artery

Figure 5.11: Velocity and pressure waveforms taken at the start (black), mid-way (red) and end (blue) of arteries 1, 18, 7 and 38. These figures show significant variation in the long arteries 7, 18 and 38.

5.2.4 Waveforms in the tapered network

We now proceed to analyse the computational results for the tapered network constructed from the MRI data. In a similar manner to the previous network we compare the computational results for the four different types of inflow boundary condition. These results are presented for the new arterial network in the same set of arteries as before in section 4.3.8. We are in the fortunate position of having a set of clinical measurements for the same subject, figure 5.7 and we compare our computed results with these in section 5.2.6. The waveforms for this new network are also compared with those of the well-matched arterial network, figure 4.15, in section 5.2.8. For brevity the results for the parameters examined in Chapter 4 that have very similar effects in this network, such as heart rate are not reproduced here.

It was shown in the previous section that where we record our information along the length of an artery is important. We have therefore presented our computational results at approximately the same location in the artery as the clinical measurements were made. Figure 5.12 shows the velocity and pressure in eight arteries of the tapered network for the four different inflow boundary conditions. The waveforms are presented at the origin of the femoral (artery 38), mid-way along the ascending aorta (artery 1), brachial (artery 7), radial (artery 8) and thoracic aorta (artery 18) and at the distal end of the abdominal aorta (artery 18 (18b)) and the common carotid (artery 15).

The computational results for arteries 15, 7, 8, 38 and 42 can be compared directly with the 5 clinical measurements taken from the same subject shown in figure 5.7 (bottom five figures). However, as we were unable to obtain any clinical readings in the aorta for the subject, the waveforms in arteries 1, 18 and 18b will be compared with the three generic diagrammatic waveforms shown in figure 5.7 (top three figures). The waveforms studied have not only been taken in the same place along the artery for the tapered network and the clinical results but also for the well-matched system of Chapter 4 so all waveforms can be easily compared. (Note the numbering in the figures of the arteries in the well-matched network may be slightly different to the MRI network, but the layout of the waveforms on the page is the same for all three sets of results.) As before the waveforms are coloured according to the inflow boundary conditions where the black lines are the results for

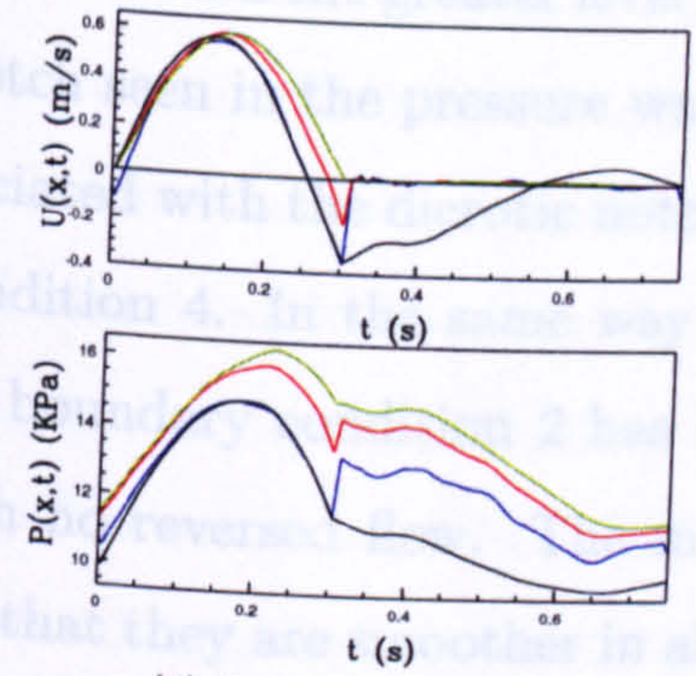
boundary condition 1, green for boundary condition 2, red for boundary condition 3 and blue for boundary condition 4.

Another factor that must be considered when comparing the waves is the heart rate. The heart rate of the female subject varied between 75 b.p.m. and 86 b.p.m. whilst the clinical measurements were taken, equivalent to a time period of 0.7 s to 0.8 s per heart beat. We have therefore chosen to take a value of 0.75 s as the time period for the computational results in the new tapered model. It should be noted that the results in figure 5.12 are for the tapered network with a reflection coefficient of zero applied to the terminal vessels. The waveforms are therefore solely due to the effects of the tapered vessels and any reflections produced at the bifurcations, which are not well-matched in this tapered network. The effect of terminal resistance in the tapered network will be studied in section 5.2.9.

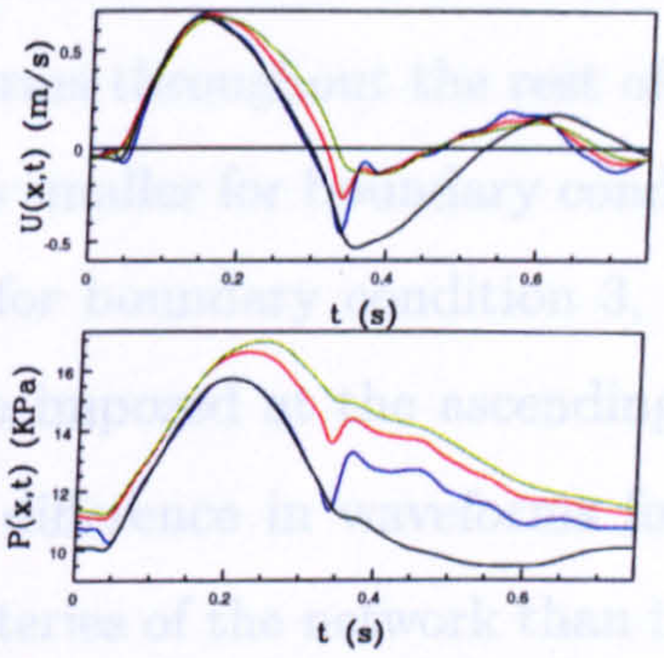
5.2.5 Comparison of the effects of the inflow boundary conditions

In this section we compare the differences between the waveforms seen in the tapered arterial network for the four inflow boundary conditions, figure 5.12. As for the previous network (section 4.3.8) the overall shapes of the waves throughout the network are similar for boundary conditions 2, 3 and 4. Boundary conditions 3 and 4 exhibit more notches in their waveforms and are not as smooth as the waveforms produced using boundary condition 2, which is again presumably related to the dicrotic notch and reversed flow seen in the ascending aorta.

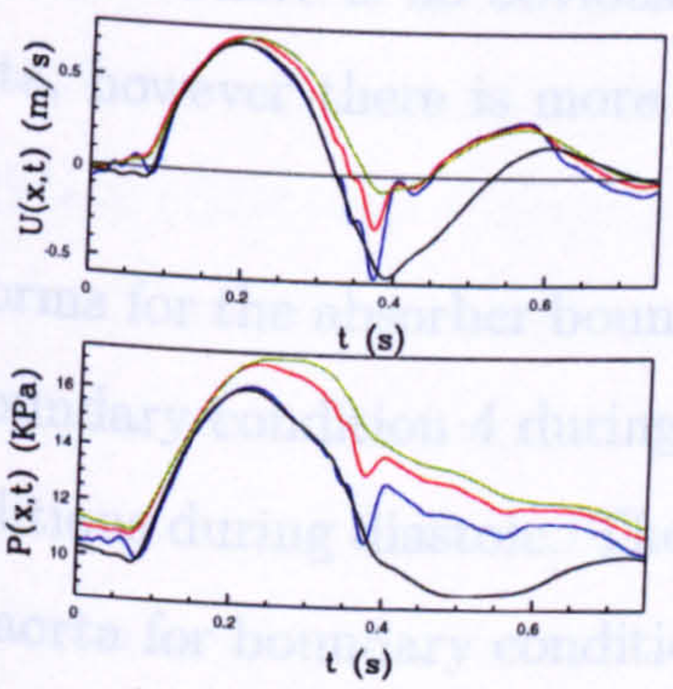
The reversed flow in the ascending aorta for boundary condition 3 is imposed, but for boundary condition 4 it is produced by the reflections in the system. This reversed flow is larger for boundary condition 4 and hence in the arteries throughout the network the related periods of reversed flow are also larger for boundary condition 4 than for boundary condition 3. Not only is there more reversed flow in the ascending aorta for boundary condition 4 but also the overall flow is lower, despite the fact that the peak velocity is similar. This is reflected in the higher pressure for boundary condition 3 in the ascending aorta and throughout the network. The velocity is even greater for boundary condition 2 and this is also seen in a higher pressure throughout the network. Boundary condition 4 exhibits a greater dicrotic notch in the pressure wave in the ascending aorta than for boundary condition 3,



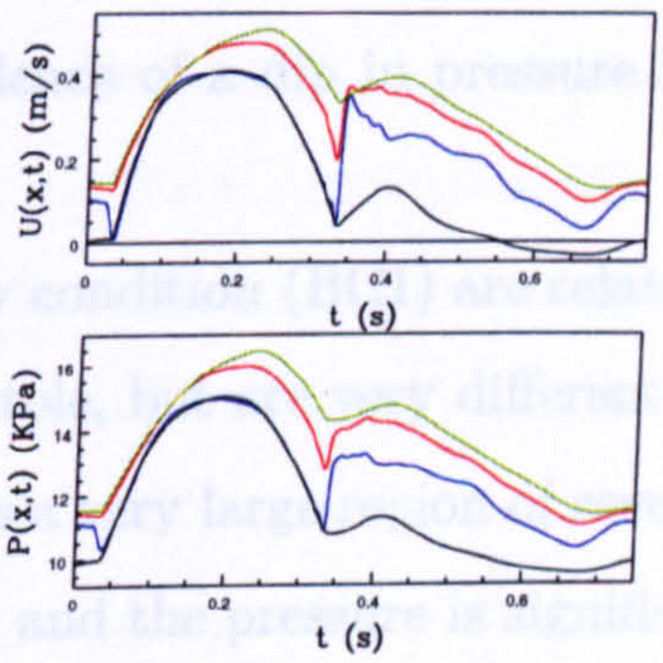
(1) Ascending Aorta



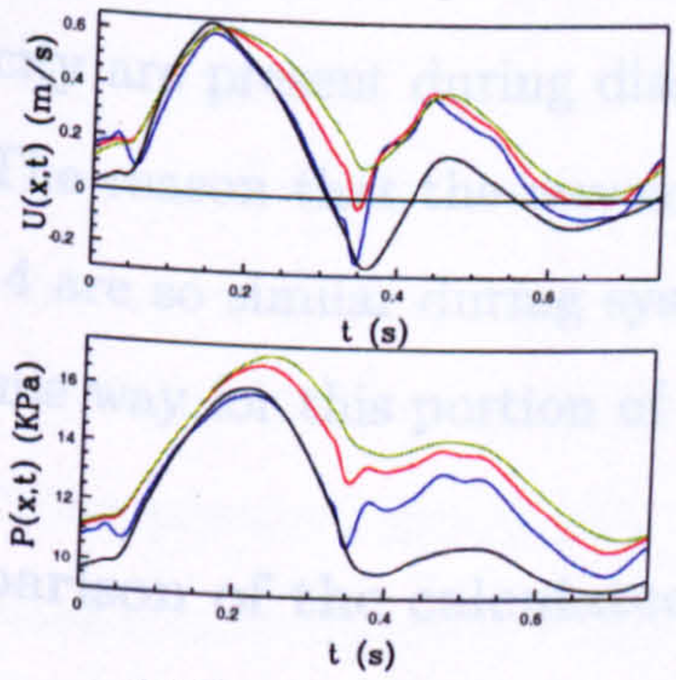
(18) Thoracic Aorta



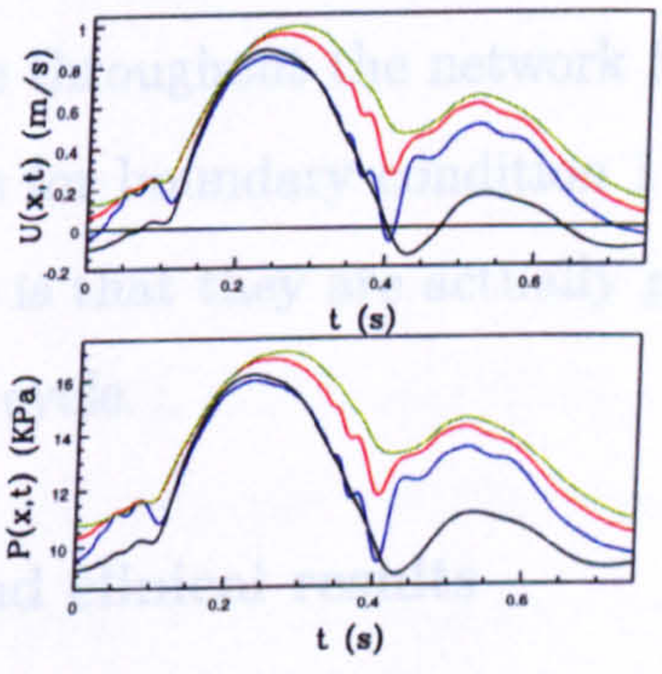
(18b) Abdominal Aorta



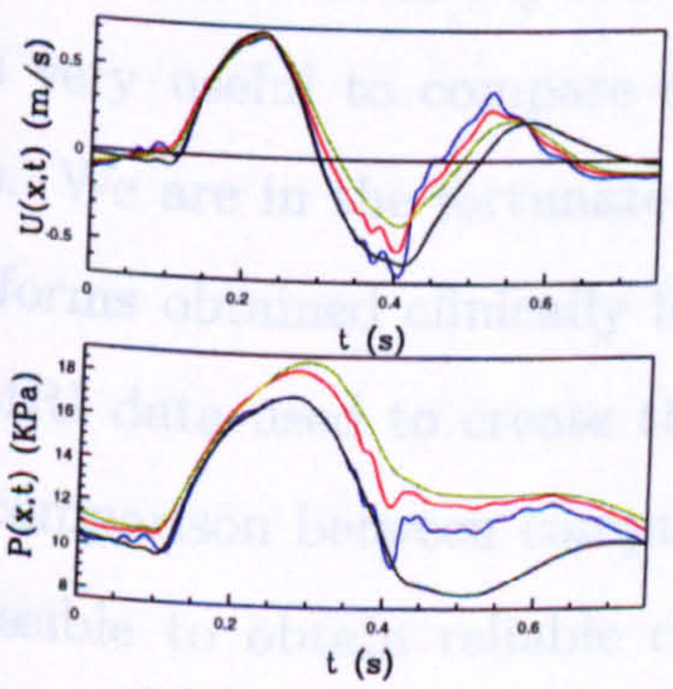
(15) Common Carotid



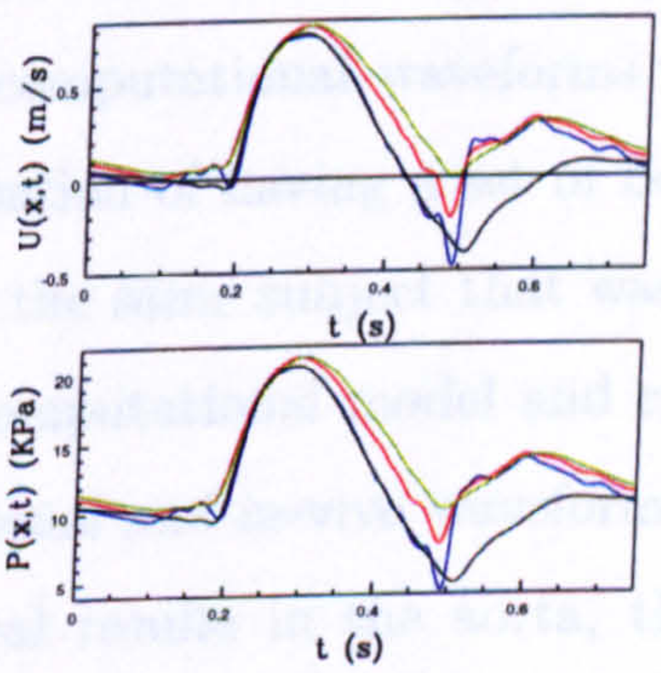
(7) Brachial Artery



(8) Radial Artery



(38) Femoral Artery



(42) Posterior Tibial

Figure 5.12: Computational results for waveforms in the MRI tapered network. The results are shown for four different boundary conditions 1 (black), 2 (green), 3 (red) and 4 (blue). The waveforms have been taken in the same locations as in Chapter 4 and are for a time period of 0.75 seconds. Note that the waveforms exhibit physiological features despite the fact that no terminal resistance has been applied to the end vessels.

which is associated with the greater level of reversed flow seen in the ascending aorta. Again any notch seen in the pressure waveforms throughout the rest of the system, which is associated with the dicrotic notch, is smaller for boundary condition 3 than boundary condition 4. In the same way as for boundary condition 3, the velocity waveform for boundary condition 2 has been imposed at the ascending aorta, but this time with no reversed flow. The main difference in waveforms for boundary condition 2 is that they are smoother in all arteries of the network than in boundary conditions 3 and 4. There is no obvious dicrotic notch in the pressure wave in the ascending aorta, however there is more evidence of a dip in pressure further from the heart.

The waveforms for the absorber boundary condition (BC1) are relatively similar to those for boundary condition 4 during systole, but are very different to all three boundary conditions during diastole. There is a very large region of reversed flow in the ascending aorta for boundary condition 1 and the pressure is significantly lower than the other three boundary conditions. The much lower levels of both pressure and velocity are present during diastole throughout the network for boundary condition 1. The reason that the waveforms for boundary condition 1 and boundary condition 4 are so similar during systole is that they are actually prescribed in exactly the same way for this portion of the cycle.

5.2.6 Comparison of the calculated and clinical results

Since we are interested in the ability of our code to accurately model the physiological situation it is very useful to compare our computational waveforms with clinical measurements. We are in the fortunate situation of having a set of both flow and pressure waveforms obtained clinically from the same subject that was scanned to produce the MRI data used to create the computational model and can therefore make a valid comparison between computational and in-vivo waveforms. However, it was not possible to obtain reliable clinical results in the aorta, therefore the computational results in the aorta are compared with the diagrammatic waveforms in figures 5.7 (1), (18) and (18b). This section details the differences between our computational results and the in-vivo waveforms for the four boundary conditions in some detail.

A small period of flow reversal is seen in the ascending aorta immediately after the systolic flow in clinical measurements. In the computational results, figure 5.12 (1), the absorber boundary condition (BC1) has too much flow reversal, which continues well into diastole and there is a secondary flow later in the cycle, neither of which occur in-vivo in the ascending aorta and imply aortic valve leakage. The simple velocity boundary condition (BC2) is prescribed to have no flow reversal. The velocity waveforms in the ascending aorta look more physiological for boundary conditions 3 and 4. The near physiological velocity boundary condition (BC3) is prescribed with a small amount of flow reversal and the part absorber/reflector boundary condition (BC4) has a larger region of flow reversal after the systolic flow. It is possible that this flow reversal maybe a little large compared with what is usually seen in-vivo, however the basic features are typical.

The pressure waveforms in the ascending aorta for boundary conditions 3 and 4 both have a dicrotic notch after the systolic flow, at the time of the aortic valve closure, followed by a gradual decline in pressure. This appears physiological, although the dicrotic notch maybe a little too large for boundary condition 4. Boundary condition 2 exhibits a levelling of pressure after the peak pressure, followed by a decline in pressure, but does not have the characteristic dicrotic notch. The pressure waveform for the absorber boundary condition (BC1) also does not exhibit a dicrotic notch; the pressure drops very rapidly after the systolic pressure and in diastole the pressure is much lower when compared with the clinical results and the other three boundary conditions. In fact the pressure dips below its base value (9.9 kPa), which is not physiologically correct. For boundary conditions 2 and 3, where the velocity has been prescribed, the peak pressure occurs in late systole, which is associated with typical waveforms for a human adult.

It is useful to compare the values of volume flux for the different computations and in-vivo to give an idea of the accuracy of the velocity magnitudes. Measurements of the volume flux were taken near to the ascending aorta using the MRI scanner and the average value was 3.8 litres/minute. The volume flux in the ascending aorta has been calculated for our computations and is shown in table 5.3 for all four boundary conditions.

The volume flux for the absorber boundary condition (BC1) is far too low and

	Volume flux (litres per minute)
BC 1	1.9
BC 2	4.4
BC 3	4.0
BC 4	3.0
From MRI data	3.8

Table 5.3: Volume fluxes in the ascending aorta.

is due to the very long period of reversed flow seen in the ascending aorta during diastole. The volume flux for the part absorber/reflector boundary condition (BC4) is also probably slightly too low with the reversed flow being too large. For the velocity boundary conditions (BC2) and (BC3) the volume flux is closer to the correct physiological value in the ascending aorta as measured.

In all four boundary conditions the peak velocity is possibly a little low in the ascending aorta. For boundary conditions 2 and 3, where the velocity is prescribed, although the peak velocity appears a little low, the mass flux is the right order of magnitude. This may indicate that the modelling assumptions of the prescribed waveform are not quite correct, i.e. the half-sine wave has a rounded peak, and we should perhaps use a more spiked or a shorter waveform.

Overall, the waveforms in the ascending aorta appear the most physiological for boundary condition 3. Boundary condition 4 also appears physiological, but has slightly too much reversed flow and the dicrotic notch is also slightly too large in the pressure waveform. This is probably due to too much reflection in the system propagating back to the ascending aorta, combined with our modelling of the aortic valve closure (section 5.2.1) but as mentioned in previous sections this boundary condition is attractive, because fewer assumptions need to be made about the waveform in the ascending aorta than for boundary condition 3.

As discussed in Chapter 4, further down the network in the thoracic aorta and the abdominal aorta the peak pressure rises, the dicrotic notch falls in pressure, is further away from the peak pressure and is generally less significant in in-vivo measurements. In our computational results it is true that the peak pressure has risen and the dicrotic notch is less significant in arteries 18 and 18b (figures 5.12 (18) and (18b)) when compared with the pressure wave in the ascending aorta. However, there is little difference in these features between the thoracic and abdominal aortas

figures 5.12 (18) and (18b). This is because the measurements have been taken at different positions along the length of what is essentially the same vessel in this tapered network. Although the vessel is tapered, there are no vessels branching off the aorta in this region for this network, because the vessels were not clear in the MRI data. At the distal end of the aorta (figure 5.12 (18b)) the dicrotic notch is further away from the peak pressure and is a little lower than mid-way along artery 18 and the ascending aorta, but the changes are not as pronounced as those seen in-vivo. Looking at the boundary conditions the pressure waveforms for the absorber boundary condition (BC1) are again the least physiological, due to a very low diastolic pressure and no sign of any notch. For the velocity boundary condition (BC2) the pressure gradually declines and is similar to in-vivo measurements, but again there is no notch. For boundary conditions 3 and 4, which have the dicrotic notch present in the ascending aorta, then there is also a notch in the lower sections of the aorta, which is more similar to the clinical results, figures 5.7 (18) and (18b). It is interesting to note that the notches are more rounded in the more distal sections of the aorta for the computational results, which reflects the trend in-vivo.

The velocity waveforms for boundary conditions 2, 3 and 4 again all look more physiological in arteries 18 and 18b than for the absorber boundary condition, because they show some reversed flow after the systolic flow and is followed by some positive flow. Boundary condition 1 again produces too much reversed flow during diastole in arteries 18 and 18b. The magnitude of the peak velocity mid-way along and at the distal end of the aorta, arteries 18 and 18b, has actually increased from the value in the ascending aorta, whereas in-vivo we would expect a decrease in peak velocity. This increase is due to the aorta being a long tapered artery with the velocity increasing as the area decreases. This artery is not actually solely tapered in the body and would have more branching arteries off the main vessel which would take some of the blood flow and consequently reduce the velocity in the lower sections of the aorta.

The computational waveforms and the clinical waveforms can be compared directly with each other in the remaining arteries, 15, 7, 8, 38 and 42 as the clinical waveforms for these arteries are clinical measurements from the same female subject from which the MRI data was obtained.

The pressure waveforms in the common carotid have approximately the same pulse pressure of 4 kPa for all four boundary conditions, figure 5.12 (15), and the clinical results, figure 5.7 (15), however the mean pressure is slightly higher for the velocity boundary conditions (BC2) and (BC3). Despite this the pressure waveforms for boundary conditions 2 and 3 appear the most similar in shape to the clinical waveform, which has a second, smaller peak of pressure later in diastole, followed by a gradual decline. For the part absorber/reflector boundary condition (BC4) there is also a second peak of pressure but it is too pronounced and for the absorber boundary condition (BC1) the pressure drops rapidly to a value that is too low in diastole.

The velocity waveforms in the common carotid do not appear as similar to the physiological results, as the pressure waveforms. They all show a second peak of velocity, but this is too high and also occurs relatively early in the cycle and the separation of the peaks of velocity needs to be greater. The velocity waveform is also much less peaked and has a lower maximum (0.4 - 0.5 m/s) when compared with the clinical results (0.9 m/s). In fact the peak in the carotid is also low when compared to the ascending aorta (0.6 m/s) in the computational results. However, some of the features of the waveform are more encouraging because in the clinical results it can be seen that all the flow is positive and for the computational results the flow is also all positive for boundary conditions 2, 3 and 4. This is particularly obvious for boundary conditions 2 and 3 where there is a higher mean velocity. The fact that the flow is all positive is a well known physiological result.

For both the pressure and velocity waveform in the clinical results of the common carotid there is a sharp peak, whereas in the computational results the waveforms show more of a rounded peak. This maybe due to an incorrectly prescribed inflow boundary condition or a lack of detail in the network.

In the clinical measurements for the brachial artery, figure 5.7, (7) the velocity waveform shows only a very small region of reversed flow and two very small secondary regions of positive flow during diastole. In the computational results for boundary conditions 1 and 4, figure 5.12 (7), we see some reversed flow followed by a very large region of secondary flow. The velocity waveforms for boundary conditions 2 and 3 are all mainly positive and appear closer to the clinical results, but again

the second peak of flow is excessively large. The peak velocity for the waveforms for all boundary conditions are similar in magnitude to the clinical measurements (0.6 m/s). The pressure magnitudes for the computational results are also very similar to the clinical measurements in the brachial artery, but for boundary conditions 2 and 3 the mean arterial pressures are again a little too high. The pressure waveforms appear more similar to the clinical measurements than the velocity waveforms and it can be seen from boundary conditions 2, 3 and 4 that there is a lower second peak of pressure later in the cycle in our computational results, which is consistent with in-vivo measurements. Again the second peak of pressure in diastole for boundary condition 1 is far too low.

The pressure magnitudes in the radial artery, figure 5.12 (8) are also similar to those seen in the clinical measurements. There is again a second peak of pressure seen later in the cycle in the computational results, but the second pressure peak seen in diastole for boundary condition 1 is slightly too low. The peaks of pressure are also slightly too early in these computational results. Again the pressures for boundary conditions 2 and 3 are slightly higher than the clinical measurements.

The velocity waveform in the clinical results of the radial artery exhibits a small period of reversed flow after the systolic flow, but the computational results for boundary conditions 2, 3 and 4 have a large second peak of flow. The velocity waveform could improve once terminal resistance is applied to this end vessel later in section 5.2.9. In fact the velocity waveforms for boundary condition 1 looks the most physiological because it has a small region of reversed flow after the systolic flow followed by a second small region of positive flow. The waveforms for velocity and pressure both look similar in this case because there is no terminal resistance applied to any of the terminal vessels such as this. The peak of the velocity has increased from the brachial to the radial which is not seen in-vivo, this again is probably due to the tapered vessels increasing the velocity as the area decreases and the high magnitudes are due to a lack of arteries branching off the current network. This section of arteries could also be improved with more arteries coming off the main arteries in the arm. It is also interesting to note that the waveforms for pressure and velocity from the clinical measurements are very similar in arteries 7 and 8 and that our computational results look far better for artery 7 than they

do for artery 8, which may be related to the fact that artery 7 is one generation of bifurcations further up the arterial tree than artery 8.

The pressure waveform for boundary condition 2 in the femoral, figure 5.12 (38), appears very similar to the clinical results, figure 5.7 (38). Boundary conditions 3 and 4 also have a similar shaped waves to boundary condition 2, but there exists a small dip in pressure after the systolic pressure due to the dicrotic notch, especially in boundary condition 4. The pulse pressure magnitude is a little too high, but this has been the case throughout the network and is probably due to a slightly high pressure being prescribed at the ascending aorta. The velocity waveform in the clinical results has a period of reversed flow after the peak velocity followed by a period of positive flow. This is seen in the computational results, but the reversed flow and the secondary positive flow again appear excessive for all boundary conditions. It is however interesting to note that there is more flow reversal seen in our computational results in the femoral than in the brachial artery which is consistent with the clinical measurements seen in figure 5.7.

In the posterior tibial, artery 42, the pressure and velocity waves, figure 5.12 (42), are similar in shape, because it is another end vessel in our computational network and no terminal resistance has been added. In the clinical results there is a large negative flow after the peak velocity and the velocity waveform for boundary condition 1 looks most similar to this. Boundary conditions 2, 3 and 4 all fail to show enough reversed flow. The peak velocity for this artery is also high in our computational results. The pressure waveform in the posterior tibial looks relatively physiological for boundary condition 2. For boundary condition 3 there is perhaps too much of a dip after systole, for boundary condition 4 the pressure decreases too sharply before increasing rapidly again and for boundary condition 1 the pressure also declines slightly too much. The pressure magnitudes in the computational results show the increase in peak pressure that is typically seen in-vivo for arteries down the network.

Generally the pressure waveforms and magnitudes in the arterial network are more similar to the clinical results than the velocity waveforms. In particular the pressure waveforms for boundary condition 2 look very similar to the clinical measurements for the more distal arteries in figure 5.7. The pressure magnitudes were

also very similar and any discrepancies could be due to incorrectly prescribing the input velocity waveform, the physical properties of the network and the base line pressure as these input values were only simple approximations. Boundary conditions 3 and 4 waveforms are very similar to those for boundary condition 2, but they exhibit extra notches in their waveforms due to the dicrotic notch and reversed flow seen in the ascending aorta. These features are generally seen in the aorta, but are not present in the clinical waveforms for later arteries and may be damped in the human system. Also our computational results may be very sensitive to this feature, or perhaps the applanation tonometry used to obtain the clinical readings is not accurate enough to detect some of the smaller features of the pressure wave. Although we were unable to obtain clinical pressure waveforms in the aorta, these are relatively well known and our computational pressure waveforms also appear physiological in these arteries. The pressure waveforms for boundary condition 2 in the aorta do not possess any extra features related to the dicrotic notch in the ascending aorta, which is also not present. However, we expect to see notches in these waveforms and do so in the waveforms for boundary conditions 3 and 4, which appear very physiological.

The computed velocity waveforms also have many of the characteristic features of in-vivo waveforms, but many of the secondary features are too large. The magnitudes for the velocity waveforms are also not as good as those for the pressure waveforms. The pressure waveforms also look relatively physiological in the terminal arteries in this system even though no terminal resistance is applied to these vessels. The velocity waveforms appear the least physiological in these end vessels as there is no reversed flow seen in some of our computations and the second peak of velocity is also very high. This suggests that, as expected, the more arteries there are to the end of the network the more accurate the waveform is. Many of the pressure and velocity waveforms appear to have a sharper peak velocity and pressure waveform where our computational results are more rounded, which is probably due to our over simplified input condition.

The length of time it has taken the wave to reach the brachial from the radial and from the femoral to the posterior tibial is approximately 0.03 seconds and 0.06 seconds respectively in the clinical measurements, this is slightly faster than the

wave in the computations which has taken approximately 0.05 seconds and 0.10 seconds respectively. This may suggest that the wavespeed we have chosen in the arteries is a little low at least in this region.

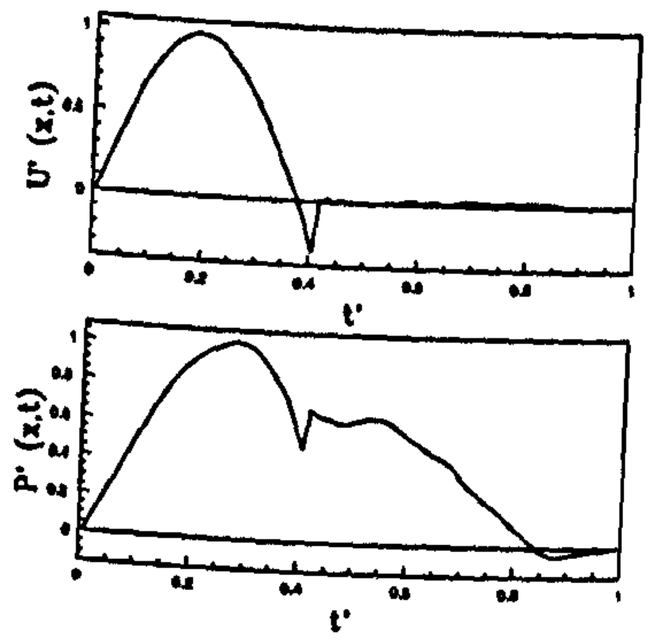
Overall the computational predictions in this novel comparison of computational and clinical results for the same human subject are reasonably encouraging. We investigate the effects of some alterations to our modelling in the hope of improving the results in later sections.

5.2.7 Magnitudes of pressure and velocity waveforms in the MRI arterial network

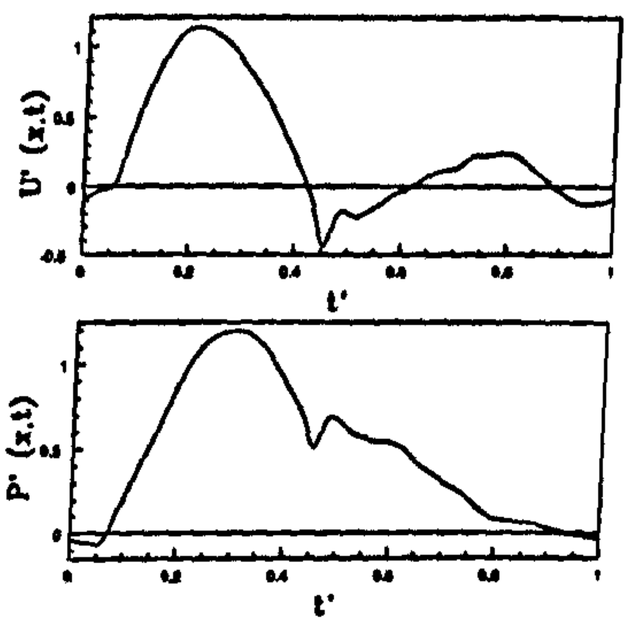
In section 5.2.6 the manner in which the magnitudes of pressure and velocity varied throughout the arterial network was discussed. In order to more clearly visualise some of these variations, particularly the amplification of the pulse pressure that is known to occur in-vivo, we have presented the non-dimensionalised waveforms for the imposed velocity boundary condition (*BC3*) in figure 5.13. The pressure and velocity waves have been non-dimensionalised by the peak values in the ascending aorta. The diastolic pressure at time equal to zero in the ascending aorta has been subtracted from the pressure waves so that the non-dimensionalised pressure waveforms essentially show the pressure pulse. The time has also been non-dimensionalised by the size of the time period, 0.75 s.

It can be clearly seen from figure 5.13 that the peak pressure in systole increases and the diastolic pressure slowly decreases, the further away from the heart the waveform is taken. In arteries close to the ascending aorta the peak pressures are slightly above one, but in more distal arteries the amplification of the pressure pulse is much greater. In the femoral artery the peak pressure is approximately one and a half times that in the ascending aorta and in the posterior tibial it increases to as much as twice the aortic pressure. In contrast the diastolic pressure in the femoral artery is -0.2 and in the posterior tibial it is -0.9. Therefore the pulse pressure increases as well as the peak pressure and the diastolic pressure declines, which is all in accordance with typical clinical findings [95, 101].

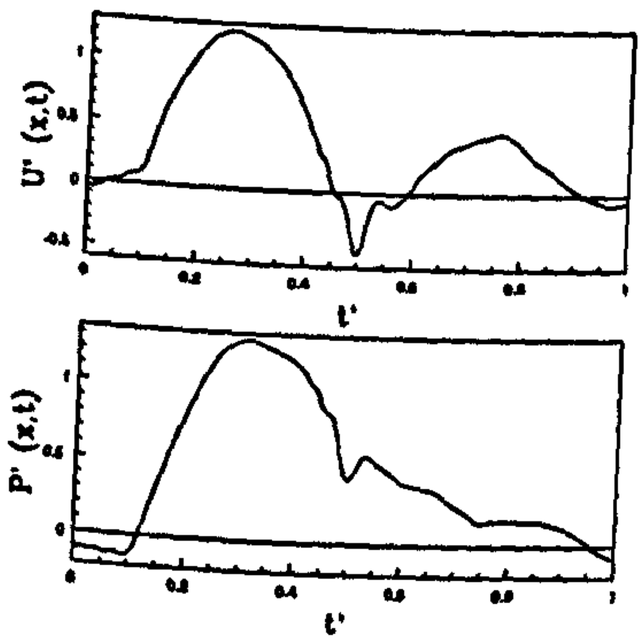
In-vivo the velocity decreases with distance from the ascending aorta, but it can now be clearly seen that this does not occur in the computational results. The only



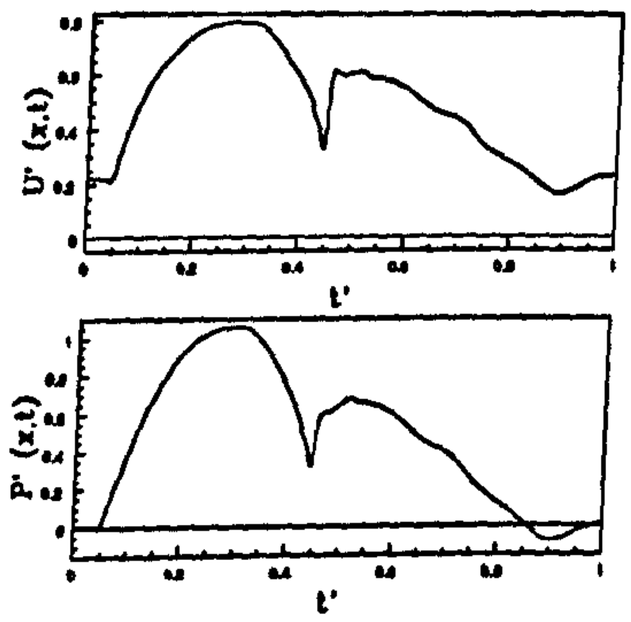
(1) Ascending Aorta



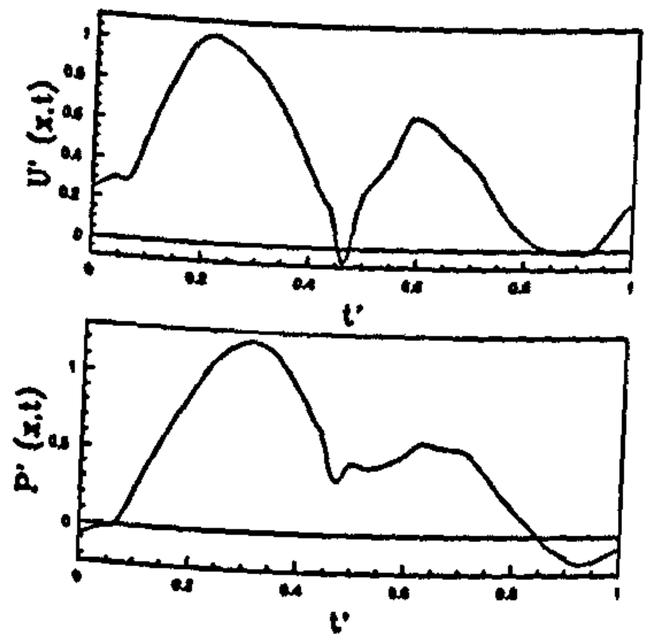
(18) Thoracic Aorta



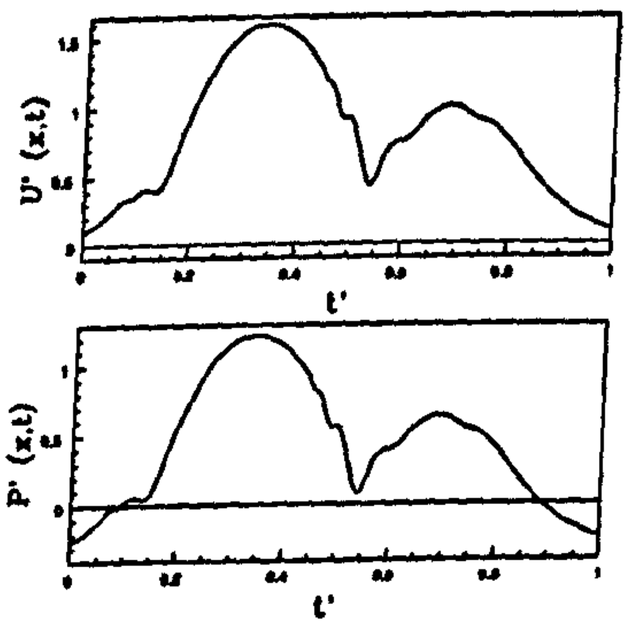
(18b) Abdominal Aorta



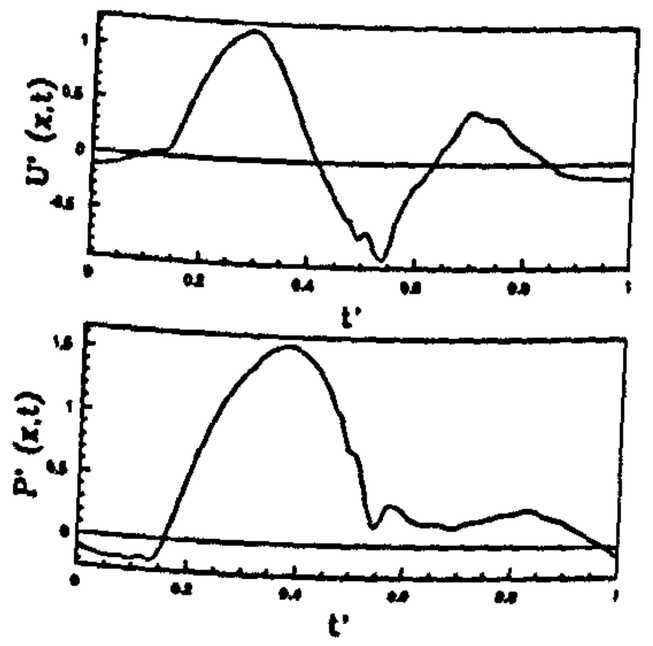
(15) Common Carotid



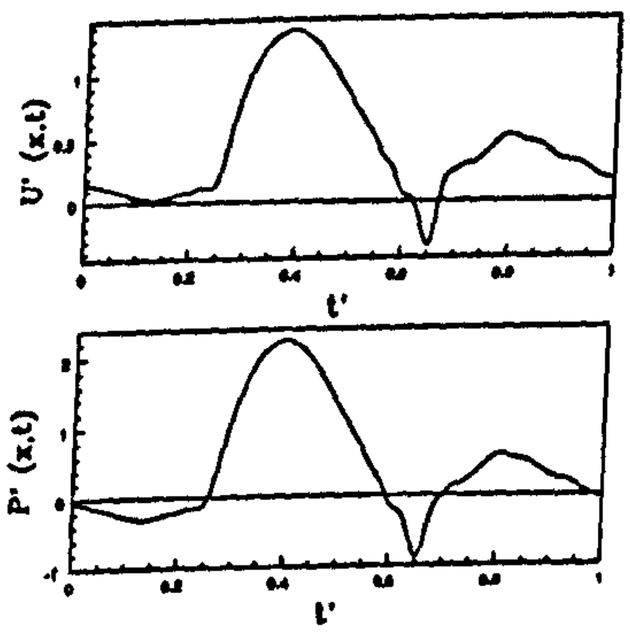
(7) Brachial Artery



(8) Radial Artery



(38) Femoral Artery



(42) Posterior Tibial

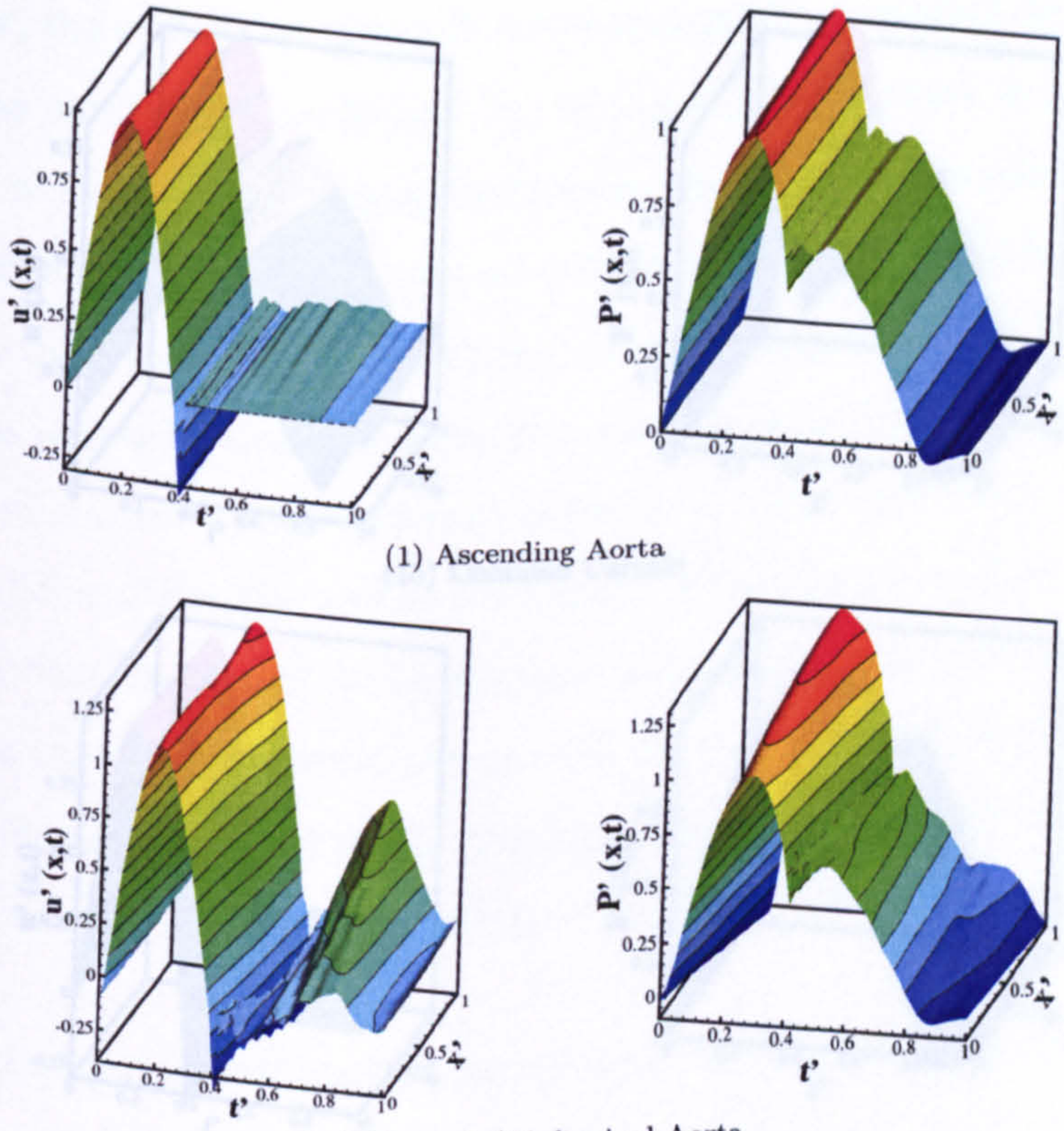
Figure 5.13: Non-dimensionalised results obtained in the MRI network for velocity inflow boundary condition 3. The velocities and pressures have been normalised by the peak and baseline values in the ascending aorta. Time has been normalised by the time period for 1 cycle. These plot show typical physiological amplification of the pressure pulse with distance from the heart, but also that there is no decline in velocity, which is not physiological.

vessel where velocity decreases is the common carotid artery and in all the other arteries in the system the velocity increases. This is mainly due to the fact that not enough vessels are modelled in the system. For example the major organs, such as the kidneys and liver are known to require a substantial portion of the resting blood flow [95, 61] and the arteries supplying them have not been modelled. The lack of other arteries also accentuates the effect of taper in more peripheral arteries where some of the decline in cross-sectional area should actually be compensated by vessels that have not been considered.

The velocity magnitude in arteries 18, 18b, 7 and 38, which are not terminal vessels, are all above one and the increases in velocity in these vessels are similar to those seen in the well-matched system. In the terminal vessels in this system (arteries 8 and 42) the velocity has substantially increased which again is not physiological, however for these two vessels in the well-matched system the velocity did decrease when terminal resistance was applied and a similar effect was seen when terminal resistance was applied to this system (section 5.2.9).

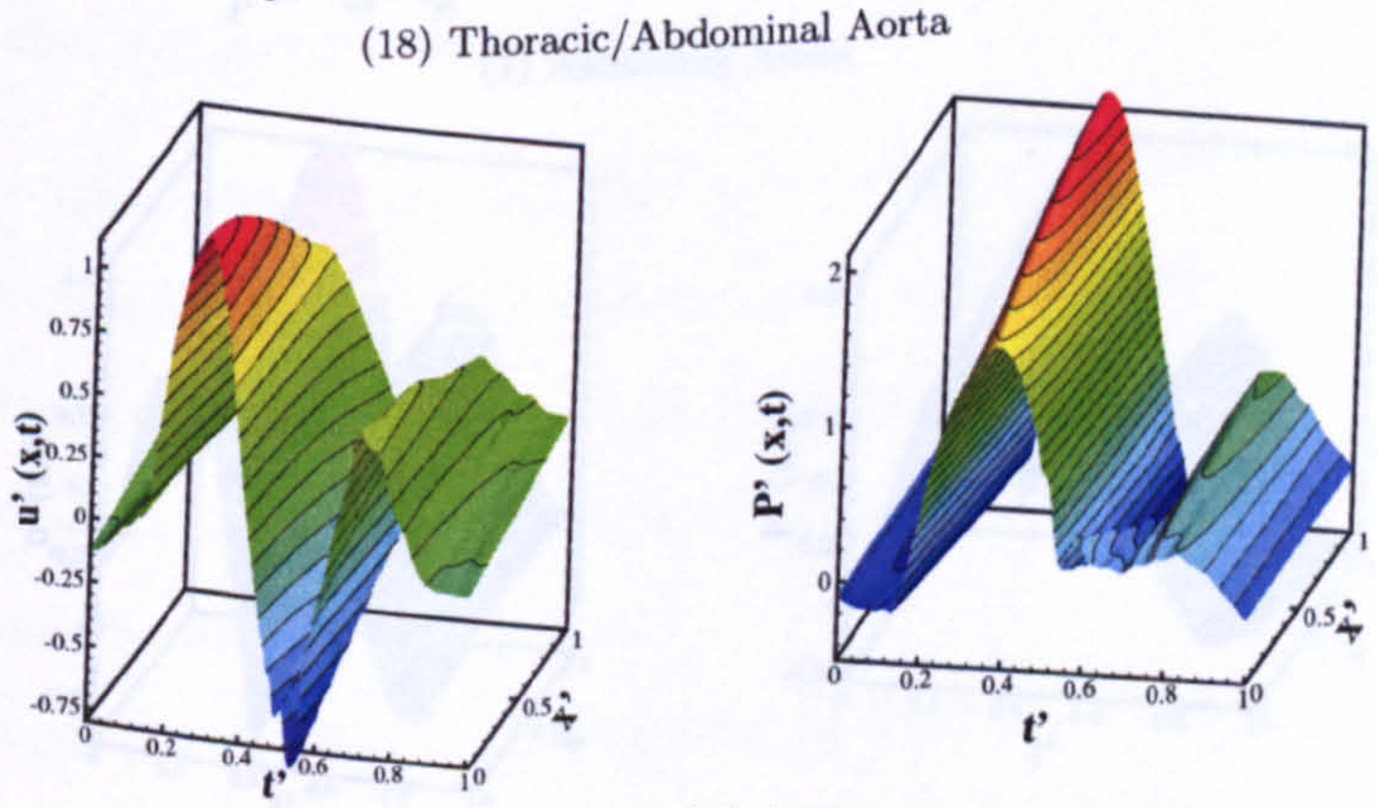
Three-dimensional images, figures 5.14 and 5.15, of the non-dimensionalised data have also been made, which show how the pressure and velocity vary along the length of the vessel and with time, for the same 8 arteries. For these images the location along each vessel has also been non-dimensionalised by the length of that vessel. The velocity waveforms are shown in the first column of figures 5.14 and 5.15 and the pressures are shown in the second column. Figure 5.14 shows the waves from the ascending aorta and down along the aorta to the legs (arteries 1, 18, 38 and 42). The waves in four arteries of the upper body are shown in figure 5.15, arteries 15 (carotids), 1 (ascending aorta) and 7 and 8 (arteries in the arms). As was shown in the previous figure the pressure increases with distance from the heart but what also can be seen from these figures is that the pressure increases along the length of each vessel, which also appears physiological.

The velocity waveforms have also increased in magnitude along the lengths of arteries 18, 42, 15 and 7. All these arteries have a relatively large reflection coefficient due to the taper, 0.36, 0.35, 0.45 and 0.42 respectively. This indicates that these vessels reduce in size and the blood is squeezed through a smaller cross-sectional area, which increases the velocity due to mass conservation arguments, see section

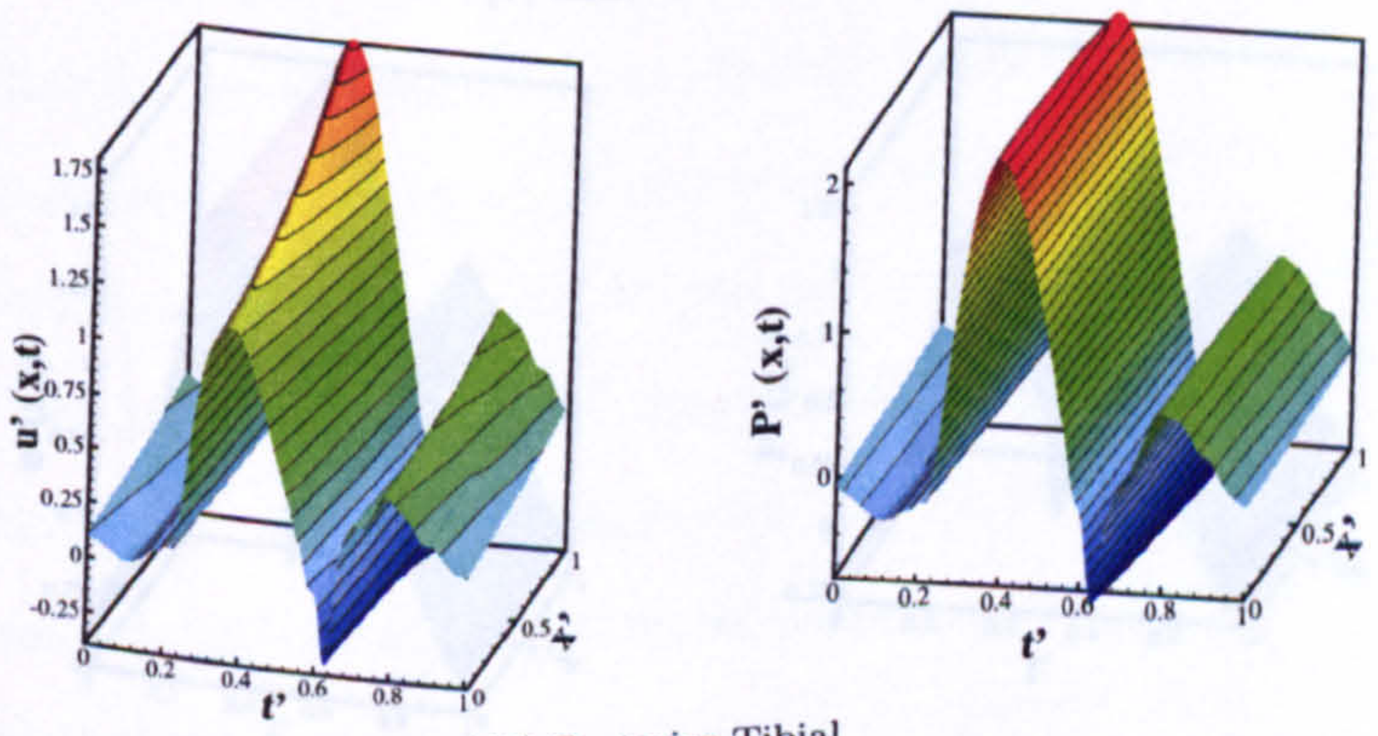


(1) Ascending Aorta

(18) Thoracic/Abdominal Aorta

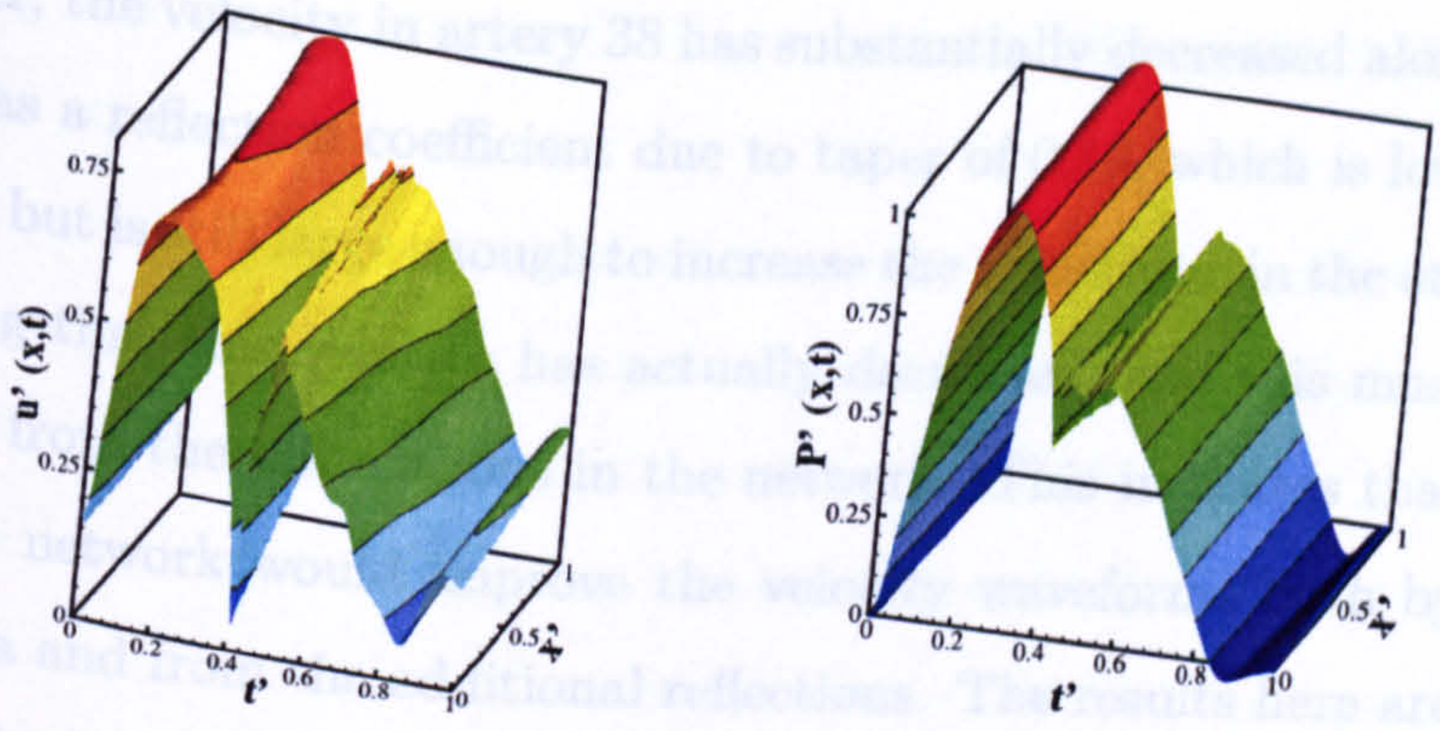


(38) Femoral Artery

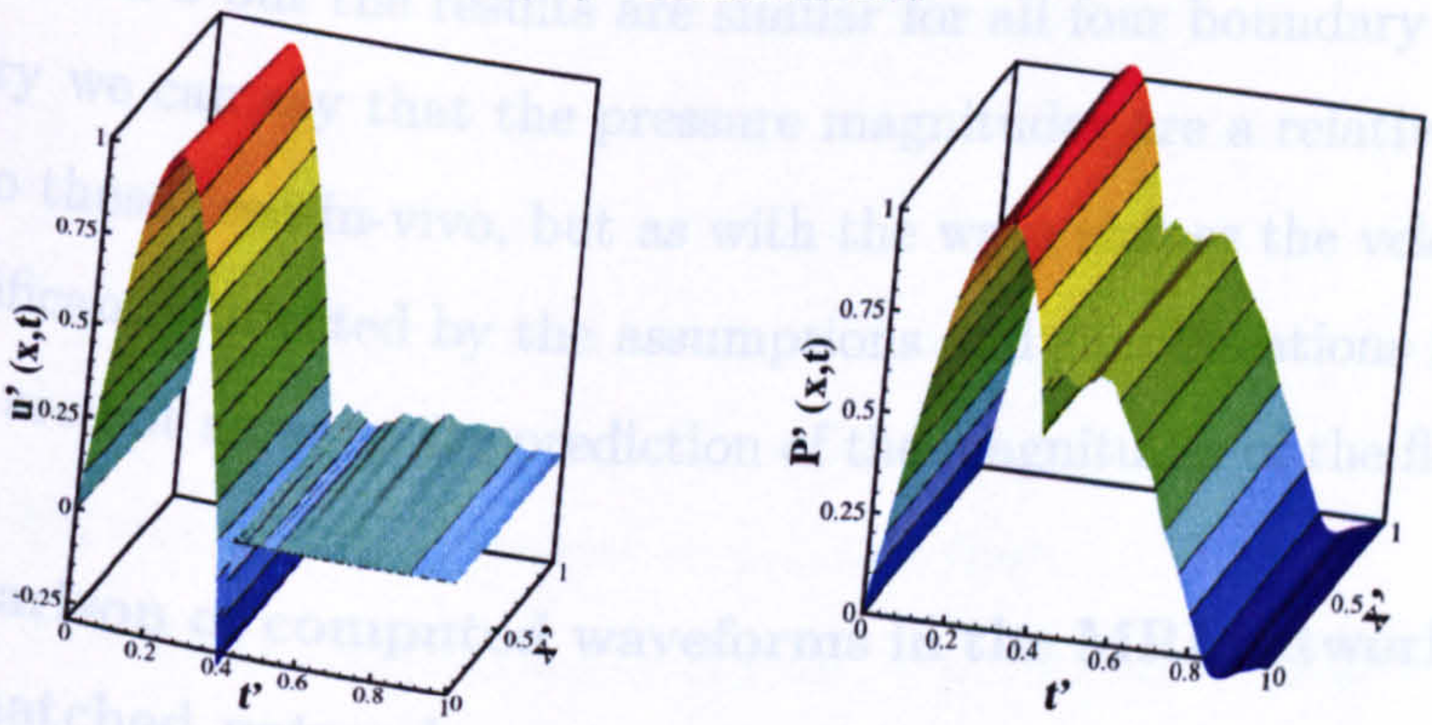


(42) Posterior Tibial

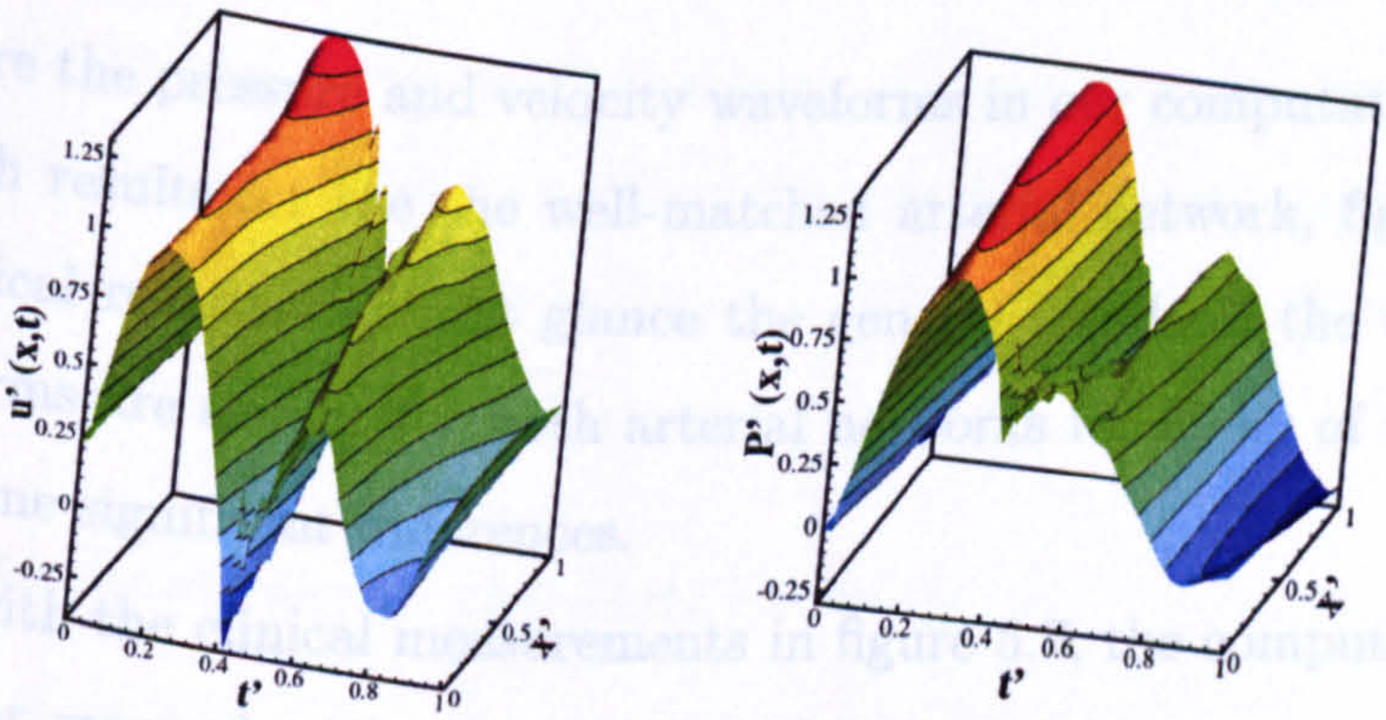
Figure 5.14: Three dimensional images of the non-dimensionalised data of the ascending aorta (1) and arteries into the legs, with velocity in the left hand column and pressure in the right. The distance along the artery has been non-dimensionalised by the length of the artery. These show quite significant changes in magnitudes along the length of some of the arteries.



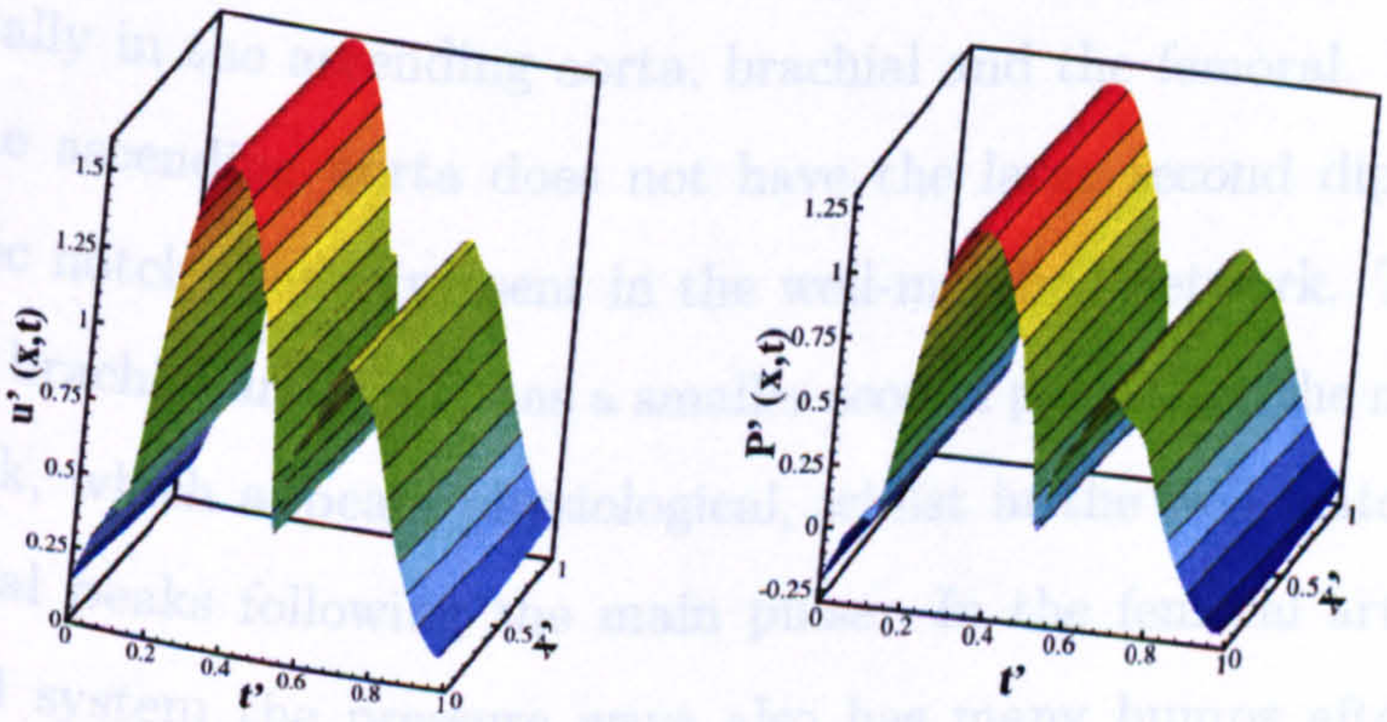
(15) Common Carotid



(1) Ascending Aorta



(7) Brachial Artery



(8) Radial Artery

Figure 5.15: Three dimensional images of the non-dimensionalised data of the common carotid in the head (15), ascending aorta (1) and arteries into the arms (7) and (8), with velocity in the left hand column and pressure in the right. The distance along the artery has been non-dimensionalised by the length of the artery.

2.1.1. However, the velocity in artery 38 has substantially decreased along its length. This artery has a reflection coefficient due to taper of 0.19, which is lower than the other arteries, but is still large enough to increase the velocity as in the other arteries. It is interesting that this velocity has actually decreased, and this must be due to the reflections from the bifurcations in the network. This indicates that modelling of more of the network would improve the velocity waveforms both by providing the correct area and from the additional reflections. The results here are shown for boundary condition 3 but the results are similar for all four boundary conditions.

In summary we can say that the pressure magnitudes are a relatively good approximation to those seen in-vivo, but as with the wave shapes the velocity magnitudes are significantly affected by the assumptions and simplifications made in our modelling and are not an accurate prediction of the magnitudes of the flows in-vivo.

5.2.8 Comparison of computed waveforms in the MRI network with the well-matched network

We now compare the pressure and velocity waveforms in our computational results, figure 5.12, with results for the the well-matched arterial network, figure 4.15, as well as our clinical results. At first glance the general trends of the velocity and pressure waveforms are similar for both arterial networks for many of the arteries, but there are some significant differences.

Comparing with the clinical measurements in figure 5.7, the computed pressure waveforms appear more physiological in the MRI network than the well-matched network, especially in the ascending aorta, brachial and the femoral. The pressure waveform in the ascending aorta does not have the large second dip in pressure after the dicrotic notch that is present in the well-matched network. The pressure waveform in the brachial artery (7) has a smaller second peak after the main peak in the MRI network, which appears physiological, whilst in the well-matched system there were several peaks following the main pulse. In the femoral artery (52) of the well-matched system the pressure wave also has many bumps after the peak pressure. The smoother pressure waves for the MRI network are much more similar to the clinical results, particularly for boundary condition 2. In fact throughout the network the differences in the overall wave shapes are most obvious for the results

produced using boundary condition 2. The magnitudes of pressure in both networks are of the right order.

The velocity waveforms have similar features to each other and both have secondary waveforms that appear a little too large. The velocity magnitudes have decreased substantially in the terminal vessels of the well-matched network unlike those in the MRI network but this may be altered when terminal resistance is added to the end vessels of the MRI network and is also related to the fact that arteries such as the renals have not been modelled in the MRI network. However the velocity magnitudes do not gradually decline through the system in either networks.

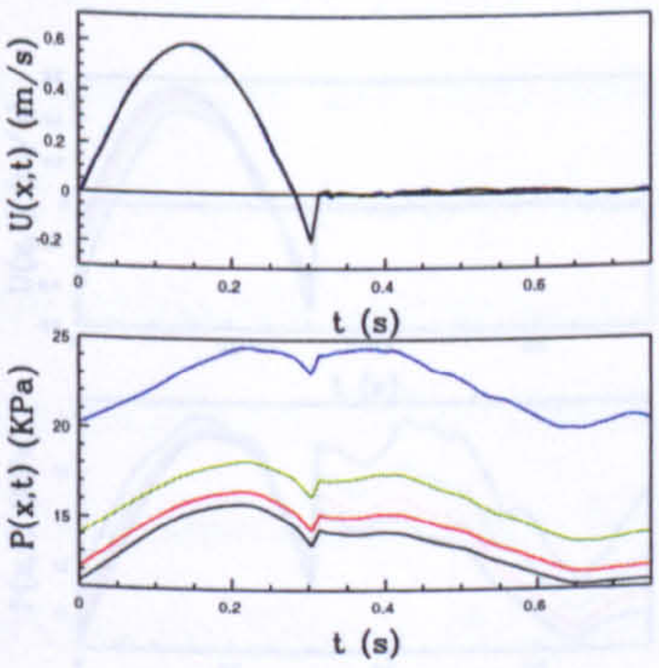
One interesting difference is that in our MRI model the mean flow is substantially above zero flow in the common carotid artery (15) especially for boundary conditions 2 and 3, but all positive flow does not occur in the well-matched system for this artery. Physiologically we expect to see all positive flow.

Overall the waveforms are reasonably similar, but they do appear more physiologically correct for the tapered MRI model. A main difference is that the waveforms in the well-matched network are much lumpier, whereas those in the tapered network are relatively smooth. This is perhaps because the tapered network provides a smooth set of reflections throughout the whole system rather than in discrete locations at the terminal vessels.

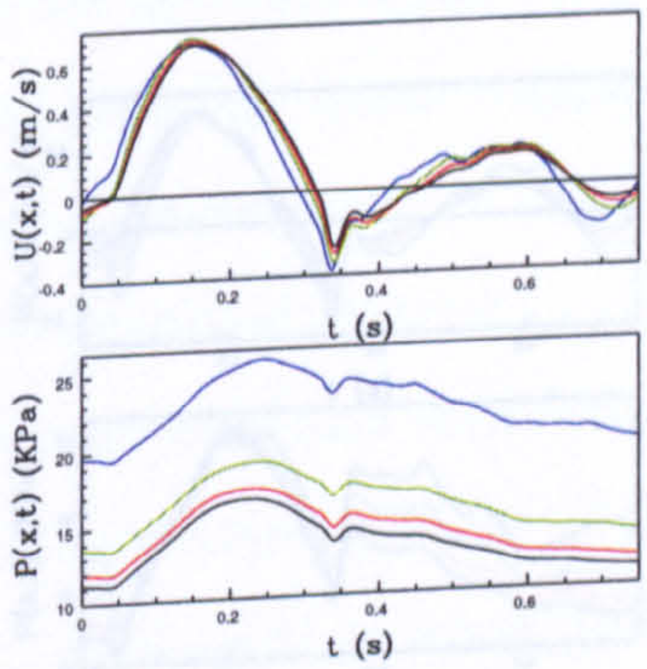
5.2.9 Terminal resistance in the MRI network

The preceding sections have shown that for this tapered network constructed from MRI data reflections have occurred despite the fact that no terminal resistance was applied to the end vessels. This is in contrast to the network studied in Chapter 4, where all the reflected waves were initially produced by the terminal resistance. We now apply terminal resistance to the terminal vessels of the tapered network to assess the effect this has on the pressure and velocity waveforms. Different levels of terminal resistance have been applied and the results are presented for boundary conditions 3 and 4 (figures 5.16 and 5.17). The waveforms have been coloured according to the value of the reflection coefficient applied to the end vessels, $R_t =$ 0.0 (black), 0.1 (red), 0.25 (green) and 0.5 (blue).

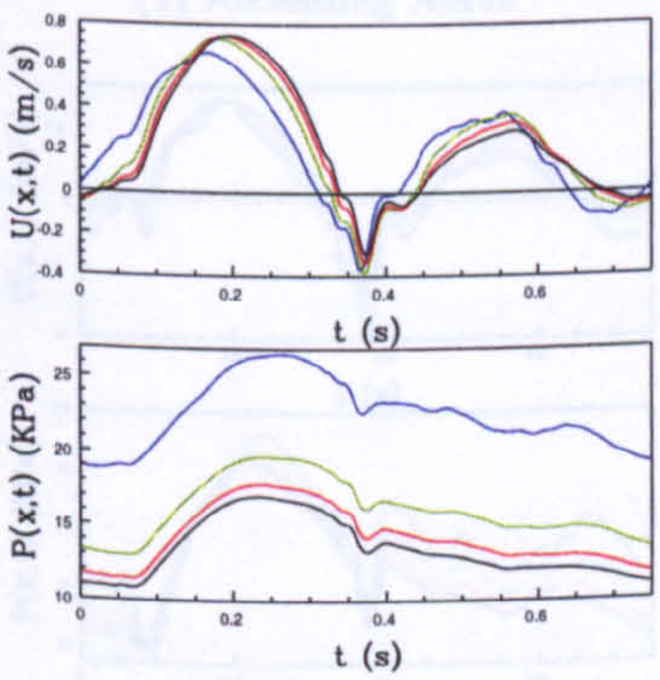
Looking first at the overall trends, it is seen that for an increasing terminal



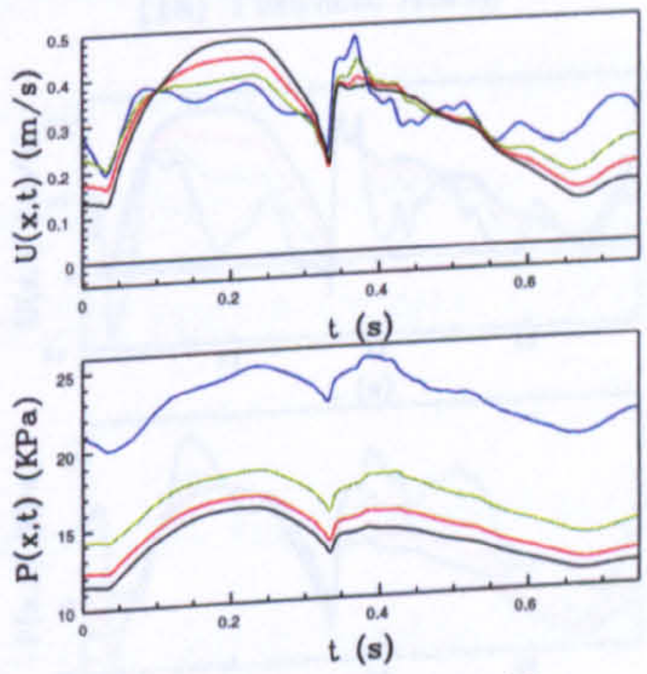
(1) Ascending Aorta



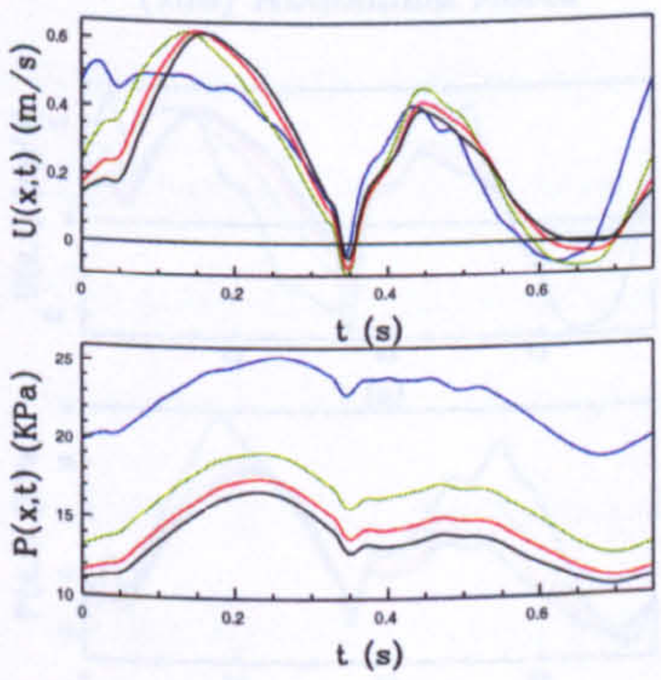
(18) Thoracic Aorta



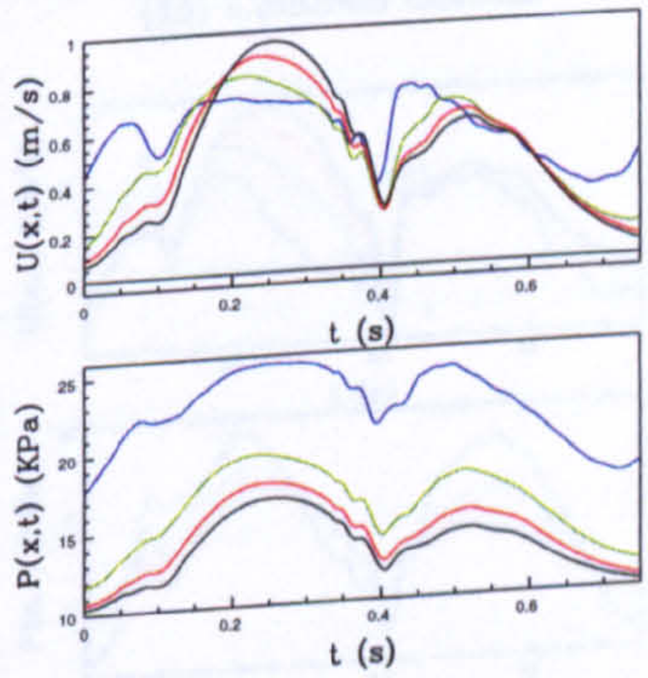
(18b) Abdominal Aorta



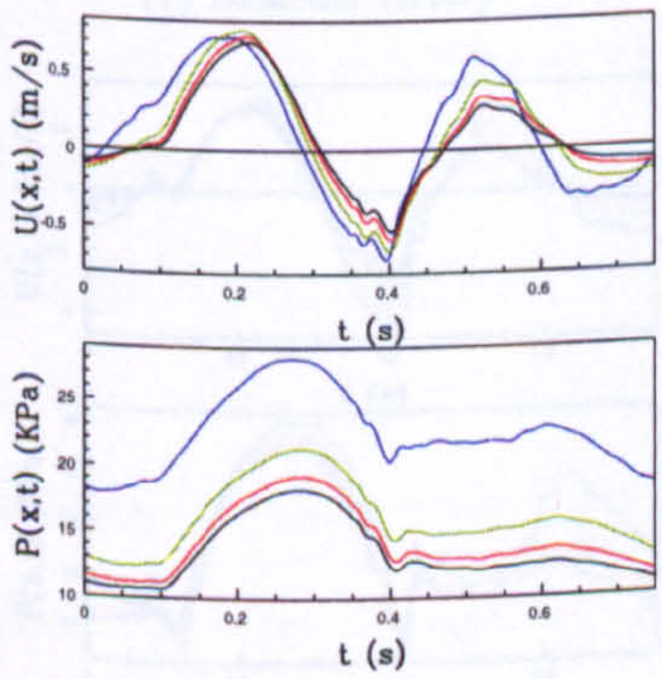
(15) Common Carotid



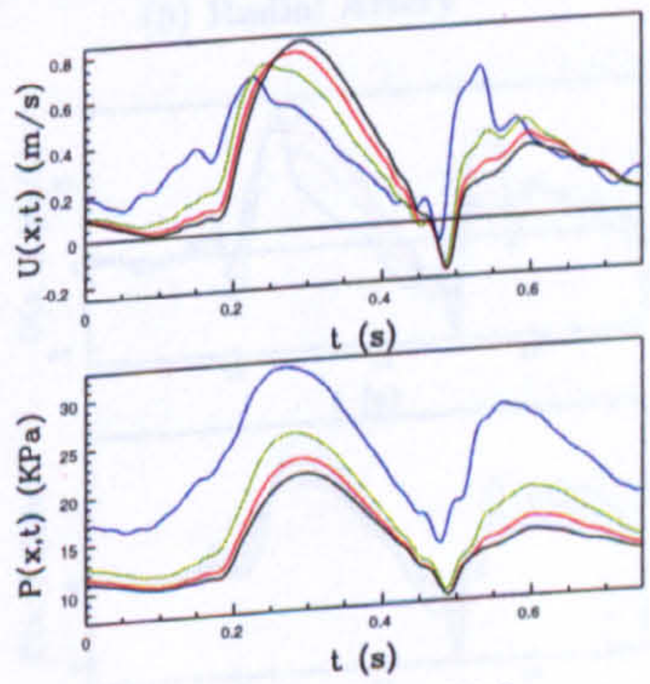
(7) Brachial Artery



(8) Radial Artery

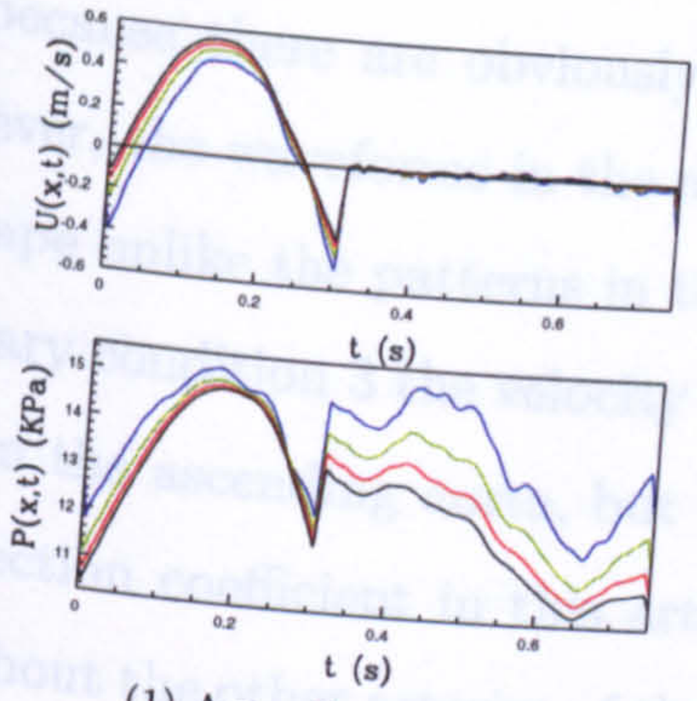


(38) Femoral Artery

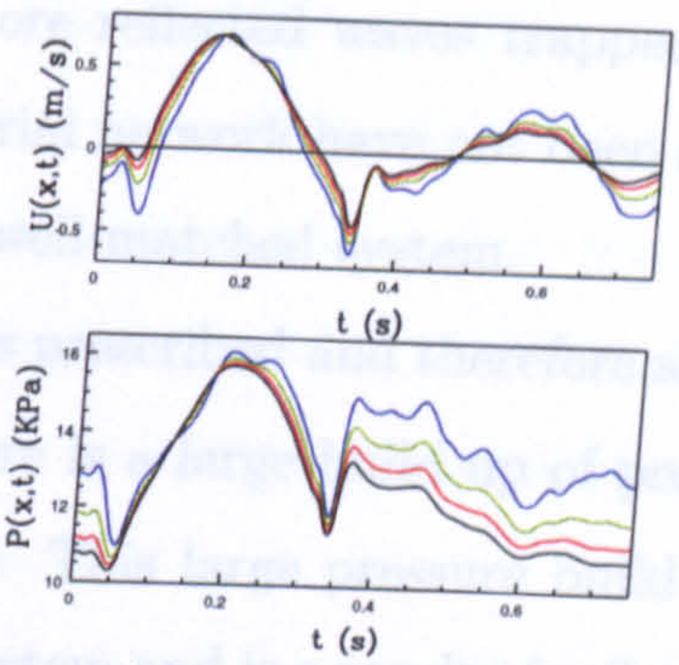


(42) Posterior Tibial

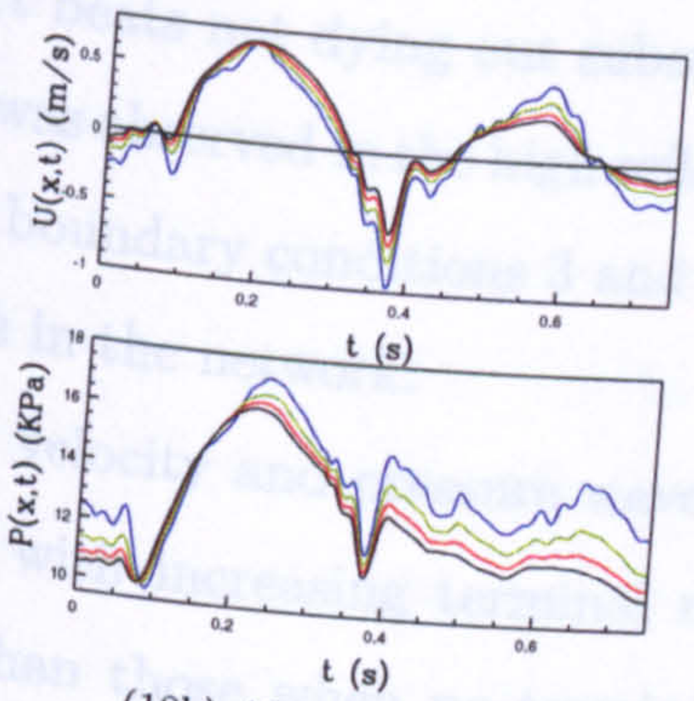
Figure 5.16: Computational results for the MRI tapered network for an imposed velocity boundary condition (BC3) with different values of reflection coefficients applied to the terminal vessels, Black = 0.0, Red = 0.1, Green = 0.25 and Blue = 0.5. The main features of the waves are relatively similar, but amplified and there is a large build up of pressure throughout the network (note the different pressure scale).



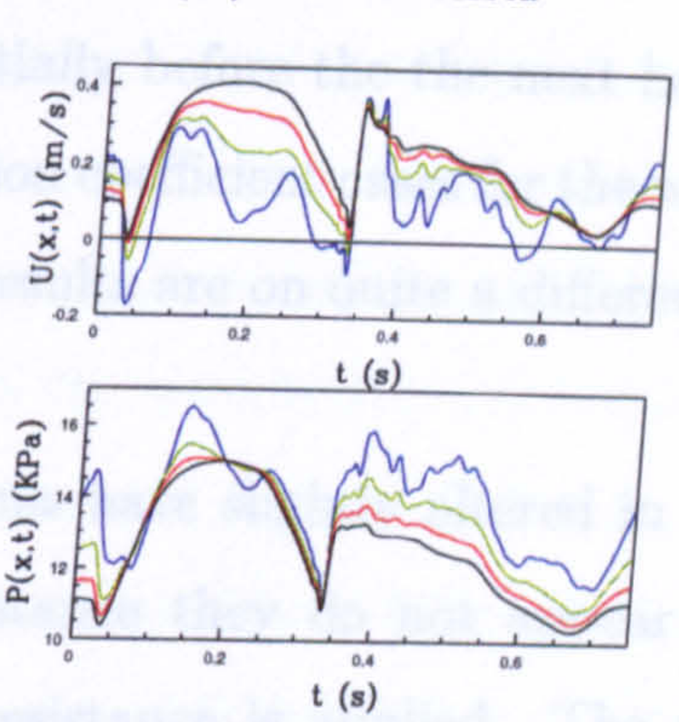
(1) Ascending Aorta



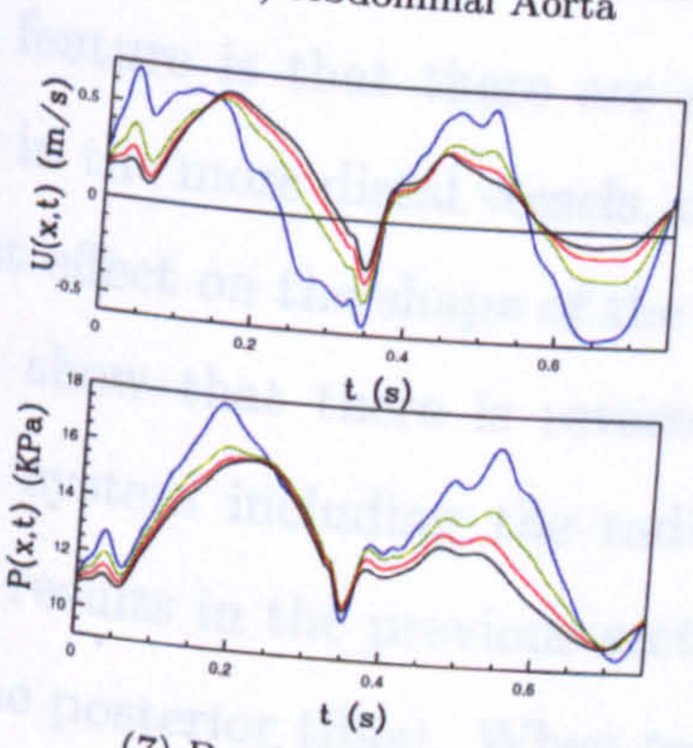
(18) Thoracic Aorta



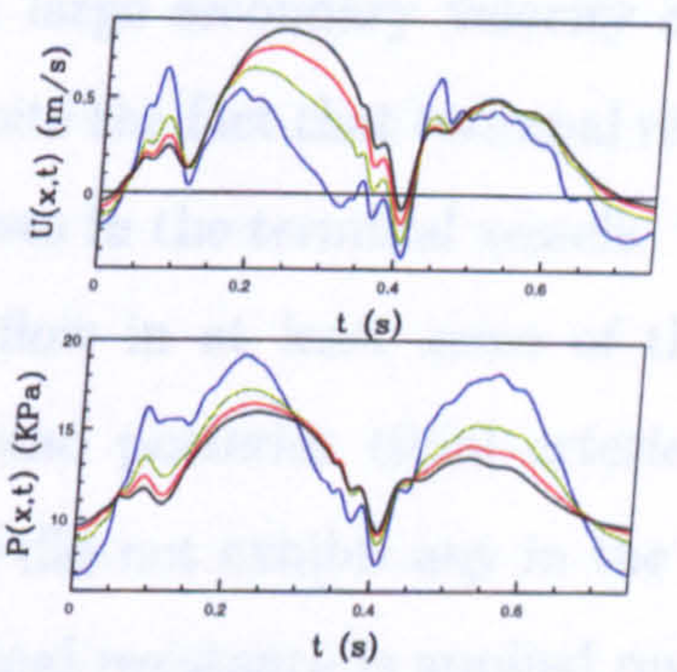
(18b) Abdominal Aorta



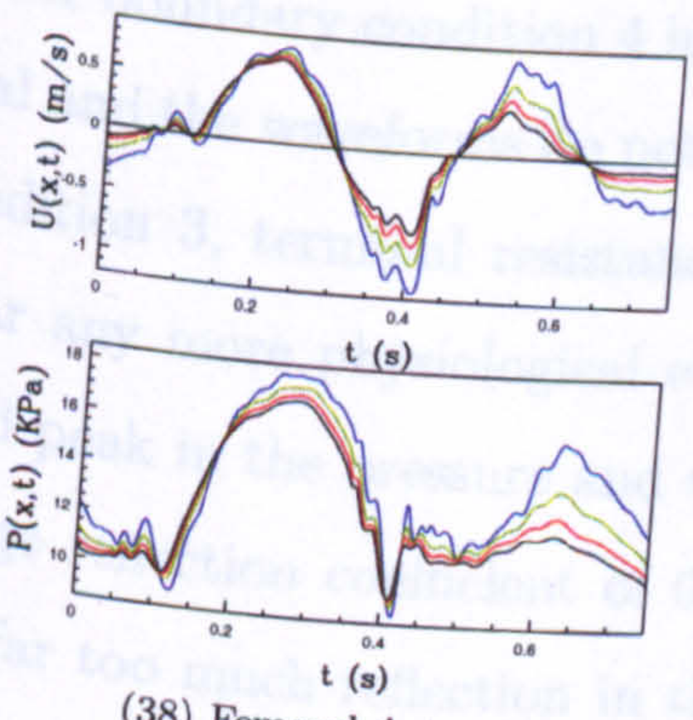
(15) Common Carotid



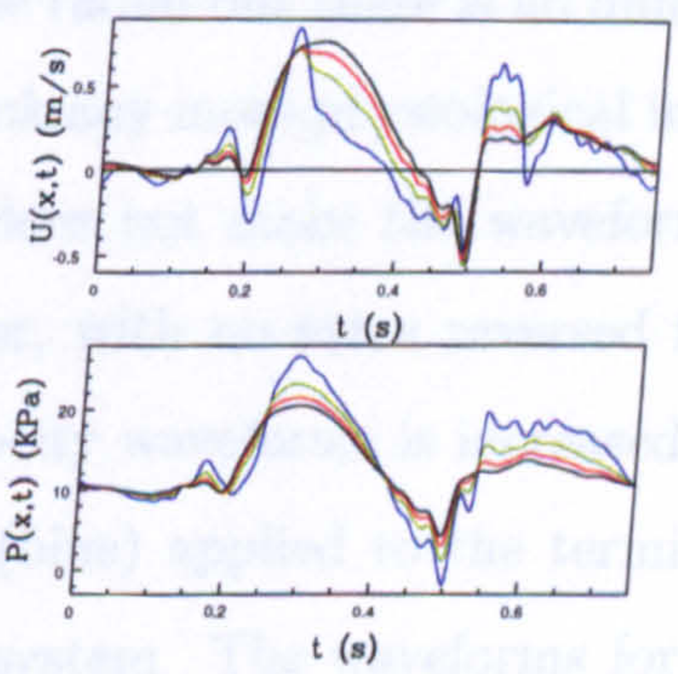
(7) Brachial Artery



(8) Radial Artery



(38) Femoral Artery



(42) Posterior Tibial

Figure 5.17: As for figure 5.16, but with an absorber/reflector boundary condition (BC4) applied at the inflow. This time there is no large build up of pressure, but instead a greater alteration of the velocity waveforms.

resistance the magnitudes of pressure increase for both boundary conditions, which is expected because there are obviously more reflected waves trapped within the system. However, the waveforms in the arterial network have not been significantly affected in shape unlike the patterns in the well-matched system.

For boundary condition 3 the velocity was prescribed and therefore always looks physiological in the ascending aorta, but there is a large build up of pressure with increasing reflection coefficient in this artery. This large pressure build up is also evident throughout the other arteries of the system and is a result of reflections from previous heart beats not dying out substantially before the the next heart beat. A similar effect was observed in the high reflection coefficient cases for the well-matched system. Note boundary conditions 3 and 4 results are on quite a different scales for all the arteries in the network.

Whilst the velocity and pressure waveforms have slightly altered in the vessels in the system with increasing terminal resistance they do not appear any more physiological than those when no terminal resistance is applied. The main non-physiological feature is that there are still large secondary velocity and pressure waves present in the more distal vessels, despite the fact that terminal resistance has had the largest effect on the shape of the waves in the terminal vessels. The clinical measurements show that there is reversed flow in at least some of the terminal vessels of this system including the radial and posterior tibial arteries, but our computational results in the previous section did not exhibit any in the radial and very little in the posterior tibial. When terminal resistance is applied reversed flow does increase for boundary condition 4 in the radial but there is no difference in the posterior tibial and the waveforms do not look any more physiological in either. For boundary condition 3, terminal resistance does not make the waveforms in these arteries appear any more physiological either, with no extra reversed flow and in fact the second peak in the pressure and velocity waveforms is increased.

With a large reflection coefficient of 0.5 (blue) applied to the terminal vessels there appears far too much reflection in the system. The waveforms for boundary conditions 3 and 4 do not look physiological throughout the network and they no longer appear similar to the waveforms for zero and low values of reflection coefficient. The most obvious differences are the high build up of pressure for boundary

condition 3, which was also seen in the well-matched system, and the lumped velocity waves for both boundary conditions. For boundary condition 4 the pressure in the ascending aorta is very high for more of the cycle and does not decline substantially until t $\sim$ 0.5 s when it drops sharply before a very large second pressure pulse. There is also a large reversed flow region before the main velocity wave in the ascending aorta, which is probably due to an increased level of reflected waves and a consequent change in the W_2 characteristic.

The effect of terminal resistance on the waveforms for boundary condition 4 is different to the boundary condition 3 case, because the inflow boundary condition is a W_1 characteristic rather than velocity. This means that for boundary condition 4 there is no large build up with pressure when terminal resistance is applied, rather there is a decline in the velocity. Comparing the boundary condition 4 waveforms for different levels of reflection coefficient shows that the main effect is an increase in pressure during diastole when the heart is acting as a reflector. This occurs throughout the network, but is limited to an increase in the magnitude of the features rather than altering the underlying shape of the waveforms. The velocity waves are relatively similar throughout the network for all values of reflection coefficient other than $R_t = 0.5$ and the waveform in the carotid also seems very sensitive to the level of reflection coefficient.

In conclusion, the effect of adding terminal resistance to the network is relatively small for lower values of reflection coefficient. For both boundary conditions the waveforms appeared reasonably physiological when only taper and ill-matched bifurcations produced reflections in the system and the addition of a reflection coefficient has merely been to reinforce the features of the wave. As with the well-matched case the effect of adding terminal resistance is dependent on the inflow boundary conditions. Also for high levels of reflection coefficients the waveforms look unphysiological.

5.3 Alterations to the geometry of the arterial tree

5.3.1 Arteries branching from the aorta

In the MRI network the arteries that branch off from the thoracic and abdominal aorta have not been modelled, because no data was acquired for these vessels. These arteries lie in the plane of the axial MR images and were therefore not clearly visible in our images, as discussed in section 5.1.1. However, these arteries supply the major internal organs, such as the liver and kidneys, and at rest in the human body we would therefore expect there to be a significant blood flow through these vessels. We are therefore interested in assessing the effect that modelling the aorta as one long single tapered vessel may have had on the magnitudes and waveforms of velocity and pressure throughout the system. This has been modelled by adding extra arteries to artery 18 to represent any missing arteries coming off the aorta. The missing arteries have been approximated using the data for the aorta and the branching arteries from the well-matched network to replace the long single tapered artery 18. The data for the well-matched network was for a male, therefore has been appropriately scaled to fit in with the female tapered network. The inlet and the outlet of this new section of network were reduced to the the same areas as the inlet and outlet of the old tapered artery 18, therefore the reflection coefficients at the top and bottom of the aorta have remained the same. Note that due to the limitations of this data all the bifurcations in this new section of arterial vessels are well-matched and the arteries do not taper. The details of the new tapered aorta are shown in figure 5.18.

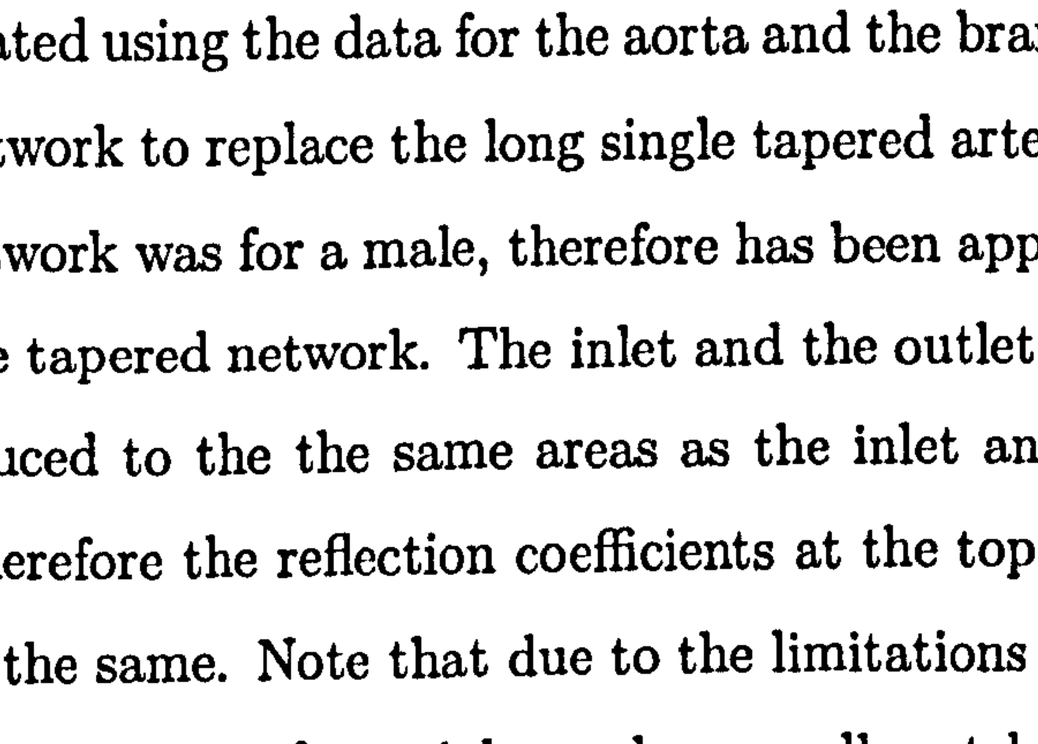
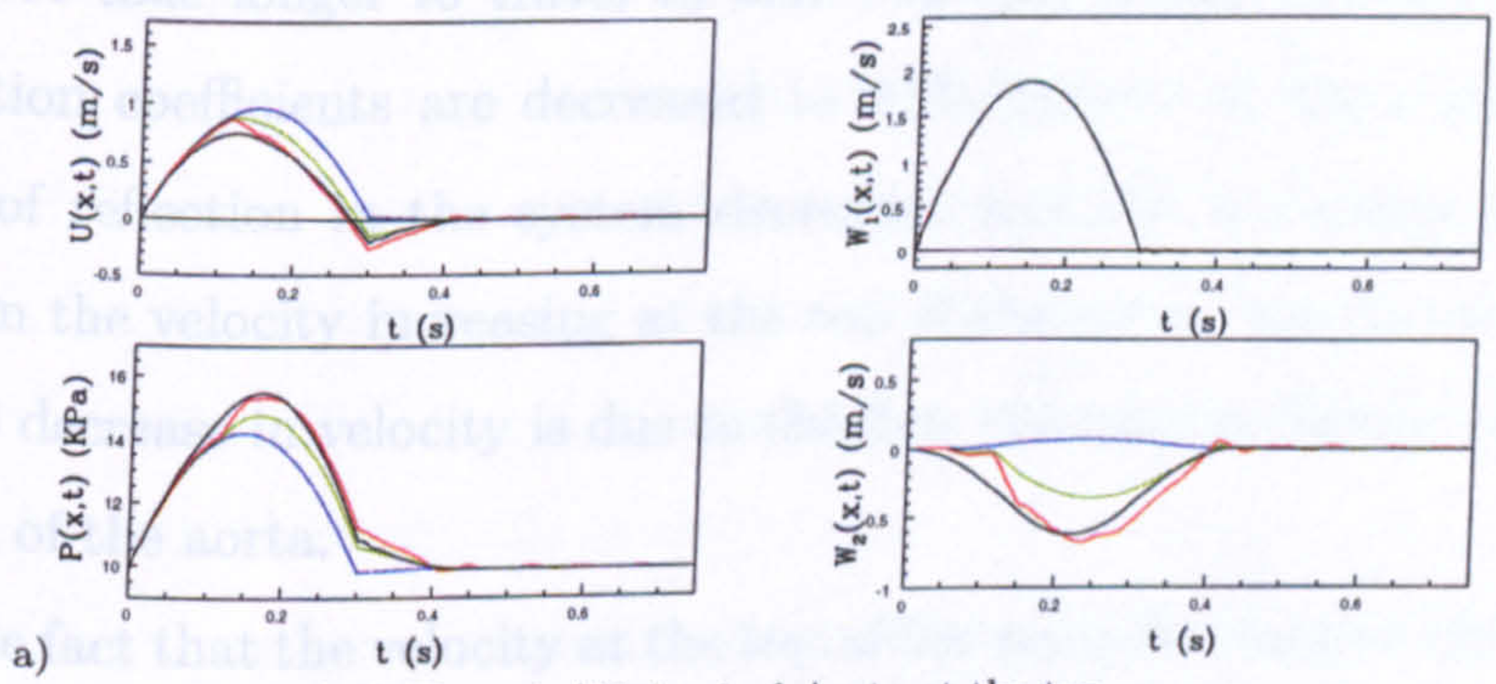
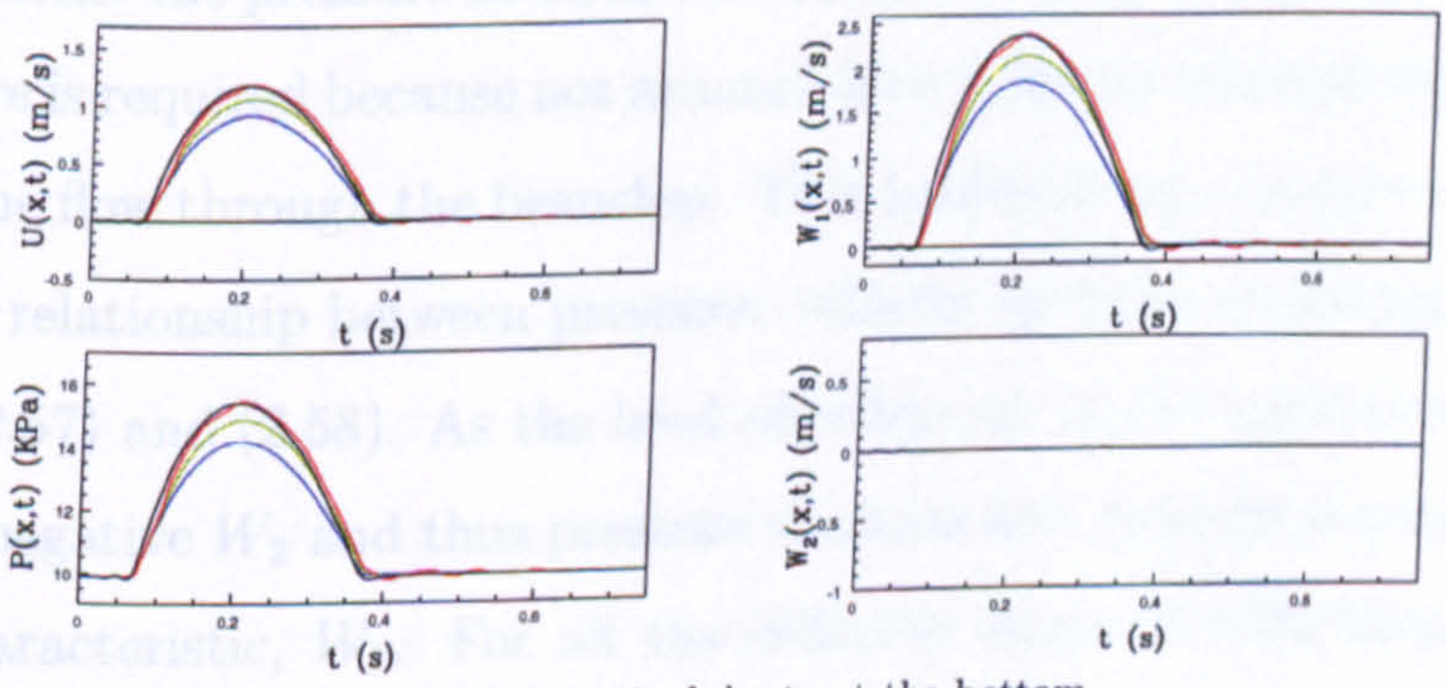


Figure 5.18: Schematics of the two different models for the lower section of the aorta. The left hand side figure is the tapered original and the right hand side figure is the well-matched branching network with no taper.

We have first studied the aorta in isolation with different levels of reflection coefficient applied to the end of the arteries coming off the aorta and compared the waveforms with the results for the tapered original version of artery (18). A half sine wave was imposed as the W_1 characteristic at the top of the descending aorta in the form of boundary condition 1 (an absorber), therefore no waves were reflected back into the network at the inlet. Figure 5.19 shows the velocity, pressure and the characteristic variables, W_1 and W_2, at the start (figures 5.19 (a)) and distal end (figures 5.19 (b)) of the aorta. The black lines in the figures are results for the original artery 18, the blue lines show results for the branching network when zero terminal resistance was applied to the arteries coming off the aorta, the green line when the reflection coefficient was 0.5 and the red line when the reflection coefficient was 1.0. No terminal resistance has been applied at the end of the abdominal aorta in either the tapered case or in the straight tube case (artery 53).



a) (18) Thoracic/Abdominal Aorta at the top



b) (18) Thoracic/Abdominal Aorta at the bottom

Figure 5.19: Comparison of the waveforms in the tapered aorta in isolation (black) with the well-matched, branched aorta with reflection coefficients of 0.0 (blue), 0.5 (green) and 1.0 (red) applied to the branch vessels. The same W_1 input was used for all cases and there was no reflection coefficient on the bottom of the aorta. These show the reflected waves and the effect these have on the pressures and velocities at respectively (a) the top and (b) the bottom of the main vessel.

It can be seen in the characteristic plot that, as expected, W_2 does not change at the outflow for all cases, figure 5.19 (b). With terminal resistance equal to 1.0 on the side branches off the aorta (red) all the waveforms are remarkably similar to the original tapered case (black). These results are however not surprising when the network for this case is considered in more detail. The area change along the length of the aorta is the same for both networks and when the reflection coefficient is one there is no outflow through the branches and the two networks are thus nearly equivalent. The difference between the two networks is that the reflection sites are discrete for the new model, whereas for the tapered artery reflections occur throughout the vessel. This leads to the reflections seen at the start of the vessel starting earlier in the tapered network as seen in the W_2 waveforms in figure 5.19 (a). In the altered network the waves reflect at the ends of the vessels in the arteries coming off the aorta, so the distance to the reflection sites is larger and the reflected waves therefore take longer to travel to and from the reflection sites. Obviously, as the reflection coefficients are decreased to 0.25 (green) on these side branches the amount of reflection in the system decreases and the W_2 waves are smaller. This results in the velocity increasing at the top of the aorta, but decreasing at the bottom. This decrease in velocity is due to the flow exiting the domain through the side branches of the aorta.

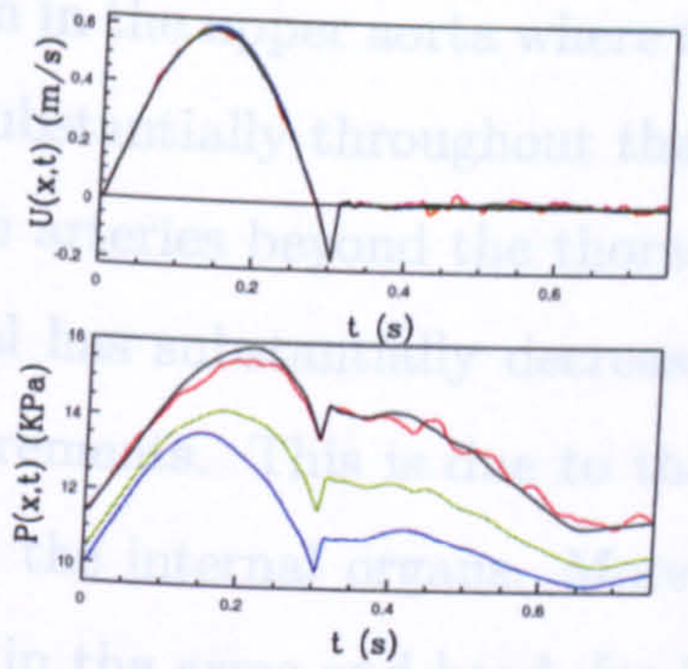
Despite the fact that the velocity at the top of the aorta increases with decreasing reflection coefficient the pressure at both the top and bottom of the aorta decreases. A lower pressure is required because not as much flow is forced through the narrowing aorta, due to the flow through the branches. This is clear if we consider the problem in terms of the relationship between pressure, velocity and the characteristics given by equations (2.57) and (2.58). As the level of reflection in the system falls so does the amount of negative W_2 and thus pressure declines and velocity increases for the same inflow characteristic, W_1. For all the different levels of reflections the peak pressure magnitudes still remain at approximately the same level at the top and bottom of the aorta. When the terminal resistance equals zero (blue) there is little change in W_2 at the inlet and therefore there is no reversed flow at the inlet and the pressure wave remains approximately the same at the inlet and the outlet. This is unlike the cases with reflection where there is a dip in velocity and increase in

pressure following the main pulse.

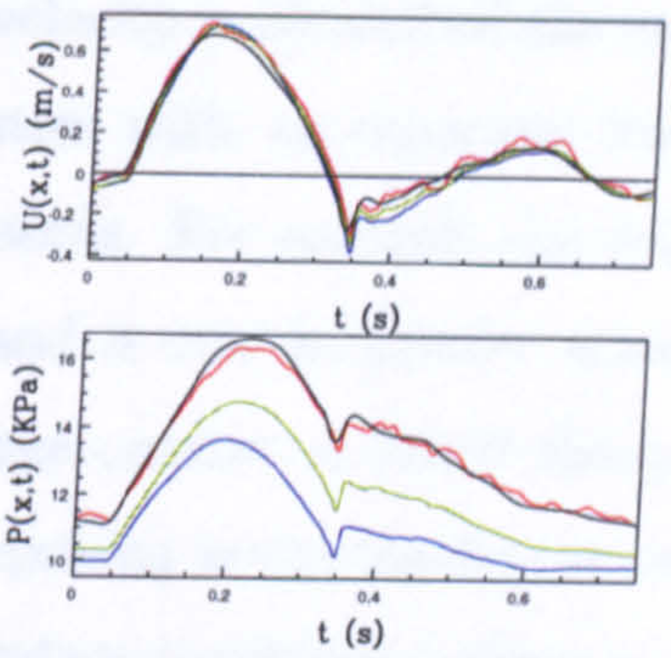
We now discuss the overall effect of modelling the arteries coming off the aorta by inserting the network discussed above into the full tapered arterial network. Artery 18 (descending/abdominal aorta) in the tapered model has been replaced with the new set of arteries shown in figure 5.18. For these computations the velocity boundary condition (BC3) was imposed at the inlet. The velocity and pressure waveforms are shown in figure 5.20 for the standard set of arteries which are labelled 1, 46, 53, 15, 7, 8, 38 and 42 for this modified network. The terminal resistance was set to zero on all the outlet vessels of the network, but it was varied on the side branches of the aorta as in the previous example. Again the waveforms are coloured with $R_t = 0.0$ (blue), $R_t = 0.5$ (green) and $R_t = 1.0$ (red) and the black line shows results for the original tapered network.

From our investigations in the aortic segment, we would expect the results for the case with a reflection coefficient equal to one (red) on the vessels coming off the aorta to be very similar to those for the original network (black). This is indeed the case, but differences between the two are now more noticeable. The red line is not as smooth as the black, with many obvious bumps which are due to the discrete reflection sites off the aorta in contrast to the smooth reflections produced by the tapered vessel. However, the overall shapes of the waves are not significantly altered and adding these extra branches does not change the character of any of the waveforms throughout the network.

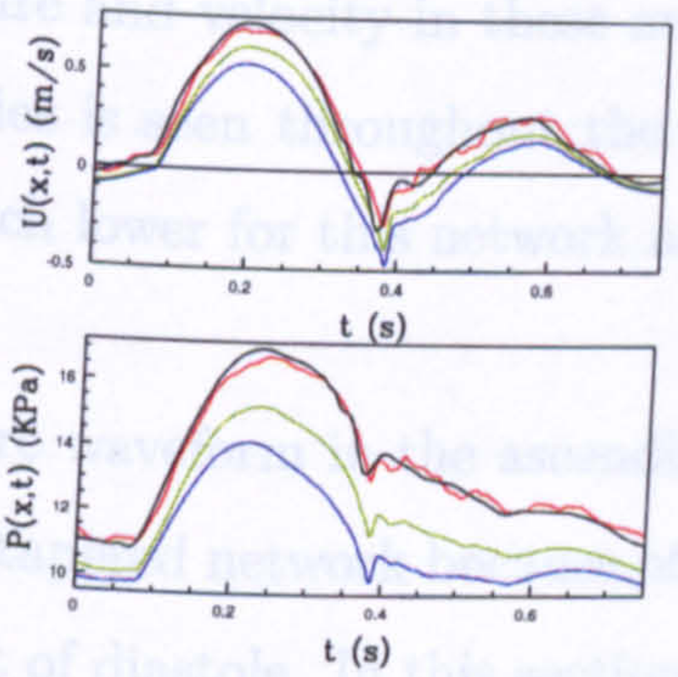
When the reflection coefficients on the vessels are lower, the effects throughout the network are pronounced. The pressure has changed throughout the system with the most obvious feature being that the mean pressure has dropped substantially. Remember that the base value is only approximate so can be altered. The pulse pressure has also decreased, but is still the right order of magnitude, and the waveform itself has changed in shape with the peak pressure now occurring earlier in the cycle. It is also surprising to see how little reflection there is in the ascending aorta when there is no reflection coefficient applied to the vessels coming off the lower sections of the aorta. The pressure in the ascending aorta has dropped by quite a large amount during diastole and there is a large difference in pressure compared to the original tapered case.



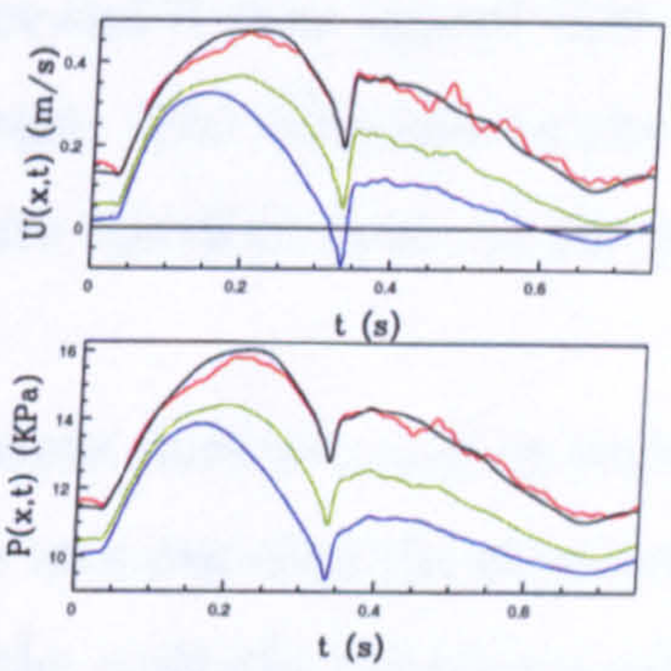
(1) Ascending Aorta



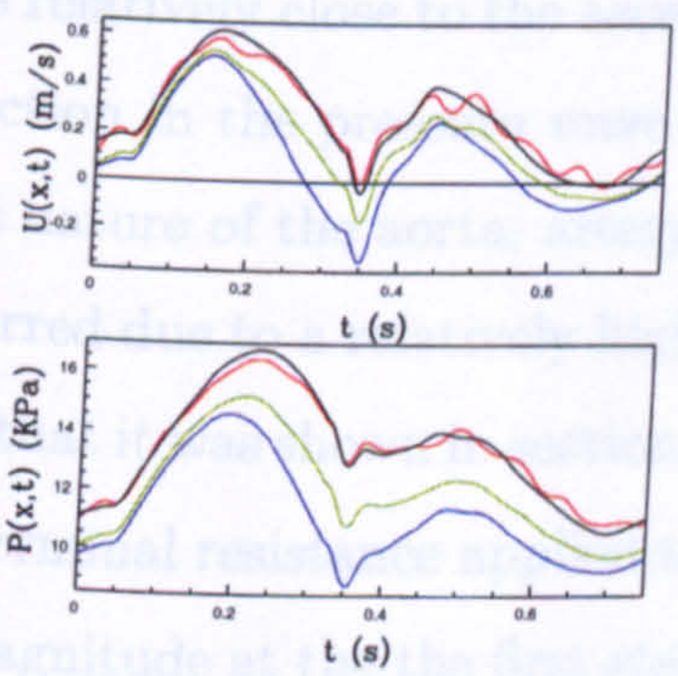
(46) Thoracic Aorta



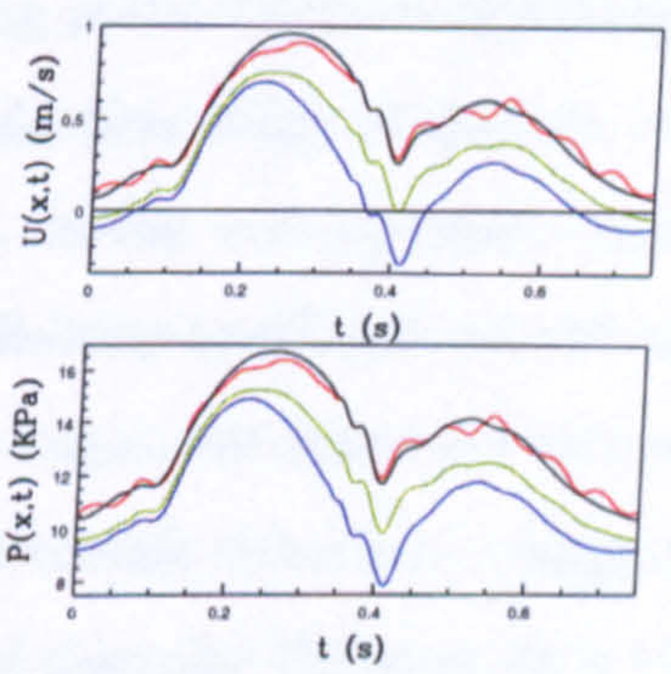
(53) Abdominal Aorta



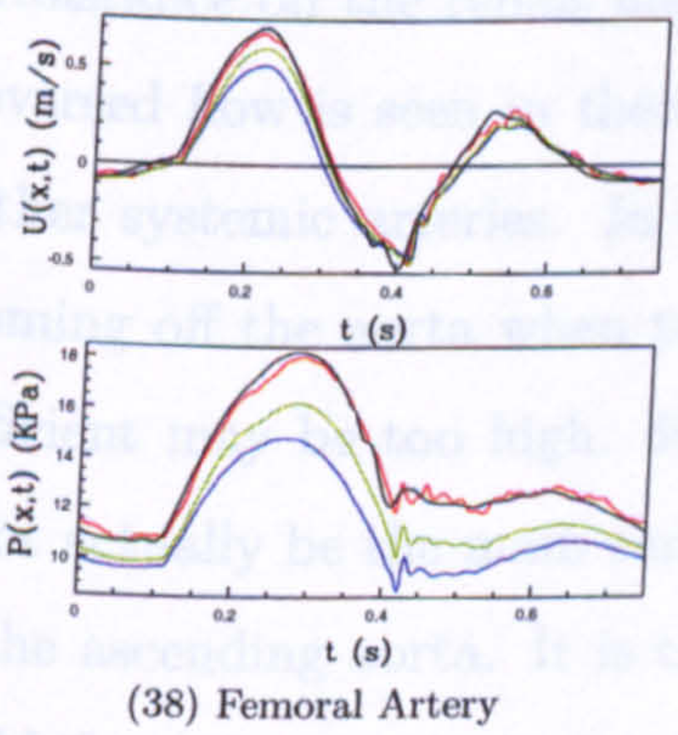
(15) Common Carotid



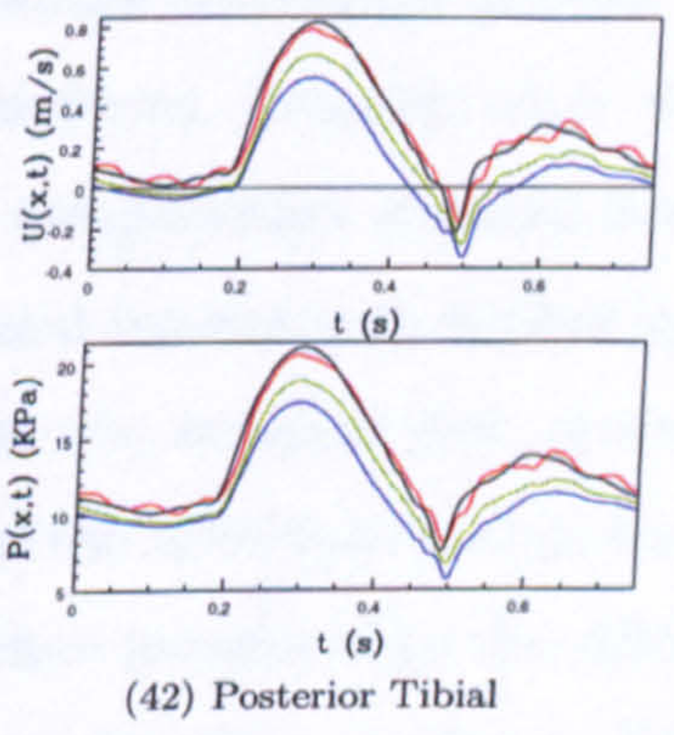
(7) Brachial Artery



(8) Radial Artery



(38) Femoral Artery



(42) Posterior Tibial

Figure 5.20: Computational results showing the effect of adding the vessels that branch off the aorta to supply the organs, such as the liver and kidneys. All computed using boundary condition 3 and with no terminal resistance on the terminal vessels other than the new additions where the reflection coefficients is 1.0 (red), 0.5 (green) and 0.0 (blue). The black line is the original network. Graphs are shown for the same locations as before despite the numbering changes. Note the large drop in pressure throughout the networks and the drop in velocity beyond the new vessels.

Other than in the upper aorta where the velocity is prescribed the velocities have also altered substantially throughout the system with, as expected, lower values of velocity in the arteries beyond the thoracic aorta. For example the velocity in the posterior tibial has substantially decreased and is now in greater accord with the clinical measurements. This is due to the large outflow of blood through the new vessels feeding the internal organs. More surprising is the decline in velocity seen in the arteries in the arms and head, for boundary condition 4 there is also a drop in both pressure and velocity in these arteries and it does appear that the addition of these arteries is seen throughout the system. The velocities in the more distal vessels are much lower for this network and are therefore closer to the physiological values.

The pressure waveform in the ascending aorta does not look as physiological as in the original tapered network because of the very low diastolic pressure, especially in the first part of diastole. In this section of the cycle the reflections will be due to reflecting sites relatively close to the ascending aorta. In the original tapered system the large reflection in the pressure wave in the first stage of diastole occurred, due to the tapered nature of the aorta, artery 18. In the well-matched system the early reflection occurred due to a relatively high reflection coefficient on the aortic branch arteries. Note that it was shown in section 4.3.2 that when the arteries coming off the aorta had no terminal resistance applied to their ends there was a large reduction in the pressure magnitude at the the first stage of diastole. However, it is thought that the terminal resistance on the renals and perhaps the hepatic arteries are actually low and no reversed flow is seen in their waveforms, although other vessels in the gut are like other systemic arteries. In our computations reversed flow is seen in the arteries coming off the aorta when terminal resistance is applied and thus the reflection coefficient may be too high. Hence, the terminal sites of some of these arteries may not actually be the main cause of the reflections seen in the first stage of diastole in the ascending aorta. It is therefore possible that the effects of taper and ill-matched bifurcations in the aorta are actually more significant. This suggests that we have probably neglected significant reflecting sites by using a well-matched aorta.

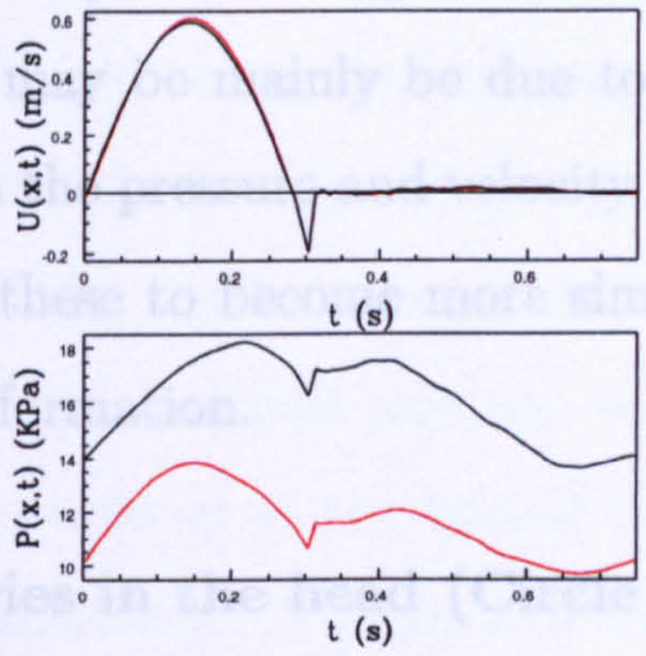
This example was to show the effect that this new aorta has on the system. The

terminal resistance was higher on the arteries coming off the aorta than on the rest of the terminal vessels of the system, but in the human body we would not expect this to be the case. Therefore we also show results for a reflection coefficient of 0.25 everywhere other than on the arteries coming off the aorta, where a lower reflection coefficient of 0.1 was used. These results are shown in red in figure 5.21, where they are compared with the results for the original tapered network with a reflection coefficient equal to 0.25 on all terminal vessels, black waveforms. The results show similar changes as to the previous case, the magnitude of velocity has decreased in the vessels beyond the aorta which is more physiological and the mean pressure has decreased throughout the network. Again though, the mean flow in the common carotid artery has substantially decreased and there is now reversed flow, which is not as physiological. The peak velocity does however appear more spiked and occurs in early systole, which is more similar to the in-vivo waveforms, but the magnitudes are low.

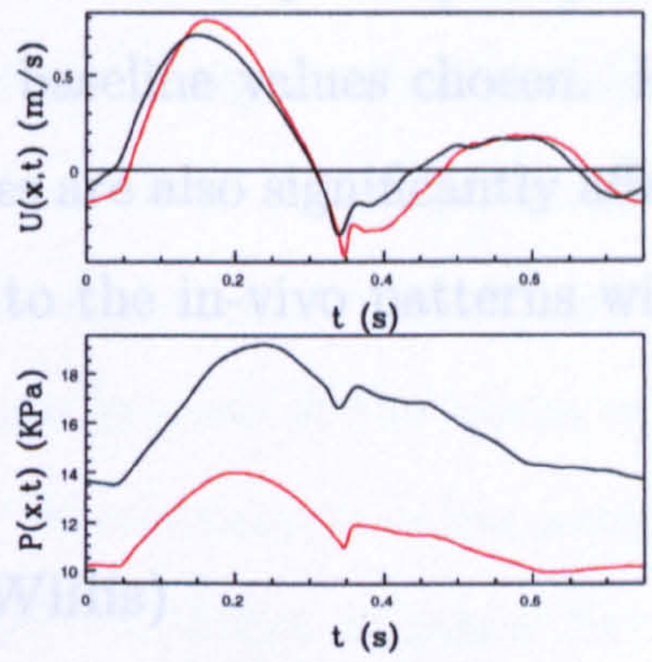
Although using this data for the aorta from the well-matched network is not ideal, in that there are no reflections from bifurcations and no tapering, it is useful for assessing how the magnitudes of velocity and pressure may be altered by the presence of these vessels. The waveforms themselves may not be predicted correctly and they do indeed appear less physiological than for the tapered network (for example, the ascending aorta pressure waveform). Even with the incorrect geometry data there is a substantial change in the velocity magnitudes seen in the waveforms of the system to more physiological values and it would therefore be very interesting to obtain the correct data for the female subject.

Although the arteries branching off the aorta are the most obvious arteries neglected in the tapered network and probably have the largest effect on the waveforms, the large impact that modelling these arteries has on the velocity magnitudes shows that it would be advantageous to model as many arteries branching off the major arteries as possible. To obtain accurate physiological velocity magnitudes, these vessels and other smaller arteries also need to be modelled, either directly, or with a sink term.

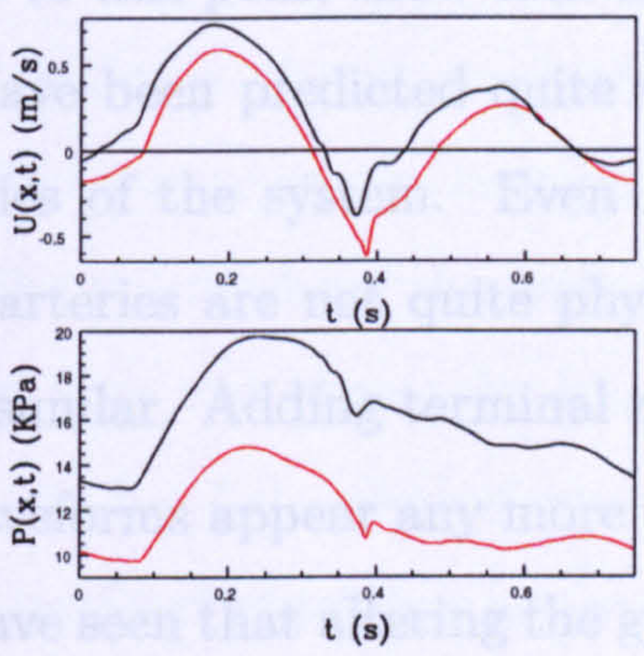
What is certainly proved from these investigations is that there is a great need for accurate and full geometrical data in order to accurately model the velocity



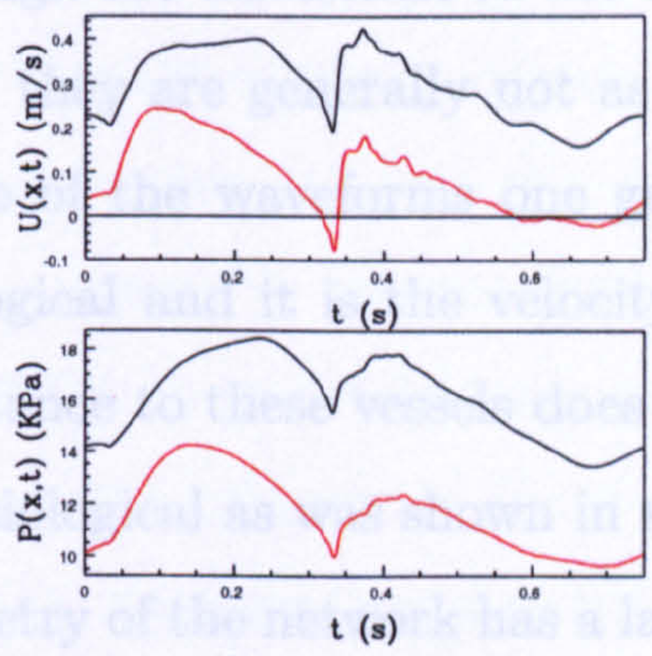
(1) Ascending Aorta



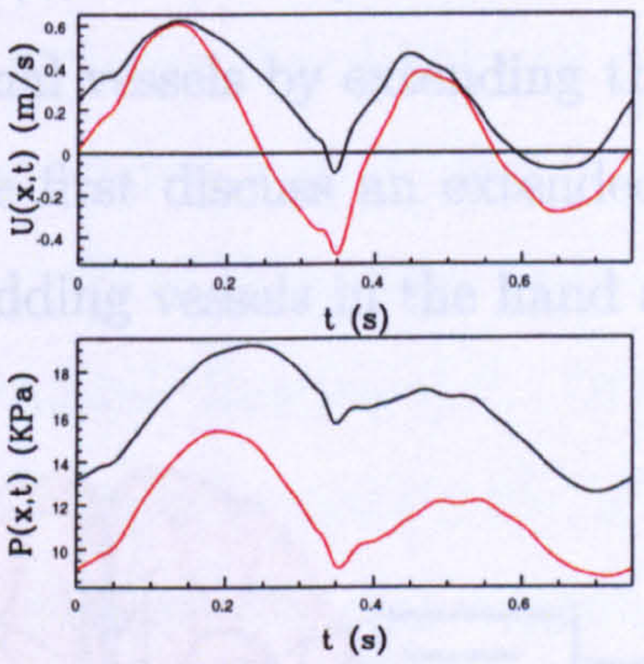
(46) Thoracic Aorta



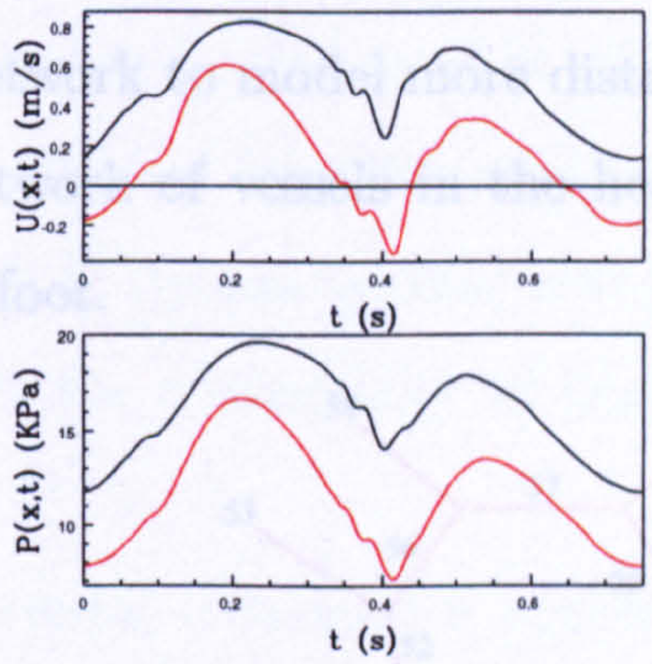
(53) Abdominal Aorta



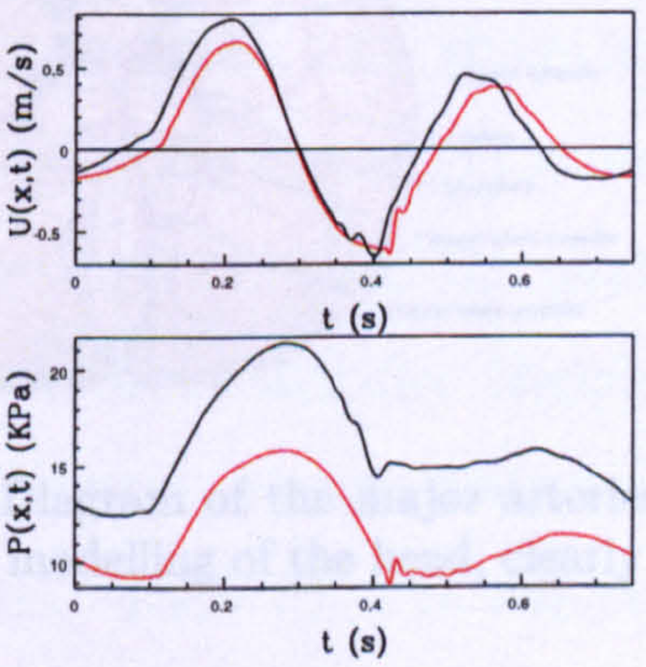
(15) Common Carotid



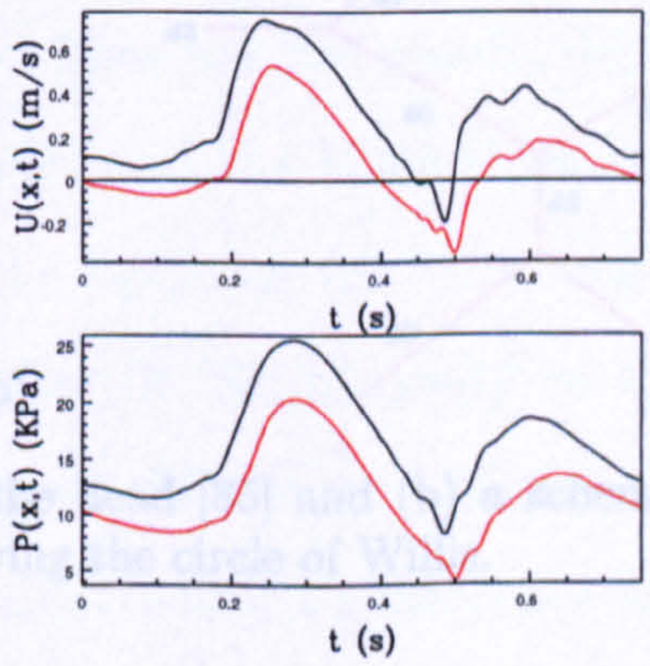
(7) Brachial Artery



(8) Radial Artery



(38) Femoral Artery



(42) Posterior Tibial

Figure 5.21: Computational results for the network with vessels added to the aorta with $R_t = 0.1$ on the new vessels and 0.25 on the terminal vessels (red) compared with the original tapered network with $R_t = 0.25$ on the terminal vessels (black). Boundary condition 3 was applied at the inflow and the waveforms are quite similar, but there is again a large drop in pressure and velocity magnitude.

magnitudes. The pressure magnitudes are also affected by the quality of the network although this may be mainly be due to the baseline values chosen. However, the shapes of both the pressure and velocity waves are also significantly affected and we would expect these to become more similar to the in-vivo patterns with improved geometrical information.

5.3.2 Arteries in the head (Circle of Willis)

The results up to this point show that although the waveforms in the arteries close to the heart have been predicted quite well, they are generally not as good in the terminal arteries of the system. Even some of the waveforms one generation up from the end arteries are not quite physiological and it is the velocity waveforms that are least similar. Adding terminal resistance to these vessels does not actually make these waveforms appear any more physiological as was shown in section 5.2.9, however, we have seen that altering the geometry of the network has a large effect on the waveforms (section 5.3.1). We would therefore like to try and improve our model at these terminal vessels by extending the network to model more distal vessels. In this section we first discuss an extended network of vessels in the head and then comment on adding vessels in the hand and foot.

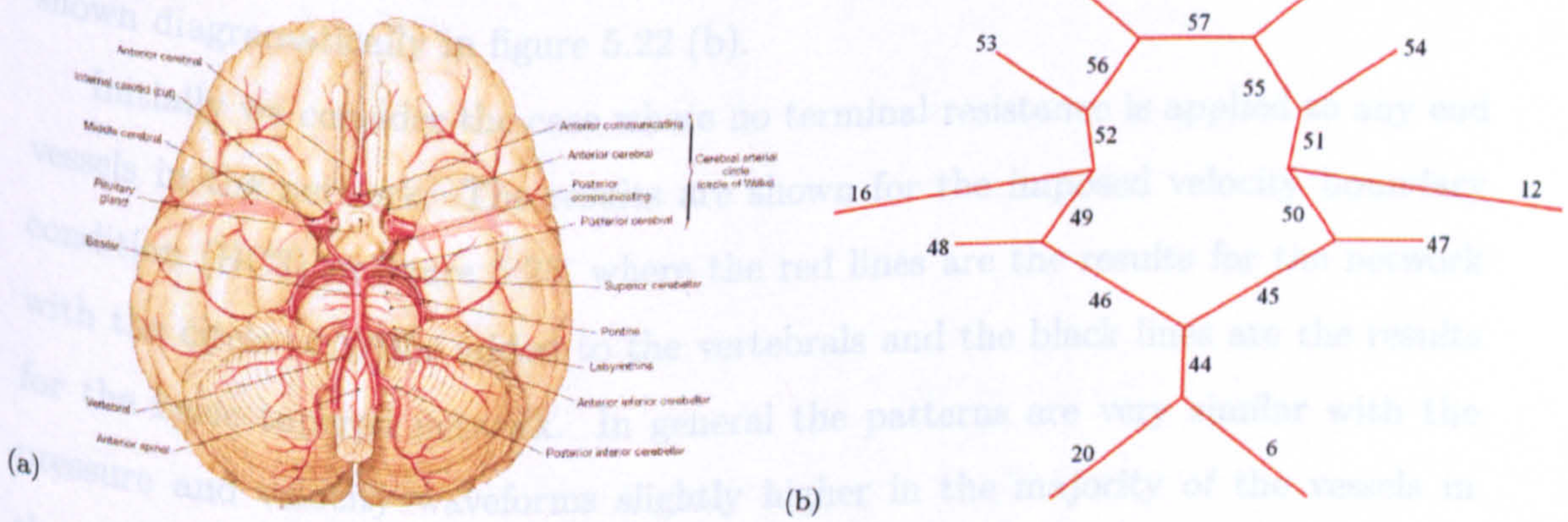


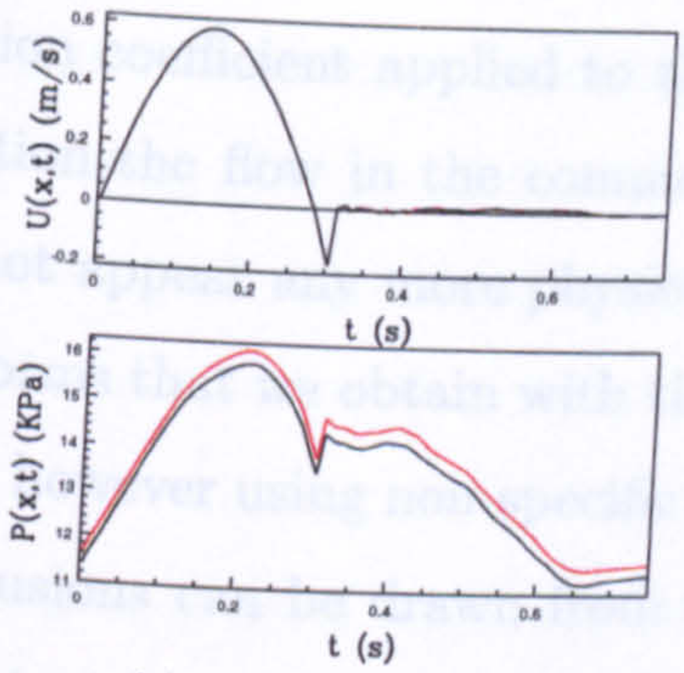
Figure 5.22: Diagram of the major arteries in the head [85] and (b) a schematic of the vessels in our modelling of the head, clearly showing the circle of Willis.

The waveform in the common carotid artery (15), is particularly interesting because it is relatively unusual in that the velocity is all positive and has a relatively high mean velocity, as can be seen in the clinical results in figure 5.7. The carotids also perform the vital task of supplying blood to the brain. The common carotid

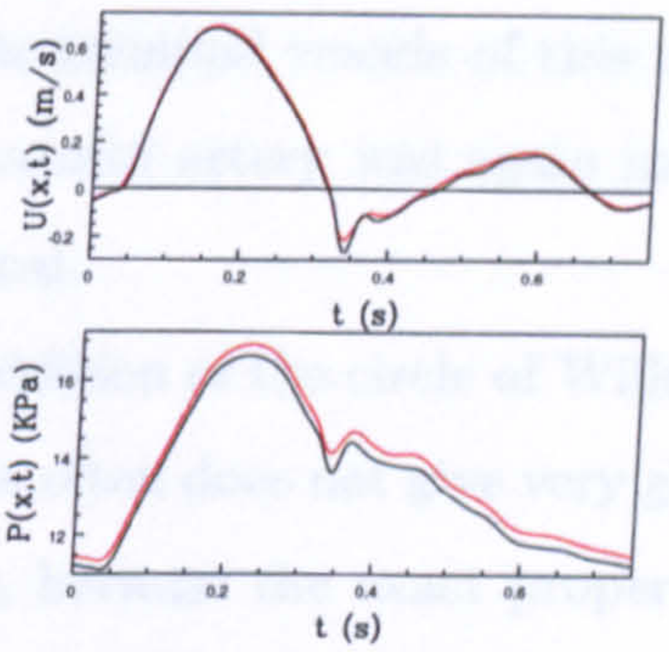
artery is one generation away from the terminal vessel in the tapered network and we are interested in seeing whether the addition of any further arteries in the head improves the waveforms. The arteries in the head form an interesting network called the circle of Willis, which connects the vertebrals and the internal carotids together in a circle with the cerebral arteries. A unique feature of the circle of Willis is the merging of two arteries at the basilar artery in contrast to other arterial junctions which are bifurcations. A picture of the circle of Willis is taken from [85] and is shown in figure 5.22 (a).

We were unable to obtain good enough images of these arteries in the MRI scanner in order to measure the lengths and diameters. We only managed to obtain images up to the point where the vertebrals converge to become the basilar artery and even these were not clear. An image of the three-dimensional reconstruction is shown in figure 5.4 (b), which demonstrates the complexity of the network and the difficulties involved obtaining accurate data. We have therefore tried to improve our tapered network model by adding the extra arteries of the circle of Willis to the vertebrals (arteries 6 and 20) and the internal carotid arteries (arteries 12 and 16) using appropriately scaled generic data. Typical lengths and diameters of the arteries in the circle of Willis were provided by S. Byrd a vascular sonographer from St. Mary's Hospital, London [14]. Detail of the connectivity of these arteries is shown diagramatically in figure 5.22 (b).

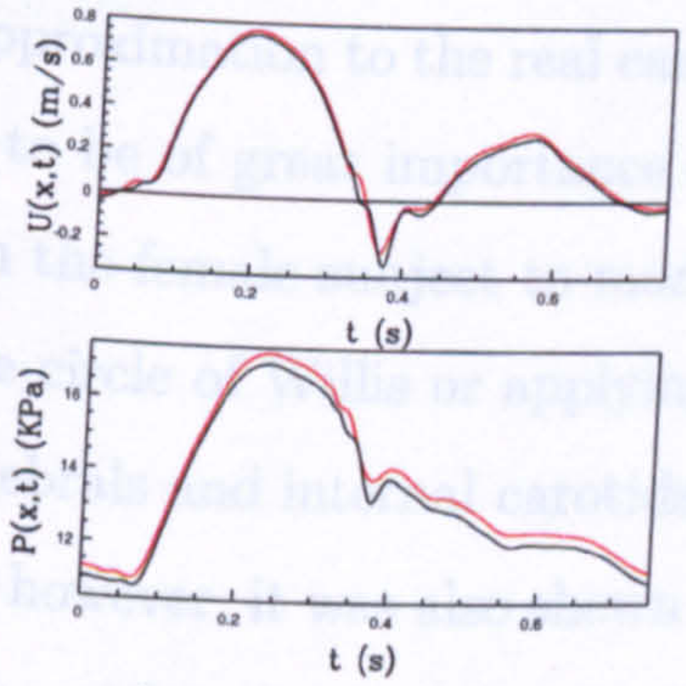
Initially we consider the case where no terminal resistance is applied to any end vessels in the network. The results are shown for the imposed velocity boundary condition (BC3) in figure 5.23, where the red lines are the results for the network with the circle of Willis added to the vertebrals and the black lines are the results for the basic tapered network. In general the patterns are very similar with the pressure and velocity waveforms slightly higher in the majority of the vessels in the network. However, as expected, the greatest difference is seen in the common carotid waveform, artery 15. The velocity has decreased significantly in magnitude, especially during systole, and in general the waveform does not look any more physiological. Some of the decrease in velocity may be due to the fact that in adding these extra vessels with ill-matched bifurcations we are in effect adding a resistance to the arteries leading to the head. To counteract this, as the arterial network is



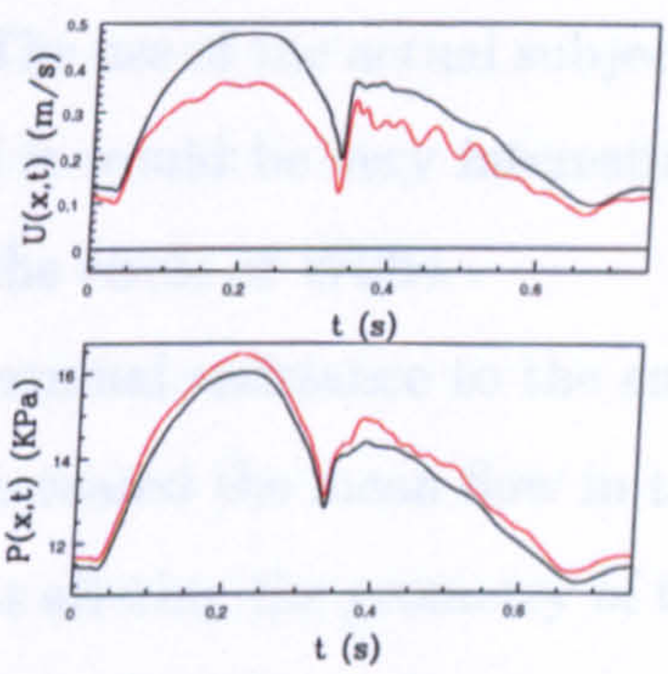
(1) Ascending Aorta



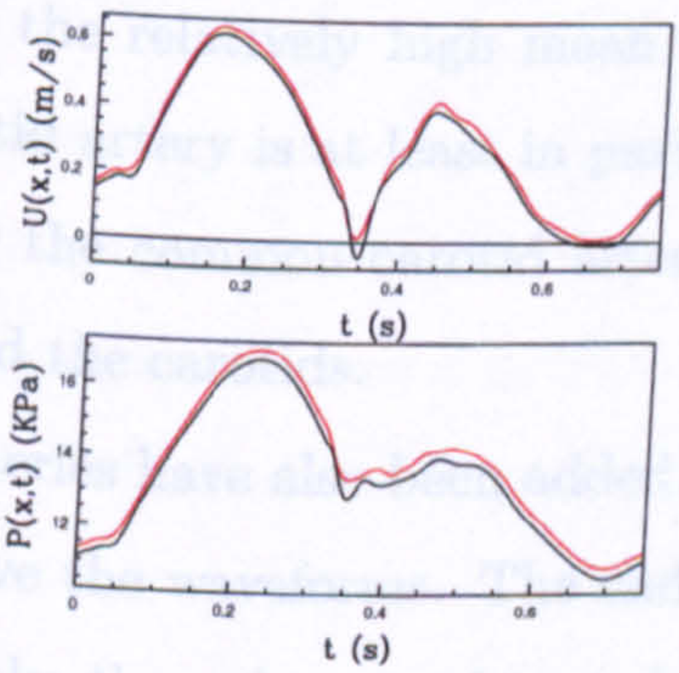
(18) Thoracic Aorta



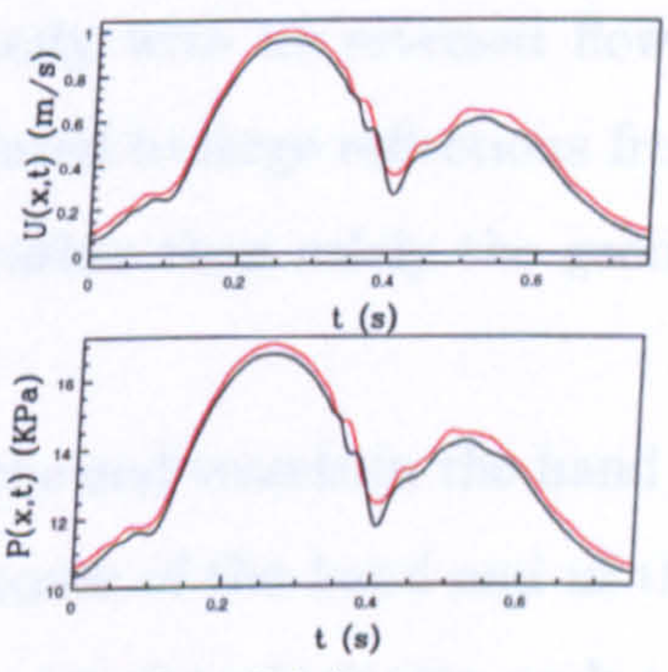
(18b) Abdominal Aorta



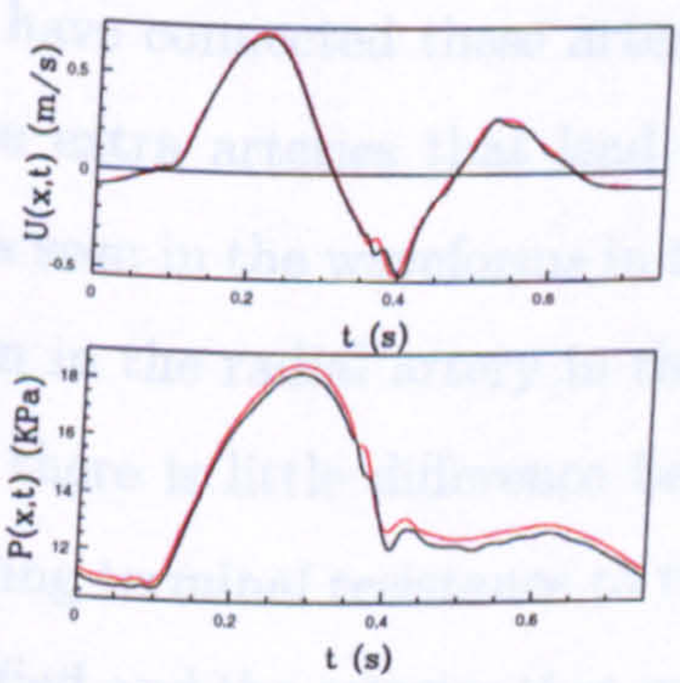
(15) Common Carotid



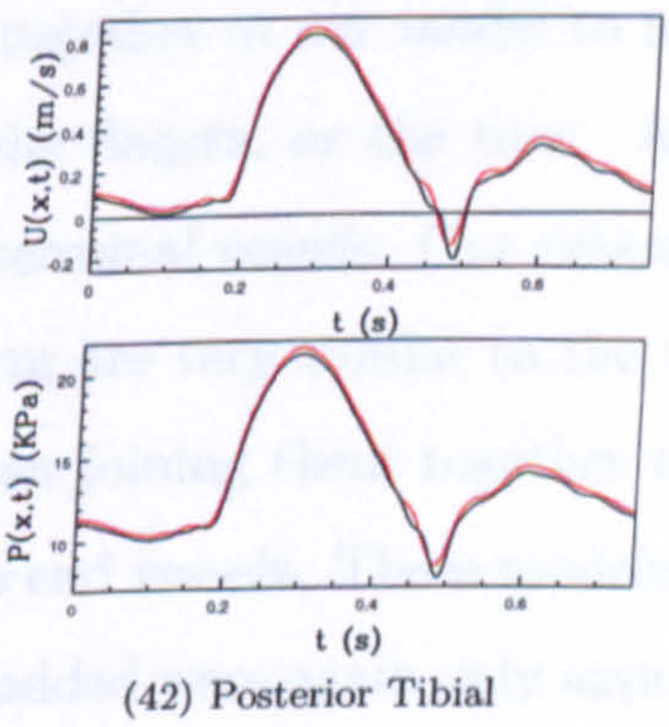
(7) Brachial Artery



(8) Radial Artery



(38) Femoral Artery



(42) Posterior Tibial

Figure 5.23: Computational results for the tapered network with (red) and without (black) the circle of Willis. This inflow was specified using boundary condition 3 and no terminal resistance was applied to the end vessels. The waveforms are relatively unaffected, apart from the velocity waveform in the common carotid (15).

thought to have terminal resistance at the end vessels we have also produced results with a reflection coefficient applied to all the terminal vessels of this network. For this computation the flow in the common carotid artery was again most affected, but also did not appear any more physiological.

The waveforms that we obtain with the addition of the circle of Willis are rather disappointing, however using non-specific data often does not give very good results. No solid conclusions can be drawn from this, because the exact properties as well as the geometries are unknown for the circle of Willis and this system was only a speculative approximation to the real case. The use of the actual subject's geometry data appears to be of great importance and it would be very interesting to obtain this data from the female subject to model the circle of Willis.

Adding the circle of Willis or applying terminal resistance to the end vessels in the head (vertebrals and internal carotids) decreased the mean flow in the common carotid artery, however, it was also shown that altering the geometry of the network in the aorta in section 5.3.1 had a large impact on the flow in artery 15. This suggests that the relatively high mean velocity with no reversed flow seen in the common carotid artery is at least in part related to large reflections from the lower body entering the common carotid artery, rather than solely the geometry of the arteries beyond the carotids.

Further arteries have also been added to the end vessels in the hand and foot to try and improve the waveforms. The end arteries of the hand and in the foot join together to make the palmar arches and the dorsal and plantar arch respectively. Therefore we have connected these arteries together in our model to make an arch and added the extra arteries that lead to the fingers, or the toes. Again no improvement was seen in the waveforms in the terminal vessels. One reason is that the waveforms seen in the radial artery in the arm are very similar to the ulnar artery waveforms, so there is little difference between joining them together to make the arch and applying terminal resistance to these end vessels. These models were probably too simplified and the arteries that were added were again only approximations as we do not know the actual properties or geometry of these arteries.

In summary, our predictions have not been improved by the addition of extra distal arteries to the network, but no definite conclusions can be drawn until we

have modelled the system using in-vivo data from the subject. It is also possible that by adding geometry more distant from the heart we have added detail to the network in the wrong places and that more accurately modelling the larger arteries of the aorta for example may actually have a greater influence on the waveforms in the more peripheral arteries.

5.4 Wavespeed and ageing in arteries

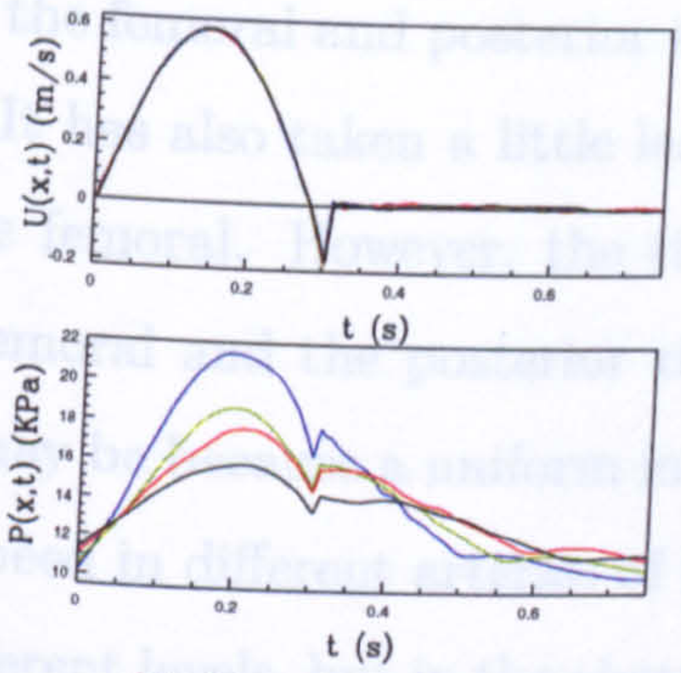
5.4.1 Wavespeed

The wavespeed in the tapered arterial network may perhaps be a little slow, because in section 5.2.6 it was shown from figure 5.12 and figure 5.7 that the time taken for the wave to travel to the posterior tibial from the femoral is larger in our calculations than in the clinical results. Although this difference could be due to inaccuracies in the clinical measurements, such as the location of the history points or an incorrect time offset, it could also be due to incorrect arterial properties, such as the wall thickness and the Young's modulus, which are both related to the wavespeed, c. These were unknown for the female subject and therefore the values from the well-matched system were also used for the tapered network.

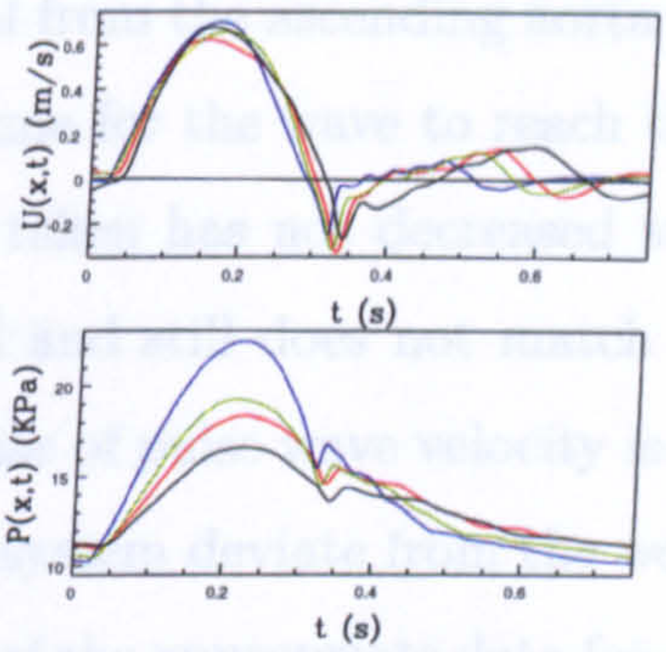
The wavespeed was increased by 20 percent in every artery of the tapered system to see what effect a moderate change in wavespeed has on the waveforms. The results for this increased wavespeed are shown for the velocity boundary condition (BC3) in figure 5.24 where they are coloured red. These can be compared with the waveforms for the original tapered network, which, as before, are the black lines.

The overall wave shapes are very similar to the original case, although a small peak of pressure and velocity now occurs late in the cycle in arteries 7, 8 and 15, which did not exist before. This is more physiological for artery 7 (brachial), because there are now two peaks. The peak pressure and velocities during systole have also increased in many of the arteries, but because the velocity was imposed at the inflow the systolic peak velocity has stayed approximately the same magnitude in the aorta. Also as expected the main features of the flow and pressure have moved closer together.

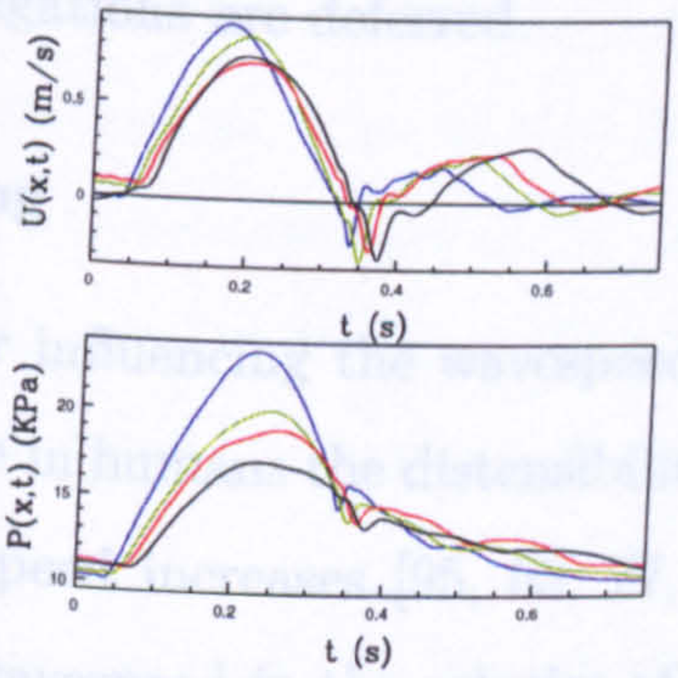
From figures 5.24 (38) and (42) it can be seen that it has taken less time for the



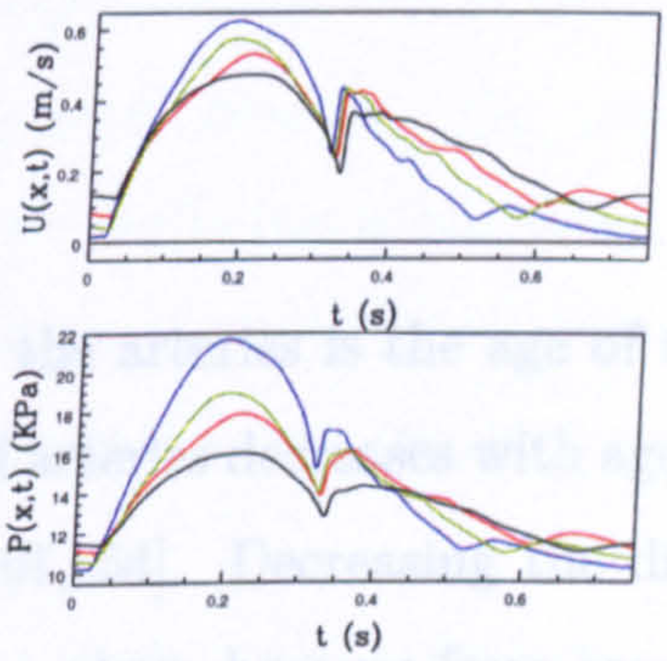
(1) Ascending Aorta



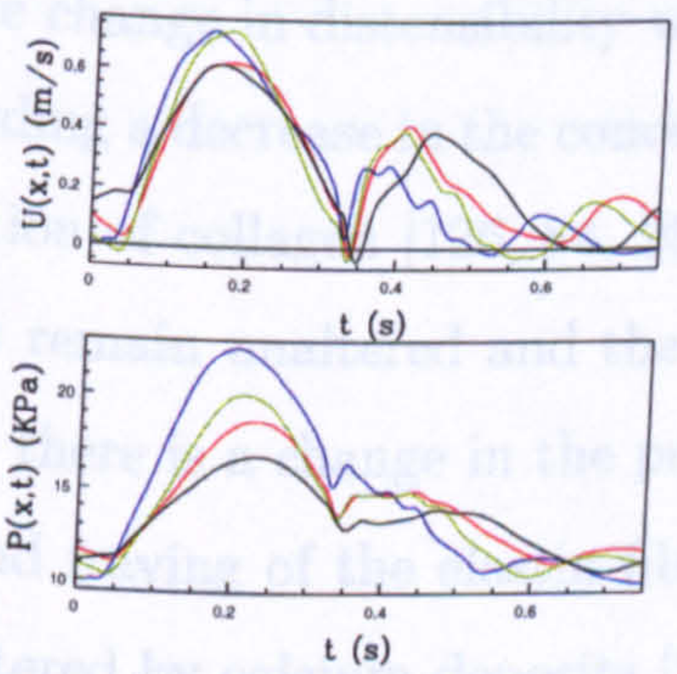
(18) Thoracic Aorta



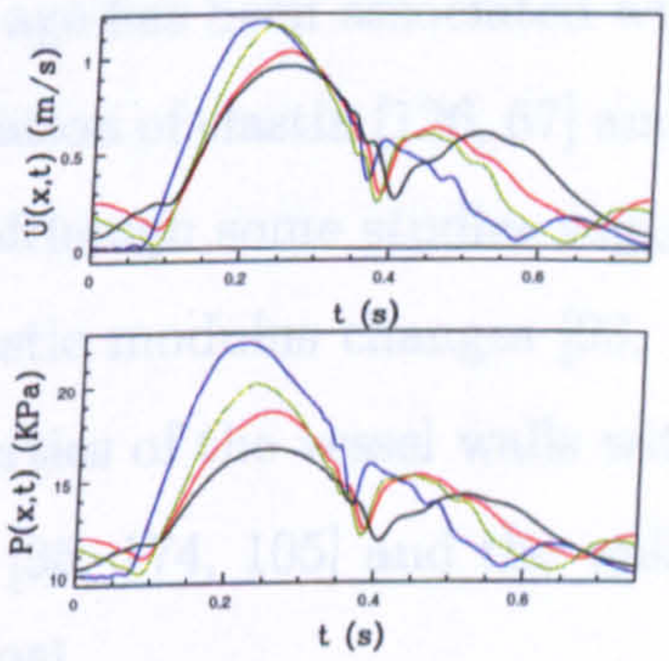
(18b) Abdominal Aorta



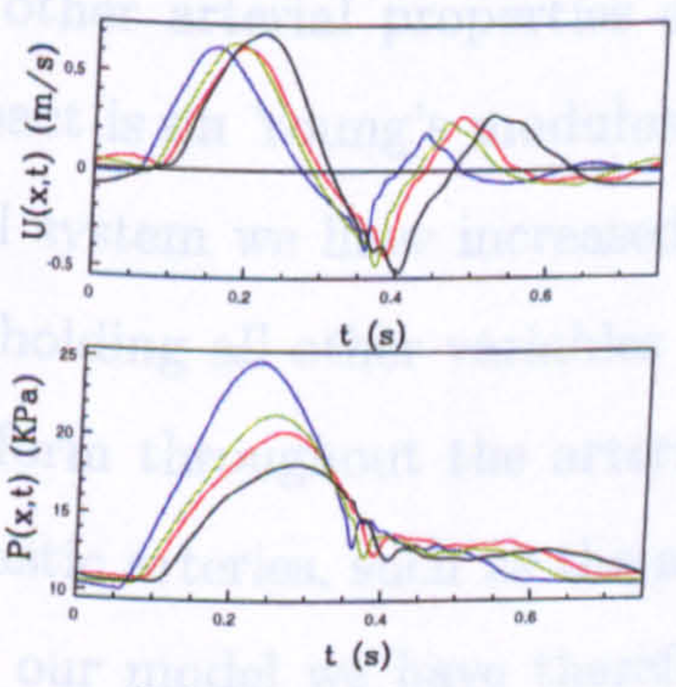
(15) Common Carotid



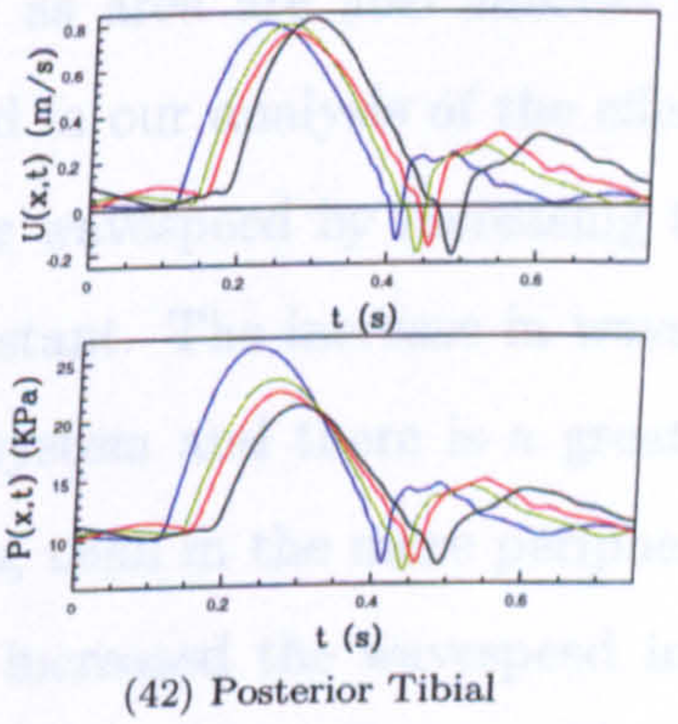
(7) Brachial Artery



(8) Radial Artery



(38) Femoral Artery



(42) Posterior Tibial

Figure 5.24: Computational results showing the effect of altering the wavespeeds in the tapered arterial network for boundary condition 3 and no terminal resistance. The black lines are the original waveforms and the red lines are for a moderate increase in wavespeed of 20% throughout the network. The green and blue lines are to simulate the effects of aging with respectively increases of 50% in the aorta and 25% elsewhere and 100% and 50%. The major effects of increasing wavespeed are an increase in systolic pressure and a decrease in separation of the main features of the waves.

wave to reach the femoral and posterior tibial from the ascending aorta than for the original case. It has also taken a little less time for the wave to reach the posterior tibial from the femoral. However, the time taken has not decreased substantially between the femoral and the posterior tibial and still does not match the clinical results. This may be because a uniform increase of pulse wave velocity is not correct and the wavespeed in different arteries of the system deviate from the well-matched network by different levels, but in the absence of the appropriate data for each artery further investigations are deferred.

5.4.2 Ageing

Another factor influencing the wavespeed in the arteries is the age of the subject. This is because in humans the distensibility of arteries decreases with age and therefore the wavespeed increases [95, 68, 77, 8, 91, 54]. Decreasing the distensibility increases the wavespeed in the arteries of the system, because from equation (2.5), $c^2 \propto 1/D$. The change in distensibility with age has been associated with a number of effects including a decrease in the concentration of elastin [126, 67] and an increase in the proportion of collagen [126, 84, 95], although some studies suggest that the concentrations remain unaltered and the elastic modulus changes [93, 177]. What is clear is that there is a change in the properties of the vessel walls with a general degradation and fraying of the elastin fibres [95, 174, 105] and the wall properties may also be altered by calcium deposits [27, 95].

Although other arterial properties such as area are also affected by age, the dominant impact is on Young's modulus and in our analysis of the effect of ageing on the arterial system we have increased the wavespeed by increasing the Young's modulus, but holding all other variables constant. The increase in wavespeed with age is not uniform throughout the arterial system and there is a greater increase in the more elastic arteries, such as the aorta, than in the more peripheral arteries [95, 68, 7]. In our model we have therefore increased the wavespeed in the aorta more than the other arteries in the network. The results are also shown in figure 5.24, where the green lines are the results when the aortic pulse wave velocity was increased by 50 percent and the wavespeed was increased by 25 percent in the other arteries in the system and the blue lines are results for increases in the aortic pulse

wave velocity of 100 percent and wavespeed increases of 50 percent in the remainder of the arteries.

Examining the results it can be seen that again the characteristic features have not greatly changed. The most significant difference in the waveforms is that the peak pressure in systole increases greatly, which is in accord with in-vivo measurements and is the main feature associated with age [64, 96, 103, 36, 95]. The waveforms are also beginning to exhibit the early wave return found in older patients [92]. Whilst velocity has also increased in many of the arteries of the arm and head this increase was not as large as that in the peak pressure. The velocity did not increase at all at the ascending aorta, because we imposed boundary condition 3 which keeps the velocity constant. The results for boundary condition 4 were also investigated and again the largest change in the waveforms was again an increase in systolic pressure.

These waveforms may also be relevant to those seen in smokers, because an increase in arterial stiffness is often observed in people who smoke [20]. In summary, increasing the wavespeed predominantly affected the magnitudes rather than the shape of the waves, although there are some features developing earlier in the cycle.

5.5 Surgical interventions

Arteries in the human body are susceptible to disease and of particular significance is atherosclerosis, which is directly responsible for over 30 % of deaths in developed countries and 75 % of cardiovascular related deaths [4]. Atherosclerosis involves the build up of fatty plaques on the inside of the artery wall, which causes the arterial lumen to narrow (stenose) restricting the blood flow through the artery [128, 81]. In the worst cases, the narrowing can lead to a complete blockage, which stops the blood flow altogether and can be fatal. The initial developement of atherosclerosis is typically asymptomatic and often by the time it is detected there are no drug treatments that are effective and surgical intervention is necessary. Two common surgical procedures which are used routinely to restore blood flow throughout the circulation are: balloon angioplasty, now often with stenting, and bypass grafting [85, 158, 138]. Balloon angioplasty involves the insertion of a catheter mounted balloon into the stenosed artery; once the catheter is inserted the balloon is inflated, which widens the calibre of the artery. The artery is however often subject to rapid restenosis and recently the procedure has been adapted with a stent being inserted into the opened artery in an effort to keep the flow path open for longer. Bypass grafting does not attempt to re-open the artery but instead provides an alternative conduit through which the blood can travel.

In sections 5.5.1 and 5.5.2 we assess the effect these two surgical interventions may have on the blood flow and pressure waveforms in the tapered arterial network. The more physiological velocity boundary condition (BC3) was imposed at the inlet for both cases and the results of these computations are shown in figures 5.25 and 5.27. Boundary condition 4 was also imposed for these networks but the results were not significantly different to those for boundary condition 3, therefore only the latter results are shown and discussed in the following sections. The terminal resistance was set equal to zero on all of the terminal vessels for these computations, because this is the simplest case and therefore the easiest to assess. Since we are primarily interested in the differences between the waveforms before and after intervention, the effect of terminal resistance is not of great importance.

5.5.1 Stents

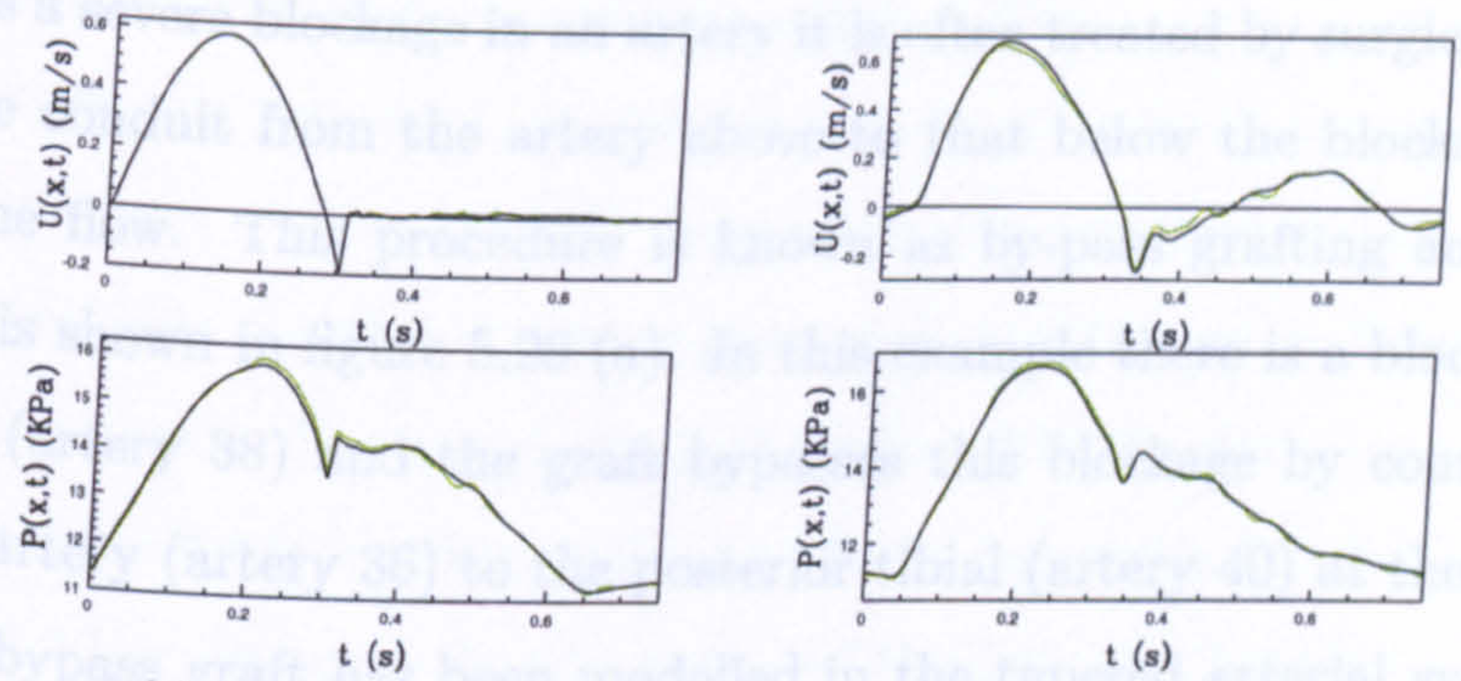
A stent is a thin cylindrical tube constructed of metal with "memory" properties. It resembles a metal gauze or mesh and is inserted into arteries to help keep the conduit open. The stent is inserted in a compressed form and then opens up into its "memorised" shape forcing the artery open. Stents are substantially stiffer than arteries, therefore it is possible that the presence of a stent may have an effect on the waveforms in the system. For our investigation the stent was modelled in the arterial system simply by increasing the Young's modulus in the location of the stent.

The stent was inserted into the right external iliac artery (36) in our system and for simplicity was assumed to extend for the full length of the artery, which is 0.117 m. The assumed increased Young's modulus due to the presence of the stent was twenty times the original in this artery. The waveforms for arteries 1, 18, 26, 27 36 and 38 are shown in figure 5.25. The black lines are the original results and the green lines are the waveforms for the system with a stent in artery 36.

It is striking that the overall waveforms have hardly changed throughout the arterial system, in particular the waveforms in the upper arteries (1 and 18) are almost unchanged. The differences in the stented artery (36), where the waveform is taken mid-way along the stent are also slight, but discernible, as they are in artery 38, which is located beyond the stent. From figures 5.25 (36) and (38) it can also be seen that the waves have reached the locations in arteries 36 and 38 faster than the original results due to the increase in wavespeed in the stented artery. However, the shapes of the waveforms are very similar overall.

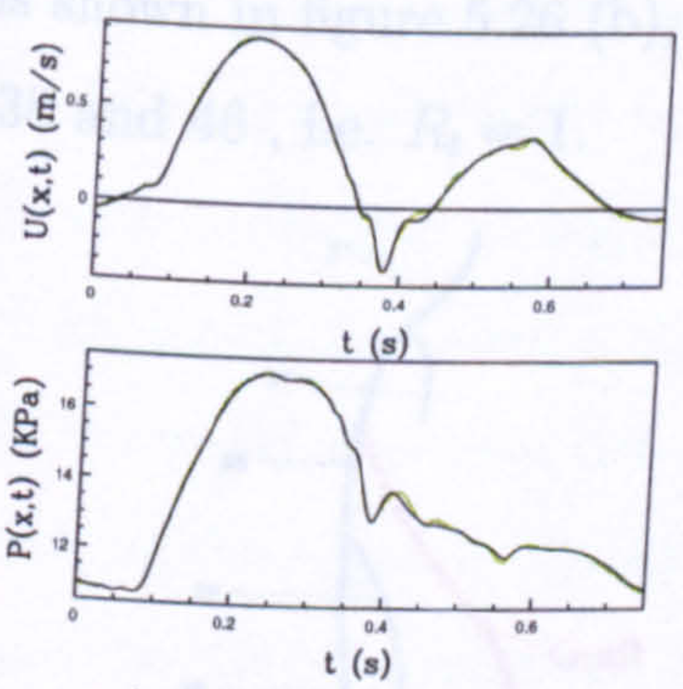
There is little difference in the waveforms in artery 26, which is just above the stent (artery 36). The largest difference in the waveforms is actually seen in artery 27, where there is a small drop in systolic velocity. This is surprising because this waveform is taken in the same position as artery 26, but in the other leg, however the differences are still very minor.

Although, it is difficult to know how a stent will affect the stiffness of an artery, because it is a structure with gaps, we believe the case modelled is quite an extreme case. It is rather long, 0.117 m and has a Young's modulus of twenty times the normal artery stiffness. From the waveforms in figure 5.25 we therefore conclude

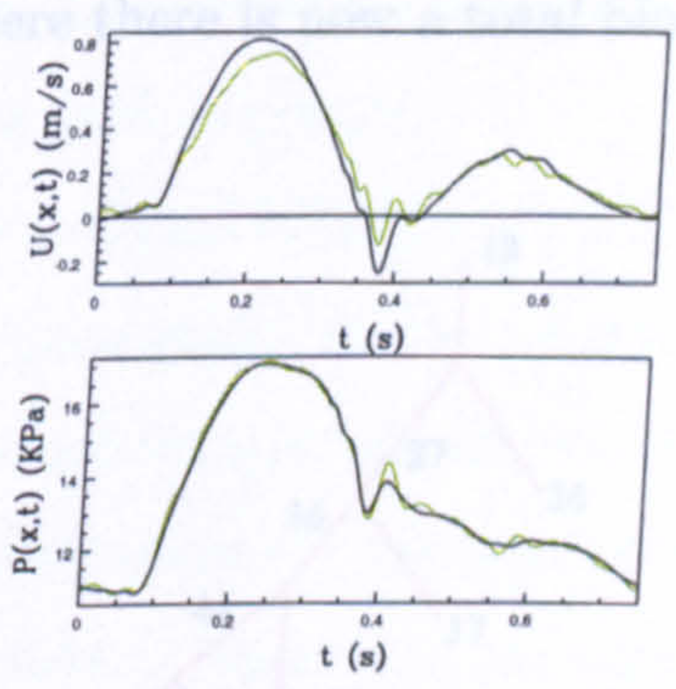


(1) Ascending Aorta

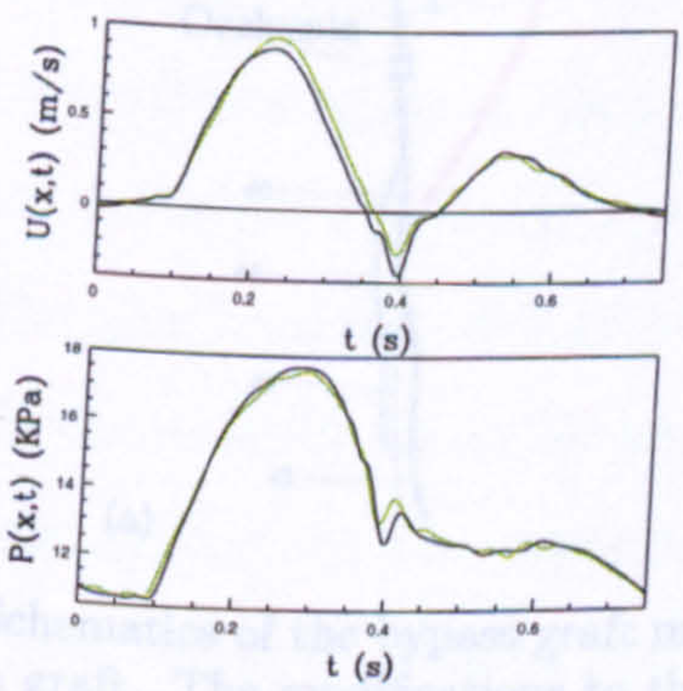
(18) Thoracic Aorta



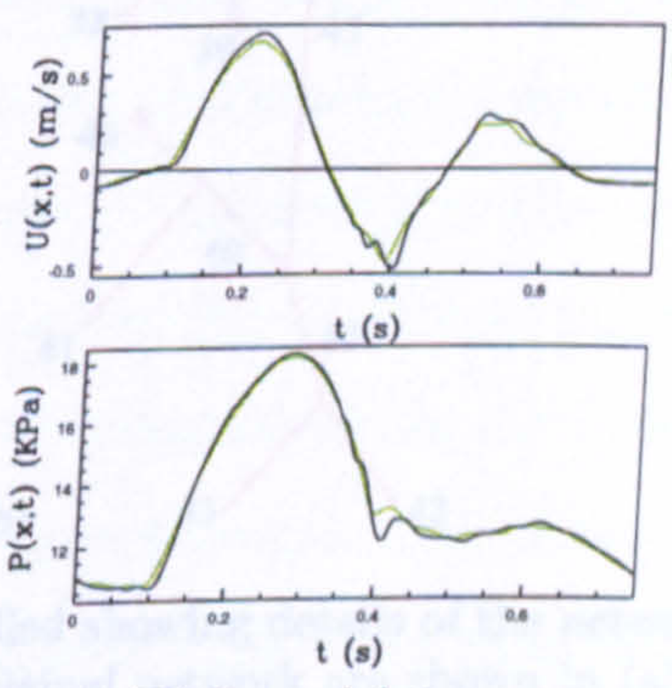
(26) Left Iliac



(27) Right Iliac



(36) External Iliac (Stent)



(38) Femoral Artery

Figure 5.25: Computational results showing that adding a stent to the arterial network (green) has little effect on the waveforms throughout the network when compared with the original (black). The differences are localised to the vicinity of the stent. The computations were performed with boundary condition 3 and no terminal resistance.

that stents do not significantly change the overall shapes of the waves seen in the arterial network.

5.5.2 By-pass grafts

When there is a severe blockage in an artery it is often treated by surgically grafting an alternative conduit from the artery above to that below the blockage in order to re-route the flow. This procedure is known as by-pass grafting and a typical by-pass graft is shown in figure 5.26 (a). In this example there is a blockage in the right femoral (artery 38) and the graft bypasses this blockage by connecting the external iliac artery (artery 36) to the posterior tibial (artery 40) at the bottom of the leg. This bypass graft has been modelled in the tapered arterial system. The new network is shown in figure 5.26 (b), where there is now a total blockage at the end of artery 38 and 46 , i.e. $R_t = 1$.

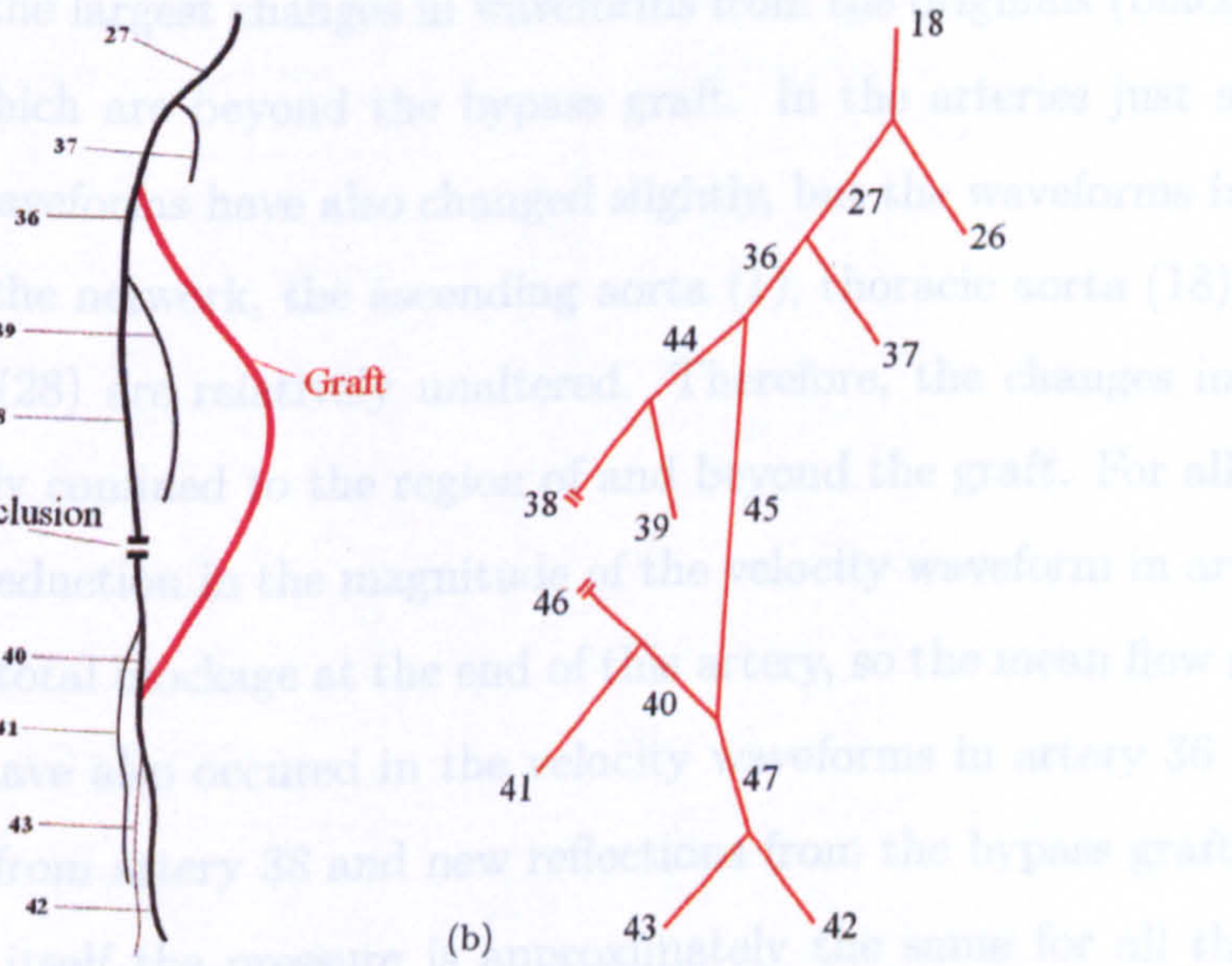


Figure 5.26: Schematics of the bypass graft modelled showing details of the network in the vicinity of the graft. The modifications to the original network are shown in (a) and the renumbered computational network is shown in (b).

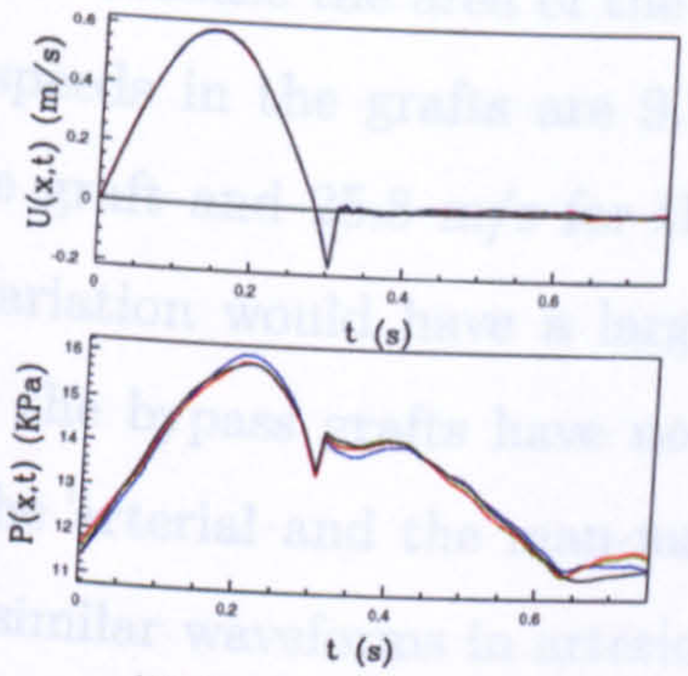
There are three typical categories of materials from which a graft can be made: 1) an arterial graft, 2) a venous graft and 3) a man-made, or prosthetic graft. All three different by-pass grafts were modelled in the tapered system as artery 45 in the network shown in figure 5.26 (b). The arterial graft was modelled with typical properties to that of a normal artery, but was not tapered along its length. Venous grafts are made from excised veins that have been reversed. These grafts are usually

of larger area than arterial grafts and, because they are now operating at arterial rather than venous pressure, are also stiffer. We have assumed the area was twice the size of the arterial graft and the Young's modulus was ten times larger. The last graft which was modelled was a man-made graft. This was assumed to have the same area as the arterial graft but was ten times stiffer.

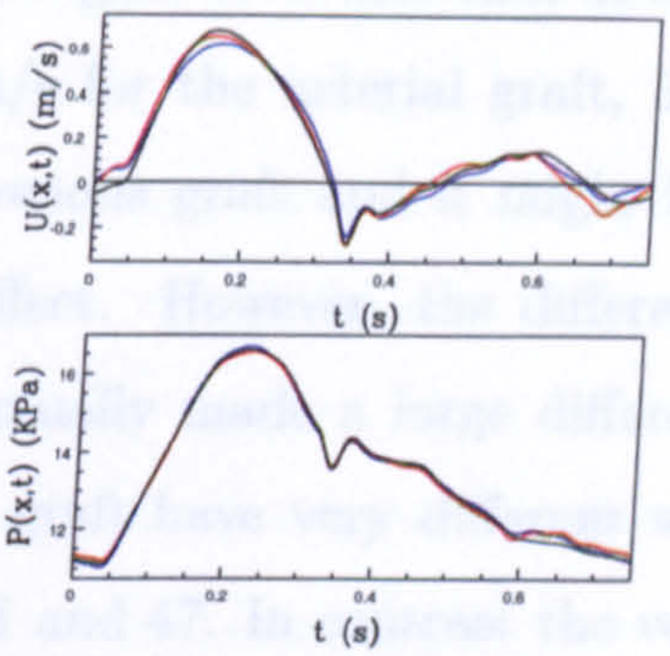
The waveforms for arteries 1, 18, 28, 36, 38, 45, 41 and 47 are shown in figure 5.27. The black lines are the original waveforms, the red lines are for the arterial bypass graft, the blue for the venous bypass graft and the green lines are for the man-made bypass graft. The waveform at the take-off of the bypass graft is that in artery 45. The waveforms in arteries 36 and 38 are just above the bypass, whereas arteries 41 and 47 are beyond the distal end of the bypass. Arteries 1, 18 and 28 are arteries numbered as before, which are in other locations in the arterial network rather than the right leg in which the bypass graft is present.

The arteries with the largest changes in waveforms from the originals (black) are arteries 41 and 47, which are beyond the bypass graft. In the arteries just above the bypass graft the waveforms have also changed slightly, but the waveforms in the arteries in the rest of the network, the ascending aorta (1), thoracic aorta (18) and the left external iliac (28) are relatively unaltered. Therefore, the changes in the waveforms are primarily confined to the region of and beyond the graft. For all the grafts there is a great reduction in the magnitude of the velocity waveform in artery 38, which is due to the total blockage at the end of this artery, so the mean flow rate is now zero. Changes have also occured in the velocity waveforms in artery 36 due to the large reflections from artery 38 and new reflections from the bypass graft.

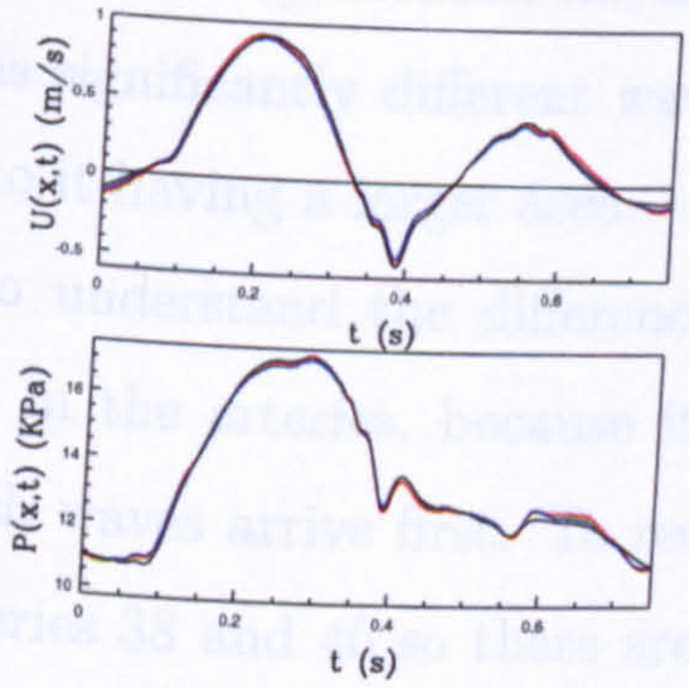
In the bypass graft itself the pressure is approximately the same for all three grafts, but the velocity for the venous graft is significantly lower than for the arterial and man-made graft. This is easily explained as it is due to the larger cross-sectional area for the venous graft. Less easily explained are the waveforms in arteries beyond the bypass graft which have now substantially changed from the original. These differences appear to be related to the total blockage at the end of artery 46 and the altered waveforms from the bypass graft. The reflection coefficient at the end of the graft appears to be important but the geometry itself seems to be most critical. The waveforms for the arterial and man-made graft are significantly different from



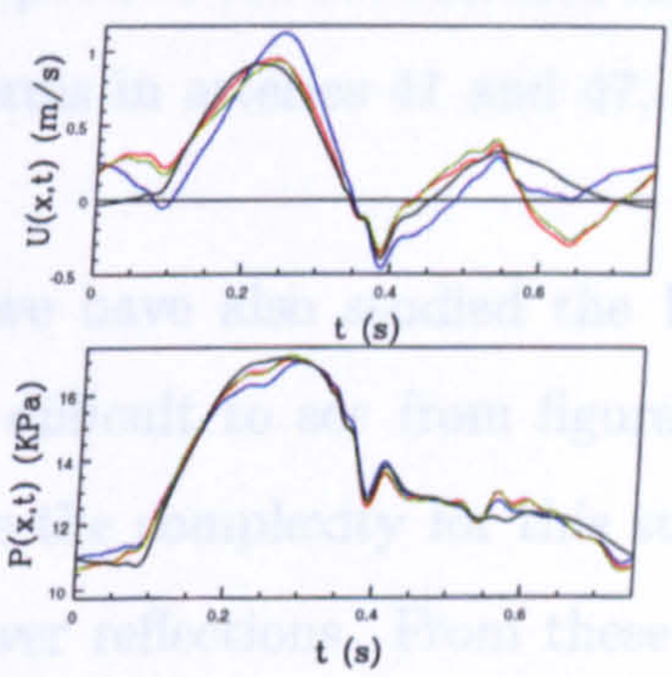
(1) Ascending Aorta



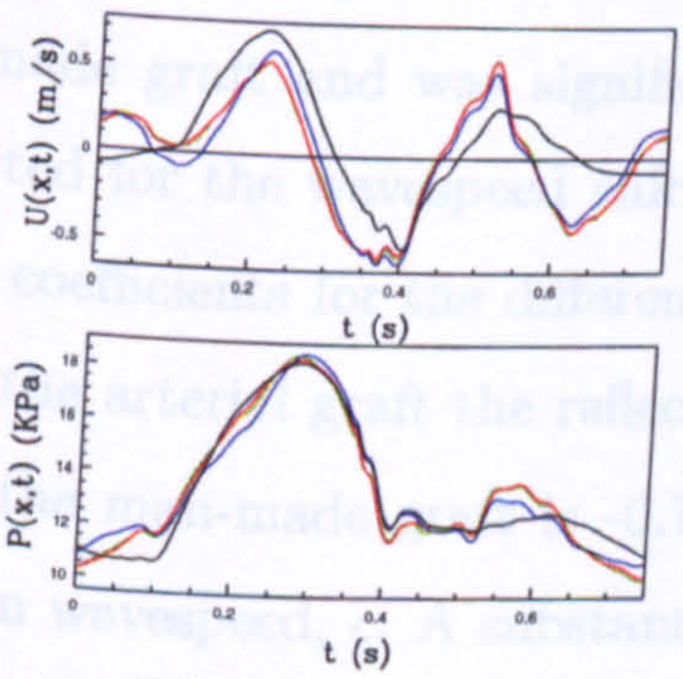
(18) Thoracic Aorta



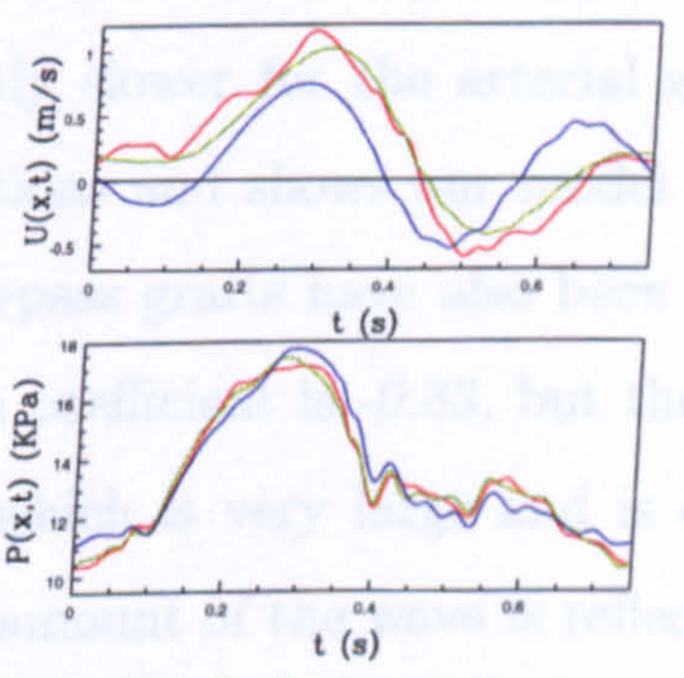
(28) Left External Iliac



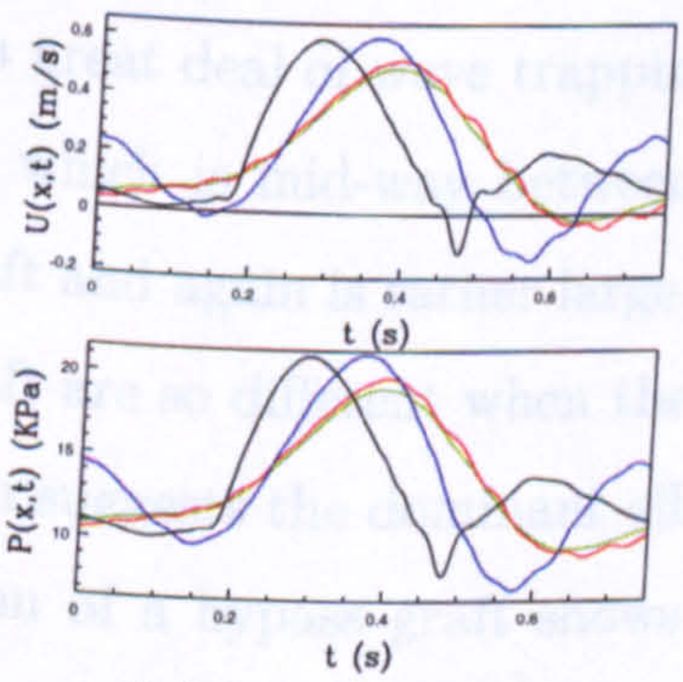
(36) Right External Iliac



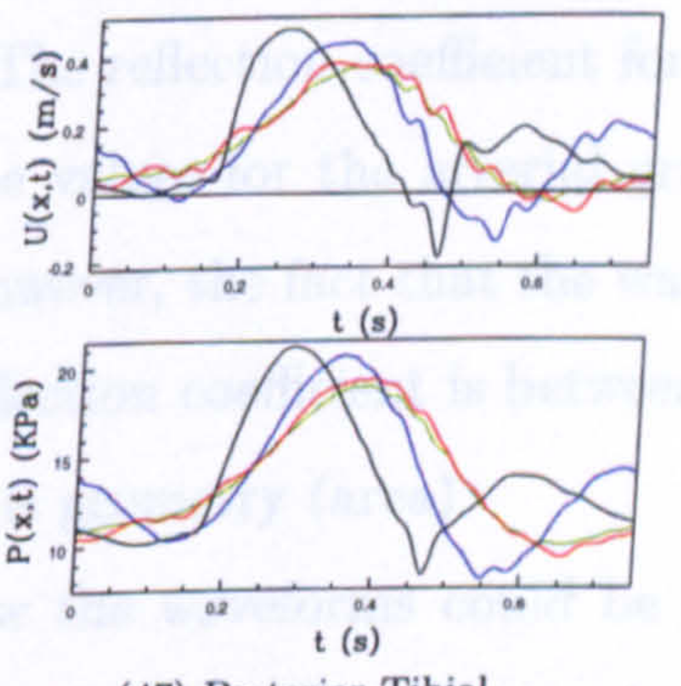
(38) Femoral Artery



(45) Graft



(41) Anterior Tibial



(47) Posterior Tibial

Figure 5.27: Computational results showing that the effects of adding a bypass graft to the leg of the original network is pronounced in the region of the graft and beyond, but relatively small elsewhere in the arterial tree. The inflow was boundary condition 3 and no terminal resistance was applied. The black lines are the original results, red are for arterial grafts, blue for venous and green for man-made grafts.

the venous graft because the area of the latter graft is double that of the others.

The wavespeeds in the grafts are 9.7 m/s for the arterial graft, 30.7 m/s for the man-made graft and 25.8 m/s for the venous graft and it might be expected that such a variation would have a large effect. However, the differences in the wavespeeds in the bypass grafts have not actually made a large difference to the waveforms. The arterial and the man-made graft have very different wavespeeds, but have very similar waveforms in arteries 41 and 47. In contrast the venous graft has a wavespeed mid-way between the wavespeed of the arterial and the man-made grafts, but has significantly different waveforms in arteries 41 and 47, which again must be due to it having a larger area.

In order to understand the differences we have also studied the W_1 and W_2 characteristics in the arteries, because it is difficult to see from figures 5.27 (41) and (47), which waves arrive first. To reduce the complexity for this study we set $R_t = 0$ on arteries 38 and 46 so there are fewer reflections. From these figures we found that the reflected W_2 characteristic reached the top of the bypass graft faster for the man-made graft and was significantly slower for the arterial graft, which is to be expected for the wavespeed calculations and shows our model is working. The reflection coefficients for the different bypass grafts have also been calculated. At the end of the arterial graft the reflection coefficient is -0.33, but the reflection coefficient for the man-made graft is -0.73, which is very large and is due to the large increase in wavespeed, c. A substantial amount of the wave is reflected at the end of this graft. The reflection coefficient at the take-off of the graft is also large so there will be a great deal of wave trapping. The reflection coefficient for the venous graft is -0.45, which is mid-way between the values for the arterial graft and the man-made graft and again is rather large. However, the fact that the waveforms for the venous graft are so different when the reflection coefficient is between the other two cases again suggests the dominant effect is geometry (area).

The addition of a bypass graft shows how the waveforms could be altered by changes to the arterial network and that there is a significant change in the waveforms below the graft when compared with the original waveforms. This is due to the blockage in the femoral, the new connectivity and the new vessel properties. It was also shown that the choice of graft is important because large changes in area

can significantly change the waveforms beyond the bypass graft and indeed the area of the graft is shown to be of great importance.

In conclusion we can say that surgically intervening in the human body with a stent or a bypass graft results in changes in the waveforms that are localised to the vicinity of the intervention and the arteries beyond. The waveforms in the rest of the network have hardly been affected. It would be of great interest to compare the results with those observed in-vivo. The change in waveforms beyond the intervention is particularly pronounced for the bypass graft case, there are also significant differences depending on the size of the graft itself. Both sets of results show that the geometry is much more significant than the local wall properties with regard to the shape of the waves.

5.6 Damping in the system

Due to the assumptions that we have made in deriving the governing equations for our one-dimensional model, no damping is incorporated in the system. When combined with the fact that the numerical scheme is not very diffusive and that there can be reflector boundary conditions on the inflow and outflow there is no mechanism for the waves to be dissipated. This is not the case in-vivo where damping is known to occur [2, 3, 11, 89, 88]. Therefore, in this section we investigate possible effects of damping on the waveforms. Damping of the waves in the system could occur from several different sources. For example, arteries are tethered in the arterial system, i.e. they are held into position by outside tissue, which can constrain them longitudinally and radially, the surrounding tissue may damp the waves as might the viscoelastic properties of the arterial wall itself and the viscosity of the blood may also be significant [89, 60]. We now study the effect of a simplified damping model on the pressure and velocity waves in the system.

Since we are currently only interested in the broad effects of damping we have not re-written the governing equations to incorporate the different effects, but we have assumed that the waves in the system are exponentially damped with time. Therefore as the time increases the magnitude of the waves decreascs. We have post-processed our results by multiplying the waveforms for a single heart beat by the exponential function $f(t) = e^{-at}$. Figure 5.28 shows a graph of the exponential function plotted against time for several different values of a. Altering the variable a is equivalent to changing the level of damping. The function was applied to only a single heart beat, because we have no means of damping the reflections from previous heart beats by the correct amount before they meet the next wave i.e. the reflections from the previous beat will not be sufficiently damped considering they have been in the system for over a cycle. For this simple analysis of damping it has also been assumed that the waveforms in all the different arteries throughout the tapered arterial network are uniformly damped, but in reality it is more likely that some arteries damp the waves more than others.

The damping in the system was assessed for the velocity boundary condition (BC3). Damping in the system is considered with and without terminal resistance

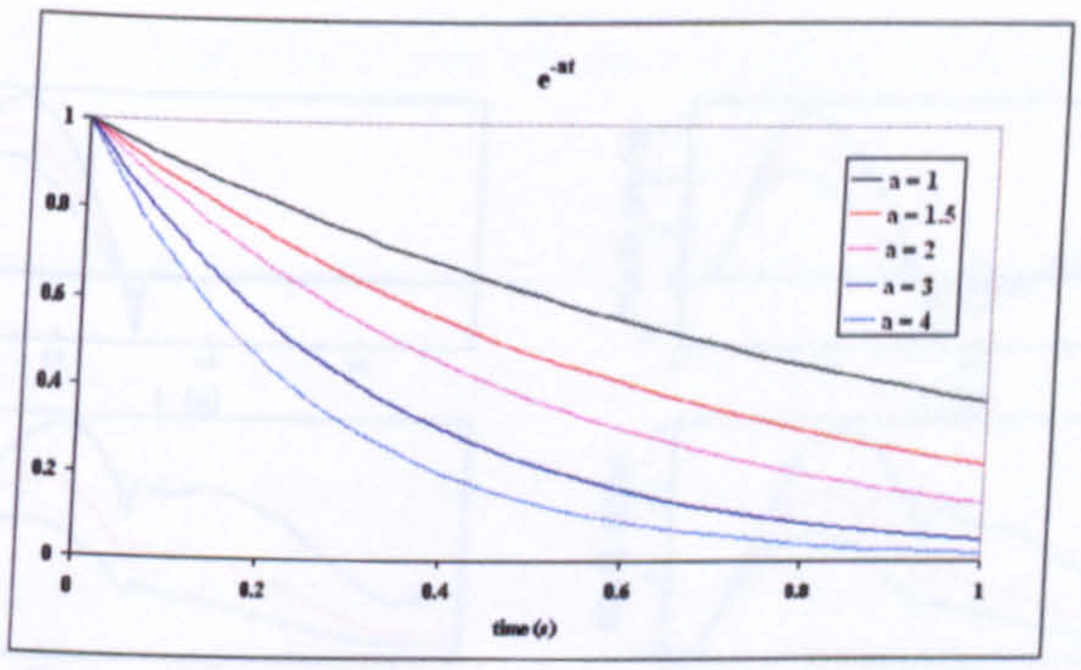
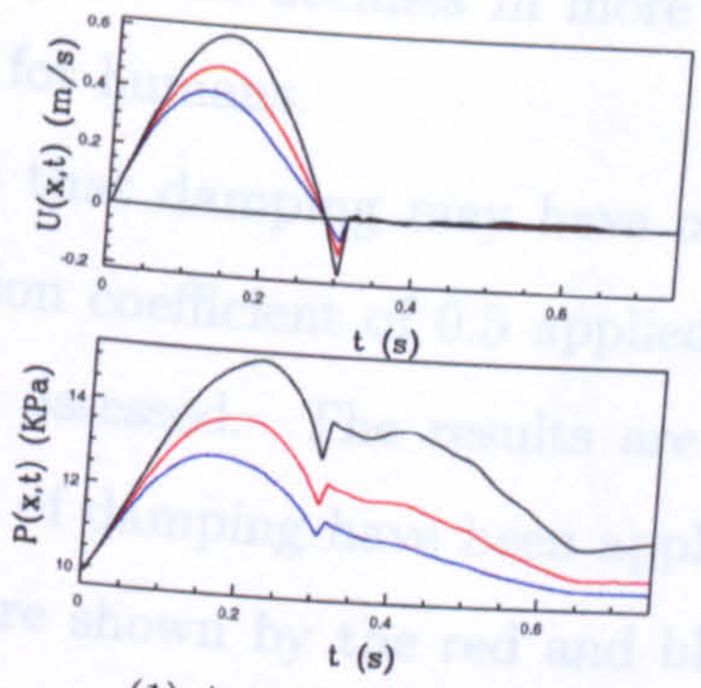


Figure 5.28: The exponential functions used as damping factors for the waves in figures 5.29 and 5.30.

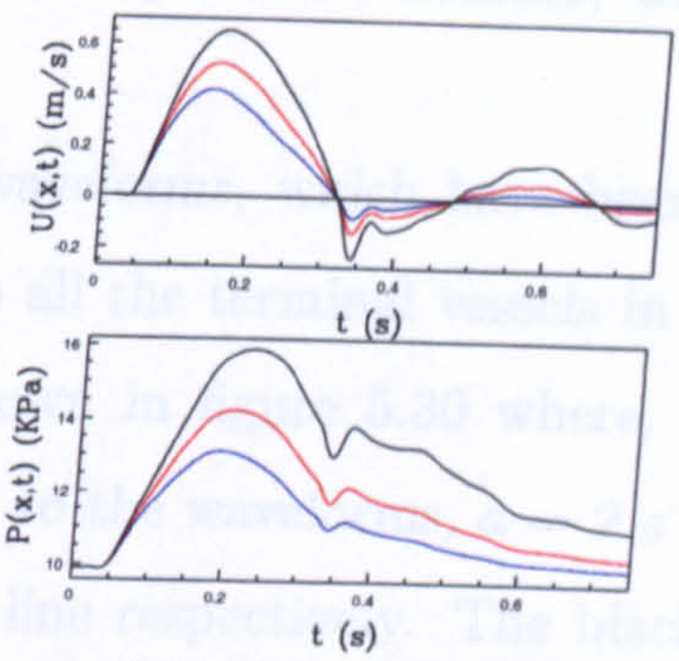
on the terminal vessels of the network, i.e. $R_t = 0.0$ and 0.5. The waveforms with no terminal resistance are shown in figure 5.29 for two different levels of damping, $a = 1.5\ s^{-1}$ and $a = 3\ s^{-1}$, red and blue lines respectively. The black lines are the original results with no damping applied. As the waves are only for one heart beat the waveforms do not incorporate the effects of any reflections from previous waves, which is why in figure 5.29 there is zero flow and a constant baseline pressure before the main wave arrives in the arteries more distal than the ascending aorta.

Comparing the waveforms with different levels of damping with the original shows that the waveforms have the same features, which is to be expected given the way the damping has been applied. The main difference is that the feature of the waves are smaller, especially in diastole, for a higher level of damping. The magnitudes of the waveforms for the red and blue lines may now appear too low, especially for the ascending aorta, but these can be altered by imposing a higher peak velocity at the inflow.

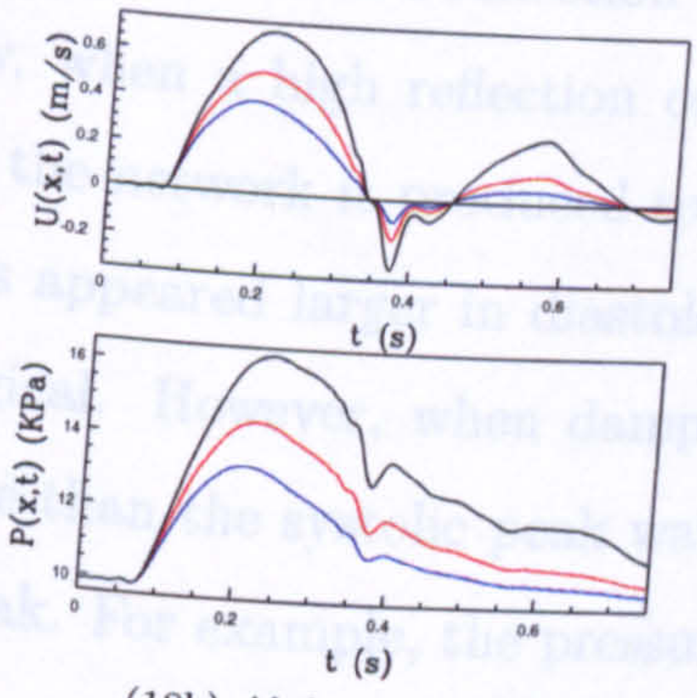
From previous sections it was found that for many of the arteries, especially for waveforms further away from the heart, that the features of the pressure and velocity waveforms were rather larger than those in-vivo later in the cycle, see the black waveforms in figures 5.29 (7), (8), (38) and (42). The damping has the greatest effect later in the cycle, because the wave is damped due to the exponential decay with time. This effect therefore causes the second features, which were originally very large, to become significantly smaller and means that the waveforms look far more physiological. This is particularly true for velocity, which did not look very physiological in the later portion of the cycle when damping was not applied. With no damping the aortic pressure was not as smooth, but with damping the pressure



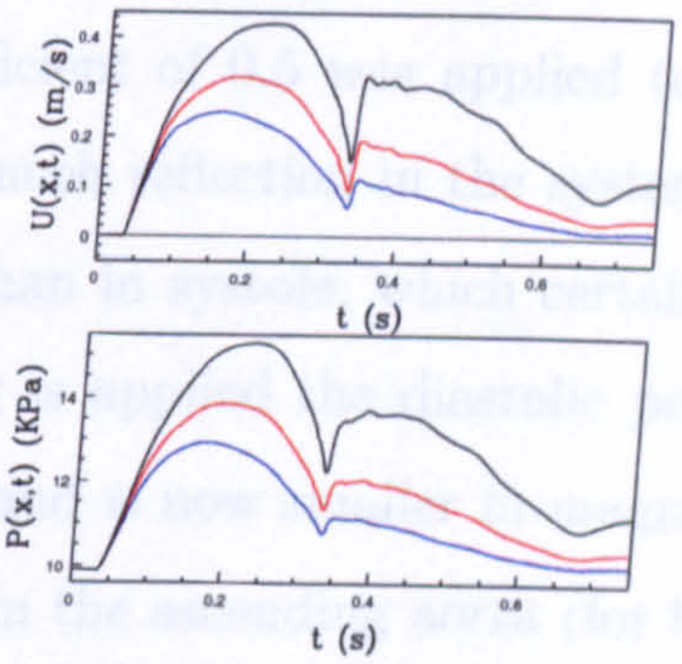
(1) Ascending Aorta



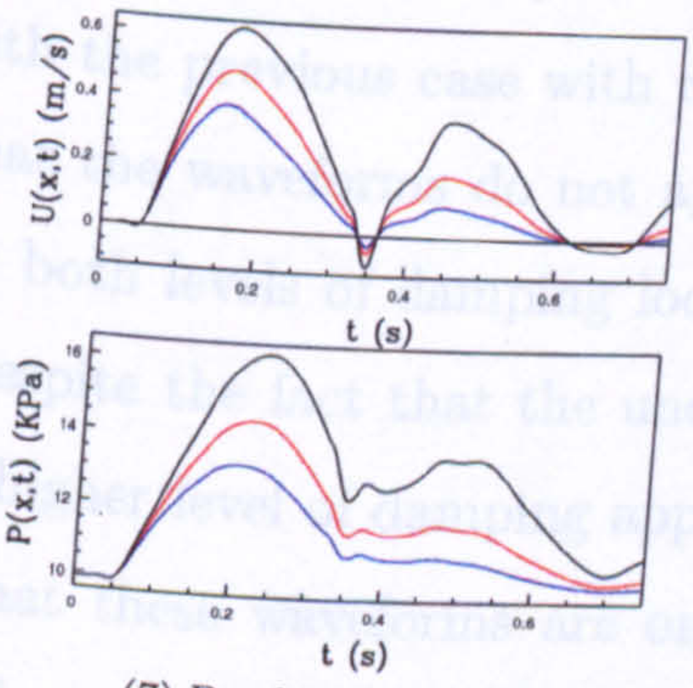
(18) Thoracic Aorta



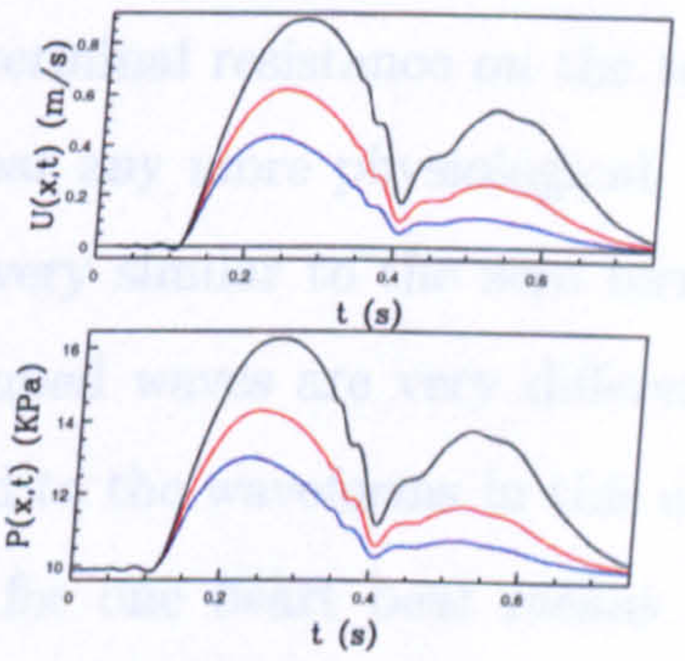
(18b) Abdominal Aorta



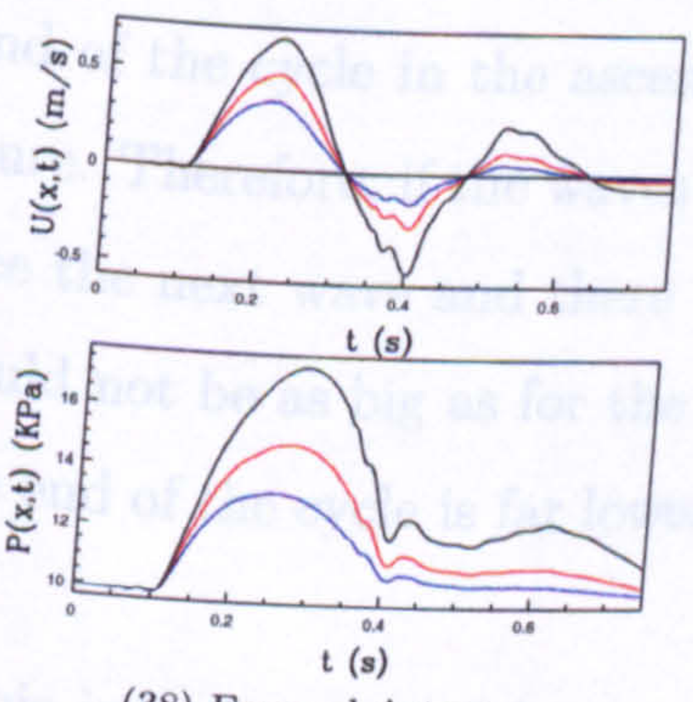
(15) Common Carotid



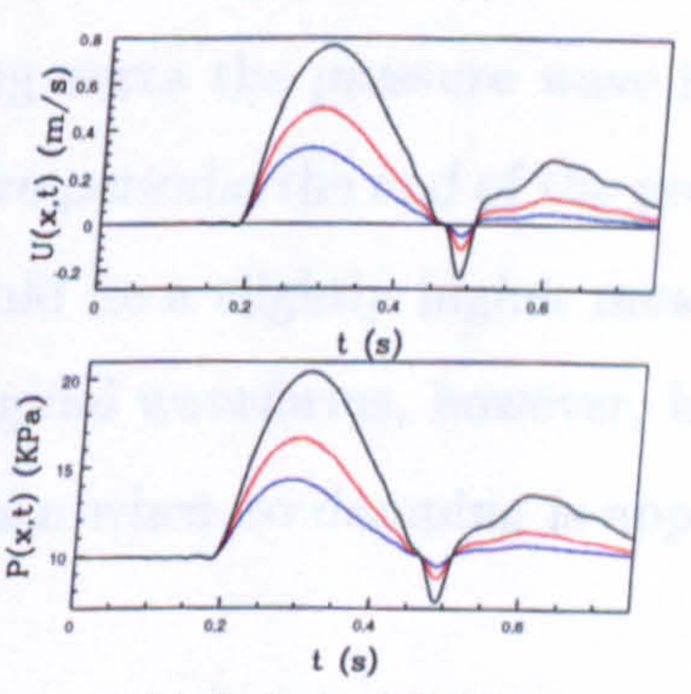
(7) Brachial Artery



(8) Radial Artery



(38) Femoral Artery



(42) Posterior Tibial

Figure 5.29: Computational results for a single heart beat showing the effects of applying an exponential damping factor to the waveforms is to reduce the secondary features of the waves during diastole. The black lines are results for the tapered network with boundary condition 3 and no terminal resistance, the red lines are for a damping factor of $a = 1.5$ s^{-1} and blue for $a = 3$ s^{-1}.

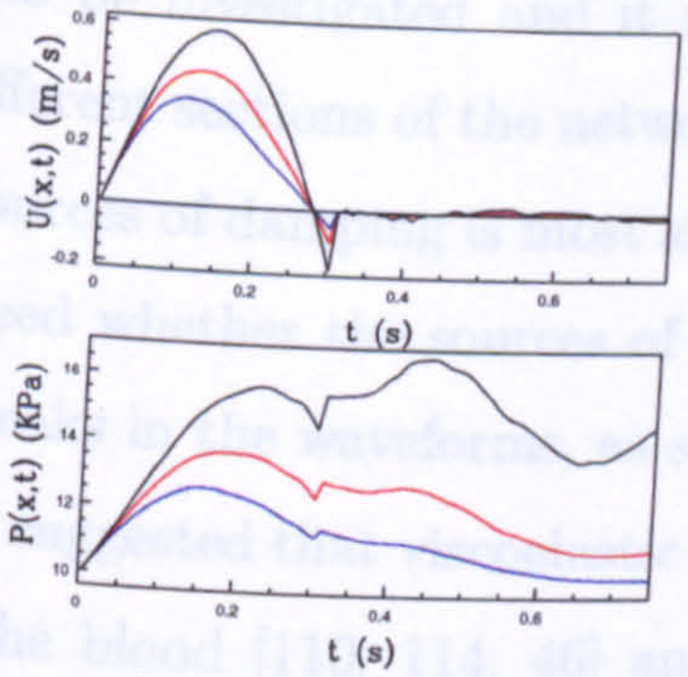
wave is smoother and declines in more of an exponential manner, which is more physiological for humans.

The effect that damping may have on waveforms, which have been calculated with a reflection coefficient of 0.5 applied to all the terminal vessels in the system has also been assessed. The results are shown in figure 5.30 where, again, two different levels of damping have been applied to the waveforms, $a = 2\ s^{-1}$ and $a = 4\ s^{-1}$, which are shown by the red and blue line respectively. The black lines are the original waveforms with a reflection coefficient of 0.5 on the terminal vessels.

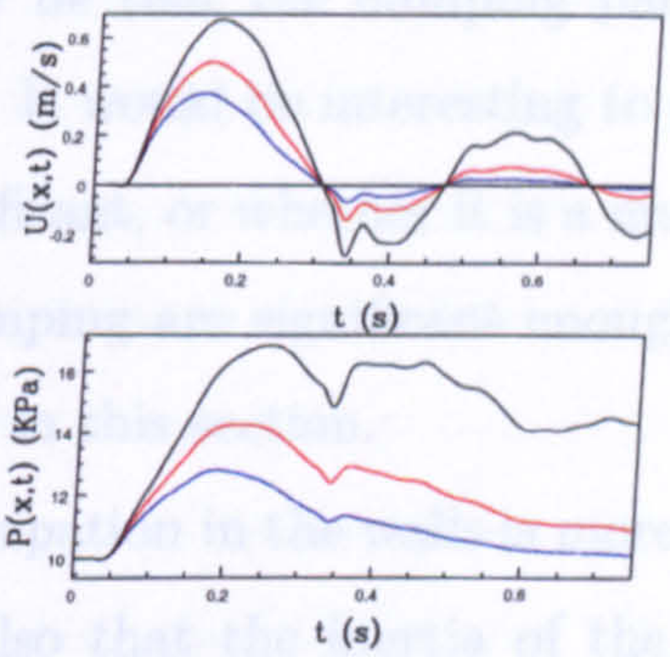
Previously, when a high reflection coefficient of 0.5 was applied to the terminal vessels of the network it produced too much reflection in the system. Many of the waveforms appeared larger in diastole than in systole, which certainly did not look physiological. However, when damping is applied the diastolic peak wave is decreased more than the systolic peak wave and is now smaller in magnitude than the systolic peak. For example, the pressure in the ascending aorta (for both levels of damping) has now substantially decreased in diastole. Comparing the damped waveforms with the previous case with no terminal resistance on the terminal vessels, shows that the waveforms do not appear any more physiological. In fact the waveforms for both levels of damping look very similar to the zero terminal resistance cases, despite the fact that the undamped waves are very different. This is related to the higher level of damping applied to the waveforms in this case.

The fact that these waveforms are only for one heart beat means reflections from previous beats do not build up, which is not physiological. It can be seen that at the end of the cycle in the ascending aorta the pressure wave is above the baseline pressure. Therefore, if the waves were periodic the end of the pressure wave would reinforce the next wave and there would be a slightly higher mean pressure. This effect would not be as big as for the original waveforms, however, because the pressure at the end of the cycle is far lower than when no damping is applied to the wave.

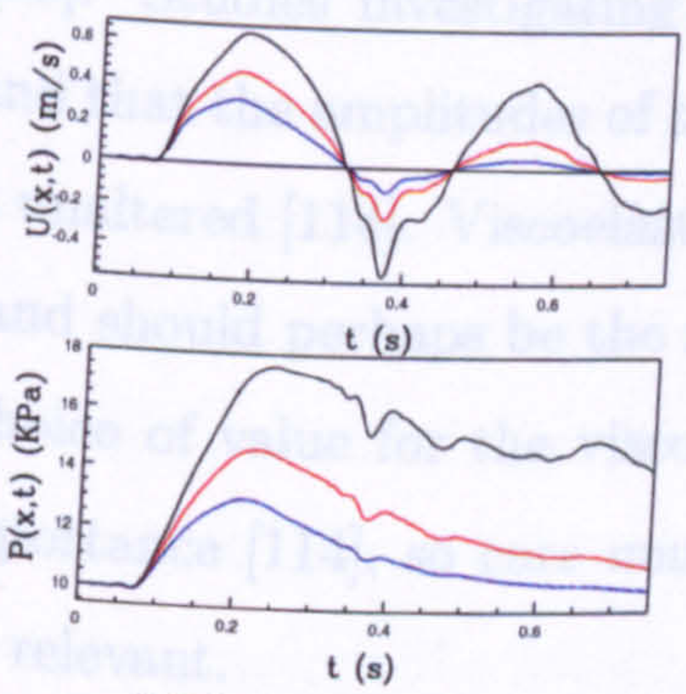
Although this investigation of damping is very simplified it does indicate that the modelling of damping within the system is worth investigating further. The effects are to improve the comparison between our predicted waveforms and those found in-vivo, which is encouraging. The damping needs to be incorporated into



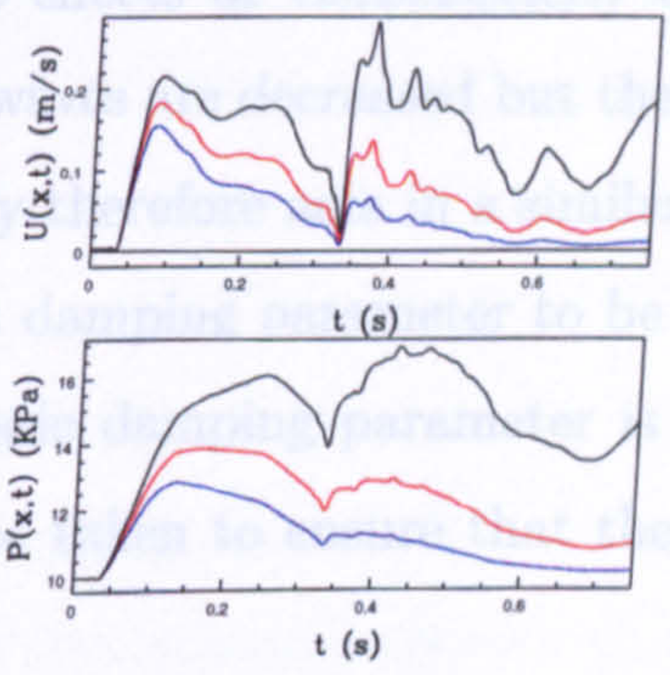
(1) Ascending Aorta



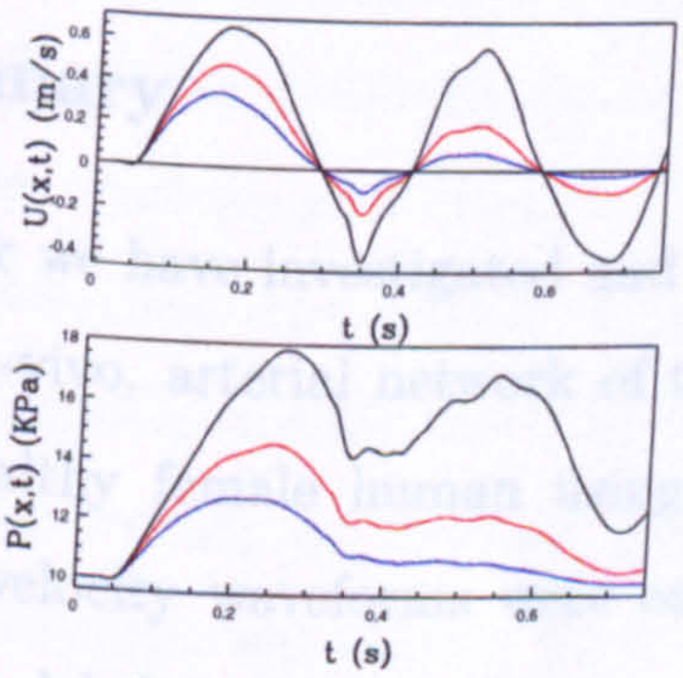
(18) Thoracic Aorta



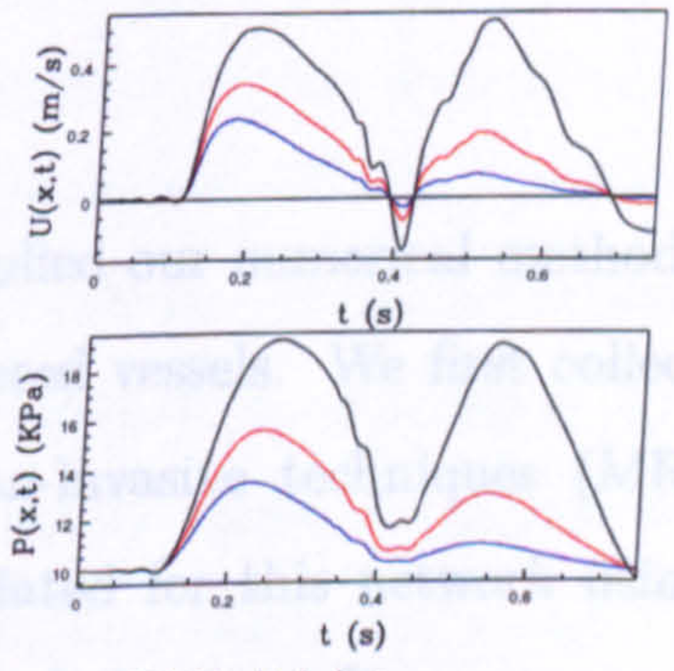
(18b) Abdominal Aorta



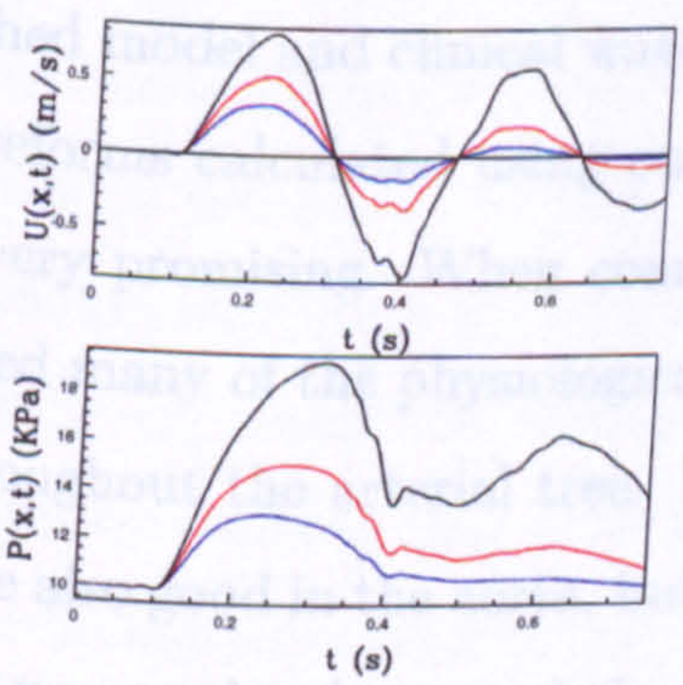
(15) Common Carotid



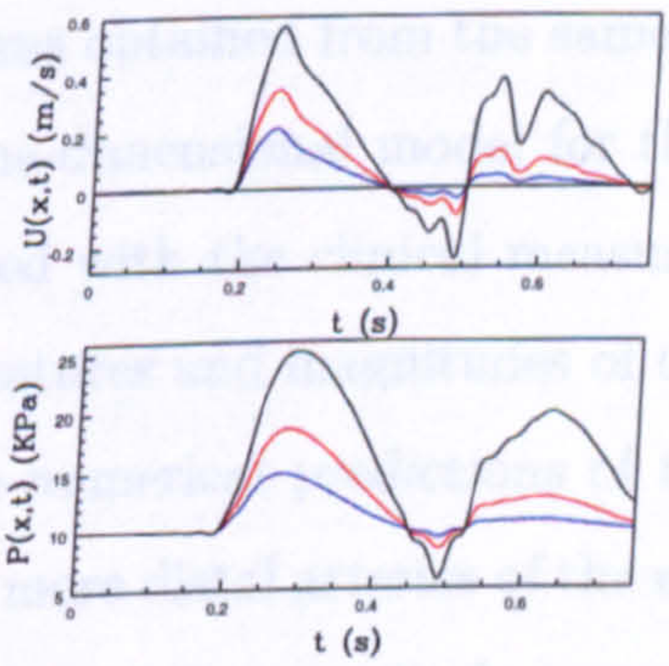
(7) Brachial Artery



(8) Radial Artery



(38) Femoral Artery



(42) Posterior Tibial

Figure 5.30: As for figure 5.29 but with a terminal resistance of 0.5 applied to the terminal vessels and damping factors of $a = 2\ s^{-1}$ (red) and $a = 4\ s^{-1}$ (blue).

the governing equations and also the correct levels of damping occurring within the system need to be investigated and it may be that the damping parameters are different in different sections of the network. It would be interesting to see which of the possible sources of damping is most significant, or whether it is a multi-factorial effect and indeed whether the sources of damping are significant enough to reduce the diastolic peaks in the waveforms, as seen in this section.

It has been suggested that viscoelastic dissipation in the walls is more important than that in the blood [110, 114, 46] and also that the inertia of the wall mass is negligible [30]. Studies investigating the effects of viscoelasticity of the vessel walls have found that the amplitudes of the waves are decreased but their frequency and phase are unaltered [114]. Viscoelasticity therefore acts in a similar manner to our damping and should perhaps be the first damping parameter to be considered, however the choice of value for the viscoelastic damping parameter is thought to be of great importance [114], so care must be taken to ensure that the values are physiologically relevant.

5.7 Summary

In this chapter we have investigated and applied our numerical methods to a completely new in-vivo, arterial network of tapered vessels. We first collected in-vivo data for a healthy female human using non-invasive techniques (MR imaging). Pressure and velocity waveforms were calculated for this network using the one-dimensional model described in Chapter 2 and these results were compared with the well-matched model and clinical waveforms obtained from the same female subject. The waveforms calculated using our one-dimensional model for this new network appear very promising. When compared with the clinical measurements, we have reproduced many of the physiological features and magnitudes of the pressure waveforms throughout the arterial tree. The numerical predictions of the velocity waveforms were also good in the aorta, but in more distal arteries of the network the diastolic peaks were rather large and the peak systolic magnitude increased rather than decreased.

A surprising property of the tapered network is that we have managed to re-

produce many of the physiological features of the waveforms without applying any terminal resistance to the end vessels of the system. This may be due to the increased number of reflection sites in our network compared with the well-matched system. The only reflection sites for the well-matched network are at the ends of the terminal vessels, whereas in the tapered network reflections occur at the ill-matched bifurcations and significant reflections also occur from the tapered vessels. It is suggested in section 5.3 that some of these tapered arteries had other arteries branching off them which were not visible from the MRI images. These vessels may not produce quite as much reflection due to taper in-vivo as our model suggests. Nevertheless the taper tests in section 5.2.2 showed that even small amounts of taper can produce significant reflections in the system and therefore should be considered when modelling the arterial tree.

Studies were also performed that involved altering the network, by including stents or bypass graft, to show how sensitive the waveforms are to changes in arterial properties and geometry. The waveforms were significantly altered beyond the bypass graft, but these changes were very localised to the leg in which the bypass graft is located and few significant changes were seen in the waveforms in the rest of the arterial tree. Had the graft been further up the arterial tree waveforms may have been altered thoughout the system. Changes due to alterations in wall properties were relatively minor in comparison to the effects of the geometry. These investigations could potentially be used for assessing the effect of surgical interventions in the arterial network and helping the surgeon to identify any possible circulatory problems that could develop post-operatively [150].

From our studies in Chapters 4 and 5, we have also identified modelling assumptions that should be considered in more detail in future research and may improve the one-dimensional prediction of the waveforms in the arterial system. Geometry appears to be very significant and although it is appealing to model only the largest arteries of the network due to time and data constraints, the results in section 5.3.1 suggest that modelling more arteries may improve the waveforms significantly. The magnitudes of velocity waves would be improved dramatically and maybe even the shapes of the waveforms might better resemble the clinical measurements. This, of course, can become very time consuming particularly when constructing the model.

It has been shown that MRI techniques are a relatively successful method of collecting data regarding lengths and areas for the arterial network. This is particularly attractive because it enables in-vivo data to be collected for living humans, which has obvious benefits with regard to surgical planning and also overcomes the problems associated with measuring the diameter of flow paths in arteries that are no longer at arterial pressure and may have undergone vaso-constriction. The detail of the MR images of the arterial network could be improved either by spending more time obtaining higher quality images or by the use of contrast agent, which would give very clear arterial information.

Considering that the inflow boundary conditions we have used are essentially simple half-sine waves, the results are surprisingly good, although the peaks of these waves appeared to be a little too rounded. The precise form of the inflow condition could be improved in future modelling, for example obtaining a clinical waveform at the ascending aorta for the human model, which we could directly impose at the inflow would be particularly interesting. Although the waveforms do not seem too sensitive to the shape of the inlet wave they are very sensitive to the type of inflow boundary condition. We found that the part absorber/reflector boundary condition (BC4) was an interesting condition to impose at the inflow, because it produced a dicrotic notch in the pressure waveform and reversed flow in the ascending aorta despite the fact the inflow shape was so simplified. Waveforms, other than a half-sine wave, need to be considered for the W_1 characteristic for this boundary condition and the modelling of valve closure could be altered, to see if these could improve the overall waveforms. Boundary condition 3 requires precise details about the flow in the ascending aorta in each case and is therefore less general.

The outflow boundary conditions were less significant for the tapered network. Adding terminal resistance did not significantly improve the waveforms in the terminal vessels, but the velocity waveforms were more physiological a few generations up the arterial tree. To improve the waveforms in the more distal vessels of our network, we could try to obtain further data for arteries beyond the radials, ulnars and tibials, for the arches in the hands and feet and arteries beyond the carotids and vertebrals and for the circle of Willis in the head. The other option is to include an impedance model or fractal model for the outflow boundary condition to model

the physiological situation more closely (sections 1.2.1.4 and 7.2).

Our model does not currently incorporate any damping of the waves, but in section 5.6 we showed that this could have a significant effect on the waveforms in the system. Therefore it would be worthwhile altering the governing equations to model the sources of damping in any further research. We believe that this could be one of the most significant improvements to the one-dimensional model.

Finally, the Young's modulus and wall thickness were unknown for the new system so we used the old data from the well-matched system. It would certainly be preferable to obtain data for a 26 year old female.

In conclusion we have modelled the waveforms in a new, in-vivo, detailed physiological arterial network of a single human using the one-dimensional numerical code and have obtained reasonably physiological waveforms, when compared with the clinical data. The current modelling has revealed many interesting features and the new arterial network is a substantial improvement on the previous computational data and results. The waveforms are sensitive to a number of parameters, the most important of which is geometry. These results provide a good basis for further research and we believe that the predicted waveforms from the numerical model could be further improved both by developments in the modelling and by the use of more accurate physiological data.

Chapter 6

Monochorionic placentas

This chapter illustrates another application of the one-dimensional modelling, namely the calculation of waveforms in the arterial networks of monochorionic twin pregnancies where two fetuses share a single placenta. The fact that the circulations of the twins are connected may have implications with regards to the development of the fetuses, as described in section 6.2, therefore it is of considerable clinical interest to understand the blood flows in these cases. Our investigations focus on the physiological arterial systems of three monochorionic placentas, which have been modelled using the one-dimensional code. Geometrical data for the arterial systems was obtained by casting monochorionic placentas to make plastic models of the placental circulations. These were then measured to acquire the data needed for the computational model. The placentas were cast within 1-2 hours of delivery, thereby mitigating the effects of vasoconstriction and cell death. The casting of placentas also suffers from fewer problems than measuring excised blood vessels, because the vessels are held in position by the surrounding tissue. The casting techniques are described in section 6.3. A total of seven placentas have been cast so far and images of the plastic models are shown in section 6.4 where the fetoplacental circulations are also briefly discussed for each model.

The computational results for the three fetoplacental circulations calculated using the one-dimensional model are shown in sections 6.6, 6.7 and 6.8. Initially, these fetoplacental circulations are modelled as two completely separate systems then the results are extended to the actual situation of modelling the arterial network as a monochorionic placenta. The velocity waveforms in-vivo can be quite distinctive and

the computational results are compared with physiological data. The mass fluxes into and out of these placentas are also calculated. The more complicated of the three placentas has been studied in greater detail in section 6.6 by altering different parameters in the model to determine the effect these have on the waveforms and the mass fluxes in the system. In sections 6.7 and 6.8 the main results for the two remaining systems are shown and are discussed.

6.1 The fetal circulation

In utero the fetus is connected via an umbilical cord to its placenta, which is attached to the uterus wall of the mother. There are two arteries and one vein in the umbilical cord, that are the flow conduits for the blood to travel from the fetus to the placenta and back to produce one circulatory system. The arteries within the umbilical cord are linked to the systemic circulation of the fetus and a proportion of the fetus' blood, therefore passes through the placenta. The blood is pumped through this circulatory system by the fetus' heart. The primary function of the placenta is to provide the fetus with nourishment and oxygen and to remove waste products such as carbon dioxide. The source of the metabolic products is the maternal blood and this also removes the waste products. The maternal blood supplied to the placenta is part of the mothers circulation and therefore the metabolites and waste products are treated in the usual manner by the mothers organs (lungs etc). It must be emphasised that the maternal and fetal circulations are completely separate and that no blood is common. The metabolites are exchanged by diffusion across thin dividing walls between the two circulations in features called cotyledons.

Identical twins occur when a fertilised embryo splits and these twin fetuses may share a single placenta. If there are two membranes, chorions, surrounding the placenta, one for each of the twin fetuses, then the two fetoplacental circulatory systems will be completely separate. This is called a dichorionic placenta, however only 25 % of monozygotic twins have dichorionic placentas, the remainder have only one chorion enveloping the placenta [156] and are called monochorionic placentas and the fetoplacental circulations may not be entirely separate. In fact it is thought that most, if not all, circulations in monochorionic placentas are linked [132, 26].

6.2 Twin-to-twin transfusion syndrome

In monochorionic placentas there can be anastomoses (joining routes) between the blood vessels of the two fetoplacental circulations, which result in a transfer of blood between the two fetuses. These connections may result in unbalanced transfer of blood from one fetus to the other. If this occurs, one fetus receives too much blood to the detriment of itself and the other twin. Discordant growth results and in extreme cases can lead to a medical condition called twin-to-twin transfusion syndrome (TTTS), which can be fatal. There are three types of anastomoses that can occur in between the fetoplacental circulations: arterio-arterial anastomoses (AAA), arterio-venous anastomoses (AVA) and venous-venous anastomoses (VVA). In TTTS the fetuses are described as the donor and recipient, but strict medical criteria must be met for the cases to be classified as TTTS, so to avoid confusion throughout this chapter we will denote the fetuses as smaller and larger in reference to the mis-matched growth that often occurs [156].

In the case of a typical arterio-venous anastomosis an artery from the smaller fetus crosses the surface of the placenta, before dipping below the surface and supplying blood to a cotyledon belonging to the venous system of the larger rather than smaller fetus. The blood then leaves the cotyledon through a vein belonging to the larger fetus' circulation. Strictly speaking this is an incorrectly connected cotyledon rather than an anastomosis, but is termed an AVA. Blood is transfusing from the high pressure arterial system of the smaller fetus to the low pressure venous system of the larger fetus, and due to the pressure difference can only travel in this direction. It is thought that the clinical outcome is usually worse when only arterio-venous anastomoses of a given direction are present as there is then no route for the blood to return from the larger fetus, that has too much blood, to the smaller fetus, which is now lacking in blood [156, 155]. With only this type of anastomosis the wave pattern often appears normal in the arteries of the placenta and the umbilical artery (i.e. non-reversing/mono-directional) and can therefore potentially go unrecognised if Doppler ultrasound is used as a diagnostic tool. It may, however be possible to visually identify arterio-venous anastomoses on the surface of the placenta, either by colour Doppler ultrasound or endoscopy [153, 120]. However, the long procedure

times that can be required for endoscopy are associated with complications [121] and although colour Doppler ultrasound is non-invasive it is not as yet a proven technique for detecting all AVA's [153]. Diagnosing that TTTS is present is usually achieved from the characteristic features of the fetuses: the recipient fetus will be larger and have an elevated level of amniotic fluid, whereas the donor fetus may have almost none, is lacking in nutrients and is usually smaller [156]. Where the imbalance between the fetuses is large often neither survives.

Arterio-arterial anastomoses are present in approximately 85% of monochorionic pregnancies, but are not necessarily associated with a negative outcome for the fetuses. Indeed there is some evidence that the existence of these anastomoses may be protective [25, 26], with a lower incidence of TTTS, and even if TTTS develops, a better survival than in the TTTS cases with only arterio-venous anastomoses [149, 151, 152]. The importance of AAAs has been recognised clinically and identical twins are already routinely scanned for their presence. The arterio-arterial anastomoses are easier to detect than AVAs and can be identified in the majority of monochorionic twins [25, 152]. Arterio-arterial anastomoses are thought to be protective because they provide a flow path for blood to transfuse from the larger fetus back into the smaller fetus [26]. From pressure considerations, in an AVA blood can only travel in one direction, whereas in an AAA blood can travel in either direction, thus balancing the system. In a typical arterio-arterial anastomosis an artery belonging to one fetoplacental circulation connects directly with an artery belonging to the other fetoplacental circulation and does not enter a cotyledon first. This usually occurs on the surface of the placenta and can often be seen by colour Doppler ultrasound or through an endoscope. The anastomosis connects the high pressure arterial systems of the fetuses and the blood in the anastomosis can travel in either direction depending on which fetus' blood is at the higher pressure at that moment in time and can have a significant effect on the waveforms. The waveforms in the arteries in the placenta of a healthy fetus are periodic and positive, therefore when two flows meet in opposite directions in an arterio-arterial anastomosis they produce a flow that oscillates between positive and negative velocity depending on the phase of the waves [154]. Typically the heart rates of the fetuses are different, which results in a wave pattern which is repeated periodically with a frequency dependent on the

difference in heart rates [154]. Venous-venous anastomoses are rare and maybe associated with a lower survival rate [26] and will not be considered here.

Surgical interventions are sometimes performed in an attempt to improve the outcome of fetuses that exhibit TTTS [156] and one type of intervention that has caused some controversy [35] involves laser ablation of anastomoses between the circulations and has had some recent success [80, 55]. However, the surgical interventions are not always beneficial and may actually be detrimental if indeed AAAs are protective and not all AVAs have been detected [156]. Therefore understanding the flow distributions in the placenta before decisions are made regarding surgical interventions would be of great benefit.

6.3 Casting the placentas

The placental topology and dimensions for the numerical model were obtained by casting placentas using plastic resin. In order to understand the circulatory system of each placenta both the arterial and venous systems of the placentas were cast. This section details the casting processes used for a typical placenta. The placental models were made by the following people from Imperial College London: Victoria Franke from the Aeronautical Engineering department, Professor Kim Parker and Nick Watkins from the Bioengineering department and Dr. Ling Wee from Queen Charlotte's hospital.

Within 1-2 hours following the delivery of the twin fetuses and the monochorionic placenta at Queens Charlotte's Hospital, London, the placenta is brought to the Bioengineering department for casting. A fresh placenta is shown in figure 6.1 (a). It can be seen that the placenta has two umbilical cords, one of which would have been attached to each fetus. The arteries and the veins on the surface of the placenta are not very clear and any connections could go unrecognised if only the surface of the placenta is visualised. Figure 6.1 (b) shows a close up of the umbilical cord joining the surface of the placenta.

In order to be able to inject the liquid plastic into the circulatory system of the placenta, cannulas are first inserted into the arteries and veins of the umbilical cords. Note each umbilical cord has two arteries and one vein. The largest possible sized

cannulas are inserted into the lumens, because this eases the process of injecting the liquid plastic. This can be very difficult, especially in the arteries, where the size of the artery lumen can be very small as a result of vasoconstriction. The cannulas inserted into the arteries are therefore much smaller than those inserted into the veins.

The difficulties of inserting the cannula into the lumen, which often cannot be seen, means that the umbilical cord typically needs to be cut down a little in order to find an entrance. Once the cannula has been inserted a little it still may not go further down the vessel, which can be due to the cannula splitting the vessel wall or going down a false passage.

Several techniques have been attempted in order to insert the cannulas further into the arteries:

1) Injecting a small amount of saline solution can often open up the artery lumen, if the saline does not enter easily the hole is unlikely to be the artery lumen;

2) The arteries are wrapped around the vein, so twisting the umbilical cord to straighten the arteries can often help the cannula slip into the artery;

3) Cutting between the arteries and veins to separate them helps, but this must be done very carefully so that the vessel walls are not compromised.

Once the cannulas are in place they need to be secured to ensure that they cannot fall out of the lumen. We have generally tied the cannulas to the umbilical cord with surgical thread to help keep them in place. A picture of three cannulas inserted into the two umbilical arteries and one umbilical vein is shown in figure 6.1 (e). Before tying them securely in place it is advisable to inject a small amount of saline to ensure that it goes down the vessels easily.

At this stage the main arteries and veins on the placenta surface are still full of blood, as can be seen in figure 6.1 (a). Blood clots are invariably present in the vessels, therefore saline is injected into the 6 cannulas before the liquid plastic, to help remove any clots which may have started to form in the vessels. The placenta with the arteries and veins filled with saline is shown in figure 6.1 (c).

Now that the cannulas have been inserted and tied into place, all the ingredients for the liquid plastic can be mixed together. There is only about 20 minutes to inject the liquid plastic once the ingredients have been combined before it begins to set, so

this should not be done before the placenta is completely ready. The ingredients for the plastic model have come from the Batson's No. 17 Plastic Replica and Corrosion Kit and is based on the procedure by Professor Batson [10]. The ingredients for the plastic model are a partially polymerised monomer, a catalyst and a promoter. More information on the exact proportions of the ingredients for the model and making the model can be found in [9]. The plastic models made from the kit are durable, do not shrivel and can capture the very small microcirculation in impressive detail. The resin was coloured to distinguish between the two fetoplacental circulations and the arterial (red and yellow) and venous (blue and green) systems. Colouring is particularly attractive for the circulatory system of monochorionic placentas as it will identify any arteries and veins which link the two fetoplacental circulations.

The liquid plastic is injected into the cannulas using disposable polyethylene syringes, figure 6.1 (f). The liquid plastic for the arterial side is usually inserted first. It can be seen in figure 6.1 (d) that the red liquid plastic in this placenta approached the other umbilical cord and therefore the artery probably connects with a vessel belonging to the other fetoplacental circulation. As the artery crossing over the equator of the placenta surface fills with plastic it is gently clamped, so that it does not fill too many of the vessels in the other fetoplacental circulation with the wrong coloured plastic, figures 6.1 (g) and 6.2 (h).

When as much red liquid plastic as possible has been injected into the placenta through both umbilical arteries then the top of the umbilical cord is clamped to stop the liquid plastic escaping. Note, as much liquid plastic is squeezed into the placentas as possible so we are able to capture the microcirculation, but unfortunately this means that the placentas will probably not be cast under physiological pressure. Next the other fetoplacental circulation has the yellow arterial liquid plastic injected into its umbilical arteries. Figure 6.2 (k) shows that a yellow artery does connect directly with the red artery that crossed over the equator. The clamp on this artery can now be removed so that there is a smooth connection. This is an arterio-arterial anastomosis, because an artery belonging to each fetoplacental circulation have joined together.

The liquid plastic is now injected into the venous side. It is easier to inject into the venous system, because the veins and thus the cannulas are larger. The placenta

shown in figure 6.2 (i) has both the arterial sides filled with resin and has the green resin in the venous side of the circulatory system, but no blue has been injected yet. The green liquid plastic has filled all the vessels on the yellow arterial side, but it is also starting to fill the vessels on the red arterial side belonging to the other fetoplacental circulation, indicating that an AVA is present.

After the liquid plastic has been injected into the green venous side, the umbilical cord is clamped and the blue liquid plastic is injected into the other umbilical vein. Figure 6.2 (m) shows the placenta with all the liquid plastic resin injected. It can be seen that the blue vein has now met with the green liquid plastic and therefore this is a venous-venous anastomosis.

Approximately 40 ml of red and 70 ml of yellow plastic was injected into the arterial circulations of this cast and 100 ml of blue and 120 ml of green plastic was injected into the venous circulations of the two fetoplacental circulations. More venous liquid plastic was injected because this filled the very small microcirculation and veins generally have more capacity than arteries.

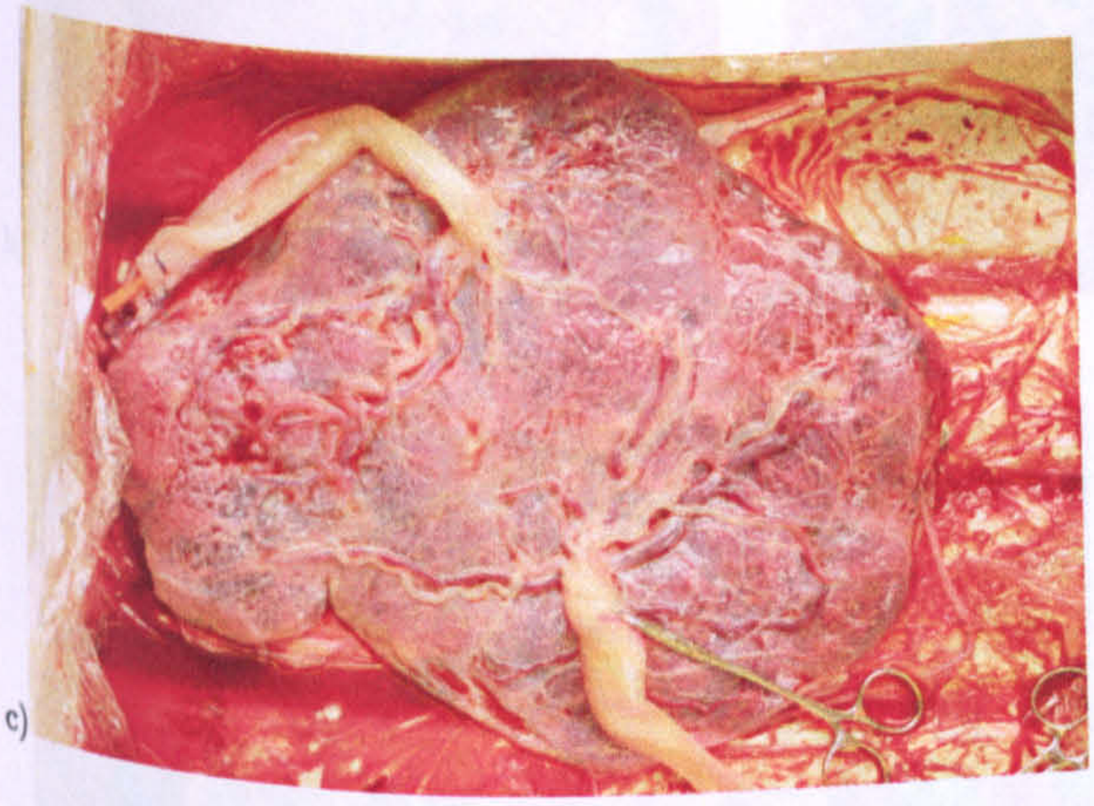
The placenta is now carefully placed in a basin where it is covered with approximately 1 litre of saline NaCl and the plastic is left to cure over night. The clamps remain on the umbilical cords during this time. Once the resin has cured the placenta is covered with 50 % hydrochloric acid (HCl) for several weeks to dissolve the surrounding tissue.

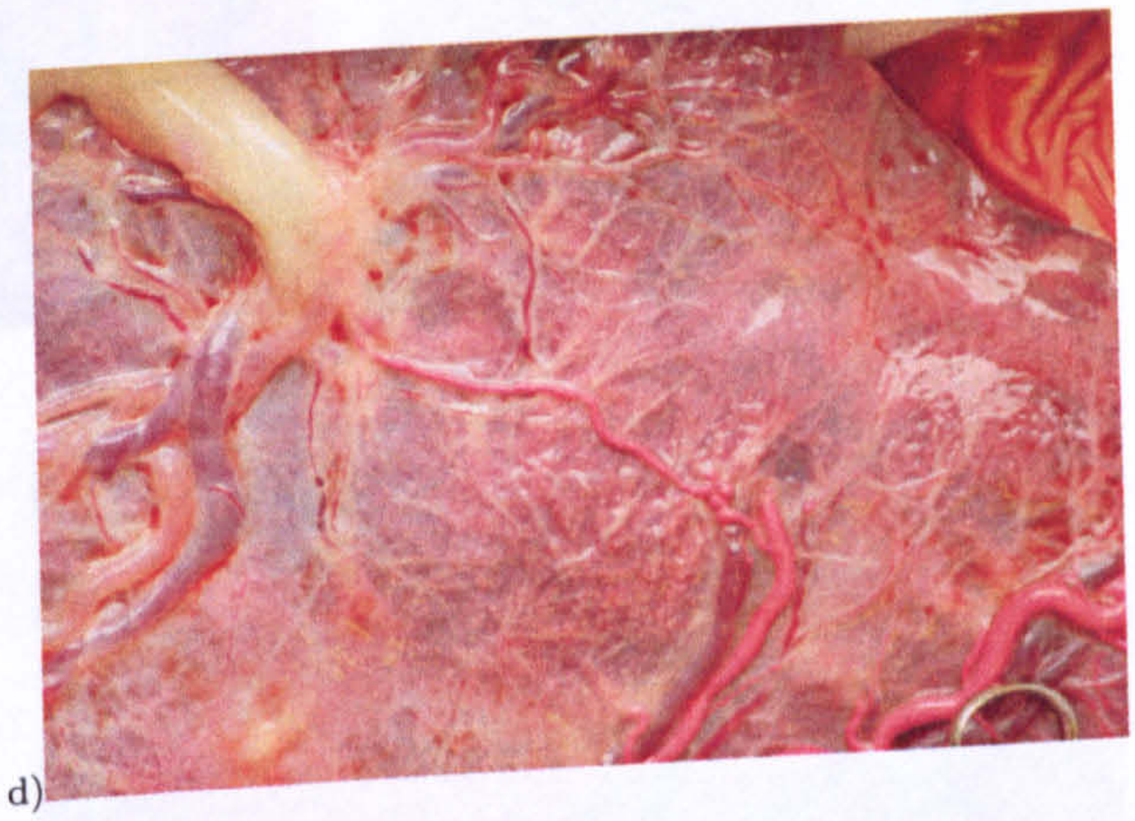
The placenta with the tissue removed is shown in figure 6.2 (n). Unfortunately, the AAA (yellow-red connection) was broken when the placenta was cleaned, but we do have a photographic record of before and after the surrounding tissue was dissolved and also a plastic model of this artery from which the geometrical data can be obtained.

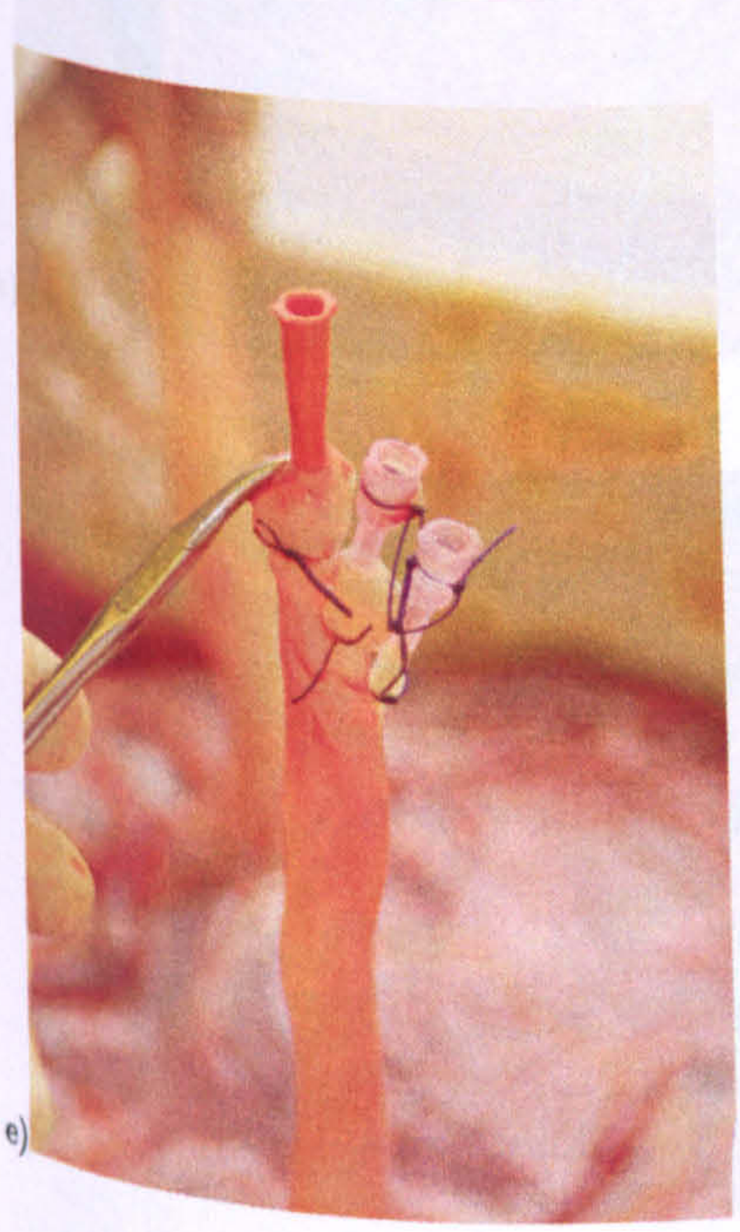
Previously, liquid dyes have been injected into placentas to show where connections occur. However, what is appealing about this method is that the circulation and microcirculation beneath the placental surface can be studied in more detail once the tissue is removed. For example figure 6.2 (l) shows that there is a connection from the green venous side to the blue venous side because one of the green veins is turning blue. This connection could not be seen on the surface of the intact placenta.













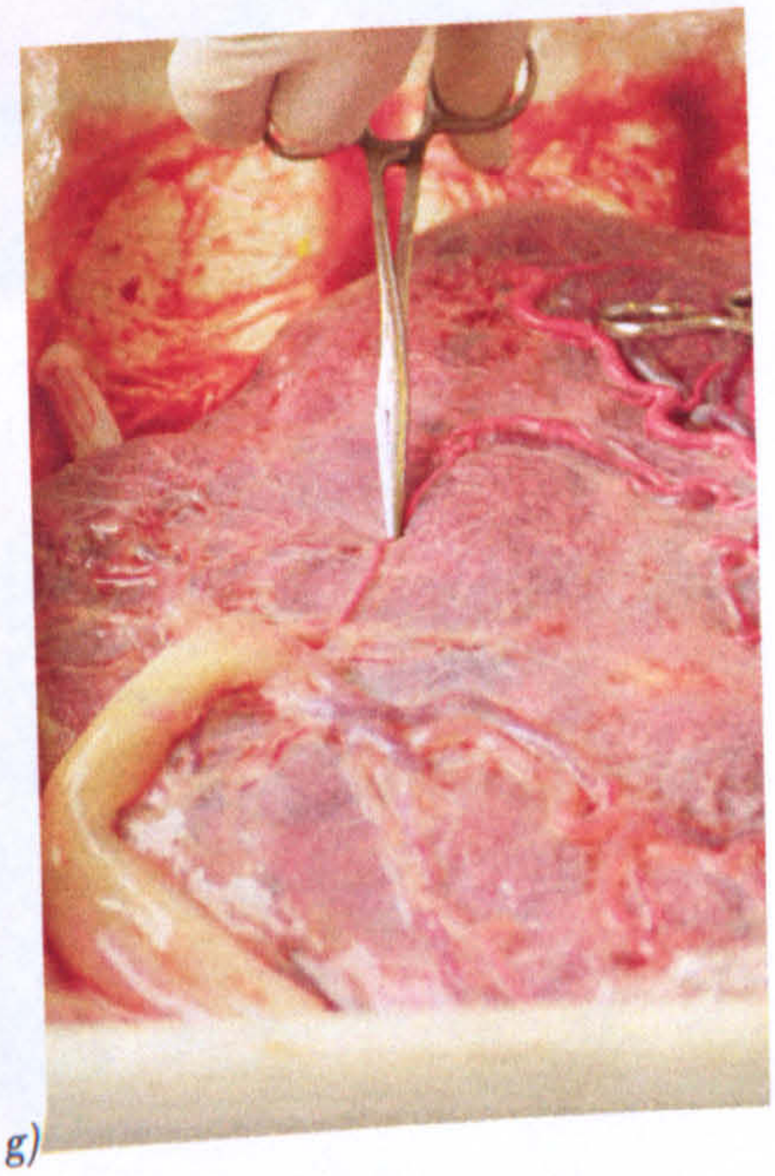


Figure 6.1: Photographs of the stages involved in casting a placenta. These images are for Placenta B. (a) The freshly delivered placenta, (b) close up of the surface of the placenta at the end of the umbilical cord, (c) vessels of the placenta flushed with saline, (e) cannulas tied in at the top of the umbilical cord, (f) injecting liquid plastic into the red artery, (d) red liquid plastic crossing over the equator of the placenta and (g) red artery is then gently clamped.

Figure 6.2: More photographs of casting a placenta showing (h) the surface of the placenta with the red artery gently clamped, (k) yellow liquid plastic meeting the red liquid plastic across the placenta's equator, (i) a vein on the other side of the network is also turning green, (j) injecting blue liquid plastic into a vein, (l) blue liquid plastic meeting the green liquid plastic, (m) the surface of the placenta with all the liquid plastic injected in and (n) the placenta once it has been dissolved using HCl for several weeks.

6.4 The plastic casts of the placentas

Altogether 6 monochorionic placentas and 1 dichorionic placenta have been cast. In this section a selection of pictures of the different placentas are shown and the fetoplacental circulations are briefly discussed. In all of the following placentas the red and blue represent the arteries and veins respectively of one fetus and yellow and green are the arteries and veins respectively of the other fetus.

6.4.1 Placenta A - large AAA

Pictures of placenta A before and after the surrounding tissue has been dissolved by hydrochloric acid are shown in figures 6.3 (a) and (b). Although, this placenta belonged to a pair of fetuses, that did not develop twin-to-twin transfusion syndrome (TTTS), there was discordant growth and the fetus on the left hand side was larger due to the intertwin transfusion. The arteries and veins of the left hand side of the placenta are coloured yellow and green respectively, the right hand system belongs to the smaller fetus and the arteries and veins are coloured red and blue.

In this particular system there is a very large arterio-venous anastomosis (red-green connection) from the smaller fetus' artery (red) via a cotyledon to the larger fetus' vein (green). There is also a large arterio-arterial anastomosis (red-yellow connection) present where blood can travel in either direction between the arterial circulations. It can be seen from figure 6.3 (a) that the two arteries meet on the surface of the placenta whereas the artery-vein connection cannot be seen on the surface and can only be seen once the surrounding tissue has been removed, figure 6.3 (b).

The characteristic features of fetoplacental circulations can also be seen in figure 6.3: the joining of the two umbilical arteries (red) and the presence of just one umbilical vein (blue). It can also be seen that the arterial system is usually formed on top of the venous system. An interesting feature of the patterns of veins and arteries that have developed is that the veins appear to have developed in straighter lines than the arteries, which are more tortuous.

6.4.2 Placenta B - medium AAA

Placenta B is shown in figure 6.4 before and after the surrounding tissue was dissolved and more photographs of this placenta can be seen in the previous section 6.3, because this was the placenta featured in the description of the casting processes.

The two sides of this placenta are connected by an arterio-arterial anastomosis with a medium sized cross-sectional area, that is relatively small compared with the previous case. The arteries connect directly on the surface of the placenta, this is seen as the red-yellow connection in figure 6.4 (a). Due to the fact that a vein on the blue venous side also appears green we know that there is also a venous-venous anastomosis. This connection cannot be seen on the surface in figure 6.4 (a) but once the tissue has been removed it can be seen that the veins are both connected to the same cotyledons. A red artery, which is of similar size, also follows the blue vein to this same cotyledon, which probably helps the balance of the two fetoplacental circulations. Blood from the yellow arterial system may join either circulation and could lead to an imbalance in the system if it were to enter the blue system, but blood from this red artery may also enter the blue or the green venous system and assist in balancing the systems. This anastomosis may also be considered as two linked arterio-venous anastomoses.

Observing the patterns of the arterial and venous systems, the branches in the venous system appear straighter and the arteries once again appear to wind around more. However, for this placenta the large arteries appear to follow the veins closely. In contrast, looking back at placenta A, figure 6.3 (b), the arteries and veins do not follow the same paths. This is interesting because the fetuses which belonged to placenta B were of similar sizes, and arteries and veins of similar sizes appear to join cotyledons together. Whereas for placenta A, where the fetuses were of very different sizes and therefore were at more risk of developing TTTS, the arteries and veins from the same fetoplacental circulation do not follow one another and appear to connect randomly with the other fetus' circulation system, hence the large arterio-venous anastomosis and the arterio-arterial anastomosis.

6.4.3 Placenta C - small AAA

The photographs for placenta C are shown in figure 6.5. Again the twin fetuses were thought to have been of similar sizes and did not develop TTTS. This placenta has a very small diameter arterio-arterial anastomosis. Figure 6.5 (b) shows a close up of this arterio-arterial anastomosis (red-yellow connection) and there are no other obvious connections in figure 6.5 (a). In the close up of the arterio-arterial anastomosis, figure 6.5 (b), there does appear the possibility that there are connections of the very small yellow arteries with the blue microcirculation of the other fetoplacental circulation. These may be very small arterio-venous anastomosis and of course these would not be detected from the surface of the placenta. Although these small arteries may go to the blue cotyledon, the main yellow artery which they have branched off from does connect correctly to a green cotyledon. If there are any very small arterio-venous anastomoses the transfusion of blood from the yellow arterial system to the blue venous system is probably extremely small. Any small transfer can probably be compensated by the presence of the AAA, where the flow can travel in either direction. Again the veins in this network appear to have developed as relatively straight vessels, whereas the arteries are again not as straight, but do follow the direction of the veins more closely than for placenta A. The AAA is surprisingly long considering its very small cross-sectional area and it appears to cross the equator of the placenta in isolation.

6.4.4 Placenta D

Figure 6.6 shows a picture of placenta D once the surrounding tissue has been dissolved. This placenta has a medium sized arterio-arterial anastomosis (red-yellow connection). It also appears to have some small red and blue vessels at the equator that join to a yellow-green cotyledon, which was not apparent on the surface of the placenta when the surrounding tissue was present.

6.4.5 Placenta E

Placenta E is shown in figure 6.7 before the surrounding tissue is dissolved. This too has a medium sized arterio-arterial anastomosis visible on the surface of the

placenta. There is also a single arterio-venous anastomosis between the red arterial side and the green venous side, which was only visible once the surrounding tissue was removed.

6.4.6 Placenta F

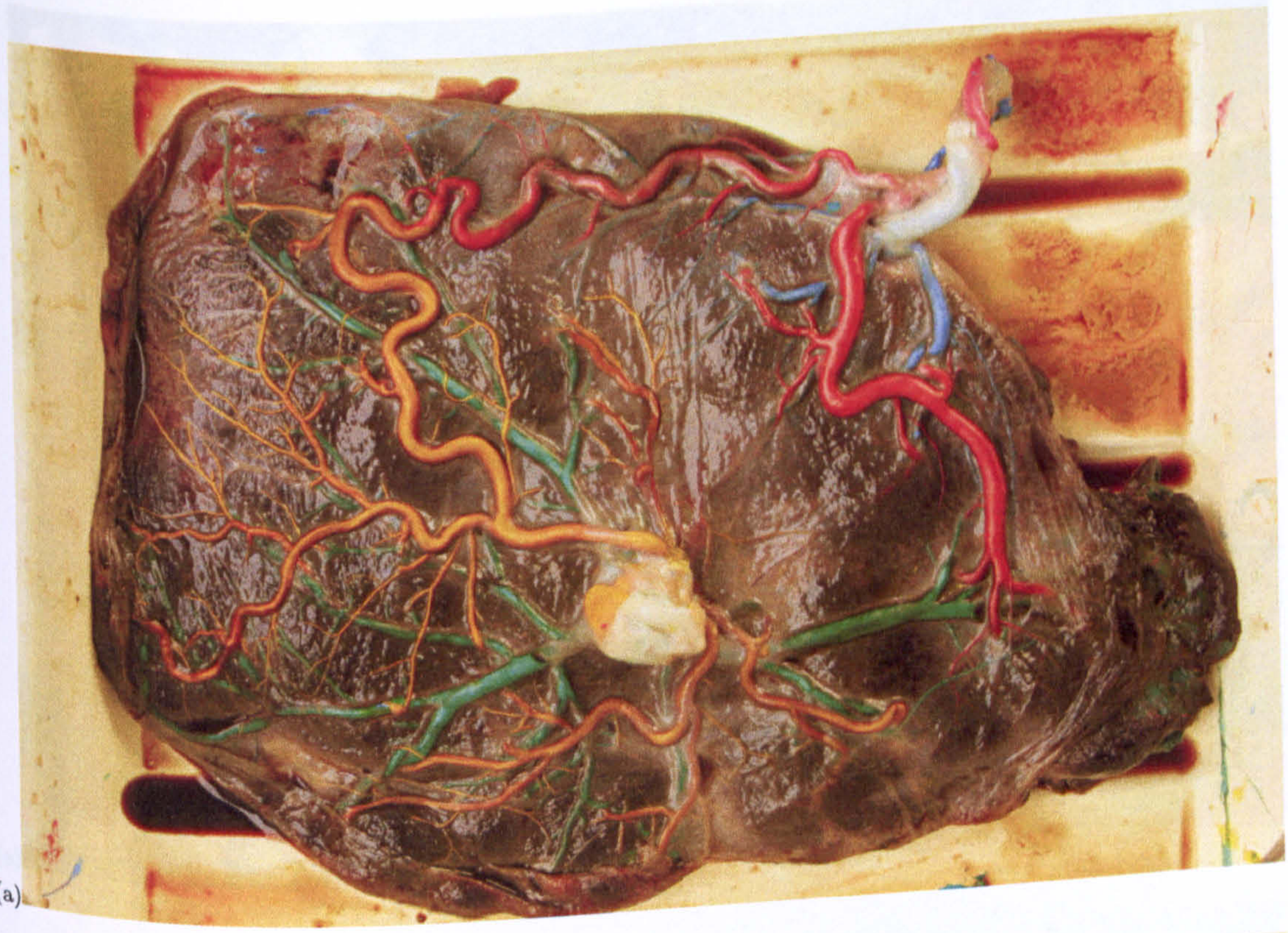
The photographs for placenta F are shown in figure 6.8. The circulatory system for this monochorionic placenta is different to the others in that it is very complicated and there are many connections between the two fetoplacental circulations. The two umbilical cords are extremely close together and it is difficult to distinguish between the two fetoplacental circulations. There is one very large arterio-arterial anastomosis, which is obvious on the surface of the placenta. There is also a very large venous-venous anastomosis, where two veins actually directly connect into each other, rather than through a cotyledon. This was also obvious from the surface of the placenta and is a rare feature. The red arteries may connect with veins at cotyledons which belong to the other fetoplacental circulation, forming an arterio-venous anastomosis. The blood for these two fetuses undoubtedly must get mixed together and perhaps is more like a single circulatory system, than two connected systems.

6.4.7 Placenta G

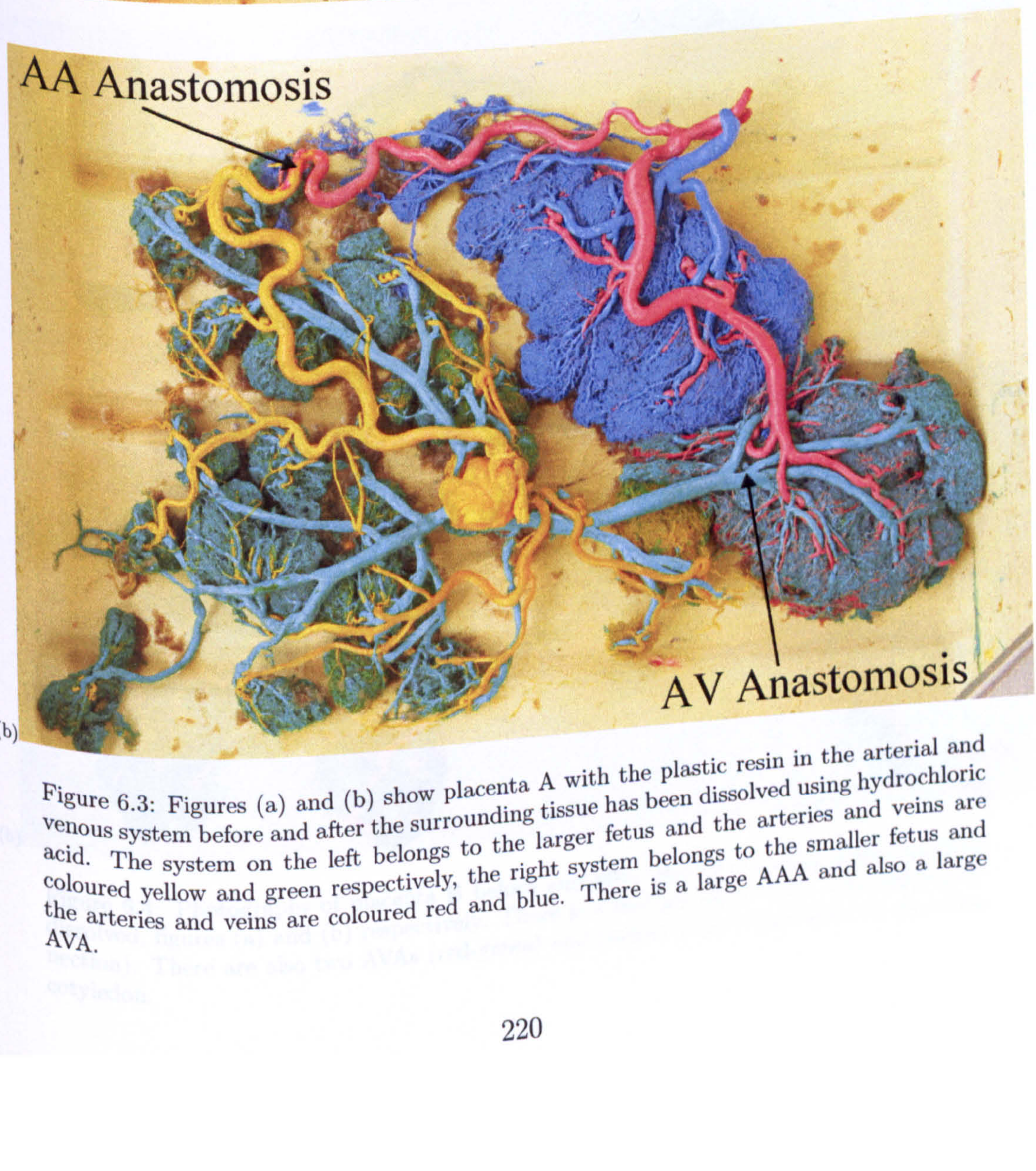
Placenta G is a dichorionic placenta, which means that there are two chorions, one surrounding each circulation, and the two fetoplacental circulations are separate, as shown in figure 6.9. Similar to the previous placenta, F, the two umbilical cords are very close to each other and it can be seen that the arteries from the two circulatory systems run parallel to one another and almost touch, but they never join. The presence of the two chorions ensures that there are no connections between the two fetoplacental circulations, which is fortunate because if this was a monochorionic system, the close proximity of the two umbilical cords means that there could well have been significant connections between the two circulatory systems as in placenta F.

6.4.8 Summary of cast placentas

What is interesting about these plastic models of the placental circulations is that they are all so very different. Unlike the human arterial tree, there is no significant repeated pattern of the arteries. Arteries often appear to follow veins to a cotyledon, but for the case where there was a very large AVA and large AAA the arteries did not follow the veins. Another feature is that the arteries are more tortuous than the veins which appear to be quite straight. All possess Hyrtyl's equilibrating anastomosis where the two umbilical arteries join and most arteries develop above the veins on the surface of the placenta.



(a)



(b)

Figure 6.3: Figures (a) and (b) show placenta A with the plastic resin in the arterial and venous system before and after the surrounding tissue has been dissolved using hydrochloric acid. The system on the left belongs to the larger fetus and the arteries and veins are coloured yellow and green respectively, the right system belongs to the smaller fetus and the arteries and veins are coloured red and blue. There is a large AAA and also a large AVA.

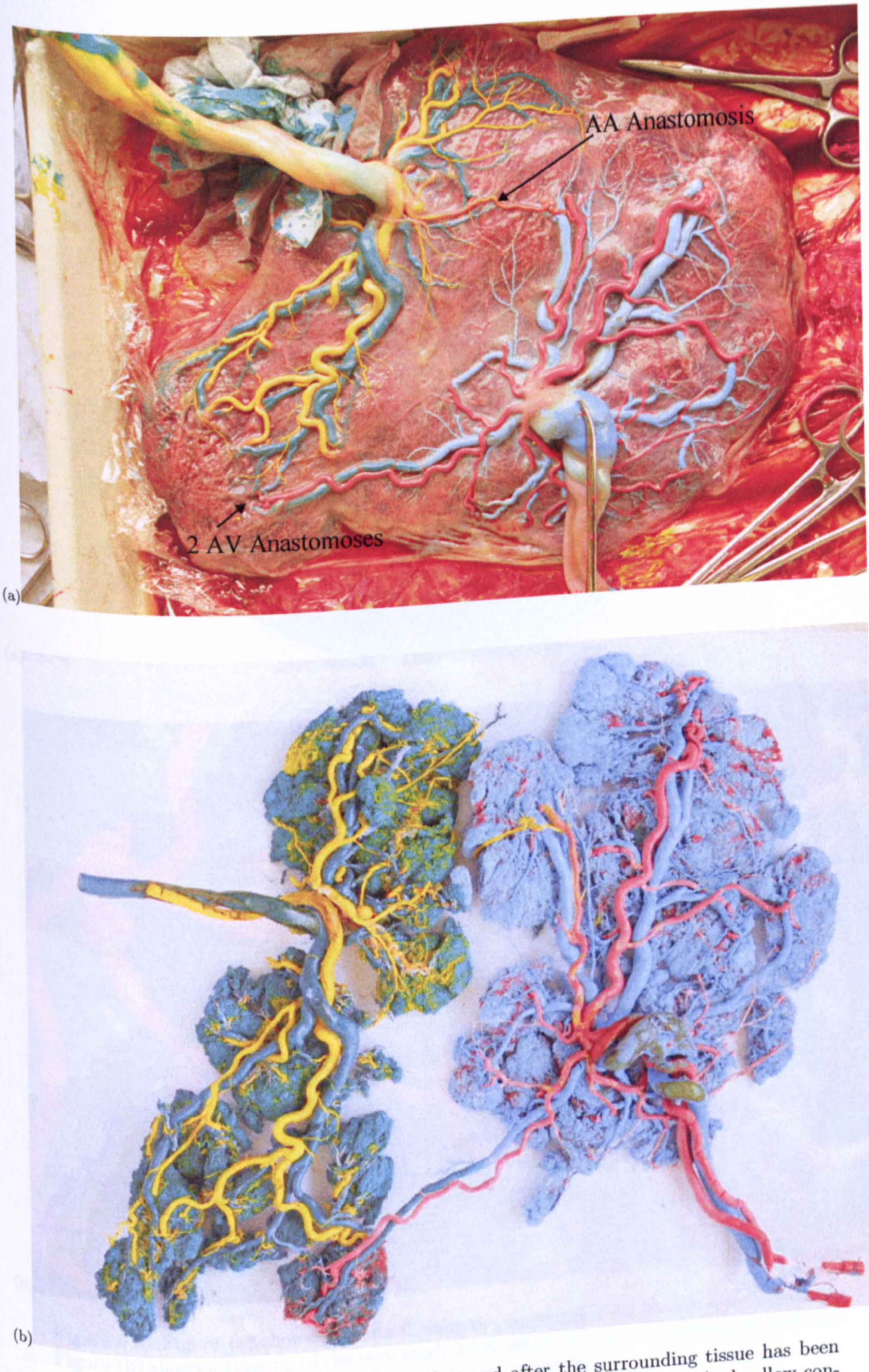
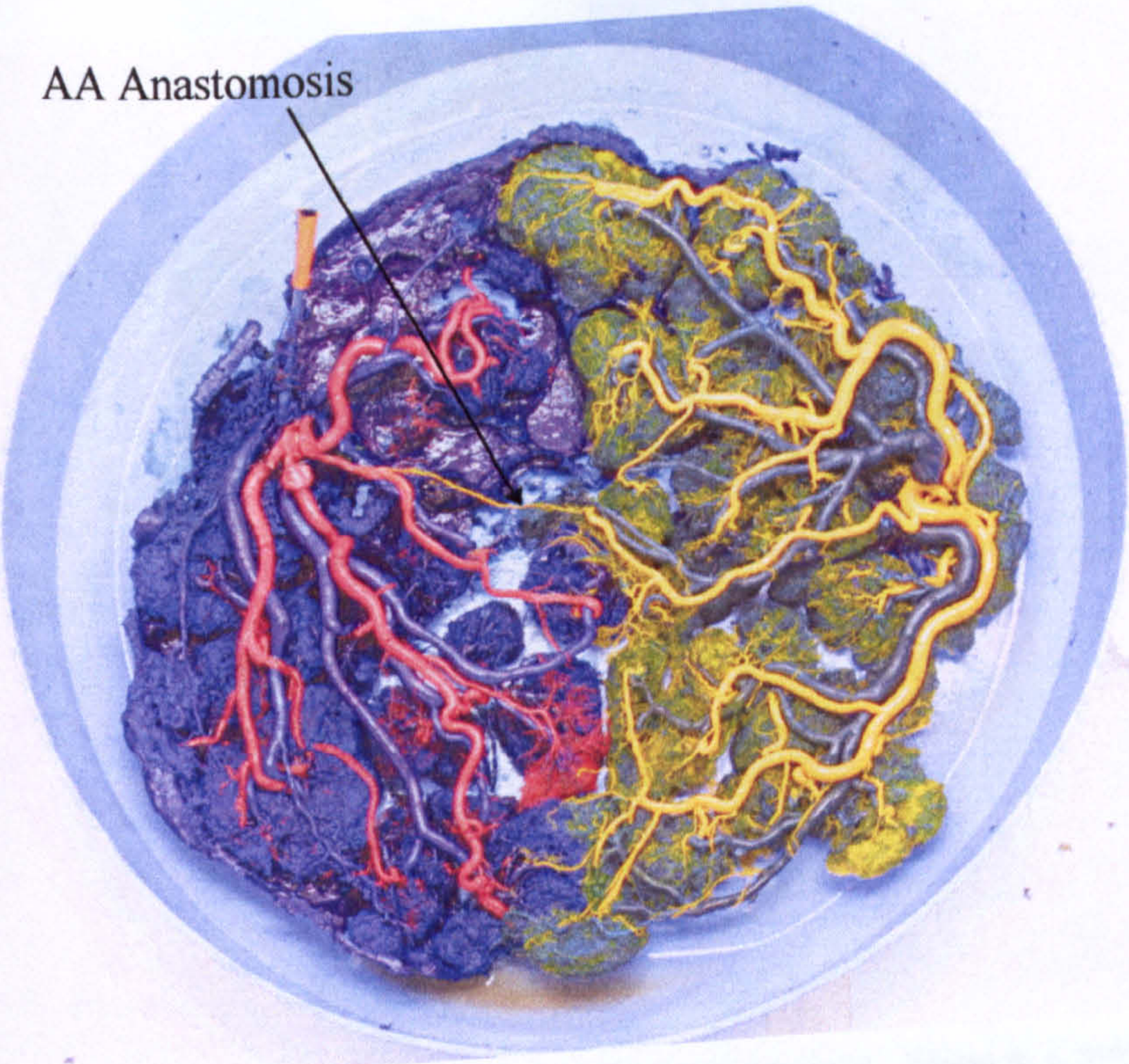
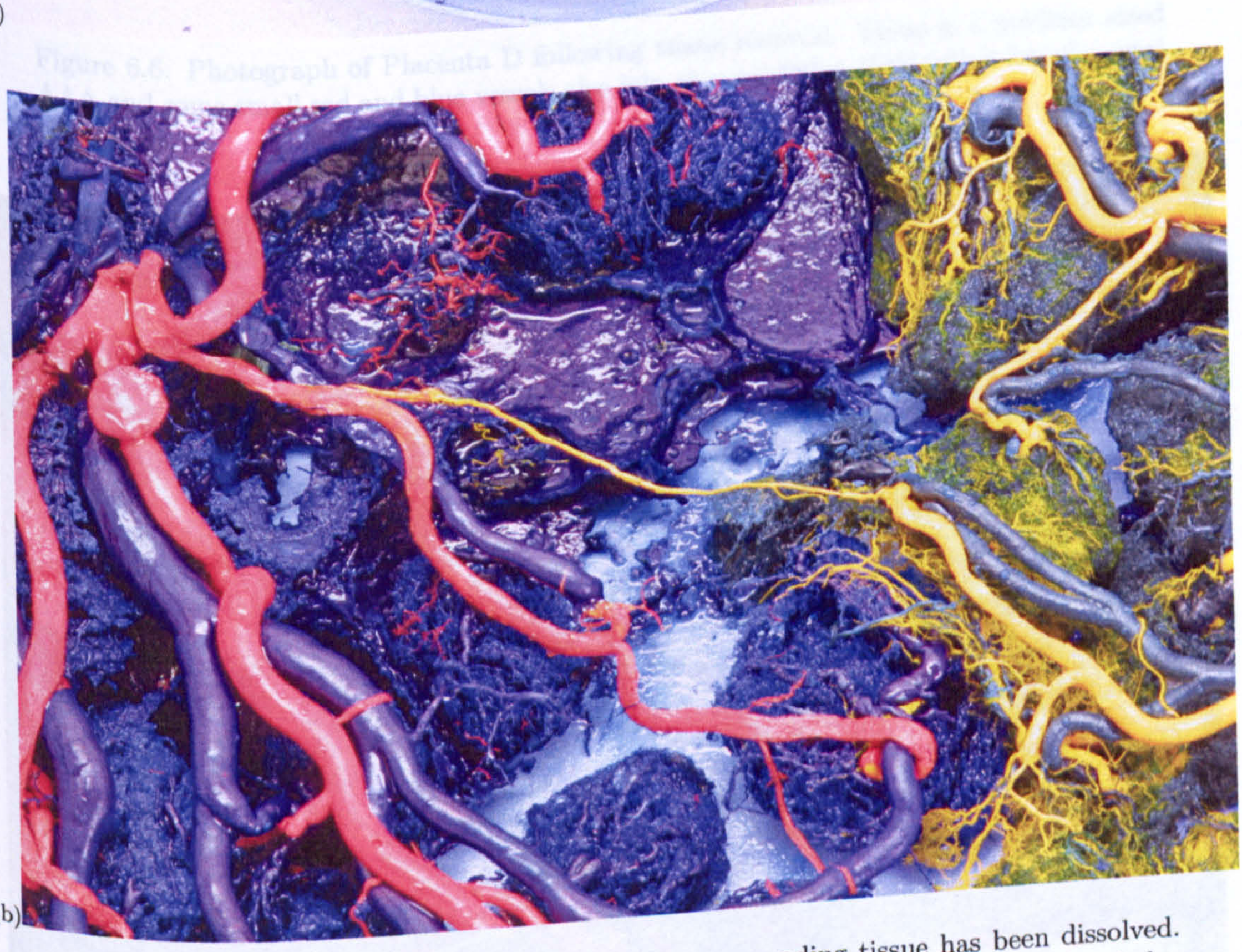


Figure 6.4: Photographs of placenta B before and after the surrounding tissue has been dissolved, figures (a) and (b) respectively. There is a medium sized AAA (red-yellow connection). There are also two AVAs (red-green) and (yellow-blue) which meet at the same cotyledon.



(a)



(b)

Figure 6.5: Figure (a) shows placenta C once the surrounding tissue has been dissolved. Figure (b) shows a close up of the very small AAA, which this placenta possesses, and also details of the microcirculation, which has been cast successfully.

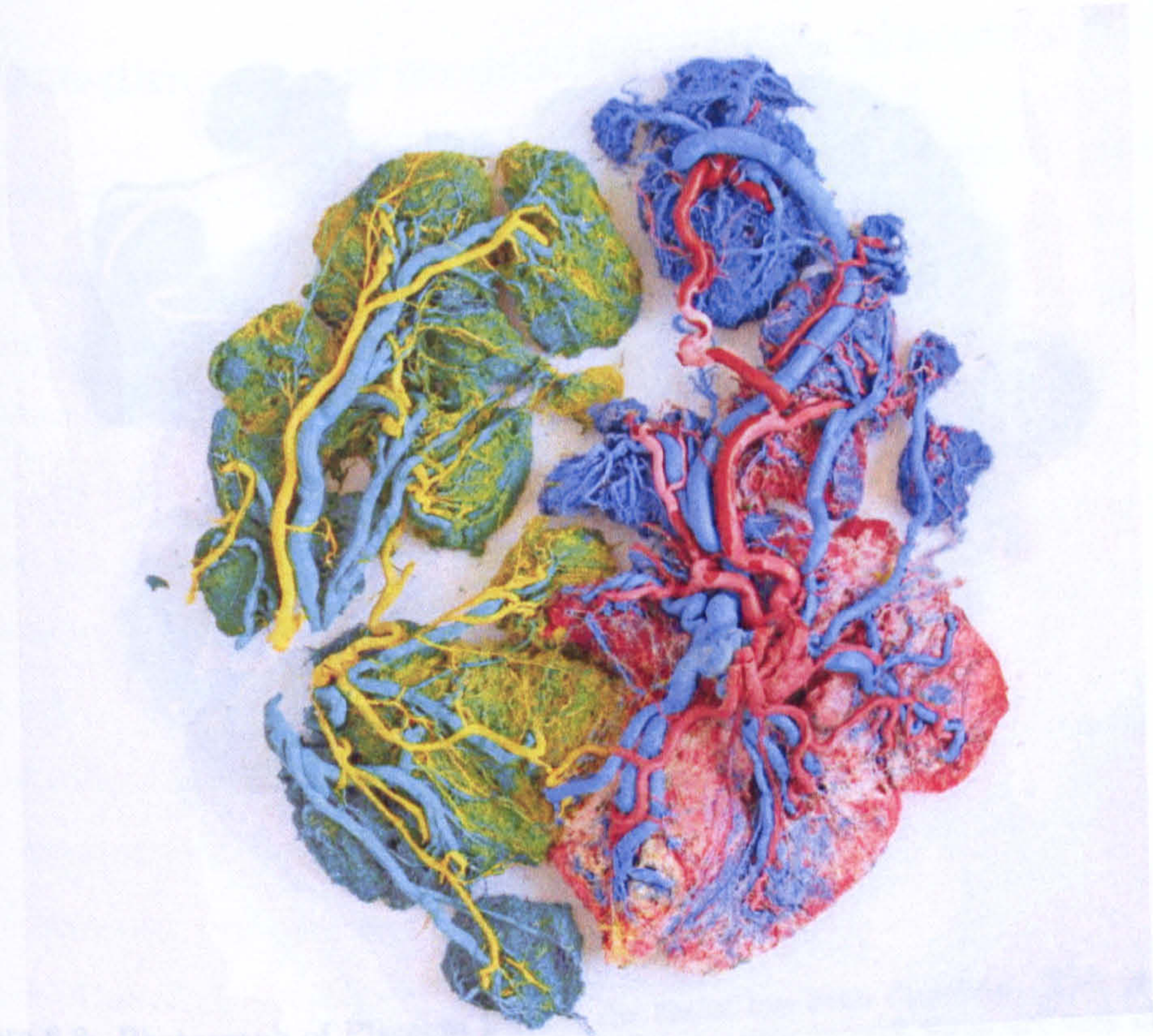


Figure 6.6: Photograph of Placenta D following tissue removal. There is a medium sized AAA and some small red and blue vessels also join at a cotyledon of the other fetoplacental circulation.

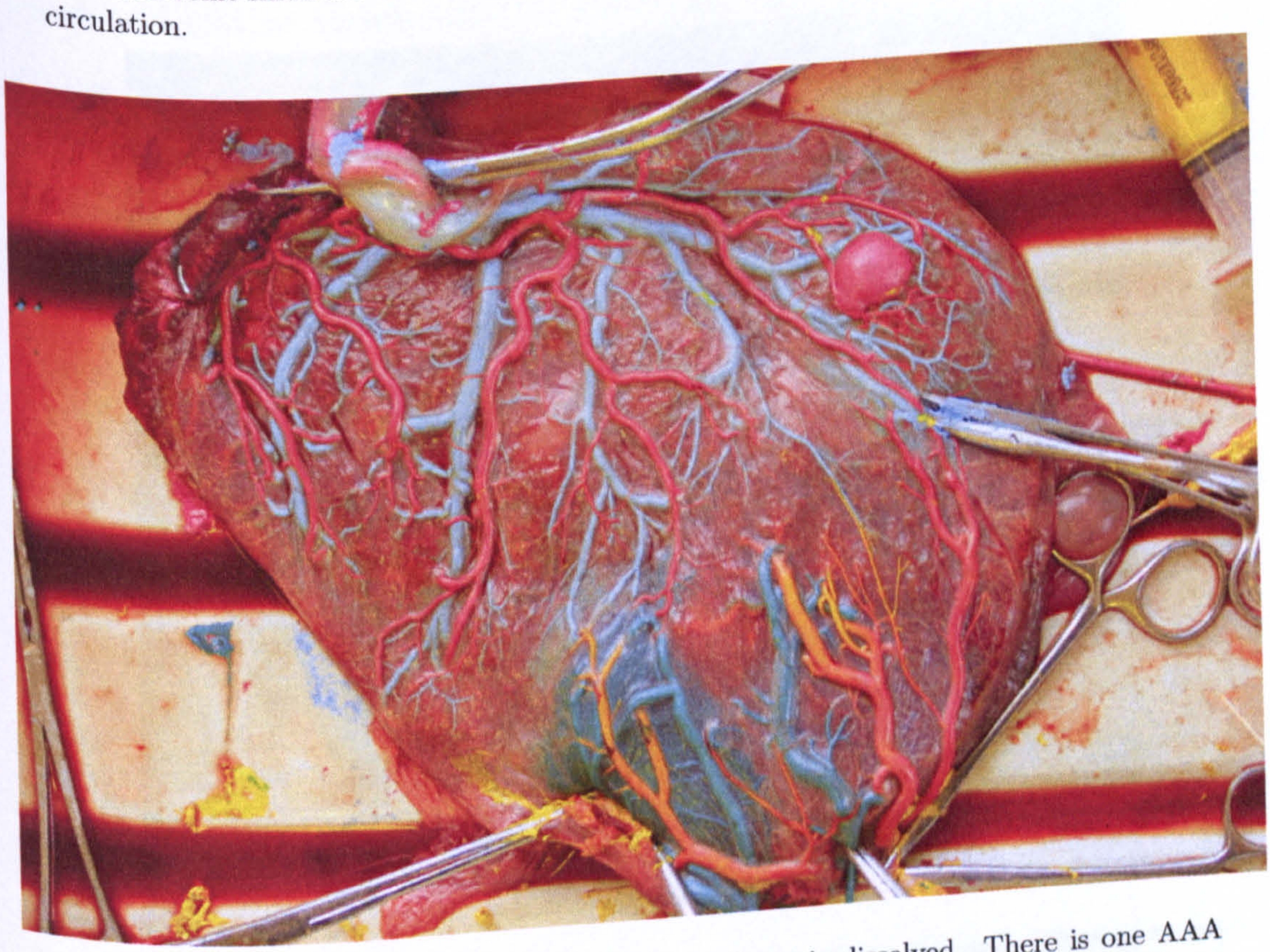


Figure 6.7: Photograph of Placenta E before the tissue is dissolved. There is one AAA visible on the surface and an AVA (red-green connection) was also identified once the tissue was removed.

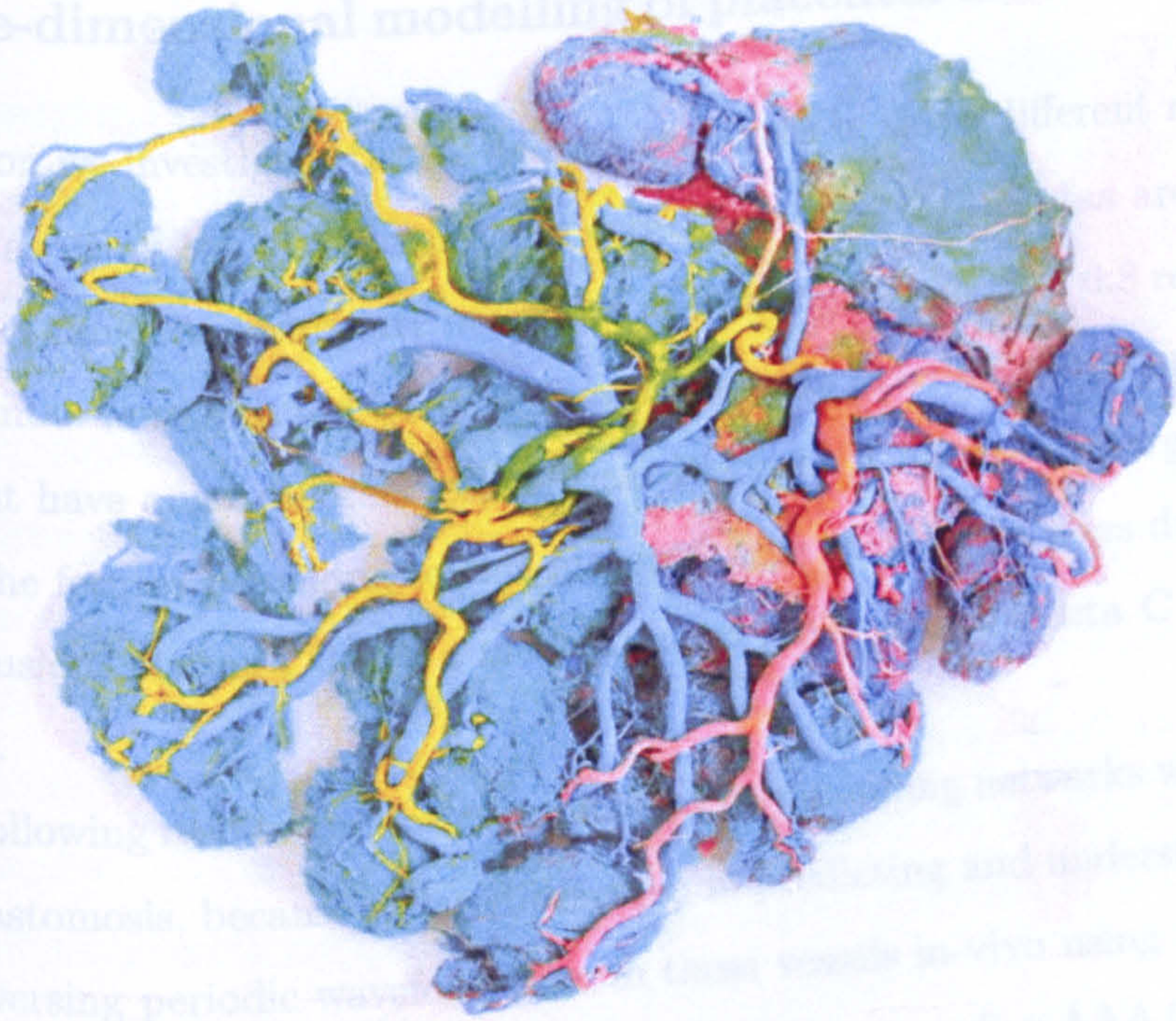


Figure 6.8: Photograph of Placenta F after the tissue has been dissolved. This is also a monochorionic placenta, but the umbilical cords belonging to each fetus are very close to each other. There are many connections between the two circulatory systems and it is difficult to distinguish between them.

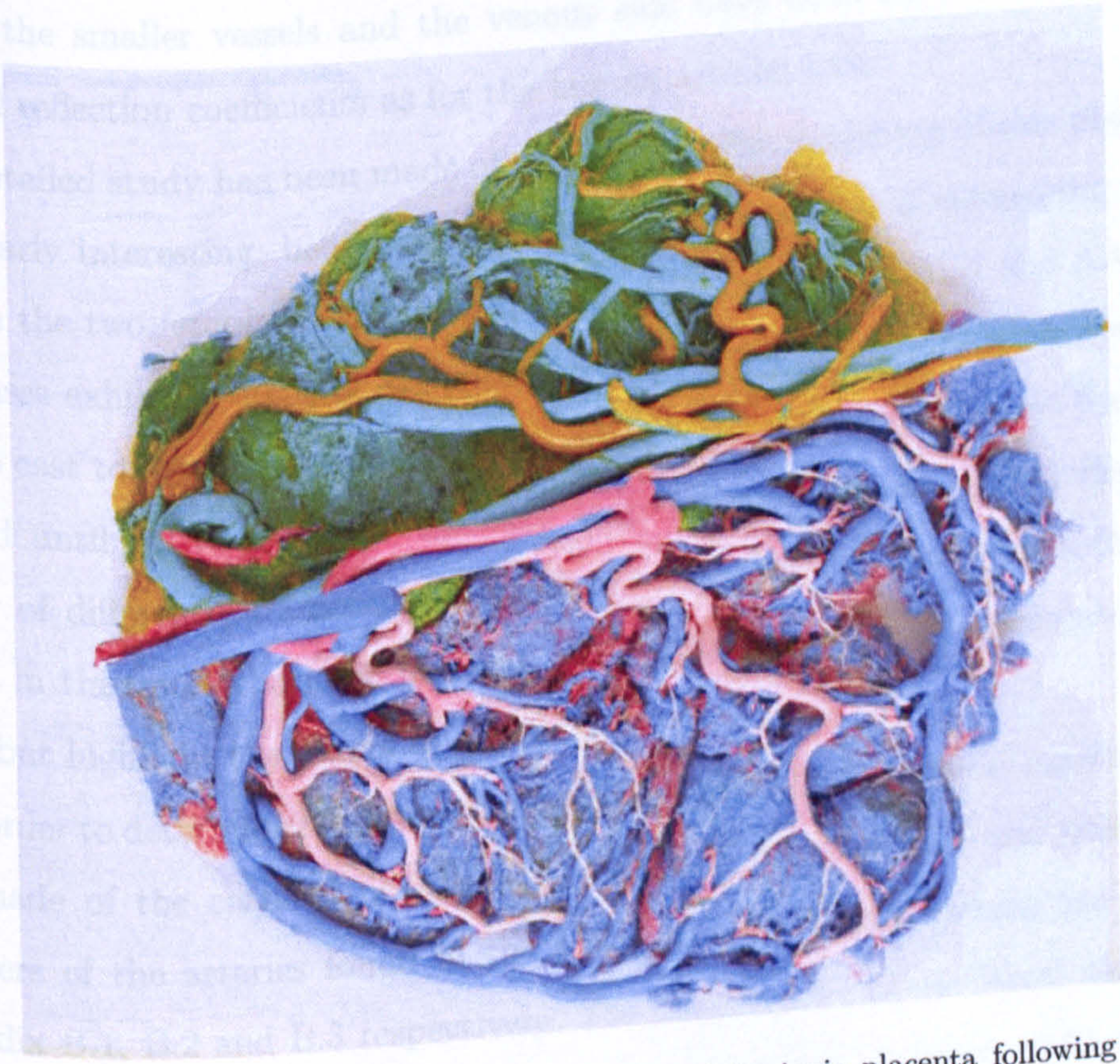


Figure 6.9: Photograph of Placenta G, which is a dichorionic placenta following tissue removal. The arteries and veins from each fetoplacental circulation are extremely close to each other but they never meet.

6.5 One-dimensional modelling of placental arterial networks

In this section we investigate the waveforms and flows in three different monochorionic placentas using the one-dimensional code. The chosen placentas are A, B and C (section 6.4) and the results are presented in sections 6.6, 6.7 and 6.8 respectively. These placentas were selected because they all contain arterio-arterial anastomoses (AAA's) but have quite different geometries. Placenta A has a very large diameter AAA and the fetuses belonging to this placenta were of different sizes due to inter-twin transfusion, placenta B has a medium sized AAA and placenta C has a very small AAA.

In the following results we have concentrated on modelling networks with arterio-arterial anastomosis, because we are interested in predicting and understanding the unusual reversing periodic waveform seen in these vessels in-vivo using Doppler ultrasound. Also clinicians are of the opinion that the presence of an AAA is protective and would like to understand the fluid dynamics of the system better both in general and also in specific cases (section 6.2). We have modelled only the major arterial vessels, the smaller vessels and the venous side have been modelled by applying terminal reflection coefficients as for the human arterial tree.

A detailed study has been made of placenta A. The modelling of this placenta is particularly interesting, because it has quite an extreme set of connecting arteries between the two fetoplacental circulations (i.e. the very large AVA and AAA) and the fetuses exhibited signs of discordant growth. This case is therefore the closest of those cast to having developed twin-to-twin transfusion syndrome yet the fetuses survived until delivery despite the very large interconnections. The effects of a number of different parameters on the flow waveforms and the volume fluxes are studied in this monochorionic placenta. The other placentas are examined in less detail, but highlight the effects of geometry.

In order to determine the geometry of the computational domains, measurements were made of the casts of placentas A, B and C to determine the lengths and diameters of the arteries found in the placental circulations, details are given in Appendix B.1, B.2 and B.3 respectively. The connectivity of the blood vessels was also observed and the computational networks are shown in figures 6.10, 6.22 and

6.25. In common with the previous modelling, several assumptions have been made in order to compute the waveforms in the placental arterial circulation, however we know even less about the wall properties for these networks. As far as we are aware, there is no published data on the mechanical properties of the large arteries in the placenta, we have therefore constructed our networks on the assumption that they have similar properties to similar sized vessels in the systemic arteries of a human. The wall thicknesses of the arteries in the placenta are taken to be 10 percent of the vessel radius and the Young's modulus, E, is assumed to be 400 kPa throughout. The terminal resistance in the placenta is thought to be low [95], so we have initially modelled the system with zero terminal resistance. The density of blood is assumed to be 1021 kg/m^3. The input wave was imposed by specifying the W_1 characteristic at the umbilical arteries making this boundary a pure absorber. An inflow profile of a half sine squared wave was applied for half a period, i.e.

$$W_1 = u_0 + 4\sqrt{\frac{\beta}{2\rho}}(A_l^{1/4} - A_0^{1/4}) \tag{6.1}$$

where

$$A_l = \begin{cases} A_0 + \Delta A_{lmax} \sin^2\left(\frac{\pi t^*}{0.25}\right) & 0 < t^* < 0.25 \\ \\ A_0 & 0.25 < t^* < T \end{cases}$$

where t^* is the time within the cycle given by $t^* = t - (cycle * T)$, T is the period for one cycle, *cycle* is the cycle number of the periodic input, u_0 is a reference initial velocity, A_0 is the initial value of the area of the umbilical artery (appendix B.1) and ΔA_{lmax} is the maximum change in area for the W_1 characteristic, A_l, and is calculated from the desired change in pressure from equations (2.98) and (2.100) from section 2.6.1.

The period for the calculations is around 0.5 s, which corresponds to a heart rate of 120 b.p.m. and the aortic valve is modelled to be open for 0.25 seconds. In a normal fetus the heart rate is typically in the range of 110 b.p.m. to 150 b.p.m., considerably higher than that in an adult. As our modelling is for a fetus close to delivery we have chosen a value towards the lower end of this range, because the rate tends to decrease with gestational age. The change in pressure over the waveform has been taken as 800 Pa. As discussed, a terminal reflection coefficient, R_t, was

applied at the ends of the arterial tree, where a value of $R_t = 0$ implies a completely absorbing boundary and a value of $R_t = 1$ implies a pure reflector.

The reflection coefficients at the bifurcations for forward travelling waves have been calculated using linear theory and are shown in the tables of data in the Appendix. For this particular network the equation to calculate the reflection coefficients at the bifurcations for forward travelling waves can be simplified to equation (6.2) because we have assumed that density, ρ and wave-speed, c, are constant throughout the placenta.

$$R_c = \frac{A_0 - A_1 - A_2}{A_0 + A_1 + A_2} \tag{6.2}$$

6.6 A detailed study of placenta A

We first apply the one-dimensional model to the calculation of waveforms in placenta A, which is described in more detail with photographs (figure 6.3) in section 6.4. Placenta A is of great interest due to the very large AAA (red-yellow connection) and AVA (red-green connection).

Figure 6.10 shows the connectivity of the major arteries of the placenta used for the numerical model in schematic form and for convenience is at a similar orientation to the placenta in figures 6.3(a) and (b). The measured data for these arteries of placenta A is presented in Appendix B.1.

The pairs of umbilical arteries belonging to the two fetuses are arteries 1 & 3 and 12 & 14 and arteries 2 and 13 represent the umbilical artery anastomoses (Hyrtyl's equilibrating anastomoses). Unfortunately, when casting the placentas, the umbilical cord for the left hand side fetus had to be cut down due to the difficulties described in section 6.3, so we were unable to cast the umbilical arteries belonging to this fetus. We therefore used the measurements of the umbilical arteries from the right hand side fetus for both systems. The inputs to the system are through these umbilical arteries.

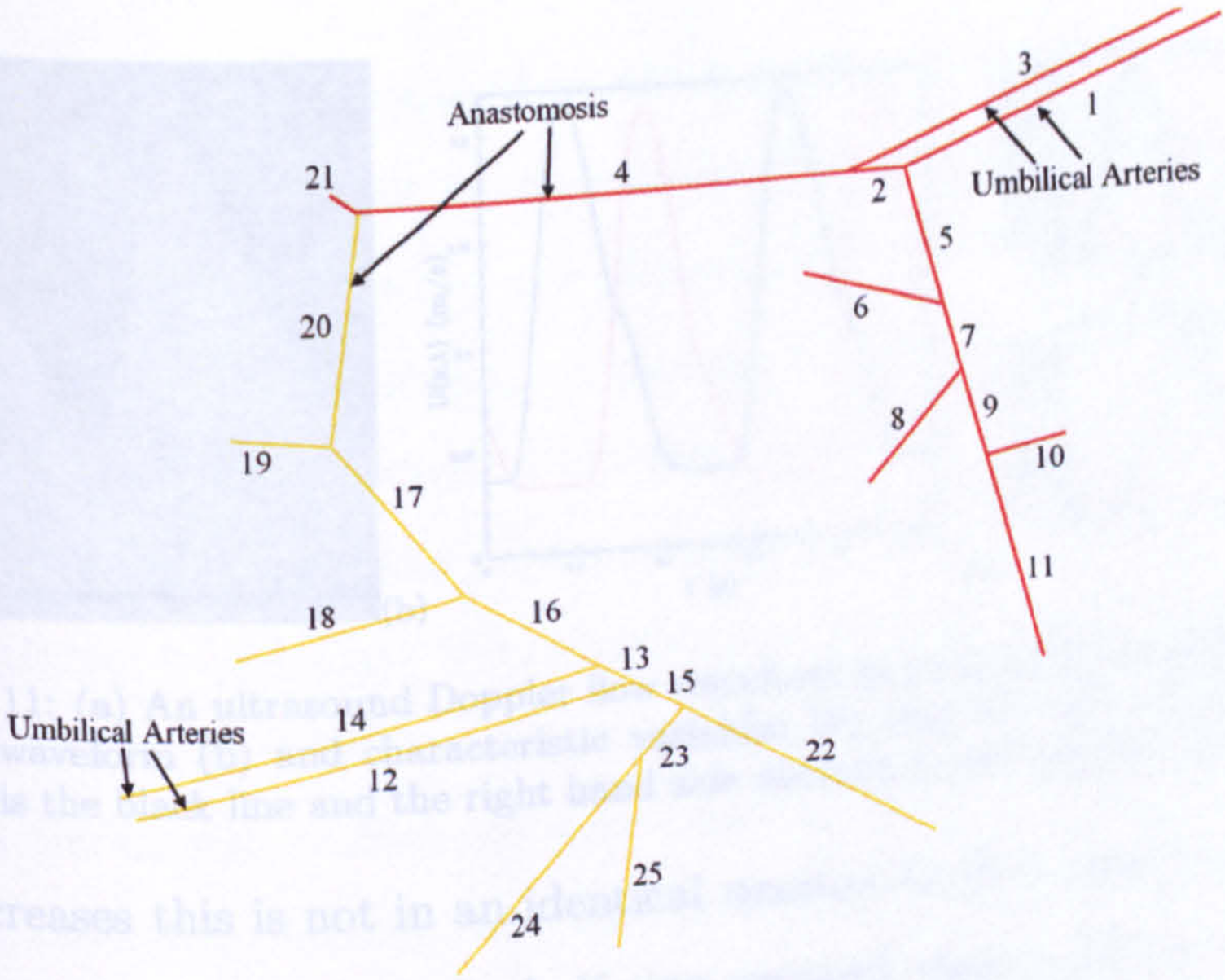


Figure 6.10: Schematic showing the connectivity of the arterial intertwin placenta network of placenta A.

6.6.1 Single placenta waveforms

Before analysing a monochorionic placenta with anastomoses, it is instructive to consider the waveforms found in a normal placenta, where in a healthy fetus the velocity waveform in the umbilical arteries is typically of the form shown in figure 6.11 (a). To examine the properties of this placenta we have first modelled the intertwin network as two separate systems using equation (6.1) as the input. To produce two separate systems we have used the two fetoplacental circulations shown in figure 6.10 but have not connected arteries 4 and 20 at artery 21, therefore no anastomoses are present and the networks can be considered as a pair of single placentas. This allows comparisons to be made between the numerical results and those observed in a healthy fetal circulation of a single placenta, figure 6.11, as well as the intertwin network.

Figures 6.11(b) and (c) are velocity waveforms for the two unconnected systems at the mid-point of umbilical arteries 1 (red line) and 12 (black line). The input time period in the left hand side network has been set as $T = 12/23$ which is equivalent to 115 b.p.m. and the heart rate in the right hand side network is 120 b.p.m.. The velocity waveforms are shown in figure 6.11(b) and similarities are seen with the clinical results in figure 6.11(a). The flow is periodic and mono-directional i.e. no negative flow, but although in our results the velocity does decline more slowly

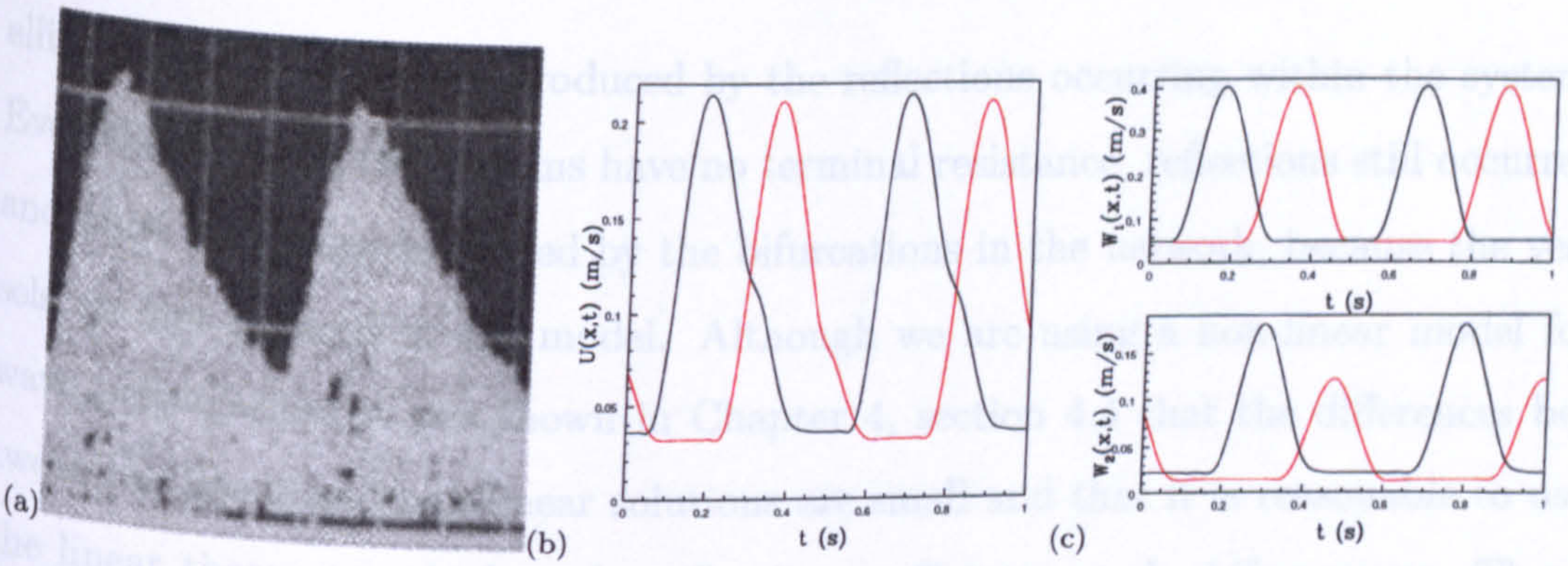


Figure 6.11: (a) An ultrasound Doppler flow waveform in an healthy fetus [95]. Calculated velocity waveform (b) and characteristic variables W_1 and W_2 (c). The left hand side network is the black line and the right hand side network is the red line in the plots.

than it increases this is not in an identical manner to that seen in a healthy fetus. This is not unexpected since the half sine squared wave used as the input to the system is only an approximation to the physiological conditions. However, as we do not know the physiological waveform for these cases and they will vary from placenta to placenta we will continue to use this simplified input waveform, because we believe that it captures most of the relevant physiological features. We have also investigated a number of different input waves and the results are all similar. The fact that these networks are actually two parts of a joined placenta may also mean that the waveforms do not correspond exactly to a healthy waveform, because these placental arterial systems may have developed slightly differently due to the presence of the anastomoses.

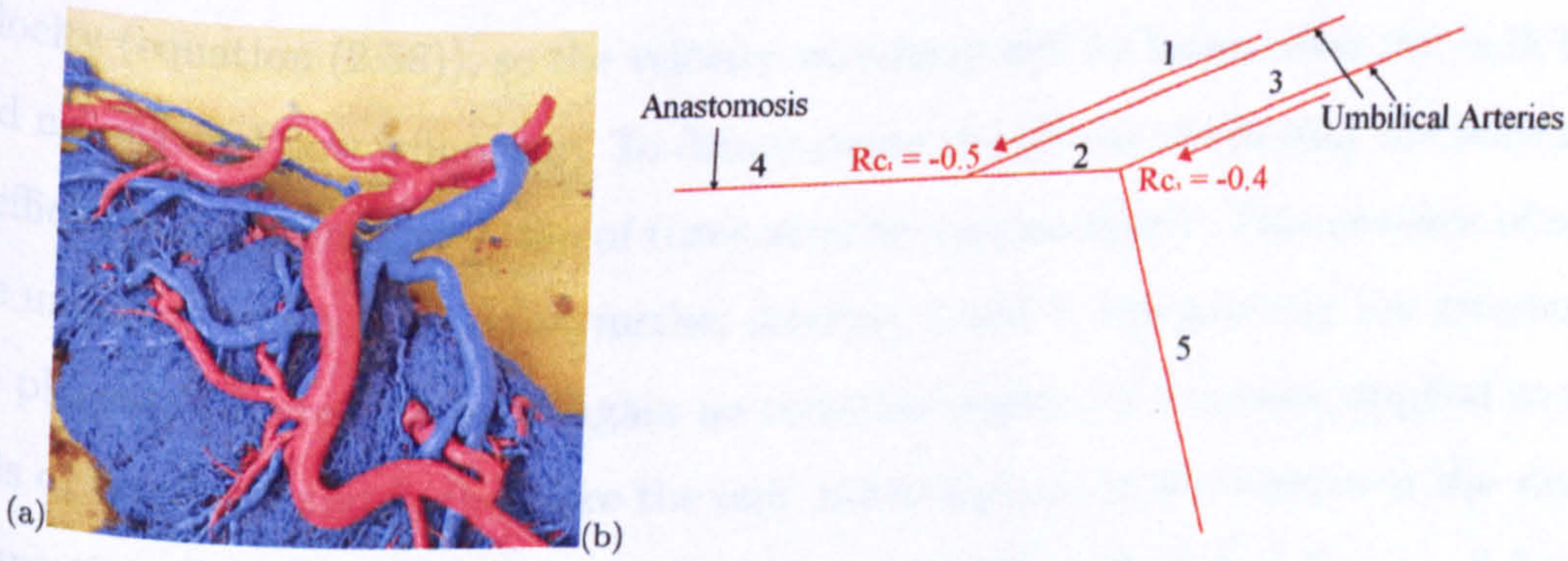


Figure 6.12: (a) Resin cast of the umbilical artery. (b) Reflection coefficients in the umbilical arteries for forward travelling waves.

The characteristic variables W_1 and W_2 are shown for the umbilical arteries in figure 6.11(c). The top figure shows the forward travelling characteristic, W_1, which is the input to the system only, because the inflows have been modelled as pure absorbers so produce no reflections. The bottom figure shows the backwards trav-

elling wave, W_2, which is produced by the reflections occurring within the system. Even though both the systems have no terminal resistance, reflections still occurred and must have been produced by the bifurcations in the network, because the vessels are not tapered in our model. Although we are using a non-linear model for wave propagation, it was shown in Chapter 4, section 4.4 that the differences between the linear and non-linear solutions are small and that it is reasonable to use the linear theory to calculate the reflection coefficients at the bifurcations. These were calculated for forward travelling waves throughout the whole network. It was found that the largest coefficients were those at the end of the umbilical arteries where they meet the placenta, whereas the bifurcations further down the network are fairly well-matched (Appendix B.1). Figure 6.12(a) shows the resin cast of the umbilical arteries found in the placenta and figure 6.12(b) shows the connectivity of the arteries and the reflection coefficients for forward travelling waves at the ends of arteries 1 and 3. The reflection coefficients are -0.5 and -0.4 for a wave travelling as indicated at the bifurcation where the umbilical artery meets the arteries in the placenta. Note that due to the equilibrating anastomoses it is impossible to have all the arteries in the placenta well-matched for forward waves.

The large negative reflection coefficients at the end of the umbilical artery may explain why there is no reversed flow seen in the umbilical arteries. Negative reflection coefficients have an additive effect on the characteristics and therefore the velocity (equation (2.58)), so the velocity waveform will be larger after the bulk flow and no reversed flow will occur. To demonstrate the effects of altering the reflection coefficients a simple bifurcation of three arteries was modelled. This consists of only one umbilical artery, 1, and two further arteries, 2 and 3, representing the arteries in the placenta (figure 6.13 (a)). Again no terminal resistance has been applied to the ends of arteries 2 and 3, therefore the only reflection site in the system is the single bifurcation. The initial reflection coefficient at the bifurcation was $Rc_1 = -0.5$ and different reflection coefficients were achieved by reducing the area of arteries 2 and 3 until the reflection coefficient at the bifurcation was well-matched, $Rc_2 = 0.0$ and the areas were further reduced to give $Rc_3 = 0.5$. The waveforms taken half way along the umbilical artery, 1, are shown in figures 6.13 (b) and (c). The red lines are the results for $Rc_1 = -0.5$, the black line for $Rc_2 = 0.0$ and the blue for $Rc_3 = 0.5$.

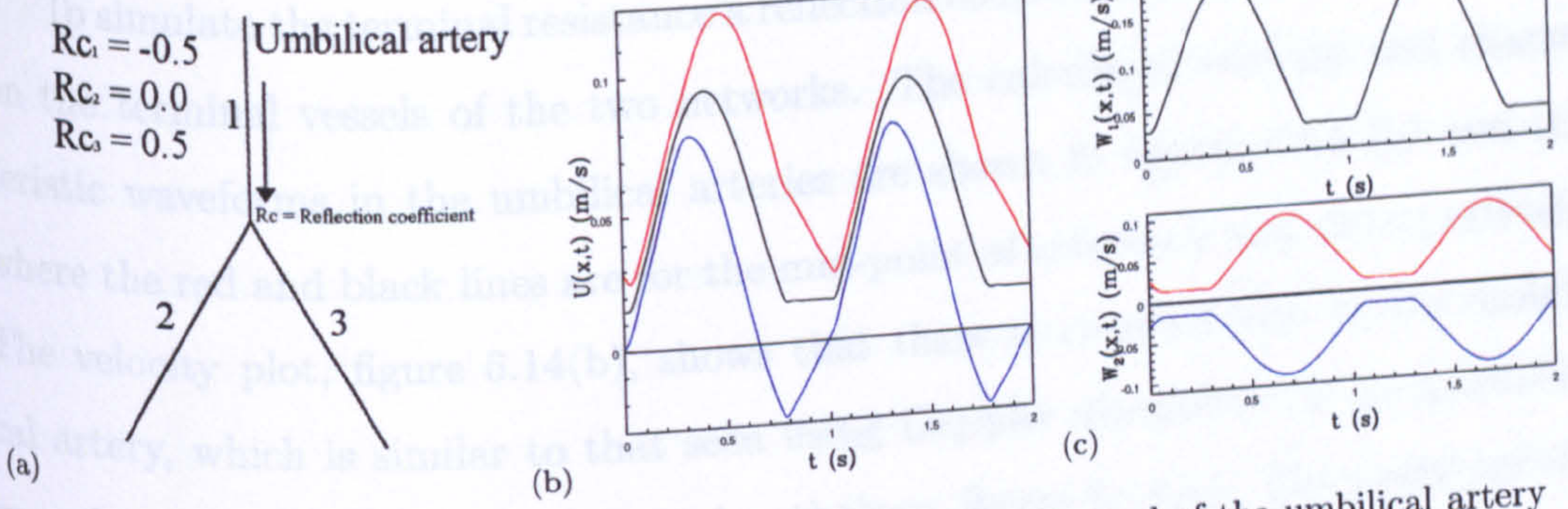


Figure 6.13: Effect of changing the reflection coefficient at the end of the umbilical artery in a simple placental network, (a). The velocity and characteristic variables (W_1 and W_2) waveforms are shown in (b) and (c) respectively.

No reflection occurred at the bifurcation in the case when $Rc_2 = 0.0$. The velocity waveform is very similar to the input characteristic, W_1, and W_2 remained constant throughout the cycle. The characteristic variable, W_2, for the $Rc_1 = -0.5$ and the $Rc_3 = 0.5$ cases have the same magnitude, but are opposite in sign. When $Rc_3 = 0.5$, the characteristic variable W_2 has a subtractive effect and the final velocity has negative flow following the bulk flow.

6.6.1.1 Terminal resistance

In the placenta it is thought that terminal resistance is low, which is consistent with the observation that there is no reversed flow in the umbilical arteries of a healthy fetus. It is also thought that when a fetus is unhealthy the terminal resistance in the placenta is higher [95] and reversed flow is often seen in the umbilical artery as a result, figure 6.14(a).

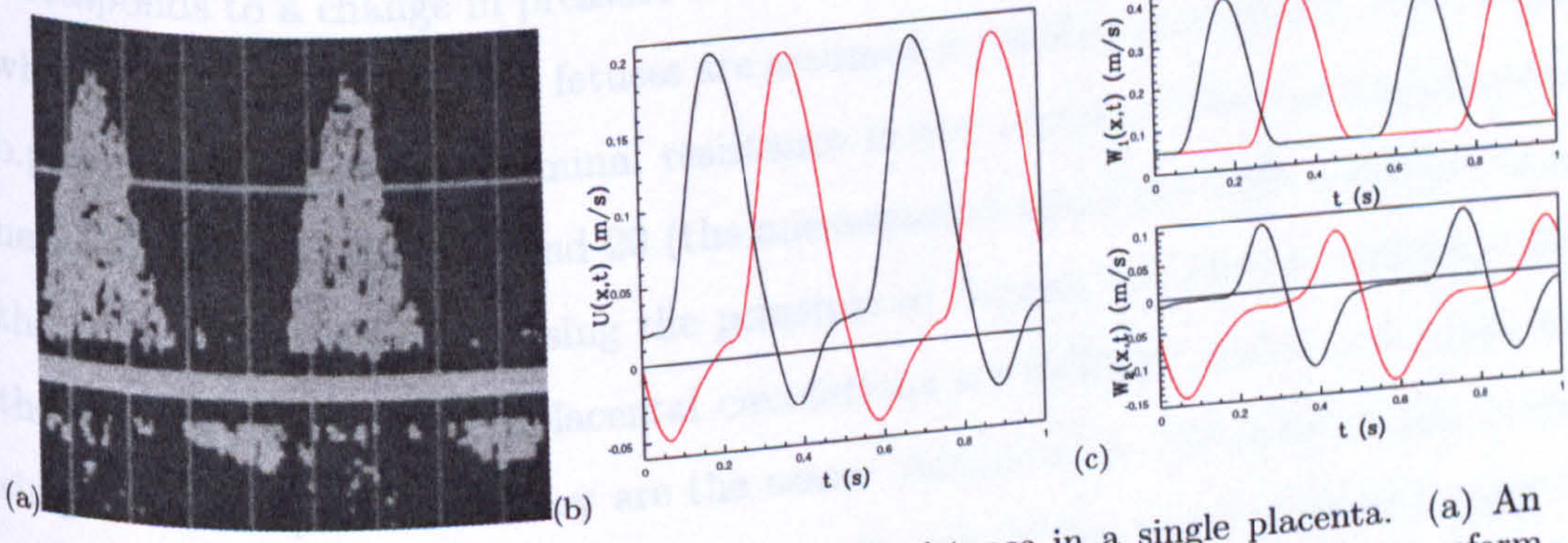


Figure 6.14: The effects of increasing terminal resistance in a single placenta. (a) An ultrasound Doppler flow waveform in an unhealthy fetus [95]. Calculated velocity waveform (b) and characteristic variables W_1 and W_2 (c) using our one-dimensional wave propagation code. The left hand side network is the black line and the right hand side network is the red line.

To simulate the terminal resistance a reflection coefficient of 0.5 has been imposed on the terminal vessels of the two networks. The calculated velocity and characteristic waveforms in the umbilical arteries are shown in figures 6.14 (b) and (c), where the red and black lines are for the mid-point of arteries 1 and 12 respectively. The velocity plot, figure 6.14(b), shows that there is reversed flow in the umbilical artery, which is similar to that seen using Doppler ultrasound in an unhealthy growth-restricted fetus with placental pathology, figure 6.14(a). The characteristic variables are shown in figure 6.14(c) and it can be seen that the W_2 characteristic firstly increases due to reflections from the bifurcation, similar to figure 6.11(c), but then decreases due to the system having a reflection coefficient of 0.5 at the end of the placental network causing a negative backward W_2 wave. This decrease in W_2 has a subtractive effect on the velocity waveform and hence reversed flow results. This demonstrates that the reversed flow seen in the placenta of compromised fetuses can be produced by an increase in terminal resistance of the placenta.

6.6.2 Waveforms in the joined monochorionic placenta

6.6.2.1 Identical heart rates and phases

Having examined the features of the placenta in isolation we now consider the joined monochorionic placental network shown in figure 6.10. The input to the system was imposed as a half sine squared wave through the W_1 characteristic using equation (6.1) at arteries 1, 3, 12 and 14. The change in characteristic area in the input wave corresponds to a change in pressure of 800 Pa. Initially we consider the simple case where the heart rates of both fetuses are assumed to be the same with $T = 0.5\ s$ (120 b.p.m.) and there is no terminal resistance in the system. The two fetoplacental networks join at arteries 4 and 20 (the anastomosis) and have been modelled using the same wall properties. Using the principle of Occam, we have no evidence that the arteries in the two fetoplacental circulations are different and so we adopt the simplest assumption that they are the same. Artery 21 in the network has a very small area and the reflection coefficient at the end of the vessel is equal to one. It is included in the model merely to join the two networks together and only has a very small flow which has a negligible effect on the results in the rest of the system. The volume fluxes into and out of the larger and smaller fetus and through the

arterio-arterial anastomosis have been calculated and are shown in table 6.1. The volume fluxes are of interest because we can calculate whether the smaller and larger fetoplacental circulation systems balance, or if there is a net transfer of blood. In later computations various parameters are altered and the volume fluxes for these systems are also shown in table 6.1. In calculating the volume flux we note that artery 11 is an arterio-venous anastomosis (AVA) and therefore connects to a vein in the larger fetus' circulation (left hand side).

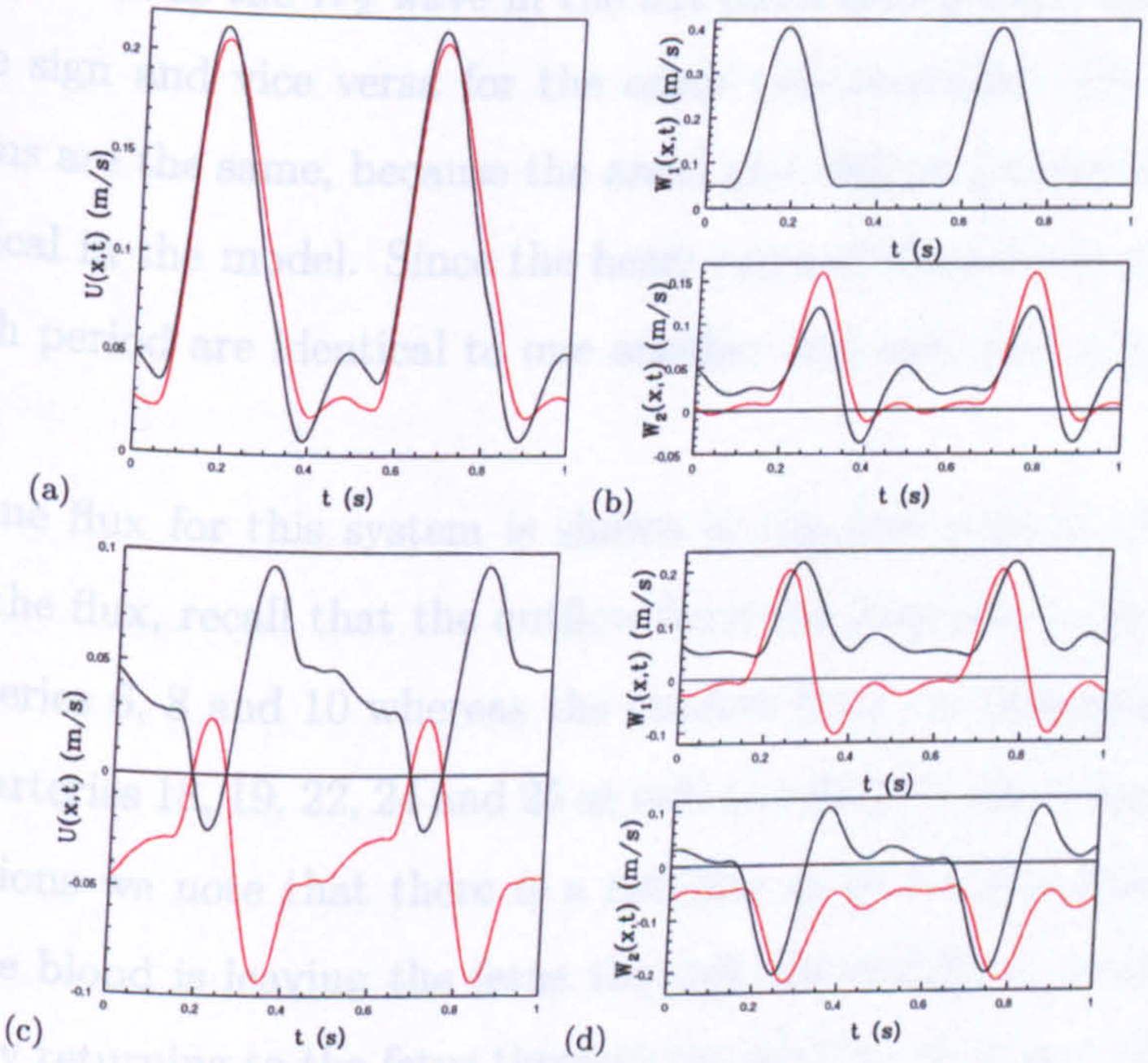


Figure 6.15: Numerically calculated waveforms in the joined monochorionic network, with the same period and phase. The velocity and characteristic variables in the umbilical arteries 1 (red line) and 12 (black line) are shown in (a) and (b) and the velocity and characteristic variables in the arterio-arterial anastomosis 4 (red line) and 20 (black line) are in (c) and (d).

The velocity waveforms in the umbilical arteries and the anastomosis are shown in figures 6.15 (a) and (c) and the characteristic variables, W_1 and W_2, are shown in figures 6.15 (b) and (d). Results are shown in figures 6.15 (a) and (b) for the umbilical arteries 1 (red line) and 12 (black line) at the mid-point in the arteries. The magnitudes of the velocities in figure 6.15 (a), have decreased slightly when compared with the equivalent plots for the unconnected networks, figure 6.11 (b). This is due to the small change in magnitude in the W_2 characteristic, figure 6.15 (b). Again no reversed flow is present and the waveforms are similar in the two fetuses. Figures 6.15 (c) and (d) are the velocity waveforms taken at the ends of

arteries 4 (red line) and 20 (black line), i.e. where the two arteries meet. The plots of arteries 4 and 20 at this point show the same results but the reference for positive and negative flow is in the opposite direction i.e. the flow in the end of artery 4 shows negative flow and blood is flowing towards the right hand side fetus (smaller fetus) and the flow at the end of artery 20 shows positive flow which also indicates that the blood is flowing towards the right hand side fetus. In the characteristic plot it can be seen that the W_1 wave for the right hand side system, artery 4, has the same waveform as the W_2 wave in the left hand side system, artery 20, but has the opposite sign and vice versa for the other two variables. The magnitudes of the waveforms are the same, because the areas and wall properties of arteries 4 and 20 are identical in the model. Since the heart rates of the fetuses are identical the waves in each period are identical to one another and only one period needs to be studied.

The volume flux for this system is shown in the first column of table 6.1. In determining the flux, recall that the outflow from the placenta to the smaller fetus comprises arteries 6, 8 and 10 whereas the outflow from the placenta to the larger fetus include arteries 18, 19, 22, 24 and 25 as well as artery 11 which is an AVA. From these calculations we note that there is a net flux of 62 ml/min from the smaller fetus i.e. more blood is leaving the fetus through the umbilical arteries (1 and 3) than is actually returning to the fetus through the arteries (6, 8 and 10) that supply the venous system of the smaller fetus. The larger fetus gains blood at a rate of 62 ml/min. From a numerical perspective we observe that the overall fluxes in and out of the placenta balance to within 1×10^{-7} litres per minute. Since this system does not balance, it clearly cannot represent the in-vivo situation. In later sections we investigate the effect of varying other parameters, such as terminal resistance and the input pressures on the balance between the systems.

It is interesting to note that the total volume flux out of the right hand side network when the arterio-venous anastomosis is included (arteries 6, 8, 10 and also 11 this time) is larger than that from the left hand side. There is therefore a net flux through the arterio-arterial anastomosis from the larger fetus' side to the net smaller fetus' side. All the parameters are the same for the system i.e. input pressure (similar output fluxes), properties and zero terminal resistance, except the size and the

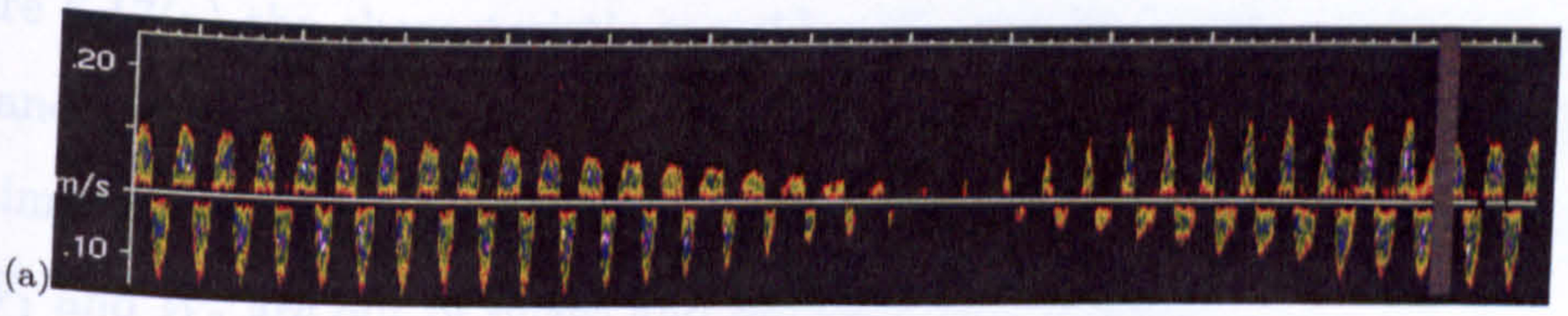
connectivity of the arteries in the two fetoplacental circulations. This suggests that the connectivity and dimensions of the arteries affect the transfusion of the blood and for this particular placenta the arteries may have developed in such a manner that they help blood transfuse back from the larger fetus to the smaller fetus through the arterio-arterial anastomosis. As a percentage of the average inflow into both fetuses, 10.8 % of blood transfuses through the arterio-arterial anastomosis. This effect alone is not adequate to balance the systems as the arterio-venous anastomosis (artery 11) is so large and transfuses much of the blood from the right hand side into the venous system of the left hand side. In fact, in this system there is more blood leaving the right hand side network through artery 11 to the larger fetus than is returning through arteries 6, 8 and 10 to the smaller fetus.

6.6.2.2 Different heart rates

In-vivo the fetuses often have slightly different heart rates, which produces flow waveforms that vary in time as the two hearts go in and out of synchronicity. Figure 6.16 shows a Doppler ultrasound waveform in the arterio-arterial anastomosis of this intertwin pregnancy. In this waveform the pattern is repeated approximately every 24 cycles with the frequency related to the difference in the heart rates. The flow in the anastomosis also alternates in direction, which is not seen in arteries in a normal placenta.

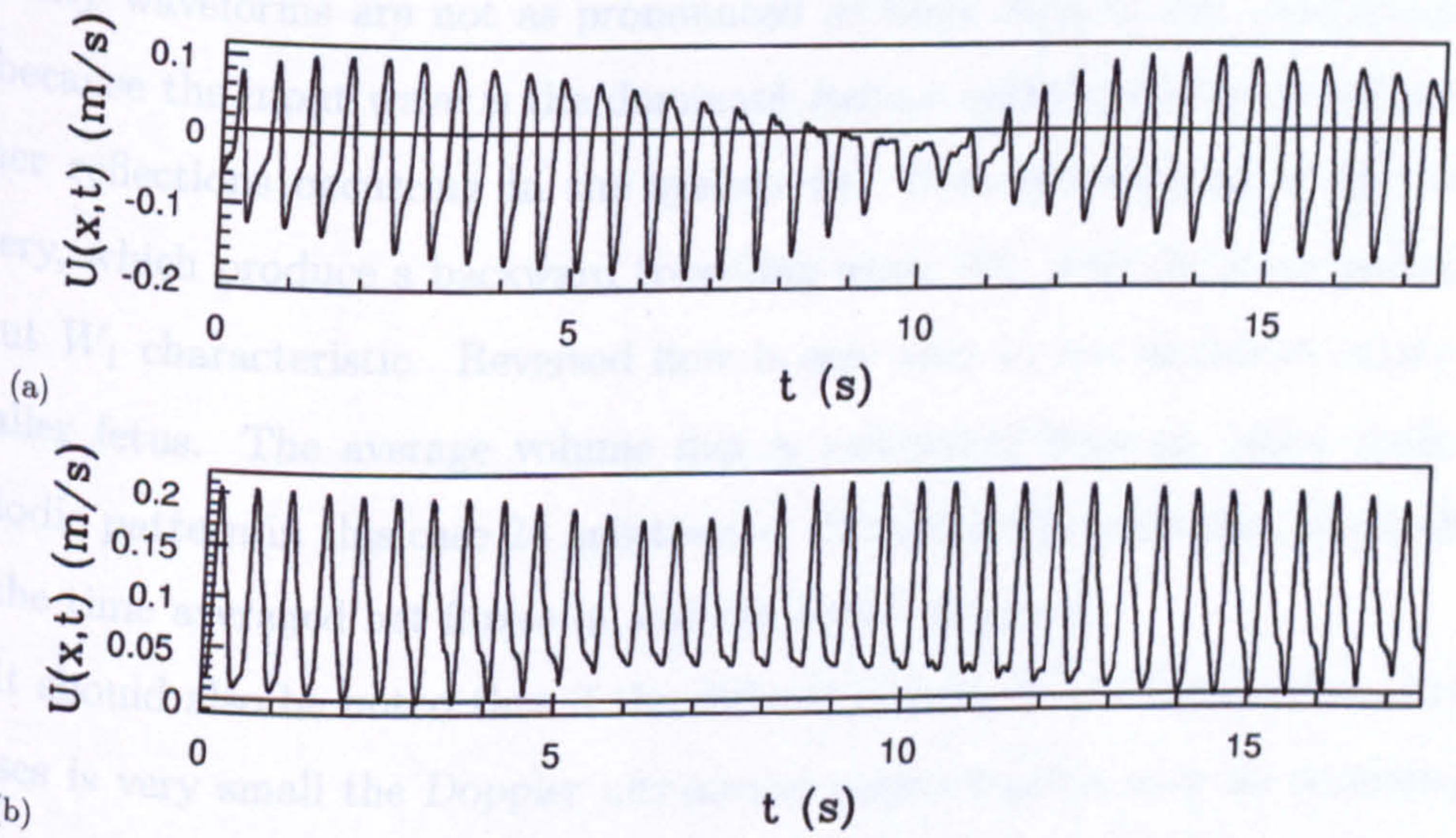
To simulate the variation in the waveforms the period, T, in the input equation (6.1) has been changed to 12/23 for the larger fetus, which is equivalent to a heart rate of 115 b.p.m. and the smaller fetus was modelled with a heart rate of 120 b.p.m.. Figure 6.17(a) shows the results in the anastomosis (artery 4) and figures 6.17(b) and (c) show the results in the umbilical arteries (1 and 12 respectively). The waveform in figure 6.17(a) repeats every 24 cycles and the velocity changes in a similar manner to the waveform obtained in-vivo.

In the previous example both the period and the phase were assumed to be exactly the same for both the larger and the smaller fetuses. The velocity plots shown in figures 6.15(a) and (c) are the resultant velocity waveforms and are exactly the same for every period. When the heart rates are different the alignment of W_1 and W_2 in the anastomosis is not the same for each period and hence the resultant veloc-

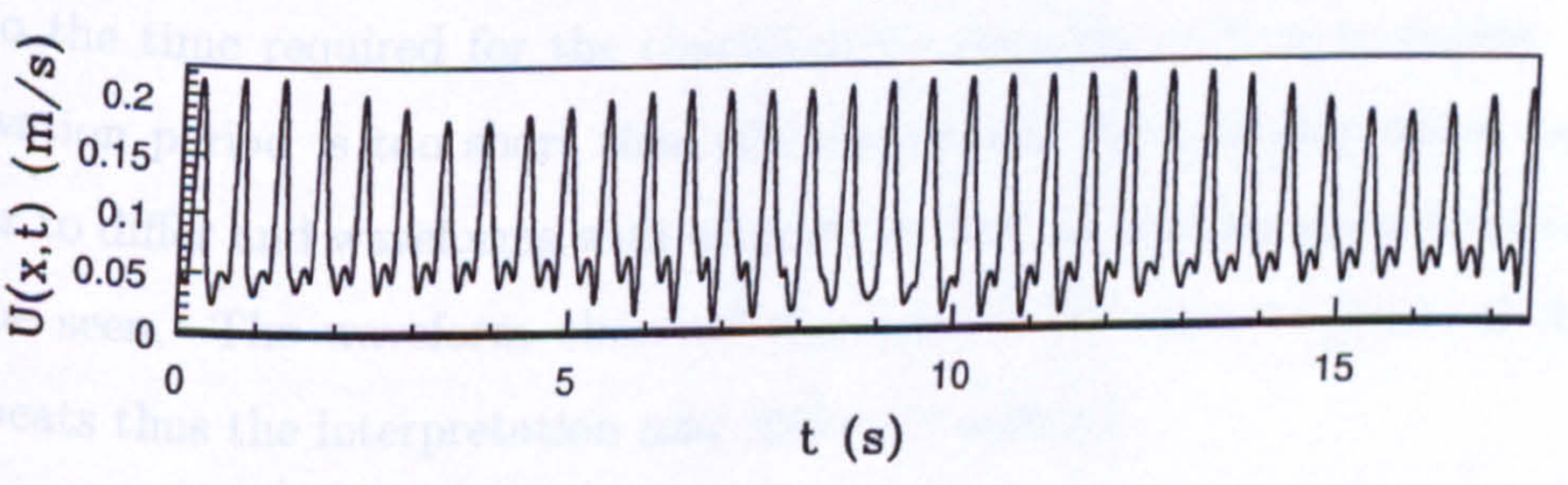


(a)

Figure 6.16: An in-vivo flow waveform in the arterio-arterial anastomosis of placenta A, obtained using Doppler ultrasound.



(a)



(b)

(c)

Figure 6.17: The effect of altering the time period of the two fetuses' input. Predicted velocity waveforms from the one-dimensional mathematical model at the end of the anastomosis, (a), artery 4 and at the start of the umbilical arteries 1 (smaller fetus) and 12 (larger fetus), (b) and (c).

ity waveform is slightly altered with each cycle. After 12 seconds, which is 24 cycles of the faster heart rate and 23 cycles of the slower heart rate, the characteristics are once again in the same alignment as for the first cycle and the different heart rates cause the velocity waveform to alternate in direction. At approximately $t = 11$ in figure 6.17(a) the characteristic variables W_1 and W_2 in the anastomosis are in phase and tend to cancel each other out, resulting in a small velocity. Similarly at approximately $t = 5$ the magnitudes of the velocity in the anastomosis are largest since W_1 and W_2 are out of phase and reinforce one another.

The umbilical artery velocity plots in figures 6.17 (b) and (c) are also periodic with the pattern repeated every 24 cycles, but the differences between successive velocity waveforms are not as pronounced as those seen in the anastomosis. This is because the input wave is the dominant feature and there is more influence from other reflections occurring in the system i.e. from bifurcations at the umbilical artery, which produce a backward travelling wave, W_2, with the same period as the input W_1 characteristic. Reversed flow is now seen in the umbilical artery of the smaller fetus. The average volume flux is calculated from an entire cycle of the periodic pattern in this case 24 heartbeats. Changing the heart rate has little effect on the time averaged net fluxes in and out of the placenta.

It should also be noted that if the difference between the heart rates of the two fetuses is very small the Doppler ultrasound measurements may be misinterpreted due to the time required for the characteristic periodic pattern to repeat. If the observation period is too short then the magnitudes of successive waves may not appear to differ and waveforms with all positive flow, or all with some negative flow may be seen. The waveform observed depends on the relative phase of the two heartbeats thus the interpretation may differ accordingly.

6.6.2.3 Different inputs

When, as in this system, the two fetuses are of different size, the smaller fetus is weaker than the larger fetus and the reversing periodic pattern is predominantly seen in the smaller fetus' umbilical artery [166]. During gestation the larger fetus was overloaded with blood and thus received more oxygen and nutrients than the under supplied smaller fetus and therefore grew more. The excess blood in the larger

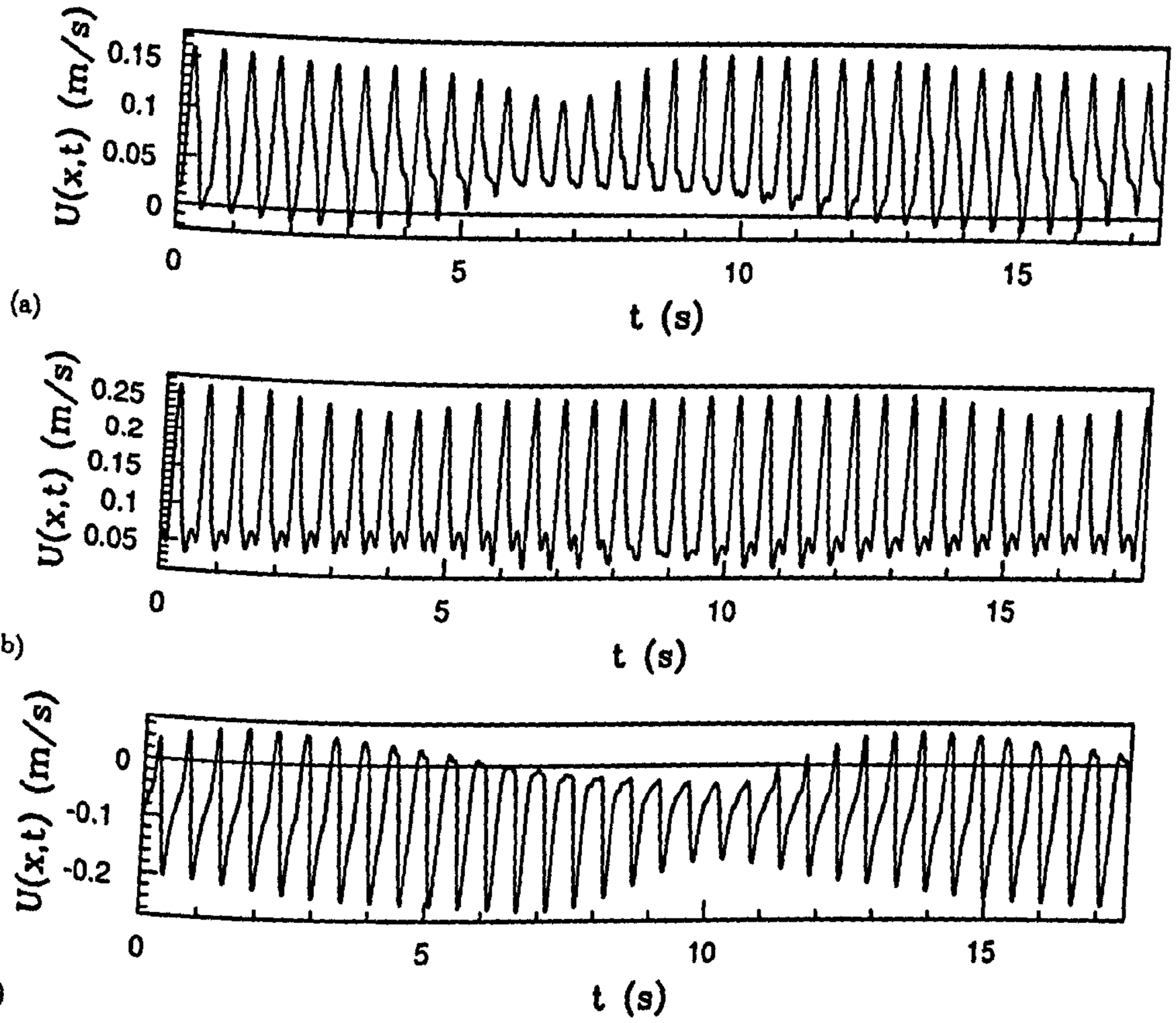


Figure 6.18: The effect of altering the magnitude of the input pressures on the predicted velocity waveforms in (a) and (b) the umbilical arteries, 1 (smaller fetus) and 12 (larger fetus) and (c) the anastomosis, artery 4.

fetus increases its venous blood pressure, its heart has to work far harder to pump the excess blood and the excess waste products can accumulate in the larger fetus [156]. Indeed clinically, it is often the larger fetus which does not survive [165].

To model the effect of the different sized fetuses, we have increased the change in pressure of the input waveform to 1000 Pa in the larger fetus and decreased the change in pressure to 600 Pa in the smaller fetus. These are extreme values for the difference in pressures so that we can clearly assess the effects. The results illustrate the effect that differing input pressures in the umbilical arteries have on the waveforms and volume fluxes in the system. The waveforms in the umbilical arteries are shown in figures 6.18 (a) and (b). The smaller fetus, figure 6.18 (a), has negative flow in its umbilical artery and its velocity magnitude appears to oscillate more than in the previous example, figure 6.17 (b). This is because the magnitude of the input characteristic, W_1, has been reduced and the influence from the larger fetus through the W_2 characteristic is greater. In contrast the larger fetus' velocity plot,

figure 6.18 (b), has all positive flow and the magnitude does not oscillate as much as it did previously, figure 6.17 (c), because this fetus has a greater W_1 input and the influence from the smaller fetus is less significant. This waveform looks more like a normal single placental waveform and this is commonly seen in the umbilical arteries of the larger fetuses. In the anastomosis, figure 6.18 (c), the flow is more negative and the velocity magnitude does not vary as much as in the previous case. The fluxes for this system are shown in column 3 of table 6.1. The volume fluxes returning to the fetuses have not changed significantly, although the imposed volume flux has increased for the larger fetus and has decreased in the smaller fetus. This difference has been overcome by a large increase of 64 ml/min through the anastomosis (23.79 % of the average input into the placenta). The balance of volume flux in and out of the fetuses has also improved and the difference is now only 26 ml/min, which means that this arrangement is closer to the in-vivo situation than the previous case where the inputs were the same. However, this has occurred, because the smaller fetus' input has now decreased and not because there is a reduced flow through the arterio-venous anastomosis.

6.6.2.4 Terminal resistance

The presence of the arterio-venous anastomosis in the modelled fetoplacental circulation means that there is a tendency for blood to be transfused from the smaller fetus to the larger fetus, as we have seen in the previous sections, but there is only a limited blood capacity in the larger fetus' circulation and the blood pressure will rise, which will affect the flow patterns. To simulate this effect we have applied a terminal resistance to the terminal vessels belonging to the larger fetus by imposing a reflection coefficient of 0.5. These are arteries 18, 19, 22, 24, 25 and also artery 11, which although it belongs to the smaller fetus, is part of the arterio-venous anastomosis and so connects with a vein belonging to the larger fetus. The pressure change for both inputs has been modelled as 800 Pa.

The volume fluxes in the system are shown in column 4 of table 6.1. For this configuration the volume fluxes into and out of the smaller and larger fetuses are approximately the same, therefore the systems are nearly balanced. This has occurred due to both the volume flux increasing through the arterio-arterial anastomosis and

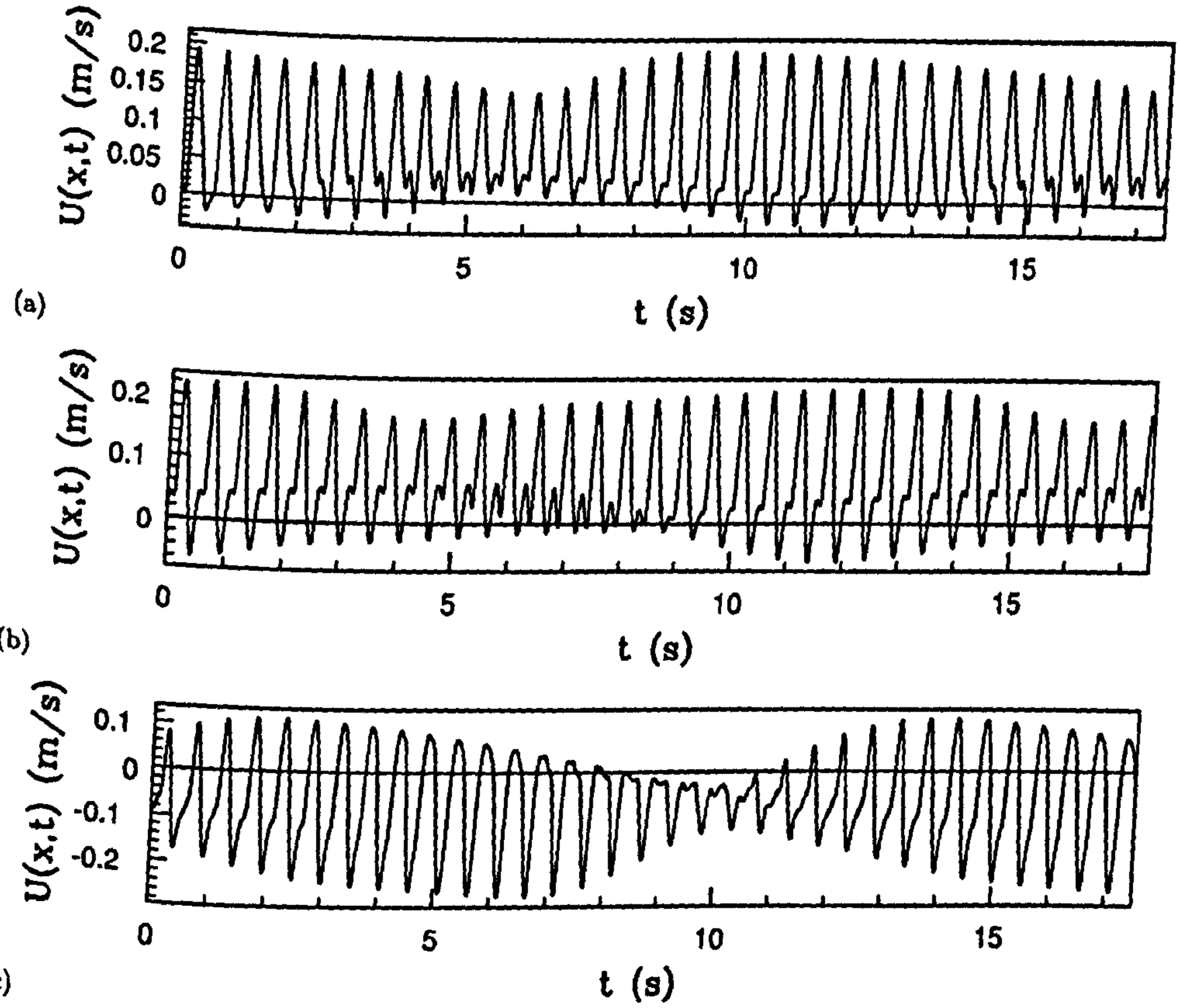


Figure 6.19: The effect of adding terminal resistance to the placental circulation of the larger fetus. Predicted velocity waveforms from the one-dimensional mathematical model in (a) and (b) the umbilical arteries, 1 (smaller fetus) and 12 (larger fetus) and (c) the anastomosis, artery 4.

decreasing through the arterio-venous anastomosis, so they are now approximately equal, which is essential for the systems to balance. The total volume flux returning to the larger fetus has decreased due to the increase in terminal resistance. An increase in terminal resistance has also caused a large reduction in volume flux into the placentas of both the larger and smaller fetuses, which may not be ideal. We would need to model the entire circulation, including the two fetuses, to determine the real effect on the placental circulations relative to the fetal circulations. With the improved algorithms we are using, there is no reason why we could not include many more vessels into the model, if the data were available for the fetal circulations. Comparing the system with no terminal resistance, table 6.1 column 2, with this system shows that there is now more blood returning to the smaller fetus from arteries 6, 8 and 10 than transfusing to the larger fetus through artery 11.

Figures 6.19 (a) and (b) show the velocity waveforms at the mid-points of the umbilical arteries 1 and 12. In both of these plots there is negative flow and the

magnitudes vary due to a large influence from the other fetus. As mentioned earlier, reversed flow is often only seen in the smaller fetuses umbilical artery, therefore in the previous example the velocity plots, figure 6.18 (a) and (b), were perhaps more appropriate for physiological conditions. The flow in the anastomosis is shown in figure 6.19 (c) and the waveform looks very similar to figure 6.17 (a), but the velocity magnitudes are greater due to the increase in volume flux. These waveforms indicate that the choice of a reflection coefficient of 0.5 in this example is possibly too large, however the AAA in this case is very large. Measurements of the physiological waveforms in the umbilical arteries of this network would have aided our investigations.

6.6.2.5 Different inputs and terminal resistance

In the previous sections it was shown that both increasing the output from the larger fetus and the terminal resistance of the larger fetus helped to balance the fetal circulations, but neither effect balances the system in a physiological manner. In-vivo, there is a complex interaction between arterial blood pressure and the resistance of the microcirculation, which is beyond the capability of our simple model to predict in its current form. Our results however, do indicate that it is probably more realistic to model the network with both a higher terminal resistance and an increase in the input to the larger fetus' placental circulation.

The results of combining different input pressures and an elevated terminal resistance for the larger fetus' circulation are shown in figure 6.20. In this system, input pressures of 600 Pa and 1000 Pa and a reflection coefficient of 0.2 on the larger fetus' terminal vessels have been used. The velocity waveform in the smaller fetus' umbilical artery has a periodically negative flow , figure 6.20 (a), whereas the flow waveform in figure 6.20 (b) for the larger fetus is now largely positive, similar to what is typically observed for in-vivo waveforms. The volume fluxes for this case are very closely balanced and the flow waveform in the anastomosis is also similar to that seen in the Doppler ultrasound measurements. The volume flux through the arterio-arterial anastomosis as a percentage of the average input to the placentas has increased to 30.0 % compared to the two previous cases, the increased input (23.8 %) and the terminal resistance (24.2 %). The general patterns are therefore

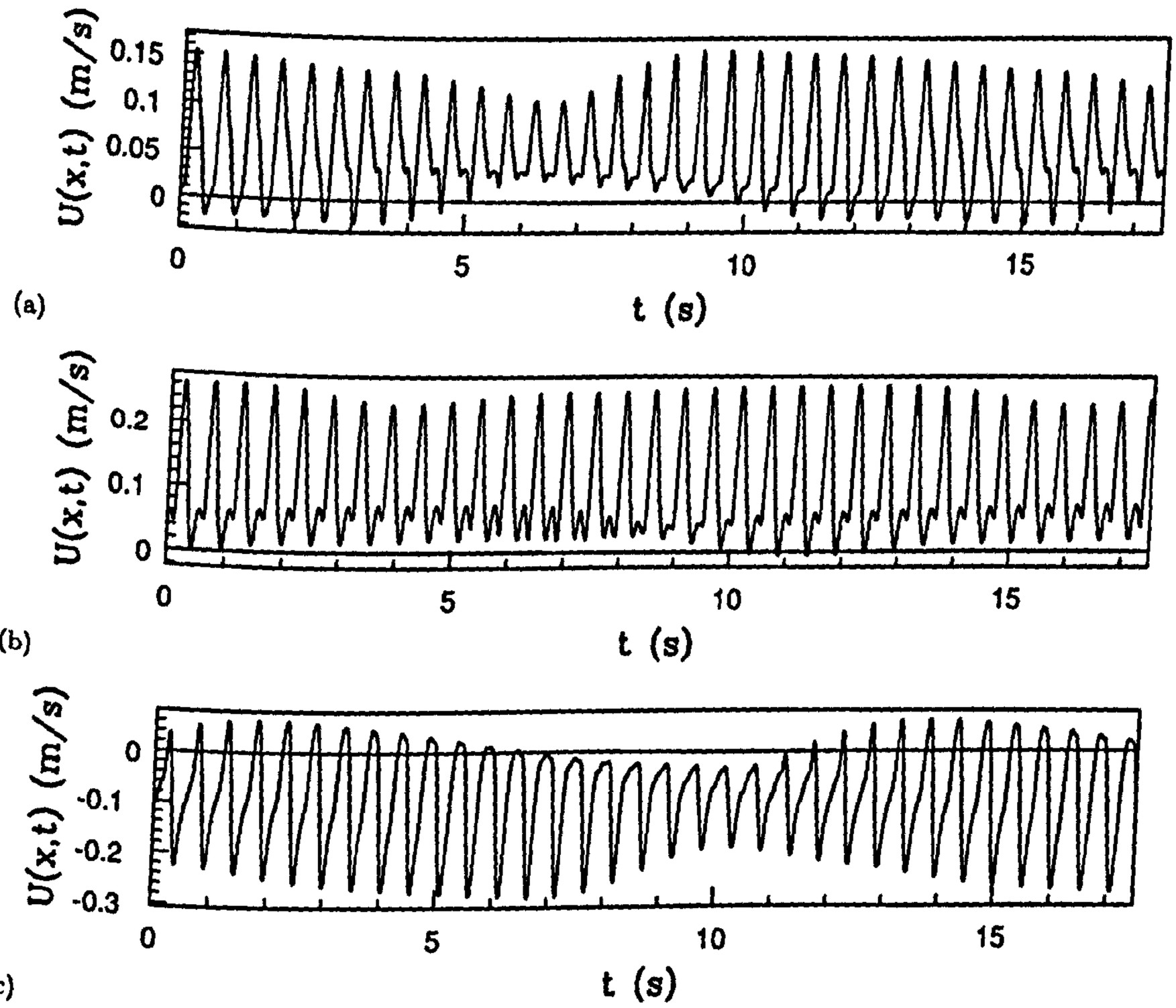


Figure 6.20: The effect of altering pressure to 600 and 1000 Pa in the smaller and larger fetus respectively and a reflection coefficient of 0.2 in the larger fetus on the predicted velocity waveforms in (a) and (b) the umbilical arteries of 1 (smaller fetus) and 12 (larger fetus) and (c) the anastomosis, artery 4.

very encouraging although the precise form of each wave is not identical to the physiological case due to the simplifications and assumptions made about the network and the input conditions.

6.6.2.6 Anastomosis area

In this fetoplacental circulation the arterio-arterial anastomosis has a very large cross-sectional area, but in other circulations arterio-arterial anastomoses are generally smaller. We have therefore reduced the area of the anastomosis in this case to investigate the effects a smaller conduit would have on the waveforms in the umbilical arteries. The area of the anastomosis, artery 20, was reduced to 3.14 mm^2 and the areas of arteries 19 and 21 were increased to 16.6 mm^2 and 9.62 mm^2 respectively so that no new reflections would occur at these bifurcations. Other fetoplacental circulations with smaller AAA's are investigated in the following sections.

The waveforms in the umbilical arteries (figures 6.21(a) and (b)) show that there

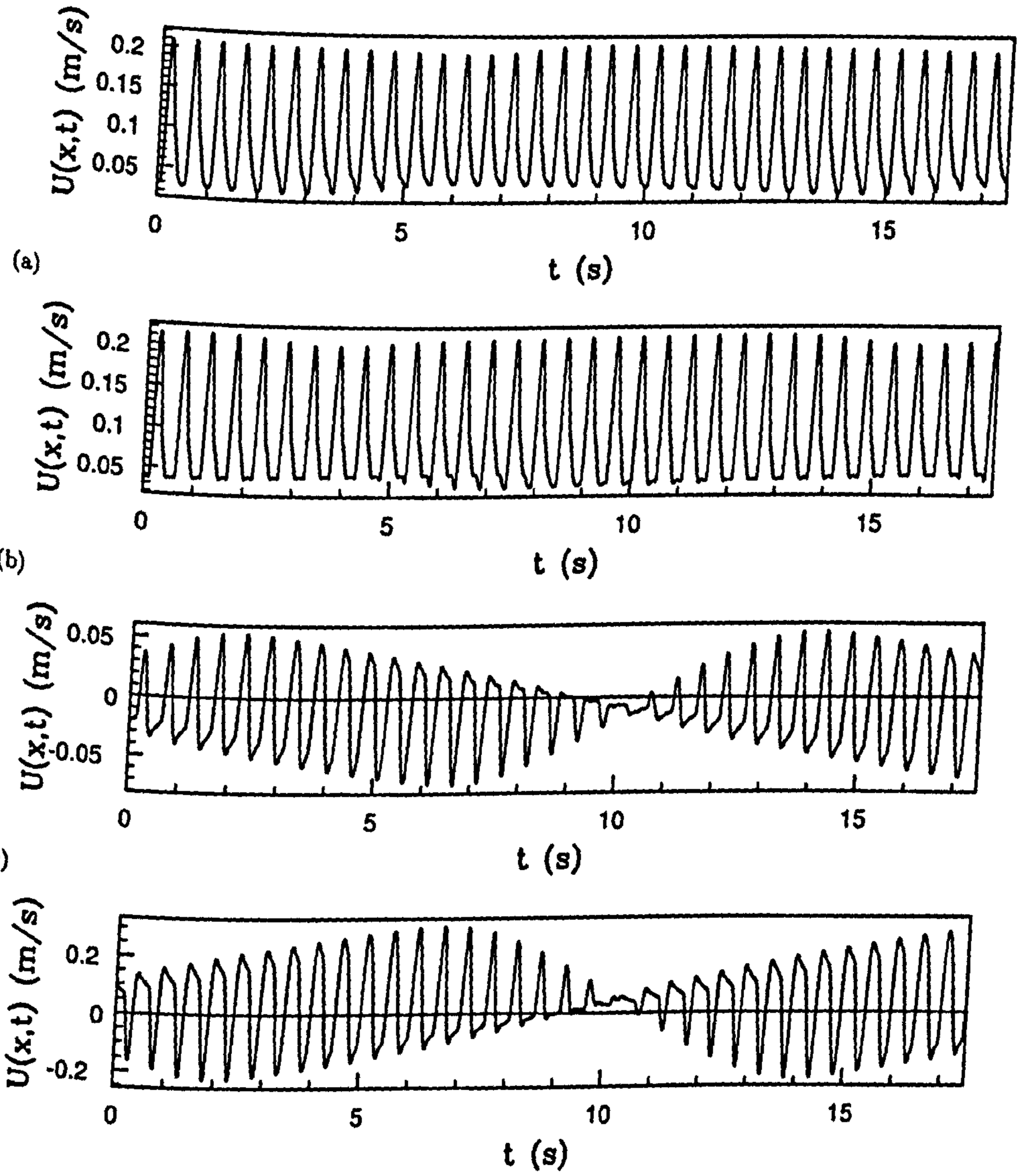


Figure 6.21: The effect of reducing the area of the arterio-arterial anastomosis, artery 20, on the predicted velocity waveforms in (a) and (b) the umbilical arteries, 1 (smaller fetus) and 12 (larger fetus) and (c) and (d) the anastomosis, arteries 4 and 20.

is no reversed flow and only a slight change in velocity magnitude between successive beats. The waveforms have not been greatly influenced by any other waves from the other fetus and appear more similar to those found in a normal healthy fetus, figure 6.11(a). The velocity waveforms in the anastomosis are shown in figures 6.21(c) and (d). Figure 6.21(c) is the velocity waveform in artery 4, which has remained the same area as the previous cases, and figure 6.21(d) is that in artery 20, which has been reduced in area. They both have the same periodic pattern but artery 4 is the reverse of artery 20, as for the example shown in figure 6.15(c). The velocity magnitude has increased in artery 20 because the area has been reduced, but has decreased in artery 4 even though this artery has the same area as before. This is due to the reduction in area of the other section of the arterio-arterial anastomosis, which reduces the efficiency of the AAA as a flow conduit. The volume flux through the anastomosis shown in column 6 of table 6.1, has reduced to 7.7 ml/min (2.73 % as an average of the inputs to the placenta), so hardly any blood is transfusing through this anastomosis, consequently the imbalance between the fetuses circulations is large with the smaller fetus now lacking 7.5 ml/min. In the previous examples the arterio-arterial anastomosis was the channel for blood to transfuse to the smaller fetus, but with a small anastomosis as in this case the protective effect of the arterio-arterial anastomosis is more limited.

Volume Flux (litres per minute)	1	2	3	4	5	6
	Same input Same period	Same input Different period	Increase input from larger fetus	Increase TR on larger fetus	Pressure and TR diff	Reduce area of AAA
Input flux into placenta from smaller fetus $u_1A_1 + u_3A_3 =$	0.134	0.134	0.099	0.099	0.084	0.141
Output flux from placenta into smaller fetus $u_6A_6 + u_8A_8 + u_{10}A_{10} =$	0.072	0.072	0.072	0.103	0.085	0.066
Net Flux Smaller Fetus Output - Input Flux =	**−0.062**	**−0.062**	**−0.026**	**0.0041**	**0.0005**	**−0.075**
Input flux into placenta from larger fetus $u_{12}A_{12} + u_{14}A_{14} =$	0.134	0.134	0.170	0.099	0.156	0.141
Output flux from placenta into larger fetus $u_{18}A_{18} + u_{19}A_{19} + u_{22}A_{22} +$ $u_{24}A_{24} + u_{25}A_{25} =$ $u_{11}A_{11}(AV anastomoses) =$	0.105 0.091	0.105 0.091	0.105 0.091	0.051 0.044	0.084 0.072	0.134 0.083
Net Flux Larger fetus Output - Input Flux =	**0.062**	**0.062**	**0.026**	**−0.0041**	**−0.0005**	**0.075**
Flux through AA Anastomoses $u_4A_4 =$	-0.029	-0.029	-0.064	-0.048	-0.072	-0.0077
As a percentage of the average inflow=	10.82%	10.82%	23.79%	24.24%	30.00%	2.73%

Table 6.1: Table of fluxes in the intertwin network, showing the effect of varying different parameters in the network.

6.7 A study of placenta B

This section discusses the waveforms in placenta B modelled using the one-dimensional code. The photographs for this placenta are shown in figure 6.4 and there are more detailed pictures of this placenta in the section describing the casting of the placentas, section 6.3, figures 6.1 and 6.2. This placenta has a medium sized AAA (red-yellow connection). It also has a connection where the artery and vein (red-blue) from one fetus meet at the same cotyledons, with an artery and vein (yellow-green) from the other fetus. This could be considered as two AVAs or one VVA.

The measurements for placenta B are given in Appendix B.2. The connectivity of the placenta was observed from the plastic cast shown in figure 6.4 and the connectivity tree is shown in a similar orientation to this in figure 6.22.

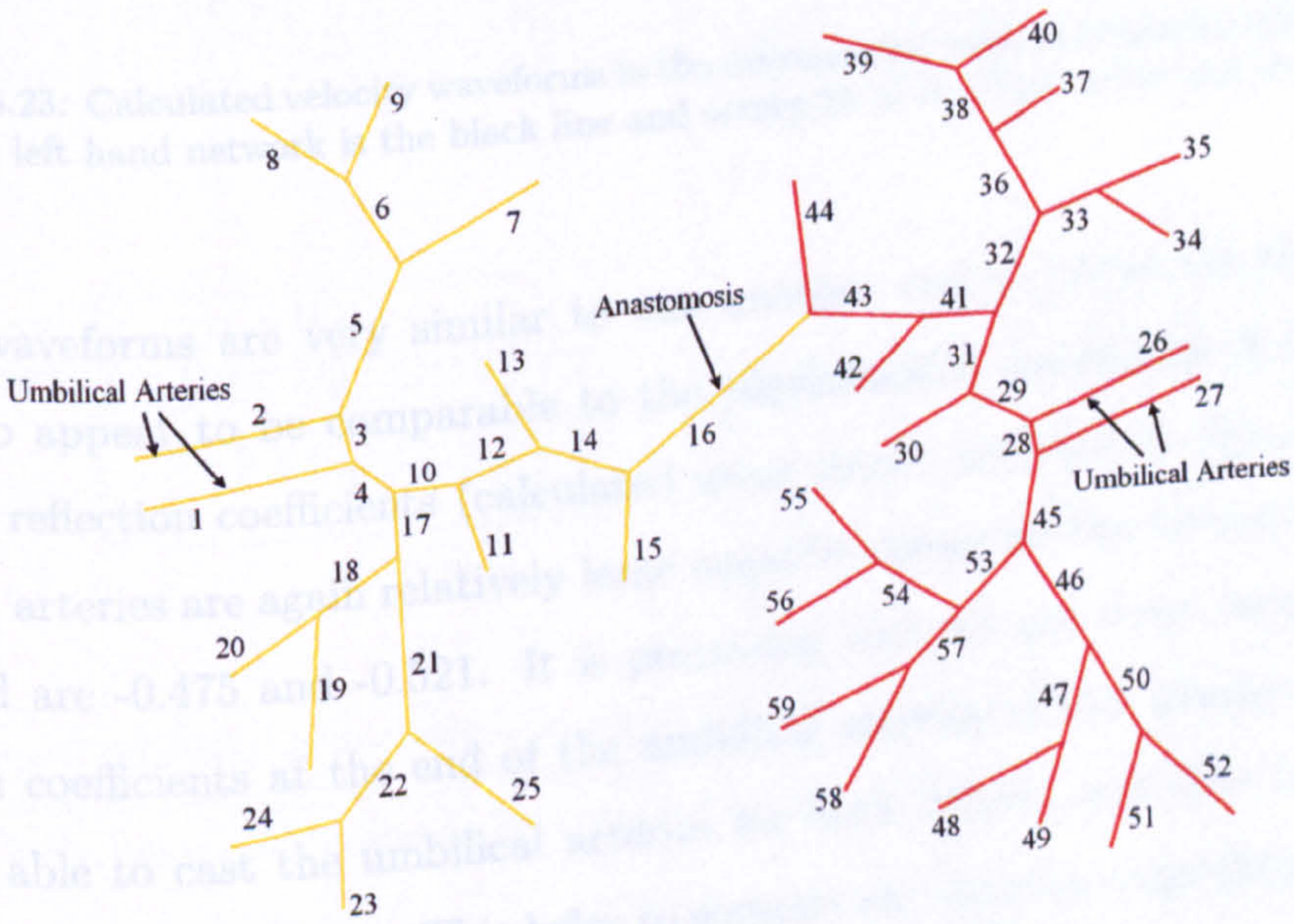


Figure 6.22: Connectivity of the arterial network of monochorionic placenta B.

The boundary conditions at the inlet of the umbilical arteries, 1 & 2 and 26 & 27, of the fetoplacental network were imposed using equation 6.1. The input time period for the yellow arterial network was $T = 0.5$, which is equivalent to 120 b.p.m. and the period for the red arterial network was $T = 12/23$, which is equivalent to 115 b.p.m.. Again the wall and vessel properties are assumed to be the same for both circulations. As for the previous network we again first investigate the two arterial systems in isolation before studying the linked network.

6.7.1 Single placenta waveforms

To model this placenta as two separate systems the connection between arteries 16 and 43 has been removed. The velocity waveforms for umbilical arteries 1 and 26 are shown in figure 6.23. The black line (artery 1) is the waveform for the yellow arterial network and the red line (artery 26) is for the red arterial network.

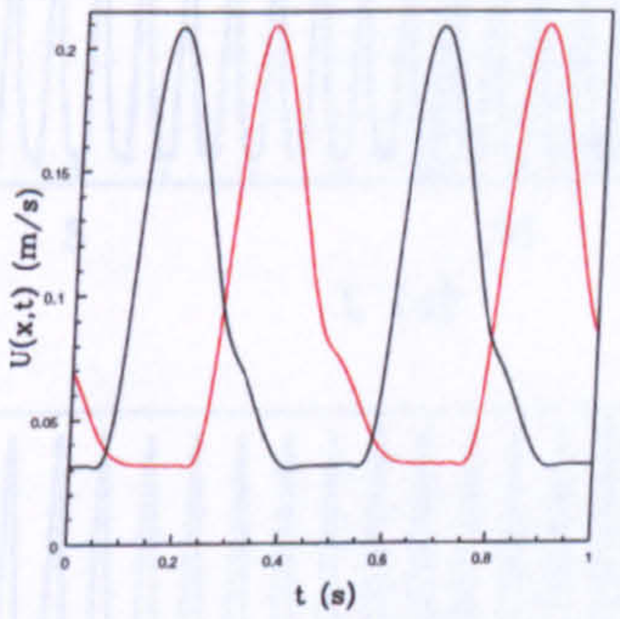


Figure 6.23: Calculated velocity waveforms in the unconnected version of placenta B. Artery 1 of the left hand network is the black line and artery 26 of the right is the red line in the plot.

The waveforms are very similar to one another and to those for placenta A. They also appear to be comparable to the physiological waveforms in figure 6.11 (a). The reflection coefficients (calculated using linear analysis) at the ends of the umbilical arteries are again relatively large negative values for the forward travelling wave and are -0.475 and -0.521. It is promising that we get these large negative reflection coefficients at the end of the umbilical arteries of this placenta, because we were able to cast the umbilical arteries for both fetuses and thus take proper physiological measurements. This helps to support our opinions regarding why there is no reversed flow in the umbilical arteries as was discussed in section 6.6.1.

6.7.2 Monochorionic placenta waveforms

The velocity waveforms are now investigated for the entire monochorionic network shown in figure 6.22. The velocity waveforms for umbilical arteries 1 and 26 are shown in figures 6.24 (a) and (b) respectively. There is a very small change in the velocity magnitudes in the periodic pattern, but this is not as substantial as in the similar case for placenta A. This is presumably due to the AAA being significantly smaller in area, which also helps to confirm the results for section 6.6.2.6. The

waveform in the AAA is shown in figure 6.24 (c) and exhibits the reversing periodic pattern, which is actually quite significant, at least in terms of velocity. Again this is due to the two different heart rates imposed into each of the fetoplacental's umbilical arteries, which interact to a significant extent in the anastomosis.

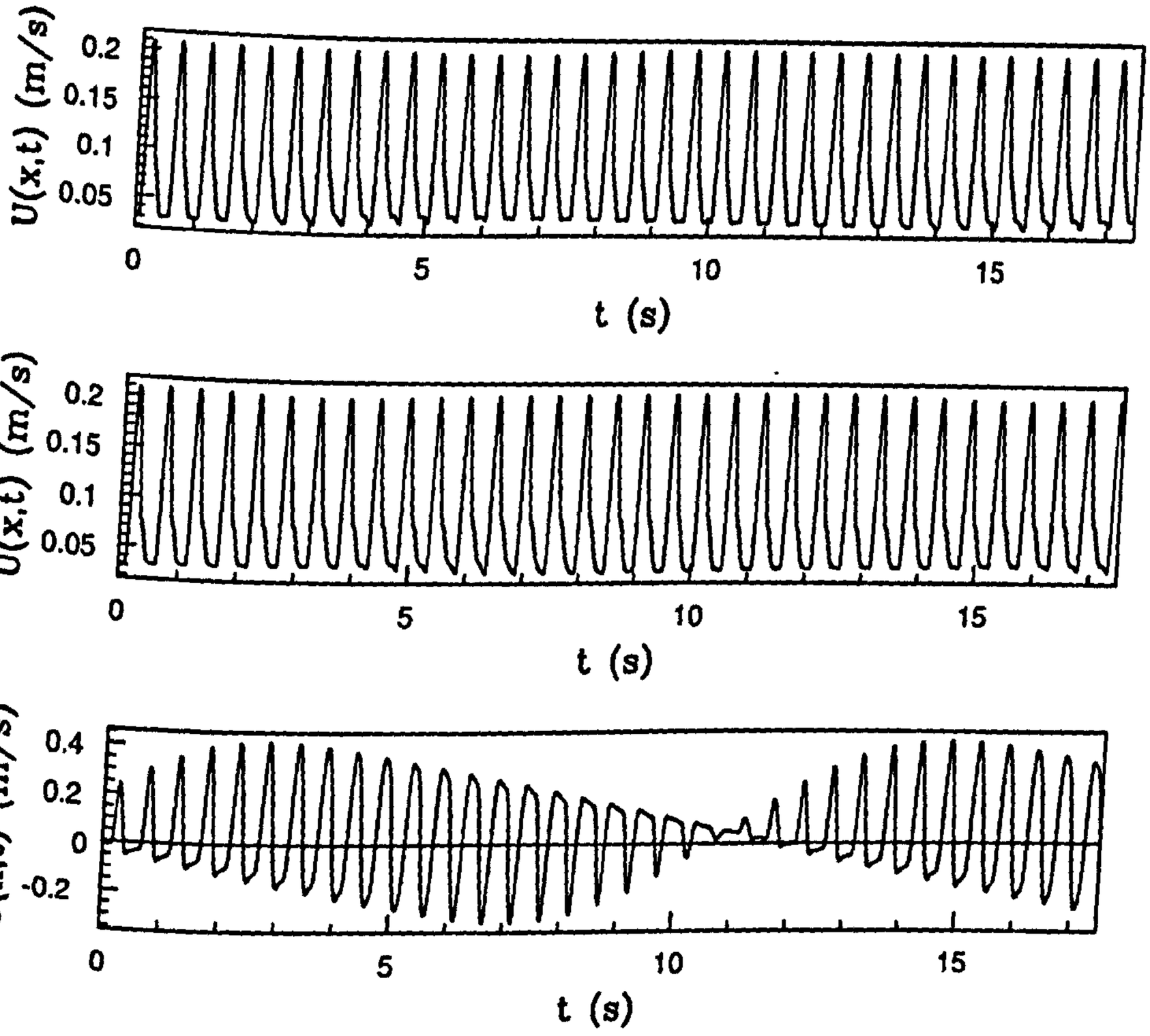


Figure 6.24: The effect of applying inputs with different time periods to the two circulations of placenta B. Predicted velocity waveforms (a) and (b) in umbilical arteries 1 and 26 respectively and (c) in the arterio-arterial anastomosis, artery 16.

The volume fluxes into and out of the two arterial systems have been calculated and are shown in table 6.2. The volume fluxes into and out of the yellow arterial network are 189 ml/min and 184 ml/min respectively and for the red arterial network are 185 ml/min and 190 ml/min respectively. This shows that the fluxes in these fetuses almost balance, which is due to the fact that the only connection is a relatively small AAA. The volume flux through the AAA is 5.4 ml/min and as a percentage of the average inflow is 2.9%, which is relatively small compared with the similar modelling for placenta A, where the flow through the AAA was 10.8% of the average inflow. However, the two networks do not quite balance and there is still some blood transfusing from the yellow arterial network to the red arterial

network, with the fetus belonging to the yellow arterial system losing 5.4 ml/min of blood and the fetus belonging to the red arterial system gaining 5.4 ml/min of blood. The reasons why this network does not balance may be the slightly different inputs resulting from the different areas of the umbilical arteries, or could be due to the connectivity of the fetoplacental circulations. Although, in this placenta the blood outflow from arteries 25 and 58 from the two fetoplacental circulations can enter either twin due to this being two AVAs, we have modelled this as if the blood from these arteries returns to the correct twin in the volume flux table 6.2. Of course this may not happen in reality at this cotyledon where blood could transfuse from the red artery (58) to the other fetoplacental circulation (green venous system) and the blood transfusing through the AAA, which we calculated to be 5.4 ml/min, could be balancing the systems.

It is promising that in this monochorionic placenta, where we were able to measure all the umbilical arteries that the inflows into the placentas are very similar in size, because we would expect the fetuses to grow at approximately the same rate and therefore have similar inflows.

Placenta B	**Volume Flux (litres per minute)**
Input flux into yellow placenta from fetus $u_1A_1 + u_2A_2 =$	0.189
Output flux from yellow placenta into fetus $u_7A_7 + u_8A_8 + u_9A_9 + u_{11}A_{11} + u_{13}A_{13} + u_{15}A_{15} + u_{19}A_{19} + u_{20}A_{20} + u_{23}A_{23} + u_{24}A_{24} + u_{25}A_{25} =$	0.184
Net Flux to Fetus (Yellow) Output - Input Flux =	**−0.00538**
Input flux into red placenta from fetus $u_{26}A_{26} + u_{27}A_{27} =$	0.185
Output flux from red placenta into fetus $u_{30}A_{30} + u_{34}A_{34} + u_{35}A_{35} + u_{37}A_{37} + u_{39}A_{39} + u_{40}A_{40} + u_{42}A_{42} + u_{44}A_{44} + u_{48}A_{48} + u_{49}A_{49} + u_{51}A_{51} + u_{55}A_{55} + u_{56}A_{56} + u_{58}A_{58} + u_{59}A_{59} =$	0.190
Net Flux to Fetus (Red) Output - Input Flux =	**0.00538**
Flux through AA Anastomoses $u_{16}A_{16} =$	0.00538
As a percentage of the average inflow =	2.88%

Table 6.2: Table of fluxes in the monochorionic network of placenta B for the same magnitude inputs, but with different periods.

6.8 A study of placenta C

As a final example placenta C is now modelled. The photographs for placenta C are shown in figure 6.5 of section 6.4. This placenta has a very small AAA (red-yellow connection) and may also have some extremely small AVAs (figure 6.5 (b)), but these have not been considered.

The measured data for placenta C is presented in Appendix B.3 and the connectivity of the arteries is shown in figure 6.25. The umbilical arteries supplying the monochorionic placenta are arteries 1 & 3 in the yellow arterial network and 31 & 33 in the red arterial network and the characteristic equation 6.1 was imposed as the inflow at these arteries. Umbilical arteries 1 & 3 had a heart rate of 120 b.p.m. and umbilical arteries 31 & 33 had a heart rate of 115 b.p.m. imposed for both the single and twin placental modelling.

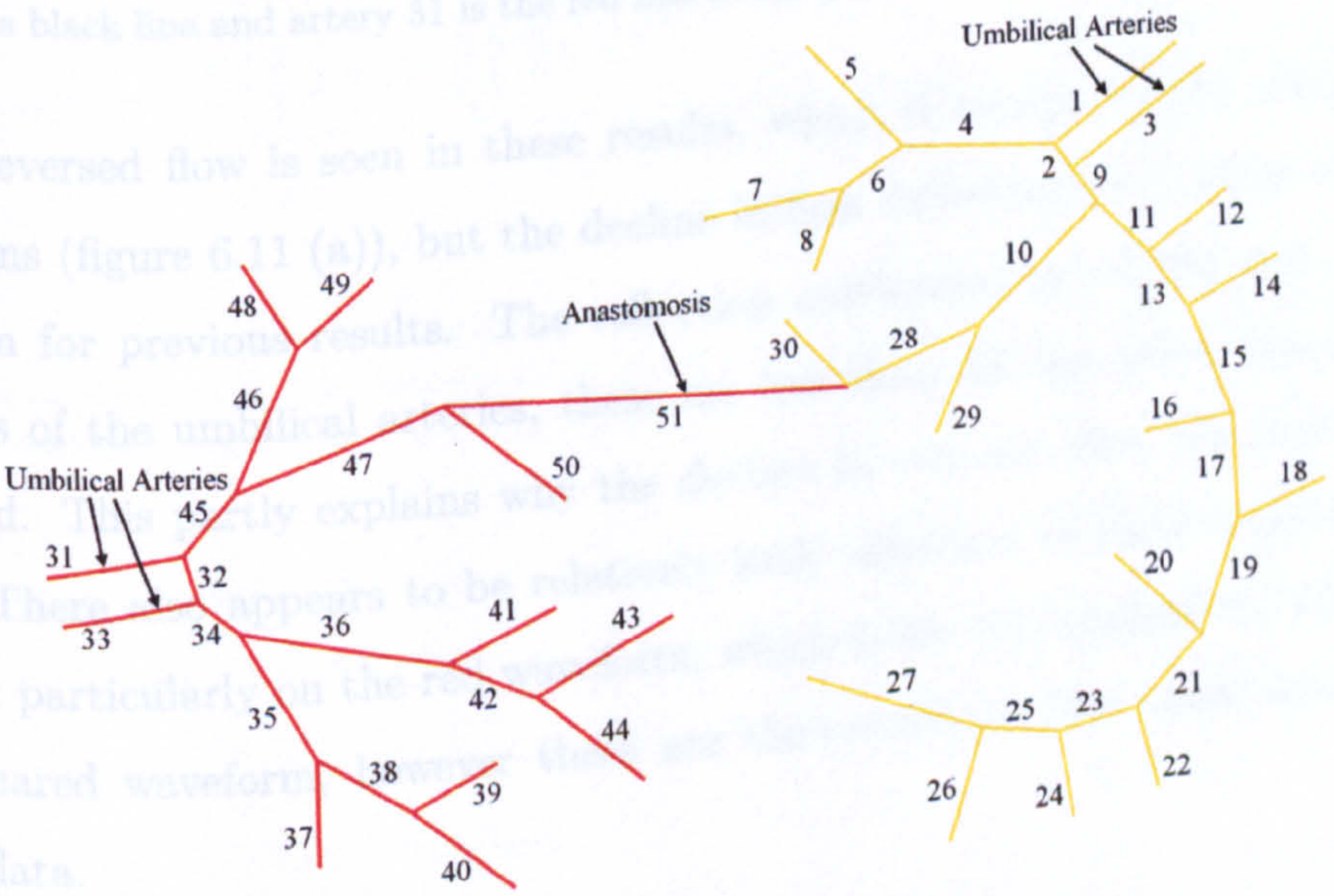


Figure 6.25: Connectivity of the arterial network for monochorionic placenta C.

Unfortunately, due to the difficulties described in section 6.3 it was not possible to obtain any data for umbilical arteries 31 & 33 of the red arterial network. Initially the measurements from the yellow arterial network were used for the red umbilical arteries, but it was found that the area for the input arteries to this placenta had to be reduced in size, as explained in section 6.8.2, and all results are shown for this reduced area.

6.8.1 Single placenta waveforms

The velocity waveforms were first calculated as though the placenta was two separate systems, with no connection at arteries 28 & 51. The waveforms are shown in figure 6.26, where the black waveform is for umbilical artery 1 (yellow network) and the red waveform is for umbilical artery 31 (red network).

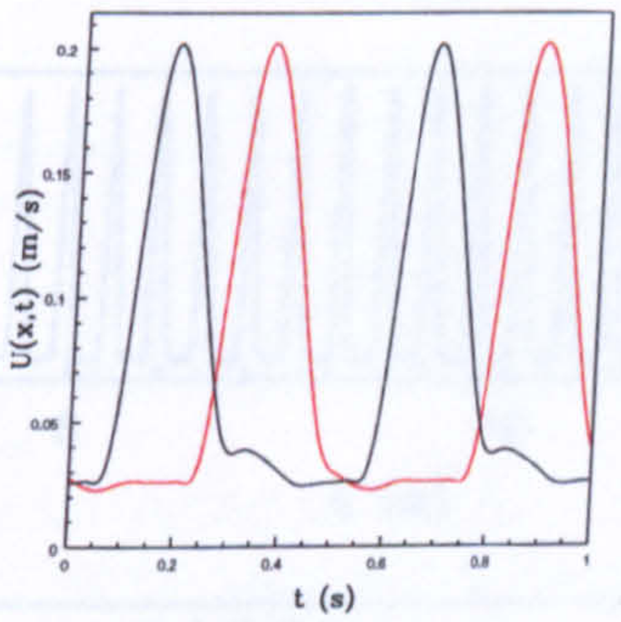


Figure 6.26: Calculated velocity waveform in the individual sections of placenta C. Artery 1 is the black line and artery 31 is the red line in the plots.

No reversed flow is seen in these results, which is similar to the physiological waveforms (figure 6.11 (a)), but the decline in flow following the peak is more sudden than for previous results. The reflection coefficients are 0.008 and -0.333 at the ends of the umbilical arteries, these are less than for the other two placentas modelled. This partly explains why the decline in velocity after the peak is more rapid. There also appears to be relatively little influence of the remainder of the network particularly on the red waveform, which looks very similar to the imposed sine squared waveform, however these are the results for the made up umbilical artery data.

6.8.2 Monochorionic placenta waveforms

In this section the entire monochorionic network in figure 6.25 is investigated. Figure 6.27 shows the velocity waveforms in umbilical arteries 1 and 31 of the yellow and red arterial networks respectively. The magnitudes hardly change from cycle to cycle and the periodic pattern is difficult to discern. This shows that the very small AAA in this network has not significantly affected the flow in the umbilical arteries. The velocity waveform in the AAA itself is also shown and in contrast to the flows in the umbilical arteries, there is a significant change in velocity magnitude with time

in this vessel.

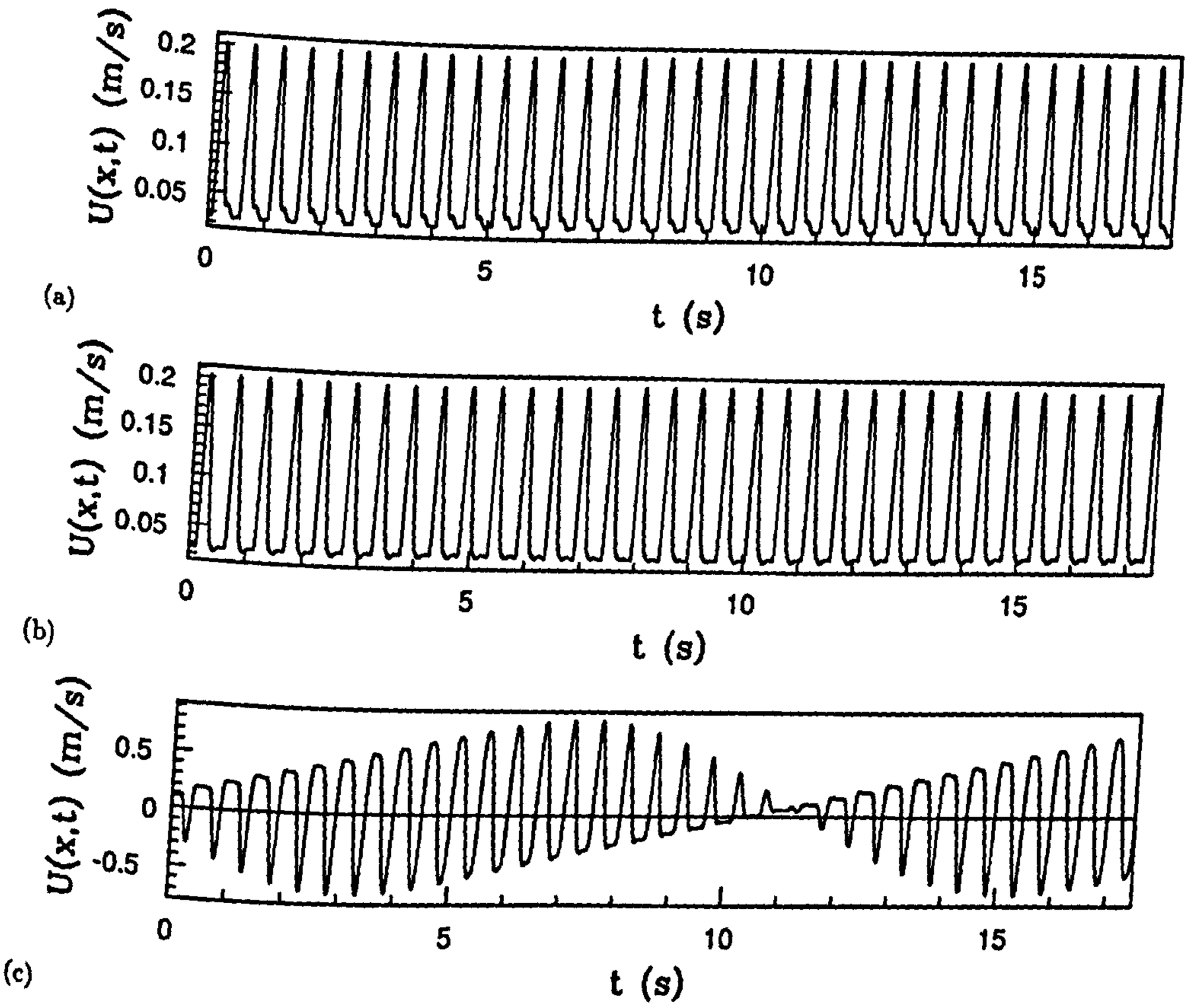


Figure 6.27: The effect of mismatched heart rates on the velocity waveforms in the two fetuses in placenta B. The waveforms in umbilical arteries 1 and 31 are in figures (a) and (b) respectively and (c) is in the arterio-arterial anastomosis, artery 51.

The mass fluxes for the system calculated into and out of each placental circulation are shown in table 6.3. The inflow and the outflow of the yellow arterial system are 224 ml/min and 225 ml/min respectively and the inflow and outflow of the red arterial system are 150 ml/min and 149 ml/min respectively. Therefore the net flux through the AAA is very small 1.2 ml/min, which is equivalent to only 0.65 % of the average inflow for the two placentas, and the transfusion from the red network to the yellow network is low. This small flux through the AAA may be balancing the flow through the very small AVAs seen in the microcirculation (yellow-blue connections), which we have not considered. The tiny flux in this network and the small effect seen on the umbilical arteries of the network despite the large variations in the velocity in the AAA show how important the area of the AAA is.

Originally the umbilical artery data for the yellow side was also used for the data on the red side, but the computations failed due to a diverging velocity through the

Placenta C	**Volume Flux (litres per minute)**
Input flux into yellow placenta from fetus $u_1A_1 + u_3A_3 =$	0.224
Output flux from yellow placenta into fetus $u_5A_5 + u_7A_7 + u_8A_8 + u_{12}A_{12} + u_{14}A_{14} + u_{16}A_{16} + u_{18}A_{18} + u_{20}A_{20} + u_{22}A_{22} + u_{24}A_{24} + u_{26}A_{26} + u_{27}A_{27} + u_{29}A_{29} + u_{30}A_{30} =$	0.225
Net Flux Donor (Yellow) Output - Input Flux =	**0.00121**
Input flux into red placenta from fetus $u_{31}A_{31} + u_{33}A_{33} =$	0.150
Output flux from red placenta into fetus $u_{37}A_{37} + u_{39}A_{39} + u_{40}A_{40} + u_{41}A_{41} + u_{43}A_{43} + u_{44}A_{44} + u_{48}A_{48} + u_{49}A_{49} + u_{50}A_{50} =$	0.149
Net Flux Receptor (Red) Output - Input Flux =	**−0.00121**
Flux through AA Anastomoses $u_{51}A_{51} =$	0.00121
As a percentage of the average inflow =	0.647%

Table 6.3: Table of fluxes in the arterial network of the monochorionic placenta C for the same input pressure magnitudes, but different heart rates.

AAA. Therefore the umbilical arteries of the red network were reduced to produce more physiological waveforms and more appropriate input conditions.

The yellow network is about the same size either side of the umbilical arteries, but the umbilical anastomosis (Hyrtyl's equilibrating anastomosis) on the yellow side is unusually small compared with others we have modelled. Each umbilical artery on the yellow network therefore fed about the same size network, but for the red network one side was far bigger than the other. The AAA was present on the smaller network, which resulted in a large flow down the AAA. On reflection we decided it was wrong to use the data from the yellow side for the red network, therefore we have adapted the red umbilical arteries slightly to suit the network. This has been done mainly by increasing the size of the umbilical anastomosis and slightly reducing the size of the umbilical artery, which is associated with the side of the network that channels blood to the AAA, artery 51. This will in effect reduce the inflow to the red arterial network. If one side of the network develops more and therefore needs more blood, the umbilical anastomosis allows blood to enter into a different section of the placenta, and shows the importance of the size of umbilical anastomosis. These results illustrate how important it is to obtain correct physiological data for the umbilical arteries, anastomoses and arteries in the placentas.

6.9 Summary

Our investigations into the flows in monochorionic placentas have involved two main steps: the acquisition of the anatomy and simple flow modelling. Several monochorionic placentas have been successfully cast (section 6.4), which showed that the connectivity of the arteries varies significantly and it is not obvious whether there is any particular order to the development of the vessels.

The results obtained using the one-dimensional wave propagation code to model waveforms in arterial networks of monochorionic placentas were promising in that they exhibit the same main features as those observed in-vivo. This suggests that the time domain one-dimensional code is a reasonable and useful method of predicting and analysing flow waveforms and fluxes throughout fetoplacental networks. Due to the lack of knowledge about the inflow and outflow boundary conditions and the wall properties of these placental networks, we have not attempted to model the precise form of the waveforms seen in-vivo, unlike our modelling in previous chapters. Instead we have concentrated on the dynamic interaction between the two inputs in the overall domains and the flow distribution and mass fluxes. The inflow condition will probably be the greatest influence because the input should be the waveform from the systemic circulation of the fetus rather than the output of the heart as in previous chapters. The effects of a number of different parameters on the waveforms have been considered for three monochorionic fetoplacental circulations where the two fetoplacental circulations are connected by arterio-arterial anastomoses and arterio-venous anastomoses. For the twin fetuses modelled in this chapter to have survived, homeostasis must have been maintained. This is the existence of a stable internal environment required for all organisms to survive and would not have occurred if one of the fetuses received too much blood. However, the twin fetuses were healthy and did survive until birth, therefore the mass-fluxes in the fetoplacental circulations must have balanced for all three cases and the use of the one-dimensional code to investigate the mass fluxes is very interesting.

By modelling the fetoplacental circulation in the intertwin case with different heart rates for each fetus the characteristic periodic pattern in the arterio-arterial anastomoses and umbilical arteries was produced. For these waveforms it can be

seen that for several beats one fetus will be receiving too much blood and then vice-versa and the mass-flux oscillates around the average blood flow. This should maintain homeostasis on average and the mass fluxes calculated in this chapter were the averages over the entire pattern.

For the detailed study of placenta A, the magnitude and shape of the waveforms in the intertwin case were altered by variations in the input magnitude and the terminal resistance, but the most significant effect was on the volume fluxes. It was found that a combination of different input pressures and increased terminal resistance on the larger fetus' placental circulation was required for the fluxes to balance in each fetus. This combination can be justified physiologically and gave encouragingly similar waveforms in the anastomosis and umbilical cords to those seen in-vivo. These results suggest that the arterio-arterial anastomosis does indeed have a 'protective' influence because it provides a flow path for blood to return to the smaller fetus which mitigates the effects of the flow through the large arterio-venous anastomosis. Since there is such a large volume flux through the arterio-arterial anastomosis, it is clearly an important conduit in the fetoplacental circulation for this case and thus any surgical alteration to arterio-arterial anastomoses identified in intertwin placentas in-vivo should certainly not be automatic.

It was shown that when the arterio-arterial anastomosis was reduced in area for placenta A then there was a very large imbalance of mass-flux in the fetoplacental circulation and the chances of the fetus' survival would be greatly reduced. Indeed for this case the arterio-arterial anastomosis may have developed into a vessel of large cross-sectional area in order to maintain homeostasis. For the other two placentas, B and C, which had smaller AAAs then the area of the arterio-arterial anastomosis has also been proportionate to that of the arterio-venous anastomosis. In fact, in the casts of all of the placentas we have not found one large arterio-venous anastomosis without balancing anastomoses of some sort. This tallies with the results of the numerical modelling and we expect that for these fetuses to survive to delivery as these have, either a large or several smaller arterio-arterial anastomoses or an arterio-venous anastomosis from the larger fetus to the smaller fetus would need to co-exist.

From a clinical perspective, the waveforms in the umbilical artery reveal the

presence of any significant arterio-arterial anastomoses through the periodic variation in the velocity waves. Once an arterio-arterial anastomosis has been identified, its waveform can be very revealing, particularly if the net volume fluxes are calculated. This could be done straight from Doppler ultrasound flow-probe readings providing sufficient area data is available. A high net flux indicates that there must be another significant flow conduit in the placental circulation and may indicate the presence of an arterio-venous anastomosis, which are generally more difficult to identify than arterio-arterial anastomoses using current methods. The identification of any potential unbalancing arterio-venous anastomoses is vital before laser ablation is performed.

Chapter 7

Conclusions and suggestions for further work

7.1 Conclusions

In conclusion, we can say that the broad objectives set out in section 1.3 have been achieved. A one-dimensional model has been developed to solve the pressure and velocity waveforms in arterial networks. Two types of arterial networks have been successfully modelled: the human systemic arterial tree and the arterial networks in monochorionic placentas. Little geometry data is available in the literature for both of these systems and therefore new physiological geometry data has been obtained for single examples of the two networks as an input into the one-dimensional code. Clinical waveforms were obtained for the measured arterial networks and the pressure and velocity waveforms calculated using the one-dimensional model. The calculated waveforms compared well with the in-vivo waveforms and the majority of the features were captured even using simple generic boundary conditions and properties. This demonstrates the great importance of the geometry and we believe that it is probably of primary significance in producing the flow and pressure waves observed in-vivo.

7.1.1 Numerical model

The governing equations for one-dimensional wave propagation have been successfully implemented in a computer model that can be applied to the calculation of

flow and pressure waveforms in arterial networks. They were discretised using a high order spectral/hp discontinuous Galerkin method that was extended to model a network of vessels using the upwinded characteristic information with the conservation of mass and momentum at the boundary of the vessels. The modelling was performed in the time domain and allows for simple interpretation and a direct link between observable wave features and physiological parameters. The discontinuous Galerkin method is ideally suited to the modelling of arterial networks, because it allows discontinuities in vessel properties to be incorporated, such as may occur at a stent, or bifurcation, and propagates the waves with minimal dispersion. The use of a spectral/hp method is also attractive in arterial networks, because the solution is generally smooth, so rapid numerical convergence can be achieved. This was demonstrated by the convergence computations in Chapter 3, where accurate solutions were obtained very quickly ($\sim$ 9 minutes for 6 cycles for the 55 arterial network, figure 3.6). The results were validated by comparing the numerical solution with the analytic solution of a simple test case in section 3.4.2. In section 3.5 the code was further validated by comparing predicted waveforms with those calculated using a Taylor Galerkin finite element solver.

The governing equations for both linear and non-linear models were implemented successfully and comparisons were made for a simple tube and a bifurcation in section 3.4 and for a whole arterial network in section 4.4. The results from the linear and non-linear analyses were found to be very similar for the arterial tree. However, the linear analysis is restricted to modelling only constant area vessels, i.e. the arteries can not taper, which is shown to be excessively restricted.

7.1.2 Human arterial tree

Two versions of the human systemic arterial tree have been studied. In Chapter 4 the waveforms in a well-matched arterial network were computed. The network has been studied by many other authors, but it is a composite of many different measurements including diameter information from dogs. In Chapter 5 the velocity and pressure waveforms were computed for a new tapered arterial network. This new model was successfully constructed from in-vivo magnetic resonance images and was for a single living human (figures 5.3 - 5.5).

Clinical waveforms were obtained for pressure and velocity waveforms for the same subject as the MRI system for a variety of arteries in the body (figure 5.7). These in-vivo waveforms provide a direct comparison with the computational results (figure 5.12) for the MRI network with no uncertainties about typical physiological variation. There was a great similarity in magnitude and shape for many of the waveforms including those in the terminal vessels. The pressure waveforms were particularly good and the overall shapes of the waves calculated for the new network were a significant improvement on the waveforms obtained for the well-matched network. It was also shown that many of the features of the waveforms were produced by the tapering and bifurcations of the large arteries and that it is probably not true to say that all reflections occur at the periphery.

Terminal resistance must be applied to the well-matched system for the waveforms in the system to appear at all physiological. However, for the new tapered arterial network no terminal resistance was needed for the waveforms to appear physiological. It was shown in section 5.2.2 that substantial reflections occur from the tapered vessels and the ill-matched bifurcations and in section 5.2.9 that applying a simple reflecting boundary condition at the terminal vessels did not make the waveforms any more physiological in any of the arteries of the network.

The geometry of the network was found to have a significant effect on the waveforms and magnitudes in the arterial system and therefore it is of great importance to have good geometry data. We believe that the tapered network constructed from the MR images provides a good basis for further research.

The effects of altering parameters were assessed for both networks. It was found that the inflow boundary condition had a significant effect on the waveforms throughout the arterial tree. The imposed velocity waveform with the reversed flow after the systolic flow (BC3) gave consistently similar waveforms to the clinical waveforms. However, the imposed W_1 characteristic, which was modelled as an absorber for the first 0.3 seconds and then as a reflector for the rest of the cycle (BC4) is a more attractive boundary condition because it produces good waveforms with fewer assumptions about the actual physiological input and can be applied generally.

The potential of the one-dimensional wave propagation model for use in surgical planning was demonstrated in section 5.5, where the addition of a stent and a bypass

graft to the arterial network were modelled.

7.1.3 Monochorionic networks

In Chapter 6 the velocity waveforms and volume fluxes in monochorionic placentas were studied using the one-dimensional code. These networks are relatively unstudied compared with those of the human arterial system and as far we know there is no published geometry data for these models. The connectivity and geometry data for these networks was obtained by producing plastic casts of newly delivered placentas (figures 6.1 and 6.2).

The computed waveforms successfully predict the main features of the umbilical artery waveforms and in section 6.6.2 the unusual periodic waveform seen in-vivo in the arterio-arterial anastomosis of placenta A (figure 6.16) was also calculated computationally for this placenta (figure 6.17 (a)). The volume fluxes were calculated and the parameters were altered until the fluxes balanced in the two fetoplacental circulations. This simulates the homeostasis that must have been maintained for the fetuses to survive until delivery. It was shown that for these volume fluxes to balance then there needs to be a substantial flow through the arterio-arterial anastomosis (table 6.1) in placenta A. This suggests that the arterio-arterial anastomosis was indeed protective in this placenta and that surgical interference with arterio-arterial anastomoses should not be automatic.

With regard to diagnosis, it appears that the presence of any significant arterio-arterial anastomoses are obvious in the periodic variation of the umbilical artery waveforms. It may then be possible to diagnose the presence of the harder to detect arterio-venous anastomoses by integrating the volume fluxes over the cycle in the arterio-arterial anastomoses. If this is not close to zero then another significant flow conduit must be present.

We hesitate to suggest that this simplistic model should form the basis of any clinical decisions, however, even these simple models can illuminate the reasons for clinical observations and suggest mechanisms for these observations. We hope that given improvements in the modelling and suitable testing and validation that it could eventually become a clinical tool. Until then, it can only be a model which helps us interpret what is seen clinically, but we feel that the understanding of the effects of

waves and their reflections and re-reflections in these idealised model networks can help us to understand the complex flows in real arterial systems.

7.2 Suggestions for further work

The importance of accurate geometry data has been demonstrated throughout this work and we are very keen to extend the network by modelling more arteries of the human subject, which we believe would improve the predicted waveforms. We believe that incorporating accurate data for the arteries branching off the aorta would be particularly beneficial, especially with respect to the velocity magnitudes. The entire fetal circulation could also be modelled with the monochorionic placentas, which would improve the accuracy of the waves in the umbilical arteries and also allow for a more direct assessment of the effect of surgical interventions on the fetuses in utero. Improvements in imaging techniques ought to make it possible to obtain better geometry data non-invasively and to incorporate smaller vessels.

Imposing an actual in-vivo velocity waveform at the ascending aorta taken from the subject would also be very interesting and a significant improvement on a half-sine wave, however, these can be difficult to obtain and would be case specific.

It would also be attractive to have specific data for the wall properties of the tapered network and the monochorionic placentas, including Young's modulus and wall thickness. Such data may be difficult to obtain in-vivo, but it should be possible to determine some of the parameters for the placentas.

Many of the modelling assumptions we have made in the thesis are quite simple and there is great scope for incorporating additional variables. However, some of the improved models require a great deal of data that is not available. One feature that we think would be very useful to incorporate is viscoelasticity of the vessel wall, which is thought to significantly damp the waves without altering their phase [114, 38] and we think this would lend to more accurate predictions of the diastolic wave features (section 5.6).

Modelling the non-linearity of the wall distensibility could be rapidly incorporated into our model by changing the relationship between area and pressure (equation (2.3)).

The vast number of vessels in the microcirculation means that solving the entire circulation would be computationally expensive and also some of the assumptions made in deriving the one-dimensional model are not valid in the microcirculation. We have modelled this terminal resistance using a simple reflector boundary condition, however, it may be more attractive to model this using multiscale techniques, as proposed by Formaggia *et al.* [40, 117] and Smith *et al.* [140], where the 1D model is coupled to a lumped 0D model that represent the smallest vessels. Olufsen [100] suggests that a fractal structure represents the reflection from the terminal vessels more physiologically and some preliminary work on fractal techniques has been performed by Parker.

These suggestions could all be incorporated in future work, however, their physiological relevance is reliant upon relevant parameter information and these properties are difficult to predict.

Once a validated one-dimensional model has been established, the one-dimensional wave propagation model could be used for a number of purposes. As well as the diagnosis and predictive tools mentioned previously, the one-dimensional model could be linked with three-dimensional modelling and used as a boundary condition. The predicted local areas in the arteries calculated from the one-dimensional model could be used as a boundary condition for the local wall displacement in a three-dimensional Arbitrary Lagrangian-Eulerian (ALE) fluid solver and the velocity could be used as the inflow boundary condition [37].

Appendix A

Human arterial network data

A.1 55 well-matched arterial data

#	Name	Radius r (mm)	Diastolic area A_0 (mm^2)	Wall thickness h (mm)	Length l (mm)	Young's modulus E (MPa)	Wavespeed c_0 (m/s)
1	Ascending Aorta	14.70	678.87	1.63	40	0.4	4.66
2	Aortic Arch I	12.63	501.14	1.26	20	0.4	4.42
3	Brachiocephalic	6.99	153.50	0.8	34	0.4	4.73
4	R. Subclavian I	5.41	91.95	0.67	34	0.4	4.93
5	R. Carotid	4.73	70.29	0.63	177	0.4	5.11
6	R. Vertebral	2.40	18.10	0.45	148	0.8	8.57
7	R. Subclavian II	5.15	83.32	0.67	422	0.4	5.05
8	R. radius	3.67	42.31	0.43	235	0.8	6.78
9	R. Ulnar I	4.54	64.75	0.46	67	0.8	6.30
10	R. Interosseous	1.94	11.82	0.28	79	1.6	10.63
11	R. Ulnar II	4.33	58.90	0.46	171	0.8	6.45
12	R. internal Corotid	3.82	45.84	0.45	176	0.8	6.79
13	R. ext. Carotid	3.82	45.84	0.42	177	0.8	6.56
14	Aortic Arch II	11.95	448.63	1.15	39	0.4	4.34
15	L. Carotid	4.13	53.59	0.63	208	0.4	5.47
16	L. int. Carotid	3.34	35.05	0.45	176	0.8	7.27
17	L. ext. Carotid	3.34	35.05	0.42	177	0.8	7.02
18	Thoracic Aorta I	11.20	394.08	1.1	52	0.4	4.39
19	L. Subclavian II	4.74	70.58	0.66	34	0.4	5.22
20	Vertebral	2.03	12.95	0.45	148	0.8	9.32
21	L. Subclavian II	4.55	65.04	0.67	422	0.4	5.37
22	L. Radius I	3.24	32.98	0.43	235	0.8	7.21
23	L. Ulnar I	4.01	50.52	0.46	67	0.8	6.70
24	L. Interosseous	1.72	9.29	0.28	79	1.6	11.29
25	L. Ulnar II	3.83	46.08	0.46	171	0.8	6.86
26	Intercoastals	3.17	31.57	0.49	80	0.4	5.50
27	Thoracic Aorta II	10.71	360.35	1	104	0.4	4.28
28	Abdominal I	9.20	265.90	0.9	53	0.4	4.38
29	Celiac I	5.88	108.62	0.64	20	0.4	4.62
30	Celiac II	2.00	12.57	0.64	10	0.4	7.92
31	Hepatic	4.58	65.90	0.49	66	0.4	4.58
32	Gastric	3.75	44.18	0.45	71	0.4	4.85
33	Splenic	3.86	46.81	0.54	63	0.4	5.23
34	Sup. Mensenteric	4.99	78.23	0.69	59	0.4	5.20
35	Abdominal II	8.43	223.26	0.8	10	0.4	4.31
36	L. Renal	3.50	38.48	0.53	64	0.4	5.45
37	Abdominal III	7.94	198.06	0.8	10	0.4	4.44
38	R. Renal	3.50	38.48	0.53	32	0.4	5.45
39	Abdominal IV	6.65	138.93	0.75	106	0.4	4.70
40	Inf. Mesenteric	1.94	11.82	0.43	50	0.4	6.59
41	Abdominal V	6.31	125.09	0.65	10	0.4	4.49
42	R. common Iliac	4.70	69.40	0.6	59	0.4	5.00
43	L. common Iliac	4.70	69.40	0.6	58	0.4	5.00
44	L. ext. iliac	4.82	72.99	0.53	144	0.8	6.56
45	L. int. Iliac	3.01	28.46	0.4	50	1.6	10.20
46	L. Femoral	3.61	40.94	0.5	443	0.8	7.37
47	L. deep Femoral	3.56	39.82	0.47	126	0.8	7.19
48	L. post. Tibial	3.76	44.41	0.45	321	1.6	9.68
49	L. ant. Tibial	1.98	12.32	0.39	343	1.6	12.42
50	R. ext. Iliac	4.82	72.99	0.53	145	0.8	6.56
51	R. int. Iliac	3.01	28.46	0.4	50	1.6	10.20
52	R. Femoral	3.61	40.94	0.5	444	0.8	7.37
53	R. deep Femoral	3.56	39.82	0.47	127	0.8	7.19
54	L. post. Tibial	3.75	44.18	0.45	322	1.6	9.70
55	R. ant. Tibial	1.97	12.19	0.39	344	1.6	12.45

Table A.1: Data for the well-matched network. (Density, $\rho = 1021\ kg/m^3$).

#	Name	$A/A_0\|_1$	Beta β (MPa/m)	Strouhal number St	Terminal reflection coefficient R_t
1	Ascending Aorta	1.000	1.702	0.00841	-
2	Aortic Arch I	0.738	1.783	0.00762	-
3	Brachiocephalic	0.226	3.695	0.00394	-
4	R. Subclavian I	0.135	5.166	0.00293	-
5	R. Carotid	0.104	6.355	0.00247	-
6	R. Vertebral	0.027	35.262	0.00075	0.906
7	R. Subclavian II	0.123	5.701	0.00272	-
8	R. radius	0.062	14.410	0.00144	0.82
9	R. Ulnar I	0.095	10.073	0.00192	-
10	R. Interosseous	0.017	67.158	0.00049	0.956
11	R. Ulnar II	0.087	11.074	0.00179	0.893
12	R. internal Corotid	0.068	13.919	0.00150	0.784
13	R. ext. Carotid	0.068	12.991	0.00155	0.79
14	Aortic Arch II	0.661	1.817	0.00734	-
15	L. Carotid	0.079	8.335	0.00201	-
16	L. int. Carotid	0.052	18.207	0.00123	0.784
17	L. ext. Carotid	0.052	16.993	0.00127	0.791
18	Thoracic Aorta I	0.580	1.979	0.00681	-
19	L. Subclavian II	0.104	6.629	0.00242	-
20	Vertebral	0.019	49.287	0.00058	0.906
21	L. Subclavian II	0.096	7.304	0.00226	-
22	L. Radius I	0.049	18.488	0.00120	0.821
23	L. Ulnar I	0.074	12.912	0.00160	-
24	L. Interosseous	0.014	85.437	0.00041	0.956
25	L. Ulnar II	0.068	14.154	0.00149	0.893
26	Intercoastals	0.047	11.004	0.00154	0.627
27	Thoracic Aorta II	0.531	1.967	0.00668	-
28	Abdominal I	0.392	2.400	0.00560	-
29	Celiac I	0.160	4.177	0.00340	-
30	Celiac II	0.019	36.108	0.00067	-
31	Hepatic	0.097	5.272	0.00267	0.925
32	Gastric	0.065	7.222	0.00206	0.921
33	Splenic	0.069	8.179	0.00197	0.93
34	Sup. Mensenteric	0.115	6.254	0.00256	0.934
35	Abdominal II	0.329	2.541	0.00521	-
36	L. Renal	0.057	9.764	0.00171	0.861
37	Abdominal III	0.292	2.864	0.00477	-
38	R. Renal	0.057	9.764	0.00171	0.861
39	Abdominal IV	0.205	3.827	0.00377	-
40	Inf. Mesenteric	0.017	25.784	0.00079	0.918
41	Abdominal V	0.184	3.684	0.00375	-
42	R. common Iliac	0.102	6.130	0.00251	-
43	L. common Iliac	0.102	6.130	0.00251	-
44	L. ext. iliac	0.108	10.297	0.00196	-
45	L. int. Iliac	0.042	39.854	0.00079	0.925
46	L. Femoral	0.060	17.317	0.00131	-
47	L. deep Femoral	0.059	16.738	0.00132	0.885
48	L. post. Tibial	0.065	28.733	0.00104	0.724
49	L. ant. Tibial	0.018	89.801	0.00043	0.716
50	R. ext. Iliac	0.108	10.297	0.00196	-
51	R. int. Iliac	0.042	39.854	0.00079	0.925
52	R. Femoral	0.060	17.317	0.00131	-
53	R. deep Femoral	0.059	16.738	0.00132	0.888
54	L. post. Tibial	0.065	28.887	0.00103	0.724
55	R. ant. Tibial	0.018	90.715	0.00042	0.716

Table A.2: Table of parameters for the well-matched network.

A.2 MRI tapered arterial network

#	Name	Diameter d (mm)	Diastolic area A_0 (mm^2)	Wall thickness h (mm)	Length l (mm)	Young's modulus E (MPa)	Wavespeed c_0 (m/s)
1	Ascending Aorta	22.98	384.55	1.217	36	0.4	4.64
2	Aortic Arch 1	18.41	244.99	0.883	6	0.4	4.43
3	Brachiocephalic	11.47	95.78	0.607	27	0.4	4.64
4		9.14	60.75	0.484		0.4	4.64
5	Right subclavian 1	5.97	26.25	0.376	6	0.4	5.05
6	Right common carotid	6.22	28.61	0.422	103	0.4	5.24
7		6.04	26.99	0.410		0.4	5.24
8	Right vertebrals	3.87	11.51	0.383	235	0.8	8.85
9		3.14	7.59	0.311		0.8	8.85
10	Right subclavian 2	4.47	14.68	0.281	446	0.4	5.05
11	Right Brachial	2.98	6.55	0.188		0.4	5.05
12	Right Radial	2.11	3.38	0.124	231	0.8	6.86
13	Right Ulnar 1	2.68	5.44	0.145	27	0.8	6.56
14	Right Interosseous	1.48	1.70	0.110	123	1.6	10.84
15	Right Ulnar 2	1.42	1.53	0.077	204	0.8	6.56
16	Right sinus carotid	5.41	22.19	0.319	144	0.8	6.86
17	Right internal carotid	4.14	13.03	0.244		0.8	6.86
18	Right external carotid	2.73	5.63	0.161	65	0.8	6.86
19		2.16	3.54	0.127		0.8	6.86
20	Aortic Arch 2	18.41	246.81	0.975	5	0.4	4.64
21	Left common carotid	6.81	34.26	0.462	141	0.4	5.24
22		5.87	25.45	0.398		0.4	5.24
23	Left sinus carotid	5.15	20.07	0.303	137	0.8	6.86
24	Left internal carotid	4.18	13.25	0.246		0.8	6.86
25	Left external carotid	3.01	6.87	0.177	65	0.8	6.86
26		1.90	2.72	0.112		0.8	6.86
27	Descending/Abdominal Aorta	18.41	244.99	0.883	312	0.4	4.43
28		13.40	129.66	0.642		0.4	4.43
29	Left subclavain 1	7.78	44.57	0.490	24	0.4	5.05
30		6.36	29.74	0.400		0.4	5.05
31	Left vertebral	3.40	8.87	0.336	74	0.8	8.85
32		2.97	6.80	0.294		0.8	8.85
33	Left subclavain 2	4.47	14.68	0.281	446	0.4	5.05
34	Left Brachial	2.98	6.55	0.188		0.4	5.05
35	Left Radial	2.11	3.38	0.124	231	0.8	6.86
36	Left Ulnar 1	2.68	5.44	0.145	27	0.8	6.56
37	Left Interosseous	1.48	1.70	0.110	123	1.6	10.84
38	Left Ulnar 2	1.42	1.53	0.077	204	0.8	6.56
39	Left Iliac	9.37	64.66	0.590	69	0.4	5.05
40		8.90	58.33	0.560		0.4	5.05
41	Right Iliac	9.35	64.38	0.588	69	0.4	5.05
42		8.41	52.09	0.529		0.4	5.05
43	Left External Iliac	7.85	46.59	0.424	117	0.8	6.56
44	Left internal Iliac	5.50	23.40	0.355	42	1.6	10.09
45	Left femoral	7.19	39.39	0.496	471	0.8	7.41
46		5.52	23.22	0.381		0.8	7.41
47	Left deep femoral	5.57	23.56	0.356	120	0.8	7.14
48		4.61	16.13	0.295		0.8	7.14
49	Left Posterior tibial 1	4.11	13.02	0.244	21	1.6	9.70
50	Left Anterior tibial	2.45	4.66	0.244	312	1.6	12.52
51		1.55	1.87	0.154		1.6	12.52
52	Left Posterior tibial 2	2.49	4.80	0.148	309	1.6	9.70
53		1.93	2.87	0.115		1.6	9.70
54	Left Peroneal	2.82	6.11	0.167	189	1.6	9.70
55		1.67	2.16	0.100		1.6	9.70
56	Right External Iliac	7.69	44.67	0.415	117	0.8	6.56
57	Right internal Iliac	4.64	16.60	0.299	42	1.6	10.09
58	Right femoral	6.65	33.74	0.459	414	0.8	7.41
59		5.75	25.20	0.397		0.8	7.41
60	Right deep femoral	5.69	24.61	0.364	126	0.8	7.14
61		4.66	16.50	0.298		0.8	7.14
62	Right Posterior tibial 1	3.99	12.26	0.237	96	1.6	9.70
63	Right Anterior tibial	3.33	8.61	0.331	375	1.6	12.52
64		2.41	4.53	0.240		1.6	12.52
65	Right Posterior tibial 2	2.50	4.82	0.149	291	1.6	9.70
66		1.93	2.87	0.115		1.6	9.70
67	Right Peroneal	2.91	6.51	0.173	171	1.6	9.70
68		1.66	2.11	0.098		1.6	9.70

Table A.3: Data for the MRI tapered network. (Density, $\rho = 1021\ kg/m^3$).

#	Name	$A/A_0\|_1$	Beta β (MPa/m)	Strouhal number St	R_c (Bifurcation)	R_c (Taper)
1		1.000	2.244	0.00636	0.043	-
2	Ascending Aorta	0.637	2.556	0.00532	-0.038	-
3	Aortic Arch 1	0.249	4.496	0.00317	-	-
4	Brachiocephalic	0.158	5.645	0.00253	0.102	0.34
5	Right subclavian 1	0.068	10.150	0.00153	0.105	-
6	Right common carotid	0.074	10.469	0.00154	-	-
7	Right vertebrals	0.070	10.780	0.00149	0.119	0.041
8	Right subclavian 2	0.030	47.168	0.00058	-	-
9	Right Brachial	0.020	58.067	0.00047	-	0.28
10	Right Radial	0.038	13.571	0.00114	-	-
11	Right Ulnar 1	0.017	20.311	0.00076	-0.009	0.42
12	Right Interosseous	0.009	52.207	0.00040	-	-
13	Right Ulnar 2	0.014	37.732	0.00053	0.361	-
14	Right sinus carotid	0.004	184.070	0.00018	-	-
15	Right internal carotid	0.004	71.220	0.00028	-	-
16	Right external carotid	0.058	20.378	0.00103	-	-
17	Aortic Arch 2	0.034	26.599	0.00079	-	0.32
18	Left common carotid	0.015	26.599	0.00052	-	-
19	Left sinus carotid	0.009	40.456	0.00041	-	0.32
20	Left internal carotid	0.642	51.039	0.00509	-0.094	-
21	Left external carotid	0.089	2.801	0.00168	-	-
22	Descending/Abdominal Aorta	0.066	9.568	0.00145	0.106	0.45
23	Left subclavain 1	0.052	11.101	0.00098	-	-
24	Left vertebral	0.034	21.427	0.00080	-	0.27
25	Left subclavain 2	0.018	26.370	0.00058	-	-
26	Left Brachial	0.007	26.370	0.00036	-	0.54
27	Left Radial	0.637	36.626	0.00532	-	-
28	Left Ulnar 1	0.337	58.176	0.00387	0.068	0.32
29	Left Interosseous	0.116	2.556	0.00199	-	-
30	Left Ulnar 2	0.077	2.556	0.00163	0.202	0.27
31	Left Iliac	0.023	2.867	0.00051	-	-
32	Right Iliac	0.018	2.867	0.00044	-	0.2
33	Left External Iliac	0.038	3.513	0.00114	-	-
34	Left internal Iliac	0.017	7.789	0.00076	-0.009	0.43
35	Left femoral	0.009	9.535	0.00040	-	-
36	Left deep femoral	0.014	53.720	0.00053	0.361	-
37	Left Posterior tibial 1	0.004	61.340	0.00018	-	-
38	Left Anterior tibial	0.004	13.571	0.00028	-	-
39	Left Posterior tibial 2	0.168	20.311	0.00240	-	-
40	Left Peroneal	0.152	52.207	0.00228	0.102	0.065
41	Right Iliac	0.167	37.732	0.00239	-	-
42	Right External Iliac	0.135	184.070	0.00215	0.100	0.15
43	Right internal Iliac	0.121	71.220	0.00156	-0.097	-
44	Right femoral	0.061	6.467	0.00072	-	-
45	Right deep femoral	0.102	6.808	0.00127	-	-
46	Right Posterior tibial 1	0.060	6.481	0.00098	0.293	0.33
47	Right Anterior tibial	0.061	7.205	0.00102	-	-
48	Right Posterior tibial 2	0.042	12.893	0.00085	-	0.25
49	Right Peroneal	0.034	43.003	0.00056	0.088	-
		0.012	17.845	0.00026	-	-
		0.005	23.244	0.00016	-	0.53
		0.012	21.428	0.00034	-	-
		0.007	25.896	0.00026	-	0.34
		0.016	53.212	0.00038	-	-
		0.006	148.164	0.00023	-	0.57
		0.116	234.005	0.00153	-0.081	-
		0.043	87.661	0.00061	-	-
		0.088	113.290	0.00118	-	-
		0.066	77.644	0.00102	0.271	0.19
		0.064	130.635	0.00105	-	-
		0.043	13.167	0.00086	-	0.26
		0.032	51.051	0.00054	0.039	-
		0.022	19.281	0.00035	-	-
		0.012	22.309	0.00026	-	0.41
		0.013	20.966	0.00034	-	-
		0.007	25.607	0.00026	-	0.35
		0.017	54.839	0.00040	-	-
		0.005	109.050	0.00023	-	0.61

Table A.4: Table of parameters for the MRI tapered network.

Appendix B

Monochorionic arterial network data

B.1 Data for placenta A

#	Diameter d (mm)	Diastolic area A_0 (mm^2)	$A/A_0\|_1$	Wall thickness h (mm)	Length l (mm)	Beta β (MPa/m)	Strouhal number S_t	Reflection coefficient R_c
1	4.45	15.55	1.000	0.223	500	10.14	0.001341	-0.507
2	3.50	9.62	0.619	0.175	10	12.90	0.001054	-0.400
3	3.50	9.62	0.619	0.175	510	12.90	0.001054	-0.400
4	4.04	12.82	0.824	0.202	125	11.17	0.001217	0.000
5	6.95	37.94	2.439	0.348	50	6.49	0.002094	-0.113
6	3.60	10.18	0.654	0.180	5	12.54	0.001085	-
7	6.90	37.39	2.404	0.345	40	6.54	0.002079	0.043
8	2.00	3.14	0.202	0.100	10	22.57	0.000603	-
9	6.30	31.17	2.004	0.315	20	7.16	0.001898	-0.090
10	3.40	9.08	0.584	0.170	10	13.28	0.001024	-
11	6.00	28.27	1.818	0.300	50	7.52	0.001808	-
12	4.45	15.55	1.000	0.223	300	10.14	0.001341	-0.318
13	3.50	9.62	0.619	0.175	10	12.90	0.001054	-0.532
14	3.50	9.62	0.619	0.175	310	12.90	0.001054	-0.532
15	5.10	20.43	1.313	0.255	50	8.85	0.001536	0.004
16	5.28	21.90	1.408	0.264	60	8.55	0.001591	-0.172
17	5.00	19.63	1.262	0.250	70	9.03	0.001506	0.083
18	3.80	11.34	0.729	0.190	100	11.88	0.001145	-
19	2.20	3.80	0.244	0.110	25	20.52	0.000663	-
20	4.04	12.82	0.824	0.202	130	11.17	0.001217	0.000
21	0.10	0.0079	0.001	0.005	10	451.35	0.000030	-
22	2.84	6.33	0.407	0.142	105	15.89	0.000856	-
23	4.21	13.92	0.895	0.211	30	10.72	0.001268	0.110
24	3.18	7.92	0.509	0.159	102	14.22	0.000956	-
25	2.03	3.24	0.208	0.102	410	22.23	0.000612	-

Table B.1: Data for placenta A (large AAA). Young's modulus = 0.4 MPa, density, ρ = 1021 kg/m^3 and $c_0 = 4.43\ m/s$ for each vessel.

B.2 Data for placenta B

#	Diameter d (mm)	Diastolic area A_0 (mm^2)	$A/A_0\|_1$	Wall thickness h (mm)	Length l (mm)	Beta β (MPa/m)	Strouhal number S_t	Reflection coefficient R_c
1	5.43	23.16	1.000	0.272	500	8.31	0.001636	-0.475
2	3.94	12.19	0.526	0.197	500	11.46	0.001187	-0.210
3	2.48	4.83	0.209	0.124	5	18.20	0.000747	-0.891
4	8.76	60.27	2.603	0.438	7	5.15	0.002639	0.205
5	4.20	13.85	0.598	0.210	21	10.75	0.001265	0.142
6	3.23	8.19	0.354	0.162	15	13.97	0.000973	0.011
7	1.68	2.22	0.096	0.084	12	26.87	0.000506	-
8	2.68	5.64	0.244	0.134	33	16.84	0.000807	-
9	1.74	2.38	0.103	0.087	30	25.94	0.000524	-
10	4.09	13.14	0.567	0.205	7	11.04	0.001232	-0.120
11	2.42	4.60	0.199	0.121	25	18.65	0.000729	-
12	3.93	12.13	0.524	0.197	4	11.48	0.001184	-0.333
13	5.10	20.43	0.882	0.255	6	8.85	0.001536	-
14	2.21	3.84	0.166	0.111	6	20.42	0.000666	0.101
15	1.30	1.33	0.057	0.065	45	34.72	0.000392	-
16	1.52	1.80	0.078	0.076	85	29.79	0.000456	-0.575
17	5.82	26.60	1.149	0.291	33	7.76	0.001753	0.069
18	3.42	9.19	0.397	0.171	19	13.20	0.001030	0.062
19	2.62	5.39	0.233	0.131	37	17.23	0.000789	-
20	1.86	2.72	0.117	0.093	45	24.27	0.000560	-
21	4.22	13.99	0.604	0.211	105	10.70	0.001271	0.041
22	2.70	5.73	0.247	0.135	37	16.72	0.000813	0.006
23	2.24	3.94	0.170	0.112	17	20.15	0.000675	-
24	1.48	1.72	0.074	0.074	34	30.50	0.000446	-
25	3.02	7.16	0.309	0.151	66	14.95	0.000910	-
26	4.37	15.00	0.648	0.219	500	10.33	0.001316	-0.521
27	4.98	19.51	0.842	0.249	500	9.06	0.001501	-0.200
28	4.61	16.69	0.721	0.231	3	9.79	0.001389	-0.467
29	6.28	30.97	1.338	0.314	4	7.19	0.001892	-0.211
30	2.58	5.23	0.226	0.129	10	17.49	0.000777	-
31	7.34	42.31	1.827	0.367	2	6.15	0.002211	0.284
32	4.93	19.09	0.824	0.247	39	9.16	0.001485	0.049
33	2.56	5.15	0.222	0.128	45	17.63	0.000771	-0.256
34	2.43	4.64	0.200	0.122	15	18.57	0.000732	-
35	2.27	4.05	0.175	0.114	45	19.88	0.000684	-
36	3.94	12.16	0.525	0.197	35	11.47	0.001185	-0.066
37	1.76	2.43	0.105	0.088	28	25.64	0.000530	-
38	3.82	11.46	0.495	0.191	8	11.82	0.001151	-0.143
39	2.08	3.40	0.147	0.104	25	21.70	0.000627	-
40	3.89	11.88	0.513	0.195	65	11.60	0.001172	-
41	2.40	4.52	0.195	0.120	39	18.81	0.000723	-0.053
42	1.38	1.50	0.065	0.069	25	32.71	0.000416	-
43	2.12	3.53	0.152	0.106	50	21.29	0.000639	-0.167
44	2.00	3.14	0.136	0.100	15	22.57	0.000603	-
45	*4.00*	*12.57*	0.543	0.200	1	11.28	0.001205	-0.108
46	2.88	*6.51*	*0.281*	*0.144*	11	15.67	0.000868	-0.312
47	2.40	4.52	0.195	0.120	*2*	*18.81*	*0.000723*	0.020
48	1.92	2.90	0.125	0.096	3	23.51	*0.000578*	-
49	1.36	1.45	0.063	0.068	20	33.19	0.000410	-
50	3.17	7.89	0.341	0.159	23	14.24	0.000955	-0.032
51	2.29	4.12	0.178	0.115	24	19.71	0.000690	-
52	2.34	4.30	0.186	0.117	12	19.29	0.000705	-
53	3.40	9.08	0.392	0.170	25	13.28	0.001024	-0.015
54	2.38	4.45	0.192	0.119	3	18.96	0.000717	-0.060
55	1.52	1.81	0.078	0.076	20	29.69	0.000458	-
56	2.02	3.20	0.138	0.101	3	22.34	0.000609	-
57	2.50	4.91	0.212	0.125	13	18.05	0.000753	-0.051
58	1.10	0.95	0.041	0.055	23	41.03	0.000331	-
59	2.39	4.49	0.194	0.120	120	18.89	0.000720	-

Table B.2: Data for placenta B (medium AAA). Young's modulus = 0.4 MPa, density, ρ = 1021 kg/m^3 and $c_0 = 4.43$ m/s for each vessel.

B.3 Data for placenta C

#	Diameter d (mm)	Diastolic area A_0 (mm^2)	$A/A_0\|_1$	Wall thickness h (mm)	Length l (mm)	Beta β (MPa/m)	Strouhal number S_t	Reflection coefficient R_c
1	5.20	21.24	1.000	0.260	500	8.68	0.001567	0.008
2	1.70	2.27	0.107	0.085	10	26.55	0.000512	-0.924
3	6.10	29.22	1.376	0.305	500	7.40	0.001838	-0.022
4	4.87	18.63	0.877	0.244	75	9.27	0.001467	-0.139
5	3.53	9.79	0.461	0.177	110	12.79	0.001063	-
6	4.35	14.86	0.700	0.218	25	10.38	0.001310	0.037
7	3.63	10.35	0.487	0.182	90	12.43	0.001094	-
8	2.10	3.46	0.163	0.105	55	21.49	0.000633	-
9	6.00	28.27	1.331	0.300	1	7.52	0.001808	0.097
10	2.57	5.19	0.244	0.129	90	17.56	0.000774	0.097
11	4.80	18.10	0.852	0.240	5	9.40	0.001446	-0.036
12	2.50	4.91	0.231	0.125	20	18.05	0.000753	-
13	4.30	14.52	0.684	0.215	20	10.50	0.001295	-0.203
14	2.60	5.31	0.250	0.130	65	17.36	0.000783	-
15	4.60	16.62	0.783	0.230	65	9.81	0.001386	-0.017
16	2.43	4.64	0.218	0.122	70	18.57	0.000732	-
17	4.00	12.57	0.592	0.200	35	11.28	0.001205	-0.030
18	2.40	4.52	0.213	0.120	15	18.81	0.000723	-
19	3.35	8.81	0.415	0.168	20	13.47	0.001009	-0.043
20	1.80	2.54	0.120	0.090	30	25.08	0.000542	-
21	3.00	7.07	0.333	0.150	30	15.05	0.000904	-0.163
22	1.70	2.27	0.107	0.085	20	26.55	0.000512	-
23	3.10	7.55	0.355	0.155	15	14.56	0.000934	0.131
24	1.13	1.00	0.047	0.057	35	39.94	0.000340	-
25	2.47	4.79	0.226	0.124	8	18.27	0.000744	0.359
26	1.20	1.13	0.053	0.060	25	37.61	0.000362	-
27	1.20	1.13	0.053	0.060	40	37.61	0.000362	-
28	2.00	3.14	0.148	0.100	30	22.57	0.000603	0.059
29	1.20	1.13	0.053	0.060	20	37.61	0.000362	-
30	1.80	2.54	0.120	0.090	15	25.08	0.000542	-
31	4.00	12.57	0.592	0.200	500	11.28	0.001205	-0.333
32	4.00	12.57	0.592	0.200	10	11.28	0.001205	-0.521
33	5.20	21.24	1.000	0.260	500	8.68	0.001567	-0.190
34	4.87	18.63	0.877	0.244	5	9.27	0.001467	-0.154
35	3.57	10.01	0.471	0.179	65	12.64	0.001075	-0.249
36	4.43	15.41	0.726	0.222	85	10.19	0.001335	0.061
37	2.60	5.31	0.250	0.130	55	17.36	0.000783	-
38	3.80	11.34	0.534	0.190	5	11.88	0.001145	0.354
39	2.00	3.14	0.148	0.100	20	22.57	0.000603	-
40	1.70	2.27	0.107	0.085	100	26.55	0.000512	-
41	1.60	2.01	0.095	0.080	60	28.21	0.000482	-
42	3.85	11.64	0.548	0.193	25	11.72	0.001160	0.027
43	2.60	5.31	0.250	0.130	20	17.36	0.000783	-
44	2.70	5.73	0.270	0.135	95	16.72	0.000813	-
45	4.00	12.57	0.592	0.200	6	11.28	0.001205	-0.048
46	4.00	12.57	0.592	0.200	80	11.28	0.001205	0.169
47	1.27	1.27	0.060	0.064	20	35.54	0.000383	-0.491
48	2.53	5.03	0.237	0.127	35	17.84	0.000762	-
49	2.23	3.91	0.184	0.112	50	20.24	0.000672	-
50	2.10	3.46	0.163	0.105	90	21.49	0.000633	-
51	0.56	0.25	0.012	0.028	70	80.60	0.000169	-0.917

Table B.3: Data for placenta C (small AAA). Young's modulus = 0.4 MPa, density, ρ = 1021 kg/m^3 and $c_0 = 4.43\ m/s$ for each vessel.

Bibliography

[1] N. Ackroyd, R. W. Gill, K. A. Griffiths, G. Kossoff, and M. Appleberg. Quantitative common carotid artery blood flow: prediction of internal carotid artery stenosis. *Journal of Vascular Surgery*, 3:846–53, 1986.

[2] M. Anliker, M. B. Histand, and E. Ogden. Dispersion and attenuation of small artificial pressure waves in the canine aorta. *Circulation Research*, 23:539–551, 1968.

[3] M. Anliker, W. E. Moritz, and E. Ogden. Transmission characteristics of axial waves in blood vessels. *Journal of Biomechanics*, 1:235–246, 1968.

[4] American Heart Association. 2002 heart and stroke stastical update. 2001.

[5] A. Avolio. Aging and wave reflection. *Journal of Hypertension*, 10(suppl. 6):S83–S86, 1992.

[6] A. P. Avolio. Multibranched model of the human arterial system. *Medical and Biological Engineering and Computing*, 18:709–718, 1980.

[7] A.P. Avolio, S. Chen, and R. Wang *et al.*. Effects of aging on changing arterial compliance and left ventricular load in a northern Chinese urban community. *Circulation*, 68:50–58, 1983.

[8] H. Bader. Dependence of wall stress in the human thoracic aorta on age and pressure. *Circulation Research*, 20:354–61, 1967.

[9] O. V. Batson. *Batson's No. 17 Plastic Replica and Corrosion Kit.* Polysciences, Inc. Warrington.

[10] O. V. Batson. *Meeting American Association Anatomists (68th session)*, PA(1955).

[11] D. H. Bergel. The dynamic elastic properties of the arterial wall. *Journal of Physiology*, 156:458–469, 1961.

[12] D. H. Bergel and W. R. Milnor. Pulmonary vascular impedance in the dog. *Journal of Physiology*, 156:458–469, 1961.

[13] D. S. Berger, J. Li, W. Laskey, and A. Noordergraaf. Repeated reflection of waves in the systemic arterial system. *American Journal of Physiology*, 264(H269-H281), 1993.

[14] S. Byrd. *Personal communication.* Imperial College London, St. Mary's Hospital, London, 2002.

[15] K. B. Campbell, L. C. Lee, H. F. Frasch, and A. Noordergraaf. Pulse reflection sites and effective length of the arterial system. *American Journal of Physiology*, 256:H1684–H1689, 1989.

[16] C. Canuto, M.Y. Hussaini, A. Quarteroni, and T. Zang. *Spectral Methods in Fluid Dynamics.* Springer-Verlag, 1987.

[17] C. G. Caro, T. J. Pedley, R. C. Schroter, and W. A. Seed. *The Mechanics of the Circulation.* Oxford University Press, Oxford, 1978.

[18] C.G. Caro, D.J. Doorly, and M. Tarnawski et.al. Non-planar curvature and branching of arteries. *The Journal of Physiology*, 475(P):60P, 1994.

[19] C.G. Caro, D.J. Doorly, and M. Tarnawski et.al. Non-planar curvature and branching of arteries and non-planar type flow. *Proceedings of the Royal Society of London*, A452:185–197, 1996.

[20] C.G. Caro, M.J. Lever, K.H. Parker, and P.J. Fish. Effect of cigarette smoking on the pattern of arterial blood flow: possible insight into mechanisms underlying the development of arteriosclerosis. *The Lancet*, Jul 4;2:11–13, 1987.

[21] S. E. Charm and G. S. Kurland. *Blood Flow and the Microcirculation.* John Wiley and Sons, New York, 1974.

[22] B. Cockburn and C.W. Shu. TVB Runge-Kutta projection discontinous Galerkin finite element methods for conservation laws II general framework. *Mathematical Communications*, 52:411–435, 1989.

[23] G. R. Cokelet. The rheology of human blood. In Y. Fung, N. Perrone, and M. Anliker, editors, *Biomechanics: Its Foundations and Objectives*. Prentice Hall, 1972.

[24] G.R. Cokelet. The rheology and tube flow of blood. In R. Skalak and S. Chen, editors, *Handbook of Bioengineering*. McGraw-Hill, 1987.

[25] M. L. Denbow, P. Cox, D. Talbert, and N. M. Fisk. Colour doppler energy insonation of placental vasculature in monochorionic twins: absent arterio-arterial anastomoses in association with twin-to-twin transfusion syndrome. *British Journal of Obstetrics and Gynecology*, 105:760–765, 1998.

[26] N. M. Denbow, P. Cox, M. Taylor, D. M. Hammal, and N. M. Fisk. Placental angioarchitecture in monochorionic twin pregnancies: relationship to fetal growth, feto-fetal transfusion syndrome, fetofetal transfusion syndrome, and pregnancy outcome. *American Journal of Obstetrics and Gynecology*, 182:417–26, 2000.

[27] P. B. Dobrin. Mechanical properties of arteries. *Physiological Reviews*, 58:397–460, 1978.

[28] D. J. Doorly, S. J. Sherwin, P. T. Franke, and J. Peiro. Vortical flow structure identification and flow transport in arteries. *Computer Methods in Biomechanics and Biomedical Engineering*, 5 (3):261–275, 2002.

[29] D. H. Bergel (ed.). *Cardiovascular Fluid Dynamics*, volume 2. Academic Press, London and New York, 1972.

[30] H. A. Erbay, S. Erbay, and S. Dost. Wave propagation in fluid filled nonlinear viscoelastic tubes. *Acta Mechanica*, 95:87–102, 1992.

[31] L. Euler. Principia pro motu sanguinis per arterias determinando. *Opera posthuma mathematica et physica anno 1844 detecta*, 2:814–823, 1775. ediderunt PH Fuss et N Fuss Petropoli; Apund Eggers et Socios.

[32] A. Feinberg and H. Lax. Studies of the arterial pulse wave. *Circulation*, 18:1125–1130, 1958.

[33] J. H. Ferziger. *Numerical methods for Engineering Application.* Wiley Interscience, New York, 1981.

[34] J. H. Ferziger and M. Perić. *Computational Methods for Fluid Dynamics.* Springer, Berlin, 1996.

[35] N. M. Fisk, R. Bajoria, and J. Wigglesworth. Twin twin transfusion syndrome. *New England Journal of Medicine*, pages 33–38, 1995.

[36] B. Folkow and A. Svanborg. Physiology of cardiovascular aging. *Physiological Reviews*, 73(4):725–764, 1993.

[37] L. Formaggia, J.-F. Gerbeau, F. Nobile, and A. Quarteroni. On the coupling of 3D and 1D Navier-Stokes equations for flow problems in compliant vessels. *Computer Methods in Applied Mechanical Engineering.*, 191:561–582, 2001.

[38] L. Formaggia, D. Lamponi, and A. Quarteroni. One-dimensional models for blood flow in arteries. Submitted to *Journal of Engineering Mathematics*, 2003.

[39] L. Formaggia, F. Nobile, and A. Quarteroni. A one-dimensional model for blood flow: application to vascular prosthesis. In I. Babuska, T. Miyoshi, and P.G. Ciarlet, editors, *Mathematical Modeling and Numerical Simulation in Continuum Mechanics*, volume 19 of *Lecture Notes in Computational Science and Engineering*, pages 137–153. Springer-Verlag, Berlin, 2002.

[40] L. Formaggia and A. Veneziani. Geometric multiscale modelling of the cardiovascular system: from lumped parameter models to 3D simulations. VKI Lecture Series on "Biological Fluid Dynamics", May 12–16 2003.

[41] O. Frank. Die grundform des arteriellen pulses. *Z. Biol.*, 37:483–526, 1899.

[42] O. Frank. Die theorie der pulswellen. *Z. Biol.*, 85(91-130), 1926.

[43] O. Frank. Schatzung des schlagvolumens des menschlichen herzens auf grund der wellen-und-windkesseltheorie. *Z. Biol.*, 90(405-409), 1926.

[44] P. T. J. Franke. *Blood flow and transport in artificial devices.* PhD Thesis, Aeronautical Engineering. Imperial College London, 2002.

[45] V. E. Franke, K. H. Parker, L. Y. Wee, N. M. Fisk, and S. J. Sherwin. Time domain computational modelling of 1D arterial networks in monochorionic placentas. *ESAIM: Mathematical Modelling and Numerical Analysis*, 37(4):557–580, 2003.

[46] Y. C. Fung. *Biomechanics: Mechanical properties of living tissues.* Springer-Verlag, New York, Second edition, 1993.

[47] C. W. Gear. *Numerical Initial value problems in Ordinary Differential Equations.* Prentice-Hall, Eaglewood Cliffs, NJ, 1971.

[48] R. G. Gosling, D. L. Newman, N. L. R. Bowden, and K. W. Twinn. The area ratio of normal aortic junctions - aortic configuration and pulse wave reflection. *British Journal of Radiology*, 44:850–853, 1971.

[49] D. Gottlieb and S.A. Orszag. Numerical Analysis of Spectral Methods: Theory and Applications. SIAM-CMBS, 1977.

[50] S. Hales. *Statistical essays: Containing haemastaticks.* No 22 History of Medicine Series: Library of New York Academy of Medicine, New York, 1733 (1964).

[51] W. F. Hamilton and P. Dow. An experimental study of the standing waves in the pulse propagated through the aorta. *American Journal of Physiology*, 125:48–59, 1939.

[52] V. Hardung. Zur mathematischen behandlung der dampfung und reflection der pulswellen. *Arch. Kreislaufforsch.*, 18:167–72, 1952.

[53] W. Harvey. *De Motu Cordis. Translated as Movement of the heart and blood in animals.* Blackwell Scientific, Oxford, 1628 (1957).

[54] K. Hayashi, M. Sato, H. Handa, and K. Moritake. Biomechanical study of the constitutive laws of vascular walls. *Experimental Mechanics*, 14:440–444, 1974.

[55] K. Hecher, W. Diehl, and L. Zikulnig *et al.*. Endoscopic laser coagulation of placental anastomoses in 200 pregnancies with severe mid-trimester twin-to-twin transfusion syndrome. *European Journal of Obstetrics Gynecology and Reproductive Biology*, 92:135–139, 2000.

[56] B. Hillen, H. W. Hoogstraten, and L. Post. A mathematical model of the flow in the circle of Willis. *Journal of Biomechanics*, 19:187–194, 1986.

[57] C. Hirsch. *Numerical computation of internal and external flows vol. I and II.* Wiley, New York, 1991.

[58] H. Holden and N.H. Risebro. Riemann problems with a kink. *SIAM Journal of Mathematical Analysis*, 30(3):497–515, 1999.

[59] J. P. Hornak. *The Basics of MRI.* http://www.cis.rit.edu/htbooks/mri/inside.htm 2003.

[60] J. D. Humphrey. Mechanics of the arterial wall: Review and directions. *Critical Review in Biomedical Engineering*, 23:1–162, 1995.

[61] A. S. Iberall. Anatomy and steady flow characteristics of the arterial system. *Mathematical Biosciences*, 1:375–395, 1967.

[62] G. N. Jager, N. Westerhof, and A. Noordergraaf. Oscillatory flow impedance in electrical analog of arterial system. *Circulation Research*, 16:121–133, 1965.

[63] C. J. H. Jones, K. H. Parker, R. Hughes, and D. J. Sheridan. Nonlinearity of human arterial pulse wave transmission. *Journal of Biomechanical Engineering*, 114:10–14, 1992.

[64] W. B. Kannel, P. A. Wolf, D. L. McGee, T. R. Dawber, P. McNamara, and W. P. Castelli. Systolic blood prssure, arterial rigidity, and risk of stroke. *Journal of the American Medical Association*, 245(12):1225–1229, 1981.

[65] M. Karamanoglu, D. Gallagher, A. Avolio, and M. O'Rourke. Functional origin of reflected pressure waves in a multibranched model of the human arterial system. *American Journal of Physiology*, 267:H1681–H1688, 1994.

[66] G. Karniadakis and S.J. Sherwin. *Spectral/hp Element Methods for CFD.* Oxford University Press, 1999.

[67] H. E. Karrer. An electron microscope study of the aorta in young and in aging mice. *Journal of Ultrastructure Research*, 5:1–27, 1961.

[68] T. Kawasaki, S. Sasayama, S. Yagi, T. Asakawa, and T. Hirai. Non-invasive assessment of the age related changes in stiffness of major branches of the human arteries. *Cardiovascular Research*, 21:678–687, 1987.

[69] D.J. Korteweg. Über die Fortpflanzungesgechwindigkeit des Schalles in elastischen Rohern. *Ann. Phys. Chem. (NS)*, 5:525–527, 1878.

[70] E. J. Kroeker and E. H. Wood. Beat-to-beat alterations in relationship of simultaneously recorded central and peripheral arterial pressure pulses during valsalva maneuver and prolonged expiration in man. *Journal of Applied Physiology*, 8:483–94, 1956.

[71] Sir Horace Lamb. *Hydrodynamics.* Dover, 1945.

[72] D. Lamponi. *Personal communication.* Institut de Mathematiques, EPFL, Lausanne, 2002.

[73] R. D. Latham, B. J. Rubal, N. Westerhof, and P. Sipkema. Non-human primate model for regional wave travel and reflections along aortas. *American Journal of Physiology*, 253:H299–H306, 1987.

[74] R. D. Latham, N. Westerhof, P. Sipkema, B. J. Rubal, P. Reuderink, and J. P. Murgo. Regional wave travel and reflections along the human aorta: a study with six simultaneous micromanometric pressures. *Circulation*, 72:1257–1269, 1985.

[75] H. Lax and A. Feinberg. Abnormalities of the arterial pulse wave in young diabetic subjects. *Circulation*, 20:1106–1110, 1959.

[76] H. Lax, A. Feinberg, and B. M. Cohen. The normal pulse wave and its modification in the presence of human atherosclerosis. *Journal of Chronic Diseases*, 3:618–631, 1956.

[77] B. M. Learoyd and M. G. Taylor. Alterations with age in the viscoelastic properties of human arterial walls. *Circulation Research*, 18:278–92, 1966.

[78] J. R. Levick. *An Introduction to Cardiovascular Physiology.* Butterworth-Heinemann Ltd., Oxford, Second edition, 1995.

[79] J. Li, J. Melbin, and A. Noordergraaf. Directional disparity of pulse reflection in the dog. *American Journal of Physiology*, 247:H95–H99, 1984.

[80] J. E. De Lia, R. S. Kuhlmann, and K. P. Lopez. Treating previable twin-twin transfusion syndrome with fetoscopic laser surgery: outcomes following the learning curve. *Journal of Perinatal Medicine*, 27:61–67, 1999.

[81] P. Libby. Atherosclerosis: the new view. *Scientific American*, 286(5):46–55, 2002.

[82] J. Lighthill. *Waves in fluids.* Cambridge University Press, Cambridge, 1978.

[83] I. Lomtev, C.W. Quillen, and G. Karniadakis. Spectral/*hp* methods for viscous compressible flows on unstructured 2D meshes. *Journal of Computational Physics*, 1998.

[84] T. Looker and C. L. Berry. The growth and development of the rat aorta ii. changes in nucleic acid and scleroprotein content. *Journal of Anatomy*, 113:17–34, 1972.

[85] F. H. Martini. *Fundamentals of Anatomy and Physiology.* Prentice Hall International, Inc., New Jersey, Fifth edition, 2001.

[86] D. A. McDonald and M. G. Taylor. The hydrodynamics of the arterial circulation. *Progress in Biophysics and Chemistry*, 9:107–173, 1959.

[87] D.A. McDonald. *Blood flow in arteries.* Williams and Wilkins, Baltimore, 1960.

[88] C. J. Mills, I. T. Gabe, J. H. Gault, D. T. Mason, J. Ross, E. Braunwald, and J. P. Shillingford. Pressure-flow relationships and vascular impedance in man. *Cardiovascular Research*, 4:405–417, 1970.

[89] W. R. Milnor. *Hemodynamics.* Williams and Wilkins, Baltimore, USA, Second edition, 1989.

[90] A.I. Moens. Over de voortplantingssnelheid von den pols. Technical report, Leiden, 1877.

[91] K. Moritake, H. Handa, A. Okumura, K. Hayashi, and H. Niimi. Stiffness of cerebral arteries: its role in the pathogenesis of cerebral aneurysms. *Neurologia Medico-Chirurgica*, 14:47–53, 1974.

[92] J. P. Murgo, N. Westerhof, J. P. Giolma, and S. A. Altobelli. Aortic input impedance in normal man: relationship to pressure wave shapes. *Circulation*, 62:105–116, 1980.

[93] S. Nagasawa, H. Handa, A. Okumura, Y. Naruo, K. Moritake, and K. Hayashi. Mechanical properties of human cerebral arteries. part 1: effects of age and vascular smooth muscle activation. *Surgical Neurology*, 12:297–304, 1972.

[94] W. W. Nichols and M. F. O'Rourke. *McDonald's Blood Flow in Arteries. Theoretical, experimental and clinical principles.* Edward Arnold, London, Third edition, 1990.

[95] W. W. Nichols and M. F. O'Rourke. *McDonald's Blood Flow in Arteries. Theoretical, experimental and clinical principles.* Arnold, London, Fourth edition, 1998.

[96] W. W. Nichols, M. F. O'Rourke, and A. P. Avolio *et al.*. Effects of age on ventricular-vascular coupling. *American Journal of Cardiology*, 55:1179–1184, 1985.

[97] A. Noordergraaf. *Physical Basis of Ballistocardiography.* PhD thesis, Univ. of Utrecht, 1956.

[98] A. Noordergraaf, P. D. Verdouw, and H. B. K. Boom. The use of an analogue computer in a circulation model. *Progress in Cardiovascular Diseases*, 5:419–439, 1963.

[99] J. Nunn. *Nunn's Applied Respiratory Physiology.* Butterworth Heinemann, Fourth edition, 1997.

[100] M. S. Olufsen. Structured tree outflow condition for blood flow in larger systemic arteries. *American Journal of Physiology*, 276:257–268, 1999.

[101] M. F. O'Rourke. Pressure and flow waves in systemic arteries and the anatomical design of the arterial system. *Journal of Applied Physiology*, 23:139–49, 1967.

[102] M. F. O'Rourke. Vascular impedance in studies of arterial and cardiac function. *Physiological Reviews*, 62:570–623, 1982.

[103] M. F. O'Rourke. Arterial stiffness, systolic blood pressure and logical treatment of arterial hypertension. *Hypertension*, 15:339–347, 1990.

[104] M. F. O'Rourke and A. P. Avolio. Pulsatile flow and pressure in human systemic arteries: studies in man and in a multibranched model of the human systemic arterial tree. *Circulation Research*, 46(3):363–372, 1980.

[105] M. F. O'Rourke, A. P. Avolio, and P. D. Lauren *et al.*. Age-related changes of elastic lamellae in the human thoracic aorta. *Journal of the American College of Cardiology*, 9:53A, 1987.

[106] M. F. O'Rourke, R. P. Kelly, and A. P. Avolio. *The Arterial Pulse.* Lea and Febiger, Philadelphia, 1992.

[107] M. F. O'Rourke and M. G. Taylor. Vascular impedance of the femoral bed. *Circulation Research*, 18:123–139, 1966.

[108] G. L. Papageorgiou and N. B. Jones. Wave reflection and hydraulic impedance in the healthy arterial system: a controversial subject. *Medical and Biological Engineering and Computing*, 26:237–42, 1988.

[109] P. K. Paulsen and J. M. Hasenkam. Three-dimensional visualisation of velocity profiles in the ascending aorta in dogs, measureed with a hot film anemometer. *Journal of Biomechanics*, 16:201–10, 1983.

[110] T. J. Pedley. *The fluid mechanics of large blood vessels.* Cambridge University Press, Cambridge, 1980.

[111] J. Peiró, S.J. Sherwin, K.H. Parker, V. Franke, L. Formaggia, D. Lamponi, and A. Quarteroni. Numerical simulation of arterial pulse propagation using one-dimensional models. In *Wall-fluid Interaction for Physiological Flows.* WIT Press, 2003.

[112] L. H. Peterson and P. H. Gerst. Significance of reflected waves within the arterial system. *Federation Proceedings*, 15:145, 1956.

[113] G. H. Pollack, R. V. Reddy, and A. Noordergraaf. Input impedance, wave travel and reflections in the human pulmonary arterial tree. studies using an electrical analog. *Transactions in Biomedical Engineering*, 15:151–164, 1968.

[114] G. Pontrelli. Nonlinear problems in arterial flows. *Nonlinear analysis*, 47:4905–4915, 2001.

[115] F. Pythoud, N. Stergiopulos, C. D. Bertram, and J. J. Meister. Effects of friction and nonlinearities on the seperation of arterial waves into their forward and backward components. *Journal of Biomechanics*, 11:1419–1423, 1996.

[116] A. Quarteroni. Simulation of fluid and structure interaction. Lecture Notes for European Mathematical Society, Euro Summer School, Prague, 2001.

[117] A. Quarteroni, S. Ragni, and A. Veneziani. Coupling between lumped and distributed models for blood problems. *Computing and Visualisation in Science*, 4:111–124, 2001.

[118] A. Quarteroni, M. Tuveri, and A. Veneziani. Computational vascular fluid dynamics: Problems, models and methods. *Computing and Visualisation in Science*, 2:163–197, 2000.

[119] C. Quick, D. S. Berger, and A. Noordergraaf. Constructive and destructive addition of forward and reflected arterial pulse waves. *American Journal of Physiology*, 280:H1519–H1527, 2001.

[120] R. A. Quintero, W. J. Morales, G. Mendoza, M. Allen, C. S. Kalter, G. Giannina, and J. L. Angel. Selective photocoagulation of placental vessels in twin-twin transfusion syndrome: evolution of a surgical technique. *Obstetrical and Gynecological Survey*, 53:S97–103, 1998.

[121] R. A. Quintero, R. Romero, H. Reich, L. Goncalves, M. P. Johnson, C. Carreno, and M. I. Evans. In utero percutaneous umbilical cord ligation in the management of complicated monochorionic multiple gestations. *Ultrasound in Obstetrics and Gynecology*, 8:16–22, 1996.

[122] J. W. Remington. Quantitative synthesis of head and foreleg arterial pulses in the dog. *American Journal of Physiology*, 208(968-983), 1965.

[123] J. W. Remington and L. J. O'Brien. Construction of aortic flow pulse from pressure pulse. *American Journal of Physiology*, 218(437-447), 1970.

[124] R. D. Richtmyer and K. W. Morton. *Difference methods for initial value problems.* Wiley, New York, 1967.

[125] G.F.B. Riemann. Ein Beitrag zu den Untersuchungen über die Bewegung eines flussigen gleichartigen Ellipsoides. Technical report, Göttingen, 1866.

[126] M. R. Roach and A. C. Burton. The effect of age on the elasticity of human iliac arteries. *Canadian Journal of Biochemistry*, 35:681–90, 1959.

[127] I. Robertson. *Free Surface Flow Simulations Using High Order Algorithms.* PhD thesis, University of London, 2000.

[128] R. Ross. The pathogenesis of atherosclerosis: a perspective for the 1990s. *Nature*, 362:801–9, 1993.

[129] T. Sarpkaya. Reflection and transmission of pulse waves in distensible bifurcating vessels. *Digest of 7th International Conference on Medical and Biological Engineering*, 1967.

[130] B. W. Schaaf and P. H. Abbrecht. Digital computer simulation of human systemic arterial pulse wave transmission: a nonlinear model. *Journal of Biomechanics*, 5:345–364, 1972.

[131] D. J. Schultz, D. S. Tunstall-Pedoe, G. de J. Lee, A. J. Gunning, and B. J. Belhouse. *Velocity distributions and transition in the arterial system. In Ciba Symposium on Circulatory and Respiratory and Mass Transport.* GEW Wolstenholme and J Knight eds., Churchill, London, 1969.

[132] N. J. Sebire, D. Talbert, and N. M. Fisk. Twin-to-twin transfusion syndrome results from dynamic asymmetrical reduction in placental anastomoses: A hypothesis. *Placenta*, 22:383–391, 2001.

[133] P. Segers and P. Verdonck. Role of tapering in aortic wave reflection: hydraulic and mathematical model study. *Journal of Biomechanics*, 33:299–306, 2000.

[134] S. J. Sherwin, V. Franke, J. Peiro, and K. Parker. One-dimensional modelling of a vascular network in space-time variables. *Submitted to Journal of Engineering Mathematics*, 2002.

[135] S.J. Sherwin. Dispersion analysis of the continuous and discontinuous Galerkin formulations. In *International Symposium on Discontinuous Galerkin Methods*, 1999. Newport, RI.

[136] S.J. Sherwin, D.J. Doorly, P. T. Franke, and J. Peiró. Unsteady near wall residence times and shear exposure in model distal arterial bypass grafts. *Biorheology*, 39(3-4):365–371, 2002.

[137] S.J. Sherwin, L. Formaggia, J. Peiró, and V. Franke. Computational modelling of 1D blood flow with variable mechanical properties and its application to the simulation of wave propagation in the human arterial system. *International Journal of Numerical Methods in Fluids*, 43:673–700, 2003.

[138] M. L. Simoons. Myocardial revascularization - bypass surgery or angioplasty. *New England Journal of Medicine*, 335:275–277, 1996.

[139] R. Skalak. The synthesis of a complete circulation. In D. Bergel, editor, *Cardiovascular Fluid Dynamics*, volume 2, pages 341–376. Academic Press, London, 1972.

[140] N. P. Smith, A. J. Pullan, and P. J. Hunter. An anatomically based model of transient coronary blood flow in the heart. *SIAM Journal of Applied Mathematics*, 62:990–1018, 2002.

[141] J. A. E. Spaan, N. P. W. Breuls, and J. D. Laird. Diastolic-systolic coronary flow differences are caused by intramyocardial pump action in the anesthetised dog. *Circulation Research*, 49:584–593, 1981.

[142] I. Starr and A. Schild. Studies made by simulating systole at necropsy. ix. a test of the aortic compression chamber hypothesis and of two stroke volume methods based upon it. *Journal of Applied Physiology*, 11:169–173, 1957.

[143] B. N. Steele, J. Wan, J. P. Ku, T. J. R. Hughes, and C. A. Taylor. In-vivo validation of a one-dimensional finite element method for simulation-based medical planning for cardiovascular bypass surgery. *IEEE Transactions of Biomedical Engineering*, 50(6):649–56, 2003.

[144] N. Stergiopulos, B. E. Westerhof, and N. Westerhof. Total arterial inertance as the fourth element of the windkessel model. *American Journal of Physiology*, 276:H81–88, 1999.

[145] N. Stergiopulos and D.F. Young. Computer simulation of arterial flow with applications to arterial and aortic stenoses. *Journal of Biomechanics*, 25(12):1477–1488, 1992.

[146] J.C. Stettler, P. Niederer, and M. Anliker. Theoretical analysis of arterial hemodynamics including the influence of bifurcations. part I: Mathematical model and prediction of normal pulse patterns. *Annals of Biomedical Engineering*, 9:145–164, 1981.

[147] J.C. Stettler, P. Niederer, and M. Anliker. Theoretical analysis of arterial hemodynamics including the influence of bifurcations, part II: Critical evaluation of theoretical model and comparison with noninvasive measuresments of flow patterns in normal and pathological cases. *Annals of Biomedical Engineering*, 9:165–175, 1981.

[148] Y. Sun, T. J. Anderson, *K. H. Parker, and J. V.* Tyberg. Wave-intensity analysis: a new approach to coronary hemodynamics. *Jornal of Applied Physiology*, 89:1636–1644, 2000.

[149] T. Y. T. Tam, M. J. O. Taylor, L. Y. Wee, T. Vanderheydem, and N. M. Fisk. Modified Quintero staging system for twin-twin transfusion syndrome. *Submitted to Ultrasound in Obstetrics and Gynecology*, 2003.

[150] C. A. Taylor, M. T. Draney, J. P. Ku, D. Parker, B. N. Steele, K. Wang, and C. K. Zarins. Predictive medicine: Computational techniques in therapeutic decision-making. *Computer Aided Surgery*, 4:231–247, 1999.

[151] M. J. O. Taylor, M. L. Denbow, K. R. Duncan, T. G. Overton, and N. M. Fisk. Anatenatal factors at diagnosis that predict outcome in twin-twin transfusion syndrome. *American Journal of Obstetrics and Gynecology*, pages 1023–1028, 2000.

[152] M. J. O. Taylor, M. L. Denbow, S. Tanawattanacharoen, C. Gannon, P. Cox, and N. M. Fisk. Doppler detection of arterio-arterial anastomoses in monochorionic twins: feasibility and clinical application. *Human Reproduction*, 15:1632–1636, 2000.

[153] M. J. O. Taylor, D. Farquaharson, P. M. Cox, and N. M. Fisk. Identification of arterio-venous anastomoses *in vivo* in monochorionic twin pregnancies: preliminary report. *Ultrasound in Obstetrics and Gynecology*, 16:218–222, 2000.

[154] M. J. O. Taylor, D. G. Talbert, and N. M. Fisk. Mapping the monochorionic equator. *Ultrasound in Obstetrics and Gynecology*, 14:372–4, 1999.

[155] M. J. C. van Gemert and H. J. C. M. Sterenborg. Hemodynamic model of twin-twin transfusion syndrome in monochorionic twin pregnancies. *Placenta*, 19:195–208, 1998.

[156] M. J. C. van Gemert, A. Umur, J. G. P. Tijssen, and M. G. Ross. Twin-twin transfusion syndrome: etiology, severity and rational management. *Current Opinion in Obstetrics and Gynecology*, 13:193–206, 2001.

[157] S. Čanić. Blood flow through compliant vessels after endovascular repair: wall deformations induced by the discontinuous wall properties. *Computing and Visualisation in Science*, 4(3):147–155, 2002.

[158] F. W. A. Verheugt. Acute coronary syndromes: interventions. *The Lancet*, 353(suppl. II):16–19, 1999.

[159] J. Wan, B. Steele, S. A. Spicer, S. Strohband, G. R. Feijoo, T. J. Hughes, and C. A. Taylor. A one-dimensional finite element method for simulation-based medical planning for cardiovascular disease. *Computer Methods in Biomechanics and Biomedical Engineering*, 5(3):195–206, 2002.

[160] J. J. Wang. *Wave propagation in a model of the human arterial system.* PhD thesis, University of London, 1997.

[161] J. J. Wang. *K. Parker's web page.* http://pfsg.bg.ic.ac.uk/KHP/khphome.htm, 2003.

[162] J.J. Wang, A. B. O'Brien, N. G. Shrive, K.H. Parker, and J. V. Tyberg. Time-domain representation of ventricular-arterial coupling as a windkessel and wave system. *American Journal of Physiology*, 284(4):H1358–H1368, 2003.

[163] J.J. Wang and K.H. Parker. Wave propagation in a model of the arterial circulation. *Journal of Biomechanics, In Press, Corrected Proof*, Available online 13 November 2003.

[164] E. H. Weber and W. E. Weber. *Wellenlehre.* Fleischer, Leipzig, 1825.

[165] L. Y. Wee and N. M. Fisk. The twin-twin transfusion syndrome. *Seminars Neonatology*, 7:187–202, 2002.

[166] L. Y. Wee, M. J. Taylor, T. Vanderheyden, D. Talbert, and N. M. Fisk. Transmitted arterio-arterial anastomosis waveforms causing cyclically intermittent absent/reversed end-diastolic umbilical artery flow in monochorionic twins. *To appear in Placenta*, 2003.

[167] N. Westerhof, F. Bosman, C.J. De Vries, and A. Noordergraaf. Analog studies of the human systemic arterial tree. *Journal of Biomechanics*, 2:121–143, 1969.

[168] N. Westerhof, C. G. Van den Bos, and S. Laxminarayan. Arterial reflection. In R. D. Bauer and R. Busse, editors, *The Arterial System*, pages 48–62. Springer, 1978.

[169] N. Westerhof, P. Sipkema, G. C. Van Den Bos, and G. Elzinga. Forward and backward waves in the arterial system. *Cardiovascular Research*, 6:648–656, 1972.

[170] E. Wetterer. Die wirkung der herztätigkeit auf die dynamik des arterien-systems. *Verhandlungen der Deutschen Gesellschaft für Kreislaufforschung*, 22(26-60), 1956.

[171] E. Wetterer, R. D. Bauer, and R. Busse. Arterial dynamics. *Cardiovascular and Pulmonary Dynamics*, 71(7-42), 1977.

[172] K. Wezler and A. Boger. Die dynamik des arteriellen systems. der arterielle blutdruck und seine komponenten. *Ergebn. Physiol.*, 41(292-606), 1939.

[173] G. B. Whitham. *Linear and Non-Linear Waves*. Wiley, New York, 1974.

[174] H. Wolinsky. Long-term effects of hypertension on the rat aortic wall and their relation to concurrent aging changes. *Circulation Research*, 30:301–9, 1972.

[175] J.R. Womersley. An elastic tube theory of pulse transmission and oscillatory flow in mammalian arteries. Technical Report WADC Technical Report TR 56-614, Wright Air Development Center, 1957.

[176] G. Yang. *CMRTools*. VIP Group, Imperial College London, 2003.

[177] F. C. P. Yin, H. A. Spurgeon, and C. H. Kallman. Age-associated alterations in viscoelastic properties of canine aortic strips. *Circulation Research*, 53:464–72, 1983.

[178] T. Young. Hydraulic investigations, subservient to an intended Croonian lecture on the motion of the blood. *Philosophical Transactions of the Royal Society, London*, 98:164–186, 1808.

[179] A. Zambanini. *Personal communication*. Imperial College London, St. Mary's Hospital, London, 2002.